

Les Rencontres de Physique de la Vallée d'Aoste

Results and Perspectives in Particle Physics

edited by M. Greco

La Thuile, Aosta Valley

February 27th - March 5th, 2011



ISTITUTO NAZIONALE DI FISICA NUCLEARE
Laboratori Nazionali di Frascati

Les Rencontres de Physique de la Vallée d'Aoste

Results and Perspectives in Particle Physics



FRASCATI PHYSICS SERIES

Series Editor

Daniilo Babusci

Technical Editor

Marcella Missiroli

Volume LIII - Special Issue

Jointly published by:

Istituto Nazionale di Fisica Nucleare - Laboratori Nazionali di Frascati
Divisione Ricerca - SIDS - Ufficio Biblioteca e Pubblicazioni
Via Enrico Fermi 40, I-00044 Frascati (Roma), Italy
e-mail: sis.publications@lnf.infn.it

Società Italiana di Fisica
Via Saragozza 12, I-40123 Bologna, Italy
<http://www.sif.it>

FRASCATI PHYSICS SERIES

Les Rencontres de Physique de la Vallée d'Aoste

RESULTS AND PERSPECTIVES IN PARTICLE PHYSICS

Copyright © 2012 SIF, Bologna – INFN-Laboratori Nazionali di Frascati
SIDS-Ufficio Biblioteca e Pubblicazioni

All rights reserved. No part of this publication may be reproduced, stored in a retrieval system or transmitted in any form or by any means, electronic, mechanical, photocopying, recording or otherwise, without the prior permission of the copyright owner.

ISBN: 978-88-7438-068-8

Printed in Italy by Compositori Industrie Grafiche
Via Stalingrado 97/2
40128 Bologna

FRASCATI PHYSICS SERIES

Volume LIII

**Les Rencontres de Physique
de la Vallée d'Aoste**

Results and Perspectives in Particle Physics

Editor
Mario Greco

Conference Organizers

Giorgio Bellettini	Pisa
Giorgio Chiarelli	Pisa
Mario Greco	Roma Tre
Gino Isidori	Laboratori Nazionali di Frascati

Chairpersons

Marina Artuso	Syracuse
Toni Baroncelli	INFN - Roma Tre
Giorgio Bellettini	Pisa
Giorgio Chiarelli	Pisa
Alvaro De Rújula	CERN
Mario Greco	Roma Tre
Gino Isidori	Laboratori Nazionali di Frascati
Michelangelo Mangano	CERN
Antonio Masiero	Padova
Eduard Masso	Barcelona
Piero Monacelli	L'Aquila
Marcello Piccolo	Laboratori Nazionali di Frascati
Giovanni Punzi	Pisa

Preface

The 2011 Rencontres de Physique de la Vallée d'Aoste were held at the Planibel Hotel of La Thuile, Aosta Valley, on February 27th - March 5th, with the twenty-fifth edition of "Results and Perspectives in Particle Physics".

The physics programme included various topics in particle physics, also in connection with present and future experimental facilities, as cosmology and astrophysics, neutrino physics, CP violation and rare decays, electroweak and hadron physics with e^+e^- and hadron colliders, heavy flavours, search for new physics and prospects at future facilities.

A special Session, in honour of my 70th birthday was organized by my friends Giorgio, Giorgio and Gino, together with other dear friends. I would like to thank warmly Guido Altarelli, Albert Bramon, Yogi Srivastava and Matteo Cacciari for their participation and their nice words, and also many other friends and colleagues who made this edition of the Rencontres quite special for me. On the other side I am very grateful to my wife Halina and all my family for their enthusiastic support.

The Session on "Physics and Society" included special colloquia on "Status of the SESAME Project", "CERN and the Future of Particle Physics" and "Quantitative Biology". We are very grateful to Amor Nadji, Rolf-Dieter Heuer and Michele Caselle for their participation and contribution.

Giorgio Bellettini, Giorgio Chiarelli, Gino Isidori and I would like to warmly thank the session chairpersons and the speakers for their contribution to the success of the meeting.

The regional government of the Aosta Valley, in particular through the Minister of Public Education and Culture Laurent Vierin, has been very pleased to offer its financial support and hospitality to the Rencontres of La Thuile. Also on behalf of the participants, representatives of some major Laboratories and Institutes in the world, we would like to thank all the Regional Authorities. Special thanks are also due to Bruno Baschiera, local coordinator of the Rencontres.

We are grateful to the President of INFN Roberto Petronzio, the Directors of INFN Laboratori Nazionali di Frascati, Mario Calvetti and INFN Sezione di Pisa, Giovanni Batignani, for the support in the organization of the Rencontres. We would like to thank also Cristina D'Amato, Lucia Lilli, Claudia Tofani and Paolo Villani for their help in both planning and running the meeting. We are also grateful to Alessandra Miletto for her valuable contribution to the local organization of the meeting. The excellent assistance provided by Mauro Giannini made it possible to set up the computer link to the international network.

Finally we would like to thank the Mayor Gilberto Roullet and the local authorities of La Thuile and the “Azienda di Promozione Turistica del Monte Bianco” for their warm hospitality, and the Planibel Hotel staff for providing us an enjoyable atmosphere.

November 2011

MARIO GRECO

CONTENTS

M. GRECO – Preface.....	page	VII
HONORING THE 70TH BIRTHDAY OF MARIO GRECO		
G. ALTARELLI – The early days of QCD (as seen from Rome).....	”	1
A. BRAMON – From Vector Meson Dominance to Quark-Hadron Duality.....	”	9
G. PANCHERI and Y. SRIVASTAVA – Frascati resummation schemes for IR radiation in QED and QCD.....	”	15
M. CACCIARI – Heavy quarks, from discovery to precision.....	”	23
COSMOLOGY AND ASTROPHYSICS		
D. SAMTLEBEN for the QUIET COLLABORATION – Measuring the Cosmic Microwave Background Radiation.....	”	31
L. LOPEZ-HONOREZ – Scalar dark matter: A revision of the Inert Doublet Model ..	”	39
A. D. DOLGOV – Contemporary gravitational waves from primordial black holes ...	”	47
ASTROPARTICLE AND NEUTRINO PHYSICS		
A. V. GRIGORIEV, A. V. LOKHOV, A. I. STUDENIKIN and A. I. TERNOV – New bounds on neutrino magnetic moment and re-examination of plasma effect in neutrino spin light.....	”	57
L. BALDINI and L. TIBALDO on behalf of the FLAT COLLABORATION – Science highlights from the <i>Fermi</i> Large Area Telescope.....	”	63
P. BERNARDINI for the ARGO-YBJ COLLABORATION – Cosmic rays in the TeV region with the ARGO-YBJ detector.....	”	75
M. BOHACOVA on behalf of the PIERRE AUGER COLLABORATION – Highlights from the Pierre Auger Observatory.....	”	83
S. DADO, A. DAR and A. DE RÚJULA – Origin of the ultrahigh-energy cosmic rays and their spectral break.....	”	89
P. NATOLI, C. BURIGANA, A. GRUPPUSO and N. MANDOLESI – The Planck mission: From first results to cosmology.....	”	97
R. TONER for the MINOS COLLABORATION – The latest results from the MINOS oscillation experiment.....	”	111
U. KOSE on behalf of OPERA COLLABORATION – Search for $\nu_\mu \rightarrow \nu_\tau$ oscillations in appearance mode in the OPERA experiment.....	”	119
J. V. DAWSON on behalf of the DOUBLE CHOOZ COLLABORATION – Commissioning the Double Chooz detector.....	”	127
B. CACCIANIGA on behalf of the BOREXINO COLLABORATION – Neutrino physics with the Borexino experiment.....	”	133
C. GIUNTI – Recent progress in neutrino physics.....	”	141

PHYSICS OF HADRONIC INTERACTIONS

G. TONELLI – First physics results from the CMS experiment at the LHC.....	”	151
E. SCOMPARIN for the ALICE COLLABORATION – Early pp physics at ALICE.....	”	163
E. MEONI on behalf of the ATLAS COLLABORATION – QCD physics at ATLAS....	”	171
J. ROJO – Parton distributions and LHC data.....	”	179
P. STEINBERG for the ATLAS COLLABORATION – Heavy-ion physics with the ATLAS detector at the LHC.....	”	187
A. DAINESE for the ALICE COLLABORATION – First ALICE results from heavy-ion collisions at the LHC.....	”	197

FLAVOUR PHYSICS, *CP* VIOLATION AND RARE DECAYS

V. TISSERAND on behalf of the BABAR COLLABORATION – Recent results from BABAR.....	”	209
J. D. LEWIS – <i>CP</i> violation and suppressed B_s decays at CDF.....	”	217
C. H. CHENG – Charmless B decays in B -factories.....	”	225
A. CRIVELLIN – Chiral enhancement in the MSSM — An overview.....	”	233
V. NOVIKOV – Comments on CPT.....	”	243
D. M. STRAUB – New physics searches in flavour physics.....	”	249
S. BALEV – New results on K physics from NA48 and NA62 experiments.....	”	257
S. FIORE on behalf of the KLOE-2 COLLABORATION – The KLOE-2 project at the DAΦNE accelerator upgraded in luminosity.....	”	265
M. D. CORCORAN for the CDF and D0 COLLABORATIONS – <i>CP</i> violation and rare B_s decays at the Tevatron.....	”	273
OLIVIER LEROY on behalf of the LHCb COLLABORATION – Prospects for <i>CP</i> violation in $B_s^0 \rightarrow J/\psi\phi$ from first LHCb data.....	”	281

ELECTROWEAK AND TOP PHYSICS

J. SEKARIC for the CDF and DØ COLLABORATIONS – Electroweak physics at the Tevatron.....	”	293
A. R. SANDSTRÖM on behalf of the ATLAS COLLABORATION – Electroweak and Top physics at ATLAS.....	”	299
M. DE GRUTTOLA on behalf of the CMS COLLABORATION – Measurement of W, Z and Top properties with CMS.....	”	307
HYUN SU LEE on behalf of the CDF and D0 COLLABORATIONS – Top physics at Tevatron.....	”	319
D. AMIDEI on behalf of the CDF COLLABORATION – Forward-backward asymmetry in $t\bar{t}$ production.....	”	327

HIGGS SEARCHES, HOT TOPICS

WEI-MING YAO for the CDF and DØ COLLABORATION – Search for the low mass Higgs boson at the Tevatron.....	”	335
M. BUEHLER on behalf of the CDF and DØ COLLABORATIONS – Search for a high mass SM Higgs boson at the Tevatron.....	”	345
A. DJOUADI – The Tevatron Higgs exclusion limits and theoretical uncertainties...	”	353
M. REDI – The non-standard model Higgs.....	”	363
M. I. VYSOTSKY – Coulomb law and energy levels in a superstrong magnetic field..	”	371

SEARCHING FOR NEW PHYSICS

L. GALLI on behalf of the MEG COLLABORATION – $\mu^+ \rightarrow e^+ \gamma$ search with the MEG experiment: Results and perspectives.....	”	383
G. LANFRANCHI on behalf of the LHCb COLLABORATION – Search for the rare decays $B_s^0 \rightarrow \mu^+ \mu^-$ and $B^0 \rightarrow \mu^+ \mu^-$ with the LHCb experiment.....	”	389
P. PARADISI – Theoretical review on lepton flavour violation.....	”	399
S. ROLLI – Search for New Physics the Fermilab Tevatron $p\bar{p}$ collider.....	”	405
H. U. FLÄCHER on behalf of the CMS COLLABORATION – Searches for New Physics at CMS.....	”	415
M. NARDECCHIA – Working Technicolor at the LHC.....	”	425

PHYSICS AND SOCIETY

R.-D. HEUER – CERN and the future of particle physics.....	”	435
--	---	-----

PERSPECTIVES

A. FAVA for the ICARUS COLLABORATION – Icarus and status of Liquid-Argon technology.....	”	447
C. L. NAUMANN on behalf of the CTA CONSORTIUM – The (future) Cherenkov Telescope Array CTA.....	”	455
G. WORMSER – Status of the SuperB project.....	”	463
Y. HORII – Status and physics prospects of the SuperKEKB/Belle II project.....	”	471
Participants.....	”	479

SESSION IX - PERSPECTIVES

<i>Angela Fava</i>	Icarus and status of Liquid-Argon technology
<i>Christopher Naumann</i>	The (future) Cherenkov Telescope Array CTA
<i>Guy Wormser</i>	Status of the SuperB project
<i>Yasuyuki Horii</i>	Status and physics prospects of the SuperKEKB/Belle II project

The early days of QCD (as seen from Rome)

G. ALTARELLI

*Dipartimento di Fisica "E. Amaldi", Università di Roma Tre and INFN
Sezione di Roma Tre - I-00146 Rome, Italy and
Department of Physics, Theory Unit, CERN - CH-1211 Geneva 23, Switzerland*

(ricevuto il 29 Settembre 2011; pubblicato online il 26 Gennaio 2012)

Summary. — In honour of Mario Greco I present my recollections on the QCD studies in Rome in the 70s and early 80s and on our very friendly group of people involved.

PACS 11.15.-q – Gauge field theories.
PACS 12.38.-t – Quantum chromodynamics.

I have a half-century-long friendship with Mario. We met when we were students at the University of Rome in the early 60s. Then in 1964 I went to Florence and in 1968 to the USA. When back in Rome in 1970 we came in closer contact, also with our families. In fig. 1 one can get an idea of how different we looked at the time. At present we are both at Roma Tre and our offices are a few meters away. In the early 70s QCD and the physics of hard processes was an area of common interest for many of us in Rome and a number of good results were obtained by the different members of our group. Here I will review these results and try to convey the collaborative atmosphere in the group that, for example, led to different collaborations among us to be formed to work on related problems. Of course, while I will talk of the Rome group and of its activity, I am well aware that much more important work on QCD was done at the time in the world, so that I stress that this is not an essay on the history of QCD, but simply a recollection on QCD studies in Rome and on the group of people involved. For a review of the development of QCD in the 70s one can go back, for example, to my 1982 review of the subject [1].

One can argue that QCD really started being a part of the Standard Model with the Nobel-Prize-winning papers by Gross and Wilczek [2] and by Politzer [3] in 1973. Sure enough in previous years there have been very important ground-breaking theoretical works, like those on quarks [4], on the naive parton model [5], on QCD field theory [6], on the renormalization group [7] and the short distance operator expansion [8]. Also Khriplovich, first, and 't Hooft (according to Symanzik), after, apparently discovered asymptotic freedom but did not jump on it as the key property for a theory of strong interactions. In fact the systematic application of QCD to physics only started in 1973.



Fig. 1. – From the left: Mario Greco, Yogi Srivastava and Guido Altarelli in 1979 at the Accademia dei Lincei, Rome.

At that time three groups were active in Rome, located at Roma 1 “La Sapienza”, the Istituto Superiore di Sanita and the Laboratori Nazionali di Frascati (today in Rome there are three Universities while only “La Sapienza” existed at that time: Roma 2, Tor Vergata was born in 1982 and Roma Tre in 1992). I was in Roma 1 with Nicola Cabibbo and Roberto Petronzio (in 1973 he was a student working at his thesis). Luciano Maiani was at the Istituto Superiore di Sanita, a short walk away from Roma 1, so that Luciano was with us all the time, and Mario Greco with Lia Pancheri, Giorgio Parisi and Yogi Srivastava were at the Laboratori Nazionali di Frascati. Later, important additions to the QCD group in Rome were achieved when Giuseppe Curci, Keith Ellis and Guido Martinelli joined our team.

Even before 1973 our group of people was working in the domain of hard processes and the parton model. Giorgio Parisi was already known and influential in the study of the physical implications of anomalous dimensions (Giorgio was very young at the time but Kurt Symanzik, a leader in the field, had already a great consideration of him). In a paper completed in 1972 [9] Giorgio studied the deep inelastic scattering structure functions in a $\lambda\phi^4$ theory with negative coupling $\lambda < 0$, a theory discussed by Symanzik as a field theory model for Bjorken scaling. This paper was cited by Gross and Wilczek [2] and also in the review by Gross, “Asymptotic Freedom and QCD—a Historical Perspective” [10], written shortly after he got the Nobel Prize. In another 1972 paper [11] Giorgio derived limits on logarithmic scaling violations in deep inelastic scattering structure functions from the existing data. This work was quoted in the asymptotic freedom paper by Politzer [3]. In 1973 at “La Sapienza” we were studying hard processes in the parton model (with scaling). Luciano Maiani and myself studied deep inelastic processes in the $\lambda\phi^3$ theory, a superrnormalisable model for scaling [12], in continuation of previous work [13]. With Cabibbo and Petronzio the two of us completed in 1973 a series of papers on the nucleon as a bound state of 3 quarks [14], where a parton picture of the structure functions was developed, with the nucleon described in terms of constituent quarks, each of them with a parton structure (so that for example the proton and the pion structure

functions could be related through the constituent structure functions). This idea is still viable and it is in competition with the picture of the nucleon as 3 valence quarks floating in a sea of quarks and gluon partons (with no separation of the 3 constituent quarks). In 1972 Mario Greco, with Bramon and Etim, evaluated the hadronic contribution to the muon anomalous magnetic moment from the data on e^+e^- cross-sections [15]. This is a problem of high current interest still today. Mario and collaborators found at the time $a_\mu = 68 \pm 9$ with a linear sum of errors, which corresponds to $a_\mu = 68 \pm 6$ with errors summed in quadrature. This value is to be compared with the modern estimate $a_\mu = 69.23 \pm 0.42$ by Davier *et al.* [16]. At that time Mario was interested in hard processes and was advocating a model for e^+e^- annihilation, deep inelastic scattering and Drell-Yan processes based on extended vector boson dominance [17]. The functional behaviour of the couplings versus mass of the tower of vector bosons was chosen as to get approximate scaling. This approach was a competitive picture with respect to the parton model for some time but it was later abandoned because it predicted no jets in e^+e^- annihilation and no suppressed ratio of longitudinal over transverse cross-sections in deep inelastic scattering.

After the Gross-Wilczek and Politzer papers we immediately turned to study the potentiality of QCD for improving the parton model. Myself and Maiani we decided to study the QCD corrections to the effective weak non-leptonic Hamiltonian, written as a Wilson expansion in terms of 4-quark operators of the $(V - A) \times (V - A)$ type obtained by integrating away the W^\pm exchange [18]. The logarithmically enhanced terms of the QCD corrections are fixed by the anomalous dimensions of these operators, much in the same way as the moments of structure functions get logarithmic corrections as computed by Gross *et al.* [2, 3] from the anomalous dimensions of the leading-twist operators in the light-cone expansion. Our hope was to find that the QCD corrections act in the direction of enhancing the $\Delta T = 1/2$ operators with respect to those with $\Delta T = 3/2$, thus explaining, at least in part, the empirical $\Delta T = 1/2$ rule (where T is the isotopic spin). The explicit calculation turned out to lead to precisely this result, as also obtained in a simultaneous work by M. K. Gaillard and B. W. Lee [19] (actually these authors had pointed out to us the crucial role of charm in this problem). These important papers were the first calculations of the QCD corrections to the coefficients of the Wilson expansion in the product of two weak currents, an approach that, suitably generalised (by considering other weak processes) and improved (for example, by computing the anomalous dimensions beyond the leading order), still represents a basic tool in this field. In the following months we applied the method to charm decays [20], before the discovery of charm, and to weak neutral current processes [21]. To this last paper also contributed Keith Ellis, a scottish PhD student of Cabibbo, who was to stay with us in Rome for a few years, eventually speaking a very good italian and fully understanding the roman way of living. Later, in 1981 Curci (who, unfortunately, is no more with us) and I, with Martinelli and Petrarca [22], computed the two-loop anomalous dimensions for the operators of the effective weak non-leptonic Hamiltonian.

Meanwhile Mario Greco, working in Frascati with Touschek (and Pancheri, Srivastava and Etim) was becoming an expert in QED radiative corrections and the resummation of soft photons. In fact, the e^+e^- collider ADONE was functioning at the time and this prompted QED studies as a main activity of the theory group of the Laboratory. For example, in 1975 Mario published two papers on the QED corrections near the J/Ψ [23]. This work has been later generalized to the production of the Z boson, preparing the stage for the analysis of LEP/SLC experiments [24]. With the advent of QCD he could profit of the acquired expertise in QED naturally turning into resumming soft gluons (see later).

I remember that I learned from Mario's papers the techniques and the results of the exponentiation of logs in QED.

In 1975 Cabibbo and Parisi published an important work. This is one of the first papers where quark deconfinement is discussed [25]. In this work they argue that an exponentially growing hadronic spectrum (*à la* Hagedorn), which is compatible with the ever increasing population of observed hadronic resonances, can be naturally associated to a 2nd-order phase transition that one could identify with the deconfining transition from the hadronic phase into that corresponding to the quark-gluon plasma.

At about the same time myself, in collaboration with Parisi and Petronzio, we studied the QCD corrections to neutrino deep inelastic cross-sections and distributions [26]. We found that the corrections, also including those due to the onsetting of the charm threshold, are rather large at the energy of the then available experimental data. In the absence of these corrections the data appeared at variance with respect to the predictions of the parton model. This paper contributed to the downgrading of the observed so-called y -anomaly from a signal of new physics (right-handed charged currents were invoked) down to a less exciting charm threshold plus QCD-logs effect.

In 1977 the well known work on the QCD evolution equations by myself and Parisi was published [27]. In the academic year 1976-77 both of us were on sabbatical in Paris. I was at the Ecole Normale Supérieure (ENS) and Giorgio at the Institut des Hautes Etudes Scientifiques at Bures-sur-Yvette. Giorgio often preferred to stay downtown, spending some time at the ENS to discuss with the people there and, in particular, with me on QCD phenomenology, a subject of great interest for both of us at that time. Out of these regular contacts our work on the evolution equations was developed. The main virtue of our approach was to formulate the evolution of parton densities as a branching process with probabilities determined (at leading order) by the splitting functions (proportional to the running coupling). In our paper a particular emphasis was devoted to prove that the splitting functions are a property of the theory and do not depend on the process (in particular the evolution does not apply only to deep inelastic scattering). On this issue I remember a discussion some months before with Cabibbo, who was asking what remains of the parton model if the scaling violations modify the parton densities in different ways for different processes. I argued that an appealing possibility was that the leading logarithmic corrections are universal and that general Q^2 -dependent parton densities could be defined in this limit and used for the description of a variety of hard processes (what is now denoted as the "factorization" theorem). With this idea in mind, in our paper, completely formulated in parton language, with running coupling, the splitting functions were directly derived from the QCD vertices, using the formalism of the "old" perturbation theory (because the 3 partons in the vertex cannot all be on their mass shell), with no reference to the particular diagram where the splitting leg is attached to, thus making clear that the splitting functions are the same for all processes. The polarized splitting functions were also derived by us with the same method in agreement with the results of refs. [28] obtained by the operator method.

The evolution equations are now often called DGLAP equations (Dokshitzer-Gribov-Lipatov-Altarelli-Parisi). The first article by Gribov and Lipatov was published in 1972 [29] (even before the works by Gross and Wilczek and by Politzer!) and was followed in 1974 by a paper by Lipatov [30] (these dates correspond to the publication in Russian). All these articles refer to an Abelian vector theory (treated in parallel with a pseudoscalar theory). Seen from the point of view of the evolution equations, these papers, in the context of the Abelian theory, ask the right question and extract the relevant logarithmic terms from the dominant class of diagrams. But from their formal

presentation the relation to real physics is somewhat hidden (in this respect the 1974 paper by Lipatov makes some progress and explicitly refers to the parton model). The article by Dokshitzer [31] was exactly contemporary to ours. It now refers to the non-Abelian theory (with running coupling) and the discussion is more complete and explicit than in the Gribov-Lipatov articles. But, for example, the notion of the evolution as a branching process and the independence of the kernels from the process are not emphasised. An important point is also that the Gribov-Lipatov papers were known to Dokshitzer (while they were not to us). Their works were in fact his starting point and are quoted among the references given in his article.

Back to Rome I met Guido Martinelli, who at that time was a post-doc with a contract for doing accelerator physics at Frascati, and I rescued him into particle physics, with a work on the transverse momentum distributions for jets in lepto-production final states [32]. In the same paper we derived an elegant formula for the longitudinal structure function F_L , also an effect of order $\alpha_s(Q^2)$, as a convolution integral over $F_2(x, Q^2)$ and the gluon density $g(x, Q^2)$. I find it surprising that it took 40 years since the start of deep inelastic scattering experiments to get meaningful data on the longitudinal structure function. The present data, recently obtained by the H1 experiment at DESY, are in agreement with this LO QCD prediction but the accuracy of the test is still far from being satisfactory for such a basic quantity.

Meanwhile Mario Greco started producing an impressive series of works where the tools developed over the years for QED were applied to the resummation of soft gluons in different QCD processes. In a first group of papers [33,34] the QED formalism of coherent states was adapted to the non-Abelian context of QCD. In particular this technique was applied by Mario with Curci and Srivastava [34] to compute the probability that a fraction ϵ of the total energy $2E$ falls outside a cone of semi-aperture δ . This amounts to upgrading the Sterman-Weinberg perturbative result obtained in 1977 [35] by including soft gluon resummed effects.

Resummation near the phase space boundaries is an important issue in QCD. Mario authored with Curci one of the early papers on this subject [36], with applications to deep inelastic scattering near $x = 1$ and to Drell-Yan processes near $\tau = Q^2/s = 1$. The resummation of the “large π^2 terms” (those arising from the continuation of Q^2 from negative values in deep inelastic scattering, where the parton densities are measured, to the positive values of the Drell-Yan process), was also included in this paper (Parisi also studied this problem nearly at the same time [37]). In fig. 2 we can see Mario at work during a Moriond meeting where he presented those results.

In those years the Rome group contributed very much to the theory of Drell-Yan processes. In addition to the works just mentioned, important progress was made in 1978-79 with the calculation of the next-to-the-leading-order (NLO) corrections to Drell-Yan processes by myself with Keith Ellis and Martinelli [38]. This was one of the first calculations of NLO corrections in QCD. We started by defining the quark parton densities beyond leading order in a precise way (for quarks we adopted the structure function F_2 as the defining quantity: the naive parton model expression is taken by definition to hold unchanged at NLO; gluons only enter at NLO in Drell-Yan processes). Then the calculation of NLO diagrams for both deep inelastic scattering and the Drell-Yan process allows to derive the corrective terms for the Drell-Yan cross-section, as function of Q^2 . The resulting corrections turned out to be surprisingly large. The ratio of corrected to uncorrected (Born) cross-sections was found to be rather constant in Q^2 and in rapidity. So we decided to denote it as the “ K -factor”, because K sounded to us as the typical symbol for a constant. The origin of the main part of this correction can be traced back



Fig. 2. – Mario Greco at a Moriond meeting in 1980 where he gave the talk “Soft gluon effects in QCD processes”.

to effects that can be resummed (like the “large π^2 terms” that we have just mentioned). Today with much larger values of Q^2 and s accessible to present accelerators and with the next-to-next-to-leading-order (NNLO) calculations completed the K -factor is under control (for example, there is not too much difference between NLO and NNLO estimates, especially when some resummations are also implemented)

Another by now classic theoretical problem for Drell-Yan processes that was first attacked in those years is the evaluation of the transverse momentum (p_T) distribution of the produced virtual boson (a γ or a W^\pm or a Z_0). The study of the LO perturbative p_T distribution, valid for $p_T \sim Q$, was completed in 1978 by myself with Parisi and Petronzio [39]. The NLO perturbative calculation followed in 1981-83 by K. Ellis, Martinelli and Petronzio [40]. The study of the Sudakov double logs, important at intermediate values of p_T (between Λ_{QCD} and Q) was started in 1979 by Mario with Curci and Srivastava [34] and by Parisi and Petronzio [41] (in this paper the completely correct formula for the LO Sudakov factor was first obtained, correcting a small bug in a previous paper by Dokshitzer, Dyakonov and Troyan [42]). Then, in the early 80s, the problem was attacked of realizing a smooth matching between the perturbative and the Sudakov component. Mario worked on this problem with Pierre Chiappetta [43]. As

soon as the data on the W and Z production from $U1$ and $U2$ at CERN were first available, an adequate theoretical prediction was ready in a paper signed by myself, K. Ellis, Greco and Martinelli [44]. This is an important paper, first because it is a paper that I signed with Mario, and then because it essentially contained all the crucial ingredients that describe the physics of this phenomenon. In the subsequent years the accuracy was much improved with the computation of subleading effects and with several different refinements, but the essential points were all present in our paper and the accuracy of our treatment was adequate for the quality of the first data. The same techniques are at present applied to the calculation of the p_T distribution of the Higgs boson produced by gluon fusion (see, for example, ref. [45]).

I leave to the following speakers to describe other aspects of the scientific activity of Mario and also what he did later in QCD. I stop here by making my best wishes to him of a long and happy sequel of celebrations for 75, 80, 85, . . . , 100 anniversaries. And also I congratulate with him for the co-foundation of these by now classical meetings in La Thuile.

* * *

I thank the Organizers of Les Rencontres, for giving me the opportunity to celebrate the 70th anniversary of my old friend and colleague MARIO GRECO.

REFERENCES

- [1] ALTARELLI G., *Phys. Rep.*, **81** (1982) 1.
- [2] GROSS D. and WILCZEK F., *Phys. Rev. Lett.*, **30** (1973) 1343; *Phys. Rev. D*, **8** (1973) 3633; *Phys. Rev. D*, **9** (1974) 980.
- [3] POLITZER H. D., *Phys. Rev. Lett.*, **30** (1973) 1346.
- [4] GELL-MANN M., *Phys. Lett.*, **8** (1964) 214; ZWEIG G., CERN Report No. TH401, 4R12 (1964) (unpublished); HAN M. Y. and NAMBU Y., *Phys. Rev. B*, **139** (1965) 1006; GREENBERG O. W., *Phys. Rev. Lett.*, **13** (1964) 598.
- [5] BJORKEN J., *Phys. Rev.*, **179** (1969) 1547; FEYNMAN R. P., *Phys. Rev. Lett.*, **23** (1969) 1415.
- [6] FRITZSCH H. and GELL-MANN M., in *Proceedings of the XVI International Conference on High Energy Physics*, Vol. **2** (CERN) 1972, p. 164; FRITZSCH H., GELL-MANN M. and LEUTWYLER H., *Phys. Lett. B*, **47** (1973) 368.
- [7] GELL-MANN M. and LOW F., *Phys. Rev.*, **95** (1954) 1300; STUECKELBERG E. and PETERMANN A., *Helv. Phys. Acta*, **26** (1953) 499; BOGOLIUBOV N. N. and SHIRKOV D. V., *Introduction to the Theory of Quantized Fields* (Interscience, New York) 1959; CALLAN C. G., *Phys. Rev. D*, **2** (1970) 1541; SYMANZIK K., *Commun. Math. Phys.*, **18** (1970) 227.
- [8] WILSON K., *Phys. Rev.*, **179** (1969) 1499; *Phys. Rev. D*, **3** (1971) 1818; FRISHMAN Y., *Ann. Phys.*, **66** (1971) 373; BRANDT R. and PREPARATA G., *Nucl. Phys. B*, **27** (1971) 541.
- [9] PARISI G., *Lett. Nuovo Cimento*, **7** (1973) 84.
- [10] GROSS D., *Nucl. Phys. B (Proc. Suppl.)*, **135** (2004) 193.
- [11] PARISI G., *Phys. Lett. B*, **43** (1973) 207.
- [12] ALTARELLI G. and MAIANI L., *Phys. Lett. B*, **41** (1972) 480; *Nucl. Phys. B*, **51** (1973) 509; **56** (1973) 477.
- [13] ALTARELLI G. and RUBINSTEIN H. R., *Phys. Rev.*, **187** (1969) 2111.
- [14] ALTARELLI G., CABIBBO N., MAIANI L. and PETRONZIO R., *Nucl. Phys. B*, **69** (1974) 531; *Phys. Lett. B*, **48** (1974) 435; *Nucl. Phys. B*, **92** (1975) 413.
- [15] BRAMON A., ETIM E. and GRECO M., *Phys. Lett. B*, **39** (1972) 514.

- [16] DAVIER M. *et al.*, ArXiv:1010.4180.
- [17] BRAMON A., ETIM E. and GRECO M., *Phys. Lett. B*, **41** (1972) 609; GRECO M., *Nucl. Phys. B*, **63** (1973) 398.
- [18] ALTARELLI G. and MAIANI L., *Phys. Lett. B*, **52** (1974) 351.
- [19] GAILLARD M. K. and LEE B. W., *Phys. Rev. Lett.*, **33** (1974) 108.
- [20] ALTARELLI G., CABIBBO N. and MAIANI L., *Phys. Lett. B*, **57** (1975) 277; *Nucl. Phys. B*, **88** (1975) 285.
- [21] ALTARELLI G., ELLIS R. K., MAIANI L. and PETRONZIO R., *Nucl. Phys. B*, **88** (1975) 215.
- [22] ALTARELLI G., CURCI G., MARTINELLI G. and PETRARCA S., *Phys. Lett. B*, **99** (1981) 141; *Nucl. Phys. B*, **187** (1981) 461.
- [23] GRECO M., PANCHERI-SRIVASTAVA G. and SRIVASTAVA Y., *Phys. Lett. B*, **56** (1975) 367; *Nucl. Phys. B*, **101** (1975) 234.
- [24] GRECO M., PANCHERI-SRIVASTAVA G. and SRIVASTAVA Y., *Nucl. Phys. B*, **171** (1980) 118.
- [25] CABIBBO N. and PARISI G., *Phys. Lett. B*, **59** (1975) 67.
- [26] ALTARELLI G., PARISI G. and PETRONZIO R., *Phys. Lett. B*, **63** (1976) 183.
- [27] ALTARELLI G. and PARISI G., *Nucl. Phys. B*, **126** (1977) 298.
- [28] AHMED M. A. and ROSS G. G., *Phys. Lett. B*, **56** (1975) 385; *Nucl. Phys. B*, **111** (1976) 441.
- [29] GRIBOV V. N. and LIPATOV L. N., *Sov. J. Nucl. Phys.*, **15** (1972) 438.
- [30] LIPATOV L. N., *Sov. J. Nucl. Phys.*, **20** (1975) 94.
- [31] DOKSHITZER Y. L., *Sov. Phys. JETP*, **46** (1977) 691.
- [32] ALTARELLI G. and MARTINELLI G., *Phys. Lett. B*, **76** (1978) 89.
- [33] GRECO M., PALUMBO F., PANCHERI-SRIVASTAVA G. and SRIVASTAVA Y., *Phys. Lett. B*, **77** (1978) 282; CURCI G. and GRECO M., *Phys. Lett. B*, **79** (1978) 406.
- [34] CURCI G., GRECO M. and SRIVASTAVA Y., *Phys. Rev. Lett.*, **43** (1979) 834; *Nucl. Phys. B*, **159** (1979) 451.
- [35] STERMAN G. F. and WEINBERG S., *Phys. Rev. Lett.*, **39** (1977) 1436.
- [36] CURCI G. and GRECO M., *Phys. Lett. B*, **92** (1980) 175.
- [37] PARISI G., *Phys. Lett. B*, **90** (1980) 295.
- [38] ALTARELLI G., ELLIS R. K. and MARTINELLI G., *Nucl. Phys. B*, **143** (1978) 521; **157** (1979) 461.
- [39] ALTARELLI G., PARISI G. and PETRONZIO R., *Phys. Lett. B*, **76** (1978) 351; 356.
- [40] ELLIS R. K., MARTINELLI G. and PETRONZIO R., *Phys. Lett. B*, **104** (1981) 45; *Nucl. Phys. B*, **211** (1983) 106.
- [41] PARISI G. and PETRONZIO R., *Nucl. Phys. B*, **154** (1979) 427.
- [42] DOKSHITZER YU. L., D'YAKONOV D. I. and TROYAN S. I., *Phys. Lett. B*, **78** (1978) 290.
- [43] CHIAPPETTA P. and GRECO M., *Nucl. Phys. B*, **221** (1983) 269; *Phys. Lett. B*, **135** (1984) 187.
- [44] ALTARELLI G., ELLIS R. K., GRECO M. and MARTINELLI G., *Nucl. Phys. B*, **246** (1984) 12.
- [45] BOZZI G., CATANI S., DE FLORIAN D. and GRAZZINI M., *Nucl. Phys. B*, **791** (2008) 1.

From Vector Meson Dominance to Quark-Hadron Duality

A. BRAMON

*Departament de Física, Universitat Autònoma de Barcelona - 08193, Bellaterra
Barcelona, Spain*

(ricevuto il 29 Settembre 2011; pubblicato online il 24 Gennaio 2012)

Summary. — A short review of the many contributions to hadron physics made by Mario Greco is presented. The review roughly covers his production between 1971 and 1974, just before the advent of QCD, when quark-model ideas, duality principles and vector meson dominance were widely accepted, developed and applied. The present author had the privilege to collaborate with Mario in most of these contributions and looking backward in time to remember the good old days we spent together in Frascati has been a great pleasure.

PACS 12.40.Vv – Vector-meson dominance.

PACS 13.66.Bc – Hadron production in e^+e^- interactions.

PACS 14.40.Be – Light mesons ($S = C = B = 0$).

1. – Vector Mesons and Vector Meson Dominance

In 1960 J.J. Sakurai published an influential paper [1], *Theory of Strong Interactions*, proposing the still to be discovered vector mesons ($J^{PC} = 1^{--}$) as gauge bosons of the strong interactions of hadrons. In this way, the successful gauge principle of QED, generating universal couplings via covariant derivatives, was exported to the much more involved field of hadron physics. The special role given to vector mesons was in clear contrast with the “hadronic democracy” ideas widely accepted at that time and during the forthcoming 1960’s. Indeed, all hadrons were expected to be treated at the same level using the unitarity and analyticity properties of the S -matrix, organizing hadron resonances along Regge trajectories and unitary symmetry multiplets of $SU(3)$, or proposing crossing-symmetric amplitudes, as in the Veneziano model.

Low-mass vector mesons had been predicted just a few years before Sakurai’s paper in order to understand the structure and size of protons and neutrons [2]. The pionic cloud surrounding the nucleons was assumed to be responsible for their structure, usually expressed in terms of the so-called electromagnetic form factors. Form factor data required, at least, two low-mass vector mesons: an isoscalar, $I = 0$, ω -resonance and the neutral member, ρ^0 , of an isovector triplet, $I = 1$. Both states, ω [3] and ρ [4], were experimentally identified in 1961 short after Sakurai’s proposal [1]. Other low-mass vector resonances were discovered and organized in a complete $SU(3)$ -nonet which became paradigmatic in applying $SU(3)$ arguments. In particular, the almost ideal mixing

between the ω and ϕ isoscalar states and the so-called Zweig-rule, strongly suggested the existence of quarks in 1964 and, almost immediately, the “quark model” became an extremely popular and successful tool in hadron physics.

It was soon realized that Sakurai’s ideas could explain only a few features of the strictly *strong* interactions of hadrons and that a new theory—QCD, to be formulated some ten years later—was needed. However, restricting to the more specific context of the *electromagnetic* interactions of hadrons, the gauge principles of ref. [1] turned out to be extremely successful. The key ingredient, proposed in 1961 by Gell-Mann and Zachariassen [5], was the complete vector meson dominance (VMD) of the electromagnetic form factors of hadrons. On the one hand, vectors mesons were universally coupled to the various hadrons—thus making the model extremely predictive—and, on the other, the three relevant vector mesons, $V = \rho^0, \omega$ and ϕ , were coupled to the photon via the constants

$$(1) \quad \frac{em_V^2}{f_V} \quad \text{with } V = \rho^0, \omega, \phi.$$

The values of the masses, m_V^2 , and coupling constants, f_V , were soon accurately measured by the Orsay, Novosibirsk and Frascati e^+e^- storage rings and found to be in nice agreement with quark model arguments.

One of the first and cleanest applications of VMD was the establishment of the following relation between the total photoproduction cross section off nucleons, $\sigma_{\text{tot}}(\gamma p)$, and the forward photoproduction cross section of V ’s, $\frac{d\sigma_0}{dt}(\gamma p \rightarrow Vp)$,

$$(2) \quad \sigma_{\text{tot}}(\gamma p) = \sum_{V=\rho^0, \omega, \phi} \frac{4\pi e}{f_V} \sqrt{\frac{1}{1 + \eta_V^2} \frac{d\sigma_0}{dt}(\gamma p \rightarrow Vp)},$$

which is an immediate consequence of the couplings (1) and the optical theorem (in this context, η_V accounts for the real part of the V -production amplitude). A second, well-known VMD result is illustrated by the following three decay chains:

$$(3) \quad \omega \rightarrow \rho\pi \rightarrow \pi^+\pi^-\pi^0, \quad \omega \rightarrow \pi^0\rho^0 \rightarrow \pi^0\gamma, \quad \pi^0 \rightarrow \omega\rho^0 \rightarrow \gamma\gamma,$$

which allowed to relate the $\Gamma(\omega \rightarrow \pi^+\pi^-\pi^0)$, $\Gamma(\omega \rightarrow \pi^0\gamma)$ and $\Gamma(\pi^0 \rightarrow \gamma\gamma)$ decay widths. In all these cases, VMD predictions turned out to be in reasonable agreement with the available data.

2. – Extended Vector Meson Dominance

Just after 1970, when more accurate data on the above processes became available, some discrepancies with the VMD predictions started to appear and to be discussed. Data on the $\sigma_{\text{tot}}(\gamma p)$ cross section were found to be some 20% larger than predicted by the right-hand side of eq. (2). This discrepancy strongly suggested the convenience to extend the sum in this equation to include further contributions from new, higher-mass vector mesons. This generalized VMD model was proposed by Sakurai and Schildknecht [6] and has recently been reviewed in detail in [7].

Somewhat earlier and along the same lines, Mario Greco and the present author [8] discussed the convenience to extend VMD with a second $SU(3)$ -nonet of vector mesons, V' , to account for new data on $V \rightarrow PPP$, $V \rightarrow P\gamma$ and $P \rightarrow \gamma\gamma$ decays, where V

and P stand for the various members of the vector- and pseudoscalar-meson nonets thus generalizing the two-step processes quoted in (3). A fit to these data led to an estimate of the relevant coupling strengths of the higher-mass vector mesons, V' , and to a few predictions such as

$$(4) \quad \sigma_{e^+e^- \rightarrow \omega\pi^0 \rightarrow \pi^0\pi^0\gamma}(m_{\rho'}^2) \simeq 3 \text{ nb},$$

$$(5) \quad \sigma_{e^+e^- \rightarrow \rho\eta \rightarrow \pi^+\pi^-\eta}(m_{\rho'}^2) \simeq 2 \text{ nb},$$

where we assumed a ρ' mass around 1.5 GeV. Such a value was in the mass region being explored those days by the ADONE e^+e^- storage ring in Frascati, where Greco's group was placed. The hope was that our next-door experimental colleagues could confirm these predictions but, due to the smallness of the estimated cross sections, we had to wait for more than 30 years. Only the quite recent measurements from DM2, CMD-2 and SND, which can reasonably be averaged to the peak-values $\sigma_{e^+e^- \rightarrow \omega\pi^0 \rightarrow \pi^0\pi^0\gamma}(m_{\rho'}^2) \simeq 1.5 \text{ nb}$ and $\sigma_{e^+e^- \rightarrow \rho\eta \rightarrow \pi^+\pi^-\eta}(m_{\rho'}^2) \simeq 3 \text{ nb}$, have shown some agreement with our rough estimates (4) and (5).

Nowadays it is rather well established that the dominant decay mode of the ρ' , with a mass around 1.5 GeV, is into four pions and not into the above two channels (4) and (5) to which our extended VMD approach could be directly applied. The $e^+e^- \rightarrow \rho' \rightarrow \pi^+\pi^-\pi^+\pi^-$ was experimentally observed in Frascati in 1971 [9] and further theoretical analyses of this process were discussed in [10] and [11]. Interestingly enough, in [10] M. Greco insisted in making the final remark that “*it is very tempting to speculate on what can be the overall contribution of (an infinite set of) vector mesons coupled to the photon*”. A naive extrapolation of our results, modifying eq. (2) through the introduction of an infinity of higher mass vector mesons, led to a surprising good agreement with the available photoproduction data and, more importantly, opened the door to an interesting new idea.

3. – Vector Meson Dominance, scale invariance and a “new” duality

Starting in 1971, deep inelastic scattering experiments established the “scale invariant” behaviour of the structure functions of the nucleons. A related behaviour, implying that the total cross section of hadron production in e^+e^- annihilations, $\sigma_{\text{had}}(s)$, scales as $1/s$ for large values of the CM energy \sqrt{s} , had been suggested by Bjorken. As a result, the “quark-parton” model, and improved versions of it, were proposed to explain these deep inelastic phenomena in terms of point-like constituents or “partons”. An interesting possibility was to attempt a *VMD approach to scale invariance*. With this explicit title we published a short paper in 1972 [12], which was further developed and reviewed by Mario somewhat later [13]. The central points of this proposal were favourably accepted and defended, among others, by Sakurai in a nice paper [14], where our original contribution [12] was reanalyzed and rephrased in terms a “new kind of duality”.

According to Sakurai's presentation, the assumption in [12] and [13] that the total cross section of hadron production in e^+e^- annihilation is completely dominated by the formation of vector mesons can be written as

$$(6) \quad \begin{aligned} \sigma_{\text{had}}(s) &= \frac{12\pi}{s} \sum_V \frac{m_V^2 \Gamma_V \Gamma_{V \rightarrow e^+e^-}}{(s - m_V^2)^2 + m_V^2 \Gamma_V^2} \\ &= \sigma_{\mu \text{ pair}}(s) \sum_V \frac{3}{(f_V^2/4\pi)} \frac{m_V^3 \Gamma_V}{(s - m_V^2)^2 + m_V^2 \Gamma_V^2}, \end{aligned}$$

where we have introduced the $V - \gamma$ coupling (1) and the $\mu^+\mu^-$ -pair cross section at large CM energies, $s \gg m_\mu^2$,

$$(7) \quad \sigma_{\mu \text{ pair}}(s) = 4\pi\alpha^2/3s.$$

One immediately sees that if $\sigma_{\text{had}}(s)$ at high energies has to behave like $1/s$, the sum in eq. (6) has to be extended to an infinite series of vector mesons, as already suggested in [10]. Moreover, a very specific relation has to exist between the density of vector meson states per unit squared mass interval, $P_V(m^2) = 1/\Delta m_V^2$, their masses m_V and couplings to the photon f_V ; namely,

$$(8) \quad P_V(m^2)m_V^2/f_V^2 = m_V^2/\Delta m_V^2 f_V^2 = \text{const.}$$

The other assumptions of our model [12] and [13] were that a) the $1/s$ behaviour is obtained on the average even for the prominent low-mass vector mesons (precocious scaling), b) the isovector meson spectrum is given by

$$(9) \quad m_n^2 = m_\rho^2(1 + 2n), \quad n = 0, 1, 2, \dots,$$

as in the Veneziano model, and c) the isoscalar sector contributes, as usual, an additional $1/3$ to the isovector contribution. Taking all this into account, the model proposed in [12] and [13] reached two relevant predictions: on the one hand, a reasonable description of the nucleon structure functions was achieved and, on the other, the remarkably simple prediction

$$(10) \quad R \equiv \lim_{s \rightarrow \infty} \sigma_{\text{had}}(s)/\sigma_{\mu \text{ pair}}(s) = 2\pi/(f_\rho^2/4\pi) \simeq 2.5,$$

which was expected to be valid for large s (but below the opening of the yet undiscovered new flavour's channels) and turned out to be quite important for our present purposes, was obtained.

Indeed, it is this latter equation what probably suggested Sakurai to rephrase our findings as a “new” duality in e^+e^- -annihilations into hadrons. In our model, the numerical prediction $R \simeq 2.5$, which is in good agreement with the data for \sqrt{s} between 2 and 3 GeV, follows exclusively from the value of f_ρ (plus analogous isoscalar contributions) which is a low-mass resonance parameter. For asymptotic, large values of s , the ratio R and the $1/s$ scaling of the e^+e^- cross section into hadrons are well predicted by the quark-parton model, much in the same way as in high energy hadron-hadron collisions the relevant asymptotic amplitudes are well described by the exchange of Regge trajectories. The “old” strong interaction duality between the high-energy Regge amplitudes (in the t and u channels) and the low-energy resonance formation (in the s channel) thus admits a vivid analogue in e^+e^- interactions: on the average, the contributions from low-energy vector mesons are dual to the contributions from the corresponding point-like quarks. These contributions should not be added (this would imply a “double counting” of the contributions), they rather satisfy “finite energy sum rules” (see the final paragraphs for some examples) as in the well-known case of strong interaction amplitudes. Possibly the name of “quark-hadron duality” captures the essence of this “new” kind of duality. On the average, it is expected to work locally, *i.e.*, for reasonable finite intervals of s , and in a sense this “quark-hadron duality” can be considered as a precursor of more accurate

and important developments such as the SVZ-sum rules that appeared once QCD was proposed.

4. – Quark-hadron duality, sum rules and the “new” vector mesons

Up to now, our discussion of quark-hadron duality has been restricted to processes involving u , d and s quarks and the corresponding nonets of $SU(3)$ vector mesons. New applications appeared as soon as new flavours were discovered and the value of R was correspondingly increased. Just after the discovery of the J/ψ resonances, M. Greco with C. A. Domínguez [15]—and some time later with G. Pancheri and Y. Srivastava [16], taken now radiative corrections into account—applied quark-hadron duality to estimate the averaged increase in R produced by the new charmed quark. The results of these papers,

$$(11) \quad \begin{aligned} R &= R_{u,d,s} + R_{\text{charm}} \\ &\simeq 2.5 + 1.2 \text{ (no rad. corrections)} \\ &\simeq 2.5 + 1.8 \text{ (with rad. corrections),} \end{aligned}$$

are in good agreement with the available data for R in the \sqrt{s} region between around 3 GeV (where the charmed channel opens) and 10 GeV (where the b -channel starts).

In 1978, when the Υ resonances appeared above $\sqrt{s} \simeq 10$ GeV but the electric charge of the b -quark was not firmly established, M. Greco [17] used again duality ideas to estimate the further increase in R in the new energy region predicting the decay width

$$(12) \quad \Gamma(\Upsilon(b\bar{b}) \rightarrow e^+e^-) \simeq 1.2 \text{ keV,}$$

which favours a b -quark electric charge of $-1/3$.

Other, more formal developments were also considered. From canonical trace anomalies of the energy-momentum tensor, E. Etim and M. Greco [18] derived the following general, n -valued family of quark-hadron duality sum rules:

$$(13) \quad \int_{s_0}^{\bar{s}} ds s^n \text{Im} \Pi(s) = \frac{\alpha R}{3} \frac{\bar{s}^{n+1}}{n+1} - \frac{c_n}{n+1},$$

where the limits of integration define the region where the two dual contributions are averaged and the imaginary part of the vacuum polarization function is related to the e^+e^- annihilation cross section into hadrons via

$$(14) \quad \text{Im} \Pi(s) = \frac{s}{4\pi\alpha} \sigma_{\text{had}}(s)$$

$$(15) \quad = 4\pi^2 \alpha \frac{m_\rho^2}{f_\rho^2} \sum_n \delta(s - m_n^2)$$

if one adopts the narrow width approximation for vector resonances in the final expression.

In particular, for $n = 0$ the preceding equation takes a much more familiar and simple form,

$$(16) \quad \int_{s_0}^{\bar{s}} ds \left(\text{Im} \Pi(s) - \frac{\alpha R}{3} \right) = 0,$$

whose generalization to axial-vector channels and to channels with open strangeness was also discussed by E. Etim, M. Greco and Y. Srivastava in [19].

As previously stated, both the general form of these sum rules and their extension to different channels suggest that a part of the subsequent work leading to the extremely successful SVZ or QCD sum rules of 1979 was done by a reduced group of people under Mario's direction. Certainly, this initial ideas developed around 1972 were quite simple and naive—no gluons, no condensates could be invoked during those pre-QCD days—but the central point, namely, the dual behaviour between quark and resonance contributions, was already there. For the present author it has been a great pleasure to remember those days as a postdoc member of the group enjoying a wonderful stay in Frascati.

* * *

Thanks are due to G. ISIDORI for his kind invitation to participate in the special session honoring Prof. Mario Greco and to the organizers of the meeting in La Thuile 2011 for the excellent atmosphere and organization.

REFERENCES

- [1] SAKURAI J. J., *Ann. Phys. (N.Y.)*, **11** (1960) 1.
- [2] NAMBU Y., *Phys. Rev.*, **106** (1957) 1366; FRAZER W. R. and FULCO J., *Phys. Rev. Lett.*, **2** (1959) 365.
- [3] MAGLIC B. *et al.*, *Phys. Rev. Lett.*, **7** (1961) 178.
- [4] ERWIN A. *et al.*, *Phys. Rev. Lett.*, **6** (1961) 628.
- [5] GELL-MANN Y. and ZACHARIASEN F., *Phys. Rev.*, **124** (1961) 953.
- [6] SAKURAI J. J. and SCHILDKNECHT D., *Phys. Lett. B*, **40** (1972) 121.
- [7] SCHILDKNECHT D., *Acta Phys. Polon. B*, **37** (2006) 595.
- [8] BRAMON A. and GRECO M., *Lett. Nuovo Cimento*, **1** (1971) 739.
- [9] BARBARINO G. *et al.*, *Lett. Nuovo Cimento*, **3** (1972) 689.
- [10] BRAMON A. and GRECO M., *Lett. Nuovo Cimento*, **3** (1972) 693.
- [11] BRAMON A. and GRECO M., *Nuovo Cimento A*, **14** (1973) 323.
- [12] BRAMON A., ETIM E. and GRECO M., *Phys. Lett. B*, **41** (1972) 609.
- [13] GRECO M., *Nucl. Phys. B*, **63** (1973) 398.
- [14] SAKURAI J. J., *Phys. Lett. B*, **46** (1973) 207.
- [15] DOMÍNGUEZ C. A. and GRECO M., *Lett. Nuovo Cimento*, **12** (1975) 439.
- [16] GRECO M., PANCHERI-SRIVASTAVA G. and SRIVASTAVA Y., *Phys. Lett. B*, **56** (1975) 367.
- [17] GRECO M., *Phys. Lett. B*, **77** (1978) 84.
- [18] ETIM E. and GRECO M., *Lett. Nuovo Cimento*, **12** (1975) 91.
- [19] ETIM E., GRECO M. and SRIVASTAVA Y., *Lett. Nuovo Cimento*, **16** (1976) 65.

Frascati resummation schemes for IR radiation in QED and QCD

G. PANCHERI⁽¹⁾ and Y. SRIVASTAVA⁽²⁾

⁽¹⁾ *Laboratori Nazionali di Frascati, INFN - Frascati, Italy*

⁽²⁾ *INFN, Sezione di Perugia and Dipartimento di Fisica, Università di Perugia - Perugia Italy*

(ricevuto il 29 Settembre 2011; pubblicato online il 26 Gennaio 2012)

Summary. — As part of the 70th birthday celebration of our dear friend Mario Greco, a brief history of the development of radiative effects at Frascati in QED and QCD covering the period between late sixties to the late eighties is presented. During these two decades, two parallel resummation schemes for QED were formulated and radiative corrections were made for the J/Ψ production and later for Z^0 production. The schemes were then extended to QCD to obtain realistic estimates of the e^+e^- hadronic cross-sections at all energies. It led to the introduction of several new concepts: frozen α_s and later to singular α_s and to the notion of the maximum value of transverse energy allowed in a radiative process. Some other fall outs from this research such as transverse momentum distributions and hadronic total cross-sections which are valid even now would be briefly touched upon.

PACS 13.85.Lg – Total cross sections.

PACS 13.60.Hb – Total and inclusive cross sections (including deep-inelastic processes).

1. – Resummed QED radiation

In 1960, Bruno Touschek had the seminal idea of making an electron positron machine. It led first to the construction at Frascati of ADA (in 1961, with an energy of 250 MeV) and later to ADONE (with an energy of 3 GeV). With the advent of ADONE, a sizeable theory group developed at Frascati, whose members in 1966, were Giovanni De Franceschi, Paolo Di Vecchia, Francesco Drago, Etim Etim, Giancarlo Rossi, Mario Greco and GP, one of the authors of this note (see fig. 1). Touschek understood that a proper quantitative analysis of the experimental results from ADONE (or any other e^+e^- colliding beam) necessitated precise computations of resummed finite radiative corrections. His philosophy being “We must do the administration of the radiative corrections to electron positron experiments”. In his words, “We must earn our bread and butter” [1].



Fig. 1. – Mario Greco and YS in Frascati in 1972.

The first scheme towards infra-red (IR) radiative correction to the cross-section of a process through resummation was initiated by Touschek [2] through a relativistic formulation of the Bloch-Nordseick Theorem, Poisson statistics and energy-momentum conservation. The resummed probability distribution of a 4-momentum loss K^μ carried off by soft photons in a process was obtained as

$$(1) \quad d^4P(K) = \left[\frac{d^4K}{(2\pi)^4} \right] \int d^4x \exp[-h(x) + iK \cdot x],$$

where h is defined in terms of the mean number of photons $\bar{n}(k)$ as

$$(2) \quad h(x) = \int d^3\bar{n}(\mathbf{k})(1 - \exp[-ik \cdot x]).$$

If only the distribution in ω , the total energy lost through IR radiation is required, the closed form expression is

$$(3) \quad dP(\omega) = \left[\frac{d\omega}{2\pi} \right] \int_{-\infty}^{\infty} dt \exp[i\omega t - h(t)] = \mathcal{N}(\beta)\beta \frac{d\omega}{\omega} \left(\frac{\omega}{E} \right)^\beta,$$



Fig. 2. – Mario Greco with the author (YS) and Guido Altarelli at Accademia dei Lincei, circa 1974.

where $\mathcal{N}(\beta)$ is a calculable normalization factor and β for electrons and positrons is given by

$$(4) \quad \beta = \frac{4\alpha}{\pi} \left(\log \frac{2E}{m_e} - \frac{1}{2} \right).$$

Unlike perturbation theory to any finite order, the resummed distribution in eq. (3) is integrable. If ΔE is the maximum allowed energy loss, the IR radiative correction factor to the cross-section is given by

$$(5) \quad d\sigma = \mathcal{N}(\beta) \left(\frac{\Delta E}{E} \right)^\beta d\sigma_0.$$

The method was further extended for resonant processes [3]. The width of the resonance provides an intrinsic cut-off and Γ replaces ΔE , provided $\Gamma \ll \Delta E$ (as is the case for J/Ψ) and for this case, a radiative tail also develops.

An equivalent very successful second scheme, also suggested by Touschek, —focused on correcting the scattering amplitude itself rather than the measurable cross-section— was developed by Greco and Rossi [4]. Both schemes were employed to do extensive and precise radiative corrections for the J/Ψ resonance and then for the Z^0 resonance [5].

2. – QCD radiation

During the period that QCD with its quarks and gluons was becoming the accepted theory behind hadrons largely thanks to the theoretical notion of asymptotic freedom, and the experimental observation of jets at high energies in e^+e^- and $pp/p\bar{p}$ reactions, theoretical need arose for saying something reasonable about the unknown non-perturbative IR “slavery” region of QCD. An immediate problem at hand was a description of the experimentally measured $e^+e^- \rightarrow \text{hadrons}$ at the initial energy \sqrt{s} . With point like quarks and hadrons, the famous ratio $R(s)$ was written down as

$$(6) \quad R(s) = \frac{\sigma(e^+e^- \rightarrow \text{hadrons})}{\sigma(e^+e^- \rightarrow \mu^+\mu^-)} = 3 \left[\sum_i Q_i^2 \right] [1 + \alpha_s(s)/\pi],$$

where Q_i denotes the charge ($2/3$ for an up quark and $-1/3$ for a down quark), and $\alpha_s(s)$ is the QCD running coupling constant, whose AF expression is given by

$$(7) \quad \alpha_{AF}(s) = \frac{12\pi}{(33 - 2n_f) \ln(s/\Lambda^2)}.$$

As the threshold of a given quark channel is crossed, its contribution is included in the sum leading thereby to steps in the cross-section for charm and later bottom quark thresholds. What about the lower energy region which should give an average value of 2, in the free quark model due to the almost massless u, d, s quarks? Would there be an enhancement due to some average value of α_s term as in eq. (6)? Since theoretically eq. (7) is not expected to be valid at low energies, and experimentally the low energy cross-section has much variation due to low energy resonances ($\rho, \omega, \phi, \dots$), some device has to be found to theoretically estimate the QCD correction in this region and another to compare it to the experimental value. The technique adopted in [6] was to assume that α_s is “frozen” at low energies:

$$(8) \quad \alpha_{frozen}(s) = \frac{12\pi}{(33 - 2n_f) \ln(a + s/\Lambda^2)},$$

where a is a constant (see fig. 2). To smooth out the ups and downs from resonances, a zeroth moment of the experimental $R(s)$ was constructed

$$(9) \quad M(\bar{s}) = \int_0^{\bar{s}} (ds) R_{expt}(s).$$

From fig. 3, an average value of $R_{light} \approx 2.4$ was deduced. Also, the thresholds of various flavours being sharply delineated, allowed the authors to obtain an effective charm quark mass $m_c \approx (1.45 \pm 0.5) \text{ GeV}/c^2$. By the way, it also provided a neat direct check of semi-local quark-hadron duality for light and heavy quarks.

Over the years, IR behavior of α_s would become a crucial widely discussed topic and singular but integrable versions would be proposed [7]

$$(10) \quad \alpha_{IR}(s) \rightarrow_{s \ll s_0} (s_0/s)^p,$$

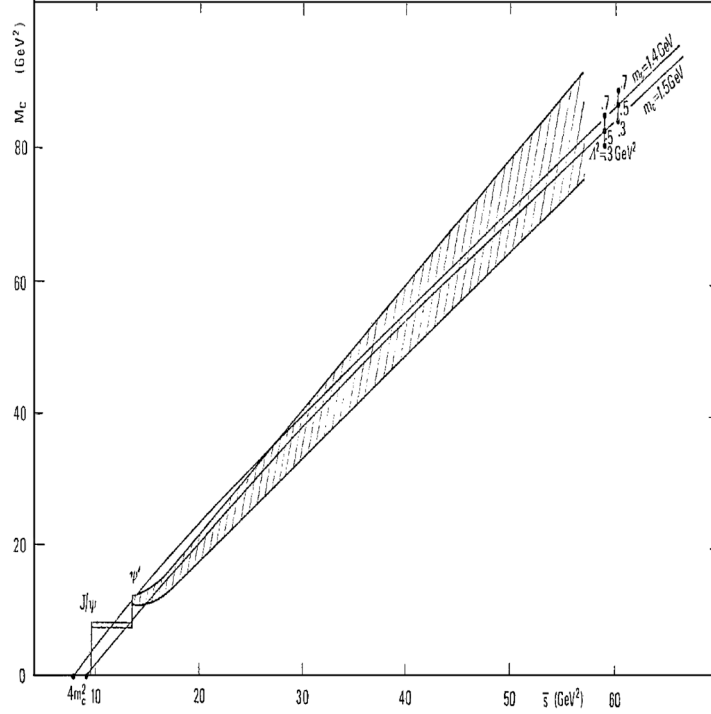


Fig. 3. – Zeroth moment of $R(s)$.

with $1/2 \leq p < 1$: the upper limit $p = 1$ being the Wilson value whereas the lower limit $p = 1/2$ corresponding to confinement but just. (α_{frozen} corresponds to $p \rightarrow 0$, which of course does not lead to confinement.)

The coherent state formalism for IR resummation in QED was successfully extended to QCD [8]. Very soon compact expressions for various jet processes in QCD were obtained using the coherent state formalism [9, 10], see fig. 5.

3. – Two applications of the QCD radiation

When transverse momentum distributions were analyzed through α_{frozen} , an arbitrary “intrinsic” transverse momentum had to be introduced. On the other hand, the singular version in eq. (10), was shown to generate spontaneously such a term with quite satisfactory results [7] as can be seen in fig. 4.

For the p_t - distribution for Drell-Yan pairs and other processes, a very useful concept of the maximum transverse momentum Q_{max} was introduced by Chiapetta and Greco [11]. The quantity Q_{max} along with an IR singular α_s have been used by us extensively in our later papers on soft-gluon resummation in total and inelastic hadronic cross-sections [12]. Recent data on inelastic cross-sections at $\sqrt{s} = 7$ TeV from LHC have been successfully analyzed using this formalism.

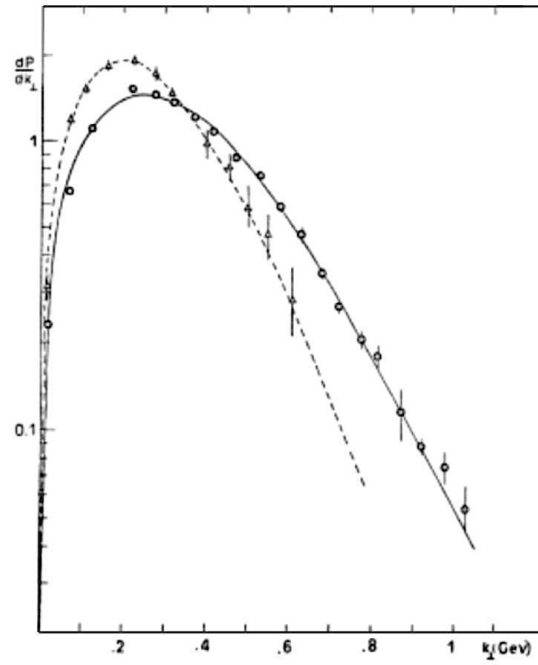


Fig. 4. – “High” transverse momentum distribution circa 1979 [7].



Fig. 5. – Mario Greco with GP.

4. – Coda

May we all meet at our 90th birthday.

REFERENCES

- [1] For a comprehensive history of this period at Frascati, see, BONOLIS L. and PANCHERI G., *Eur. Phys. J. H*, **36** (2011) 1.
- [2] ETIM E. G., PANCHERI G. and TOUSCHEK B., *Nuovo Cimento B*, **51** (1968) 362.
- [3] PANCHERI G., *Nuovo Cimento A*, **60** (1969) 321.
- [4] GRECO M. and ROSSI G., *Nuovo Cimento A*, **50** (1967) 168.
- [5] GRECO M., PANCHERI G. and SRIVASTAVA Y. N., *Nucl. Phys. B*, **101** (1975) 234.
- [6] GRECO M., PENSO G. and SRIVASTAVA Y., *Phys. Rev. D*, **21** (1980) 2520.
- [7] NAKAMURA A., PANCHERI G. and SRIVASTAVA Y., *Zeit. Phys. C*, **21** (1984) 243; GRAU A., PANCHERI G. and SRIVASTAVA Y., *Phys. Rev. D*, **41** (1990) 3360; 28; GRAU A., PANCHERI G. and SRIVASTAVA Y. N., *Phys. Rev. D*, **60** (1999) 114020 [arXiv:hep-ph/9905228].
- [8] GRECO M., PALUMBO F., PANCHERI-SRIVASTAVA G. and SRIVASTAVA Y., *Phys. Lett. B*, **77** (1978) 282.
- [9] CURCI G., GRECO M. and SRIVASTAVA Y., *Nucl. Phys. B*, **159** (1979) 451.
- [10] CURCI G., GRECO M. and SRIVASTAVA Y., *Phys. Rev. Lett.*, **43** (1979) 834.
- [11] CHIAPPETTA P. and GRECO M., *Nucl. Phys. B*, **199** (1982) 77.
- [12] ACHILLI A., GODBOLE R. M., GRAU A., PANCHERI G., SHEKHOVTSOVA O. and SRIVASTAVA Y. N., *Phys. Lett. B*, **659** (2008) 137 [arXiv:0708.3626]; BLOCK M. M. *et al.*, *Phys. Rev. D*, **84** (2011) 094009 [arXiv:hep-ph 1102.1949].

Heavy quarks, from discovery to precision

M. CACCIARI

LPTHE, UPMC and CNRS - Paris, France
Université Paris Diderot - Paris, France

(ricevuto il 29 Settembre 2011; pubblicato online il 17 Gennaio 2012)

Summary. — The discoveries of the heavy quarks are briefly reviewed, with a focus on the role played by Mario Greco in the interpretation of the experimental observations, and on his contributions to heavy quark precision phenomenology.

PACS 12.38.-t – Quantum chromodynamics.

PACS 14.40.Pq – Heavy quarkonia.

PACS 14.65.-q – Quarks.

1. – Mario's charm

In November 1974 two experimental groups simultaneously announced the discovery of a new resonance. The collaboration led by Sam Ting [1] at the Brookhaven National Laboratory and the one led by Burton Richter [2] at the Stanford Linear Accelerator Laboratory agreed on all the key characteristics of the new particle, but its name. Since the latter is not consequential, we shall rather focus here on its mass, at 3 GeV significantly larger than previously observed hadronic resonances and—more importantly—its total width, estimated at less than 1.3 MeV in [2], a surprisingly small value for a hadronic resonance. Appelquist and Politzer [3] and De Rujula and Glashow [4] are credited with the first interpretation of the new particle (eventually called J/ψ) as a bound state of the previously unobserved charm quark and its antiquark. The relatively large mass of the new quark (~ 1.5 GeV), together with the asymptotic freedom property of QCD, could elegantly explain the very small observed width.

Mario Greco was 33 years old and en route to SLAC for a seminar when the news of the discovery broke. Once at destination he was able to gather the available details, notably the mass of the resonance, and forward them to Frascati, where the observation could immediately be confirmed by the ADONE e^+e^- collider [5]. Mario then flew to Mexico City for a planned visit, and once there he learnt about the discovery of the ψ' through the local press. In collaboration with C. A. Dominguez he quickly published a paper [6] (fig. 1). Working within the Extended Vector Meson Dominance (EVMD) approach [7], and using the scarce experimental data available about the new ψ_n resonances, they were able to derive their total contribution to hadron production in e^+e^- collisions.

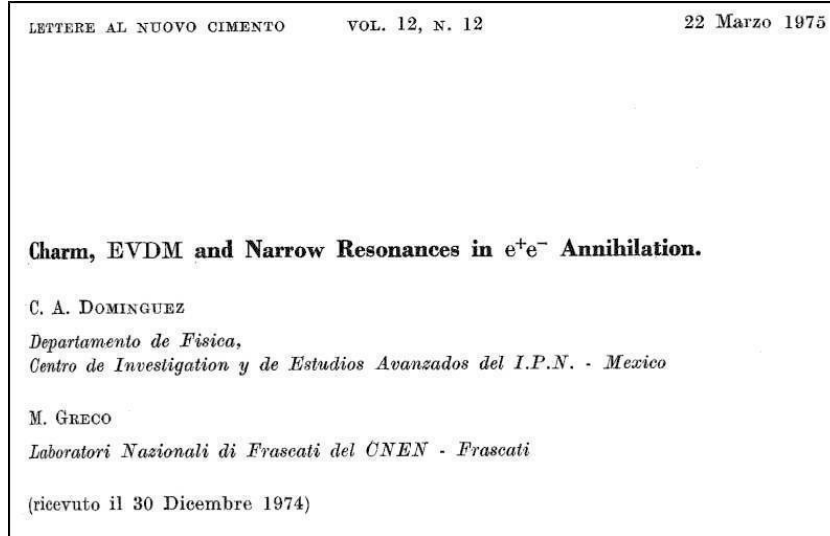


Fig. 1. – The front page of the Dominguez-Greco [6] paper interpreting the observation of the J/ψ as a charm-anticharm vector bound state. The typo in the title, EVDM rather than EVMD (a clear indication of how hectic those times must have been), bears fortunately no relation with the accuracy of the paper.

They wrote

$$\begin{aligned}
 R &= \frac{\sigma(e^+e^- \rightarrow \gamma \rightarrow \text{hadrons}) + \sigma(e^+e^- \rightarrow \psi_n \rightarrow \text{hadrons})}{\sigma(e^+e^- \rightarrow \gamma \rightarrow \mu^+\mu^-) + \sigma(e^+e^- \rightarrow \psi_n \rightarrow \mu^+\mu^-)} \\
 (1) \quad &= R_{\text{normal}} + R_{\text{charm}} \simeq 2.5 + 1.2 = 3.7.
 \end{aligned}$$

The resulting increment for the R ratio was in fair agreement with experimental data, and allowed them to interpret the newly observed resonances: “...one is naturally led to think of the new narrow resonances as charm-anticharm vector mesons”.

2. – Mario’s beauty

A few years later it was the turn of another quark to make its appearance in the form of a new resonance. In 1977 the collaboration led by Leon Lederman observed a peak around 9.5 GeV in the structure of the dimuon spectrum in 400 GeV proton-nucleus collisions at the Fermilab [8]. This was quickly interpreted as a bottom (or beauty)-antibottom bound state. Shortly thereafter, Mario Greco applied again [9] duality ideas [7, 10-14] to this discovery. These ideas led to simple relations for the electronic widths of vector mesons

$$(2) \quad \Gamma_{\rho}^{e\bar{e}} : \Gamma_{\omega}^{e\bar{e}} : \Gamma_{\varphi}^{e\bar{e}} : \Gamma_{\psi}^{e\bar{e}} : \Gamma_{\Upsilon}^{e\bar{e}} = 9 : 1 : 2 : 8 : 2(8),$$

where the last term in the equation above is related to the electric charge of the bottom quark having the value $-1/3(2/3)$. Choosing the value $-1/3$ leads to the prediction $\Gamma_{\Upsilon}^{e\bar{e}} \simeq 1.2 \text{ keV}$. This, in turn, allows one to estimate the production cross section of the Υ , for which Mario obtained a value in good agreement (within a factor of two) with the

TABLE I. – *The predictions of ref. [9] for the electronic widths of bottom-antibottom bound states, compared to modern experimental results.*

$\Gamma^{e\bar{e}}$ (keV)	Υ	Υ'	Υ''
Mario Greco [9]	1.2	0.65	0.55
PDG [15]	1.34	0.61	0.44

experimental measurement. He could therefore conclude that the charge $-1/3$ for the bottom quark was favoured by the available data: “*Our results suggest that the charge of the new constituent quark is likely $-1/3$* ”.

A by-product of this analysis were the predictions for the values for the leptonic widths of the Υ and the higher resonances, at the time unknown. Table I compares the predictions in [9] with the modern measured values. Obviously, not a bad job.

3. – Top discovery

After these two discoveries almost twenty years elapsed before the sixth quark was finally observed. The CDF collaboration at the Fermilab Tevatron collider published at first initial evidence [16] for the top quark in 1994, and followed up in 1995 with the definitive observation [17]. This last paper was also presented [18] in the 1995 edition of the La Thuile conference, one of the very first public announcements of the definitive discovery of the top quark.

The very large mass, of the order of 175 GeV, at which the top quark was finally observed would have been perhaps surprising only a few years earlier when, without any other experimental guidance, one could have expected a top quark only marginally heavier than the heavy quarks already discovered. However, by the time of the CDF discovery, a lot more information was available through the precision fits of the Standard Model parameters performed at LEP. In particular, it had become clear (see, *e.g.*, fig. 2, taken from [19]) that the top quark was going to be very heavy, with a mass of the order of 150 GeV, and a residual uncertainty that, in 1994, was probably of the order of ± 20 –30 GeV. This indirect evidence for the value of the top mass was one of the main contributions of LEP to the experimental landscape, and it was possible because of a huge amount of theoretical and phenomenological work directed at improving the predictions. As an example of Mario Greco’s contribution to this collective effort I’d like to mention two of his many papers on radiative corrections for LEP physics, refs. [20] and [21], which extensively reviewed and systematized electromagnetic corrections to Bhabha scattering at the Z^0 pole.

4. – “Precision” physics in heavy quarks and quarkonium

After the time of discoveries comes of course that of more accurate measurements and, out of necessity, more refined theoretical predictions, usually in the form of next-to-leading order (NLO) and resummed calculations. I wish to mention in particular two contributions of Mario Greco to this endeavour.

One of them is the first complete and systematic NLO calculation of heavy quarkonium total cross sections in hadronic collisions [22] within the then recently developed Non-Relativistic QCD (NRQCD) formalism [23]. This work capped a series of papers

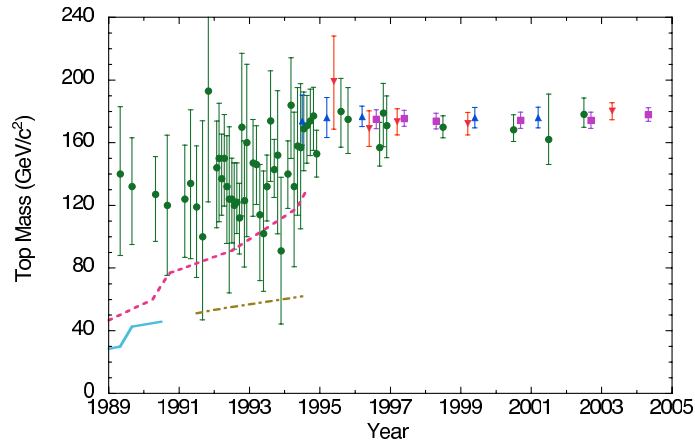


Fig. 2. – (Colour on-line) The evolution in time of the top mass value extracted from electroweak precision fits at LEP (green circles), together with the actual measurements at the Tevatron (red and blue triangles, magenta squares). Taken from ref. [19], page 24, fig. 16.

on heavy quarkonium that Mario and I wrote together, the first of them, on the role of resummed fragmentation contributions in the production of J/ψ at the Tevatron [24], as part of my doctoral thesis. Twenty years after its discovery, the J/ψ was still providing theorists with a lot of work, the focus having shifted to a detailed understanding of its production mechanism and to accurate evaluations of its cross sections, a quest that still goes on today.

A second contribution of Mario to precision phenomenology is the large transverse momentum resummation of heavy quark production in hadronic collisions [25], a paper that we wrote together in 1993 and my first foray into QCD. At the time I was a graduate student in Pavia. Mario, who eventually spent three years there, had just moved from a position with the INFN (the Italian Institute for Nuclear Physics) to a professorship in the University. He suggested that I look into combining the results of an article he had written a few years earlier with Aversa, Chiappetta and Guillet, the full set of higher-order QCD corrections to parton-parton scattering processes [26], with those from a paper from Mele and Nason [27], which calculated the boundary conditions of the fragmentation functions of massless partons into a massive quark. Together with the evolution kernels from Altarelli-Parisi [28] and Curci-Furmanski-Petronzio [29], these ingredients were what was needed to perform the resummation to next-to-leading logarithmic level of the cross section for heavy quark production at large transverse momentum. The availability of all the building blocks did not make the job look less daunting. Mario put me in touch with Jean-Philippe Guillet and with Paolo Nason (and later Michel Fontannaz), who kindly provided us with codes they had written for other projects but which contained the necessary ingredients. Then, patiently and with a keen understanding of what the correct outcome had to look like, he helped me make sense of a few thousand lines of CAPITALISED Fortran 77 code and eventually obtain physically meaningful results.

This work, also a part of my PhD thesis, has successively evolved into the so-called FONLL calculation [30] of heavy quark production, a formalism where the fixed order calculation at NLO [31] is matched with the resummed one from [25] and, at the same time, non-perturbative information extracted from LEP data is employed in predictions of

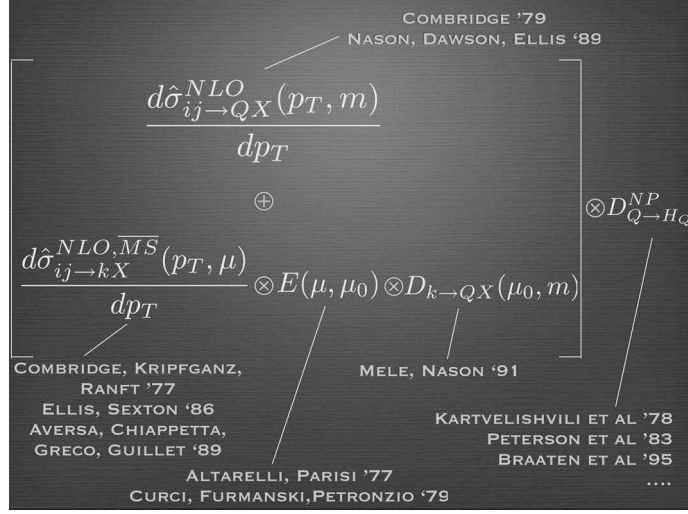


Fig. 3. – Schematic view of “previous art” used in the FONLL formalism, showing the authors of the main ingredients that enter the calculation.

heavy hadrons spectra in hadronic collisions. A schematic view of the FONLL calculation, in the form

$$(3) \quad d\sigma_{H_Q}^{FONLL} = [d\sigma_Q^{NLO} \oplus d\sigma_Q^{res}] \otimes D_{Q \rightarrow H_Q}^{non-pert},$$

where \oplus denotes a “matched” sum and \otimes a convolution, is given in fig. 3. It shows how FONLL draws from a large amount of previous work in QCD, achieving a remarkable synthesis. Eventually, this synthesis also proved to be quite effective, as it was shown capable of describing well heavy quark production in a number of different experiments, from ep collisions at HERA, to pp and $p\bar{p}$ at RHIC and the Tevatron and, more recently and almost 20 years after it was first introduced, pp collisions at the LHC.

5. – Conclusions

The history of heavy quarks is now almost forty years long, and Mario Greco’s career spanned all of it. His work has given many contributions to our present understanding, and in these proceedings I could only describe briefly some of it.

The very much abridged story of these forty years started here with the discovery of the fourth quark, charm. It may be easy, today and from the heights of our six known quarks, the heaviest of them with potential links to new physics beyond the electroweak scale, to take this fourth, barely “heavy” quark almost for granted. This would however mean doing injustice to the revolutionary proposal of Glashow, Iliopoulos and Maiani [32] which in 1970, introducing the charm quark, presciently captured the lepton-hadron symmetry which is now a cornerstone of the Standard Model. Indeed, its importance did not quite go unnoticed at the time, and Collins, Wilczek and Zee [33] could for instance write, in 1978 and before the Nobel prize effectively sealed the paternity of the Standard Model, “. . . we specialize to the standard sequential Weinberg-Salam-Glashow-Iliopoulos-Maiani model of weak interactions. . .”.

* * *

I wish to thank the Organisers of La Thuile conference for inviting me to give this talk. More importantly, I wish to thank Mario for the physics he has taught me and for the attitude towards physics that I have tried to learn from him. It has been a privilege to be his student and collaborator, and a real pleasure to work with him.

REFERENCES

- [1] AUBERT J. J. *et al.* (E598 COLLABORATION), *Phys. Rev. Lett.*, **33** (1974) 1404.
- [2] AUGUSTIN J. E. *et al.* (SLAC-SP-017 COLLABORATION), *Phys. Rev. Lett.*, **33** (1974) 1406.
- [3] APPELQUIST T. and POLITZER H. D., *Phys. Rev. Lett.*, **34** (1975) 43.
- [4] DE RUJULA A. and GLASHOW S. L., *Phys. Rev. Lett.*, **34** (1975) 46.
- [5] BACCI C., CELIO R. B., BERNA-RODINI M., CATON G., DEL FABBRO R., GRILLI M., IAROCCI E., LOCCI M. *et al.*, *Phys. Rev. Lett.*, **33** (1974) 1408.
- [6] DOMINGUEZ C. A. and GRECO M., *Lett. Nuovo Cimento*, **12** (1975) 439.
- [7] BRAMON A., ETIM E. and GRECO M., *Phys. Lett. B*, **41** (1972) 609.
- [8] HERB S. W., HOM D. C., LEDERMAN L. M., SENS J. C., SNYDER H. D., YOH J. K., APPEL J. A., BROWN B. C. *et al.*, *Phys. Rev. Lett.*, **39** (1977) 252.
- [9] GRECO M., *Phys. Lett. B*, **77** (1978) 84.
- [10] GRECO M., *Nucl. Phys. B*, **63** (1973) 398.
- [11] BOEHM M., JOOS H. and KRAMMER M., *Acta Phys. Austriaca*, **38** (1973) 123.
- [12] SAKURAI J. J., *Phys. Lett. B*, **46** (1973) 207.
- [13] GOUNARIS G. J., *Nucl. Phys. B*, **68** (1974) 574.
- [14] ETIM E. and GRECO M., *Lett. Nuovo Cimento*, **12** (1975) 91.
- [15] NAKAMURA K. *et al.* (PARTICLE DATA GROUP COLLABORATION), *J. Phys. G*, **37** (2010) 075021.
- [16] ABE F. *et al.* (CDF COLLABORATION), *Phys. Rev. D*, **50** (1994) 2966.
- [17] ABE F. *et al.* (CDF COLLABORATION), *Phys. Rev. Lett.*, **74** (1995) 2626 [hep-ex/9503002].
- [18] GERDES D., "Observation of the top quark production in $\bar{p}p$ collisions with the Collider Detector at Fermilab", in *Proceedings of 9th Les Rencontres de Physique de la Vallée d'Aoste: Results and Perspectives in Particle Physics, 5-11 Mar 1995, La Thuile, Italy*, edited by GRECO M. (Frascati Physics Series, INFN).
- [19] QUIGG C., "Beyond the standard model in many directions", Lectures given at the *2nd Latin American School Of High-Energy Physics 1-14 Jun. 2003, San Miguel Regla, Mexico*, hep-ph/0404228; *Phys. Today*, **50**, issue No. 5 (1997) 20.
- [20] GRECO M., PANCHERI-SRIVASTAVA G. and SRIVASTAVA Y., *Nucl. Phys. B*, **171** (1980) 118.
- [21] CONSOLI M., GRECO M. and LO PRESTI S., *Phys. Lett. B*, **113** (1982) 415.
- [22] PETRELLI A., CACCIARI M., GRECO M., MALTONI F. and MANGANO M. L., *Nucl. Phys. B*, **514** (1998) 245 [hep-ph/9707223].
- [23] BODWIN G. T., BRAATEN E. and LEPAGE G. P., *Phys. Rev. D*, **51** (1995) 1125 [hep-ph/9407339].
- [24] CACCIARI M. and GRECO M., *Phys. Rev. Lett.*, **73** (1994) 1586 [hep-ph/9405241].
- [25] CACCIARI M. and GRECO M., *Nucl. Phys. B*, **421** (1994) 530 [hep-ph/9311260].
- [26] AVERSA F., CHIAPPETTA P., GRECO M. and GUILLET J. P., *Nucl. Phys. B*, **327** (1989) 105.
- [27] MELE B. and NASON P., *Nucl. Phys. B*, **361** (1991) 626.
- [28] ALTARELLI G. and PARISI G., *Nucl. Phys. B*, **126** (1977) 298.
- [29] CURCI G., FURMANSKI W. and PETRONZIO R., *Nucl. Phys. B*, **175** (1980) 27; FURMANSKI W. and PETRONZIO R., *Phys. Lett. B*, **97** (1980) 437.
- [30] CACCIARI M., GRECO M. and NASON P., *JHEP*, **9805** (1998) 007 [hep-ph/9803400]; CACCIARI M., FRIXIONE S. and NASON P., *JHEP*, **0103** (2001) 006 [hep-ph/0102134].
- [31] NASON P., DAWSON S. and ELLIS R. K., *Nucl. Phys. B*, **327** (1989) 49.
- [32] GLASHOW S. L., ILIOPOULOS J. and MAIANI L., *Phys. Rev. D*, **2** (1970) 1285.
- [33] COLLINS J. C., WILCZEK F. and ZEE A., *Phys. Rev. D*, **18** (1978) 242.

SESSION I - COSMOLOGY AND ASTROPHYSICS

<i>Dorothea Samtleben</i>	Measuring the Cosmic Microwave Background Radiation
<i>Laura Lopez-Honorez</i>	Scalar dark matter: A revision of the Inert Doublet Model
<i>Alexander Dolgov</i>	Contemporary gravitational waves from primordial black holes

Measuring the Cosmic Microwave Background Radiation

D. SAMTLEBEN for the QUIET COLLABORATION

Nikhef - Science Park, Amsterdam, The Netherlands

(ricevuto il 29 Settembre 2011; pubblicato online il 24 Gennaio 2012)

Summary. — The Cosmic Microwave Background Radiation (CMBR) has over the last four decades been measured to increasingly high precision and with that provided information on the early Universe to shape and scrutinize our current cosmological model. Here we provide an overview on the status and prospects of current and future measurements.

PACS 98.80.Es – Observational cosmology (including Hubble constant, distance scale, cosmological constant, early Universe, etc.).

PACS 98.70.Vc – Background radiations.

1. – Introduction

The Cosmic Microwave Background Radiation (CMBR) is a relict from the early Universe from the time of recombination when the Universe became transparent to photons, 400000 years after the Big Bang. It provides a picture of the early Universe and with that rich information on the content and dynamics of the Universe. While its temperature pattern has already been studied in detail and was instrumental in establishing the current cosmological model experiments have only in the last decade reached the sensitivity to additionally access the fainter polarization anisotropy. We will describe the status, prospects and potential of the measurements whereby illustrating the experimental challenge of polarization measurements with a focus on the Q/U Imaging Experiment (QUIET [1]).

2. – Temperature anisotropies

The temperature anisotropies reflect the acoustic oscillation pattern in the early Universe due to the density fluctuations at the time of decoupling of photons. After the first detection of the small anisotropies by the COBE satellite a good number of ground-based and balloon experiments contributed to characterizing their detailed characteristics which by now have also been measured on all sky to a very high precision by the WMAP satellite. As a Gaussian homogeneous and isotropic field all information of the

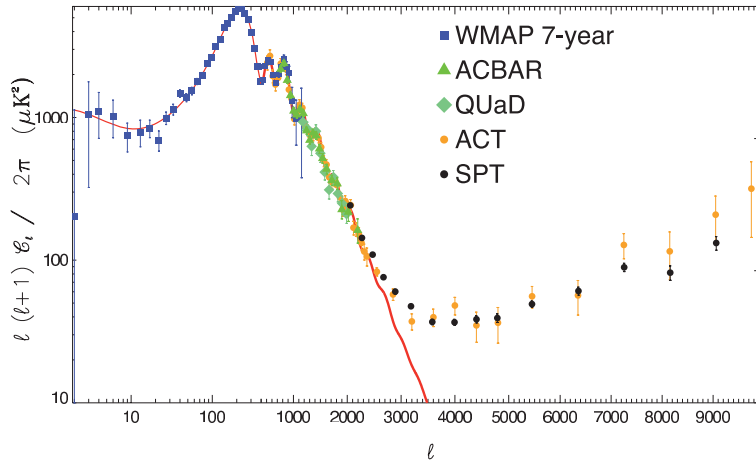


Fig. 1. – (Colour on-line) Measurements of the CMBR temperature power spectrum together with a fit of the best cosmological model in red. Foregrounds dominate above $l = 3000$ (from [2]).

anisotropy pattern can be condensed into the well-known power spectrum which allows the extraction of the parameters characterizing our cosmological model.

$$T(\theta, \phi) = \sum a_{lm} Y_{lm}(\theta, \phi) \quad C_l = \langle a_{lm} a_{lm}^* \rangle \quad \Delta T^2 = \frac{l(l+1)}{2\pi} C_l.$$

The Y_{lm} are spherical harmonics where the multipole l defines the angular scale (small l means large angular scale). To date the spectrum has been precisely measured in a multipole range of almost four decades (see fig. 1). Current measurements are fully compatible with Gaussian fluctuations. Future surveys like the Planck satellite will be able to much further constrain the level of possible non-Gaussianities and with that probe the predictions of different inflationary models.

The shape of the spectrum is determined by the content and dynamics of the Universe. The acoustic oscillation pattern of the plasma in the early Universe is imprinted on the photons released at the time of decoupling. The horizon size at that time provides a boundary condition that translates into a series of peaks at certain angular scales in the power spectrum of the CMBR anisotropies. The large power at the first peak of the spectrum is associated with the fluctuations of the size of the horizon at the time of decoupling and thus the position determines the angular size of the horizon as seen by today's observers, about 1 degree. Though seemingly large ($6000 \mu\text{K}^2$) the power at the first peak corresponds to a fluctuation of only 10^{-5} of the absolute CMBR temperature of 2.7K. Current CMBR power spectrum measurements allow determining the main parameters of the cosmological model like the baryon and dark matter content to the precision of few percent.

While the CMBR is often perceived as providing a complete picture of the early Universe it is also crucial to appreciate that its pattern can not uniquely be mapped to a single cosmological model but contains degeneracies in the allowed parameter space. The pattern that is visible today is not only affected by the conditions of the early Universe but also by the structure in the line of sight and its development as well as the curvature of the Universe.

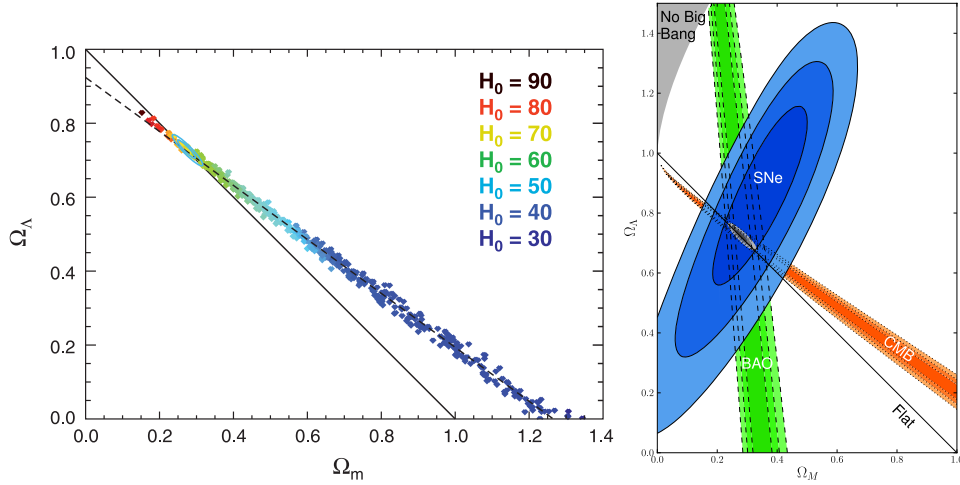


Fig. 2. – Left: Models in the Ω_Λ vs. Ω_m plane allowed by WMAP measurements for various values of the Hubble constant (from [5]). Right: Further constraints in the same plane coming also from supernovae and baryonic acoustic oscillations with systematic errors included (from [6]).

A prominent degeneracy is illustrated by the evidence that supports the existence of Dark Energy from CMBR measurements. Figure 2 from [3] shows the phase space of cosmological models in the Ω_Λ vs. Ω_m plane (energy densities of Dark Energy and matter) that is allowed by the WMAP measurements. Only when also considering external information like a measurement of the Hubble constant the phase space with no Dark Energy ($\Omega_\Lambda=0$) is ruled out⁽¹⁾. Measurements of Supernovae distances and baryonic oscillations also complement the information of the CMB to narrow the allowed parameter range considerably towards a flat Universe with a significant content of Dark Energy as seen in the right plot of fig. 2. The increasingly detailed measurements of the temperature anisotropies did not only help establish and specify the current cosmological model at high precision but also provide a rich data set to scrutinize anomalies. As to date several unresolved anomalies have been reported (see, *e.g.*, [7]). A prominent large-scale anomaly is that the quadrupole ($l = 2$) and octupole ($l = 3$) as measured by WMAP are closely aligned also with the ecliptic plane. Though a cosmological origin seems unlikely no instrumental or systematic feature could be proven to account for this distinct feature though the suspicion of possible subtle scan-induced issues has been raised [8]. The new full-sky survey by the Planck satellite will soon be able to shed more light on this with an independent measurement including different scanning and instrumental systematics.

3. – Polarization anisotropies

The polarization pattern is conventionally split into orthogonal contributions named “E”- and “B”-modes which contain gradient and curl components, respectively. E-modes

⁽¹⁾ By now the first evidence for Dark Energy from CMB measurements alone has been reported by ACT, breaking the previous degeneracy by adding CMBR lensing information [4].

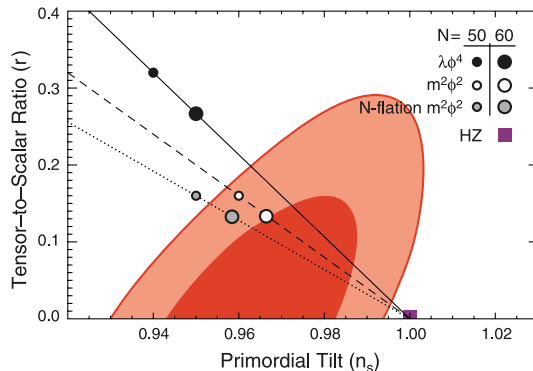


Fig. 3. – (Colour on-line) Various inflationary models are compared in the plane of $r = T/S$ and n_s to the allowed phase space from WMAP measurements which is indicated in red (from [3]).

derive from the same physical origin as the temperature anisotropies, namely the density fluctuations and the associated dynamics and are one order of magnitude smaller than the temperature anisotropies, corresponding to a signal size of μK size. The E-mode polarization directly derives from the flow of the photons between hot and cold spots. As the density fluctuations have by now been measured to high precision by the CMBR temperature data the resulting model predicts also a well-defined polarization pattern with it, that can be cross-checked with the polarization measurements and has been confirmed by current E-mode power spectrum measurements. In stacking the maps of polarization data from hot and cold temperature spots in the WMAP data the expected polarization pattern around those regions could also already be visualized [3].

B-modes are expected from lensing of the E-modes due to matter in the line of sight, but in addition most excitingly also as imprint of primordial gravitational waves in the inflationary era. The B-mode signal due to lensing is expected at more than an order of magnitude smaller size than the E-modes. The size of the B-mode signal deriving from primordial gravitational waves is dependent on the energy scale of inflation and commonly parametrized by the tensor-to-scalar ratio $r = T/S$. Current limits constrain its expected size to smaller than $\sim 100 \text{ nK}$.

The phase space of inflationary models can be parametrized by r together with the slope n_s of the primordial power spectrum whereby n_s is predicted to deviate slightly from 1. Several models are displayed in this parameter space in fig. 3 together with the current best constraints from measurements. The slope n_s has been measured to 0.97 ± 0.012 and the best constraint on r of $r < 0.2$ also still comes from the CMBR temperature measurements together with supernovae and baryonic acoustic oscillation measurements which cannot constrain it further. The best limit on r from polarization data alone comes from the measurements by BICEP at $r < 0.7$ [9].

Upcoming polarization experiments aim at providing sensitivities to reach $r = 10^{-2}$, corresponding to signal sizes of tens of nK and the interesting regime of inflationary energy scales of the order of the GUT energy scale. The CMBR polarization thus provides a unique view on the earliest moments of the Universe and accesses energies that colliders cannot explore, with this complementing the measurements in High Energy Physics laboratories in a highly interesting phase space.

4. – The experimental challenge

In order to access the subtle signature of inflation in the CMBR polarization a significant improvement in sensitivity is needed. As current technologies operate close to fundamental limits this step requires large detector arrays. Large bolometer arrays of the order of several 100 detectors are being built and some already operating. The current most sensitive CMBR array is the successor BICEP 2 of BICEP 1. It is already taking data since 2009 with 512 detectors at the South Pole. In November 2010 it has been followed by the first parts of the Keck array which in 2011 will be complemented to its final size of 5×512 detectors and will then be the most sensitive receiver operating.

Another probe of the inflationary B-modes already in the next year will come from the Planck satellite. Its sensitivity for B-modes from gravity wave reaches $r = 0.1$ and stems from large angular scales ($l = 5$) where also a big signal is expected (its size also depends on the details of reionization). With this different angular reach Planck complements the ground-based measurements in the B-mode search.

Now that the required sensitivity can technically be reached there are still two big obstacles in the way of hunting the primordial B-modes, namely systematics and astrophysical foregrounds. It has yet to be shown that the level of instrumental systematics can be controlled to the required size of nK. And the signal from the sky is not a clean view on the CMBR, but contaminated by signals from, *e.g.*, diffuse emission in our galaxy. The main foregrounds come from synchrotron and dust emission which both are polarized. As the frequency dependence of these foregrounds is different from the CMBR dependence the experiments strive to identify and eliminate the foregrounds by evaluating the sky at several frequencies. The synchrotron emission decreases with frequency and is dominant at frequencies below 100 GHz while the dust contamination is increasing with frequency and dominant above 100 GHz where current bolometer arrays are sensitive. The foregrounds can vary spatially and are at most frequencies expected to have larger signals than the tiny primordial B-mode signal, so it will be a significant challenge to prove the successful cleaning of the CMBR maps.

5. – The Q/U Imaging Experiment (QUIET)

The QUIET instrument has in contrast to most other current CMBR polarization experiments been built using coherent amplifier technology. This allows the instantaneous measurement of both linear polarization Stokes parameters Q and U in a single pixel and with this provides an excellent handle for the control of polarization systematics. Building on the planar polarimetry receiver developments at the Jet Propulsion Laboratory (JPL) [10] polarimeters at 40 GHz (Q-band) and 90 GHz (W-band) had been developed which were used to build a 19 and a 91 element receiver array, respectively. Both receivers were subsequently installed from summer 2008 till the end of 2010 on the former CBI platform in the Atacama desert in Chile. With its low frequencies QUIET complements the reach of other CMBR experiments using bolometer arrays, which are measuring at frequencies > 100 GHz. The instantaneous sensitivity of the QUIET arrays of ~ 70 (85) $\mu\text{K}\sqrt{s}$ made them the most sensitive HEMT polarization receivers in the world.

Four patches of the sky of 400 square degrees each were chosen to allow almost continuous observing and at the same time minimize the expected potential foreground contamination from the diffuse galactic emission. Two patches in the galactic plane were observed during the time when none of these selected patches were visible.

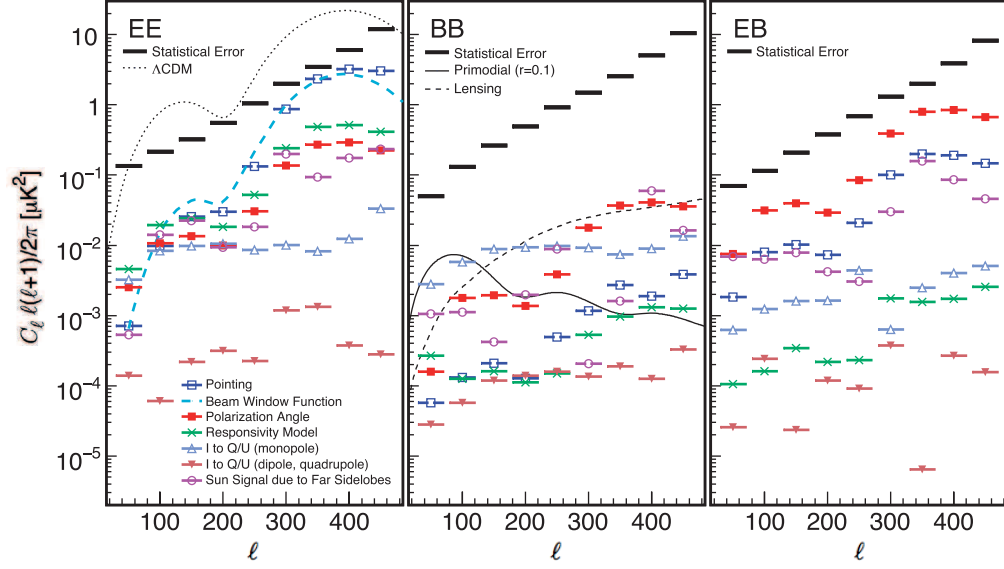


Fig. 4. – The different systematic errors as evaluated in detailed simulations for the QUIET experiment are shown for the E-mode and B-mode spectra as well as the EB-spectra also in comparison to the statistical error (from [11]).

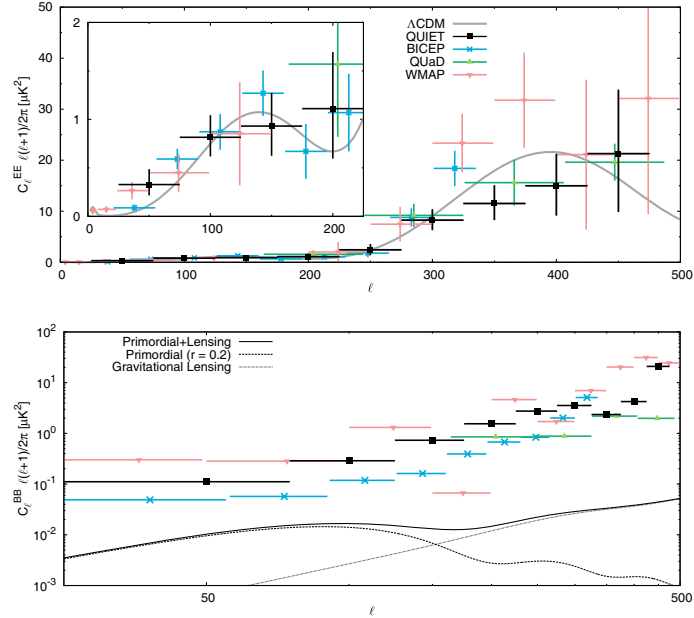


Fig. 5. – Top: Measurements of the E-mode power spectrum with 68% CL error bars together with the Λ CDM model. Bottom: 95% upper limits on the B-mode power spectrum. Expectations from the Λ CDM model are shown with the highest still allowed contribution from primordial gravity waves ($r = 0.2$) (from [11]).

The data streams were switched and differenced at two different frequencies (4 kHz and 50 Hz) in order to suppress the impact of $1/f$ noise and imperfections of the detection chains in the receiver. In addition possible ground-contamination was minimized through subtraction of ground-templates and the evaluation of the power spectrum by cross-correlating maps observed with different boresight rotations of the receiver.

The analysis of the Q-band data has been finished [11] and the analysis of W-band is underway with a data set with a factor of two better sensitivity. The analysis was performed in a blind way which means that selection criteria were chosen based on the studies of null spectra where two halves of the data were differenced. Though common in high energy physics experiments this philosophy has not yet made its way into the increasingly sophisticated analyses of complex cosmological data and this analysis is one of a few pioneering this approach for CMBR measurements.

The systematics were evaluated through multiple simulations and found to be minor compared to the statistical error. The various contributions are shown in comparison to the statistical error in fig. 4. The main contribution for B-modes comes from instrumental features leading to leakage of the temperature signal into the polarization signal (I to Q/U). The leakage could in the future be corrected for and thus suppress the systematics further by an order of magnitude. For B-modes these systematics are already the lowest reported to date ($r = 0.1$) at the angular scales relevant for the signature of primordial gravity waves ($l = 100$).

The final Q-band E-mode spectra and limits on the B-spectrum are shown in fig. 5 in comparison to other results. QUIET confirms at lower frequency the only measurement of the first peak in the E-mode power spectrum at 150 GHz. The measured B-mode spectrum is consistent with no signal.

Having successfully proven the potential of the technology with good sensitivity and low systematics the planning for an expansion of the QUIET arrays is now underway to achieve sensitivities for measuring $r \simeq 10^{-2}$.

6. – Outlook

The CMBR measurements have opened a window to rich information on the early Universe. The continuous improvements in the sensitivity allow now to start investigating on the subtle signature from primordial gravity waves from the very first moments of the Universe in the CMBR polarization pattern. Already in the upcoming years an interesting phase space can be explored which will help to shape the theoretical standard models in both cosmology and particle physics.

REFERENCES

- [1] quiet.uchicago.edu.
- [2] SHIROKOFF E. *et al.*, *Astrophys. J.*, **736** (2011) 61, arXiv:1012.4788v2.
- [3] KOMATSU E. *et al.*, *Astrophys. J. Suppl. Ser.*, **192** (2011) 18.
- [4] SHERWIN B. *et al.*, *Phys. Rev. Lett.*, **107** (2011) 021302, arXiv:1105.0419v2.
- [5] LARSON D. *et al.*, *Astrophys. J. Suppl. Ser.*, **192** (2011) 16.
- [6] AMANULLAH *et al.*, *Astrophys. J.*, **716** (2010) 712.
- [7] BENNETT C. L. *et al.*, *Astrophys. J. Suppl. Ser.*, **192** (2011) 17.
- [8] LIU HAO and LEI TI-PEI, *Astrophys. J.*, **732** (2011) 2.
- [9] CHIANG H. C. *et al.*, *Astrophys. J.*, **711** (2010) 1123.
- [10] KANGASLAHTI P. *et al.*, *Microwave Symposium Digest, IEE MTT-S International* (2006) p. 89.
- [11] QUIET COLLABORATION, *Astrophys. J.*, **741** (2011) 111, arXiv:1012.3191v2.

Scalar dark matter: A revision of the Inert Doublet Model

L. LOPEZ-HONOREZ

Service de Physique Théorique, Université Libre de Bruxelles - 1050 Bruxelles, Belgium

(ricevuto il 29 Settembre 2011; pubblicato online il 24 Gennaio 2012)

Summary. — The Inert Doublet Model (IDM) is a simple and yet very rich extension of the Standard Model which provides interesting scalar dark matter candidates. In these proceedings, we show that annihilation into 3 body final states $WW^* \rightarrow \bar{f}f'$ can significantly affect the viable parameter space of the IDM below the W threshold as well as the prospects for direct and indirect detection searches. We also show that the new viable region of the IDM between ~ 80 – 150 GeV is already almost completely ruled out by the most recent results of the Xenon 100 experiment.

PACS 95.35.+d – Dark matter (stellar, interstellar, galactic, and cosmological).

PACS 12.60.-i – Models beyond the standard model.

PACS 12.60.Fr – Extensions of electroweak Higgs sector.

1. – Introduction

Even though dark matter accounts for about 23% of the energy density of the Universe [1], we do not yet know its true substance. Among the zoo of dark matter candidates now available in the literature, the inert dark matter particle has earned a special place as a representative candidate of weakly interacting scalar dark matter.

In the inert doublet model, a Higgs doublet H_2 , odd under a new Z_2 symmetry, is added to the standard model particle content. The scalar potential of this model is given by

$$V = \mu_1^2 |H_1|^2 + \mu_2^2 |H_2|^2 + \lambda_1 |H_1|^4 + \lambda_2 |H_2|^4 + \lambda_3 |H_1|^2 |H_2|^2 + \lambda_4 |H_1^\dagger H_2|^2 + \frac{\lambda_5}{2} \left[(H_1^\dagger H_2)^2 + \text{h.c.} \right],$$

where H_1 is the Brout-Englert-Higgs doublet (referred to as Higgs in the following), and λ_i and μ_i are real parameters. Four new physical states are obtained in this model: two charged states, H^\pm , and two neutral ones, H^0 and A^0 . We choose H^0 to be the lightest inert particle, $m_{H^0}^2 < m_{A^0}^2, m_{H^\pm}^2$ and the dark matter candidate. In our study, we will use the following free parameters: the combination $\lambda_L = (\lambda_3 + \lambda_4 + \lambda_5)/2$ corresponding to the scalar coupling of a pair of H_0 to the Higgs particle h ; m_{H^0} , the H_0 mass;

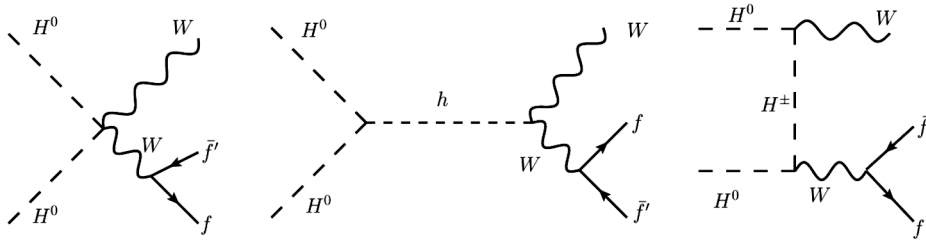


Fig. 1. – The Feynman diagrams that contribute, in the unitary gauge, to the $H^0 H^0$ annihilation into the three-body final state $WW^* \rightarrow Wf\bar{f}$ within the inert doublet model.

$\Delta m_{A^0} = m_{A^0} - m_{H^0}$ and $\Delta m_{H^\pm} = m_{H^\pm} - m_{H^0}$, two mass splittings between the inert scalars, and the Higgs mass, m_h . Notice that the λ_2 parameter has a small impact on the dark matter analysis. We take into account all the known theoretical and experimental constraints on this model—see [2] and [3]. This model has been extensively studied in a number of recent works (see [4] and references therein). It was shown that the dark matter relic density constraint can be satisfied for restricted values of m_{H^0} . Four viable regions can be distinguished: a small mass regime with $m_{H^0} \sim 8$ GeV [5, 6], a large mass regime with $m_{H^0} > 500$ GeV [7, 3, 8] and two intermediate mass regime: $m_{H^0} \lesssim M_W$ [2, 3] and $m_{H^0} \gtrsim M_W$ (as recently pointed out in [9]).

On general grounds annihilation of dark matter particles can receive large contributions from three-body final states consisting of a real and a virtual massive particle [10–12]. In [4], we pointed out that the annihilation into the three-body final state WW^* ($\rightarrow Wf\bar{f}$), are important in the intermediate mass region below the W threshold. Moreover, in ref. [9], we demonstrated the existence of a new viable region of the inert doublet model featuring dark matter masses between M_W and about 160 GeV. In that mass regime, the correct relic density is obtained thanks to cancellations between different diagrams contributing to dark matter annihilation into gauge bosons (W^+W^- and Z^0Z^0). In these proceedings, we summarize the impact of the inclusion of the three-body final state WW^* on the IDM and show that the new viable region of the IDM, just above W threshold, is almost ruled out by direct detection experiments.

2. – Impact of the WW^* annihilation processes for fixed parameters

In order to clarify how important the annihilation of dark matter into WW^* ($H^0 H^0 \rightarrow WW^* \rightarrow Wf\bar{f}$) can be in the inert doublet model, we first focus on the three-body annihilation cross section $\sigma(H^0 H^0 \rightarrow WW^*)$ fixing the free parameters of the model without imposing the WMAP relic abundance constraint [1]. In fig. 1, we represent the three diagrams contributing to the annihilation of dark matter into WW^* . For the range of parameters that we consider here ($m_{H^0} < m_{A^0}, m_{H^\pm}$ and $m_{H^0} \lesssim M_W$), their amplitudes depend weakly on m_{A^0} (only through the Higgs width) and on m_{H^\pm} (the H^+ mediated diagram is suppressed by the t -(u -)channel propagator). $\sigma(H^0 H^0 \rightarrow WW^*)$ is however much more sensitive to m_{H^0} , λ_L (sign and magnitude), and m_h .

In fig. 2, the left panels compare the two- and three-body annihilation rates at low velocity, denoted by σv , for three different Higgs masses $m_h = 120$ (top), 150 (middle) and 200 (bottom) GeV. The two-body annihilation rate that has been thought to drive indirect detection processes (well) below the W threshold is $H^0 H^0 \rightarrow h \rightarrow f\bar{f}$. It is

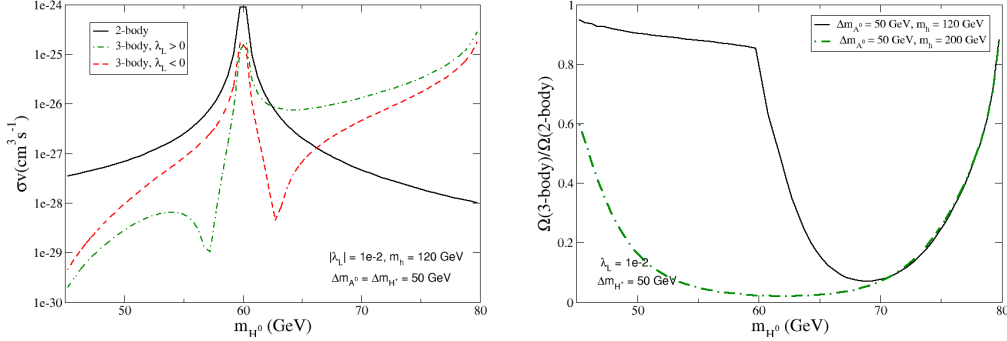


Fig. 2. – Annihilation rates and relic density ratios as a function of m_{H^0} for $|\lambda_L| = 10^{-2}$ and $\Delta m_{A^0} = \Delta m_{H^\pm} = 50$ GeV. Left panel: Comparison between the three-body and the two-body annihilation rate, σv , as a function of the dark matter mass for the two possible signs of λ_L and $m_h = 120$ GeV. Right panel: Ratio between the relic density including the three-body final state and the relic density for two-body final states only for $m_h = 120$ GeV and 200 GeV.

a Higgs-mediated process, whose amplitude depends on λ_L and on the Yukawa coupling of the outgoing fermions f to the Higgs. We see in fig. 2 that the three-body process can actually compete with the two-body ones. This is related to the Yukawa suppression present in $\sigma v_{2\text{-body}}$ and to the large multiplicity of final states associated with WW^* ($\rightarrow \sum_f W f f'$) processes. $\sigma v_{3\text{-body}}$ generically increases as m_{H^0} gets closer to M_W and its dependence in the scalar parameters λ_L, m_h is stronger around the Higgs resonance, $m_{H^0} \sim m_h/2$. More specifically, the presence of a trough in $\sigma v_{3\text{-body}}$ next to $m_{H^0} = m_h/2$ is due to the interference between the purely gauge diagram and the Higgs-mediated diagram (left and central diagrams in fig. 1). Because of such interference, the three-body cross section for $\lambda_L > 0$ (dash-dotted line) is larger than that for $\lambda_L < 0$ (dashed line) above the Higgs resonance but smaller than it below the resonance. In any case, the crucial point for us is that the three-body cross section is not negligible at all, especially next to the W threshold.

We can now compare the relic density obtained for two-body final states only (denoted as $\Omega(2\text{-body})$) with the one that includes the final state WW^* (denoted as $\Omega(3\text{-body})$ and referred to as the 3-body relic density). Let us mention that for our calculations, we have used a modified version of micrOMEGAs, see [13] and references therein, in which we incorporated the annihilation into the three-body final state WW^* . To illustrate the effect of the three-body final state on the relic abundance, we show in the right panels of fig. 2 the ratio $\Omega(3\text{-body})/\Omega(2\text{-body})$ as a function of m_{H^0} for two values of the Higgs masses $m_h = 120$ and 200 GeV.

A ratio equal to 1 means that the three-body process gives a negligible correction to the calculation of the relic density. Clearly, that is not the case. The ratio tends to 1 for m_{H^0} close to M_W , where the annihilation into W^+W^- is efficient, and for $m_{H^0} \ll M_W$, where the three-body annihilation is suppressed, but in the intermediate region the three-body final state plays a major role, giving rise to a correct relic density significantly smaller than the two-body one. An effect that is present for every Higgs mass and can lead to an overestimation of the predicted relic density by more than one order of magnitude. Notice that using smaller Δm_{A^0} , the coannihilation through the process $H^0 A^0 \rightarrow Z^* \rightarrow f \bar{f}'$ increases the effective annihilation rate that drives the relic

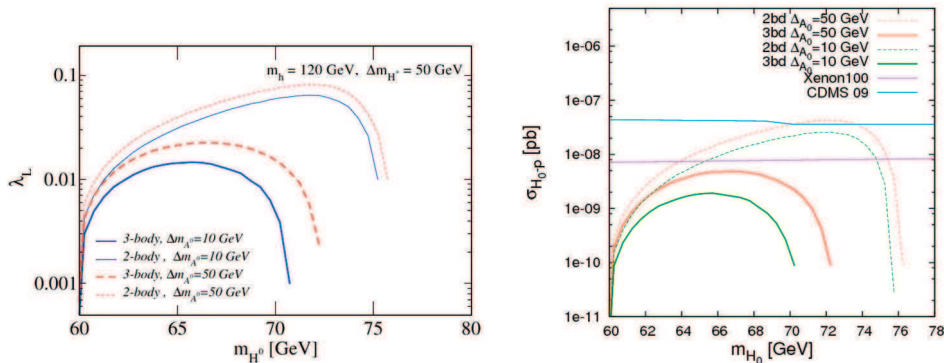


Fig. 3. – The viable parameter space for $m_h = 120$ GeV (left panel) and the corresponding WIMP-nucleon elastic scattering cross section (right panel). Along the lines $\Omega h^2 = 0.11$. The thick lines are the result including the final state WW^* , the thin lines correspond to 2-body final states only.

abundance. They also reduce the impact of three-body process on the relic density. It can be shown though [9] that the effect of the three-body final state remains important over a significant portion of the viable parameter space of the inert doublet model.

3. – The impact of WW^* on the viable parameter space

We can now study the impact of the three-body process on the viable parameter space, *i.e.* the parameter space determined by requiring that the predicted relic abundance be compatible with the observed density of dark matter [1]. For definiteness, we focus on $m_h = 120$ GeV with $\lambda_L > 0$. The left panel of fig. 3 shows the viable parameter space of the intermediate mass range of the inert dark matter model in the plane (λ_L, m_{H^0}) for $\Delta m_{H^\pm} = 50$ GeV, and two different values of Δm_{A^0} , 10 GeV (more coannihilations) and 50 GeV. The thin lines in these figures correspond to the viable regions if only two-body final states are considered. The thick lines, on the contrary, correspond to the *genuine* viable regions, those obtained by taking into account two- and three-body final states in the calculation of the relic density. We see that, as a consequence of the three-body final state contribution to the annihilation rate of inert Higgs dark matter, the required value of λ_L is smaller at any given mass, and the maximum allowed value of m_{H^0} gets reduced by several GeVs (without taking into account cancellations, see sect. 4). The modification of the viable parameter space, induced by the annihilation into the three-body final state WW^* , appears to be a generic feature of the inert doublet model. A feature that is present over a wide range of m_{H^0} quite independently of the other parameters of the model. As a consequence, the prospects for direct, indirect detection but also Higgs searches have to be reexamined.

In the inert Higgs model, the $H^0 N$ scattering cross section, $\sigma_{H^0 N}$, relevant for direct detection is Higgs-mediated and is proportional to λ_L^2 . Given the new allowed values of λ_L that were derived above, $\sigma_{H^0 N}$ appears to be significantly reduced with respect to the two-body result used, until now, in the literature. This is illustrated in the right panels of fig. 3 where the prediction for $\sigma_{H^0 N}$ are shown along the viable lines of the inert doublet model for $m_h = 120$. For comparison, in this figure we also show the current limit from CDMS [14] and the recent results of the Xenon100 experiment [15]. Notice from

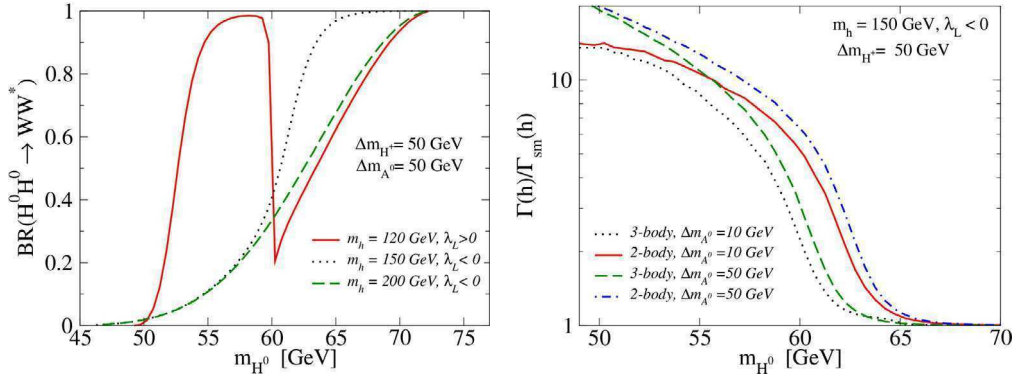


Fig. 4. – Left panel: Annihilation branching ratio into the three-body final state WW^* along the viable regions of the inert doublet model. Right panel: Ratio between the Higgs branching ratios in the inert doublet model and in the standard model along the viable regions for $m_h = 150$ GeV. λ_L was taken to be negative and $\Delta m_{H^\pm} = 50$ GeV.

the figure that the correct direct detection cross section can be more than two orders of magnitude smaller than the one obtained for two-body final states leading to less stringent constraints on the IDM from the present bounds set by direct detection searches.

The indirect detection signals of inert Higgs dark matter are also altered by the existence of the three-body final state WW^* . On the one hand, these signals should be now computed along new regions, due to the modified viable parameter space. On the other hand, in these new regions the annihilation cross section and branching ratios typically receive large corrections from the three-body final state WW^* . As a result, the spectrum of photons, neutrinos, positrons and antiprotons expected from inert Higgs annihilation will be different, changing its indirect detection prospects. In the left panel of fig. 4, we show that the three-body final state WW^* becomes dominant over a sizeable region of the viable parameter space.

In the inert doublet model, the Higgs boson can decay also into $H^0 H^0$ and $A^0 A^0$, increasing the Higgs decay width and modifying its branching ratios. The contribution to the Higgs decay with from the decay into the inert scalars is proportional to λ_L^2 , so that it will be affected by the three-body final state WW^* via the new viable parameter space. In the right panel of fig. 4, we illustrate for $m_h = 150$ GeV how the Higgs decay width can be modified when including the three-body final state in the determination of the relic abundance. This should be taken into account for Higgs searches at colliders.

4. – Cancellations in the $m_{H^0} > M_W$ regime

Above the W threshold, $m_{H^0} > M_W$, dark matter annihilation into $W^+ W^-$ becomes kinetically allowed, with the result that the total annihilation cross section tends to be rather large. Typically, the pure gauge contributions (*i.e.* setting all the inert scalar couplings to zero) give rise to annihilation cross sections much larger than those required to obtain the correct relic density ($\sigma v \sim 3 \times 10^{-26}$ cm³/s), so that it seems difficult to satisfy the dark matter constraint in this mass range. In ref. [9] we have shown⁽¹⁾ that

⁽¹⁾ See also [16] and [4].

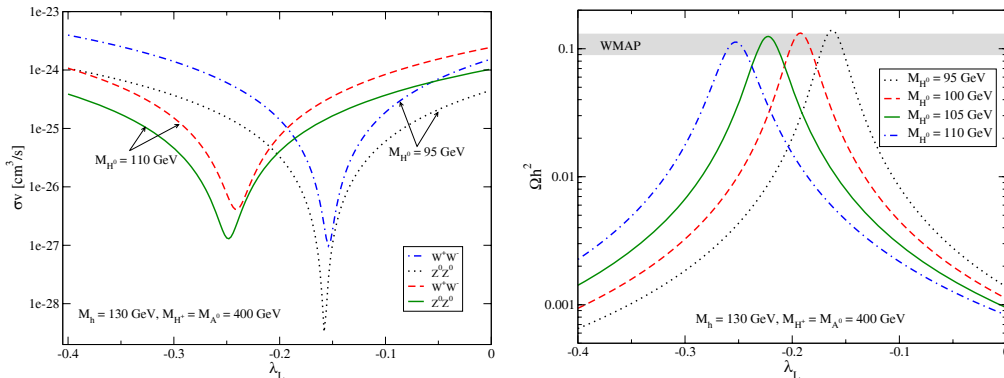


Fig. 5. – Left panel: The dark matter annihilation cross section (at low velocity) into W^+W^- and Z^0Z^0 as a function of λ_L for two different values of m_{H^0} : 95 GeV and 110 GeV. Right panel: Relic density.

taking advantage of the interference among the different diagrams that contribute to dark matter annihilation into gauge bosons, it is possible to satisfy the relic density constraint for $m_{H^0} \gtrsim M_W$. Thus, opening up a new viable region of the inert doublet model.

It is easy to show that a cancellation between the diagram contributing to the annihilation into two gauge bosons occurs for $\lambda_L \approx -2(m_{H^0}^2 - (M_h/2)^2)/v^2$. In the following, we refer to that condition as the cancellation condition. Hence, cancellations take place for $\lambda_L > 0$ if $m_{H^0} < M_h/2$ and for $\lambda_L < 0$ if $m_{H^0} > M_h/2$. Notice also that the cancellation condition is the same for both final states, W^+W^- and Z^0Z^0 , indicating that both processes will be simultaneously suppressed. Suppressing the annihilations into W^+W^- and Z^0Z^0 is not enough to ensure a small dark matter annihilation cross section. In addition, we must make sure that annihilation into the other possible final states is not kinematically allowed. In the following, we will see that the viable models taking advantage of the cancellations feature $m_{H^0} < M_h, m_t$.

5. – Examples

The cancellation effects we have described are illustrated in the left panel of fig. 5, which shows the dark matter annihilation cross sections into W^+W^- and Z^0Z^0 as a function of λ_L . For this figure we set $M_h = 130$ GeV, $M_{H^\pm} = M_{A^0} = 400$ GeV, and we consider two different values of m_{H^0} : 95 GeV and 110 GeV. The cancellation condition tells us that the cancellations should take place for negative values of $\lambda_L = -0.16$ and -0.26 , respectively, which is in good agreement with the full numerical treatment of the annihilation cross section. We observe that the larger m_{H^0} the larger the value of $|\lambda_L|$ required to obtain cancellations.

Since $\Omega h^2 \propto 1/\sigma v$, we expect these cancellations in the annihilation cross section to increase significantly the inert Higgs relic density, opening up the possibility of finding viable models for $m_{H^0} \gtrsim M_W$. This is illustrated in the right panel of fig. 5.

6. – The new viable region and the constraints from direct detection searches

In ref. [9], we have performed a systematic analysis of this new viable region of the parameter space using a Markov Chain Monte Carlo (MCMC). The left panel of fig. 6

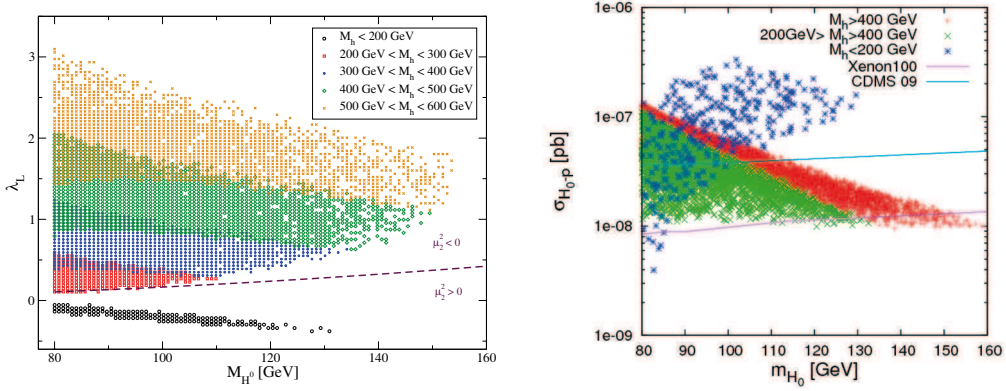


Fig. 6. – (Colour on-line) Left panel: The new viable region projected on the plane (m_{H^0}, λ_L) . The different symbols (and colors) distinguish among the possible ranges of M_h . The dashed line is the contour $\mu_2^2 = 0$. Right panel: scattering cross section relevant for direct detection searches.

shows the new viable region of the inert doublet model in the plane (m_{H^0}, λ_L) . Notice that the value of m_{H^0} over the new region extends from M_W up to about 160 GeV. In λ_L , the range of possible values extends from -0.5 to about 3.0. A sharp contrast is observed between the models with $\lambda_L < 0$ and those with $\lambda_L > 0$. In the former case ($\lambda_L < 0$), the maximum value of m_{H^0} is about 130 GeV and the Higgs boson is necessarily light, $M_h < 200$ GeV, as cancellations occur for $m_{H^0} > M_h/2$. In the latter case ($\lambda_L > 0$), the maximum value of m_{H^0} can be larger, strongly depending on the range of Higgs masses. Thus, for $200 \text{ GeV} < M_h < 300 \text{ GeV}$ the maximum m_{H^0} is only about 110 GeV whereas it can reach almost 160 GeV for the largest Higgs masses, $M_h > 500 \text{ GeV}$. It is also apparent from the figure, that for $\lambda_L > 0$ the larger the Higgs mass the larger λ_L must be.

In the inert Higgs model, the $H^0 p$ scattering process relevant for direct detection is Higgs-mediated and its cross section, $\sigma_{H_0 p}$, is directly proportional to the square of λ_L . Given the rather large values of λ_L we found, we foresee that $\sigma_{H_0 p}$ will be significant over the entire new viable region. In the right panel of fig. 6, we show the spin-independent dark matter-nucleon cross section, $\sigma_{H_0 p}$, as a function of m_{H^0} for our sample of models. $\sigma_{H_0 p}$ lies in a narrow range between 3×10^{-7} and 10^{-8} Pb. In this figure we show the constraints resulting from the present experimental (CDMS experiment [14] and Xenon100 [15]). We see that the very last results of the Xenon100 experiment exclude almost the entirety of this new viable region [15].

7. – Conclusions

We studied the impact, on the phenomenology of the inert doublet model, of dark matter annihilation into the three-body final state WW^* and of cancellations among the diagrams contributing to the annihilation just above the W threshold. The annihilation cross section into WW^* , $\sigma(H^0 H^0 \rightarrow WW^*)$, was shown to dominate the total dark matter annihilation cross section over a relevant portion of the parameter space. In consequence, the viable H_0 -coupling to the Higgs (λ_L) can be reduced by one order of magnitude. This implies that the scattering cross section ($\propto \lambda_L^2$) relevant for direct

detection searches can become two orders of magnitude smaller. Moreover, concerning the new viable parameter space of the IDM just above the W threshold, we have shown that the last results of the Xenon 100 experiment excluded almost all the models with masses $m_W < m_{H^0} < 160$ GeV.

* * *

I would like to thank the organizers of La Thuile 2011 for giving me the opportunity to present this work at the conference. The results presented in these proceedings were originally obtained in collaboration with CARLOS E. YAGUNA in ref. [4] and in ref. [9] I was supported in part by the IISN and by Belgian Science Policy (IAP VI/11).

REFERENCES

- [1] KOMATSU E. *et al.*, *Astrophys. J. Suppl.*, **180** (2009) 330.
- [2] BARBIERI RICCARDO, HALL LAWRENCE J. and RYCHKOV VYACHESLAV S., *Phys. Rev. D*, **74** (2006) 015007.
- [3] LOPEZ HONOREZ LAURA, NEZRI EMMANUEL, OLIVER JOSEF F. and TYTGAT MICHEL H. G., *JCAP*, **0702** (2007) 028.
- [4] LOPEZ HONOREZ LAURA and YAGUNA CARLOS E., *JHEP*, **09** (2010) 046.
- [5] HAMBYE THOMAS and TYTGAT MICHEL H. G., *Phys. Lett. B*, **659** (2008) 651.
- [6] ANDREAS SARAH, HAMBYE THOMAS and TYTGAT MICHEL H. G., *JCAP*, **0810** (2008) 034.
- [7] CIRELLI MARCO, FORNENGO NICOLAO and STRUMIA ALESSANDRO, *Nucl. Phys. B*, **753** (2006) 178.
- [8] HAMBYE T., LING F. S., LOPEZ HONOREZ L. and ROCHER J., *JHEP*, **07** (2009) 090.
- [9] LOPEZ-HONOREZ LAURA and YAGUNA CARLOS E., *JCAP*, **01** (2011) 002.
- [10] YAGUNA CARLOS E., *Phys. Rev. D*, **81** (2010) 075024.
- [11] CHEN XUE-LEI and KAMIONKOWSKI MARC, *JHEP*, **07** (1998) 001.
- [12] HOSOTANI YUTAKA, KO PYUNGWON and TANAKA MINORU, *Phys. Lett. B*, **680** (2009) 179.
- [13] BELANGER G., BOUDJEMA F., PUKHOV A. and SEMENOV A., *Comput. Phys. Commun.*, **180** (2009) 747.
- [14] AHMED Z. *et al.*, Results from the Final Exposure of the CDMS II Experiment (2009).
- [15] APRILE E. *et al.* (XENON100 COLLABORATION), *Phys. Rev. Lett.* **107** (2011) 131302, arXiv:1104.2549
- [16] LUNDSTROM ERIK, GUSTAFSSON MICHAEL and EDSJO JOAKIM, *Phys. Rev. D*, **79** (2009) 035013.

Contemporary gravitational waves from primordial black holes

A. D. DOLGOV

Università di Ferrara and INFN, Sezione di Ferrara - via Saragat 1, 44100 Ferrara, Italy
ITEP - Moscow, 117218, Russia

(ricevuto il 29 Settembre 2011; pubblicato online il 24 Gennaio 2012)

Summary. — Stochastic background of gravitational waves (GW) generated by the interactions between primordial black holes (PBH) in the early universe and by PBH evaporation is considered. If PBHs dominated in the cosmological energy density prior to their evaporation, GWs from the earlier stages (*e.g.*, inflation) would be noticeably diluted. On the other hand, at the PBH dominance period they could form dense clusters where PBH binary formation might be significant. These binaries would be efficient sources of the gravitational waves.

PACS 04.30.-w – Gravitational waves.

PACS 98.80.-k – Cosmology.

PACS 14.65.Jk – Other quarks (*e.g.*, 4th generations).

The registration of the gravitational waves generated in the early universe could bring an important information about inflation, possible (first order) cosmological phase transitions, topological defects, such as cosmic strings, etc. Very sensitive GW detectors such as LIGO and LISA may make the discovery opening a new era of gravitational wave astronomy. In particular, an observation of stochastic cosmological background of low frequency GWs could be a final proof of inflation. However, an absence of a such background would not mean that the universe was not in inflationary stage. First, the present day density of GWs depends upon the model of inflation and, second, there could be a mechanism which suppresses the density of GWs at post-inflationary stage. Such a mechanism is described in my talk. Though the inflationary background of GWs could be noticeably suppressed, a new higher frequency GWs would be generated by the suggested mechanism. The talk is based on two papers [1,2]. In the second one a detailed reference list is presented which is reduced here due to lack of space.

We consider GWs produced by the interactions between primordial black holes (PBH), as well as by their evaporation. PBHs are supposed to be very light, so they evaporated before the big bang nucleosynthesis (BBN) leaving no trace in the present day universe, except for GWs. The lifetime of an evaporating black hole with mass M is equal to [3]

$$(1) \quad \tau_{BH} = \frac{10240 \pi}{N_{eff}} \frac{M^3}{m_{Pl}^4},$$

where $m_{Pl} = 1.22 \cdot 10^{19} \text{ GeV} = 2.176 \cdot 10^{-5} \text{ g}$ is the Planck mass and N_{eff} is the number of particle species with masses smaller than the black hole temperature:

$$(2) \quad T_{BH} = \frac{m_{Pl}^2}{8\pi M}.$$

The corrections due to the propagation and back-capture of the evaporated particles [4], the so called grey factor, change this result by a factor of order unity and are not included here.

According to ref. [5], to avoid a conflict with BBN the lifetime of PBHs should be shorter than $t \approx 10^{-2} \text{ s}$ and thus the black holes should be lighter than

$$(3) \quad M < 1.75 \cdot 10^8 \left(\frac{N_{eff}}{100} \right)^{1/3} \text{ g}.$$

The temperature of such PBHs exceeds $3 \cdot 10^4 \text{ GeV}$ and correspondingly $N_{eff} \geq 10^2$.

Formation of PBHs from primordial density perturbations in the early Universe was considered in pioneering papers [6,7]. PBHs were formed when the density contrast, $\delta\rho/\rho$, at horizon was of the order unity or, in other words, when the Schwarzschild radius of the perturbation was of the order of the horizon scale. If PBHs were created at the radiation dominated stage, when the cosmological energy density was $\rho(t) = 3m_{Pl}^2/(32\pi t^2)$, and the horizon was $l_h = 2t$, the mass of such PBHs would be

$$(4) \quad M(t) = m_{Pl}^2 t \simeq 4 \cdot 10^{38} \left(\frac{t}{\text{s}} \right) \text{ g},$$

where t is the cosmological time.

The fraction, Ω_p , of the cosmological energy density of PBH produced by this mechanism depends upon the spectrum of the primordial density perturbations. If the usual flat Harrison-Zeldovich spectrum is assumed, then Ω_p would be quite small. We have not calculated Ω_p but have taken it as a free parameter of the model. One reason for that is that the spectrum of the density perturbations at small wavelengths is unknown. Moreover, there could be other mechanisms of PBH formation. In particular, in refs. [8,9] a model of PBH formation has been proposed which might lead to considerably larger probability of PBH formation. The mass spectrum of PBHs produced by the latter mechanism has the log-normal form

$$(5) \quad \frac{dN}{dM} = C \exp \left[\frac{(M - M_0)^2}{M_1^2} \right],$$

where C , M_0 , and M_1 are some model-dependent parameters. Quite naturally the central value of PBH mass distribution may be in the desired range $M_0 < 10^9 \text{ g}$. In this model the value of Ω_p may be much larger than in the conventional model based on the flat spectrum of the primordial fluctuations. We will not further speculate on the value of Ω_p and on the form of the mass spectrum of PBH. In what follows we assume for an order of magnitude estimate that the spectrum is well localized near some fixed mass M and that Ω_p is an arbitrary parameter. Different mechanisms of PBH production are reviewed, *e.g.*, in ref. [10].

The energy density of nonrelativistic PBHs drops down as $1/a^3$, while the energy density of the initially dominant relativistic matter drops as $1/a^4$, where $a = a(t)$ is the cosmological scale factor. So the relative contribution of PBH into the total energy density rises as

$$(6) \quad \Omega_{BH}(t) = \Omega_p a(t)/a_p = \Omega_p (t/t_p)^{1/2},$$

here $t_p = M/m_{Pl}^2$ is the PBH production time, related to their mass by eq. (4). So initially $\Omega_{BH}(t)$ rises as $t^{1/2}$ and at some stage it reaches unity and after that Ω_{BH} remains constant till the PBH evaporation. PBHs would begin to dominate in the cosmological energy density at $t = t_{eq} = M(m_{Pl}^2 \Omega_p^2)$, if $t_{eq} > \tau_{BH}$, eq. (1). This can be transformed into the lower limit on the PBH mass:

$$(7) \quad M > 6 \cdot 10^{-2} \left(\frac{N_{eff}}{100} \right)^{1/2} \frac{m_{Pl}}{\Omega_p} \simeq 10^{-7} \text{ g } \Omega_p^{-1}.$$

If condition (7) was fulfilled, the universe expansion regime was initially relativistic, radiation dominated (RD), then after $t = t_{eq}$ it became non-relativistic, matter dominated (MD). Later after PBH evaporation, $t > \tau_{BH}$ the universe returned to RD stage again, and only after very long time, $t = t_{LSS} \sim 10^5$ years, the expansion became matter dominated. After that time the large scale structures (galaxies, their clusters, etc.) began to form. As is known, cosmological structure formation took place at MD stage, when initially small primordial density perturbations started to rise due to gravitational instability. In our case the density perturbations started to rise at $t > t_{eq}$. According to the theory, at MD stage $\Delta \equiv \delta\rho/\rho \sim a(t)$, till the perturbations remain small, $\Delta \ll 1$. When Δ reaches unity, the perturbations quickly rise and as a result they become quite large, $\Delta \gg 1$. In the present day universe $\Delta \sim 10^5$ at the galactic scale.

In our scenario we expect formation of high density clusters of PBHs with density contrast which rose as $\Delta(t) = \Delta_{in}(t/t_{in})^{2/3}$, where $t_{in} \geq t_{eq}$ is the moment when the perturbation comes inside the cosmological horizon. The density contrast would reach unity at $t_1(t_{in})$ such that

$$(8) \quad \Delta[t_1(t_{in})] = \Delta_{in}[t_1(t_{in})/t_{in}]^{2/3} = 1 \quad \text{or} \quad t_1(t_{in}) = t_{in} \Delta_{in}^{-3/2}.$$

To this end the PBH lifetime should be longer than t_1 .

After the density contrast has reached unity, the cluster would decouple from the general cosmological expansion. In other words, the cluster stopped expanding together with the universe and, on the opposite, it would begin to shrink when gravity took over the free streaming of PBHs. So the cluster size would drop down and both n_{BH} and ρ_b would rise. The density contrast would quickly rise from unity to $\Delta_b = \rho_b/\rho_c \gg 1$, where ρ_c and ρ_b are, respectively, the average cosmological energy density and the density of PBHs in the cluster (bunch). It looks reasonable that the density contrast of the evolved cluster could rise up to $\Delta_b = 10^5$ – 10^6 , as in the contemporary galaxies. After the size of the cluster stabilized, the number density of PBH, n_{BH} , as well as their mass density, ρ_{BH} , would be constant too. But the density contrast, Δ_b would continue to rise as $(t/t_1)^2$ because ρ_c drops down as $1/t^2$. From time $t = t_1$ to $t = \tau_{BH}$ the density contrast

would additionally rise by the factor

$$(9) \quad \Delta(\tau_{BH}) = \Delta_b \left(\frac{\tau_{BH}}{t_1} \right)^2.$$

This rise is associated with the drop of the average cosmological energy density, $\rho \sim 1/t^2$, but not with the absolute rise of $\delta\rho$. This effect is absent in the present day universe because the time when Δ reached unity was close to the present universe age.

GWs could be generated in the processes of PBH scattering in the high density clusters and, in particular, the GW emission could proceed from the PBH binaries. Both processes are strongly enhanced in the clusters. The probability of scattering and binary formation rate are proportional to the square of the number density of PBHs, n_{BH} . However, the net effect on the cosmological energy density of the emitted GWs is linear in n_{BH} because it is normalized to the total cosmological energy density.

The cross-section of the graviton bremsstrahlung was calculated in ref. [11] for the case of two spineless particles (here black holes) with masses m and M under assumption that $m \ll M$. In non-relativistic approximation, the differential cross section is

$$(10) \quad d\sigma = \frac{64M^2m^2}{15m_{pl}^6} \frac{d\xi}{\xi} \left[5\sqrt{1-\xi} + \frac{3}{2}(2-\xi) \ln \frac{1+\sqrt{1-\xi}}{1-\sqrt{1-\xi}} \right],$$

where ξ is the ratio of the emitted graviton frequency, $\omega = 2\pi f$, to the kinetic energy of the incident black hole, *i.e.* $\xi = 2m\omega/\mathbf{p}^2$. In what follows we will use this expression for a simple estimate assuming that it is approximately valid for $m \sim M$.

The energy density of gravitational waves emitted at the time interval t and $t + dt$ in the frequency range ω and $\omega + d\omega$ is given by

$$(11) \quad \frac{d\rho_{GW}}{d\omega} = v_{rel} n_{BH}^2 \omega \left(\frac{d\sigma}{d\omega} \right) dt,$$

where n_{BH} is the number density of PBH and v_{rel} is their relative velocity. The latter is close to the virial velocity of PBHs in the cluster and can be about 0.1. As noted by the authors of ref. [11], Weizsäcker-Williams approximation is not valid. This means that there could be some difference between classical and quantum graviton emission.

The graviton bremsstrahlung proceeded till the PBH evaporation. Hence to find the total energy of the produced gravitons we need to integrate their energy spectrum over frequencies and redshift from τ_{BH} down to the moment of the cluster formation. Thus we obtain for the cosmological energy fraction of GWs:

$$(12) \quad \Omega_{GW}^{(brem.s)}(\omega_{max}, \tau_{BH}) \approx 16Q \left(\frac{v_{rel}}{0.1} \right) \left(\frac{\Delta}{10^5} \right) \left(\frac{N_{eff}}{100} \right) \left(\frac{\omega_{max}}{M} \right).$$

Here coefficient $Q > 1$ reflects the uncertainty in the cross-section due to the unaccounted for Sommerfeld enhancement [12]. Note that Δ may be considerably larger than 10^5 . For the details see ref. [2].

The frequency f_* of GW produced at time t_* during PBH evaporation, is redshifted down to the present day value, f , as

$$(13) \quad f = f_* \left[\frac{a(t_*)}{a_0} \right] = 0.34 f_* \frac{T_0}{T_*} \left[\frac{100}{g_S(T_*)} \right]^{1/3},$$

where $T_0 = 2.725$ K is the temperature of the cosmic microwave background radiation at the present time, $T_* \equiv T(t_*)$ is the plasma temperature at the moment of radiation of the gravitational waves, and $g_S(T_*)$ is the number of species contributing to the entropy of the primeval plasma at temperature T_* . It is convenient to express T_0 in frequency units, $T_0 = 2.7$ K $= 5.4 \cdot 10^{10}$ Hz.

The density parameter of the gravitational waves at the present time is related to cosmological time t_* as

$$(14) \quad \Omega_{GW}(t_0) = \Omega_{GW}(t_*) \left(\frac{a(t_*)}{a(t_0)} \right)^4 \left(\frac{H_*}{H_0} \right)^2,$$

where $H_0 = 100h_0$ km/s/Mpc is the Hubble parameter and $h_0 = 0.74 \pm 0.04$ [13].

Using expression for redshift (13) and taking the emission time $t_* = \tau_{BH}$ we obtain

$$(15) \quad \Omega_{GW}(t_0) = 1.67 \times 10^{-5} h_0^{-2} \left(\frac{100}{g_S(T_{BH})} \right)^{1/3} \Omega_{GW}(\tau_{BH}).$$

Now we find that the total density parameter of gravitational waves integrated up to the maximum frequency is

$$(16) \quad h_0^2 \Omega_{GW}(t_0) \approx 0.6 \cdot 10^{-21} \text{ K} \left(\frac{10^5 \text{ g}}{M} \right)^2,$$

where K is a numerical coefficient:

$$(17) \quad K = \left(\frac{v_{rel}}{0.1} \right) \left(\frac{\Delta}{10^5} \right) \left(\frac{N_{eff}}{100} \right) \left(\frac{Q}{100} \right) \left(\frac{100}{g_S(T_{BH})} \right)^{1/3}.$$

Presumably K is of order unity but since Δ may be much larger than 10^5 , see eq. (9), K may also be large.

Classical emission of GW at the scattering of non-relativistic bodies is well described in quadrupole approximation. If the minimal distance between the bodies is larger than their gravitational radii, the energy of gravitational waves emitted in a single scattering process is equal to

$$(18) \quad \delta E_{GW} = \frac{37\pi}{15} \frac{M^2 m^2 v}{b^3 m_{Pl}^6}, \quad v \ll 1,$$

where b is the impact parameter.

The differential cross-section of the gravitational scattering of two PBHs in non-relativistic regime, $q^2 \ll 2M^2$, is

$$(19) \quad d\sigma = \frac{M^2}{m_{Pl}^2} \frac{dq^2}{q^4} = \frac{2M^2}{m_{Pl}^2} b db$$

and the rate of the energy emission by the GWs is given by

$$(20) \quad d\rho_{GW} = \frac{74\pi v_{rel}}{15} \rho_{BH}^2 \frac{M^4}{m_{Pl}^8} \frac{d\omega}{2\pi} dt.$$

The energy density parameter of GW at the moment of BH evaporation can be obtained integrating this expression over time and frequency. Thus we obtain

$$(21) \quad \Omega_{GW}(\tau_{BH}) = 2 \cdot 10^{-10} \left(\frac{v_{rel}}{0.1} \right)^2 \left(\frac{\Delta_b}{10^5} \right) \left(\frac{N_{eff}}{100} \right) \left(\frac{10^5 \text{ g}}{M} \right).$$

If we allow for $b \sim r_g$, the energy density of GWs at the moment of PBHs evaporation might be comparable to unity.

Now we can calculate the relative energy density of GWs per logarithmic frequency interval at the present time:

$$(22) \quad \Omega_{GW}(f; t_0) \equiv \frac{1}{\rho_c} \frac{d\rho_{GW}}{d \ln f} \approx 2.4 \cdot 10^{-12} \alpha' \left(\frac{f}{\text{GHz}} \right) \left(\frac{10^5 \text{ g}}{M} \right)^{1/2},$$

where α' is the coefficient at least of order of unity:

$$(23) \quad \alpha' = \left(\frac{v_{rel}}{0.1} \right) \left(\frac{\Delta_b}{10^5} \right) \left(\frac{N_{eff}}{100} \right)^{3/2} \left(\frac{100}{g_S(T_{BH})} \right)^{1/4}.$$

It may be much larger, if $\Delta_b \gg 10^5$.

More efficient mechanism of GW emission may be radiation from the PBH binaries, if their number in the high density clusters is sufficiently high. To form the binary bound state PBHs should sufficiently cool down losing their kinetic energy. The cooling could be achieved by the energy loss to the gravitational wave radiation discussed above and by the dynamical friction [14]. A particle moving in the cloud of other particles would transfer its energy to these particles due to their gravitational interaction. However, one should keep in mind that the case of dynamical friction is essentially different from the energy loss due to gravitational radiation. In the latter case the energy leaks out of the system cooling it down, while dynamical friction does not change the total energy of the cluster. Nevertheless a particular pair of black holes moving toward each other with acceleration may transmit their energy to the rest of the system and became gravitationally captured forming a binary.

The dynamical friction time was estimated in ref. [15]. In both cases $v > \sigma$ and $v < \sigma$, where σ is the velocity dispersion, the characteristic time was of the order of

$$(24) \quad \tau_{DF} \approx \left(\frac{\sigma}{0.1} \right)^3 \left[\frac{25}{\ln(10^{-6}/\Omega_p)} \right] \left(\frac{100}{N_{eff}} \right) \left(\frac{M}{1 \text{ g}} \right) \left(\frac{10^6}{\Delta} \right) \tau_{BH}.$$

For PBH masses below a few grams dynamical friction would be an efficient mechanism of PBH cooling leading to frequent binary formation. Moreover, dynamical friction could result in the collapse of small PBHs into much heavier black hole. Even the whole high density cluster of PBHs could form a single black hole. These processes of heavier black hole formation would be accompanied by a strong burst of gravitational radiation.

The emission of GWs from a binary results in the energy loss which is compensated by a decrease of the radius of the binary and of the rotation period. As a result the system goes into the so-called inspiral regime. Ultimately the two rotating bodies coalesce and produce a burst of the gravitational waves. To reach this stage the characteristic time of the coalescence should be shorter than the lifetime of the system. In our case it is

the lifetime of PBH with respect to the evaporation. The coalescence time of the binary made of two BH with masses M_1 and M_2 can be easily calculated, see, *e.g.*, book [16]:

$$(25) \quad \tau_{co} = \frac{5R_0^4 m_{Pl}^6}{256M_1M_2(M_1 + M_2)},$$

where R_0 is the initial radius of the binary. This result is true for a circular orbit of the binary. In the case of elliptic orbit the eccentricity drops down due to GW emission and the system approaches to the circular one. We may use eq. (25) for an order of estimate of the lifetime of the binary.

There are two interesting limiting cases, when $\tau_{co} \gg \tau_{BH}$ and vice versa. In the first case the stationary orbit approximation is valid and each binary emits GWs with fixed frequency equal to twice the orbital frequency and the frequency spectrum is determined by the distribution of the binaries on their radius. As is shown in ref. [2], if the stationary regime was realized, the spectral density parameter today would be:

$$(26) \quad \Omega_{GW}^{(stat)}(f; t_0) \approx 10^{-8} \epsilon \left[\frac{N_{eff}}{100} \right]^{2/3} \left[\frac{100}{g_S(T(\tau_{BH}))} \right]^{1/18} \left[\frac{M}{10^5 \text{ g}} \right]^{1/3} \left[\frac{f}{\text{GHz}} \right]^{10/3},$$

where ϵ is the fraction of binaries with respect to the total number of PBHs in the cluster and $g_S(T(\tau_{BH}))$ is the number of the entropy degrees of freedom at the moment of PBH evaporation when the plasma temperature was equal to $T(\tau_{BH})$. Here the possibly weak redshift dilution of GWs by the factor $(\tau_{co}/\tau_{BH})^{2/9}$ is neglected.

If the system goes to the inspiral phase, then we would expect today a continuous spectrum in the range from $f_{min} \sim 10^7$ Hz to $f_{max} \sim 3 \cdot 10^{14}$ Hz. However if we take into account the redshift of the early formed binaries from the moment of their formation to the PBH decay, the lower value of the frequency may move to about 1 Hz.

PBHs could also directly produce gravitons by evaporation. The total energy emitted by BH per unit time and frequency ω (energy) of the emitted particles, is approximately given by the equation (see, *e.g.*, book [17]):

$$(27) \quad \left(\frac{dE}{dt d\omega} \right) = \frac{2N_{eff}}{\pi} \frac{M^2}{m_{Pl}^4} \frac{\omega^3}{e^{\omega/T_{BH}} - 1},$$

where T is the BH temperature (2). Due to the impact of the gravitational field of BH on the propagation of the evaporated particles, their spectrum is distorted [4] by the so-called grey factor $g(\omega)$, but we disregard it in what follows.

The frequency spectrum of the evaporated gravitons is not thermal because of the different redshifts in the course of the evaporation. According to the calculations of ref. [2] the spectral density parameter of GWs at $t = \tau_{BH}$ is equal to

$$(28) \quad \Omega_{GW}(\omega_*; \tau_{BH}) \approx \frac{2.9 \cdot 10^3 M^4 \omega_*^4}{\pi m_{Pl}^8} I \left(\frac{\omega_*}{T_{BH}} \right),$$

where

$$(29) \quad I \left(\frac{\omega_*}{T_{BH}} \right) = \int_0^{z_{max}} \frac{dz (1+z)^{1/2}}{\exp[(z+1)\omega_*/T_{BH}] - 1},$$

and

$$(30) \quad 1 + z_{max} = \left(\frac{\tau_{BH}}{t_{eq}} \right)^{2/3} \left(\frac{t_{eq}}{t_p} \right)^{1/2} = \left(\frac{32170}{N_{eff}} \right)^{2/3} \left(\frac{M}{m_{Pl}} \right)^{4/3} \Omega_p^{1/3}.$$

With respect to the thermal spectrum, spectrum (28) has more power at small frequencies due to redshift of higher frequencies into lower band and less power at high ω_* .

The spectral density of the evaporated gravitons today would be

$$(31) \quad \Omega_{GW}(f; t_0) = 2.7 \cdot 10^{-27} \left(\frac{N_{eff}}{100} \right)^2 \left(\frac{10^5 \text{ g}}{M} \right)^2 \left(\frac{f}{10^{10} \text{ Hz}} \right)^4 \cdot I \left(\frac{2\pi \cdot f}{T_0} \right),$$

where T_0 is the BH temperature redshifted to the present time:

$$(32) \quad T_0 = 4.5 \cdot 10^{15} \text{ Hz} \left(\frac{100}{g_S(T_{BH})} \right)^{1/12} \left(\frac{100}{N_{eff}} \right)^{1/2} \left(\frac{M}{10^5 \text{ g}} \right)^{1/2}.$$

The mechanisms of GWs generation considered here could create quite high cosmological fraction of the energy density of the relic gravitational waves at very high frequencies. Unfortunately at the lower part of the spectrum Ω_{GW} significantly drops down making such GWs outside the reach of LISA or LIGO. Still the planned interferometers DECIGO/BBO and detectors based on the resonance graviton-photon transformation could be sensitive to the predicted high-frequency GWs.

REFERENCES

- [1] DOLGOV A. D., NASELSKY P. D. and NOVIKOV I. D., arXiv: astro-ph/0009407.
- [2] DOLGOV A. D. and EJLLI D., *Phys. Rev. D*, **84** (2011) 024028, arXiv: 1105.2303.
- [3] HAWKING S. W., *Phys. Rev. D*, **13** (1976) 191.
- [4] PAGE D. N., *Phys. Rev. D*, **13** (1976) 198.
- [5] CARR B. J., KOHRI K., SENDOUDA Y. *et al.*, *Phys. Rev. D*, **81** (2010) 104019.
- [6] ZELDOVICH YA. B. and NOVIKOV I. D., *Astron. Zh.*, **43** (1966) 758; *Sov. Astron.*, **10** (1967) 602.
- [7] HAWKING S., *Mon. Not. R. Astron. Soc.*, **152** (1971) 75; CARR B. J. and HAWKING S. W., *Mon. Not. R. Astron. Soc.*, **168** (1974) 399.
- [8] DOLGOV A. and J. SILK J., *Phys. Rev. D*, **47** (1993) 4244.
- [9] DOLGOV A. D., KAWASAKI M. and KEVLISHVILI N., *Nucl. Phys. B*, **807** (2009) 229.
- [10] CARR B. J., in *Inflating Horizons in Particle Astrophysics and Cosmology*, edited by SUSUKI H. *et al.* (Universal Academy Press, Tokyo, Japan) 2005, pp. 119-149, astro-ph/0511743; KHLOPOV M. YU., *Res. Astron. Astrophys.*, **10** (2010) 495.
- [11] BARKER B. M., GUPTA S. N. and KASKAS J., *Phys. Rev.*, **182** (1969) 1391.
- [12] SOMMERFELD A., *Ann. Physik (Leipzig)*, **403** (1931) 257; SAKHAROV A. D., *Zh. Eksp. Teor. Fiz.*, **18** (1948) 631.
- [13] KOMATSU K. *et al.* (WMAP COLLABORATION), *Astrophys. J. Suppl.*, **192** (2011) 18; NAKAMURA K. *et al.* (PARTICLE DATA GROUP), *J. Phys. G*, **37** (2010) 075021.
- [14] BINNEY J. and TREMAINE S., *Galactic Dynamics* (Princeton University Press, Princeton USA) 2008.
- [15] BAMBI C., SPOLYAR D., DOLGOV A. D. *et al.*, *Mon. Not. R. Astron. Soc.*, **399** (2009) 1347.
- [16] LANDAU L. D. and LIFSHITZ E. M., *Course of theoretical physics: The classical theory of fields*, Vol. **2** (Butterworth-Heinemann) 2003.
- [17] FROLOV V. P. and NOVIKOV I. D., *Black hole physics: Basic concepts and new developments* (Kluwer Academic, Dordrecht, Netherlands) 1998.

SESSION II - ASTROPARTICLE AND NEUTRINO PHYSICS

<i>Alexander Studenikin</i>	New bounds on neutrino magnetic moment and re-examination of plasma effect in neutrino spin light
<i>Luca Baldini</i>	Science highlights from the <i>Fermi</i> Large Area Telescope
<i>Paolo Bernardini</i>	Cosmic rays in the TeV region with the ARGO-YBJ detector
<i>Martina Bohacova</i>	Highlights from the Pierre Auger Observatory
<i>Arnon Dar</i>	Origin of the ultrahigh-energy cosmic rays and their spectral break
<i>Paolo Natoli</i>	The Planck mission: From first results to cosmology
<i>Ruth Toner</i>	The latest results from the MINOS oscillation experiment
<i>Umut Kose</i>	Search for $\nu_\mu \rightarrow \nu_\tau$ oscillations in appearance mode in the OPERA experiment
<i>Jaime Dawson</i>	Commissioning the Double Chooz detector
<i>Barbara Caccianiga</i>	Neutrino physics with the Borexino experiment
<i>Carlo Giunti</i>	Recent progress in neutrino physics

New bounds on neutrino magnetic moment and re-examination of plasma effect in neutrino spin light

A. V. GRIGORIEV⁽¹⁾, A. V. LOKHOV⁽²⁾, A. I. STUDENIKIN⁽²⁾⁽³⁾^(*)
and A. I. TERNOV⁽⁴⁾

⁽¹⁾ *Skobeltsyn Institute of Nuclear Physics, Moscow State University - 119991 Moscow, Russia*

⁽²⁾ *Department of Theoretical Physics, Faculty of Physics, Moscow State University - 119991 Moscow, Russia*

⁽³⁾ *Joint Institute for Nuclear Research - 141980 Dubna, Moscow Region, Russia*

⁽⁴⁾ *Department of Theoretical Physics, Moscow Institute for Physics and Technology - 141700 Dolgoprudny, Russia*

(ricevuto il 29 Settembre 2011; pubblicato online il 23 Gennaio 2012)

Summary. — Recent discussion on the possibility to obtain more stringent bounds on neutrino magnetic moment has stimulated new interest to possible effects induced by neutrino magnetic moment. In particular, in this paper after a short review on neutrino magnetic moment we re-examine the effect on plasmon mass on neutrino spin light radiation in dense matter. We track the entry of the plasmon mass quantity in process characteristics and found out that the most substantial role it plays is the formation of the process threshold. It is shown that far from this point the plasmon mass can be omitted in all the corresponding physical quantities and one can rely on the results of massless photon spin light radiation theory in matter.

PACS 13.15.+g – Neutrinos interactions.

PACS 95.30.Cq – Elementary particles processes.

1. – Neutrino magnetic moment

Neutrino magnetic moments are no doubt among the most well theoretically understood and experimentally studied neutrino electromagnetic properties [1, 2].

As it was shown long ago [3], in a wide set of theoretical frameworks neutrino magnetic moment is proportional to the neutrino mass and in general very small. For instance, for the minimally extended Standard Model the Dirac neutrino magnetic moment is given

^(*) E-mail: studenik@srd.sinp.msu.ru

by [3]

$$(1) \quad \mu_{ii} = \frac{3eG_F}{8\sqrt{2}\pi^2} m_i \approx 3.2 \cdot 10^{-19} \left(\frac{m_i}{1 \text{ eV}} \right) \mu_B.$$

At the same time, the magnetic moment of hypothetical heavy neutrino (with mass $m_e \ll m_W \ll m_\nu$) is $\mu_\nu = \frac{eG_F m_\nu}{8\sqrt{2}\pi^2}$ [4]. It should be noted here that much larger values for the neutrino magnetic moments are possible in various extensions of the Standard Model (see, for instance, in [1]).

Constraints on the neutrino magnetic moment can be obtained in $\nu - e$ scattering experiments from the observed lack of distortions of the recoil electron energy spectra. Recent reactor experiments provide us with the following upper bounds on the neutrino magnetic moment: $\mu_\nu \leq 9.0 \times 10^{-11} \mu_B$ (MUNU Collaboration [5]), $\mu_\nu \leq 7.4 \times 10^{-11} \mu_B$ (TEXONO Collaboration [6]). The GEMMA Collaboration has obtained the world best limit $\mu_\nu \leq 3.2 \times 10^{-11} \mu_B$ [7]. Another kind of neutrino experiment Borexino (solar neutrino scattering) has obtained rather strong bound: $\mu_\nu \leq 5.4 \times 10^{-11} \mu_B$ [8]. The best astrophysical constraint on the neutrino magnetic moment has been obtained from observation of the red giants cooling $\mu_\nu \leq 3 \times 10^{-12} \mu_B$ [9].

As it was pointed out above the most stringent terrestrial constraints on a neutrino effective magnetic moments have been obtained in (anti)neutrino-electron scattering experiments and the work to attain further improvements of the limits is in process. In particular, it is expected that the new bound on the level of $\mu_\nu \sim 1.5 \times 10^{-11} \mu_B$ can be reached by the GEMMA Collaboration in a new series of measurements at the Kalinin Nuclear Power Plant with much closer displacements of the detector to the reactor that can significantly enhance the neutrino flux (see [7]).

An attempt to reasonably improve the experimental bound on a neutrino magnetic moment was undertaken in [10] where it was claimed that the account for the electron binding effect in atom can significantly increase the electromagnetic contribution to the differential cross section with respect to the case when the free-electron approximation is used in calculations of the cross section.

However, as it was shown in a series of papers [11-13] the neutrino reactor experiments on measurements of neutrino magnetic moment are not sensitive to the electron binding effect, so that the free-electron approximation can be used for them.

2. – Magnetic moment and neutrino propagation in matter

One may expect that neutrino electromagnetic properties can be much easier visualized when neutrino is propagating in external magnetic fields and dense matter. Also, neutrino propagation in matter is a rather longstanding research field nevertheless still having advances and obtaining a lot of interesting predictions for various phenomena.

The convenient and elegant way for description of neutrino interaction processes in matter has been recently offered in a series of papers [14, 15]. The developed method is based on the use of solutions of the modified Dirac equation for neutrino in matter in Feynman diagrams. The method was developed before for studies of different processes in quantum electrodynamics and was called as “the method of exact solutions” [16]. The gain from the introduction of the method was sustained by prediction and detailed quantum description of the new phenomenon of the spin light of neutrino in matter (the $SL\nu$), first predicted in [17] within the quasi-classical treatment of neutrino spin

evolution. The essence of the $SL\nu$ is the electromagnetic radiation in neutrino transition between two different helicity states in matter.

The simplification of the process framework, such as use of the uniform, unpolarized and non-moving matter, neglect of the matter influence on the radiated photon, makes the estimate of real-process relevance in astrophysical settings far from the practical scope. In this short paper we should like to make a step towards the completeness of the physical picture and to consider the incomprehensible at first glance question of the plasmon mass influence on the $SL\nu$. The importance of plasma effects for the $SL\nu$ in matter was first pointed out in [14]. The investigations already carried out in this area [18] indicated that the plasmon emitted in the $SL\nu$ has a considerable mass that can affect the physics of the process. However the calculation method used there does not lead to the direct confrontation of the results [18] with the analogous ones for the $SL\nu$ [14].

To see how the plasmon mass enters the $SL\nu$ quantities we appeal to the method of exact solutions and carry out all the computations relevant to the $SL\nu$. In this respect, in order to have the conformity we also set all the conditions for the task the same as for corresponding studies on the $SL\nu$. In particular, we consider only the Standard Model neutrino interactions and take matter composed of electrons.

In the exact solutions method, one starts with the modified Dirac equation for the neutrino in matter in order to have initial and final neutrino states, which would enter the process amplitude. The equation reads as follows [14]:

$$(2) \quad \left\{ i\gamma_\mu \partial^\mu - \frac{1}{2}\gamma_\mu(1 + \gamma^5)f^\mu - m \right\} \Psi(x) = 0,$$

where in the case of neutrino motion through the non-moving and unpolarized matter $f^\mu = G_f/\sqrt{2} (n, \mathbf{0})$ with n being matter (electrons) number density. Under these conditions eq. (2) has a plane-wave solution determined by 4-momentum p and quantum numbers of helicity $s = \pm 1$ and sign of energy $\varepsilon = \pm 1$. For the details of equation solving and exact form of the wave functions $\Psi_{\varepsilon,p,s}(\mathbf{r}, t)$ the reader is referred to [14] and [15], here we cite only the expression for the neutrino energy spectrum:

$$(3) \quad E = \varepsilon \sqrt{(p - s\tilde{n})^2 + m_\nu^2} + \tilde{n}, \quad \tilde{n} = \frac{1}{2\sqrt{2}} G_F n.$$

The S -matrix of the process involves the usual dipole electromagnetic vertex $\mathbf{\Gamma} = i\omega\{[\mathbf{\Sigma} \times \boldsymbol{\varkappa}] + i\gamma^5 \mathbf{\Sigma}\}$ and for given spinors for the initial and final neutrino states $u_{i,f}$ can be written as

$$(4) \quad S_{fi} = -(2\pi)^4 \mu \sqrt{\frac{\pi}{2\omega L^3}} \delta(E_2 - E_1 + \omega) \delta^3(\mathbf{p}_2 - \mathbf{p}_1 + \mathbf{k}) \bar{u}_f(\mathbf{e}, \mathbf{\Gamma}_{fi}) u_i.$$

Here \mathbf{e} is the photon polarization vector, μ is the transitional magnetic moment and L is the normalization length. The delta-functions before spinors convolution part lead to the conservation laws

$$(5) \quad E_1 = E_2 + \omega; \quad \mathbf{p}_1 = \mathbf{p}_2 + \mathbf{k},$$

with energies for the initial and final neutrinos $E_{1,2}$ taken in accordance to (3). For the photon dispersion, for the purpose of our study it is sufficient to use the simplest expression

$$(6) \quad \omega = \sqrt{k^2 + m_\gamma^2}.$$

As it was discussed in our previous studies on the $SL\nu$ [14,15] the most appropriate conditions for the radiation to manifest its properties are met in dense astrophysical objects. This is the setting we will use further for the process and in the case of cold plasma the plasmon mass should be taken as

$$(7) \quad m_\gamma = \sqrt{2\alpha}(3\sqrt{\pi n})^{1/3}.$$

The numerical evaluation at typical density gives $m_\gamma \sim 10^8$ eV, while the density parameter $\tilde{n} \sim 10^4$ eV.

3. – Plasmon mass influence

Let us now consider the influence of dense plasma on the process of spin light of neutrino. Similarly to the original spin light calculation we consider the case of initial neutrino possessing the helicity quantum number $s_1 = -1$ and the corresponding final neutrino helicity is $s_2 = 1$. Using the neutrino energies (3) with corresponding helicities one can resolve eqs. (5) in relation to plasmon momentum which is not equal to its energy since we take into account the dispersion of the emitted photon in plasma (6).

For convenience of calculations it is possible to use the following simplification. In most cases the neutrino mass appeared to be the smallest parameter in the considered problem and it is several orders smaller than any other parameter in the system. So we could first examine our process in approximation of zero neutrino mass, though we should not forget that only neutrino with non-zero mass could naturally possess the magnetic moment. This our simplification should be considered only as a technical one. It should be pointed here that in order to obtain the consistent description of the $SL\nu$ one should account for the effects of the neutrino mass in the dispersion relation and the neutrino wave functions.

From the energy-momentum conservation it follows [18] that the process is kinematically possible only under the condition (taking account of the above-mentioned simplification)

$$(8) \quad \tilde{n}p > \frac{m_\gamma^2}{4}.$$

Provided with the plasmon momentum we proceed with calculation of the $SL\nu$ radiation rate and total power. The exact calculation of total rate is an intricate problem and the final expression is too large to be presented here. However one can consider the most notable ranges of parameters to investigate some peculiarities of the rate behavior.

First of all we calculate the rate for the case of the $SL\nu$ without plasma influence. This can be done by choosing the limit $m_\gamma \rightarrow 0$ and the obtained result is in full agreement with [14]

$$(9) \quad \Gamma = 4\mu^2\tilde{n}^2(\tilde{n} + p).$$

From (9) one easily derives the $SL\nu$ rate for two important cases, *i.e.* high and ultra-high densities of matter just by choosing correspondingly p or \tilde{n} as the leading parameter in the brackets. While neutrino mass is the smallest quantity, our system falls within the range of relativistic initial neutrino energies.

The corresponding expression for the total power also covers high and ultra-high density cases [14] as well as the intermediate area where the density parameter and the neutrino momentum are comparable:

$$(10) \quad I = \frac{4}{3}\mu^2\tilde{n}^2(3\tilde{n}^2 + 4p\tilde{n} + p^2).$$

If we account for the plasma influence (thus, $m_\gamma \neq 0$) on the $SL\nu$ we can discuss two important situations. One is the area of parameters near the threshold, and the other is connected with direct contribution of m_γ into the radiation rate expression. The latter case is particularly important for this study, because it fulfills the aim of the present research in finding the conditions under which the plasmon mass cannot be neglected.

For physically reliable conditions the density parameter usually appears to be less than the plasmon mass, which in its turn is less than the neutrino momentum: $\tilde{n} \ll m_\gamma \ll p$. Obviously the threshold condition (8) should be satisfied. As we consider the conditions similar to different astrophysical objects it is natural to use high-energy neutrino.

Using the series expansion of the total rate one could obtain the rate of the process in the following form:

$$(11) \quad \Gamma = 4\mu^2 p\tilde{n}^2(1 + 6\lambda + 4\lambda \ln \lambda),$$

where $\lambda = \frac{m_\gamma^2}{4\tilde{n}p} < 1$. Approaching the threshold ($\lambda \rightarrow 1$), expansion (11) becomes inapplicable, however it is correct in a rather wide range of parameters with $m_\gamma \ll p$ and $\tilde{n} \ll p$. Near the threshold the total rate can be presented in the form $\Gamma \sim (1 - \lambda)$ but the exact coefficient is too unwieldy to be presented here.

Concerning the power of the $SL\nu$ with plasmon, one can use the expansion

$$(12) \quad I = \frac{4}{3}\mu^2 p^2 \tilde{n}^2 \left(1 - 6\lambda - 57\lambda \frac{\tilde{n}}{p} - 12\lambda \frac{\tilde{n}}{p} \ln \lambda \right).$$

Expression (12) is correct only if the system meets the requirement $\lambda \ll 1$. Otherwise one should use higher orders of quantity $\frac{m_\gamma^2}{p}$ in the expansion to achieve a reliable value of intensity. Near the threshold the power has the same dependence on the “distance” from the threshold $(1 - \lambda)$ as the rate of the process.

4. – Conclusion

There is an increasing interest to neutrino electromagnetic properties and neutrino magnetic moments in particular. This interest is stimulated, first by the progress in experimental bounds on magnetic moments which have been recently achieved, as well as theoretical predictions of new processes emerging due to neutrino magnetic moment, such as the $SL\nu$ and a belief in its importance for possible astrophysical applications.

Further developing the theory of the spin light of neutrino, we have explicitly shown that the influence of plasmon mass becomes significant (see (11) and (12)) when the

parameter λ is comparable with 1, this corresponds to the system near the threshold. As soon as the quantity $\lambda \ll 1$ (so the system is far from the threshold) one can use either $SL\nu$ radiation rate and total power from [14] or their rather compact generalizations (11) and (12) where the plasmon mass is accounted for as a minor adjustment.

Since high energy neutrinos propagating in matter could be a rather typical situation in astrophysics, for instance in neutron stars, the influence of photon dispersion in plasma on the $SL\nu$ process can be neglected and the threshold generated by the non-zero plasmon mass should not be taken into account. However, the method of exact solutions of modified Dirac equation provides us with analytical expressions for probability and intensity in the whole range of possible parameters.

* * *

One of the authors (AS) is thankful to G. BELLETTINI, G. CHIARELLI, M. GRECO and G. ISIDORI for the invitation to participate in Les Rencontres de Physique de la Vallée d'Aoste on Results and Perspectives in Particle Physics. This work has been supported by RFBR grant 11-02-01509-a.

REFERENCES

- [1] GIUNTI C. and STUDENIKIN A., *Phys. Atom. Nucl.*, **72** (2009) 2151.
- [2] STUDENIKIN A., *Nucl. Phys. Proc. Suppl.*, **188** (2009) 220; GIUNTI C. and STUDENIKIN A., *J. Phys. Conf. Ser.*, **203** (2010) 012100.
- [3] MARCIANO W. J. and SANDA A. I., *Phys. Lett. B*, **67** (1977) 303; LEE B. W. and SHROCK R. E., *Phys. Rev. D*, **16** (1977) 1444; FUJIKAWA K. and SHROCK R. E., *Phys. Rev. Lett.*, **45** (1980) 963.
- [4] DVORNIKOV M. and STUDENIKIN A., *Phys. Rev. D*, **69** (2004) 073001; *J. Exp. Theor. Phys.*, **99** (2004) 254.
- [5] DARAKCHIEVA Z. *et al.* (MUNU COLLABORATION), *Phys. Lett. B*, **615** (2005) 153.
- [6] WONG H. T. *et al.* (TEXONO COLLABORATION), *Phys. Rev. D*, **75** (2007) 012001.
- [7] BEDA A. G. *et al.*, *Particle Physics on the Eve of LHC*, edited by STUDENIKIN A. (World Scientific, Singapore) 2009, p. 112; *Phys. Part. Nucl. Lett.*, **7** (2010) 406; arXiv:0906.1926.
- [8] ARPESELLA C. *et al.* (BOREXINO COLLABORATION), *Phys. Rev. Lett.*, **101** (2008) 091302.
- [9] RAFFELT G., *Phys. Rev. Lett.*, **64** (1990) 2856.
- [10] WONG H. T., LI H. B. and LIN S. T., *Phys. Rev. Lett.*, **105** (2010) 061801; arXiv:1001.2074.
- [11] VOLOSHIN M. B., *Phys. Rev. Lett.*, **105** (2010) 201801; arXiv:1008.2171.
- [12] KOUZAKOV K. A. and STUDENIKIN A. I., *Phys. Lett. B*, **696** (2011) 252.
- [13] KOUZAKOV K. A., STUDENIKIN A. I. and VOLOSHIN M. B., *JETP Lett.*, **93** (2011) 699; *Phys. Rev. D*, **83** (2011) 113001; *Nucl. Phys. B, Proc. Suppl.* (2011) (*Proceedings of Neutrino 2010 Conference*).
- [14] STUDENIKIN A. and TERNOV A., *Phys. Lett. B*, **622** (2005) 107; GRIGOREV A., STUDENIKIN A. and TERNOV A., *Phys. Lett. B*, **608** (2005) 199; *Grav. Cosmol.*, **11** (2005) 132.
- [15] STUDENIKIN A., *J. Phys. A: Math. Gen.*, **39** (2006) 6769; *J. Phys. A: Math. Theor.*, **41** (2008) 164047.
- [16] SOKOLOV A. A. and TERNOV I. M., *Synchrotron radiation* (Pergamon Press, Oxford) 1968; RITUS V., *Issues in intense-field quantum electrodynamics*, edited by GINZBURG V. (Proc. of Lebedev Phys. Inst. 111, Moscow) 1978, p. 5; NIKISHOV A., *Issues in intense-field quantum electrodynamics*, edited by GINZBURG V. (Proc. of Lebedev Phys. Inst. 111, Moscow) 1978, p. 152.
- [17] LOBANOV A. and STUDENIKIN A., *Phys. Lett. B*, **564** (2003) 27; **601** (2004) 171.
- [18] KUZNETSOV A. V. and MIKHEEV N. V., *Int. J. Mod. Phys. A*, **22** (2007) 3211.

Science highlights from the *Fermi* Large Area Telescope

L. BALDINI⁽¹⁾ and L. TIBALDO⁽²⁾ on behalf of the FERMI LAT COLLABORATION

⁽¹⁾ *INFN, Sezione di Pisa - Pisa, Italy*

⁽²⁾ *Dipartimento di Fisica "G. Galilei", Università di Padova and INFN, Sezione di Padova Padova, Italy*

(ricevuto il 29 Settembre 2011; pubblicato online il 23 Gennaio 2012)

Summary. — During its first three years of operation, the *Fermi* γ -ray Space Telescope has provided an unprecedented view of the high energy γ -ray sky, and also performed direct measurements of the cosmic-ray leptons and searches for signals from dark matter. In this paper we present a short overview of some highlight results, shedding new light on the high-energy side of the Universe.

PACS 95.85.Pw – γ -ray.

PACS 98.70.Sa – Cosmic rays (including sources, origin, acceleration, and interactions).

PACS 95.35.+d – Dark matter (stellar, interstellar, galactic, and cosmological).

1. – The *Fermi* γ -ray Space Telescope: an observatory of the high-energy Universe

Radiation in the γ -ray domain is a privileged messenger of high-energy processes taking place in our Universe. Contrary to charged cosmic rays (CRs), which are deflected by magnetic fields and rapidly lose memory of their sources, γ -rays carry directional information. Compared to neutrinos or gravitational waves they are easier to detect thanks to their larger interaction probabilities.

Designed to survey the γ -ray sky in the broad energy range from 20 MeV to more than 300 GeV, with the additional capabilities of studying transient phenomena at lower energies and charged species, notably leptons, from GeV to TeV energies, the *Fermi* γ -ray Space Telescope⁽¹⁾ is the premier space-borne γ -ray observatory of this decade.

Fermi carries two instruments on-board: the γ -ray Burst Monitor (GBM) [1] and the Large Area Telescope (LAT) [2]. The GBM, sensitive in the energy range between 8 keV and 40 MeV, is designed to observe the full unocculted sky with rough directional capabilities (at the level of one to a few degrees) for the study of transient sources, particularly γ -Ray Bursts (GRBs). The LAT is a pair conversion telescope for photons above 20 MeV up to a few hundreds of GeV.

⁽¹⁾ Formerly γ -ray Large Area Space Telescope, *GLAST*.

1.1. *The LAT instrument and its performance.* – The LAT is a 4×4 array of identical towers, each one made by a tracker-converter module (hereafter *tracker*) and a calorimeter module. A segmented anti-coincidence detector (ACD) covers the tracker array and a programmable trigger and data acquisition system completes the instrument. Though owing most of the basic design to its predecessors—particularly the Energetic γ -Ray Experiment Telescope (EGRET) [3] on-board the *CGRO* mission—the LAT exploits the state of the art in terms of detector technology, which allows for a breakthrough leap in the instrument performance.

Each tracker module features 16 tungsten layers, promoting the conversion of γ -rays into e^+/e^- pairs, and 18 x - y pairs of single-sided silicon strip detector planes—for a total of 1.5 radiation lengths of material on-axis. The silicon-sensor technology allows precise tracking (with no detector-induced dead time and no use of consumables) and the capability to self-trigger.

Each calorimeter module consists of 96 CsI(Tl) crystals, arranged in a hodoscopic configuration (for a total depth of ~ 8.6 radiation lengths on axis). The calorimeter provides an intrinsically three-dimensional image of the shower development, which is crucial both for the energy reconstruction (especially at high-energy, where a significant part of the shower can leak out of the back of the instrument) and for background rejection.

The anti-coincidence detector, a set of plastic scintillators surrounding the tracker, is the first defense of the LAT against the overwhelming background due to charged CRs. In order to limit the “self-veto” effect—due to the back-splash of secondaries from high-energy particles hitting the calorimeter—it is segmented in 89 tiles providing spatial information that can be correlated with the signal from the tracker and the calorimeter.

The design, construction and operation of such a complex detector is a fascinating subject on its own and the interested readers can refer to [2] and references therein for further details. The LAT largely surpasses the previous generations of γ -ray telescopes in terms of effective area, energy range, instrumental dead time, angular resolution and field of view (2.5 sr). It has the ability to observe 20% of the sky at any time which, in the nominal scanning mode of operation, enables it to view the entire sky every three hours.

1.2. *Outline.* – With the observatory being well into the third year of sky survey, this paper is a short overview of the most important Science highlights, chosen in consideration of the interests of the audience and presented by the authors in two review talks at the XXV Rencontres de Physique de La Vallée d’Aoste.

Section 2 presents a short overview of the high-energy γ -ray sky unveiled by the *Fermi* observatory. The different γ -ray sources are examined to understand the non-thermal processes leading to the production of high-energy particles, and also to view them in relation to other messengers such as charged CRs, neutrinos and gravitational waves. Then, sect. 3 is devoted to the search for dark matter (DM) signals in γ -rays with the LAT. Finally, sect. 4 summarizes the experimental advances due to the LAT in the measurement of the leptonic component of the cosmic radiation, and its implications in the light of results from other experiments.

2. – The high-energy γ -ray sky seen by *Fermi*

The sky in high-energy γ -rays is dominated by diffuse emission: more than 70% of the photons detected by the LAT are produced in the interstellar space of our Galaxy

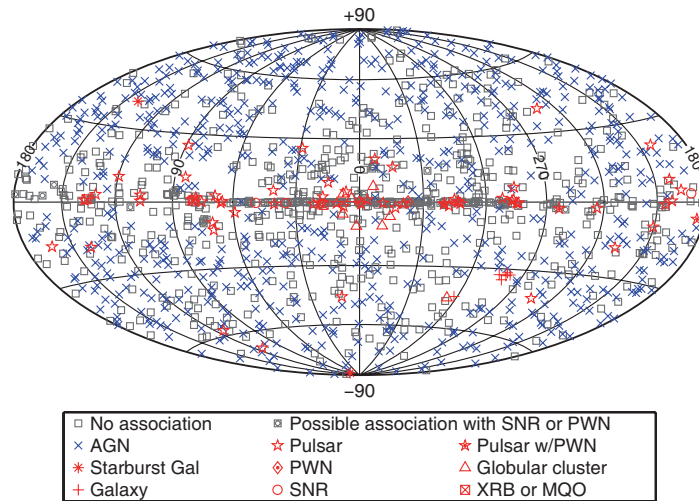


Fig. 1. – Skymap showing the positions of the 1451 1FGL sources [4] (Aitoff projection in Galactic coordinates). The different markers correspond to the association at other wavelengths most likely for each source.

by interactions of high-energy CRs with matter and low-energy radiation fields. An additional diffuse component with an almost isotropic distribution, and therefore thought to be extragalactic in origin, accounts for another sizable fraction of the LAT photon sample. The rest consists of sources detected by the LAT from a variegated zoo of objects including Active Galactic Nuclei (AGN) and normal galaxies, pulsars and their relativistic wind nebulae, globular clusters, binary systems, shock-waves remaining from supernova explosions and nearby solar-system bodies like the Sun and the Moon.

A major step forward in the understanding of the γ -ray sky was given by the first LAT source Catalog (1FGL) [4], based on the first 11 months of data, which is summarized by fig. 1. The LAT increased the number of known γ -ray sources from a few hundred to 1451, including new classes of objects like globular clusters and starburst galaxies. The mystery of the unassociated γ -ray sources, which comprise 630 out of the 1451 sources in the 1FGL sample, continues to puzzle astrophysicists. The second LAT source Catalog, based on two years of data and improved detection methods, will be released soon.

Compared to what is known at longer wavelengths, a characteristic feature of the γ -ray sky is its rapid variability over timescales from a few seconds to months. In addition to transients known for decades like γ -ray bursts and flares from AGN, the LAT observed unexpected phenomena like γ -ray emission from the nova in the symbiotic binary V407 Cygni [5] and variability from the Crab nebula [6].

2.1. γ -ray bursts. – The mysterious explosions known as γ -ray bursts (GRBs), which episodically outshine for a few seconds to minutes any other sources in the γ -ray sky, have intrigued scientists since their discovery in the '60s. There is currently a large consensus that they are produced by a release of gravitational energy (of the order of one rest solar mass) over a very short time interval (of the order of 1 s) within a very compact region (of the order of 10 km) by a cataclysmic event, either the collapse of a massive-star core into a black hole (long GRBs) or by the merging of two compact objects

(short GRBs). This energy release would mostly result in a burst of thermal neutrinos and perhaps gravitational waves, but also in a very high temperature fireball expanding at highly relativistic speed which would undergo energy dissipation, producing, among other particles, γ -rays and later developing into a blastwave which would decelerate against the external medium and give rise to the afterglow observed in γ -rays and at longer wavelengths. The explosions producing GRBs are among the few phenomena sufficiently energetic to contribute to the acceleration of CRs across the whole observed energy spectrum.

Observations indicate that GRBs are distributed isotropically in the sky and that those which have known redshift are located at cosmological distances. *Fermi*, with the LAT and the GBM, observes GRBs over 6 orders of magnitude in photon energy: it was therefore expected to shed light on some fundamental aspects of GRB Physics, including the origin of the energy and the mechanism by which it is transported, the γ -ray emission mechanism and the level of collimation (isotropic emission would require an unrealistic energy release). The GBM has, so far, observed a few hundred GRBs, of which a few tens were detected also by the LAT. The improved performance of the LAT, especially at energies > 10 GeV, led, for some bursts, to the measurement of a hard spectral component in addition to the standard Band component, *e.g.* [7], or of high-energy afterglows, *e.g.* [8].

The highest energy photon ever recorded from a burst was detected at ~ 31 GeV from GRB 090510 [9] at a redshift $z = 0.903$. In simple radiation models such as that described in [10], the temporal structure of the burst requires, in order to lower the internal opacity due to γ - γ interactions, bulk Lorentz factors larger than a few hundreds. High-energy photons traveling over cosmological distances are also a powerful tool to probe for a possible breaking of Lorentz invariance. Assuming that a photon of energy E is delayed by $\Delta t = E/(M_{\text{LIV}} c^2)$, where M_{LIV} sets the scale of the Lorentz invariance violation, the temporal structure of GRB 090510 implies $M_{\text{LIV}} > 1.19 M_{\text{Planck}}$ [9].

2.2. Active Galactic Nuclei. – The largest class of associated sources in the LAT Catalog corresponds to AGN [4, 11]. High-energy emission from AGN is thought to be powered by the accretion of matter onto a super-massive black hole. In a process not fully understood yet, this produces a jet of relativistic particles that shoots away from the central engine. There are, however, pending questions, including the emission mechanism which produces the observed γ -ray emission and the region where this process takes place. There is not even a consensus on the nature of the particles carrying the energy which is radiated in γ -rays, either leptons or nucleons. In the latter case AGN are promising neutrino sources. There is also a suggestive correlation measured by the Auger observatory between the arrival directions of ultra-high energy CRs and nearby AGN [12], which might be their primary sources.

Thanks to the improved angular resolution of the LAT, Centaurus A has become the first AGN ever resolved in high-energy γ -rays; the γ -ray flux is almost equally divided between the core of the Galaxy and the lobes, which are flooded by electrons of energies up to 1 TeV, accelerated directly in the lobes or efficiently transported from the core [13].

A γ -ray flare from the AGN 3C279, associated with a change in the optical polarization angle, proved that, in this object, the regions of γ -ray and optical emission are co-located; the change in optical polarization implies a non-axisymmetric magnetic field and a distance of the emitting material from the central engine $> 10^5$ gravitational radii [14].

2.3. Pulsars and pulsar wind nebulae. – Pulsars, *i.e.* highly-magnetized rotating neutron stars emitting periodic spikes of electromagnetic radiation, were the first class of identified γ -ray sources. The LAT brought the number of known γ -ray pulsars from 6 to > 70 and further new discoveries are foreseen. In addition to young radio pulsars discovered in γ -rays thanks to the rotational properties measured by radio astronomers, the LAT discovered two new pulsar populations:

- γ -ray selected pulsars found without any prior knowledge about their pulsation [15]; some of them did not reveal, so far, any radio emission, suggesting that the γ -ray beams may be broader than those at longer wavelengths;
- millisecond pulsars [16], *i.e.* older pulsars with weaker surface magnetic fields, which were spun up to higher velocities by accreting material from a companion object in a binary system.

There is a large consensus that the radiation is mostly due to interactions of leptons accelerated at large magnetic-field strengths. The properties illustrated in the first LAT pulsar Catalog [17] suggest that γ -ray emission largely arises from the outer magnetosphere of the neutron stars rather than the region near the magnetic poles as previously proposed by several authors.

Most of the energy lost by pulsars while spinning down goes into the production of a pulsar wind, and its termination shock further accelerate particles, primarily electrons, which produce a pulsar wind nebula (PWN). Pulsars and their wind nebulae might therefore significantly contribute to the leptonic fraction observed in cosmic rays. The enhanced sensitivity of the LAT enabled, so far, the detection of γ -ray emission from three PWNe, namely the Crab Nebula, Vela X and MSH 15 – 52 [18]. The LAT detected a surprising day-scale variability from the Crab nebula [6]: this was interpreted as synchrotron emission from an electron population reaching PeV energies in a region within 17 light days of the neutron star, *i.e.* at the termination shock of the pulsar wind.

2.4. Supernova remnants. – Shock-waves produced by supernova explosions have long been considered the most likely candidates for the parent source population of Galactic CRs, since, except for GRBs, they are the only objects sufficiently energetic to explain the CR fluxes observed at the Earth. Diffusive shock acceleration in supernova remnants (SNR) provides a plausible mechanism to sustain Galactic CRs. While multiwavelength spectra of SNRs undoubtedly prove the presence of high-energy electrons in the expanding shock-waves, only indirect evidence points to the acceleration of nuclei. In the future, the detection of high-energy neutrinos might be the smoking gun of hadron acceleration.

γ -ray observations are an important probe of non-thermal particles in SNR shock-waves. The improved angular resolution of the LAT enabled us to spatially resolve some SNRs, *e.g.*, W44 [19], and to verify that γ -ray emission is associated with the shock region. The dominant class of LAT detected SNRs, like W44, are middle-aged SNRs (with ages of the order of 10^4 years) showing interactions with molecular clouds. Their broad-band spectrum is better reproduced by assuming that the γ -radiation is mostly produced by nucleon-nucleon inelastic collisions, as shown for W51 in fig. 2. Middle-aged SNRs detected by LAT show a steep spectrum above a few GeV; on the other hand, young SNRs (ages of a few thousand years), where efficient particle acceleration is thought to occur, show in the LAT energy band hard spectra which connect with the TeV emission detected by ground-based instruments.

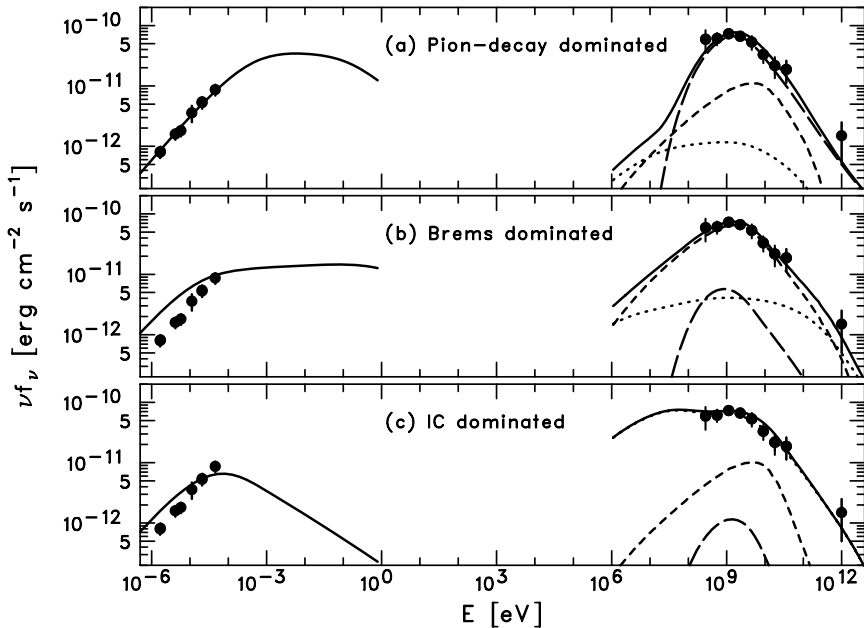


Fig. 2. – Broad-band spectral energy distribution of SNR W51 compared with different emission models [20]. The spectrum combines LAT measurements from 200 MeV to 50 GeV, with TeV measurements by the HESS telescope and radio measurements of synchrotron emission from relativistic electrons. Model (a) corresponds to the case of efficient nuclei acceleration (where the γ -ray emission is dominated by π^0 decay), models (b) and (c) two different cases of inefficient nuclei acceleration, where γ -ray emission is dominated by bremsstrahlung and inverse-Compton scattering, respectively.

2.5. Galactic interstellar emission. – Galactic interstellar emission is produced by CR interactions, via nucleon-nucleon inelastic collisions (through π^0 production and decay) and via electron bremsstrahlung and inverse-Compton scattering. It is therefore, together with synchrotron radiation from electrons at radio wavelengths, the only probe of CRs on the Galactic scale, beyond direct measurements performed in the solar system and at its outer frontiers. Previous measurements showed an excess at energies $\gtrsim 1$ GeV with respect to expectations based on the directly measured CR spectra [21], attributed either to CR spectral variations, instrumental effects or contributions from exotic phenomena.

The LAT measured the γ -ray emission from the nearby interstellar space and found that its spectrum is softer than previous measurements [22], in good agreement within 10% with production by CRs with a spectrum consistent with that directly measured near the Earth [22, 23]. The LAT is currently investigating, through interstellar emission observations, the distribution of CRs at large in the Galaxy. LAT observations reinforced the so-called CR gradient problem, with the measurement of CR densities larger than expected toward the outer Galaxy, where the putative sources, SNRs, rapidly drop off [24, 25]; this might be related to some poorly-constrained aspects in the propagation of particles (*e.g.*, a large diffusion halo, anisotropic diffusion or convection) or to large masses of target gas escaping our observations or, less likely, to unknown accelerators.

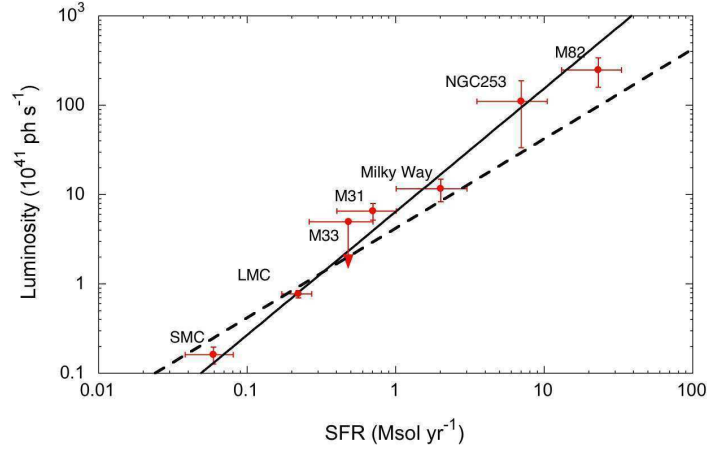


Fig. 3. – γ -ray luminosity as a function of star-formation rate for some galaxies observed by the LAT [29].

The ongoing modeling of large-scale properties of interstellar γ -ray emission in the light of LAT data [26] and the studies of other selected region will deepen our understanding of particle propagation in the Galaxy in the near future.

2.6. External galaxies. – High-energy γ -ray emission from non-active external galaxies, highlighting different emitting CR populations, is regarded as the main piece of evidence that CRs below 10^{15} eV are Galactic in origin. The only non-AGN galaxy detected before the LAT era was the nearby Large Magellanic Cloud. The LAT has so far detected γ -ray emission from galaxies of the local group, the two Magellanic clouds [27, 28] and the Andromeda galaxy [29], and from some nearby starburst galaxies [30].

Thanks to the improved angular resolution of the LAT, the Large Magellanic Cloud was the first external galaxy ever resolved in high-energy γ -rays [27], leading to the first map of CR acceleration and propagation in a galaxy. The γ -ray emission correlates with massive-star formation rather than interstellar gas. This reinforces the idea that the energy for accelerating CRs in galaxies is provided by massive stars, thanks to the catastrophic explosions taking place at the end of their lives and, perhaps, to the collective action of stellar winds in massive-star clusters. On the other hand, the lack of correlation with the distribution of gas would require propagation lengths shorter than usually assumed in the Milky Way.

The link between the acceleration of particles and massive stars is further supported by the correlation found between the γ -ray luminosity and the massive-star formation rate, see fig. 3. This correlation is not fully understood yet, but might be analogous to the correlation found between radio and infrared luminosities of galaxies. An enlarged sample of external galaxies studied by the LAT will allow us to use this correlation to evaluate the contribution by unresolved non-active galaxies to the isotropic diffuse γ -ray emission.

2.7. The isotropic diffuse γ -ray emission. – The LAT measured the spectrum of the isotropic diffuse γ -ray emission and found it to be consistent with a featureless power law of index ~ 2.4 in the energy range 200 MeV–100 GeV [31]. This is expected to be largely

due to populations of unresolved extragalactic sources. The population synthesis of AGN detected by the LAT (see subsect. 2'2) constrains their contribution to be $< 30\%$ [32]. The contribution from non-active galaxies is under evaluation, for the first time based not only on theoretical models but also on a sample detected by the LAT (see subsect. 2'6).

Yet, at present there is still room for *truly diffuse* extragalactic emission, which can be due to many different processes, like large-scale structure formation, interactions of ultra-high-energy CRs with the extragalactic low-energy background radiation, annihilation or decay of cosmological DM, *e.g.*, [33]. On the other hand, interactions of CRs with debris at the outer frontier of the solar system might partially contribute to the spectrum of the isotropic diffuse emission [34].

3. – Indirect Dark Matter searches in γ -rays

One of the major open issues in our understanding of the Universe is the existence of an extremely-weakly interacting form of matter, DM, supported by a wide range of observations including large scale structures, the cosmic microwave background and the isotopic abundances resulting from the primordial nucleosynthesis. Complementary to *direct* searches being carried out in underground facilities and at accelerators, the *indirect* search for DM is one of the main items in the broad *Fermi* Science menu.

The word “indirect” denotes here the search for signatures of Weakly Interactive Massive Particle (WIMP) annihilation or decay processes through the final products (γ -rays, electrons and positrons, antiprotons) of such processes. Among many other ground-based and spaceborne instruments, the LAT plays a prominent role in this search through a variety of distinct search targets: γ -ray lines, Galactic and isotropic diffuse γ -ray emission, dwarf satellites, CR electrons and positrons (for the latter item see sect. 4).

3'1. γ -ray lines. – The quest for a possible narrow line in the diffuse γ -ray emission arises naturally since photons can be produced in two-body DM particle annihilations $\chi\chi \rightarrow \gamma X$ or decays $\chi \rightarrow \gamma X$. Since, in most scenarios, DM particles are electrically neutral (and therefore do not couple directly to photons) such processes only occur at high orders and the branching ratios are expected to be strongly suppressed. Despite the subsequent weakness, a photon line, if present, is easy to identify and distinguish from the standard astrophysical sources of γ rays—whose flux is dominant in most situations. Therefore, this discovery channel features a distinctive experimental signature that, if observed, would incontrovertibly indicate new physics at work.

The detector response to a monochromatic line is not a monochromatic line and the effect of the finite energy resolution cannot be ignored. The response can be modeled by means of Monte Carlo simulations (see the insert in fig. 4) and verified with tests at accelerators so that it can be effectively folded into the procedure and used to assess the statistical significance of a possible line component in the measured count spectra.

No significant evidence of γ -ray line(s) has been found in the first 11 months of data, between 30 and 200 GeV [35] and work is ongoing to extend the energy range of the analysis and include more data. The detailed discussion of the upper limits obtained and their relevance in the context of specific DM models is beyond the scope of this brief overview.

3'2. DM signals from the Galactic halo. – The Milky Way halo and the Galactic center are obvious candidates for indirect dark matter searches in γ -rays: given the large DM content, a large annihilation signal can be potentially expected. The main challenge is

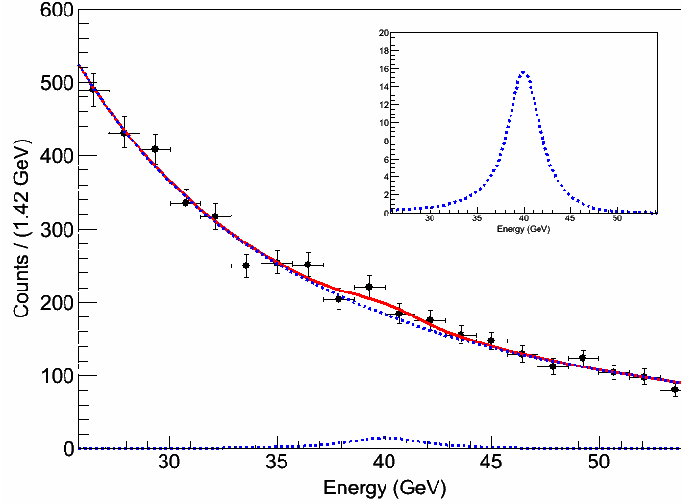


Fig. 4. – (Colour on-line) Binned representation of the fit procedure (here centered at 40 GeV) used to derive the upper limit on the flux of a possible photon line contribution in the all-sky (except for part of the Galactic plane) spectrum (from [35]). The two dotted lines represent the background (modeled with a power law) and the signal from the fit, respectively, while the red line is their sum. The insert shows a close-up of the instrument response to a monochromatic line at 40 GeV, which is used to model the signal.

presented by the strong γ -ray foreground comprising the Galactic diffuse emission (cfr. sect. 2.5). Indeed, the detailed modeling of this foreground is currently the main limiting factor for DM searches in this channel.

In the case of the Galactic center a firm assessment of the conventional astrophysical signals is furthermore complicated by the problem of source confusion, due to the limited angular resolution of the instrument, and of pile-up along the line of sight.

3.3. Dwarf galaxies. – Dwarf satellites of the Milky Way are among the cleanest targets for indirect dark matter searches in γ -rays. They are systems with a very large mass/luminosity ratio (*i.e.* systems which are largely DM dominated). The LAT detected no significant emission from any of such systems and the upper limits on the γ -ray flux allowed us to put very stringent constraints on the parameter space of well motivated WIMP models [36].

A combined likelihood analysis of the 10 most promising dwarf galaxies, based on 24 months of data and pushing the limits below the thermal WIMP cross section for low DM masses (below a few tens of GeV), is currently under preparation and will be published soon.

4. – Direct cosmic-ray measurements

The electron component of the primary CR radiation is widely recognized as a unique probe to address a number of significant questions concerning the origin of CRs and their propagation in our galaxy (see [37] for a synthetic review). Several different experiments

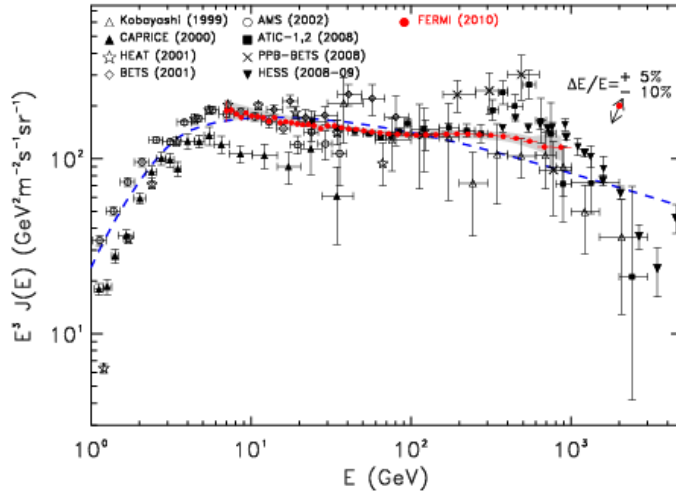


Fig. 5. – (Colour on-line) CR electron spectrum measured by the *Fermi* LAT (red points, from [39]). The gray shaded band indicates the systematic uncertainties associated with the flux values, while the blue dashed line represents the prediction of a diffusive propagation model tuned on the pre-*Fermi* data. Many other recent measurements are included for completeness.

have recently published new data of unprecedented quality and spanning energy ranges never explored before, stirring up the interest of the scientific community, mostly in connection with the possible indication of the existence of an extra component in the energy spectrum, which is not part of the standard CR paradigm.

4.1. The all-electron spectrum. – The LAT intrinsic capability for detecting high-energy CR electrons (and positrons) was already recognized by the collaboration in the early stages of the instrument development. This was demonstrated with the publication of the first high-statistics spectrum of CR $e^+ + e^-$ between 20 GeV and 1 TeV, based on the data from the first six months of the mission [38]. This capability derives from the unique combination of large acceptance and long observation time; this combination results in an effective exposure factor of the order of a few $10^8 \text{ m}^2 \text{ sr s}$ at 100 GeV (including all the effects of the event selections and instrument dead time and duty cycle), which is significantly larger than any other experiment ever flown to measure the electron component of the cosmic radiation in the LAT energy range.

Figure 5 shows the updated $e^+ + e^-$ spectrum, based on the first year of data, published in [39]. It extends the previous result [38] down to 7 GeV—the lowest accessible energy for primary electrons and positrons in the *Fermi* orbit (with an inclination of 25.6°). The spectrum does not show any evidence for a sharp spectral feature, such as the one reported by ATIC [40]. The new low-energy data points, though, exacerbate the tension with the hypothesis of a single power law spectrum, which could not be ruled out in [38].

In fact, several different authors showed that the LAT $e^+ + e^-$ spectrum, along with the positron fraction measured by the PAMELA experiment [41], can be well fitted with the addition of a separate high-energy e^+/e^- component, whose origin might be due to

nearby pulsars or annihilation of WIMP dark matter. Other authors, like [42] and [43], however, point to alternative explanations of the *lepton excesses* not invoking any extra-components.

4.2. Anisotropies in CR electrons. – Thanks to its large exposure factor, and to it being an all-sky instrument, *Fermi* offers a unique opportunity for the measurement of possible anisotropies in the arrival directions of CR electrons and positrons, that could potentially provide important information (complementary to the energy spectrum) about their origin.

With more than 1.6 million candidate electrons above 60 GeV in the first year of operation, we found no evidence for anisotropies on any angular scale [44]. The search was performed by means of integrated skymaps with different regions of interest (with radii ranging from 10° and 90°) and through a spherical harmonic analysis. For a dipole anisotropy—which is an interesting case study in the situation in which a single nearby source dominates the high-energy electron spectrum—the LAT upper limits range from 0.5% to 10%, depending on the energy range. This is close to the level where we might indeed expect some signal and it will get better as new data are analyzed.

5. – Final remarks: *Fermi* and Astroparticle Physics

The *Fermi* observatory provides a paradigmatic example of the fruitful interplay between Astrophysics and Particle Physics, which has been taking place over the last decades. On the one hand, the highlight results we presented show how the significant observational advances of the *Fermi* era are largely due to the technological developments coming from accelerator-based detectors, notably in this case to silicon tracking devices.

On the other hand, *Fermi* is contributing to a deeper understanding of high-energy processes occurring in the Universe, often much more energetic than those produced by our Earth-based particle accelerators. High-energy particles of cosmic origin played an important role in the birth of subnuclear Physics and are now regarded as a fundamental component of galaxies, as well as messengers of possible exotic phenomena beyond the standard model of Particle Physics. The LAT is mapping with unprecedented accuracy the high-energy facet of the sky, performing direct measurements of the charged cosmic radiation and searching for signatures of Physics beyond the standard model. Further advancements are foreseen in next years thanks to the complementarity with other multi-wavelength/messenger Astroparticle detectors and accelerator-based experiments.

* * *

The *Fermi* LAT Collaboration acknowledges support from a number of agencies and institutes for both development and the operation of the LAT as well as scientific data analysis. These include NASA and DOE in the United States, CEA/Irfu and IN2P3/CNRS in France, ASI and INFN in Italy, MEXT, KEK, and JAXA in Japan, and the K. A. Wallenberg Foundation, the Swedish Research Council and the National Space Board in Sweden. Additional support from INAF in Italy and CNES in France for science analysis during the operations phase is also gratefully acknowledged.

REFERENCES

- [1] MEEGAN C. *et al.*, *AIP Conf. Proc.*, **921** (2007) 13.
- [2] ATWOOD W. B. *et al.*, *Astrophys. J.*, **697** (2009) 1071.
- [3] THOMPSON D. J. *et al.*, *Astrophys. J. Suppl. Ser.*, **86** (1993) 629.
- [4] ABDO A. A. *et al.*, *Astrophys. J. Suppl. Ser.*, **188** (2010) 405.
- [5] ABDO A. A. *et al.*, *Science*, **329** (2010) 817.
- [6] ABDO A. A. *et al.*, *Science*, **331** (2010) 739.
- [7] ABDO A. A. *et al.*, *Astrophys. J. Lett.*, **706** (2009) L138.
- [8] DE PASQUALE M. *et al.*, *Astrophys. J. Lett.*, **709** (2010) L146.
- [9] ABDO A. A. *et al.*, *Nature*, **462** (2009) 331.
- [10] ABDO A. A. *et al.*, *Astrophys. J.*, **716** (2010) 1178.
- [11] ABDO A. A. *et al.*, *Astrophys. J.*, **715** (2010) 429.
- [12] ABRAHAM J. *et al.*, *Science*, **318** (2007) 938.
- [13] ABDO A. A. *et al.*, *Science*, **328** (2010) 725.
- [14] ABDO A. A. *et al.*, *Nature*, **463** (2010) 919.
- [15] ABDO A. A. *et al.*, *Science*, **325** (2010) 840.
- [16] ABDO A. A. *et al.*, *Science*, **325** (2010) 848.
- [17] ABDO A. A. *et al.*, *Astrophys. J. Suppl. Ser.*, **187** (2010) 460.
- [18] ABDO A. A. *et al.*, *Astrophys. J.*, **726** (2011) 35.
- [19] ABDO A. A. *et al.*, *Science*, **327** (2010) 1103.
- [20] ABDO A. A. *et al.*, *Astrophys. J. Lett.*, **706** (2009) L1.
- [21] STRONG A. W., MOSKALENKO I. V. and REIMER O., *Astrophys. J.*, **537** (2000) 763.
- [22] ABDO A. A. *et al.*, *Phys. Rev. Lett.*, **103** (2009) 25.
- [23] ABDO A. A. *et al.*, *Astrophys. J.*, **703** (2010) 1249.
- [24] ABDO A. A. *et al.*, *Astrophys. J.*, **710** (2011) 133.
- [25] ACKERMANN A. A. *et al.*, *Astrophys. J.*, **726** (2011) 81.
- [26] STRONG A. W., arXiv:1101.1381.
- [27] ABDO A. A. *et al.*, *Astron. Astrophys.*, **512** (2010) A7.
- [28] ABDO A. A. *et al.*, *Astron. Astrophys.*, **523** (2010) A46.
- [29] ABDO A. A. *et al.*, *Astron. Astrophys.*, **523** (2010) L2.
- [30] ABDO A. A. *et al.*, *Astrophys. J. Lett.*, **709** (2010) L152.
- [31] ABDO A. A. *et al.*, *Phys. Rev. Lett.*, **104** (2010) 101101.
- [32] ABDO A. A. *et al.*, *Astrophys. J.*, **720** (2009) 435.
- [33] ABDO A. A. *et al.*, *J. Cosm. Astropart. Phys.*, **04** (2010) 014.
- [34] MOSKALENKO I. V. and PORTER T. A., *Astrophys. J. Lett.*, **652** (2009) L54.
- [35] ABDO A. A. *et al.*, *Phys. Rev. Lett.*, **104** (2010) 091302.
- [36] ABDO A. A. *et al.*, *Astrophys. J.*, **712** (2010) 147.
- [37] MÜLLER D., *Adv. Space Res.*, **27** (2001) 659.
- [38] ABDO A. A. *et al.*, *Phys. Rev. Lett.*, **102** (2009) 181101.
- [39] ABDO A. A. *et al.*, *Phys. Rev. D*, **82** (2010) 092004.
- [40] CHANG J. *et al.*, *Nature*, **456** (2008) 362.
- [41] ADRIANI O. *et al.*, *Nature*, **458** (2009) 607.
- [42] BLASI P., *Phys. Rev. Lett.*, **103** (2009) 051104.
- [43] KATZ B. *et al.*, *Mon. Not. R. Astron. Soc.*, **405** (2010) 1458.
- [44] ABDO A. A. *et al.*, *Phys. Rev. D*, **82** (2010) 092003.

Cosmic rays in the TeV region with the ARGO-YBJ detector

P. BERNARDINI for the ARGO-YBJ COLLABORATION

Dipartimento di Fisica, Università del Salento and INFN, Sezione di Lecce - Lecce, Italy

(ricevuto il 29 Settembre 2011; pubblicato online il 23 Gennaio 2012)

Summary. — Very High Energy (VHE) γ -astronomy and cosmic ray physics are the main goals of the ARGO-YBJ experiment. The detector is located in Tibet (People's Republic of China) and is a full-coverage Extensive Air Shower array consisting of a carpet of Resistive Plate Chambers (RPCs). Altitude and full coverage ensure an unprecedented reconstruction of showers close to their maximum size. The performances of the detector and the present results concerning TeV cosmic ray physics will be presented.

PACS 96.50.sd – Extensive air showers.

1. – Introduction

The ARGO-YBJ (Astrophysical Radiation Ground-based Observatory at YangBa-Jing) experiment is located in Tibet at an altitude of 4300 m and is supported by an Italian-Chinese scientific collaboration. It is mainly devoted to VHE gamma astronomy and cosmic ray (CR) physics.

After some detail about the performances of the detector (sect. 2), this paper will be focused on CRs in the range 1–300 TeV. Many significant analyses have been completed or are under way about Moon shadow and antiproton flux (sect. 3), anisotropies (sect. 4) and proton cross section (sect. 5). Unprecedented details on the shower front are available (sect. 6) thanks to the high granularity and this information can be crucial to test the hadron interaction models. Other CR topics (as the spectrum measurement, the large-scale anisotropy or the Sun shadow analysis) will not be discussed for space limits.

2. – Detector features and performance

The detector consists of a single layer of RPCs operated in streamer mode [1], on a total area of about $110 \times 100 \text{ m}^2$ (fig. 1). The central carpet ($78 \times 74 \text{ m}^2$) is fully active and surrounded by a sampling ring with other 1000 m^2 (20% of the outer ring) equipped with RPCs. The detector is logically divided in 153 clusters, each made by 12 RPCs with a dedicated Local Station for the DAQ. The digital read-out of the RPCs is performed by means of inductive strips ($6 \times 62 \text{ cm}^2$) well suited to detect small air showers. The

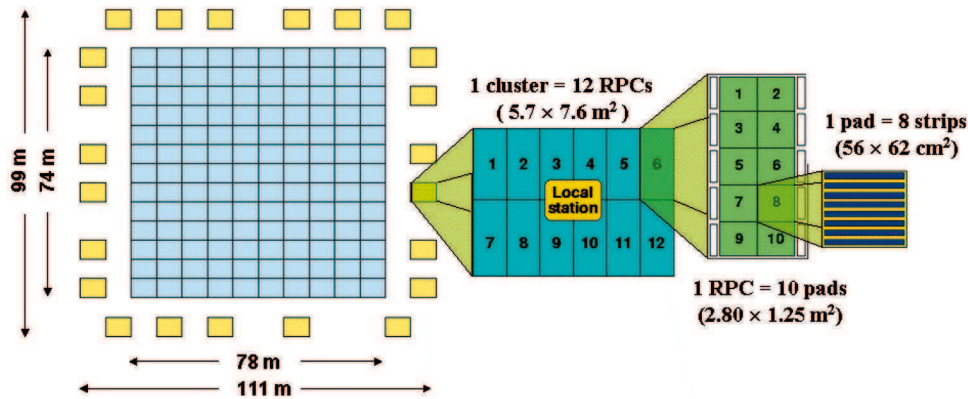


Fig. 1. – (Colour on-line) Setup of the ARGO-YBJ experiment. Two big-pads (not shown in this figure) are used for the analog charge read-out of each RPC.

fast-OR of 8 strips is called *pad* and defines the space-time pixel of the detector, with a time resolution of ~ 1.8 ns [2]. The timing calibration of the detector has been properly performed by means of an innovatory software method [3] and does not require dedicated calibration runs. Thus the data-taking is limited only by maintenance operations and the duty-cycle is higher than 86%. In order to extend the measurable energy range, each RPC has been equipped also with two large electrodes, called *big pads*, which provide an analog signal proportional to the deposited charge [4].

ARGO-YBJ collects data in scaler and shower mode. The first one does not require any trigger, it records the rate for four multiplicity bands (≥ 1 , ≥ 2 , ≥ 3 and ≥ 4) on each cluster in a time window of 0.5 s. The scaler mode allows the detection of low energy transient phenomena (*e.g.*, GRBs and solar flares) observed as non-statistical fluctuations of the background [5].

The shower mode works when the number of pads fired in a time-window of 420 ns exceeds the multiplicity required by the trigger condition. Typically the lowest multiplicity is 20 and the trigger rate is 3.5 kHz. The event is fully reconstructed (arrival direction, core position, lateral distribution and so on) looking at the space-time pattern (see fig. 2) and the size of the shower is measured by means of the fired strips. When the strip signal is saturated as in the event of fig. 3, a detailed reconstruction of the shower is always allowed by the recently implemented charge read-out. Because of this detector capability the CR studies can be extended to some thousands of TeV, in the region close to the knee.

Thanks to modularity the data-taking began during the commissioning, the central carpet was completed in 2006. Since November 2007 the experiment has been fully installed and in stable data-taking.

3. – Moon shadow and antiproton flux

Cosmic rays are hampered by the Moon, therefore a deficit of CRs in its direction is expected (the so-called Moon shadow). The same effect has been observed in the direction of the Sun [6]. The Moon shadow analysis is a crucial test of the detector

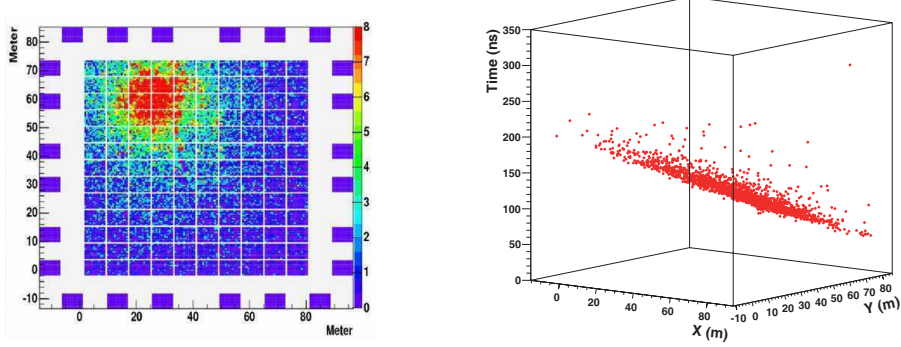


Fig. 2. – (Colour on-line) Digital display of ARGO-YBJ events. Left: x - y shower footprint, where the color scale indicates the number of strips fired on each pad. Right: x - y -time view of another shower, where each dot is a fired pad.

performance. The RMS of the deficit is related to the Point Spread Function (PSF) of the detector according to

$$(1) \quad RMS = \sqrt{\sigma^2 + \left(\frac{\phi}{4}\right)^2},$$

where σ^2 is the variance of a Gaussian PSF and $\phi = 0.52^\circ$ is the Moon angular diameter. The westward angular shift $\Delta\alpha$ of the shadow is due to the bending of CR path in the geomagnetic field and allows to calibrate the scale of the primary energy (E) according to the formula $\Delta\alpha \sim 1.58^\circ Z/E[\text{TeV}]$. Finally the deficit position for events with high rigidity (that is energy) allows to estimate the pointing accuracy.

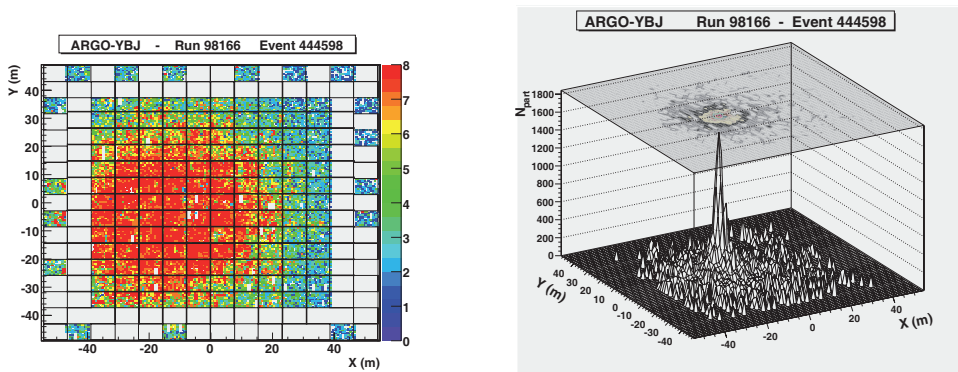


Fig. 3. – (Colour on-line) Comparison between digital and analog read-out for a high-energy event. Left: the large number of particles saturates the digital response (8 strips fired for each pad). Right: the shower core is clearly visible in the analog reconstruction (the number of particles is on the vertical axis).

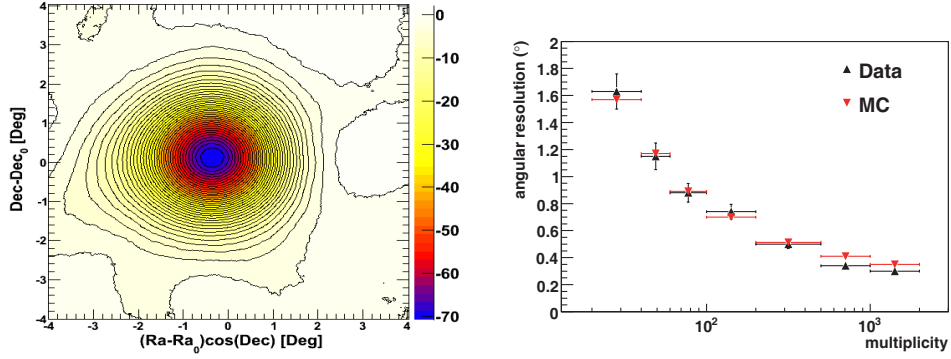


Fig. 4. – (Colour on-line) Moon shadow. Left: significance map of the Moon region. The color scale gives the deficit standard deviations. Right: angular resolution as a function of strip multiplicity. Real data and MC simulation are compared.

The data analysis (fig. 4) confirms the reliability of the ARGO-YBJ detector. The Moon shadow is observed with a significance of 9 standard deviations (s.d.) per month at TeV energy. Using the data collected in the period July 2006–November 2010 and requiring more than 100 strips fired in each event, the deficit appears with a significance higher than 70 s.d. (fig. 4, left). The Moon position turned out to be stable at a level of 0.1° . The angular resolution (fig. 4, right) is what expected.

Also the analysis of the primary CR bending due to the Earth magnetic field and the comparison with MC simulation [7] make us confident in the detector performances and in the reconstruction algorithms. In fig. 5, left the westward Moon shadow shift is shown as a function of strip multiplicity or rigidity assuming positive charged primary CRs. On the contrary it is meaningful to take into account that primary antiprotons are deflected in the opposite sense in their way to the Earth. Thus the Earth-Moon system acts as a magnetic spectrometer and allows the search for antiparticles in the opposite direction of the observed Moon shadow. Selecting CRs with low enough energy and exploiting the

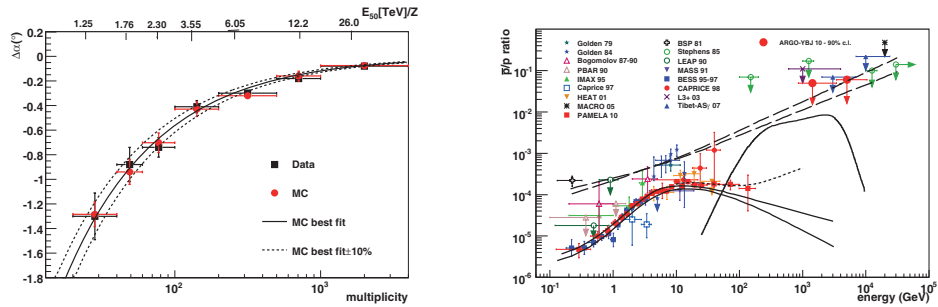


Fig. 5. – (Colour on-line) Left: westward shift ($\Delta\alpha$) of the Moon shadow as a function of strip multiplicity. Real data (black squares) and Monte Carlo simulation (red circles) are compared. The upper scale refers to the rigidity associated to the median energy in the multiplicity bins. Right: antiproton/proton ratio in the CR flux *vs.* energy. The upper limits set by ARGO-YBJ (red arrows) are compared with all measurements and with some theoretical estimate (see text).

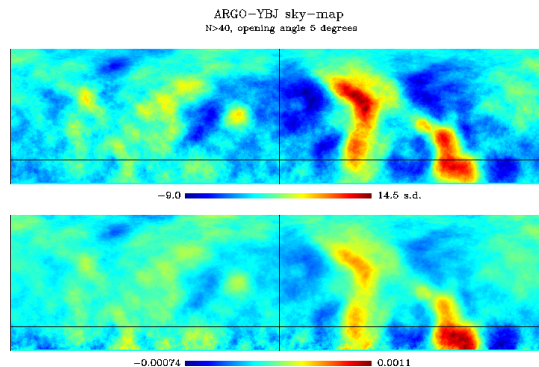


Fig. 6. – (Colour on-line) Sky-map in celestial coordinates of 3-years ARGO-YBJ data (opening angle 5°). Upper plot: the color scale indicates the statistical significance in s.d. Lower plot: the color scale indicates the percentage excess with respect to the estimated background.

angular resolution of the detector two shadows could be observed, one shifted towards West due to the positive CRs and the other one shifted towards East due to antiprotons.

The search for an antiproton signal has been performed exploiting the angular resolution, the pointing accuracy, the long-term stability and the low energy threshold of the detector [8]. The results are two upper limits shown in fig. 5, right, where also theoretical models are shown. The solid curves refer to \bar{p} production during the CR propagation in the Galaxy [9], the long-dashed lines refer to primary antiproton production by antistars [10]. The dot-dashed line represents the contribution of \bar{p} from the annihilation of heavy dark matter particles [11]. The short-dashed line shows a model [12] with secondary antiprotons and an additional antiproton component produced and accelerated at CR sources.

4. – Intermediate-scale anisotropies

The data collected in three years by the ARGO-YBJ detector show several few-degree CR excesses (fig. 6) after the removal of large angular features. This observation has high statistical significance and confirms findings by other experiments like Tibet AS- γ and Milagro. The morphological description of the phenomenon has been improved by our measurement and new localized sky zones hosting excesses have been found. Energy spectra have been measured and they are rather similar to previous measurements, though significant differences can be appreciated. So far these few-degrees anisotropies in the rigidity region 1–10 TV are not explained in terms of the standard theories of CR propagation in the galaxy. Possible explanations are a particular structure of the galactic magnetic field in the Earth neighborhood as well as the emission from nearby sources. In the last case few-degree anisotropies may reveal as an effective tool to probe the accelerated emission of CRs at sources.

5. – Proton cross section

The measurement [13] is based on the shower flux attenuation for different zenith angles (θ), *i.e.* atmospheric depths. The detector features allow to fix the energy ranges and

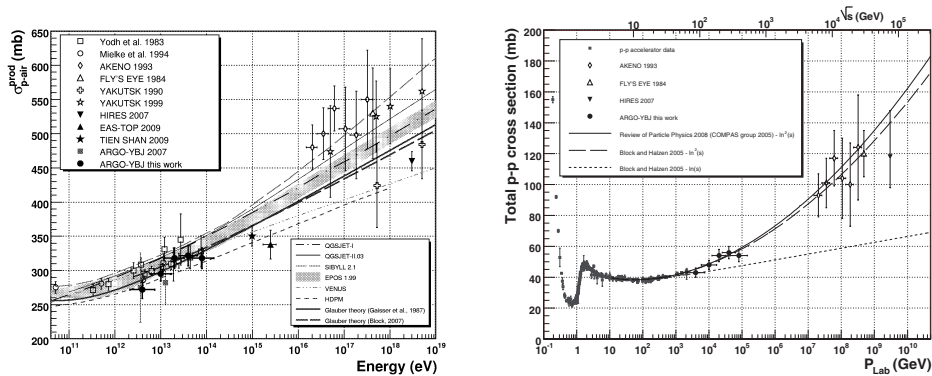


Fig. 7. – Left: the proton-air *production* cross section as measured by ARGO-YBJ and by other CR experiments. The predictions of several hadronic interaction models are also shown. Right: the p-p total cross section obtained by ARGO-YBJ data, together with results published by other CR and accelerator experiments.

to constrain the shower ages. In particular, different strip multiplicity intervals have been used to select showers corresponding to different primary energies. At the same time the information on particle density, lateral profile and shower front extension have been used to select showers having their maximum development within a given distance/grammage from the detection level. This made possible the unbiased observation of the expected exponential falling of shower intensities as a function of the atmospheric depth through the $\sec \theta$ distribution. After the event selection, the fit to this distribution with an exponential law gives the slope value γ , connected to the characteristic length Λ through the relation $\gamma = h_0/\Lambda$ ($h_0 \simeq 610 \text{ g/cm}^2$ is the vertical atmospheric depth). That is,

$$(2) \quad I(\theta) = A(\theta) I(0) e^{-\gamma (\sec \theta - 1)},$$

where $A(\theta)$ accounts for the geometrical acceptance in the angular bin. The parameter Λ is connected to the proton interaction length by the relation $\Lambda = k\lambda_{int}$, where k depends on hadronic interactions and on the shower development in the atmosphere and its fluctuations. The actual value of k has been evaluated by a full MC simulation and it depends also on the experimental approach, the primary energy range and on the detector response. The p-air *production* cross section is then obtained from the relation

$$(3) \quad \sigma_{p-air} \text{ (mb)} = 2.41 \times 10^4 / \lambda_{int} \text{ (g/cm}^2\text{)},$$

while several theoretical approaches are possible to get the corresponding p-p total cross section σ_{p-p} [14]. The results of this measurement are shown in fig. 7 for 5 energies. ARGO-YBJ experimental points lie in an energy region not yet reached by p-p colliders (and still unexplored by p- \bar{p} experiments), favouring the asymptotic $\ln^2(s)$ increase of total hadronic cross sections.

6. – Morphology of the shower front

The space-time structure of extensive air showers depends on primary mass, energy and arrival direction and on the interaction mechanisms with air nuclei. Detailed

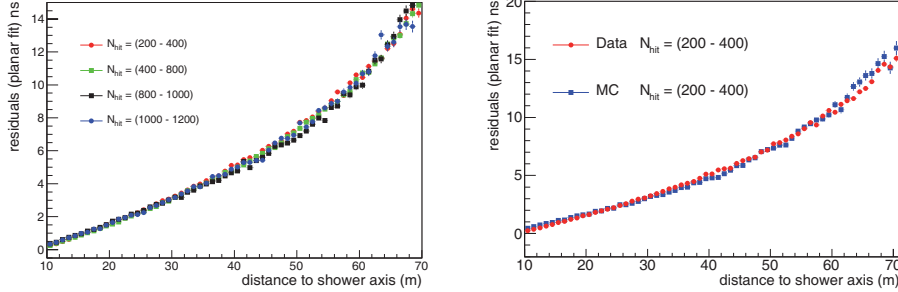


Fig. 8. – (Colour on-line) Mean of time residuals with respect to a planar fit as a function of the distance to shower axis. Left: real data measurement for different pad multiplicities. Right: real data and simulated data (proton) for pad multiplicity in the range 200–400.

measurements of many shower parameters (size, lateral distribution, arrival times, curvature and so on) would be required for a complete knowledge of the shower event.

A full-coverage array like ARGO-YBJ measures the arrival times and densities of shower particle at ground. The digital readout allows detection down to very low density and the high space-time granularity provides a fine sampling of the shower front close to the core. These unprecedented detector features allow deep studies about the shower development searching for more information about type of primary, its energy and shower age. These studies could be also a test-bed for hadronic interaction models and could give some hint about gamma-hadron separation.

The curvature and the thickness of the shower disc have been studied as a function of the distance to shower axis up to a maximum distance of 70 m for quasi-vertical showers ($\theta < 15^\circ$). Figure 8, left shows the mean value of time residuals with respect to a planar fit for different pad multiplicities. The arrival time delay from planar fit increases with distance up to 10 ns for particles landing further than 50 m from the core. No significant dependence on pad multiplicity is observed. In fig. 8, right the real data distribution for $200 < N_{pad} < 400$ is compared with a simulation where Sibyll code has been used for the hadronic interactions and Corsika for the shower development in the atmosphere. No discrepancies are visible and this make us more confident about the tools of this analysis (simulation and reconstruction algorithms).

For primaries interacting deeper in the atmosphere (young showers), due to geometrical reasons, the arrival of particles at a given lateral distance is expected to be more delayed compared to primaries that have interacted higher (old showers). Young showers will then exhibit a steeper time profile with respect to a planar fit. A study of the correlation between the measured shower conicity and the atmospheric depth of the shower maximum suggests to adopt the conicity as an estimator of the shower development stage.

Also events with particularly large time spread have been investigated. They can be grouped into two main typologies: wide shower and double front events. The first ones can be large showers with the core very far from the detector. The second ones are expected to be showers in the same trigger time window ($2 \mu\text{s}$). Some discrepancy with respect to these interpretations could be the signal of exotic effects.

7. – Conclusions

The ARGO-YBJ detector is taking data since November 2007 in the complete setup (central carpet and guard ring) in a very stable way. The detector performances are what expected and they are monitored by the analysis of the Moon shadow in the CR flux. Remarkable results have been achieved in gamma-astronomy [15]. Here a selection of CR physics measurements essentially based on the digital read-out has been presented.

We would like to stress that the analog charge read-out allows to enlarge the energy range of ARGO-YBJ measurements (for instance the p-p cross section measurement) up to thousands of TeV.

* * *

This work is supported in China by NSFC (Contract No. 10120130794), the Chinese Ministry of Science and Technology, the Chinese Academy of Sciences, the Key Laboratory of Particle Astrophysics, CAS, and in Italy by the Istituto Nazionale di Fisica Nucleare (INFN) and the Ministero dell'Istruzione, dell'Università e della Ricerca (MIUR).

REFERENCES

- [1] BACCI C. *et al.* (ARGO-YBJ COLLABORATION), *Nucl. Instrum. Methods A*, **508** (2003) 110; AIELLI G. *et al.* (ARGO-YBJ COLLABORATION), *Nucl. Instrum. Methods A*, **562** (2006) 92.
- [2] AIELLI G. *et al.* (ARGO-YBJ COLLABORATION), *Nucl. Instrum. Methods A*, **608** (2009) 246.
- [3] HE H. H. *et al.*, *Astropart. Phys.*, **27** (2007) 528; AIELLI G. *et al.* (ARGO-YBJ COLLABORATION), *Astropart. Phys.*, **30** (2009) 287.
- [4] AIELLI G. *et al.* (ARGO-YBJ COLLABORATION), *Nucl. Instrum. Methods A*, (2011) to be published.
- [5] AIELLI G. *et al.* (ARGO-YBJ COLLABORATION), *Astropart. Phys.*, **30** (2008) 85.
- [6] AIELLI G. *et al.* (ARGO-YBJ COLLABORATION), *Astroph. J.*, **729** (2011) 113.
- [7] DI SCIASCIO G. and IUPPA R., *Nucl. Instrum. Methods A*, **630** (2011) 301.
- [8] DI SCIASCIO G. *et al.* (ARGO-YBJ COLLABORATION), *Nucl. Phys. B (Proc. Suppl.)*, **212-213** (2011) 301.
- [9] DONATO F. *et al.*, *Phys. Rev. Lett.*, **102** (2009) 071301.
- [10] STEPHEN S. A. and GOLDEN R. L., *Space Sci. Rev.*, **46** (1987) 31.
- [11] CIRELLI M. *et al.*, *Nucl. Phys. B*, **813** (2009) 14.
- [12] BLASI P. and SERPICO P. D., *Phys. Rev. Lett.*, **103** (2009) 081103.
- [13] AIELLI G. *et al.* (ARGO-YBJ COLLABORATION), *Phys. Rev. D*, **80** (2009) 092004.
- [14] GAISSER T. K., *Phys. Rev. D*, **36** (1987) 1350; BLOCK M. M., *Phys. Rev. D*, **76** (2007) 111503 and references therein.
- [15] AIELLI G. *et al.* (ARGO-YBJ COLLABORATION), *Astrophys. J.*, **699** (2009) 1281; *Astropart. Phys.*, **32** (2009) 47; *Astrophys. J. Lett.*, **714** (2010) L208; BERNARDINI P. (ARGO-YBJ COLLABORATION), *Proceedings of Science: Texas 2010* (2010) 166; BARTOLI B. *et al.* (ARGO-YBJ COLLABORATION), *Astrophys. J.*, **734** (2011) 110.

Highlights from the Pierre Auger Observatory

M. BOHACOVA on behalf of the PIERRE AUGER COLLABORATION^(*)

*Institute of Physics of the Academy of Sciences of the Czech Republic - Na Slovance 2
182 21 Praha 8, Czech Republic*

(ricevuto il 29 Settembre 2011; pubblicato online il 23 Gennaio 2012)

Summary. — We present a review of recent results from the Pierre Auger Observatory, including the measurement of the cosmic ray energy spectrum above 10^{18} eV, searches for anisotropy of the arrival directions, and studies of cosmic ray mass composition. The flux exhibits hardening at 4×10^{18} eV followed by suppression consistent with the GZK effect above 3×10^{19} eV. Correlation of cosmic ray air shower arrival directions with the distribution of the nearby extragalactic matter is observed at energies above 5.5×10^{19} eV. The observed longitudinal development of air showers suggests that the interaction cross-section increases with energy more rapidly than current models predict for proton primaries, perhaps due to a transition to heavier composition. No clear candidates for neutrinos and photons in the ultra-high energy cosmic ray flux have yet been found.

PACS 95.55.Vj – Neutrino, muon, pion, and other elementary particle detectors; cosmic ray detectors.

PACS 95.85.Ry – Neutrino, muon, pion, and other elementary particles; cosmic rays.

1. – Introduction

The Pierre Auger Observatory [1] was built to study the properties of extensive air showers produced by cosmic rays with energies above 10^{18} eV. It is located in the southern hemisphere near the town of Malargüe, Argentina. The observatory features a large detection area to collect a significant number of rare cosmic ray events. It is the first experiment observing air showers simultaneously by two detection techniques, making it possible to reduce the systematic uncertainties associated with each method. The surface detector (SD) is an array of more than 1600 water Cherenkov detectors sampling the lateral distribution of the shower particles on the ground. The SD has a duty cycle of almost 100%. The fluorescence detector (FD) consists of 27 telescopes observing the longitudinal development of the showers in the atmosphere above the surface array. The light is from

^(*) Full author list available at: http://www.auger.org/archive/authors_2010_11.html

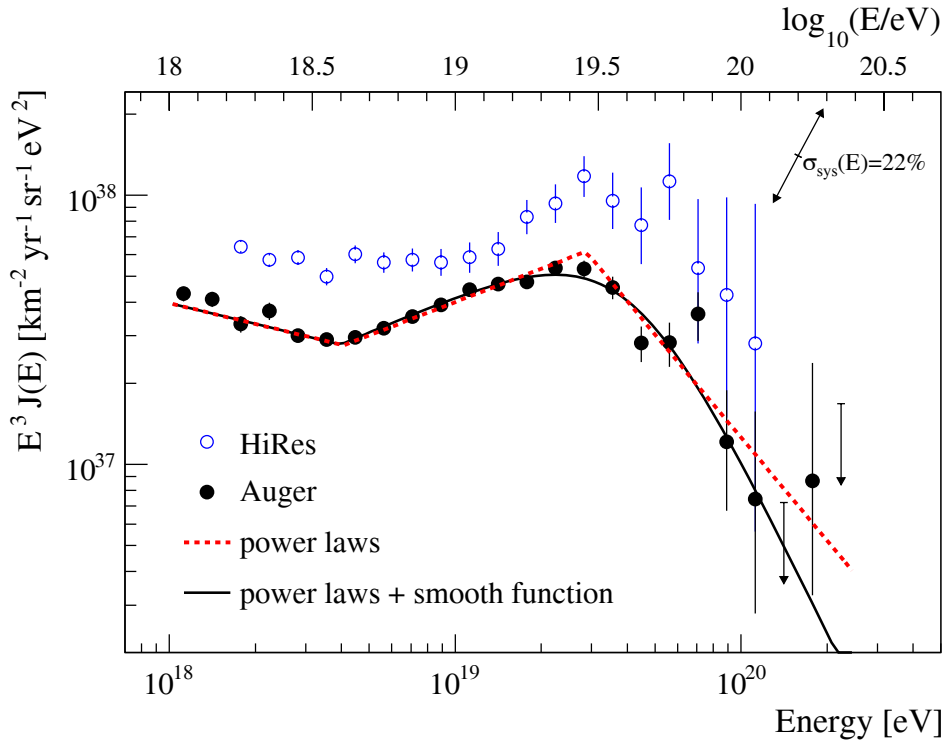


Fig. 1. – Combined hybrid and SD energy spectra from Auger [4] compared to the stereo spectrum from HiRes [5].

nitrogen emission in the near UV region and so the FD can operate only during clear moonless nights, limiting its duty cycle to less than 15% [2]. This technique provides a calorimetric and therefore essentially model-independent measurement of the shower energy, which is used to calibrate the SD measurements. The modular design of the observatory made it possible to start data taking in 2004, before the baseline configuration was completed in 2008. By the end of 2009 a total exposure of about 20 000 km² sr y was collected, significantly more than that of all previous air shower experiments combined.

2. – Energy spectrum

Measuring the cosmic ray energy spectrum is a key aspect in understanding the origin and nature of particles whose energies exceed by many orders of magnitude the energy achievable in man-made accelerators. The most direct shower energy determination is obtained by the fluorescence technique. The fluorescence yield (photons emitted per unit of electron energy deposited) characteristics are determined in laboratory measurements [3]. The total energy deposited by the shower is then given by integrating the light observed as the shower develops. A subset of hybrid events (detected by both techniques) are used to establish the relationship between the SD particle density parameter and the FD determined energy. This relation is then used to derive the energy of the full SD data sample. The combined hybrid and SD-only spectrum from the Pierre Auger Observatory is shown in fig. 1. The spectrum can be described by a broken power-law E^{-s} with the

spectral index $s = 3.26 \pm 0.04$ below the first break located at $\log(E) = 18.61 \pm 0.01$ (called the ankle). The spectral index reaches 2.59 ± 0.02 above the ankle and then steepens again to $s = 4.3 \pm 0.2$ above the second spectral feature at $\log(E) = 19.46 \pm 0.03$. The HiRes stereo spectrum is shown for comparison. The apparent overall shift of the two spectra is not yet understood, but they are consistent within systematic errors [4] (about 20% for each experiment).

Although the observed features are consistent with the GZK predictions (for proton dominated composition), one should realize that this does not necessarily mean that this is in fact the mechanism behind the suppression. For example it is also conceivable that the suppression is caused by the maximum energy achievable by the cosmic accelerators. Interpretation of the spectral features should be done using also the information from chemical composition studies and searches for photons and neutrinos. The ankle may be a result of a steep spectrum from galactic sources crossing over a flatter spectrum from the extragalactic sources.

3. – Arrival directions

With increasing energy the trajectories of cosmic ray particles become less deflected in the galactic and extragalactic magnetic fields, giving hope that astronomy at ultra-high energies will become feasible. Moreover, if the observed flux suppression is the GZK effect, then 10^{20} eV particles can not reach the Earth from distances of order 100 Mpc or beyond. Since nearby extragalactic matter is not uniformly distributed, these facts motivate a search for anisotropy in the arrival directions of cosmic rays. One class of objects believed capable of accelerating particles to ultrahigh energies are Active Galactic Nuclei (AGN). The Pierre Auger Collaboration found a significant correlation with objects from the Véron-Cetty and Véron catalog [6], the effect appearing for events with energy above 55 EeV, angular separation from catalog objects of less than 3.1° , and for AGNs less than 75 Mpc distant [7].

An update of the fraction of correlating events detected until 31 December 2009 excluding the 14 initial events used to establish the hypothesis, yields $38_{-6}^{+7}\%$, where only 21% would be expected for an isotropic distribution [8]. The 69 events with energies above 55 EeV detected in this time period are plotted in fig. 2. Note that the catalogs are incomplete near the galactic plane due to obscuration, so the lack of correlation for events in this region is expected. Details of these studies are reported in [8].

Especially interesting is the concentration of events around the location of Centaurus A, which lies only ~ 4 Mpc away from us. Plotting the number of observed events as a function of angular distance from Cen A shows the most significant excess for events within 18° , where 13 events were observed while only 3 are expected for an isotropic distribution (fig. 3). It is unclear whether the events come from the Cen A nucleus, its radio lobes, or even from other objects, perhaps in the Centaurus galaxy cluster, located about 45 Mpc behind Cen A on the same line of sight. Of course, the possibility that the excess could be a random fluctuation has not yet been ruled out.

4. – Mass composition

Information about the mass and type of the primary particle is another key component in understanding the origin of ultra-high energy cosmic rays. The chemical composition of the primaries will affect the resulting air showers most significantly in the electron/muon

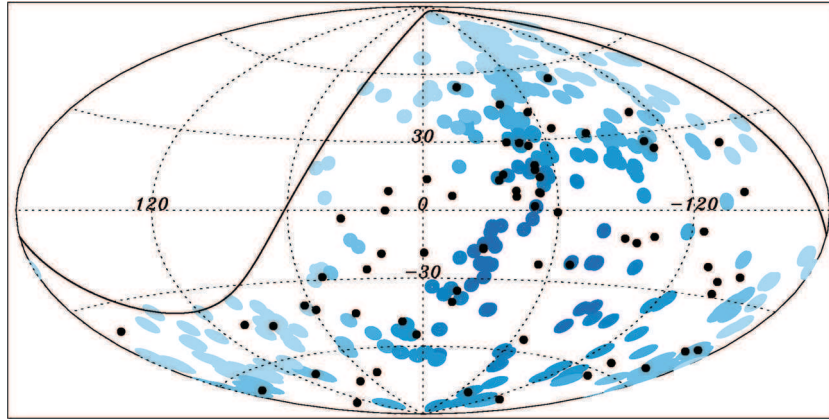


Fig. 2. – Arrival directions of the 69 events above 55 EeV (dots). The circles of 3.1° are centered around the positions of the 318 AGNs from the VCV catalog that are located within 75 Mpc distance and within the field of view of the observatory (solid curve). The shading of the circles indicates the relative exposure at these locations. Cen A is located at $l \sim -50.5^\circ$, $b \sim 19.4^\circ$.

ratios at the ground level and the depth-of-maxima in the atmosphere. A simple superposition principle gives some guidance: it approximates an interaction of a nucleus of mass A and energy E as the superposition of A nucleons each with the energy E/A . Hence, for a given energy a proton primary will penetrate deeper into the atmosphere and the

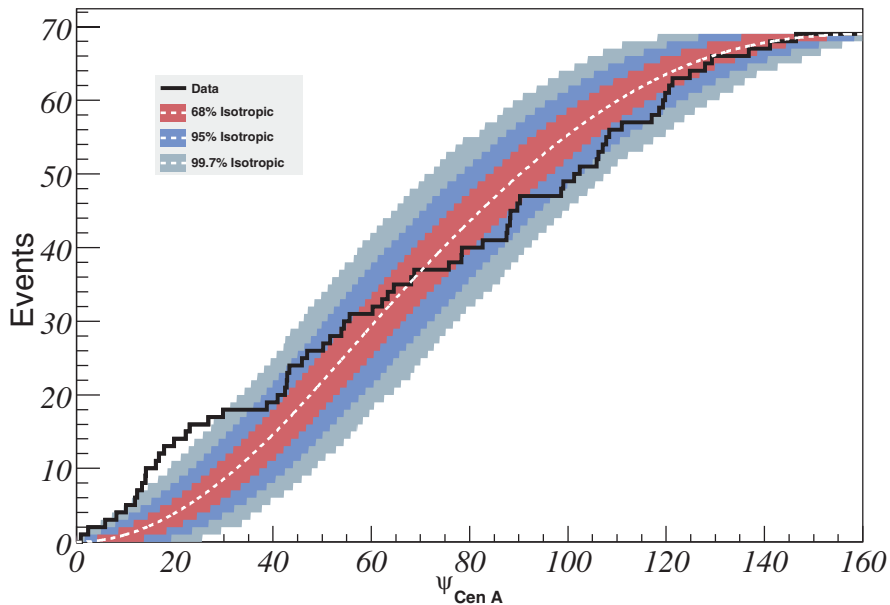


Fig. 3. – Cumulative number of events with $E \geq 55$ EeV as a function of angular distance from the direction of Cen A. The bands correspond to 68%, 95%, and 99.7% dispersion expected for an isotropic flux.

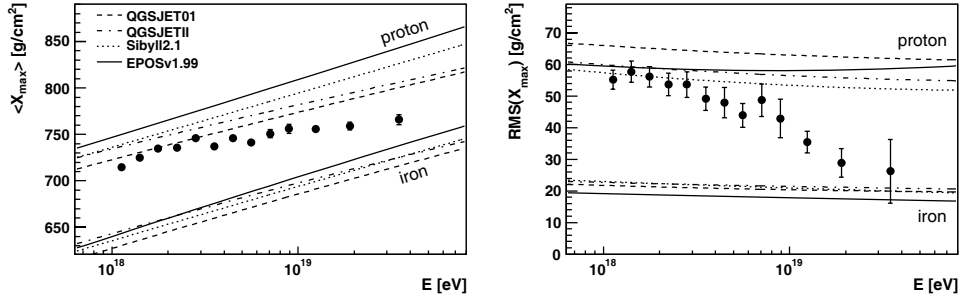


Fig. 4. – Distributions of X_{\max} (left) and $\text{RMS}(X_{\max})$ as a function of energy. Sample contains well-reconstructed hybrid events only. Monte Carlo simulations using different hadronic interaction models are shown for protons and iron nuclei.

shower-to-shower fluctuations will be larger than in the case of a heavier nucleus. Results of the studies of the X_{\max} distribution and its RMS are presented in fig. 4 together with predictions for a pure proton and a pure iron composition from various hadronic interaction models. Further details of this analysis can be found in [9]. It is necessary to invoke hadronic physics models to assess the composition, but there are no models that properly represent all observed air shower characteristics. Thus it is dangerous to make inferences using them. Current models are extrapolating the features of the hadronic interactions well beyond the region tested by accelerator data. Consequently, the systematic uncertainties of the predictions are significant. With these caveats in mind, both $\langle X_{\max} \rangle$ and $\text{RMS}(X_{\max})$ suggest a trend from a lighter composition to heavier (*e.g.* CNO). The trend coincides with the position of the ankle in the spectrum. Only the highest quality events detected by the FD are considered in this study, limiting the number of events analyzed. An unfortunate result is that the statistics do not yet allow extension of this analysis to the highest energies, where the correlations with AGNs are observed. Reconciling this composition trend with the observed anisotropy may be very challenging.

It is interesting to note that an increase in the proton-nucleus inelastic cross-section at the highest energies would bring model predictions for protons closer to the data by making X_{\max} higher in the atmosphere. Results from the LHC, particularly in the forward region, will be of great interest for the cosmic ray community as they are expected to improve the reliability of the hadronic interaction models.

Independently of the LHC experiments (and at energies beyond their reach), the Pierre Auger Observatory can investigate some aspects of hadronic interaction models. For example, several examinations of the intensity of the muon component in extensive air showers have been performed, with preliminary results suggesting that showers contain more muons than the models predict [10].

5. – Photon and neutrino limits

Photons and earth-skimming neutrinos are expected to have a characteristic signature in the data, since both produce showers that develop deep in the atmosphere. Both kinds will be seen as young showers, while an earth-skimming tau neutrino will also have a nearly horizontal trajectory. Searches for such events have yielded strong limits that exclude some of the so-called “exotic scenarios” for the production of ultra-high energy

cosmic rays. The current upper limit from the Auger data for the fraction of photons in the UHECR flux is 2% above 10 EeV and 2.4% above 2 EeV [11]. For the tau neutrino flux in the energy range $2 \times 10^{17} \text{ eV} < E_\nu < 2 \times 10^{19} \text{ eV}$, assuming a diffuse spectrum of the form E_ν^{-2} the corresponding upper limit is $6 \times 10^{-8} \text{ GeV cm}^{-2} \text{ s}^{-1} \text{ sr}^{-1}$ [12].

6. – Observatory enhancements

The Pierre Auger Observatory is now collecting around 7000 km² sr of exposure per year. New detector systems are being deployed now to compare our measurements with other experiments working at lower energy. HEAT (High Elevation Auger Telescopes) has three telescopes with their field of view pointing above the baseline Auger instruments, allowing observation of nearby lower energy showers ($\gtrsim 10^{17} \text{ eV}$) [13]. AMIGA (Auger Muon and Infill for the Ground Array) is essentially a denser grid of surface stations paired with underground muon counters and will perform a precise study of the lateral shower profile as well as the muon content in the energy region between 10^{17} eV and 10^{19} eV [14]. AERA (Auger Engineering Radio Array) is exploiting yet another detection technique, the measurement of the coherent radiation at radio frequencies emitted by secondary shower particles deflected in the geomagnetic field [15].

As the new devices are put to operation and the analysis of new data is ongoing, more interesting results can be expected.

* * *

The contribution was prepared with the support of Ministry of Education, Youth and Sports of the Czech Republic within the project LA08016.

REFERENCES

- [1] ABRAHAM J. *et al.* (PIERRE AUGER COLLABORATION), *Nucl. Instrum. Methods A*, **523** (2004) 50.
- [2] ABRAHAM J. *et al.* (PIERRE AUGER COLLABORATION), *Nucl. Instrum. Methods A*, **620** (2010) 227.
- [3] *Nucl. Instrum. Methods A*, **597** (2008).
- [4] ABRAHAM J. *et al.* (PIERRE AUGER COLLABORATION), *Phys. Lett. B*, **685** (2010) 239.
- [5] ABBASI R. *et al.* (HiRES COLLABORATION), *Astropart. Phys.*, **32** (2009) 53.
- [6] VÉRON-CETTY M.-P. and VÉRON P., *Astron. Astrophys.*, **455** (2006) 773.
- [7] ABRAHAM J. *et al.* (PIERRE AUGER COLLABORATION), *Science*, **318** (2007) 938; *Astropart. Phys.*, **29** (2008) 188.
- [8] ABREU R. *et al.* (PIERRE AUGER COLLABORATION), *Astropart. Phys.*, **34** (2010) 314.
- [9] ABRAHAM J. *et al.* (PIERRE AUGER COLLABORATION), *Phys. Rev. Lett.*, **104** (2010) 091101.
- [10] CASTELLINA A. for the PIERRE AUGER COLLABORATION, *Proceedings of the 31st ICRC, Lodz, Poland*, (2009) 0033.
- [11] ABRAHAM J. *et al.* (PIERRE AUGER COLLABORATION), *Astropart. Phys.*, **31** (2009) 399.
- [12] ABRAHAM J. *et al.* (PIERRE AUGER COLLABORATION), *Phys. Rev. D*, **79** (2009) 102001.
- [13] KLEIFGES M. for the PIERRE AUGER COLLABORATION, *Proceedings of the 31st ICRC, Lodz, Poland*, (2009) 0410.
- [14] ETCHEGOYEN A. for the PIERRE AUGER COLLABORATION, *Proceedings of the 30th ICRC, Mérida, Mexico*, (2007) 1307.
- [15] VAN DER BERG A. M. for the PIERRE AUGER COLLABORATION, *Proceedings of the 31st ICRC, Lodz, Poland*, (2009) 0232.

Origin of the ultrahigh-energy cosmic rays and their spectral break

S. DADO⁽¹⁾, A. DAR⁽¹⁾ and A. DE RÚJULA⁽²⁾

⁽¹⁾ *Department of Physics, Technion Israel Institute of Technology - Haifa 32000, Israel*

⁽²⁾ *Instituto de Física Teórica (UAM/CSIC), Universitat Autònoma de Madrid, Madrid and CIEMAT, Madrid, Spain,
CERN, 1211 Geneva 23, Switzerland,
Physics Department, Boston University, MA, USA*

(ricevuto il 29 Settembre 2011; pubblicato online il 23 Gennaio 2012)

Summary. — The energy spectrum, composition and arrival directions of ultrahigh energy cosmic rays (UHECRs) with energy above the cosmic ray ankle, measured by the Pierre Auger Observatory, appear to be in conflict if their origin is assumed to be extragalactic. Their spectrum and composition, however, are those expected from Galactic UHECRs accelerated by highly relativistic jets such as those producing short hard gamma ray bursts (SHBs). If this alternative interpretation is correct, then the observed break in the energy spectrum of UHECRs around 50 EeV is the energy threshold for free escape of UHE iron nuclei from the Galaxy and not the Greisen-Zatsepin-Kuzmin (GZK) cutoff for protons, and the arrival directions of UHECR nuclei with energy above their UHE breaks must point back to their Galactic sources rather than to active galactic nuclei (AGN) within the GZK horizon.

PACS 95.85.Ry – Neutrino, muon, pion, and other elementary particles; cosmic rays.

PACS 98.70.Rz – γ -ray sources; γ -ray bursts.

Cosmic rays (CRs), discovered by Victor Hess [1] almost a century ago, have an observed spectrum extending from $E \leq 10^6$ eV to extremely high energies, $E \geq 10^{20}$ eV. At low energies the primary CRs contain all the stable elements. At very high energies, their all-particle spectrum has not been resolved into separate elements. Their energy spectrum is well represented by a broken power law $E^{-\beta}$, with $\beta \approx 2.7$ above ~ 10 GeV until the “CR knee” at $\sim 3 \times 10^{15}$ eV, where it steepens to $\beta \approx 2.9$ up to a “second knee” near 2×10^{17} eV where it changes to $\beta \approx 3.3$. Above the “ankle” at $\sim 3 \times 10^{18}$ eV the ultrahigh energy cosmic ray (UHECR) flux has been accurately measured by the Fly’s Eye High Resolution (HiRes) experiment [2, 3] and the Pierre Auger Observatory (PAO) [4, 5]. Its energy spectrum is well described by a power-law with $\beta \approx 2.7$ until a “break” near 5×10^{19} eV where it changes to $\beta \approx 4.3$, as shown in fig. 1, which shows the energy domain we are here concerned with.

While the origin of the CR knees of different elements is still debated, the CR ankle is generally identified as the energy beyond which the deflection of CRs in the Galactic magnetic field can neither isotropise them nor prolong significantly their residence time in the Galaxy, see, *e.g.*, [6-9] and references therein, and [10] for an alternative.

A free escape of UHECRs from the Galaxy implies that they essentially suffer an angular spread $\langle\theta^2\rangle \ll 1$ by magnetic deflections on their way out of the Galactic cosmic ray halo whose typical radius is $R_G \sim 10$ kpc. For CRs of charge Z , this happens at an energy for which their Larmor radius, $R_L = E/Z e B_r$, becomes much larger than the coherence length, l_c , of the random component of the Galactic magnetic field $B_r \sim 3 \mu$ Gauss [11, 12] and their small deflections $\delta\theta \simeq l_c/R_L$ add up to

$$(1) \quad \langle\theta\rangle \simeq \left[\frac{R_G}{l_c}\right]^{1/2} \left[\frac{l_c}{R_L}\right] \leq \frac{\pi}{2}.$$

For a typical $l_c \sim 0.1$ kpc, $R_L = E/e Z B$ and $\theta = \pi/2$, eq. (1) yields a threshold energy for escape, and consequently a spectral break at $E_{break}(A, Z) = Z E_{break}(p) = 1.8 Z$ EeV. For Fe nuclei, $E_{break}(Fe) = 46.8$ EeV, which roughly coincides with the break-energy measured by HiRes [2, 3] and PAO [4, 5].

The observed ultrahigh-energy (UHE) break at $E \approx 5 \times 10^{19}$ eV was identified by both HiRes and PAO as the so-called ‘‘GZK cutoff’’. This effective threshold for energy losses of CR protons by pion production in collisions with the cosmic microwave background (CMB) radiation, which exponentially suppresses the extragalactic flux of UHECR protons with energy above 5×10^{19} eV, was predicted by Greisen [13] and by Zatsepin and Kuzmin [14] in 1966, right after the discovery of the CMB.

Further support for the identification of the UHE break with the GZK cutoff for UHECR protons came from the arrival directions of UHECRs with energy above the GZK threshold observed in the early PAO data [15]: if the UHECRs are protons, half of those with $E \geq E_{GZK}$ must come from distances < 70 Mpc. Indeed, PAO reported that a large fraction of these UHECRs (measured between 1 January 2004 and 31 August 2007) had arrival directions pointing back within ≤ 3.1 deg to active galactic nuclei (AGNs) closer than ~ 75 Mpc, while the directions of those with smaller energies were isotropic [15, 16].

The conclusion that most UHECRs with $E \geq E_{GZK}$ are protons was expected: extragalactic UHECR nuclei disintegrate in collisions with the infrared background radiations and the CMB, with a mean free path much shorter than that of UHE protons for π production above the GZK threshold [7, 17-20].

However, this early evidence for a directional correlation with AGNs, obtained by PAO from a sample of 27 UHECRs was not present in a sample of an additional 42 events seen through 31 December 2009 and has diminished significantly in the joint sample [21]. In addition, the HiRes collaboration reported [22]. that their sample of 13 events with energy above 57 EeV ($1 \text{ EeV} = 10^{18} \text{ eV}$), is incompatible with directional correlation with AGNs at 95%.

Moreover, PAO recently reported the measured depth of shower maximum of UHECRs and its root-mean-square fluctuations, which indicate that the composition of UHECRs changes progressively with energy from proton-dominated below the CR ankle to Fe-dominated as one approaches the GZK cutoff [4, 23]. The GZK cutoff for Fe-dominated composition is $\approx A = 56$ times larger than that for protons, $E_{GZK}(\text{Fe}) \approx 3 \times 10^{21}$ eV. Thus, the PAO composition of UHECRs seems to be in conflict with the identification of

the UHE break at 50 EeV as the GZK cutoff of UHECR protons. Also the spectral shape around the UHE break seems not to be compatible with that expected from the GZK cutoff [24]. Note, however, that a proton dominated composition [25] and the spectrum of UHECRs [22] that were measured by HiRes are those expected from extragalactic UHECRs [7].

All together, it appears that either the UHECRs are mainly extragalactic protons, the UHE break is due to the GZK cutoff and the Fe-dominated composition of UHECRs near the GZK cutoff that was inferred by the PAO is not correct, or the UHECR composition becomes Fe-dominated near the UHE break and the UHE break is not the GZK cutoff of UHECR protons. This composition controversy, as well as the UHECR-AGN association controversy should be resolved experimentally. But, if the UHECR composition inferred by PAO [4,23] turns out to be the correct one, is there a consistent and simple explanation for both the energy spectrum and composition measured by PAO?

In this short paper we present such an explanation. We show that, with small modifications in the assumed relative Galactic and extragalactic fluxes, the comprehensive theory of cosmic rays presented in [7] correctly predicts the energy spectrum and composition of the PAO UHECRs. All one has to do is to go back to the original assumption that the UHECRs are dominantly of Galactic origin [6]. We show that a rough knowledge of the properties of the Galactic accelerators of UHECRs without an exact knowledge of their identity can reproduce the spectrum and composition of UHECRs which were reported by PAO.

In [7] we posited that CRs are a mixture of Galactic and extragalactic fluxes, accelerated in gamma ray bursts (GRBs) [26]. They are the GRB-ionized interstellar medium (ISM) collisionally accelerated by the highly relativistic jets of plasmoids (cannonballs) that produce Galactic and extragalactic GRBs, most of which are beamed away from Earth [6]. The ones trapped in the Galactic magnetic field have produced its CR halo. In a steady state, the escape rate from the CR halo equals its filling rate. The two CR populations are steadily injected into the Galactic CR halo and the intergalactic medium (IGM) with roughly the same energy spectrum and composition. But they suffer different losses in the host galaxies of the GRBs and in the IGM due to the different environments and residence times.

The CR energy spectrum and composition above the second knee reflect the A-dependent threshold energy (roughly proportional to A) for photo-dissociation of extragalactic CR nuclei in collisions with the CMB and the infrared background radiations during their long residence time in the IGM [7]. The second knee is the threshold for photo-dissociation of ^4He . The CR composition changes progressively from that of low-energy CRs near the second knee to almost a pure protons below the CR ankle, as more heavy nuclei and their fragments disintegrate. The photo-disintegration of the primary nuclei and their fragments changes the power-law index of the all-particle energy spectrum from ~ 2.9 below the second knee to ~ 3.3 above it. We do not discuss in detail this computationally complex subject here (DADO and DAR, in preparation) since we are focusing on the understanding of UHECRs above the ankle. The Galactic component, whose residence time in the Galaxy is too short to imply a significant photo-disintegration in the ISM, starts to dominate before the energy reaches the CR ankle.

Above $E = E_{break}(p) \approx 1.9 \text{ EeV}$, UHECR protons are not isotropised and their free escape is not delayed by the Galactic magnetic field. Their flux predictably decreases with increasing energy beyond the proton UHE break. The CR nuclei of ^4He , that at fixed particle energy are only slightly less abundant than protons (by a factor ~ 0.8), have a UHE break at $E_{break}(^4\text{He}) \approx 2 \times 1.9 \text{ EeV}$, beyond which Fe dominates the CR

composition. The UHE Fe break is at $\approx 26 \times 1.9 \approx 50$ EeV. We shall interpret the UHE all-particle break as the UHE Fe break beyond which Fe CRs are not isotropised nor confined. In order to validate this possibility, we proceed to derive the corresponding spectrum of UHECRs.

At the energies at which CR nuclei are isotropised by the Galactic magnetic field, their density is enhanced by their energy-dependent residence time in the Galaxy. At relatively low (sub TeV) energies this time was empirically estimated [27] to behave as $\tau(E, Z) \propto (E/Z)^{-\beta_r}$ with $\beta_r \approx 0.5 \pm 0.1$, yielding a CR number density [7]

$$(2) \quad \frac{dn_A}{dE} \propto \tau(E, Z) \frac{dn_A^{inj}}{dE} \propto X(A, Z) A^{\beta-1} E^{-\beta},$$

where n_A^{inj} are the injection rates of nuclei, $X(A, Z)$ are their relative abundances in the ISM and $\beta = \beta_{inj} + \beta_r$. For Fermi acceleration in highly relativistic jets, $\beta_{inj} = 13/6$ for all CR nuclei [7], while β_r is not known above the spectral knees. If β_r is E -independent, using its low-energy value one obtains [7] a spectral index of Fe UHE nuclei $\beta = 2.67 \pm 0.1$, for $E < E_{break}(\text{Fe}) \sim 50$ EeV, *i.e.*,

$$(3) \quad \frac{dn_{Fe}}{dE} \propto E^{-2.67 \pm 0.1}.$$

Consider now the arrival of CR nuclei with $E > E_{break}(A, Z)$ from Galactic sources. Their small deflections by the Galactic magnetic field along their path to Earth spread their arrival directions according to eq. (1) and their mean arrival times by

$$(4) \quad \langle \tau_d(E, Z) \rangle \sim \frac{R_G \langle \theta^2 \rangle}{2c}$$

and their residence time in the Galaxy as a function of E approaches rapidly their energy-independent free escape time, $\langle \tau_r(E, Z) \rangle \sim (R_G/c) [1 + \langle \theta^2 \rangle / 2] \rightarrow R_G/c$. A distribution of N_s Galactic transient sources of UHECRs that *isotropically emit* CRs can produce a quasi-isotropic distribution of arrival directions provided their Galactic rate satisfies $\dot{N}_s \tau_d > 4/\langle \theta^2 \rangle$. Their spectral index, however, will remain $\beta = \beta_{inj} \approx 13/6$.

In our theory [7] the injection of CRs is *narrowly beamed*: CRs are accelerated by highly relativistic very narrow jets emitted in the birth or death of compact stars, in supernova explosions, in phase transitions in compact stars, in their mergers, and in accretion episodes onto compact stars, all of which produce observable GRBs when their jets point towards Earth.

For collimated sources eq. (1) implies that the probability for an UHECR to reach Earth is $\langle \theta^2 \rangle / 4 \propto E^{-2}$. Consequently, if the effective number of sources during $\tau_d(E)$ satisfies $N_{eff} = \dot{N}_s \tau_d(E) \ll 4/\langle \theta^2 \rangle$, the probability that the rays reach us during a time $\delta t \ll \tau_d(E)$ is $\propto E^{-2}$. The flux of UHECR nuclei beyond their $E_{break}(Z) = Z E_{break}(p)$ then satisfies

$$(5) \quad \frac{dn_A}{dE} \propto E^{-\beta_{inj}-2} \sim E^{-4.17}.$$

This result is valid in the cannonball model of GRBs [28] where the jets have typical bulk-motion Lorentz factor $\gamma \sim 10^3$ and the UHECRs are beamed into a cone with an opening angle $\theta \sim 1/\gamma \sim 10^{-3}$ much smaller than their angular spread by Galactic

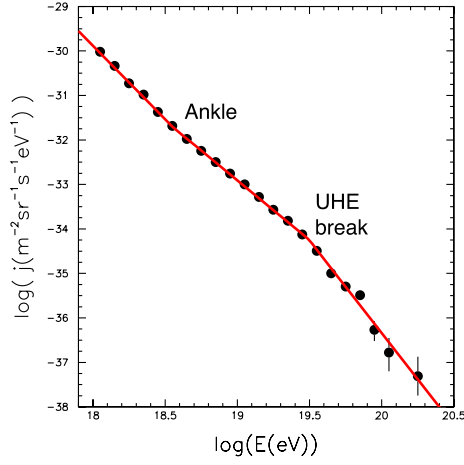


Fig. 1. – Comparison between the predicted slopes of the broken power-law spectrum of UHECRs and the PAO data [5]. The overall normalization and the energy of the cosmic ray ankle which depend on poorly known astrophysical parameters, were adjusted by a best fit to the data.

magnetic deflections. It is not valid in GRB fireball models with spherical ejecta or conical jets of opening angle much larger than the angular spread due to deflections by the Galactic magnetic field.

In fig. 1 we compare the PAO spectrum [5] of UHECRs (multiplied by E^3 in fig. 2 for clarity) and the approximate power-law spectrum with the predicted indexes $\beta = 3.3$ between the second knee and the ${}^4\text{He}$ UHE break (Dado and Dar, in preparation), $\beta = 2.67$ between this energy and the Fe break and $\beta = 4.17$, as given in eqs. (3), (5), which follow from our current update of [7]. The broken power-laws is a best fit to the data. The theoretical power-law indexes and break points agree well with their best fit

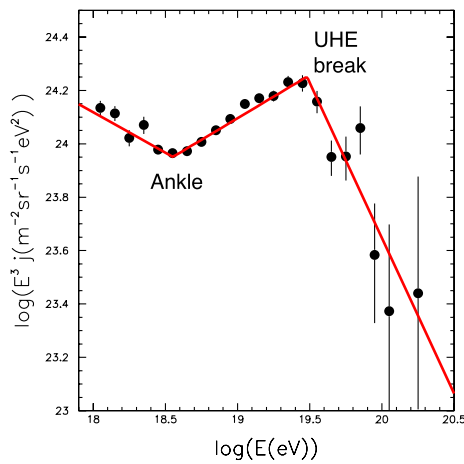


Fig. 2. – The predicted broken power-law spectrum of UHECRs, compared to the PAO data [5], both multiplied by E^3 .

values: a best fit yields power-law indexes 2.68 and 4.16 below and above the UHE break at 50 EeV, and 3.3 below the ankle at 3.6 EeV.

A similar interpretation of the spectrum and composition of UHECRs has been proposed [29]. It is based on the assumption that the origin of UHECRs is Galactic GRBs, as first suggested in [6]. Yet, we maintain that their derivation in [29] of the spectrum at energies above the UHE iron break is flawed⁽¹⁾.

In conclusion, if the UHECRs with energy above the UHE break are mostly iron nuclei, as inferred from the PAO measurements, then the spectrum and composition of the UHECRs are those expected from CRs that are accelerated by the highly relativistic jets emitted in Galactic GRBs, most of which are mercifully beamed away from Earth. In particular, the UHE break in the spectrum of UHECRs around 50 EeV is not the GZK cutoff, but the energy threshold for “free” escape of UHE Fe nuclei from the Galaxy. The energy spectrum of UHECRs above the UHE break is a trivial consequence of the energy dependence of the magnetic deflection of Galactic UHE Fe nuclei: It is the steepening by two units of the spectrum at the break, eq. (5) that reflects the “rigidity” of a UHECR trajectory in the randomly directed domains of the Galactic magnetic field. Finally the UHECR nuclei above their respective UHE breaks should point back towards young remnants of Galactic GRBs. These may be supernova remnants, magnetars, young neutron stars and accreting compact objects in close binaries (the expected angular-clustering properties of UHECRs will be discussed elsewhere).

If the UHECRs are extragalactic protons, as implied by the Fly’s Eye HiRes observations, then the UHE break near 50 EeV is the GZK cutoff, and the UHECRs must be accompanied by the UHE neutrinos and photons from the decay of the charged and neutral GZK pions. Their expected spectral index between the CR ankle and the GZK cutoff is their injection index below the CR ankle, *i.e.* $\beta = 3.2 - \beta_r \approx 2.7 \pm 0.1$, their spectrum above the UHE break is the GZK spectrum, and their arrival directions should point towards their nearby extragalactic sources.

REFERENCES

- [1] HESS V., *Phys. Zeit.*, **13** (1912) 1084.
- [2] FLY’S EYE HIRES COLLABORATION (ABBASI R. U. *et al.*), *Phys. Rev. Lett.*, **100** (2008) 101101.
- [3] FLY’S EYE HIRES COLLABORATION (SOKOLSKY P.), *eprint*, arXiv:1010.269 (2010).
- [4] PIERRE AUGER COLLABORATION (CRONIN J. W.), *eprint*, arXiv:0911.4714 (2009).
- [5] PIERRE AUGER COLLABORATION (ABRAHAM J. *et al.*), *Phys. Lett. B*, **685** (2010) 239.
- [6] DAR A. and PLAGA R., *Astron. Astrophys.*, **349** (1999) 259.
- [7] DAR A. and DE RÚJULA A., *Phys. Rep.*, **466** (2008) 179.

⁽¹⁾ The number density of Galactic CRs is roughly their injection rate times their residence time in the Galaxy. At energies beyond which they are not isotropised by the Galactic magnetic field, their mean residence time in the Galaxy tends to their free escape time $\sim R_G/c$, which is constant and does not decrease like E^{-2} as was assumed in [29] in order to argue that $\beta = \beta_{inj} + 2$ for $E(A, Z) > E_{break}(A, Z)$. At energy well above the UHE break, the random angular deflections are in steps $|\delta\theta| \sim l_c/R_L \propto (Z/E)^2$ perpendicular to the motion and the magnetic field, while the advance along the direction of motion is not by random walk but in steps of an approximate length l_c yielding $\tau_r \approx R_G/c$. Quite generally, theoretical estimates of the diffusion coefficient below the escape breaks, like that in [29] did not yield an energy dependence of the Galactic residence time of CRs consistent with measurements at low CR energies [27].

- [8] HILLAS A. M., *J. Phys. G*, **31** (2005) R95.
- [9] WIBIG T. and WOLFENDALE A. W., *J. Phys. G*, **31** (2005) 255.
- [10] BEREZINSKY V., GAZIZOV A. Z. and GRIGORIEVA S. I., *Phys. Rev. D*, **74** (2006) 043005.
- [11] RAND R. J. and KULKARNI S. R., *Astrophys. J.*, **343** (1989) 760.
- [12] BECK R., *Space Sci. Rev.*, **99** (2001) 243.
- [13] GREISEN K., *Phys. Rev. Lett.*, **16** (1966) 748.
- [14] ZATSEPIN G. T. and KUZMIN V. A., *Sov. Phys. JETP Lett. (Engl. Transl.)*, **4** (1966) 78.
- [15] THE PIERRE AUGER COLLABORATION (ABRAHAM J. *et al.*), *Science*, **318** (2007) 938.
- [16] THE PIERRE AUGER COLLABORATION (ABRAHAM J. *et al.*), *Astropart. Phys.*, **29** (2008) 188.
- [17] PUGET J. L., STECKER F. W. and BREDEKAMP J. J., *Astrophys. J.*, **205** (1976) 638.
- [18] EPELE L. N. and ROULET E., *Phys. Rev. Lett.*, **3295** (1999) 81.
- [19] ALLARD D. *et al.*, *J. Cosmol. Astropart. Phys.*, **10** (2008) 033.
- [20] ALOISIO R., BEREZINSKY V. and GRIGORIEVA S., *eprint*, arXiv:1006.2484 (2010).
- [21] THE PIERRE AUGER COLLABORATION (ABREU P. *et al.*), to be published in *Astropart. Phys.*, *eprint*, arXiv:1009.1855 (2010).
- [22] THE FLY'S EYE HiRES COLLABORATION (ABBASI R. U. *et al.*), *Astrophys. J.*, **713** (2010) L64.
- [23] ABRAHAM J. *et al.*, *Phys. Rev. Lett.*, **104** (2010) 1101.
- [24] ALOISIO R., BEREZINSKY V. and GAZIZOV A., *eprint*, arXiv:0907.5194 (2009).
- [25] THE FLY'S EYE HiRES COLLABORATION (ABBASI R. U. *et al.*), *Phys. Rev. Lett.*, **104** (2010) 1101.
- [26] The association between high-energy CRs and GRBs was suggested by DAR A., KOZLOVSKY B., NUSSINOV S. and RAMATY R. (*Astrophys. J.*, **388** (1992) 164). WAXMAN E. (*Phys. Rev. Lett.*, **75** (1995) 386), MILGROM M. and USOV V. (*Astrophys. J.*, **449** (1995) 37) and VIETRI M. (*Astrophys. J.*, **453** (1995) 883) proposed that extragalactic relativistic fireballs that allegedly produce GRBs are the source of UHECRs. DAR A. and PLAGA R. maintained [6] that the relativistic jets launched in Galactic core-collapse supernova explosions are the main source of CRs at all energies. These explosions are also the alleged source of extragalactic narrowly beamed long-duration GRBs (SHAVIV N. and DAR A., *Astrophys. J.*, **447** (1995) 863) and of GRB afterglows (DAR A., astro-ph/9704187 and *Astrophys. J.*, **500** (1998) L93). These ideas have been further developed into a theory of CRs at all energies [7].
- [27] SWORDY S. P. *et al.*, *Astrophys. J.*, **330** (1990) 625.
- [28] DAR A. and DE RÚJULA A., *Phys. Rep.*, **405** (2004) 203.
- [29] CALVEZ A., KUSENKO A. and NAGATAKI ALEXANDER S., *Phys. Rev. Lett.*, **105** (2010) 091101.

The Planck mission: From first results to cosmology

P. NATOLI⁽¹⁾⁽²⁾⁽³⁾, C. BURIGANA⁽³⁾, A. GRUPPUSO⁽³⁾ and N. MANDOLESI⁽³⁾

⁽¹⁾ *Dipartimento di Fisica, Università degli Studi di Ferrara - via Giuseppe Saragat 1
I-44100 Ferrara, Italy*

⁽²⁾ *Agenzia Spaziale Italiana Science Data Center, c/o ESRIN - via Galileo Galilei
Frascati, Italy*

⁽³⁾ *INAF-IASF Bologna, Istituto di Astrofisica Spaziale e Fisica Cosmica di Bologna
Istituto Nazionale di Astrofisica - via Piero Gobetti 101, I-40129 Bologna, Italy*

(ricevuto il 29 Settembre 2011; pubblicato online il 25 Gennaio 2012)

Summary. — *Planck* is a ESA satellite, currently in operation, whose main objective is to accurately image the anisotropies of the Cosmic Microwave Background Radiation in intensity and polarization. Benefiting from an unprecedented combination of sensitivity, angular resolution, and frequency leverage, *Planck* will provide high quality data to be mined in cosmology and astrophysics. The first *Planck* results have been released in January 2011 and include both Galactic and extragalactic source catalogues, a list of galaxy clusters selected by the Sunyaev-Zel'dovich effect, and a cold cores catalogue. The first cosmological data products are awaited for early 2013. *Planck* has a wide list of scientific targets. Here we focus on one specific aspect which is also of interest to the high energy physics community: constraining the Parity and *CPT* symmetries through CMB datasets. We describe the basic formalism, the relevant estimators and the overall analysis strategy. We provide marginal evidence for large scale Parity anomaly in the WMAP data that may be soon confirmed or discarded by the *Planck* satellite. *Planck* is currently measuring CMB anisotropies and their polarization with a level of precision that will remain unparalleled for many years to come. We also show how the CMB can be used to constrain fundamental symmetry violations in the photon sector through the so-called cosmological birefringence phenomenon.

PACS 98.80.-k – Cosmology.

1. – Introduction

Planck⁽¹⁾, is the third generation mission devoted to the Cosmic Microwave Background (CMB), after the COsmic Background Explorer (COBE) and Wilkinson Microwave Anisotropy Probe (WMAP)⁽²⁾, and at the frontier of precision cosmology today [1-3]. It is equipped with a 1.5-m effective aperture telescope with two actively-cooled instruments observing the sky in nine frequency bands from 30 GHz to 857 GHz: the Low Frequency Instrument (LFI) operating at 20 K with pseudo-correlation radiometers, and the High Frequency Instrument (HFI) with bolometers operating at 100 mK. A summary of the LFI and HFI performances is reported in table I. *Planck* is sensitive to linear polarization up to 353 GHz. The constraints on the thermal behavior, required to minimize systematic effects, resulted in a cryogenic architecture that is one of the most complicated ever conceived for space. Moreover, the spacecraft has been designed to exploit the favorable thermal conditions of the orbit around the second Lagrangian point of the Sun-Earth system. *Planck* is a spinning satellite. Thus, its receivers will observe the sky through a sequence of (almost great) circles following a scanning strategy aimed at minimizing systematic effects and achieving all-sky coverage for all receivers [4].

After launch on 14 May 2009, *Planck* has already mapped the sky about four times (at the time of writing this proceedings paper) and it is planned to complete another full sky survey with both instrument operational, and yet another one for LFI only. The HFI is expected to reach end of life after the end of the fifth sky survey, due to cryogenic helium consumption.

The first scientific results of *Planck* have been released on January 2011 [6]. They describe the instrument performance in flight including thermal behaviour [7-9], the HFI and LFI data analysis pipelines [10,11], the main astrophysical results about Galactic science [12-18], extragalactic sources and far-IR background [19-24], and Sunyaev-Zel'dovich effects and cluster properties [25-29], providing to the scientific community the *Planck* Early Release Compact Source Catalog (ERCSC) [30]. The first publications of the main cosmological implications are expected in early 2013.

The anisotropy pattern of the CMB, measured by WMAP, probes cosmology with unprecedented precision (see [31,32] and references therein). WMAP data are largely consistent with the concordance Λ cold dark matter (Λ CDM) model, but there are some interesting deviations from it, in particular on the largest angular scales [33]. See also [34] for a critical point of view upon the subject.

A large number of papers dealing with these anomalies have been published in the last years. We briefly list below those that are the most studied: a) lack of power on large angular scales [35,36]; b) hemispherical asymmetries [37-43]; c) unlikely alignments of low multipoles [44-48,35,49-53]; d) non-Gaussianity [43,54,55]; e) spots and/or excess of signal [56,57,42], possibly linked to non-Gaussianity; f) Parity asymmetry. This anomaly represents one subject of the present paper. It has been suggested in [58] that an estimator built upon the point Parity symmetry might be used as a practical tool for detecting foregrounds. In particular these authors consider whether the observed

⁽¹⁾ <http://www.esa.int/Planck>. is a project of the European Space Agency—ESA—with instruments provided by two scientific Consortia funded by ESA member states (with France and Italy as lead countries), contributions from NASA (USA), and telescope reflectors provided in a collaboration between ESA and a scientific Consortium led and funded by Denmark.

⁽²⁾ <http://lambda.gsfc.nasa.gov/>

TABLE I. – *Planck performances. The average sensitivity, $\delta T/T$, per FWHM² resolution element (FWHM is reported in arcmin) is given in CMB temperature units (i.e. equivalent thermodynamic temperature) for 28 months of integration. The white noise (per frequency channel for LFI and per detector for HFI) in 1 sec of integration (NET, in $\mu\text{K} \cdot \sqrt{\text{s}}$) is also given in CMB temperature units. The other used acronyms are: DT = detector technology, N of R (or B) = number of radiometers (or bolometers), EB = effective bandwidth (in GHz). Adapted from [5, 2] and [3].*

LFI			
Frequency (GHz)	30	44	70
InP DT	MIC	MIC	MMIC
FWHM	33.34	26.81	13.03
N of R (or feeds)	4 (2)	6 (3)	12 (6)
EB	6	8.8	14
NET	159	197	158
$\delta T/T$ [$\mu\text{K}/\text{K}$] (in T)	2.48	3.82	6.30
$\delta T/T$ [$\mu\text{K}/\text{K}$] (in P)	3.51	5.40	8.91
HFI			
Frequency (GHz)	100	143	
FWHM in T (P)	(9.6)		7.1 (6.9)
N of B in T (P)	(8)		4 (8)
EB in T (P)	(33)		43 (46)
NET in T (P)	100 (100)		62 (82)
$\delta T/T$ [$\mu\text{K}/\text{K}$] in T (P)	2.1 (3.4)		1.6 (2.9)
Frequency (GHz)	217	353	
FWHM in T (P)	4.6 (4.6)		4.7 (4.6)
N of B in T (P)	4 (8)		4 (8)
EB in T (P)	72 (63)		99 (102)
NET in T (P)	91 (132)		277 (404)
$\delta T/T$ [$\mu\text{K}/\text{K}$] in T (P)	3.4 (6.4)		14.1 (26.9)
Frequency (GHz)	545	857	
FWHM in T	4.7		4.3
N of B in T	4		4
EB in T	169		257
NET in T	2000		91000
$\delta T/T$ [$\mu\text{K}/\text{K}$] in T	106		4243

low CMB quadrupole in temperature could more generally signal odd point-Parity, *i.e.* suppression of even multipoles. However they claim that WMAP dataset never supports Parity preference beyond the meagre 95% confidence level. Later, [59] found that the Parity symmetry in the temperature map of WMAP 3 and 5 year data is anomalous at the level of 4 out of 1000 in the range $\delta\ell = [2, 18]$. This analysis have been repeated in the WMAP 7 year data confirming the anomaly at same level for a slightly wider range $\delta\ell = [2, 22]$ [60]. We report in this paper that analysis and its extension to polarization [61]. In fact, the CMB polarization pattern can provide information on symmetry-violating physics beyond the standard model.

In general, the breakdown of spacetime symmetries is a potential tracer of new physics [62]. Several models exist that predict non-standard \mathcal{P} and \mathcal{CP} violations (“ \mathcal{C} ” standing for charge conjugation), as well as \mathcal{CPT} violations (“ \mathcal{T} ” being time reversal) and the related (through the anti- \mathcal{CPT} theorem [63, 64]) breakdown of Lorentz invariance. A number of tests have been suggested and (in many cases) performed, either in terrestrial and orbital laboratories [65, 66] or through cosmological observations [67-69]. These violations may also be seen as anomalies the CMB polarization pattern, since its statistical properties are constrained by the assumption of symmetry conservation.

The paper is organized as follows. In sect. 2 we describe the basic formalism, the performed analysis, and the relevant symmetry estimators. Current results on symmetry estimators based on WMAP data are given in sect. 3 while in sect. 4 we focus on the implications for birefringence. The forecasts for *Planck* about these topics are provided in sect. 5. The precise extraction of the cosmological information from microwave observations requires an extremely accurate and efficient data analysis and a careful separation of CMB and astrophysical emissions (see, *e.g.*, [70] for a discussion of this topics in the context of the *Planck* surveys). Finally, our conclusions are drawn in sect. 6.

2. – Description of the analysis

2.1. Introduction. – All-sky temperature maps, $T(\hat{n})$, are usually expanded in Spherical Harmonics $Y_{\ell m}(\hat{n})$, with \hat{n} being a direction in the sky, namely depending on the couple of angles (θ, ϕ) :

$$(1) \quad a_{T, \ell m} = \int d\Omega Y_{\ell m}^*(\hat{n}) T(\hat{n}),$$

where $a_{T, \ell m}$ are the coefficients of the Spherical Harmonics expansion and $d\Omega = d\theta d\phi \sin\theta$. Under reflection (or Parity) symmetry ($\hat{n} \rightarrow -\hat{n}$), these coefficients behave as

$$(2) \quad a_{T, \ell m} \rightarrow (-1)^\ell a_{T, \ell m}.$$

Analogously for polarizations maps, taking into account the usual combination of Stokes parameters ($Q(\hat{n})$ and $U(\hat{n})$)

$$(3) \quad a_{\pm 2, \ell m} = \int d\Omega Y_{\pm 2, \ell m}^*(\hat{n}) (Q(\hat{n}) \pm iU(\hat{n})),$$

where $Y_{\pm 2, \ell m}(\hat{n})$ are the Spherical Harmonics of spin 2 and $a_{\pm 2, \ell m}$ are the corresponding

coefficients, it is possible to show that under Parity

$$(4) \quad a_{E,\ell m} \rightarrow (-1)^\ell a_{E,\ell m},$$

$$(5) \quad a_{B,\ell m} \rightarrow (-1)^{\ell+1} a_{B,\ell m},$$

where

$$(6) \quad a_{E,\ell m} = -(a_{2,\ell m} + a_{-2,\ell m})/2,$$

$$(7) \quad a_{B,\ell m} = -(a_{2,\ell m} - a_{-2,\ell m})/2i.$$

Equations (2), (4) and (5) show that the cross-correlations $C_\ell^{TB} = C_\ell^{EB} = 0$.

Further details can be found for example in [71], [72] and explicit algebra is present in the Appendix of [61].

In order to evaluate the angular power spectrum (APS) we adopt the quadratic maximum likelihood (QML) estimator, introduced in [73] and extended to polarization in [74]. Further details can be found in [75].

2.2. Angular power spectrum estimation, data set and simulations. – In order to evaluate the angular power spectrum (APS) we adopt the quadratic maximum likelihood (QML) estimator, introduced in [73] and extended to polarization in [74]. Further details can be found in [75]. Now, we describe the data set that we have considered. We use the temperature ILC map smoothed at 9.8 degrees and reconstructed at HEALPix⁽³⁾ [76] resolution $N_{side} = 16$, the foreground cleaned low resolution maps and the noise covariance matrix in (Q, U) publicly available at the Legacy Archive for Microwave Background Data Analysis (LAMBDA) website⁽⁴⁾ for the frequency channels Ka, Q and V as considered by [31] for the low ℓ analysis. These frequency channels have been co-added as follows [77]:

$$(8) \quad m_{tot} = C_{tot} \left(C_{Ka}^{-1} m_{Ka} + C_Q^{-1} m_Q + C_V^{-1} m_V \right),$$

where m_i , C_i are the polarization maps and covariances (for $i = Ka, Q$ and V) and

$$(9) \quad C_{tot}^{-1} = C_{Ka}^{-1} + C_Q^{-1} + C_V^{-1}.$$

This polarization data set has been extended to temperature considering the ILC map. We have added to the temperature map a random noise realization with variance of $1 \mu K^2$ as suggested in [78]. Consistently, the noise covariance matrix for TT is taken to be diagonal with variance equal to $1 \mu K^2$.

We have also performed Monte-Carlo simulations in order to assess the significance of our results. A set of 10000 CMB + noise sky realizations has been generated: the signal extracted from the WMAP 7 years best fit model, the noise through a Cholesky decomposition of the noise covariance matrix. We have then computed the APS for each of the 10000 simulations by means of *BolPol* and build two figures of merit as explained in the next subsection.

⁽³⁾ <http://healpix.jpl.nasa.gov/>

⁽⁴⁾ <http://lambda.gsfc.nasa.gov/>

2.3. Estimators. – We define the following quantities:

$$(10) \quad C_{+/-}^X \equiv \frac{1}{(\ell_{max} - 1)} \sum_{\ell=2, \ell_{max}}^{+/-} \ell(\ell + 1) 2\pi \hat{C}_\ell^X,$$

where \hat{C}_ℓ^X are the estimated APS obtained with the *BolPol* code [75] for the power spectrum $X = \text{TT}, \text{TE}, \text{EE}$ and BB . The sum is meant only over the even or odd ℓ (and this is represented respectively by the symbol $+$ or $-$) with $\ell_{max} \geq 3$.

Therefore, two estimators can be built from eq. (10) as follows: the ratio R^X , as performed in [59] or [60],

$$(11) \quad R^X = C_+^X / C_-^X,$$

and, in analogy to what performed for the hemispherical symmetry in [41], the difference D^X

$$(12) \quad D^X = C_+^X - C_-^X,$$

of the two aforementioned quantities. In the following, we drop the index X for R and D specifying every time we use them which is the spectrum they refer to.

For our application to WMAP data, both estimators have been considered for the TT spectrum but only the second one for the other spectra (EE, TE and BB). This is due the unfavorable signal-to-noise ratio of the WMAP data in polarization.

For $X = \text{TB}$ and EB we simply use the average power

$$(13) \quad C^X \equiv \frac{1}{(\ell_{max} - 1)} \sum_{\ell=2, \ell_{max}} \frac{\ell(\ell + 1)}{2\pi} \hat{C}_\ell^X.$$

3. – Results

In fig. 1 we show the estimator R and D for TT averaged in $\delta\ell = [2, 22]$ and in $\delta\ell = [2, 33]$. The probability to obtain a smaller value than the WMAP one is 0.47% for R in the range $\delta\ell = [2, 22]$ and 3.17% in the range $\delta\ell = [2, 33]$. For the D estimator the probability is 0.63% in the range $\delta\ell = [2, 22]$ and 3.17% in the range $\delta\ell = [2, 33]$. The upper left panel of fig. 1 recovers the same level of anomaly claimed in [60].

In fig. 2 we plot the percentage related to the WMAP 7y Parity anomaly for TT versus ℓ_{max} in the range [10,40] for the two considered estimators. As evident there is not a single ℓ_{max} for which the TT anomaly shows up, but rather a characteristic scale, see also [60]. For the estimator of eq. (11) the percentage anomaly is well below 1% for almost any choice of ℓ_{max} in the range [15,25]⁽⁵⁾. As also shown in fig. 2, the estimator of eq. (12) follows closely the other estimator although it is slightly less sensitive. Therefore, we find a whole multipole range, rather than a single ℓ_{max} value, where the WMAP 7y Parity anomaly holds. This dims significantly the case for posterior biasing.

⁽⁵⁾ Only for $\ell_{max} = 21$ the estimator of eq. (11) exhibits a percentage which is of the order of 1%.

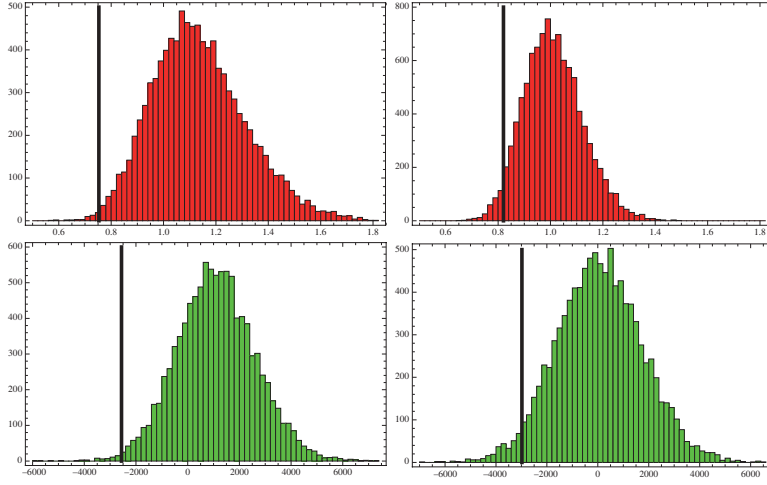


Fig. 1. – TT. Counts (y -axis) vs. the estimator (x -axis). Upper histograms: Ratio for the range $\delta\ell = [2, 22]$ (left panel) and for the range $\delta\ell = [2, 33]$ (right panel). Lower histograms: Difference for the range $\delta\ell = [2, 22]$ (left panel) and for the range $\delta\ell = [2, 33]$ (right panel). Units for the estimator D are μK^2 . The vertical line stands for the WMAP 7 year value.

In table II we provide the results for EE, TE and BB. As mentioned above, only D is considered and computed for the four following multipoles range $\delta\ell = [2, 4]$, $[2, 8]$, $[2, 16]$ and $[2, 22]$. No anomalies have been found and compatibility with Parity symmetry is obtained.

In table III we provide the results for EB and TB where the estimator C is considered and computed for the same aforementioned four multipoles range. Both the spectra are well consistent with zero. Only the EB spectrum shows a mild anomaly in the range $\delta\ell = [2, 22]$ at the level of 97.7%. This is due to five estimates from $\ell = 18$ to $\ell = 22$ that

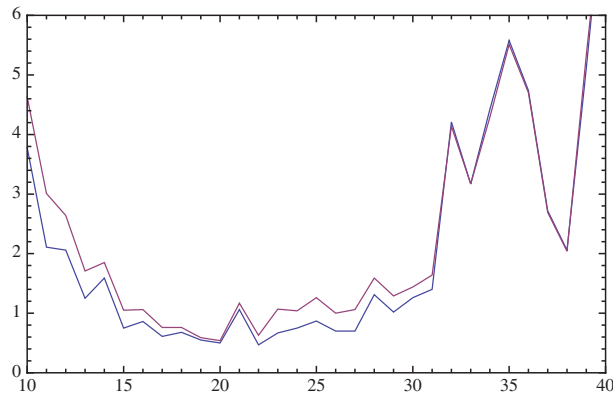


Fig. 2. – TT. Percentage of the WMAP 7 y value (y -axis) vs. ℓ_{max} (x -axis). Blue line is for the ratio and the red line for the difference. This analysis shows that there is no single ℓ_{max} for which the TT anomaly shows up, but rather suggests the existence of a characteristic scale, see also [60].

TABLE II. – Probabilities (in percentage) to obtain a smaller value than the WMAP 7y one.

D	$\delta\ell = [2, 4]$	$\delta\ell = [2, 8]$	$\delta\ell = [2, 16]$	$\delta\ell = [2, 22]$
EE	93.09	76.21	44.27	46.61
TE	56.35	38.88	24.79	22.77
BB	7.97	13.42	11.70	44.31

are systematically larger than zero. When these points are excluded this mild anomaly drops. For example in the range $\delta\ell = [2, 16]$ the probability to obtain a smaller value than the WMAP one is 55.35%. The latter two estimators are shown in fig. 3.

4. – Birefringence

As shown above, if the physics controlling CMB fluctuations is Parity conserving then the cross spectra C_l^{TB} and C_l^{EB} must vanish due to the different handedness of the B and (T, E) harmonics. Therefore, if the standard cosmological model holds, we should expect no relevant information from TB and EB . On the other hand, detection of non-zero primordial TB and/or EB may probe fundamental physics in the early universe, such as the presence of a primordial homogeneous [79] or helical [80, 81] magnetic field which would induce Faraday rotation and non-zero TB correlations. Parity-asymmetric gravity dynamics during inflation may generate a discrepancy among left and right-handed gravitational waves, so that TB and EB are non-zero [82, 83]. Particle physics models with non-standard Parity-violating interactions also predict non-vanishing TB and EB signals [84-86].

In this section we focus on a class of models that exhibit Parity violations in the photon sector [87]. A Chern-Simons term can be introduced in the effective Lagrangian [68, 69]:

$$\Delta\mathcal{L} = -\frac{1}{4} p_\mu \epsilon^{\mu\nu\rho\sigma} F_{\rho\sigma} A_\nu,$$

where $F^{\mu\nu}$ is the Maxwell tensor and A^μ the 4-potential. The 4-vector p_μ may be interpreted as the derivative of the quintessence field or the gradient of a function of the Ricci scalar [88, 89]. In either case a \mathcal{P} violation always arises provided that p_0 is non-zero, while \mathcal{C} and \mathcal{T} remain intact. Hence, \mathcal{CP} and \mathcal{CPT} symmetries are also violated, as well as Lorentz invariance, since p^μ picks up a preferred direction in space-time. The net effect on a propagating photon is to rotate its polarization direction by an angle $\Delta\alpha$, hence the name “cosmological birefringence”. Historically, the effect has been constrained by measuring polarized light from high redshift radio galaxies and quasars [68, 69, 90-94].

TABLE III. – Probabilities (in percentage) to obtain a smaller value than the WMAP 7y one.

C	$\delta\ell = [2, 4]$	$\delta\ell = [2, 8]$	$\delta\ell = [2, 16]$	$\delta\ell = [2, 22]$
TB	51.78	39.42	6.71	10.55
EB	62.73	69.83	55.35	97.70

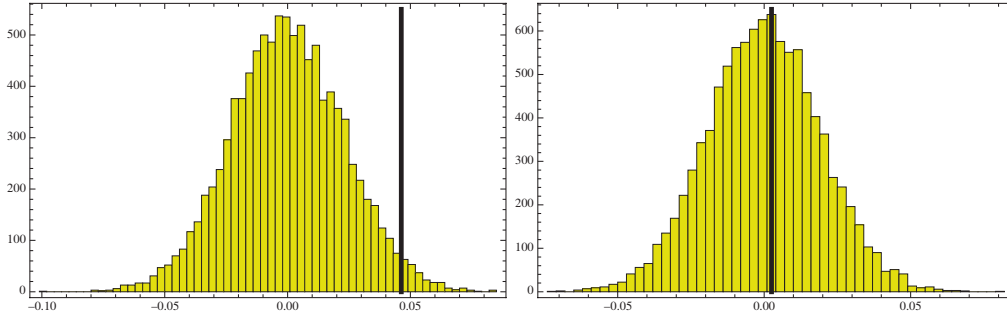


Fig. 3. – EB . Counts (y -axis) vs. the estimator C (x -axis). Distribution of C for $\delta\ell = [2, 22]$ (left panel) and $\delta\ell = [2, 16]$ (right panel). Units are μK^2 . The vertical line stands for the WMAP 7y data.

Obviously, the CMB photons would also be affected and, due to their longer journey, may get a larger rotation. A consequence for the CMB pattern is the mixing of E and B modes: the TB and EB correlations still vanish at last scattering surface, but the observable CMB spectra are distorted as [82, 83, 95]:

$$(14) \quad C_l'^{TB} = C_l^{TE} \sin 2\Delta\alpha,$$

$$(15) \quad C_l'^{EB} = \frac{1}{2} (C_l^{EE} - C_l^{BB}) \sin 4\Delta\alpha,$$

$$(16) \quad C_l'^{TE} = C_l^{TE} \cos 2\Delta\alpha,$$

$$(17) \quad C_l'^{EE} = C_l^{EE} \cos^2 2\Delta\alpha + C_l^{BB} \sin^2 2\Delta\alpha,$$

$$(18) \quad C_l'^{BB} = C_l^{BB} \cos^2 2\Delta\alpha + C_l^{EE} \sin^2 2\Delta\alpha,$$

where the primed quantities are rotated. In [32] a limit $\Delta\alpha = 0.9^\circ \pm 1.4^\circ$ was derived for the multipole range $\delta\ell = [23, 800]$, whereas for $\delta\ell = [2, 23]$ they find $\Delta\alpha = -3.8^\circ \pm 5.2^\circ$. The reason for this distinction is that the low ℓ polarization pattern is only influenced by the reionization epoch, which happened at redshift $z \simeq 10$. The primary fluctuations at higher multipoles, on the other hand, can be traced to last scattering at $z \simeq 1100$ so the corresponding angular scales allow for a much longer journey of the CMB photons. A slightly more stringent limit based on QUaD⁽⁶⁾ data has been set in [96] as $\Delta\alpha = 0.83^\circ \pm 0.94^\circ \pm 0.5^\circ$, the second error being systematic.

5. – Planck forecast

In this section we discuss how *Planck* will improve the present constraints on the symmetry violations discussed above. We first take into account the case of the low ℓ Parity anomaly. We then discuss briefly the case of birefringence.

5.1. Simulated dataset. – We consider the white noise level for 143 GHz channel of *Planck*. As in [41], we consider the nominal sensitivity of the *Planck* 143 GHz channel,

⁽⁶⁾ QUaD stands for “QUEST at DASI”. In turn, QUEST is “Q & U Extragalactic Survey Telescope” and DASI stands for “Degree Angular Scale Interferometer”.

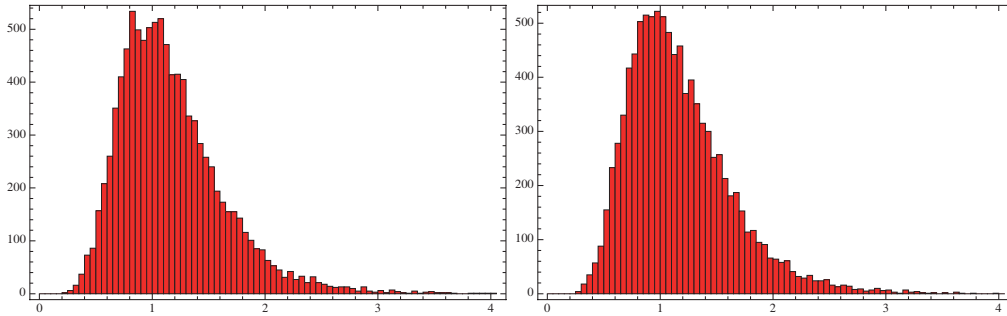


Fig. 4. – EE . Counts (y -axis) vs. the estimator R (x -axis). Distribution of R for $\delta\ell = [2, 22]$ (left panel) and $\delta\ell = [2, 16]$ (right panel).

taken as representative of the results which can be obtained after the foreground cleaning from various frequency channels. The 143 GHz channel has an angular resolution of $7.1'$ (FWHM) and an average sensitivity of $6 \mu\text{K}$ ($11.4 \mu\text{K}$) per pixel—a square whose side is the FWHM size of the beam—in temperature (polarization), after 2 full sky surveys. We assume uniform uncorrelated instrumental noise and we build the corresponding diagonal covariance matrix for temperature and polarization, from which, through Cholesky decomposition we are able to extract noise realizations. For this low noise level we apply the same procedure adopted for the Monte Carlo simulations in subsect. 2.2.

5.2. Forecasts. – From the set of 10000 CMB + noise sky realizations, we find that: The T based estimators (both R and D) do not change much since at large scale the APS for T is dominated by cosmic variance and not by the noise. For EE , TE and BB it is possible to consider even the R estimator. See for example fig. 4 where the R estimator is computed for EE in the range $\delta\ell = [2, 22]$ (left panel) and $\delta\ell = [2, 16]$ (right panel). The standard deviations for the D and C are evaluated in table IV for $\delta\ell = [2, 22]$ and compared to the WMAP 7y ones.

The case of birefringence has been investigated in [97] where the expected standard error for *Planck* in constraining the rotation angle α is given as $\Delta\alpha = 0.057^\circ$. Note

TABLE IV. – Upper Table: standard deviation for the D estimator computed in the range $\delta\ell = [2, 22]$. Lower Table: standard deviation for the C estimator computed in the range $\delta\ell = [2, 22]$. Units are μK^2 .

σ_D	WMAP 7y	<i>Planck</i>
TT	1517.17	1509.21
TE	20.19	9.08
EE	0.65	0.10
BB	0.69	0.04
σ_C	WMAP 7y	<i>Planck</i>
TB	0.95	0.19
EB	0.023	0.001

however that this error purely considers the noise level. Realistic measurements of α may be affected by systematic errors, especially arising from the uncertainties in the orientation of the polarimeters. The latter need to be properly taken into account [98].

6. – Conclusions

The *Planck* satellite is measuring CMB anisotropies and their polarization with a level of precision that will remain unparalleled for many years to come. The results derived from the *Planck* dataset will set a benchmark for precision cosmology. In this paper we have focused on fundamental information that the CMB may reveal about the breaking of fundamental discrete symmetries in the early universe. We have reviewed the present constraints, due to WMAP, for the cases of a hinted low resolution Parity anomaly as well as for cosmic birefringence. For the latter, the QUaD dataset has provided the most stringent limits to date. We have also presented *Planck* forecasts. *Planck* may be able to confirm or deny the existence of the low resolution Parity anomaly. Moreover, it is expected to greatly improve the knowledge of the polarization pattern of the CMB. *Planck* will also probe photon birefringence, improving the present constraints by over an order of magnitude.

* * *

We acknowledge the use of the BCX and SP6 at CINECA under the agreement INAF/CINECA and the use of computing facility at NERSC. We acknowledge use of the HEALPix [76] software and analysis package for deriving the results in this paper. We acknowledge the use of the LAMBDA. Support for LAMBDA is provided by the NASA Office of Space Science. Work supported by ASI through ASI/INAF Agreement I/072/09/0 for the Planck LFI Activity of Phase E2.

REFERENCES

- [1] TAUBER J. *et al.*, *Astron. Astrophys.*, **520** (2010) A1.
- [2] BERSANELLI M. *et al.*, *Astron. Astrophys.*, **520** (2010) A4.
- [3] LAMARRE J. M. *et al.*, *Astron. Astrophys.*, **520** (2010) A9.
- [4] DUPAC X. and TAUBER J., *A&A*, **430** (2005) 363.
- [5] MANDOLESI N. *et al.*, *Astron. Astrophys.*, **520** (2010) A3.
- [6] PLANCK COLLABORATION *et al.*, arXiv:1101.2022 [astro-ph.IM].
- [7] PLANCK HFI CORE TEAM *et al.*, arXiv:1101.2039 [astro-ph.IM].
- [8] MENNELLA A. *et al.*, arXiv:1101.2038 [astro-ph.CO].
- [9] PLANCK COLLABORATION *et al.*, arXiv:1101.2023 [astro-ph.IM].
- [10] PLANCK HFI CORE TEAM *et al.*, arXiv:1101.2048 [astro-ph.CO].
- [11] ZACCHEI A. *et al.*, arXiv:1101.2040 [astro-ph.IM].
- [12] PLANCK COLLABORATION *et al.*, arXiv:1101.2037 [astro-ph.GA].
- [13] PLANCK COLLABORATION *et al.*, arXiv:1101.2036 [astro-ph.GA].
- [14] PLANCK COLLABORATION *et al.*, arXiv:1101.2034 [astro-ph.GA].
- [15] PLANCK COLLABORATION *et al.*, arXiv:1101.2035 [astro-ph.GA].
- [16] PLANCK COLLABORATION *et al.*, arXiv:1101.2032 [astro-ph.GA].
- [17] PLANCK COLLABORATION *et al.*, arXiv:1101.2031 [astro-ph.GA].
- [18] PLANCK COLLABORATION *et al.*, arXiv:1101.2029 [astro-ph.GA].
- [19] PLANCK COLLABORATION *et al.*, arXiv:1101.2047 [astro-ph.GA].
- [20] PLANCK COLLABORATION *et al.*, arXiv:1101.2046 [astro-ph.CO].
- [21] PLANCK COLLABORATION *et al.*, arXiv:1101.2045 [astro-ph.CO].
- [22] PLANCK COLLABORATION *et al.*, arXiv:1101.2044 [astro-ph.CO].

- [23] PLANCK COLLABORATION *et al.*, arXiv:1101.1721 [astro-ph.CO].
- [24] PLANCK COLLABORATION *et al.*, arXiv:1101.2028 [astro-ph.CO].
- [25] PLANCK COLLABORATION *et al.*, arXiv:1101.2043 [astro-ph.CO].
- [26] PLANCK COLLABORATION *et al.*, arXiv:1101.2027 [astro-ph.CO].
- [27] PLANCK COLLABORATION *et al.*, arXiv:1101.2026 [astro-ph.CO].
- [28] PLANCK COLLABORATION *et al.*, arXiv:1101.2025 [astro-ph.CO].
- [29] PLANCK COLLABORATION *et al.*, arXiv:1101.2024 [astro-ph.CO].
- [30] PLANCK COLLABORATION *et al.*, arXiv:1101.2041 [astro-ph.CO].
- [31] LARSON D. *et al.*, arXiv:1001.4635 [astro-ph.CO].
- [32] KOMATSU E. *et al.*, *Astrophys. J. Suppl.*, **192** (2011) 18.
- [33] COPI C. J., HUTERER D., SCHWARZ D. J. and STARKMAN G. D., arXiv:1004.5602 [astro-ph.CO].
- [34] BENNETT C. L. *et al.*, arXiv:1001.4758 [astro-ph.CO].
- [35] COPI C. J., HUTERER D., SCHWARZ D. J., STARKMAN G. D., *Phys. Rev. D*, **75** (2007) 023507.
- [36] COPI C. J., HUTERER D., SCHWARZ D. J. and STARKMAN G. D., *Mon. Not. Roy. Astron. Soc.*, **399** (2009) 295.
- [37] ERIKSEN H. K., BANDAY A. J., GORSKI K. M., HANSEN F. K. and LILJE P. B., *Astrophys. J.*, **660** (2007) L81.
- [38] HANSEN F. K., BANDAY A. J., GORSKI K. M., ERIKSEN H. K. and LILJE P. B., *Astrophys. J.*, **704** (2009) 1448.
- [39] HOFUFT J., ERIKSEN H. K., BANDAY A. J., GORSKI K. M., HANSEN F. K. and LILJE P. B., *Astrophys. J.*, **699** (2009) 985.
- [40] ERIKSEN H. K., HANSEN F. K., BANDAY A. J., GORSKI K. M. and LILJE P. B., *Astrophys. J.*, **605** (2004) 14; **609** (2004) 1198 (E).
- [41] PACI F., GRUPPUSO A., FINELLI F., CABELLA C., DE ROSA A., MANDOLESI N. and NATOLI P., *Mon. Not. Roy. Astron. Soc.*, **407** (2010) 399.
- [42] PIETROBON D., CABELLA P., BALBI A., CRITTENDEN R., DE GASPERIS G. and VITTORIO N., *Mon. Not. Roy. Astron. Soc. Lett.*, **402** (2009) L34.
- [43] VIELVA P., MARTINEZ-GONZALEZ E., BARREIRO R. B., SANZ J. L. and CAYON L., *Astrophys. J.*, **609** (2004) 22.
- [44] TEGMARK M., DE OLIVEIRA-COSTA A. and HAMILTON A., *Phys. Rev. D*, **68** (2003) 123523.
- [45] COPI C. J., HUTERER D. and STARKMAN G. D., *Phys. Rev. D*, **70** (2004) 043515.
- [46] SCHWARZ D. J., STARKMAN G. D., HUTERER D. and COPI C. J., *Phys. Rev. Lett.*, **93** (2004) 221301.
- [47] WEEKS J. R., arXiv:astro-ph/0412231.
- [48] LAND K. and MAGUELJO J., *Phys. Rev. Lett.*, **95** (2005a) 071301.
- [49] ABRAMO L. R., BERNUI A., FERREIRA I. S., VILLELA T. and WUENSCHKE C. A., *Phys. Rev. D*, **74** (2006) 063506.
- [50] WIAUX Y., VIELVA P., MARTINEZ-GONZALEZ E. and VANDERGHEYNST P., *Phys. Rev. Lett.*, **96** (2006) 151303.
- [51] VIELVA P., WIAUX Y., MARTÍNEZ-GONZÁLEZ E., VANDERGHEYNST P., *Mon. Not. R. Astron. Soc.*, **381** (2007) 932.
- [52] GRUPPUSO A. and GORSKI K. M., *J. Cosmol. Astropart. Phys.*, **1003** (2010) 019.
- [53] GRUPPUSO A. and BURIGANA C., *J. Cosmol. Astropart. Phys.*, **0908** (2009) 004.
- [54] BERNUI A. and REBOUCAS M. J., *Phys. Rev. D*, **81** (2010) 063533.
- [55] BERNUI A., REBOUCAS M. J. and TEIXEIRA A. F. F., arXiv:1005.0883 [astro-ph.CO].
- [56] CRUZ M., MARTINEZ-GONZALEZ E., VIELVA P. and CAYON L., *Mon. Not. Roy. Astron. Soc.*, **356** (2005) 29.
- [57] CRUZ M., MARTINEZ-GONZALEZ E. and VIELVA P., arXiv:0901.1986 [astro-ph]
- [58] LAND K. and MAGUELJO J., *Phys. Rev. D*, **72** (2005) 101302.
- [59] KIM J. and NASELSKY P., *Astrophys. J.*, **714** (2010a) L265.
- [60] KIM J. and NASELSKY P., (2010b) arXiv:1002.0148 [astro-ph.CO].

- [61] GRUPPUSO A., FINELLI F., NATOLI P., PACI F., CABELLA P., DE ROSA A. and MANDOLESI N., *Mon. Not. Roy. Astron. Soc.*, **411** (2011) 3.
- [62] LENHNERT R., hep-ph/0611177.
- [63] GREENBERG O. W., *Phys. Rev. Lett.*, **89** (2002) 231602.
- [64] GREENBERG O. W., *Found. Phys.*, **36** (2006) 1535.
- [65] BLUHM R., hep-ph/0112318.
- [66] MEWES M., hep-ph/0307161.
- [67] AMELINO-CAMELIA G. *et al.*, *Nature*, **393** (1998) 763.
- [68] CARROLL S. M., FIELD G. B. and JACKIW R., *Phys. Rev. D*, **41** (1990) 1231.
- [69] CARROLL S. M. and FIELD G. B., *Phys. Rev. D*, **43** (1991) 3789.
- [70] LEACH S. M. *et al.*, *Astron. Astrophys.*, **491** (2008) 597.
- [71] ZALDARRIAGA M., *Astrophys. J.*, **503** (1998) 1 [arXiv:astro-ph/9709271].
- [72] ZALDARRIAGA M. and SELJAK U., *Phys. Rev. D*, **55** (1997) 1830.
- [73] TEGMARK M., *Phys. Rev. D*, **55** (1997) 5895.
- [74] TEGMARK M. and DE OLIVEIRA-COSTA A., *Phys. Rev. D*, **64** (2001) 063001.
- [75] GRUPPUSO A., DE ROSA A., CABELLA P., PACI F., FINELLI F., NATOLI P., DE GASPERIS G. and MANDOLESI N., *Mon. Not. Roy. Astron. Soc.*, **400** (2009) 1.
- [76] GORSKI K. M., HIVON E., BANDAY A. J., WANDELT B. D., HANSEN F. K., REINECKE M. and BARTELMANN M., HEALPix: A Framework for High-resolution Discretization and Fast Analysis of Data Distributed on the Sphere, *Astrophys. J.*, **622** (2005) 759.
- [77] JAROSIK N. *et al.* [WMAP COLLABORATION], *Astrophys. J. Suppl.*, **170** (2007) 263.
- [78] DUNKLEY J. *et al.* (WMAP), *Astrophys. J. SS*, **180** (2009) 306.
- [79] SCANNAPIECO E. S. and FERREIRA P. G., *Phys. Rev. D*, **56** (1997) 7493.
- [80] POGOSIAN L., VACHASPATI T. and WINITZKI S., *Phys. Rev. D*, **65** (2002) 083502.
- [81] GIOVANNINI M., *Phys. Rev. D*, **71** (2005) 021301.
- [82] LUE A., WANG L. and KAMIONKOWSKI M., *Phys. Rev. Lett.*, **83** (1999) 1506.
- [83] SAITO S., ICHIKI K. and TARUYA A., arXiv:0705.3701, 2007.
- [84] MAITY D., MAJUMDAR P., SENGUPTA S., *J. Cosmol. Astropart. Phys.*, **0406** (2004) 005.
- [85] LEPORA N. F., gr-qc/9812077, 1998.
- [86] BALAJI K. R. S., BRANDENBERGER R. H. and EASSON D. A., *J. Cosmol. Astropart. Phys.*, **12** (2003) 008.
- [87] CABELLA P., NATOLI P. and SILK J., *Phys. Rev. D*, **76** (2007) 123014.
- [88] DAVOUDIASL H. *et al.*, *Phys. Rev. Lett.*, **93** (2004) 201301.
- [89] LI H., LI M. and ZHANG X., *Phys. Rev. D*, **70** (2004) 047302.
- [90] CARROLL S. M. and FIELD G. B., *Phys. Rev. Lett.*, **79** (1997) 2394.
- [91] CARROLL S. M., *Phys. Rev. Lett.*, **81** (1998) 3067.
- [92] NODLAND B. and RALSTON J. P., *Phys. Rev. Lett.*, **78** (1997) 3043.
- [93] EISENSTEIN D. J. and BUNN E. F., *Phys. Rev. Lett.*, **79** (1997) 1957.
- [94] LEAHY J. P., astro-ph/9704285, 1997.
- [95] FENG B., LI H., LI M., ZHANG X., *Phys. Lett. B*, **620** (2005) 27.
- [96] WU E. Y. S. *et al.* [QUAD COLLABORATION], *Phys. Rev. Lett.*, **102** (2009) 161302.
- [97] XIA J. Q., LI H., ZHAO G. B. *et al.*, *Int. J. Mod. Phys. D*, **17** (2009) 2025.
- [98] PAGANO L. *et al.*, *Phys. Rev. D*, **80** (2009) 043522.

The latest results from the MINOS oscillation experiment

R. TONER for the MINOS COLLABORATION

Cavendish Laboratory, University of Cambridge - Madingley Road, Cambridge, CB3 0HE, UK

(ricevuto il 29 Settembre 2011; pubblicato online il 19 Gennaio 2012)

Summary. — The MINOS experiment is a long-baseline neutrino oscillation experiment, which utilizes neutrinos from the Fermilab NuMI muon neutrino beam. The neutrino flux from this beamline is studied before and after oscillation with two separate magnetized tracking calorimeter detectors. MINOS has recently carried out several studies in the field of neutrino oscillations, using 7.2×10^{20} protons on target of neutrino data, and 1.71×10^{20} protons on target of antineutrino data. These studies include a precision study of the atmospheric neutrino oscillation parameters $\sin^2(2\theta_{23})$ and $|\Delta m_{23}^2|$, a comparative study of the atmospheric antineutrino oscillation parameters $\sin^2(2\bar{\theta}_{23})$ and $|\Delta \bar{m}_{23}^2|$, an attempt to measure θ_{13} by looking for $\nu_\mu \rightarrow \nu_e$ oscillations, and a search for oscillations to an additional sterile state.

PACS 14.60.Pq – Neutrino mass and mixing.

PACS 14.60.Lm – Ordinary neutrinos (ν_e, ν_μ, ν_τ).

PACS 29.27.-a – Beams in particle accelerators.

1. – The MINOS experiment

The MINOS experiment studies neutrinos provided by the Fermilab NuMI beamline using both a Near and a Far Detector, which measure the flux of these neutrinos, respectively before and after oscillations. The NuMI beamline [1] is an on-axis muon neutrino beamline. Neutrino production begins when the Main Injector collides 120 GeV protons with a graphite target, producing pions and kaons. These hadrons are then focused by two separate magnetic focusing horns. K^- and π^- are focused to create a neutrino beam, while K^+ and π^+ are focused to create an antineutrino beam. The hadrons then travel down a 675 m long decay pipe. The final product is a beamline with 91.7% ν_μ , 7.0% $\bar{\nu}_\mu$, and 1.3% ν_e and $\bar{\nu}_e$. The current in the focusing horns, along with the relative positions of the target and horns, can be adjusted to create different beam configurations. The beam is normally run in “low energy” mode to produce a beam peak at 3.1 GeV (rms 1.1 GeV), in order to best explore the region of atmospheric oscillations [2]. The analyses discussed in this paper employ 7.2×10^{20} protons on target worth of neutrino data, and 1.71×10^{20} protons on target worth of antineutrino data.

The neutrinos are then studied by two separate functionally equivalent magnetized tracking calorimeter detectors [3]. The Near Detector is smaller (with a 0.029 kT fiducial mass) and is situated 1 km down the beamline at Fermilab; this detector measures neutrinos in their unoscillated state. The beam then travels 735 km northwest through the Earth to the Far Detector in Soudan, Minnesota. This detector has a larger mass of 4.0 kT and is located (for cosmic shielding purposes) at a depth of 2100 mwe. The Far Detector is intended to measure neutrinos after they have oscillated. Both detectors consist of a series of octagonal planes with two separate layers: first, a layer of 1 inch thick steel, which forms the target mass for neutrino interaction, and second, a layer of 1 cm thick by 4 cm wide strips of plastic scintillator, which collect photons from the interactions. The detectors are also magnetized with a 1.3 T field, to allow discrimination between muon tracks from ν_μ and $\bar{\nu}_\mu$.

2. – Recent analysis results from MINOS

2.1. ν_μ disappearance. – The MINOS detectors have been primarily designed to look for the disappearance of muon neutrinos. The survival probability for muon neutrino oscillation is as follows:

$$(1a) \quad P(\nu_\mu \rightarrow \nu_\mu) = 1 - \sin^2(2\theta_{23}) \sin^2(1.27\Delta m_{32}^2 L/E).$$

It is presumed that the remainder of the muon neutrinos oscillate to tau neutrinos; tau neutrinos are not directly observed in MINOS, however (due to the high production threshold for τ), so this oscillation is seen as disappearance. MINOS, having a fixed oscillation length L and energy range E , is capable of searching for the behavior in eq. (1) to make a precision measurement of the oscillation parameters θ_{23} and Δm_{32}^2 . Muon neutrinos are detected in MINOS via ν_μ Charged Current interactions, which leave a hadronic shower and a distinctive muon track. The Near Detector spectrum is used to make a prediction of the spectrum at the Far Detector in the absence of oscillations. The (presumably oscillated) data spectrum is then compared to the unoscillated prediction. For this analysis, 2451 ± 60 events are predicted in the Far Detector without oscillations, and 1986 events are observed in the data. The predicted and data spectra, along with their ratio, can be seen in fig. 1. When a fit for the oscillation in eq. (1) is performed, best fit values of $|\Delta m_{32}^2| = 2.32_{-0.08}^{+0.12} \times 10^{-3} \text{ eV}^2$ and $\sin^2(2\theta_{23}) > 0.90$ (90% CL) are obtained, along with the allowed regions in fig. 2. Comparisons to the previous Super-K [4, 5] and K2K results [6] are also shown. This MINOS result is the most precise measurement of these parameters to date. The $\nu_\mu \rightarrow \nu_\tau$ hypothesis is also well-supported by the data, with the alternative hypotheses of pure decoherence [7] and pure decay [8] ruled out respectively at greater than 9 and 7 sigma. Further details of this analysis can be found in reference [9].

2.2. $\bar{\nu}_\mu$ disappearance. – In addition to this precision study of neutrino oscillation, MINOS also has the unique ability to do a direct comparative measurement of the antineutrino oscillation parameters $\bar{\theta}_{23}$ and $\Delta \bar{m}_{32}^2$:

$$(2a) \quad P(\bar{\nu}_\mu \rightarrow \bar{\nu}_\mu) = 1 - \sin^2(2\bar{\theta}_{23}) \sin^2(1.27\Delta \bar{m}_{32}^2 L/E).$$

As stated earlier, the current in the NuMI focusing horn can be reversed to focus the opposite charge sign of hadrons, producing a beam with an enhanced antineutrino

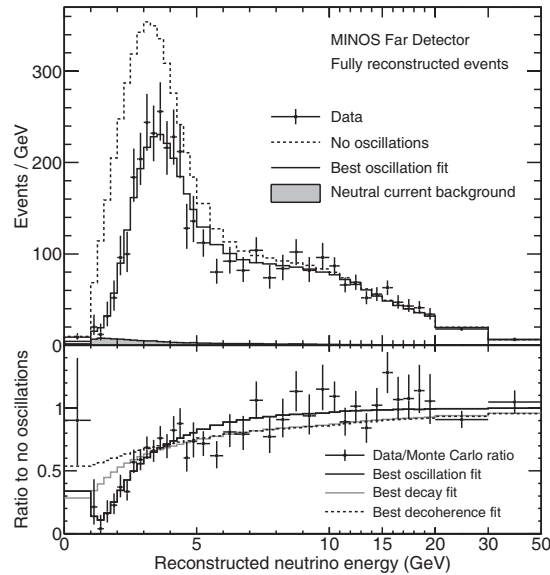


Fig. 1. – The top plot shows the predicted and observed energy spectra distributions for fully reconstructed ν_μ Charged Current events in the MINOS Far Detector. The dashed line indicates the prediction for the no-oscillation case. The solid line shows the best fit for oscillations. The black markers indicate the data distribution. The bottom plot shows the background-subtracted ratio of the data and the no-oscillation prediction, with best fits for oscillation, decoherence, and decay. This plot is for an exposure of 7.2×10^{20} protons on target.

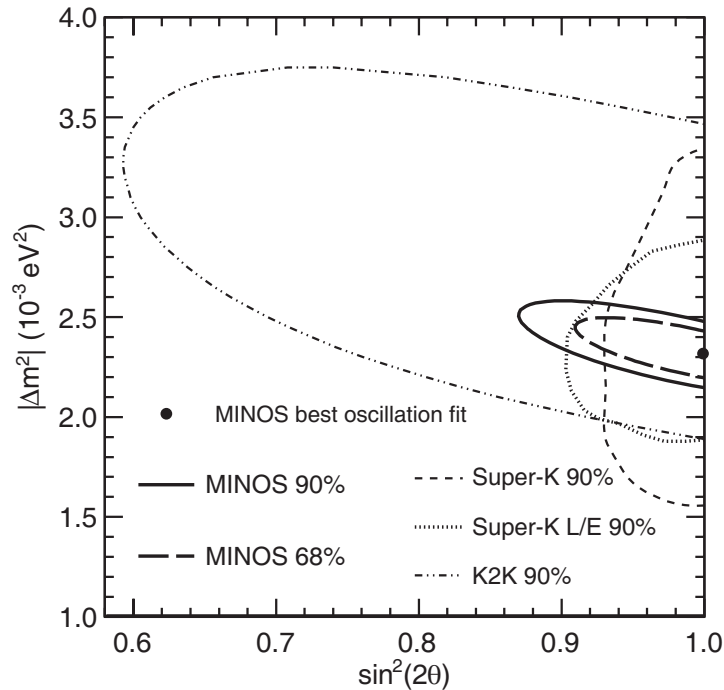


Fig. 2. – 90% and 68% CL for allowed regions of $\sin^2(2\theta_{23})$ and $|\Delta m_{32}^2|$ for the 2010 MINOS analysis. Previous results from Super-K [4, 5] and K2K [6] are shown for comparison.

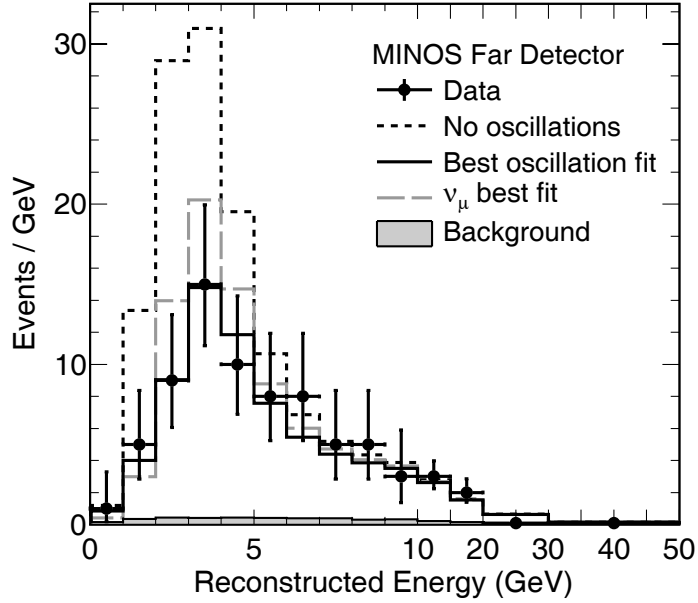


Fig. 3. – Predicted and observed energy spectra distributions for fully reconstructed $\bar{\nu}_\mu$ Charged Current events in the MINOS Far Detector. The black dashed line indicates the prediction for the no-oscillation case. The black markers indicate the observed spectrum. The solid black line shows the best fit for antineutrino oscillations. The grey dashed line shows the expected distribution if the same best fit values as the neutrino analysis were obtained.

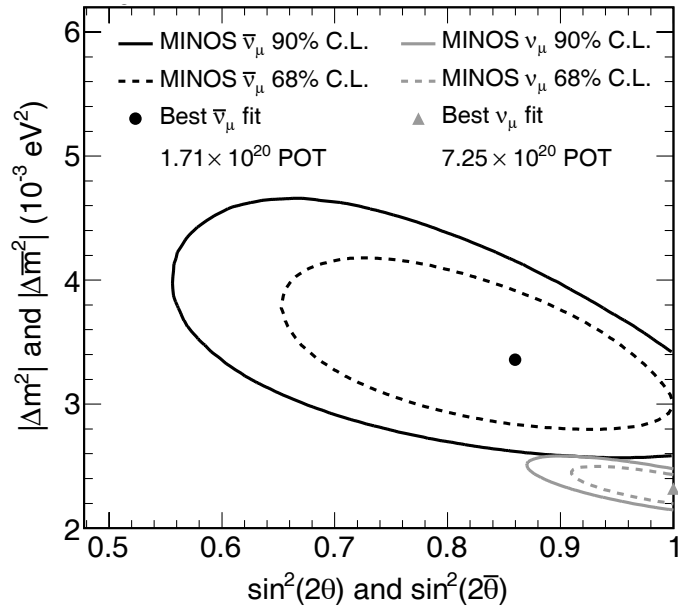


Fig. 4. – 90% (solid line) and 68% CL (dashed line) for allowed regions of $\sin^2(2\theta_{23})$ and $|\Delta m_{32}^2|$ for antineutrino (black) and neutrino (grey) oscillations, with best fits.

flux. Muon antineutrinos can then be separated from muon neutrinos by examining the curvature of the $\mu^{-(+)}$ track from a muon neutrino Charged Current interaction. The Near Detector selection is again used to make a prediction of the unoscillated muon antineutrino Far Detector spectrum. 156 events are expected, while 97 are observed, as seen in fig. 3. For this analysis, the final result is dominated by low statistics, including a 30% uncertainty on contamination by the muon neutrino background. Best fit values of $|\Delta m_{32}^2| = 3.36_{-0.40}^{+0.46}(\text{stat.}) \pm 0.06(\text{syst.}) \times 10^{-3} \text{ eV}^2$ and $\sin^2(2\theta_{23}) = 0.86_{-0.12}^{+0.11}(\text{stat.}) \pm 0.01(\text{syst.})$ are obtained. As can be seen in contour in fig. 4, there is some tension between this result and the earlier neutrino oscillation result, with the two measurements consistent at the 2.0% confidence level (for identical true oscillation parameters). An effort will be made in 2011 to double the 1.71×10^{20} protons on target antineutrino data set which was used in this analysis. Further details of the current analysis can be found in [10].

2'3. $\nu_\mu \rightarrow \nu_e$ oscillations. – The standard explanation for ν_μ disappearance is oscillation to tau neutrinos. This does not rule out other modes of oscillation, and in particular, the oscillation of muon neutrinos to electron neutrinos. Observing this mode of oscillation would allow MINOS to set a limit or possibly make a measurement of the as-yet-unmeasured mixing angle θ_{13} . A non-zero θ_{13} in turn would allow for the possibility of neutrinos exhibiting CP violation. The two-neutrino approximation of this mode is the following:

$$(3a) \quad P(\nu_\mu \rightarrow \nu_e) \approx \sin^2(2\theta_{13}) \sin^2(2\theta_{23}) \sin^2(1.27\Delta m_{32}^2 L/E).$$

The current best limit for θ_{13} comes from the CHOOZ reactor experiment, which finds $\sin^2(2\theta_{13}) < \sim 0.16$ (at the current MINOS best-fit limit for Δm_{32}^2) [11]. Unlike a reactor experiment like CHOOZ, however, the MINOS measurement of θ_{13} is also dependent on the CP violation phase δ_{CP} , $\sin^2(2\theta_{23})$, and the choice of mass hierarchy (normal or inverted).

A MINOS observation of $\nu_\mu \rightarrow \nu_e$ is difficult, due in large part to a small expected signal (ν_e Charged Current events) and a large expected background contamination (mostly from Neutral Current hadronic shower events). To separate signal from background, a series of preselection cuts are applied, followed by a particle ID consisting of an artificial neural network trained on eleven separate variables quantifying event shape and energy profile. These cuts have an efficiency of 40% for ν_e signal events and result in a predicted Far Detector sample with a purity of Signal:Background = 1:2 for a CHOOZ-size signal. This set of selection cuts is applied to the Near Detector to make a prediction of the amount of background expected at the Far Detector. The predicted Far Detector background is $49.1 \pm 7(\text{stat.}) \pm 2.7(\text{syst.})$ events. 54 events are observed, corresponding to a non-significant excess of 0.7σ . The resulting contours can be seen in fig. 5. Assuming $2\sin^2(\theta_{23}) = 1$, $\delta_{\text{CP}} = 0$, and $|\Delta m_{32}^2| = 2.43 \times 10^{-3} \text{ eV}^2$, MINOS finds $\sin^2(2\theta_{13}) < 0.12$ for the normal hierarchy, and $\sin^2(2\theta_{13}) < 0.20$ for the inverted hierarchy. Further details of this analysis can be found in ref. [12].

2'4. Looking for a sterile neutrino. – Muon neutrinos in MINOS could also potentially be oscillating to other “sterile” neutrino flavors. The cross section for Neutral Current interactions is the same for all three neutrino flavors. For a three neutrino scenario, in which all three neutrinos interact, there will therefore be no change in the rate of

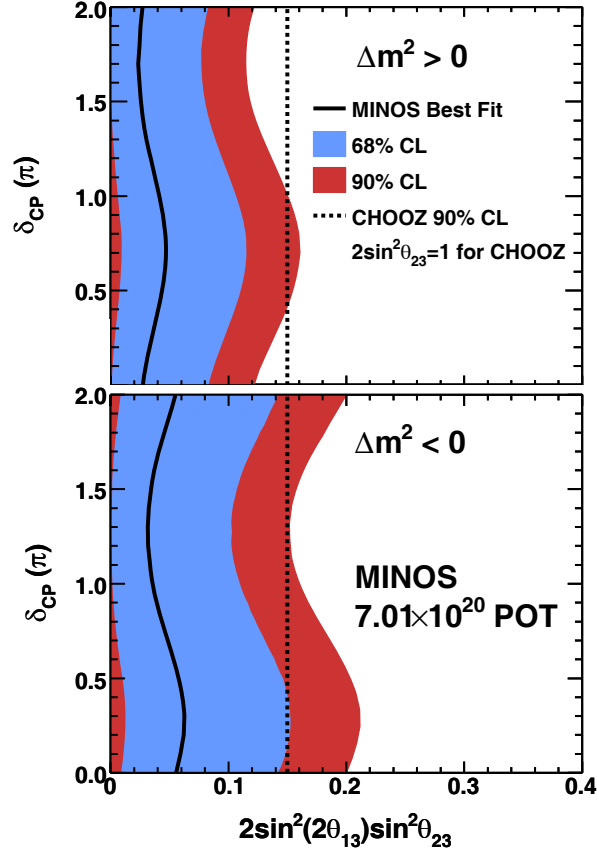


Fig. 5. – 90% and 68% exclusion limits on the value of θ_{13} (horizontal) *versus* δ_{CP} (vertical). The contours are shown for both the normal (top) and inverted (bottom) hierarchies, and assume $|\Delta m_{32}^2| = 2.43 \times 10^{-3} \text{ eV}^2$. This study was done for an exposure of 7.0×10^{20} protons on target.

NC events at the Far Detector due to oscillation. If there is oscillation to sterile states, however, there will be a deficit in the number of observed Neutral Current events.

A selection designed to select Neutral Current hadronic shower events is applied to the Near Detector to predict the rate of NC events at the Far Detector. $754 \pm 28(\text{stat.}) \pm 37(\text{syst.})$ events are expected at the Far Detector (assuming the mixing angle $\theta_{13} = 0$), and 802 events are observed. The observed distribution, as compared to the expected distribution, can be seen in fig. 6. The ratio of observed to expected NC candidate events is found to be $R = 1.09 \pm 0.06(\text{stat.}) \pm 0.05(\text{syst.}) - 0.08(\nu_e)$ (where the final term is derived from the MINOS 90% CL limit on the value of θ_{13}). A limit is therefore placed on the fraction f_s of disappearing ν_μ s which could be oscillating to a sterile state. This limit is $f_s < 0.22$, and $f_s < 0.40$ in the presence of $\nu_\mu \rightarrow \nu_e$ oscillations, at 90% CL. The full details of this analysis can be found in [13].

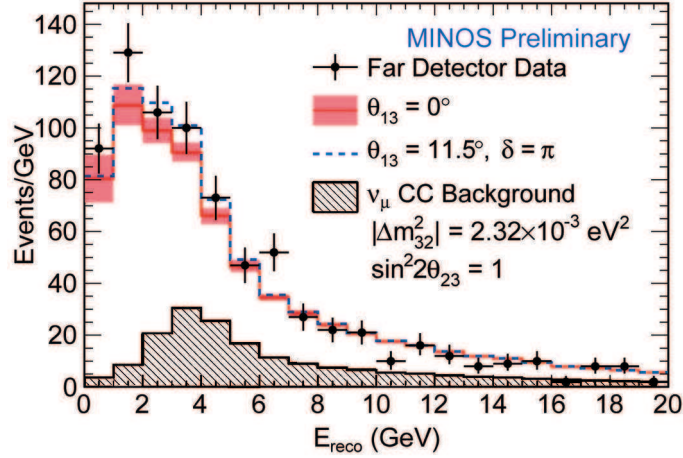


Fig. 6. – (Colour online) The Far Detector NC selected spectrum. The black markers indicate the data. The solid line (red) indicates the best fit (with error bars) for the case where $\theta_{13} = 0^\circ$, and the dotted line (blue) shows the best fit for $\theta_{13} = 11.5^\circ$ (the MINOS best fit). The expected ν_μ CC background is also shown. This plot is for an exposure of 7.2×10^{20} protons on target.

3. – Conclusion

The MINOS experiment has carried out an extensive research program looking at neutrino oscillations in several different parts of the atmospheric sector. By looking at the disappearance of muon neutrinos ($\nu_\mu \rightarrow \nu_x$) MINOS has placed the most precise limits on the mixing parameters Δm_{32}^2 and $\sin^2(2\theta_{23})$ to date, with $|\Delta m_{32}^2| = 2.32^{+0.12}_{-0.08} \times 10^{-3} \text{ eV}^2$ and $\sin^2(2\theta_{23}) > 0.90$ at 90% CL. Additionally, a measurement was also made of the equivalent antineutrino mixing parameters, finding best fits $|\Delta m_{32}^2| = 3.36^{+0.46}_{-0.40}(\text{stat.}) \pm 0.06(\text{syst.}) \times 10^{-3} \text{ eV}^2$ and $\sin^2(2\theta_{23}) = 0.86^{+0.11}_{-0.12}(\text{stat.}) \pm 0.01(\text{syst.})$. The neutrino and antineutrino are consistent at the 2.0% confidence level. In order to resolve this tension, an attempt will be made in 2011 to double the amount of antineutrino data. A search for oscillation to sterile neutrinos was also conducted, looking for a deficit in the rate of Neutral Current events in the Far Detector. No significant evidence of this oscillation mode was found, with the total fraction of muon neutrino disappearance caused by oscillation to sterile states being < 0.22 at 90% CL. Finally, an attempt was also made to search for $\nu_\mu \rightarrow \nu_e$ oscillations to measure the mixing angle θ_{13} . This study found that (for $2\sin^2(\theta_{23}) = 1$, $\delta_{\text{CP}} = 0$, and $|\Delta m_{32}^2| = 2.43 \times 10^{-3} \text{ eV}^2$) $\sin^2(2\theta_{13}) < 0.12$ for the normal hierarchy, and $\sin^2(2\theta_{13}) < 0.20$ for the inverted hierarchy. This result will also be followed up in 2011 in a new analysis which will incorporate both new data and improved analysis techniques.

REFERENCES

- [1] ANDERSON K. *et al.*, *NuMI facility technical design report*, Tech. Rep. FERMILAB-DESIGN, 1998-01, Fermilab (1998).
- [2] ADAMSON P. *et al.*, *Phys. Rev. D*, **77** (2008) 072002.
- [3] MICHAEL D. G. *et al.*, *Nucl. Instrum. Meth. A*, **596** (2008) 190.

- [4] ASHIE Y. *et al.*, *Phys. Rev. Lett.*, **93** (2004) 101801.
- [5] ASHIE Y. *et al.*, *Phys. Rev. D*, **71** (2005) 112005.
- [6] AHN M. H. *et al.*, *Phys. Rev. D*, **74** (2006) 072003.
- [7] BARGER V. D. *et al.*, *Phys. Lett. B*, **462** (1999) 109.
- [8] FOGLI G. L. *et al.*, *Phys. Rev. D*, **67** (2003) 093006.
- [9] ADAMSON P. *et al.*, *Phys. Rev. Lett.*, **106** (2011) 181801.
- [10] ADAMSON P. *et al.*, preprint arXiv:1104.0344v2 [hep-ex].
- [11] APOLLONIO M. *et al.*, *Eur. Phys. J. C*, **27** (2003) 331.
- [12] ADAMSON P. *et al.*, *Phys. Rev. D*, **82** (2010) 051102.
- [13] ADAMSON P. *et al.*, preprint arXiv:1104.3922v2 [hep-ex].

Search for $\nu_\mu \rightarrow \nu_\tau$ oscillations in appearance mode in the OPERA experiment

U. KOSE(*) on behalf of OPERA COLLABORATION

Dipartimento di Fisica dell'Università di Padova, I-35131 Padova, Italy
INFN, Sezione di Padova, I-35131 Padova, Italy

(ricevuto il 29 Settembre 2011; pubblicato online il 19 Gennaio 2012)

Summary. — The OPERA experiment in the underground Gran Sasso Laboratory (LNGS) has been designed to perform the first detection of neutrino oscillations in direct appearance mode in the muon neutrino to tau neutrino channel. The detector is hybrid, being made of an emulsion/lead target and of electronic detectors. It is placed in the CNGS neutrino beam 730 km away from the neutrino source. Runs with CNGS neutrinos were successfully carried out in 2008, 2009, and 2010. After a brief description of the beam and the experimental setup, we report on event analysis of a sample of events corresponding to 1.89×10^{19} p.o.t. in the CERN CNGS ν_μ beam that yielded the observation of a first candidate ν_τ CC interaction. The topology and kinematics of this candidate event are described in detail. The background sources are explained and the significance of the candidate is assessed.

PACS 13.15.+g – Neutrino interactions.

PACS 14.60.Pq – Neutrino mass and mixing.

PACS 29.40.Gx – Tracking and position-sensitive detectors.

PACS 29.40.Rg – Nuclear emulsions.

1. – Introduction

Two types of experimental methods can be used to detect neutrino oscillations: observing the appearance of a neutrino flavour initially absent in the beam or measuring the disappearance rate of the initial flavour. In the latter case, one must know the flux of the beam precisely. In this type of experiment one explores whether less than the expected number of neutrinos of a produced flavour arrives at a detector or whether the spectral shape changes if observed at various distances from a source. Since the final state is not observed, disappearance experiments cannot tell into which flavor a neutrino has oscillated. An appearance experiment searches for possible new flavours of neutrino, which does not exist in the original beam, or for an enhancement of an existing neutrino

(*) E-mail: umut.kose@cern.ch

flavour. The identification of the flavour relies on the detection of the corresponding lepton produced in its charged current (CC) interactions: $\nu_l N \rightarrow l^- X$ with $l = e, \mu, \tau$ and where X denotes the hadronic final state.

In the past two decades, several experiments carried out with atmospheric and accelerator neutrinos, as well as with solar and reactor neutrinos, have established the picture of a three-neutrino oscillation scenario with two large mixing angles. Atmospheric sector flavor conversion was first established by the Super-Kamiokande [1] and MACRO [2] experiments and then confirmed by the K2K [3] and MINOS [4] longbaseline experiments. The CHOOZ [5] and Palo Verde [6] reactor experiments excluded indirectly the $\nu_\mu \rightarrow \nu_e$ channel as the dominant process in the atmospheric sector. However, the direct observation of flavour transition through the detection of the corresponding lepton has never been observed. Appearance of ν_τ will prove unambiguously that $\nu_\mu \rightarrow \nu_\tau$ oscillation is the dominant transition channel at the atmospheric scale.

The OPERA experiment [7] has been designed to directly observe the appearance of ν_τ in a pure ν_μ beam on an event by event basis. The ν_τ signature is given by the decay topology and kinematics of the short lived τ^- leptons produced in the interaction of $\nu_\tau N \rightarrow \tau^- X$ and decaying to one prong (μ, e or *hadron*) or three prongs, which are [8]:

$$\begin{aligned}
 \tau^- &\rightarrow \mu^- \nu_\mu \bar{\nu}_\tau && \text{with } BR = 17.36 \pm 0.05\%, \\
 \tau^- &\rightarrow e^- \nu_e \bar{\nu}_\tau && \text{with } BR = 17.85 \pm 0.05\%, \\
 \tau^- &\rightarrow h^- (n\pi^0) \bar{\nu}_\tau && \text{with } BR = 49.52 \pm 0.07\%, \\
 \tau^- &\rightarrow 2h^- h^+ (n\pi^0) \bar{\nu}_\tau && \text{with } BR = 15.19 \pm 0.08\%.
 \end{aligned}$$

2. – The neutrino beam

The CNGS ν_μ beam produced by the CERN-SPS is directed towards the OPERA detector, located in the Gran Sasso underground laboratory (LNGS) [9] in Italy, 730 km away from the neutrino source at CERN. In order to study $\nu_\mu \rightarrow \nu_\tau$ oscillations in appearance mode as indicated in the atmospheric neutrino sector, the CERN Neutrinos to GranSasso (CNGS) neutrino beam [10] was designed and optimized by maximizing the number of ν_τ CC interactions at the LNGS.

The average ν_μ beam energy is 17 GeV, well above tau production energy threshold. The $\bar{\nu}_\mu$ contamination is $\sim 4\%$ in flux, 2.1% in terms of interactions. The ν_e and $\bar{\nu}_e$ contaminations are lower than 1%, while the number of prompt ν_τ from D_s decay is negligible. The average L/E_ν ratio is 43 km/GeV, suitable for oscillation studies at atmospheric Δm^2 . Due to the Earth's curvature neutrinos from CERN enter the LNGS halls with an angle of about 3° with respect to the horizontal plane.

With a nominal CNGS beam intensity of 4.5×10^{19} protons on target (p.o.t.) per year, and assuming $\Delta m_{23}^2 = 2.5 \times 10^{-3} \text{ eV}^2$ and full mixing, about 10 ν_τ events are expected to be observed in OPERA in 5 years of data taking, with selection criteria reducing the background to 0.75 events.

The goal is to accumulate a statistics of neutrino interactions corresponding to 22.5×10^{19} p.o.t. in 5 years. The 2008, 2009 and 2010 runs achieved a total intensity of 1.78×10^{19} , 3.52×10^{19} and 4.04×10^{19} p.o.t. respectively. Within these three years, neutrinos produced 9637 beam events. The processing of these events, particularly the scanning of emulsion films, is continuously going on. The 2011 run started on May 2011 and is still in progress.

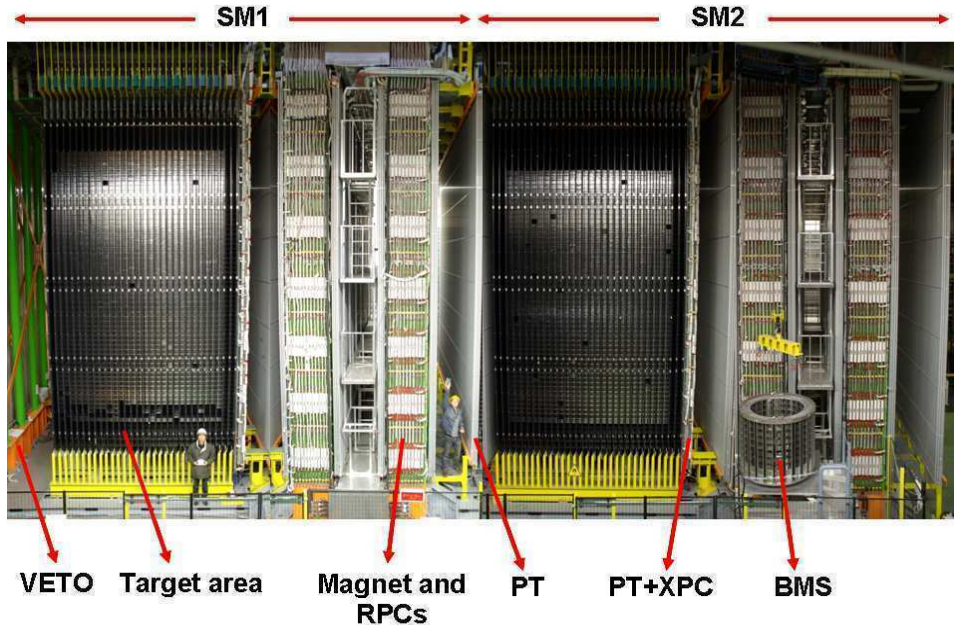


Fig. 1. – View of the OPERA detector; the neutrino beam enters from the left. Arrows show the position of detector components, the VETO planes, the target and TT, the drift tubes (PT) laid out along the XPC, the magnets and the RPC installed between the magnet iron slabs. The Brick Manipulator System (BMS) is partly shown.

At the CNGS energies the average τ^- decay length is submillimetric, so OPERA uses nuclear emulsion films as high precision tracking device in order to be able to detect such short decays. Emulsion films are interspaced with 1 mm thick lead plates, which act as neutrino target and form the largest part of the detector mass. This technique is called Emulsion Cloud Chamber (ECC). It was successfully used to establish the first evidence for charm in cosmic rays interactions [11] and in the DONUT experiment [12] for the first direct observation of the ν_τ . To date, nine ν_τ CC interactions have been observed by DONUT produced by a fixed target 800 GeV proton beam configuration.

3. – The OPERA detector

OPERA is a hybrid detector made of two identical Super Modules (SM1 and SM2), each one formed by a target section and a muon spectrometer as shown in fig. 1. Each target section is organized in 31 vertical “walls”, transverse to the beam direction. Walls are filled with “ECC bricks” with an overall mass of 1.25 kton. They are followed by double layers of scintillator planes acting as Target Trackers (TT) that are used to locate neutrino interactions occurred within the target. A target brick consists of 56 lead plates of 1 mm thickness interleaved with 57 emulsion films. The lead plates serve as neutrino interaction target and the emulsion films as 3-dimensional tracking detectors providing track coordinates with a sub-micron accuracy and track angles with a few mrad accuracy. The material of a brick along the beam direction corresponds to about 10 radiation length and 0.33 interaction length. The brick size is 10 cm \times 12.5 cm \times 8 cm and its weight is about 8.3 kg.

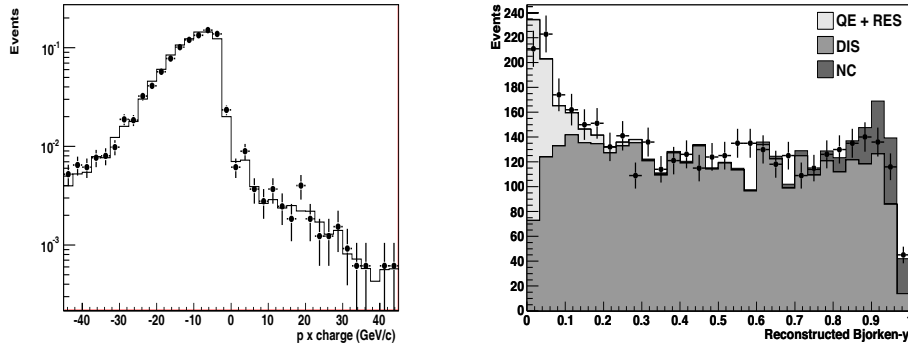


Fig. 2. – Right: Muon charge comparison (momentum \times charge): data (black dots with error bars) and MC (solid line) are normalised to one. Left: Bjorken- y variable reconstructed in data (dots with error bars) and MC (shaded areas). The MC distributions are normalised to data. The different contributions of the MC are shown in different colours: QE + RES contribution in light grey, DIS contribution in grey and the NC contamination in dark grey.

In order to reduce the emulsion scanning load, Changeable Sheets (CS) [13] film interfaces have been used. They consist in tightly packed doublets of emulsion films glued to the downstream face of each brick. Charged particles from a neutrino interaction in a brick cross the CS and produce signals in the TT that allow the corresponding brick to be identified and extracted by an automated Brick Manipulator System (BMS).

The spectrometers consist of a dipolar magnet instrumented with active detectors, planes of RPCs (Internal Tracker, IT) and drift tubes (Precision Tracker, PT). Tasks of the spectrometers are muon identification and charge measurement in order to minimize the background. For muon momenta between 2.5 GeV/ c and 45 GeV/ c , the fraction of events with wrong charge determination is 1.2%. The μ^+ to μ^- events ratio, within the selected momentum range, obtained from data can be directly compared with predictions based on Monte Carlo simulations: $3.92 \pm 0.37(\text{stat.})\%$ for data, $3.63 \pm 0.13(\text{stat.})\%$ for MC. Figure 2 left-side shows the momentum and momentum times charge distribution for data and MC.

In fig. 2 right side, Bjorken- y distribution is shown for the events with at least a muon track. The agreement between data and MC simulation is reasonable. The sum of the QE and RES processes can be clearly seen as a peak at low y values. The NC contribution shows up at values of Bjorken- y close to one. The NC contribution becomes negligible when a track with its momentum measured by the spectrometer is required.

A detailed description of the complete detector can be found in [7]. Event reconstruction procedures and a performances of the OPERA electronic detectors can be found in more detail in [14].

4. – Neutrino interaction location

Neutrino event analysis starts with the pattern recognition in the electronic detectors. Charged particle tracks produced in a neutrino interaction generate signals in the TT and in the muon spectrometer. A brick finding algorithm is applied in order to select the brick which has the maximum probability to contain the neutrino interaction. The brick with the highest probability is extracted from the detector for analysis. The efficiency of

this procedure reaches 83% in a subsample where up to 4 bricks per event were processed.

After extraction of the brick predicted by the electronic detectors, its validation comes from the analysis of the CS films. The measurement of emulsion films is performed through high-speed automated microscopes [15, 16] with a sub-micrometric position resolution and angular resolution of the order of one milliradian. If no expected charged track related to the event is found in the CS, the brick is returned back to the detector with another CS doublet attached. If any track originating from the interaction is detected in the CS, the brick is exposed to cosmic rays (for alignment purposes) and then depacked. The emulsion films are developed and sent to the scanning laboratories of the Collaboration for event location studies and decay search analysis.

All the track information of the CS is then used for a precise prediction of the tracks in the most downstream films of the brick (with an accuracy of about $100\ \mu\text{m}$). When found in this films, tracks are followed upstream from film to film. The scan-back procedure is stopped when no track candidate is found in three consecutive films and the lead plate just upstream the last detected track segment is defined as the vertex plate. In order to study the located vertices and reconstruct the events, a general scanning volume is defined with a transverse area of $1 \times 1\ \text{cm}^2$ for 5 films upstream and 10 films downstream of the stopping point. All track segments in this volume are collected and analysed. After rejection of the passing through tracks related to cosmic rays and of the tracks due to low energy particles, the tracks produced by the neutrino interaction can be selected and reconstructed.

The present overall location efficiency averaged over NC and CC events, from the electronic detector predictions down to the vertex confirmation, is about 60%.

5. – Decay search

Once the neutrino interaction is located, a decay search procedure is applied to detect possible decay or interaction topologies on tracks attached to the primary vertex. The main signature of a secondary vertex (decay or nuclear interaction) is the observation of a track with a significant impact parameter (IP) relative to the neutrino interaction vertex. The IP of primary tracks is smaller than $10\ \mu\text{m}$ after excluding tracks produced by low momentum particles. When secondary vertices are found in the event, a kinematical analysis is performed, using particle angles and momenta measured in the emulsion films. For charged particles up to about $6\ \text{GeV}/c$, momenta can be determined using the angular deviations produced by Multiple Coulomb Scattering (MCS) of tracks in the lead plates [17] with a resolution better than 22%. For higher momentum particles, the measurement is based on the position deviations. The resolution is better than 33% on $1/p$ up to $12\ \text{GeV}/c$ for particles passing through an entire brick.

A γ -ray search is performed in the whole scanned volume by checking all tracks having an IP with respect to the primary or secondary vertices lower than $800\ \mu\text{m}$. The angular acceptance is $\pm 500\ \text{mrad}$. The γ -ray energy is estimated by a Neural Network algorithm that uses the number of segments, the shape of the electromagnetic shower and also the MCS of the leading tracks.

6. – Data analysis

In the following, the analysis results [18] of about 35% of the 2008 and 2009 data sample, corresponding to the 1.89×10^{19} p.o.t are presented. The decay search procedure was applied to a sample of 1088 events of which 901 were classified as CC interactions.

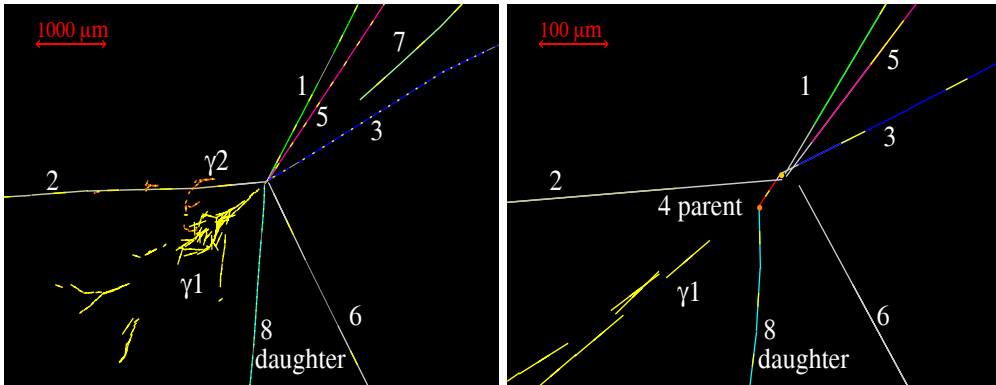


Fig. 3. – Display of the ν_τ candidate event. Left: view transverse to the neutrino direction. Right: same view zoomed on the vertices. The short track named “4 parent” is the τ^- candidate.

In the sample of CC interactions, 20 charm decay candidates were observed, in good agreement with the expectations from the Monte Carlo simulation, 16 ± 2.9 . Out of them 3 have a 1-prong topology where 0.8 ± 0.2 was expected. The background for the total charm sample is about 2 events. Several ν_e -induced events have also been observed.

Moreover, a first CC ν_τ candidate has been detected. The expected number of ν_τ events detected in the analysed sample is about $0.54 \pm 0.13(\text{syst.})$ at $\Delta m_{23}^2 = 2.5 \times 10^{-3} \text{ eV}^2$ and full mixing.

7. – The first tau neutrino candidate

In this section, the first tau neutrino candidate [18] will be described. The location and decay search procedure yielded a neutrino interaction vertex with 7 tracks. One track exhibits a visible kink with an angular change of $41 \pm 2 \text{ mrad}$ after a path length of $1335 \pm 35 \mu\text{m}$. The kink daughter momentum is estimated to be $12_{-3}^{+6} \text{ GeV}/c$ by MCS measurement and its transverse momentum to the parent direction is $470_{-120}^{+230} \text{ MeV}/c$. The event is displayed in figs. 3 and 4.

All the tracks from the neutrino interaction vertex were followed until they stop or interact. The probability that one of them is left by a muon is estimated to be less than 10^{-3} . The residual probability for being a ν_μ CC event, with a possibly undetected large angle μ track, is about 1%; a nominal value of 5% is assumed. None of the tracks is compatible with being an electron.

Two electromagnetic showers caused by γ -rays, associated with the event, have been located and studied. The energy of $\gamma 1$ is $(5.6 \pm 1.0(\text{stat.}) \pm 1.7(\text{syst.})) \text{ GeV}$ and it is clearly pointing to the decay vertex. The $\gamma 2$ has an energy of $1.2 \pm 0.4(\text{stat.}) \pm 0.4(\text{syst.}) \text{ GeV}$ and it is compatible with pointing to either vertex, with a significantly larger probability to the decay vertex.

All the selection cuts used in the analysis were those described in detail in the experiment proposal [19] and its addendum [20]. All the kinematical variables of the event and the cut applied are given in table I.

The invariant mass of the two observed γ -rays is $120 \pm 20(\text{stat.}) \pm 35(\text{syst.})$ supporting the hypothesis that they are emitted in a π^0 decay. The invariant mass of the charged decay daughter assumed to be a π^- and of the two γ -rays amount to

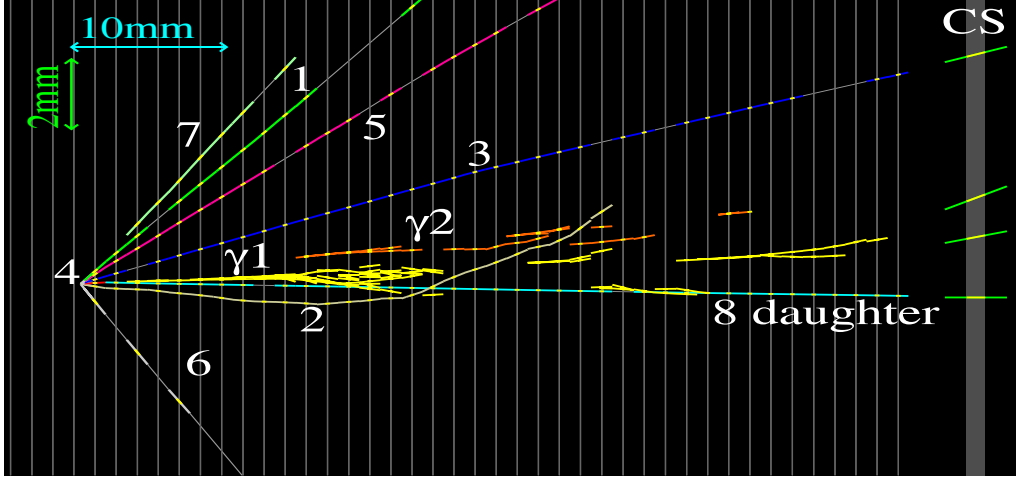


Fig. 4. – Longitudinal view of the ν_τ candidate event.

640_{-80}^{+125} (stat.) $_{-90}^{+100}$ (syst.) MeV/c, which is compatible with the $\rho(770)$ mass. So the decay mode of the candidate is consistent with the hypothesis $\tau^- \rightarrow \rho^- \nu_\tau$ (where the branching ratio is about 25%).

8. – Background estimation

The two main sources of background to the $\tau^- \rightarrow h(n\pi^0)\nu_\tau$ channel where a similar final state may be produced are:

- the decays of charmed particles produced in ν_μ CC interactions where the primary muon is not identified as well as the $c\bar{c}$ pair production in ν_μ NC interactions where one charm particle is not identified and the other decays to a 1-prong hadron channel;
- the 1-prong inelastic interactions of primary hadrons produced in ν_μ CC interactions where the primary muon is not identified or in ν_μ NC interactions and in which no nuclear fragment can be associated with the secondary interaction.

TABLE I. – Kinematical variables of ν_τ candidate event.

Variable	Measured	Selection criteria
Kink angle (mrad)	42 ± 2	> 20
Decay length (μm)	1335 ± 35	Within 2 plates
P daughter (GeV/c)	12_{-3}^{+6}	> 2
PT daughter (MeV/c)	470_{-120}^{+230}	> 300 (γ attached)
Missing PT (MeV/c)	570_{-170}^{+320}	< 1000
Angle ϕ (deg)	173 ± 2	> 90

The Monte Carlo expectation of the first background source is 0.007 ± 0.004 (syst.) event, the fraction produced in ν_e CC interactions is less than 10^{-3} events, The second type of background amounts to 0.011 ± 0.006 (syst.) event. The total background in the decay channel to a single charged hadron is 0.018 ± 0.007 (syst.) events. The probability that this background events fluctuate to one event is 1.8% (2.36σ). As the search for τ^- decays is extended to all four channels, the total background then becomes 0.045 ± 0.023 (syst.). The probability that this expected background to all searched decay channels of the τ^- fluctuates to one event is 4.5% (2.01σ). At $\Delta m^2 = 2.5 \times 10^{-3} \text{ eV}^2$ and full mixing, the expected number of observed τ^- events with the present analyzed statistics is 0.54 ± 0.13 (syst.) of which 0.16 ± 0.04 (syst.) in the one-prong hadron topology, compatible with the observation of one event.

9. – Conclusions

During 2008, 2009 and 2010 runs, a total intensity of 1.78×10^{19} , 3.52×10^{19} and 4.04×10^{19} p.o.t. respectively, was achieved. Within these three years, 9637 beam events have been collected within the OPERA target. The neutrino interaction location and decay search are going on.

A first candidate ν_τ CC interaction in the OPERA detector at LNGS was detected after analysis of a sample of events corresponding to 1.89×10^{19} p.o.t. in the CERN CNGS ν_μ beam. The expected number of ν_τ events in the analysed sample is 0.54 ± 0.13 (syst.). The candidate event passes all selection criteria, it is assumed to be a τ^- lepton decaying into $h^-(n\pi^0)\nu_\tau$. The observation of one possible tau candidate in the decay channel $h^-(\pi^0)\nu_\tau$ has a significance of 2.36σ of not being a background fluctuation.

REFERENCES

- [1] FUKUDA Y. *et al.*, *Phys. Rev. Lett.*, **81** (1998) 1562.
- [2] AMBROSIO M. *et al.*, *Eur. Phys. J. C*, **36** (2004) 323.
- [3] AHN M. H. *et al.*, *Phys. Rev. D*, **74** (2006) 072003.
- [4] MICHAEL D. G. *et al.*, *Phys. Rev. Lett.*, **101** (2008) 131802.
- [5] APOLLONIO M. *et al.*, *Eur. Phys. J. C*, **27** (2003) 331.
- [6] PIEPKE A., *Prog. Part. Nucl. Phys.*, **48** (2002) 113.
- [7] ACQUAFREDDA R. *et al.*, *JINST*, **4** (2009) P04018.
- [8] NAKAMURA K. *et al.*, *J. Phys. G*, **37** (2010) 075021.
- [9] LNGS web site: <http://www.lngs.infn.it/>.
- [10] CNGS project: <http://proj-cngs.web.cern.ch/prj-cngs/>.
- [11] NIU K., MIKUMO E. and MAEDA Y., *Prog. Theor. Phys.*, **46** (1971) 1644.
- [12] KODAMA K. *et al.*, *Phys. Lett. B*, **504** (2001) 218; *Phys. Rev. D*, **78** (2008) 052002.
- [13] ANOKHINA T. *et al.*, *JINST*, **3** (2008) P07005.
- [14] AGAFONOVA N. *et al.*, *New J. Phys.*, **13** (2011) 053051.
- [15] ARMENISE N. *et al.*, *Nucl. Instrum. Methods A*, **551** (2005) 261; DE SERIO M. *et al.*, *Nucl. Instrum. Methods A*, **554** (2005) 247; ARRABITO L. *et al.*, *Nucl. Instrum. Methods A*, **568** (2006) 578.
- [16] MORISHIMA K. and NAKANO T., *JINST*, **5** (2010) P04011.
- [17] DE SERIO M. *et al.*, *Nucl. Instrum. Methods A*, **512** (2003) 539; BESNIER M., PhD. Thesis, Université de Savoie, 2008, LAPP-T-2008-02.
- [18] AGAFONOVA N. *et al.*, *Phys. Lett. B*, **691** (2010) 138.
- [19] GULER M. *et al.*, CERN-SPSC-2000-028; LNGS P25/2000.
- [20] GULER M. *et al.*, CERN-SPSC-2001-025; LNGS-EXP 30/2001 add. 1/01.

Commissioning the Double Chooz detector

J. V. DAWSON on behalf of the DOUBLE CHOOZ COLLABORATION

*Laboratoire Astroparticule et Cosmologie - 10 rue Alice Domon et Léonie Duquet
75205 Paris, France*

(ricevuto il 29 Settembre 2011; pubblicato online il 23 Gennaio 2012)

Summary. — The Double Chooz experiment is the first of the next wave of reactor experiments searching for a non-vanishing value of the mixing angle θ_{13} . The experimental concept and detector design are presented, and the most pertinent backgrounds are discussed. Operation of the far detector began in early 2011. Installation of the near detector will occur in 2012. Double Chooz has the capacity to measure $\sin^2(2\theta_{13})$ to 3σ if $\sin^2(2\theta_{13}) > 0.05$ or exclude $\sin^2(2\theta_{13})$ down to 0.03 at 90% for $\Delta m_{31}^2 = 2.5 \times 10^{-3} \text{ eV}^2$ with three years of data with both near and far detectors.

PACS 14.60.Pq – Neutrino mass and mixing.

PACS 29.40.Mc – Scintillation detectors.

1. – Introduction

Neutrino oscillation has been clearly established via the study of solar, atmospheric, reactor and beam neutrinos. Combining these results requires the existence of (at least) three-neutrino mixing. In the current view, the PMNS mixing matrix relates the three neutrino mass eigenstates to the three neutrino flavour eigenstates parameterized by three mixing angles (θ_{12} , θ_{13} and θ_{23}) and one CP -violating phase δ_{cp} (for Dirac neutrinos). Neutrino oscillation experiments have made great progress in measuring the mixing angles and the two squared mass differences $\Delta m_{ij}^2 = m_i^2 - m_j^2$. However, one mixing angle θ_{13} remains unmeasured, and the mass hierarchy and the δ_{cp} phase are also still unknown. Upper limits to the value of θ_{13} have been made, indicating that this angle is very small with respect to the other two mixing angles. Whilst a measurement of θ_{13} would complete the knowledge of the mixing angles, even a more stringent upper limit would be useful since the size of θ_{13} has a great bearing on the possibility to observe CP violation in the leptonic sector with upcoming neutrino experiments (see, for example, [1] for a discussion of θ_{13} and CP violation discovery in forthcoming experiments).

The current value of θ_{13} is dominated by the bound given by the reactor experiment, CHOOZ [2], in which no oscillation was observed $R = 1.01 \pm 2.8\%(\text{stat.}) \pm 2.7\%(\text{sys.})$. Recent work on the calculation of neutrino fluxes from nuclear reactors [3] showed that

previous calculations under-estimated the neutrino fluxes indicating a deficit in the number of observed anti-neutrinos for all reactor experiments at baselines shorter than 100 m (the Reactor Anti-Neutrino Anomaly). A re-evaluation of the CHOOZ result leads to a new exclusion limit, $\sin^2(2\theta_{13}) < 0.10$, at 90% CL for $\Delta m_{31}^2 = 2.4 \times 10^{-3} \text{ eV}^2$ [4].

The future direction of the field of neutrino oscillations is in some way governed by the size of θ_{13} such that even a more stringent upper limit would be of great use to the community. The size of θ_{13} essentially dictates whether current and future accelerator experiments can observe CP-violation in the leptonic sector, and also determine the neutrino mass hierarchy.

Reactor experiments provide a promising method to measure θ_{13} . These experiments search for the disappearance of electron anti-neutrinos emitted from the cores of the nuclear reactors. Equation (1) gives the survival probability of a $\bar{\nu}_e$ from a reactor, where E is the neutrino energy and L is the distance from the source to the detector.

$$(1) \quad P(\bar{\nu}_e \rightarrow \bar{\nu}_e) = 1 - \sin^2(2\theta_{13}) \sin^2 \frac{\Delta m_{31}^2 L}{4E} - \cos^4 \theta_{13} \sin^2(2\theta_{12}) \sin^2 \frac{\Delta m_{21}^2 L}{4E} \\ + 2 \sin^2 \theta_{13} \cos^2 \theta_{13} \sin^2 \theta_{12} \left(\cos \frac{(\Delta m_{31}^2 - \Delta m_{21}^2)L}{2E} - \cos \frac{\Delta m_{31}^2 L}{2E} \right).$$

For short baselines only the first two terms are relevant. With a well positioned detector (such that L/E is $\sim 0.5 \text{ km/MeV}$), a detector might observe less neutrinos than anticipated indicating a non-zero value of θ_{13} and therefore these experiments are termed “disappearance” experiments. “Appearance” experiments, *i.e.* long baseline accelerator experiments, aim to measure the appearance of ν_e s in a ν_μ beam.

Reactor based θ_{13} experiments have some advantages over long baseline accelerator experiments. They suffer less from parameter degeneracies, being independent on δ_{CP} and the sign of Δm_{31} and having only a weak dependence on Δm_{21}^2 . Since the neutrino energies are low, ~ 1 to 10 MeV, and the detectors are positioned at short distances, there are no matter effects. The major drawback to this type of experiment is that there is limited knowledge on the neutrino production processes inside the reactors.

2. – Double Chooz

The Double Chooz experiment [5] is located at Chooz, the same site as the original CHOOZ experiment, in the Champagne-Ardennes region in France. The site contains two closely neighbouring nuclear reactors each with a thermal power of 4.27 GW. The Double Chooz concept is to use two identical detectors; one near, to effectively measure the neutrino spectrum and flux from the reactor, and one far, to observe any neutrino disappearance.

The far detector is located in the same underground laboratory as the original CHOOZ experiment (1 km from the two cores). This site is perfect for three reasons; a good L/E of 0.3 MeV/km, the cost is significantly reduced due to the existing laboratory, and the experimental background rate *i.e.* from muons, neutrons and rock radioactivity, etc. is already well measured with reactor-off data. The near detector underground laboratory is currently under construction at a distance of 400 m from the two reactors.

The target is a gadolinium loaded scintillator, with an interacting anti-neutrino of energy greater than 1.8 MeV causing an inverse beta decay of a proton:

$$(2) \quad \bar{\nu}_e + p \rightarrow n + e^+.$$

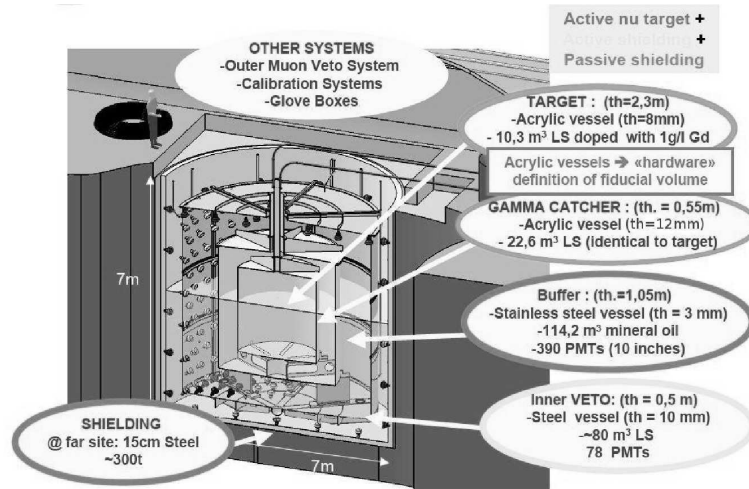


Fig. 1. – Design of the Double Chooz detectors.

The positron slows depositing its kinetic energy in the scintillator. It quickly annihilates; releasing two 511 keV gammas. The total prompt visible energy seen is some 1 to ~ 8 MeV and is directly related to the energy of the neutrino $E_\nu = E_{visible} + 0.8$ MeV. After a characteristic delay, the neutron slows and is captured; on gadolinium (absorption time of $30 \mu\text{s}$) or on hydrogen. Gamma cascades from the captures give energy deposits of ~ 8 MeV (from gadolinium) and 2.2 MeV from hydrogen.

As the interaction cross-section rises (with the square of the energy) and the reactor neutrino spectrum falls in a similar fashion, the convolution of these two, the observed spectrum is roughly Gaussian in shape with a peak visible energy of ~ 3 MeV.

3. – Detector design

Figure 1 shows the detector and laboratory design. Both detectors are identical from the buffer tank (inner-most stainless steel vessel) inwards which is a physics requirement. Shielding against the radioactivity of the rock is provided by 15 cm of demagnetised steel for the far detector but less stringent shielding is required for the near detector.

Each detector is formed from a series of nested cylinders with each volume filled with different liquids; insensitive buffer oil for shielding, Gd-doped scintillator as the target and undoped scintillators for gamma rays, fast neutrons and muons.

The two inner vessels are acrylic and transparent to photons above 400 nm. The innermost vessel is the Target, with a diameter of 2.3 m, which contains 10 m^3 of gadolinium-doped scintillator; such that the scintillator contains 1 g/l of gadolinium. In this volume neutron-capture on gadolinium can occur releasing cascade gammas with an energy of ~ 8 MeV. More than 80% of neutron captures are on gadolinium rather than hydrogen. The definition of a neutrino candidate event is one in which neutron capture on gadolinium occurs.

Enclosing the target is the Gamma-Catcher volume, with a diameter of 3.4 m, which contains 22 m^3 of undoped scintillator. The purpose of this volume is to detect the gammas emitted in both the neutron-capture process and positron annihilation in the

target, such that gammas emitted from neutrino events occurring in the outer volume of the target are detected. This results in a well-defined target volume.

Since the photomultipliers are the most radioactive component of the detector, the inner volumes are shielded by a buffer volume, with a diameter of 5.5 m, filled with non-scintillating paraffin oil. Events occurring in the acrylic volumes are detected by 390 10 inch low background photomultiplier tubes (Hamamatsu R7081 [6]) fixed to the inside of the stainless steel buffer tank. Uniquely the photomultiplier tubes are angled to improve the uniformity of light collection efficiency in the inner-most volumes.

The outer detector volume is steel walled, with a diameter of 6.6 m, and filled with scintillator. 78 8 inch photomultipliers (Hamamatsu R1408 [6]) line the outermost wall which is painted with a reflective white coating. This volume is the Inner Veto with the purpose of detecting and tracking muons and fast neutrons.

On top of the detector sits the Outer Veto. This comprises strips of plastic scintillator and wavelength-shifting fibres. The veto extends further than the detector diameter with the purpose of detecting and tracking muons. The precision of the entry point of a muon, X-Y position, will be far more precise than that achieved by the Inner Veto and detector. One of the main objectives is to tag near-miss muons, which interact in the surrounding rock (and not in the detector) but produce fast neutrons. Another important goal is to determine whether a muon entered the Inner Detector. Muons that do so can produce cosmogenic isotopes (*i.e.* via a photonuclear interaction on carbon), some of which will produce backgrounds for the experiment.

4. – Backgrounds

As each neutrino produces two time-correlated signals; that of the positron and a delayed capture of a neutron (with characteristic decay time of $30\ \mu\text{s}$), backgrounds can come from two sources; accidental and time-correlated.

The accidental component comes from the random chance that two events of appropriate energy interact within this characteristic time. Since these two events are unrelated this rate can easily be measured, based on the singles rate. The main source of events come from radioactive contamination with the dominant source being the photomultiplier tubes. For the accidental component to be well constrained, strict radioactive contamination limits have been placed on all parts.

The most difficult backgrounds to study are those that are, like our signal, time-correlated. From the experience of Chooz it is anticipated that Double Chooz will observe some ~ 1.5 events/day of false neutrino-like events. The Chooz experiment had a period of data-taking before operation of the nuclear reactors began and so the background could be very thoroughly investigated. The sources of the neutrino-like events observed were attributed to fast neutrons (muon-induced neutrons) and cosmogenically produced isotopes (also muon produced).

Fast neutrons can mimic neutrino signals by producing a proton-recoil (positron-like signal) and a delayed neutron capture. If the muon is seen by the experiment then these events can be tagged. More dangerous, however, are near-miss muons which interact in the rock releasing fast neutrons which interact in the detector. The primary purpose of the Outer Veto is to identify these events by covering an area wider than the detector itself.

Those cosmogenically produced isotopes that are dangerous for the experiment are those that result in electron emission followed by neutron emission, as these mimic well our neutrino signal. Two isotopes, ^8He and ^9Li , have long decay times (119 ms and

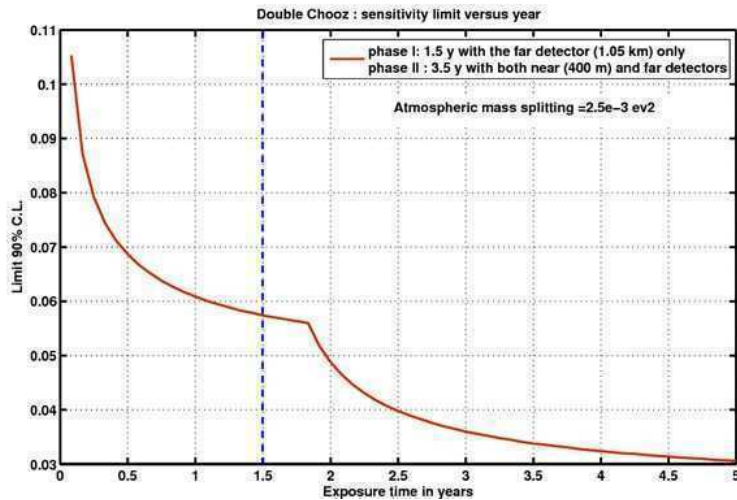


Fig. 2. – Sensitivity of the experiment, showing the first far detector only phase and the rapid improvement as the near detector is included.

174 ms, respectively) [7] rendering a hardware veto impractical. Coupling information from the Outer Veto (with precise muon entry points), Inner Veto and Inner Detector will allow reconstruction of muon tracks to identify muons that cross the Inner Detector.

5. – Improvements on Chooz

Improvements on the original Chooz experiment have been made in two ways; the detector design and the two-detector concept. The new detector target is more than twice as large as the original Chooz detector. The scintillator technology has improved as to allow the production of a Gadolinium-loaded scintillator that is very stable (on the timescale of years) allowing a longer run time of ~ 5 years. The number of neutrinos detected in the far detector assuming 3 years of running will be $\sim 60,000$ compared to $\sim 2,500$ in the Chooz experiment, reducing the statistical error, 2.8% in Chooz, to 0.4%.

The aim is to reduce the systematic error, 2.7% in Chooz, to less than 0.6%. There are three sources of systematic error; the reactor, the detector and the analysis. With two detectors, each reactor component systematic; flux and cross-section, reactor power and energy per fission, reduce to below 0.1%. Making a relative measurement, between the two detectors, reduces many of detector systematics to similar orders.

The scintillators have been produced for both detectors in one batch, reducing the systematic on the number of H and Gd atoms in each detector. With a well performing scintillator the number of observed photons should be high enough such that all of the positron signal is observed so there is no systematic introduced by cutting on the positron spectrum.

In general, controlling the relative systematics between the two detectors is far easier than the absolute. Two detectors, however, introduces one new systematic—the live time, as both detectors must operate simultaneously.

6. – The far detector

Commissioning of the far detector began in early 2011 and ended in April 2011. Preliminary results show that the main design aims have been well achieved, with the detector operating with a lower energy threshold far below the commencement of the positron spectrum and a low event rate from radioactivity.

The first neutrino physics run began in April and ended in November 2011. Whilst the experiment is less sensitive without the near detector, it will still be more sensitive than the original CHOOZ detector. With data only from the first neutrino run we expect to obtain a sensitivity at least equal to the CHOOZ limit. With one year of data the experiment should be able reach a sensitivity to $\sin^2(2\theta_{13})$ of 0.06 with only the far detector.

7. – Conclusion

Double Chooz is the first next generation reactor experiment to commence operation. The construction of the far detector of the Double Chooz experiment was completed in 2010 with detector commissioning finishing in April 2011. The first phase of data-taking will occur with the far detector only. Figure 2 shows the improvement in sensitivity as a function of time; the far detector only phase and the two detector phase. Although the experiment is less sensitive without the near detector, only a few months of data are required to equal the sensitivity of the original CHOOZ detector and the experiment should reach a sensitivity to $\sin^2(2\theta_{13})$ of 0.06 with one year of data. With two detectors, Double Chooz will be able to measure $\sin^2(2\theta_{13})$ to 3σ if $\sin^2(2\theta_{13}) > 0.05$ or exclude $\sin^2(2\theta_{13})$ down to 0.03 at 90% for $\Delta m_{31}^2 = 2.5 \times 10^{-3} \text{ eV}^2$ with three years of data with both near and far detectors.

REFERENCES

- [1] SCHWETZ T., *Phys. Lett. B*, **648** (2007) 54.
- [2] APOLLONIO M. *et al.* (CHOOZ COLLABORATION), *Eur. Phys. J. C*, **27** (2003) 331.
- [3] MUELLER T. *et al.*, arXiv: 1101.2663.
- [4] MENTION G. *et al.*, *Phys. Rev. D*, **83** (2011) 073006.
- [5] ARDELLIER F. *et al.* (DOUBLE CHOOZ COLLABORATION), Double Chooz: A search for the neutrino mixing angle θ_{13} (2006) preprint arXiv:hep-ex/0606025v4.
- [6] HAMAMATSU CORPORATION, <http://sales.hamamatsu.com/>.
- [7] HAGNER T. *et al.*, *Astropart. Phys.*, **14** (2000) 33.

Neutrino physics with the Borexino experiment

B. CACCIANIGA on behalf of the BOREXINO COLLABORATION(*)

*Dipartimento di Fisica, Università di Milano Studi e INFN, Sezione di Milano
Milano 20133, Italy*

(ricevuto il 29 Settembre 2011; pubblicato online il 26 Gennaio 2012)

Summary. — Borexino is a large mass, high radiopurity detector located under the Gran Sasso Mountain (Italy) and designed to measure in real-time the flux of low energy solar neutrinos. Borexino has been taking data continuously since May 2007. This talk is focused on the main goal of Borexino, the measurement of solar neutrinos produced in the ${}^7\text{Be}$ reaction: I will present the result on the ${}^7\text{Be}$ flux obtained in 2008 after 192 days of data-taking together with a preliminary evaluation of the day-night asymmetry of the signal. I will also discuss the impact on the analysis of the two extensive calibration campaigns performed in 2009. Thanks to these campaigns a new measurement of the ${}^7\text{Be}$ flux will be shortly published with significantly reduced error. Borexino is also able of measuring the ${}^8\text{B}$ neutrino flux with an unprecedented low threshold of 3 MeV (scattered electron kinetic energy): it is the only experiment able of probing the survival probability in the vacuum dominated oscillation regime (with ${}^7\text{Be}$ neutrinos) and in the matter enhanced oscillation regime (with ${}^8\text{B}$). Finally, I will also present another important result of Borexino, namely the first clear observation of geoneutrinos.

PACS 95.55.Vj – Neutrino, muon, pion, and other elementary particle detectors; cosmic ray detectors.

PACS 29.40.Mc – Scintillation detectors.

(*) G. Bellini, J. Benziger, D. Bick, S. Bonetti, M. Buizza Avanzini, B. Caccianiga, L. Cado-nati, F. Calaprice, C. Carraro, P. Cavalcante, A. Chavarria, D. D'Angelo, S. Davini, A. Derbin, A. Etenko, F. von Feilitzsch, K. Fomenko, D. Franco, C. Galbiati, S. Gazzana, C. Ghiano, M. Giammarchi, M. Göger-Neff, A. Goretti, L. Grandi, E. Guardincerri, S. Hardy, Aldo Ianni, Andrea Ianni, V. Kobychev, D. Korablev, G. Korga, Y. Koshio, D. Kryn, T. Lewke, E. Litvi-novich, B. Loer, F. Lombardi, P. Lombardi, L. Ludhova, I. Machulin, S. Manecki, W. Maneschg, G. Manuzio, Q. Meindl, E. Meroni, L. Miramonti, M. Misiaszek, D. Montanari, P. Mosteiro, V. Muratova, L. Oberauer, M. Obolensky, F. Ortica, M. Pallavicini, L. Papp, L. Perasso, S. Perasso, A. Pocar, R.S. Raghavan, G. Ranucci, A. Razeto, A. Re, A. Romani, A. Sabel-nikov, R. Saldanha, C. Salvo, S. Schönert, H. Simgen, M. Skorokhvatov, O. Smirnov, A. Sot-nikov, S. Sukhotin, Y. Suvorov, R. Tartaglia, G. Testera, D. Vignaud, R.B. Vogelaar, J. Winter, M. Wojcik, A. Wright, M. Wurm, J. Xu, O. Zaimidoroga, S. Zavatarelli, and G. Zuzel

1. – Introduction

Solar neutrinos have been studied for 30 years by means of radiochemical and water-Čerenkov detectors. These studies have yielded to the discovery of neutrino oscillations in the Sun and to the determination of the oscillation parameters $\Delta m^2 = 7.6 \cdot 10^{-5} \text{ eV}^2$ and $\sin^2 2\theta_{12} = 0.87$ (K. Nakamura *et al.* [1]). However, the investigation of the solar neutrino spectrum is far from being complete, having been limited on one hand by the fact that radiochemical experiments cannot measure neutrino energies, and on the other by the fact that water-Čerenkov detectors must work with a high experimental threshold ($E > 4.5 \text{ MeV}$) because of radioactive background. The Borexino experiment has opened a new chapter in the experimental history of solar neutrinos, by proving the feasibility of the solar neutrino spectroscopy in real-time down to the unprecedented energy threshold of 250 keV [2, 3]. This was made possible by employing a liquid scintillator technique which has several advantages over both radiochemical and water-Čerenkov ones: on one hand, it allows detection in real-time (unlike the radiochemical technique), on the other, it makes it possible to lower the energy threshold down to few hundred keVs. This last feature stems from two main characteristics of an organic liquid scintillator: the large light yield (with respect to the Čerenkov one) and the fact that it provides very low solubility to ions and metal impurities which makes it possible to bring it to unprecedented level of radiopurity.

In this talk we report the main results obtained so far by the Borexino experiment, which include the measurement of the ${}^7\text{Be}$ flux after 192 days of data-taking, the measurement of the ${}^8\text{B}$ neutrino flux down to the unprecedented threshold of 3 MeV. We will also discuss preliminary results on the day-night asymmetry of the ${}^7\text{Be}$ neutrinos. We will finally show the results concerning the first clear detection of geoneutrinos. More details can be found in Arpesella *et al.* [2, 3] and in [4].

2. – The Borexino detector

The Borexino detector is located under the Gran Sasso Mountain in the Laboratori Nazionali del Gran Sasso, Italy. It detects solar neutrinos via their elastic scattering on the electrons of 300 tons of liquid scintillator. The scintillator (pseudocumene as a solvent + 1.5 g/l of PPO as a solute) is contained in a large spherical nylon vessel ($R = 4.25 \text{ m}$). The scintillation light is viewed by 2214 photomultiplier tubes mounted on a Stainless-Steel Sphere (SSS) concentric with the vessel at a radius of 6.85 m (see fig. 1). In order to reduce external background (γ 's from the PMTs and γ 's + neutrons from the rock), the design of Borexino is based on the principle of graded shielding, with the inner core scintillator at the center of a set of concentric shells of increasing radiopurity.

The innermost shield is provided by 1000 tons of pure pseudocumene contained in the SSS. The outermost one consists in 2000 tons of ultrapure water contained in the cylindrical dome (diameter = 18 m, height = 16.9 m) which encloses the entire detector. The external water serves also as a Čerenkov radiator to detect residual cosmic muons crossing the detector. Besides keeping external backgrounds at a low level, the key requirement for measuring low energy neutrinos with Borexino is the extreme radiopurity of the scintillator itself: the neutrino signal, in fact, is indistinguishable from the beta-like events due to natural radioactivity. Therefore, the rate of events due to radioactive background must be lower or comparable to the expected interaction rate for the ${}^7\text{Be}$ signal, namely 50 counts/(day · 100 tons). During 15 years of dedicated R&D studies, the

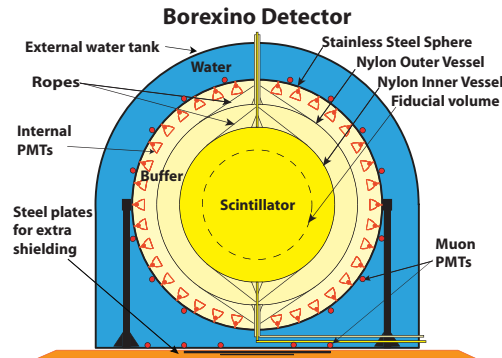


Fig. 1. – A scheme of the Borexino detector: the core of the experiment is represented by 300 tons of liquid scintillator contained in a spherical vessel (in yellow) of 4.25 m radius. The light emitted by the scintillator is viewed by 2200 photomultiplier tubes mounted on a sphere of 7 m radius.

Borexino Collaboration developed a successful purification strategy which proved to be effective in removing the most dangerous contaminants from the scintillator. In particular, the contamination due to ^{238}U and ^{232}Th was brought to the unprecedented levels of $(1.6 \pm 0.1) 10^{-17}$ g/g and $(6.8 \pm 1.5) 10^{-18}$ g/g, respectively, one order of magnitude better than the designed goal of 10^{-16} g/g. For more details concerning the Borexino detector see [5, 6].

3. – ^7Be neutrino flux

An event in Borexino is recorded when at least 25 PMT pulses occur within a time window of 99 ns (which corresponds to an energy threshold of approximately 40 keV). When a trigger occurs, a $16 \mu\text{s}$ gate is opened and time and charge of each PMT is collected. The offline software identifies the shape and length of the scintillator pulse and reconstructs the position of the energy deposit in the scintillator by means of a time of flight technique. Energy is determined by summing the photoelectrons collected for each event. The calibration of the energy scale has been obtained by means of internal contaminants, in particular ^{14}C . The scintillator Light Yield is found to be of the order of 500 photoelectrons/MeV of deposited energy.

The analysis described here refers to 192 live days of data taken in the period from May 16, 2007 to April 12, 2008. The selection cuts are needed to reject muons and residual external and internal backgrounds. For what concerns muons, they are rejected by using the combined information of the outer Čerenkov detector and the internal detector.

Events must be reconstructed within a spherical fiducial volume of 3 meters. The selection of the innermost region of the scintillator is essential to reduce external background to acceptable levels. Additionally, the z -coordinate of the event must be $|z| < 1.7$ m in order to remove background near the poles of the nylon vessel.

The resulting spectrum after applying all cuts is shown in fig. 2 on the left. The prominent peak at approximately 450 keV is due to the 5.3 MeV α 's from ^{210}Po , whose visible energy is reduced by light quenching as expected in an organic liquid scintillator. The high ^{210}Po contamination has unknown origins. However, ^{210}Po is not in equilibrium

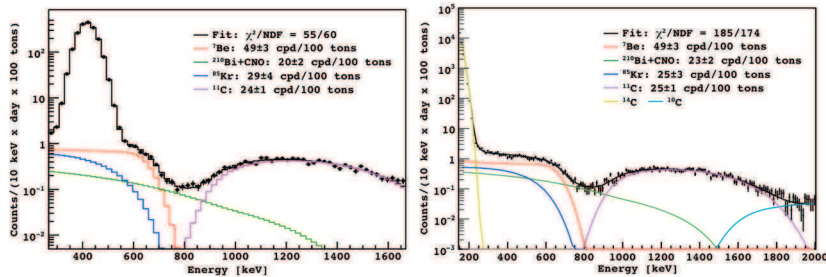


Fig. 2. – Borexino spectra obtained after applying the analysis cuts, before (left) and after (right) statistically subtracting the α 's from ^{210}Po decay. The ^7Be rate is determined by a fit to the spectra which accounts also for the residual backgrounds ^{11}C , ^{85}Kr , ^{210}Bi and for neutrinos from the CNO reactions.

with the other elements of the ^{238}U chain to which it belongs and is decaying away with the expected lifetime ($\tau = 200.2$ days). It is possible to apply a pulse-shape discrimination technique to statistically subtract from the spectrum the contribution due to ^{210}Po α 's. The resulting spectrum is shown in fig. 2 on the right. A fit is performed on both spectra including the contribution of the ^7Be neutrino signal (with its characteristic Compton-like shape), plus the spectral shapes of the expected residual internal backgrounds, namely, ^{11}C , ^{85}Kr and ^{210}Bi . Since the shapes of ^{210}Bi and CNO neutrino spectra are almost indistinguishable, they are fitted together, using a single weight. The weights of all spectral components are left as free parameters of the fit, together with the light yield. The results obtained with and without alpha subtraction are consistent with each other. The main contributions to the systematic error come from the uncertainty on the fiducial mass and on the detector response function. The total systematic uncertainty is $\pm 8.5\%$. This error will be substantially reduced thanks to the information coming from two calibration campaigns performed in 2009 (see dedicated paragraph).

The final result for the ^7Be rate in Borexino including both statistical and systematic error is $(49 \pm 3_{\text{stat}} \pm 4_{\text{sys}})$ counts/(day \cdot 100 tons). The expected signal from the Solar Standard Model⁽¹⁾ [7], in case of no-oscillation is 74 ± 4 counts/day \cdot 100 tons: the no-oscillation hypothesis is rejected by the Borexino data at the 4σ level. On the other hand, the rate expected in Borexino in case of oscillations for the current best-fit MSW-LMA parameters [1] is 48 ± 4 counts/(day \cdot 100 tons), in perfect agreement with what found experimentally. From our measurement, under the constraint from the high metallicity SSM and of the MSW-LMA scenario, our best estimate for the flux of ^7Be neutrinos is $\Phi(^7\text{Be}) = (5.18 \pm 0.51) \times 10^9 \text{ cm}^{-2} \text{ s}^{-1}$.

The Borexino measured rate can be combined with the other solar neutrino measurements to constrain the flux normalization constants for the other solar neutrino sources. In particular, using the luminosity constraint, one obtains $f_{pp} = 1.005^{+0.13}_{-0.19}$ and $f_{\text{CNO}} < 3.80$ (90% CL), where f_{pp} and f_{CNO} are the ratios between the measured and the expected fluxes of pp and CNO sources under the assumptions of the SSM and MSW-LMA.

⁽¹⁾ Depending on the assumptions made on the solar abundances of high-Z elements, the ^7Be flux predicted by the Standard Solar Model changes by approximately 10%. We arbitrarily choose as a reference the latest SSM based on abundances reported in reference [8].

4. – ${}^7\text{Be}$ neutrino day-night asymmetry

A preliminary analysis of the day-night asymmetry of the ${}^7\text{Be}$ signal has been performed. This measurement can give an independent confirmation of the LMA region: the day-night asymmetry predicted in the LMA region hypothesis is in fact very small ($< 0.1\%$) while can be as large as 80% in other regions of the oscillation parameter space (like in the so-called LOW solution region). For this analysis we use events in a Fiducial Volume defined by the $R < 3$ m cut only and we perform the fit described in the previous paragraph to extract the signal on the day and night spectra separately. The day-night asymmetry is defined as $A_{dn} = 2 \frac{R_N - R_D}{R_N + R_D}$ where R_N and R_D are the ${}^7\text{Be}$ rate for night and day respectively. A preliminary analysis based on 387.46 days during the day time and 401.57 days during the night time leads to $A_{dn} = 0.007 \pm 0.073$, consistent with zero in agreement with the LMA hypothesis. A more accurate measurement of the day-night asymmetry will be published in the near future.

5. – The ${}^8\text{B}$ neutrino flux

Borexino is the first experiment capable to probe the oscillation hypothesis both in the vacuum dominated regime at low energies (with the ${}^7\text{Be}$ neutrinos) and in the matter enhanced regime at higher energies by also measuring the ${}^8\text{B}$ neutrino flux [9]. With respect to the large Čerenkov detectors designed on purpose to measure ${}^8\text{B}$ neutrinos, Borexino has the disadvantage of a relatively small mass and is not capable to correlate the signal to the sun, since scintillation signal lacks directionality. In spite of that, the excellent radiopurity reached by the detector has made it possible not only to measure the ${}^8\text{B}$ flux, but also to reduce the energy threshold for the scattered electron energy down to the unprecedented level of 3 MeV. In Borexino, the main backgrounds affecting the ${}^8\text{B}$ analysis are the cosmogenic isotopes induced by muons and the external background from photomultipliers. The short lived cosmogenics ($\tau < 2$ s) are removed by vetoing the detector for 5 s after each muon crossing it, while ${}^{10}\text{C}$ is removed by the triple coincidence with the parent muon and the neutron capture on proton. The external background (mainly Thallium from photomultiplier tubes) is rejected by a Fiducial Volume cut of $R < 3$ m. The contribution due to the small Thallium internal contamination (0.008 counts/(day · 100 tons)) is statistically subtracted from the final spectrum. Figure 3 (left) shows the spectrum after data selection (red dots), with superimposed the expected contributions from residual backgrounds. The resulting ${}^8\text{B}$ neutrino rate above 3 MeV is found to be $(0.22 \pm 0.04_{stat} \pm 0.01_{sys})$ counts/(day · 100 tons). This result is obtained analyzing a total of 488 live days of data-taking, corresponding to an exposure of 345.3 days after all cuts. The corresponding total ${}^8\text{B}$ neutrino flux is $(2.7 \pm 0.4 \pm 0.1) \times 10^6 \text{ cm}^{-2} \text{ s}^{-1}$, in very good agreement with previous more precise measurements performed by Čerenkov detectors. Figure 3 (right) shows the electron neutrino survival probability P_{ee} for the ${}^7\text{Be}$ and ${}^8\text{B}$ energies as obtained from the Borexino data (assuming the Standard Solar Model predictions for the fluxes in [7] and [8]). Eliminating common sources of systematic errors the ratio between the two probabilities is 1.6 ± 0.33 confirming the expectations of the LMA-MSW oscillation scenario at 93% CL.

6. – Geoneutrinos

Geoneutrinos (geo- $\bar{\nu}_e$) are electron antineutrinos produced in β -decays of isotopes naturally present in the Earth like ${}^{40}\text{K}$ and several nuclides in the ${}^{238}\text{U}$ and ${}^{232}\text{Th}$ chains.

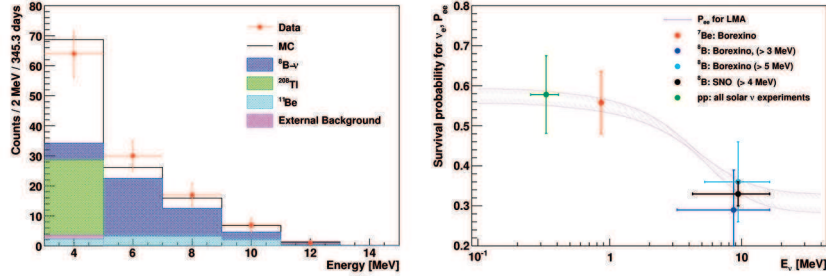


Fig. 3. – (Colour on-line) Left plot: residual spectrum after all selection cuts (red dots). The expected electron recoil spectrum (from ^8B neutrinos including oscillations) is shown in filled blue histogram, together with the expected residual backgrounds. Right plot: the electron neutrino survival probability of the LMA-MSW model and the experimental results discussed in this talk. The curve is computed for PBS09(GS98) and oscillation parameters $\tan^2\theta_{12} = 0.45$ and $\Delta m_{12}^2 = 7.69 \times 10^{-5} \text{ eV}^2$.

They can be used as a unique direct probe of the Earth interior, in particular they can give information on the content and distribution of the long-lived radioactive elements in the Earth. Radiogenic heat is generally considered as the main contribution to the total heat budget of Earth. The geochemical Bulk Silicate Earth (BSE) model predicts about 19 TW of radiogenic heat from which 9 TW is produced in the crust (mainly continental) and 10 TW in the mantle. Other models predict a much larger contribution from radiogenic heat, while more exotic ones predict possible additional heat sources such as the presence of a nuclear geo-reactor in the core. These models can be discriminated by geo- $\bar{\nu}_e$ measurements, which, especially when performed at different sites, can give information about the spatial distribution of radiogenic elements, about their concentration in the mantle, and about the compatibility of the terrestrial Th/U ratio with the chondritic value of 3.9.

Borexino detects $\bar{\nu}_e$ via the inverse β -decay reaction $\bar{\nu}_e + p \rightarrow n + e^+$. The positron comes to rest and annihilates emitting two 511 keV γ -rays, yielding a prompt event, with a visible energy of $E_p = E_{\bar{\nu}_e} - 0.782 \text{ MeV}$. The emitted neutron is typically captured on protons with a mean time of $\tau \simeq 256 \mu\text{s}$ resulting in the emission of a 2.22 MeV de-excitation γ -ray, which provides a coincident delayed event. The characteristic time and spatial coincidence of prompt and delayed events offers a clean signature of $\bar{\nu}_e$ detection. Borexino identifies 21 $\bar{\nu}_e$ candidates during 540 livedays with a total exposure after all selection cuts of 252.6 ton yr. Besides geoneutrinos, the known $\bar{\nu}_e$ sources are reactor $\bar{\nu}_e$, while supernova relic $\bar{\nu}_e$'s give a negligible contribution. The expected reactor signal with (without) neutrino oscillation and 100% detection efficiency is $5.7 \pm 0.3 \text{ events}/(100 \text{ ton} \cdot \text{yr})$ ($9.9 \pm 0.5 \text{ events}/(100 \text{ ton} \cdot \text{yr})$). The energy spectrum for the prompt signal of the 21 candidates surviving the analysis cuts is shown in fig. 4. An unbinned maximum likelihood analysis is used to extract the contribution from geoneutrino and from reactor antineutrinos: our best estimate for the number of detected geoneutrinos is $N_{geo} = 9.9_{-3.4}^{+4.1(+14.6)}$ and of reactor antineutrinos is $N_{rea} = 10.7_{-3.4}^{+4.3(+15.8)}$ at 68.4% CL (99.73% CL). By studying the profile of the log-likelihood with respect to N_{geo} we have calculated that the null hypothesis for geo- $\bar{\nu}_e$ (*i.e.*, $N_{geo} = 0$) can be rejected at 99.997%. This results hint at a higher rate for geo- $\bar{\nu}_e$ than current BSE predictions, but the present uncertainty prevents firm conclusions. We plan to accumulate at least an exposure of 1000 ton yr, which should reduce the error by a factor two.

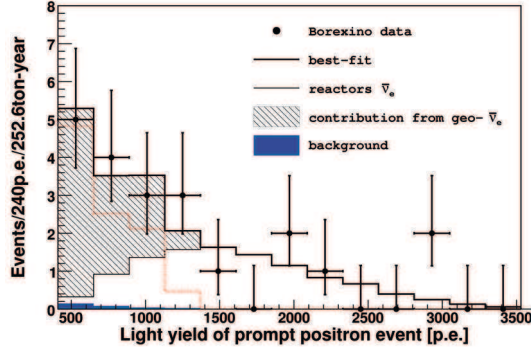


Fig. 4. – Spectrum (number of photoelectrons) for the positron prompt events of the 21 $\bar{\nu}_e$ candidates and the best-fit curve (black solid).

The observed prompt positron spectrum above 2.6 MeV is compatible with the one expected from nuclear reactors (mean baseline of approximately 1000 km). Our measurement of reactor antineutrinos excludes the non-oscillation hypothesis at 99.60% CL. Furthermore, this measurement rejects the hypothesis of an active geo-reactor in the Earth’s core with a power above 3 TW at 95% CL.

7. – Calibrations

Two calibration campaigns were performed in 2009 to study possible systematics associated to the position reconstruction of the events, and to determine the energy scale and the detector response function with high precision. Before calibrations, reconstruction of position and energy was tested and tuned on internal contaminants (like ^{14}C , ^{222}Rn and so on) in a non optimal way and this is reflected in the high systematic error associated to the ^7Be measurement described in this talk. During the two calibration campaigns several radioactive sources were inserted in many positions throughout the active volume of the detector. In order to calibrate the detector without introducing unwanted contaminations, the source containers have been carefully designed. We have used a quartz sphere (one inch diameter) either filled by ^{222}Rn loaded scintillator identical to the Borexino or filled with γ emitters in aqueous solution. The quartz sphere was attached to a set of stainless steel bars that allowed to locate the source in almost any position within the IV. The Rn source, deployed in more than 200 positions, was mainly used to study the position reconstruction and the position dependence of the detector response. The nominal source position was determined independently by a system of 7 CCD cameras located on the Stainless Steel Sphere (where also the 2200 phototubes are mounted). The calibration campaign allowed to reduce the overall systematic uncertainty on the Fiducial Volume selection from 6% down to $\approx 1\%$.

TABLE I. – Calibrations sources used to determine the energy scale. The isotopes are γ -emitters and span the energy region of interest for the ^7Be analysis.

Isotope	^{57}Co	^{139}Ce	^{203}Hg	^{85}Sr	^{54}Mn	^{65}Zn	^{60}Co	^{40}K
Energy (keV)	122	165	279	514	834	1115	1173-1332	1460

The energy scale was studied by inserting 8 different gamma-emitting sources (see table I) spanning the energy range of interest for the ${}^7\text{Be}$ analysis (from ≈ 100 keV to 1.4 MeV). An AmBe neutron source was also used, in order to have calibration points at higher energies, relevant for ${}^8\text{B}$ solar neutrinos and geo-neutrinos. Due to the quenching phenomenon, the energy scale of a scintillator is not linear and depends also on particle type. The calibration campaigns allowed to reduce the uncertainty on the energy scale between 0 and 2 MeV to less than 1.5%.

8. – Conclusions and perspectives

Borexino has performed the first direct measurement of the ${}^7\text{Be}$ solar neutrino flux in real time. The results confirm the neutrino oscillation hypothesis and are in agreement with what expected in the LMA-MSW scenario. We have also measured the flux of ${}^8\text{B}$ neutrinos thus probing oscillations both in the vacuum and in the matter enhanced regimes. Borexino has also performed the first clear detection of geoneutrinos.

The calibration campaigns performed in 2009 will have a crucial role in reducing the systematic errors and a new, more precise measurement of the ${}^7\text{Be}$ flux will be published soon. The exceptional levels of radiopurity of the experiment have opened the possibility to explore in a near future other solar neutrino sources, like the so-called pep, CNO and possibly pp. In particular, we are currently purifying the scintillator to try and reduce even further the content of ${}^{210}\text{Bi}$ and ${}^{85}\text{Kr}$, which are the main sources of background for these analyses.

REFERENCES

- [1] NAKAMURA K. *et al.* (PARTICLE DATA GROUP), *Review of Particle Physics, J. Phys. G*, **37** (2010) 075021.
- [2] ARPESELLA C. *et al.* (BOREXINO COLLABORATION), *Phys. Lett. B*, **658** (2008) 101.
- [3] ARPESELLA C. *et al.* (BOREXINO COLLABORATION), *Phys. Rev. Lett.*, **101** (2008) 091302.
- [4] BELLINI G. *et al.* (BOREXINO COLLABORATION), *Phys. Lett. B*, **687** (2010) 299.
- [5] ALIMONTI G. *et al.* (BOREXINO COLLABORATION), *Nucl. Instrum. Methods Phys. Res. A*, **600** (2009) 568.
- [6] ALIMONTI G. *et al.* (BOREXINO COLLABORATION), *Nucl. Instrum. Methods Phys. Res. A*, **609** (2009) 58.
- [7] BAHCALL J. N., SERENELLI A. M. and BASU S., *Astrophys. J. Suppl.*, **165** (2006) 400.
- [8] GREVESSE N. and SAUVAL A. J., *Space Sci. Rev.*, **85** (1998) 161.
- [9] BELLINI G. *et al.* (BOREXINO COLLABORATION), *Phys. Rev. D*, **82** (2010) 033006.

Recent progress in neutrino physics

C. GIUNTI

INFN, Sezione di Torino - Via P. Giuria 1, I-10125 Torino, Italy

(ricevuto il 29 Settembre 2011; pubblicato online il 24 Gennaio 2012)

Summary. — After a brief review of the results of solar, atmospheric and long-baseline neutrino oscillation experiments which led to the current three-neutrino mixing paradigm, we discuss indications of neutrino oscillation experiments in favor of short-baseline oscillations which require the existence of one or more sterile neutrinos. We show that the simplest possibility of existence of one sterile neutrino is not enough to fit all data of short-baseline neutrino oscillation experiments because of two tensions: a tension between neutrino and antineutrino data and a tension between appearance and disappearance data. The tension between neutrino and antineutrino data is eliminated with the addition of a second sterile neutrino which allows *CP*-violating effects in short-baseline experiments. In this case the tension between appearance and disappearance data is reduced, but cannot be eliminated.

PACS 14.60.Pq – Neutrino mass and mixing.

PACS 14.60.Lm – Ordinary neutrinos.

PACS 14.60.St – Non-standard-model neutrinos.

The results of several solar, atmospheric and long-baseline neutrino oscillation experiment have proved that neutrinos are massive and mixed particles (see ref. [1]). There are two groups of experiments which measured two independent squared-mass differences (Δm^2) in two different neutrino flavor transition channels.

Solar neutrino experiments (Homestake, Kamiokande, GALLEX/GNO, SAGE, Super-Kamiokande, SNO, BOREXino) measured $\nu_e \rightarrow \nu_\mu, \nu_\tau$ oscillations generated by $\Delta m_{\text{SOL}}^2 = 6.2_{-1.9}^{+1.1} \times 10^{-5} \text{ eV}^2$ and a mixing angle $\tan^2 \vartheta_{\text{SOL}} = 0.42_{-0.02}^{+0.04}$ [2]. The KamLAND experiment confirmed these oscillations by observing the disappearance of reactor $\bar{\nu}_e$ at an average distance of about 180 km. The combined fit of solar and KamLAND data leads to $\Delta m_{\text{SOL}}^2 = (7.6 \pm 0.2) \times 10^{-5} \text{ eV}^2$ and a mixing angle $\tan^2 \vartheta_{\text{SOL}} = 0.44 \pm 0.03$ [2]. Notice that the agreement of solar and KamLAND data in favor of ν_e and $\bar{\nu}_e$ disappearance generated by the same oscillation parameters is consistent with the equality of neutrino and antineutrino disappearance expected from CPT symmetry (see ref. [1]).

Atmospheric neutrino experiments (Kamiokande, IMB, Super-Kamiokande, MACRO, Soudan-2, MINOS) measured ν_μ and $\bar{\nu}_\mu$ disappearance through oscillations generated by $\Delta m_{\text{ATM}}^2 \simeq 2.3 \times 10^{-3} \text{ eV}^2$ and a mixing angle $\sin^2 2\vartheta_{\text{ATM}} \simeq 1$ [3]. The K2K and MINOS long-baseline experiments confirmed these oscillations by observing the disappearance of accelerator ν_μ at distances of about 250 km and 730 km, respectively. The MINOS data give $\Delta m_{\text{ATM}}^2 = 2.32_{-0.08}^{+0.12} \times 10^{-3} \text{ eV}^2$ and $\sin^2 2\vartheta_{\text{ATM}} > 0.90$ at 90% CL [4]. The equality

of muon neutrino and antineutrino disappearance expected from CPT symmetry is currently under investigation in the MINOS experiment [5], with preliminary results which hint at an intriguing difference between the muon neutrino and antineutrino oscillation parameters.

These measurements led to the current three-neutrino mixing paradigm, in which the three active neutrinos ν_e, ν_μ, ν_τ are superpositions of three massive neutrinos ν_1, ν_2, ν_3 with respective masses m_1, m_2, m_3 . The two measured squared-mass differences can be interpreted as

$$(1) \quad \Delta m_{\text{SOL}}^2 = \Delta m_{21}^2, \quad \Delta m_{\text{ATM}}^2 = |\Delta m_{31}^2| \simeq |\Delta m_{32}^2|,$$

with $\Delta m_{kj}^2 = m_k^2 - m_j^2$. In the standard parameterization of the 3×3 unitary mixing matrix (see ref. [1]) $\vartheta_{\text{SOL}} \simeq \vartheta_{12}$, $\vartheta_{\text{ATM}} \simeq \vartheta_{23}$ and $\sin^2 \vartheta_{13} < 0.035$ at 90% CL [6].

The completeness of the three-neutrino mixing paradigm has been challenged by the recent observation of a signal of short-baseline $\bar{\nu}_\mu \rightarrow \bar{\nu}_e$ oscillations in the MiniBooNE experiment [7] which agrees with a similar signal observed several years ago in the LSND experiment [8]. It is remarkable that the two signals have been observed at different values of distance (L) and energy (E), but approximately at the same L/E . Since the distance and energy dependences of neutrino oscillations occur through this ratio, the agreement of the MiniBooNE and LSND signals raised interest in the possibility of existence of one or more squared-mass differences much larger than Δm_{SOL}^2 and Δm_{ATM}^2 . These new squared-mass differences should have values larger than about 0.5 eV.

In the following, I consider first the simplest extension of three-neutrino mixing with the addition of one massive neutrino. In such four-neutrino mixing framework the flavor neutrino basis is composed by the three active neutrinos ν_e, ν_μ, ν_τ and a sterile neutrino ν_s which does not have weak interactions and does not contribute to the invisible width of the Z boson [9]. The existence of sterile neutrinos which have been thermalized in the early Universe is compatible with Big-Bang Nucleosynthesis data [10,11] and cosmological measurements of the Cosmic Microwave Background and Large-Scale Structures if the mass of the fourth neutrino is limited below about 1 eV [12,13].

So-called 2+2 four-neutrino mixing schemes are strongly disfavored by the absence of any signal of sterile neutrino effects in solar and atmospheric neutrino data [17]. Hence, we must consider the so-called 3+1 four-neutrino schemes depicted in fig. 1. Since the “ 4ν -inverted” and “totally-inverted” schemes have three massive neutrinos at the eV scale, they are disfavored by cosmological data over the “normal” and “ 3ν -inverted” schemes. In all 3+1 schemes the effective flavor transition and survival probabilities in short-baseline (SBL) experiments are given by

$$(2) \quad P_{\nu_\alpha \rightarrow \nu_\beta}^{\text{SBL} \quad (-) \quad (-)} = \sin^2 2\vartheta_{\alpha\beta} \sin^2 \left(\frac{\Delta m^2 L}{4E} \right) \quad (\alpha \neq \beta),$$

$$(3) \quad P_{\nu_\alpha \rightarrow \nu_\alpha}^{\text{SBL}} = 1 - \sin^2 2\vartheta_{\alpha\alpha} \sin^2 \left(\frac{\Delta m^2 L}{4E} \right),$$

for $\alpha, \beta = e, \mu, \tau, s$, with $\Delta m^2 = \Delta m_{\text{SBL}}^2$ and

$$(4) \quad \sin^2 2\vartheta_{\alpha\beta} = 4|U_{\alpha 4}|^2 |U_{\beta 4}|^2,$$

$$(5) \quad \sin^2 2\vartheta_{\alpha\alpha} = 4|U_{\alpha 4}|^2 (1 - |U_{\alpha 4}|^2).$$

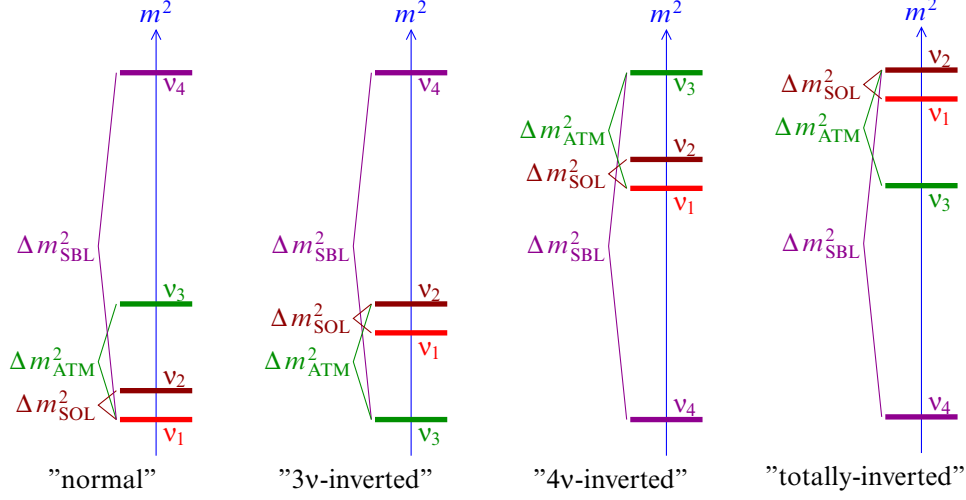


Fig. 1. – 3+1 four-neutrino schemes.

Therefore:

1. All effective SBL oscillation probabilities depend only on the largest squared-mass difference $\Delta m^2 = \Delta m_{\text{SBL}}^2 = |\Delta m_{41}^2|$.
2. All oscillation channels are open, each one with its own oscillation amplitude.
3. All oscillation amplitudes depend only on the absolute values of the elements in the fourth column of the mixing matrix, *i.e.* on three real numbers with sum less than unity, since the unitarity of the mixing matrix implies $\sum_{\alpha} |U_{\alpha 4}|^2 = 1$
4. CP violation cannot be observed in SBL oscillation experiments, even if the mixing matrix contains CP -violating phases. In other words, neutrinos and antineutrinos have the same effective SBL oscillation probabilities.

Before the recent indication of an antineutrino $\bar{\nu}_{\mu} \rightarrow \bar{\nu}_e$ signal consistent with the LSND antineutrino signal, the MiniBooNE collaboration published the results of neutrino data which do not show a corresponding $\nu_{\mu} \rightarrow \nu_e$ signal [20]. This difference between the MiniBooNE neutrino and antineutrino data may be due to CP violation.

The absence of any difference in the effective SBL oscillation probabilities of neutrinos and antineutrinos in 3+1 four-neutrino mixing schemes implies that these schemes cannot explain the difference between neutrinos and antineutrino oscillations observed in the MiniBooNE. Moreover, the dependence of all the oscillation amplitudes in eqs. (4) and (5) on three independent absolute values of the elements in the fourth column of the mixing matrix implies that the amplitude of $\bar{\nu}_{\mu}^{(-)} \rightarrow \bar{\nu}_e^{(-)}$ transitions is limited by the absence of large SBL disappearance of $\bar{\nu}_e^{(-)}$ and $\bar{\nu}_{\mu}^{(-)}$ observed in several experiments.

The results of reactor neutrino experiments constrain the value $|U_{e4}|^2$ through the measurement of $\sin^2 2\vartheta_{ee}$. The calculation of the reactor $\bar{\nu}_e$ flux has been recently improved in ref. [15], resulting in an increase of about 3% with respect to the previous value adopted by all experiments for the comparison with the data. As illustrated in fig. 2,

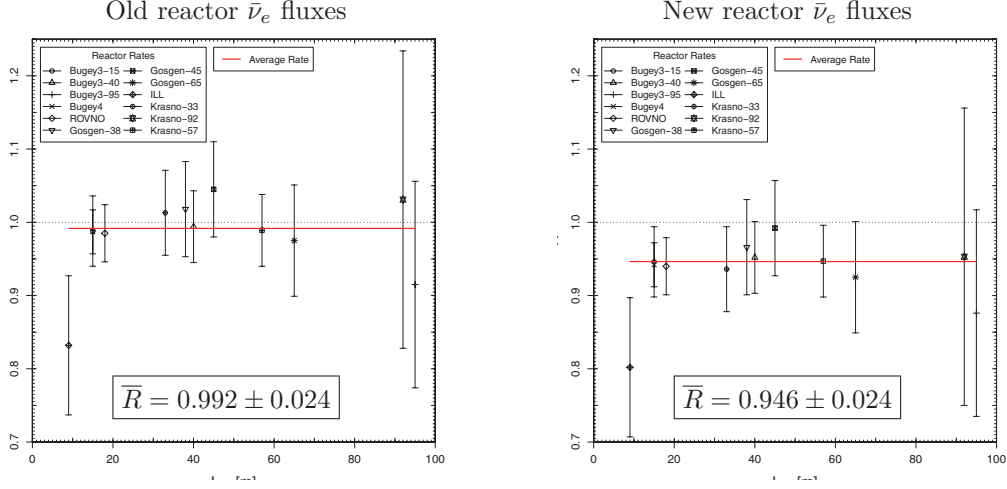


Fig. 2. – Ratio R of the observed $\bar{\nu}_e$ event rate and that expected in absence of $\bar{\nu}_e$ disappearance obtained from the old (see ref. [14]) and new [15] reactor $\bar{\nu}_e$ fluxes. The average value of R obtained with the new reactor $\bar{\nu}_e$ fluxes quantifies the reactor antineutrino anomaly [16].

the measured reactor rates are in agreement with those derived from the old $\bar{\nu}_e$ flux, but show a deficit of about 2.2σ with respect to the rates derived from the new $\bar{\nu}_e$ flux. This is the “reactor antineutrino anomaly” [16]⁽¹⁾, which may be an indication in the $\bar{\nu}_e \rightarrow \bar{\nu}_e$ channel of a signal corresponding to the $\bar{\nu}_\mu \rightarrow \bar{\nu}_e$ signal observed in the LSND and MiniBooNE experiments. However, the $\bar{\nu}_e$ disappearance is small and large values of $\sin^2 2\vartheta_{ee}$ are constrained by the exclusion curves in the left panel of fig. 3. Since values of $|U_{e4}|^2$ close to unity are excluded by solar neutrino oscillations (which require large $|U_{e1}|^2 + |U_{e2}|^2$), for small $\sin^2 2\vartheta_{ee}$ we have

$$(6) \quad \sin^2 2\vartheta_{ee} \simeq 4|U_{e4}|^2.$$

The value of $\sin^2 2\vartheta_{\mu\mu}$ is constrained by the curves in the right panel of fig. 3, which have been obtained from the lack of ν_μ disappearance in the CDHSW ν_μ experiment [18] and from the requirement of large $|U_{\mu1}|^2 + |U_{\mu2}|^2 + |U_{\mu3}|^2$ for atmospheric neutrino oscillations [19]. Hence, $|U_{\mu4}|^2$ is small and

$$(7) \quad \sin^2 2\vartheta_{\mu\mu} \simeq 4|U_{\mu4}|^2.$$

From eqs. (4), (6) and (7), for the amplitude of $\bar{\nu}_\mu^{(-)} \rightarrow \bar{\nu}_e^{(-)}$ transitions we obtain

$$(8) \quad \sin^2 2\vartheta_{e\mu} \simeq \frac{1}{4} \sin^2 2\vartheta_{ee} \sin^2 2\vartheta_{\mu\mu}.$$

⁽¹⁾ We do not consider here the “Gallium neutrino anomaly” [21-26], which may be compatible with the reactor antineutrino anomaly assuming the equality of neutrino and antineutrino disappearance imposed by the CPT symmetry.

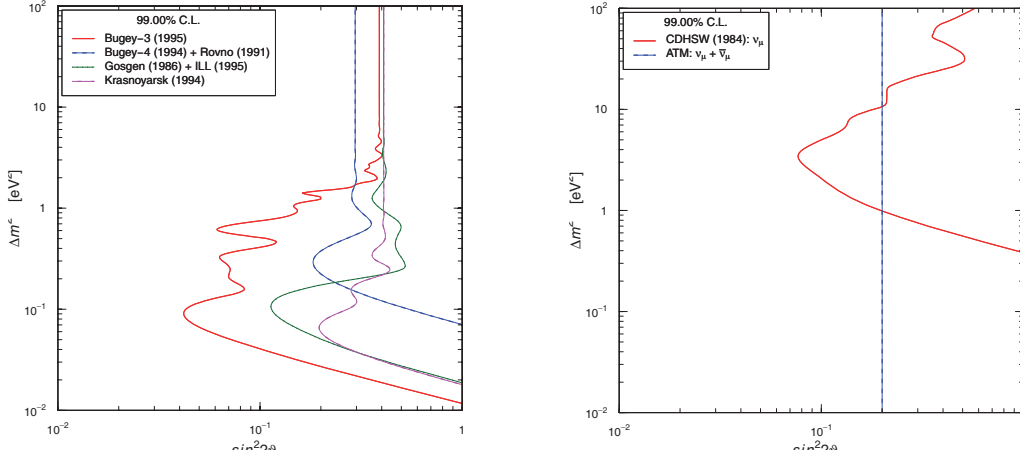


Fig. 3. – Exclusion curves obtained from the data of reactor $\bar{\nu}_e$ disappearance experiments (see ref. [16]), from the data of the CDHSW ν_μ disappearance experiment [18], and from atmospheric neutrino data (extracted from the analysis in ref. [19]).

Therefore, if $\sin^2 2\vartheta_{ee}$ and $\sin^2 2\vartheta_{\mu\mu}$ are small, $\sin^2 2\vartheta_{e\mu}$ is quadratically suppressed. This is illustrated in the left panel of fig. 4, where one can see that the separate effects of the constraints on $\sin^2 2\vartheta_{ee}$ and $\sin^2 2\vartheta_{\mu\mu}$ exclude only the large- $\sin^2 2\vartheta_{e\mu}$ part of the region allowed by LSND and MiniBooNE antineutrino data, whereas most of this region is excluded by the combined constraint in eq. (8). As shown in the right panel of fig. 4, the constraint becomes stronger by including the data of the KARMEN [27], NOMAD [28] and MiniBooNE neutrino [20] experiments, which did not observe a short-

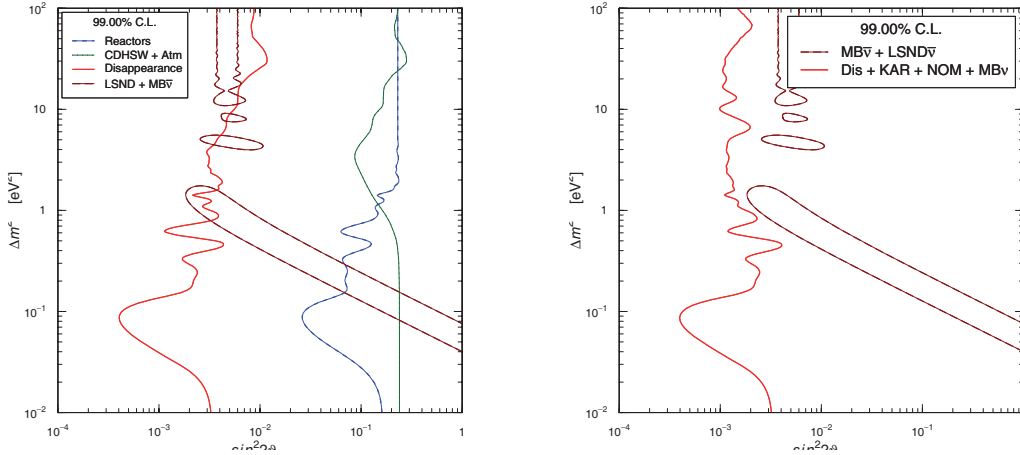


Fig. 4. – Left Panel: Exclusion curves in the $\sin^2 2\vartheta_{e\mu}-\Delta m^2$ plane obtained from the separate constraints in fig. 3 (blue and green lines) and the combined constraint given by eq. (8) (red line) from disappearance experiments (Dis). Right Panel: Exclusion curve obtained with the addition of KARMEN [27] (KAR), NOMAD [28] (NOM) and MiniBooNE neutrino [20] (MB ν) data (red line). In both panels the region enclosed by the dark-red lines is allowed by LSND and MiniBooNE antineutrino data.

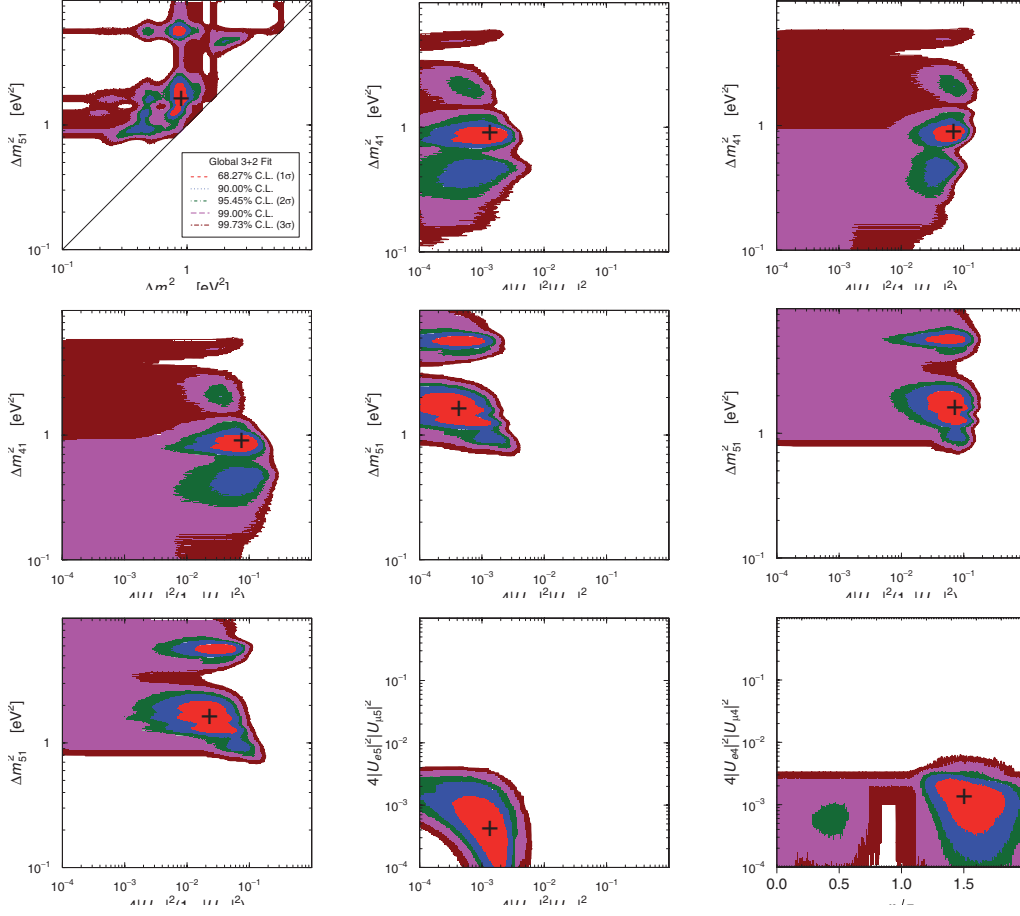


Fig. 5. – Marginal allowed regions in two-dimensional planes of interesting combinations of the oscillation parameters in 3+2 neutrino mixing.

baseline $\bar{\nu}_\mu \rightarrow \bar{\nu}_e$ signal. Since the parameter goodness-of-fit [29] is 0.0016%, 3+1 schemes are strongly disfavored by the data. This conclusion has been reached recently also in refs. [19, 30–32] and confirms the pre-MiniBooNE results in refs. [17, 33].

The CP -violating difference between MiniBooNE neutrino and antineutrino data can be explained by introducing another physical effect in addition to a sterile neutrino: a second sterile neutrino in 3+2 schemes [19, 30, 32, 34–36], non-standard interactions [30], CPT violation [31, 37]. In the following I discuss the possibility of 3+2 neutrino mixing.

In 3+2 schemes the relevant effective oscillation probabilities in short-baseline experiments are given by

$$(9) \quad P_{\nu_\mu \rightarrow \nu_e}^{\text{SBL}(-)} = 4|U_{\mu 4}|^2|U_{e 4}|^2 \sin^2 \phi_{41} + 4|U_{\mu 5}|^2|U_{e 5}|^2 \sin^2 \phi_{51} + 8|U_{\mu 4}U_{e 4}U_{\mu 5}U_{e 5}| \sin \phi_{41} \sin \phi_{51} \cos(\phi_{54} - \eta),$$

$$(10) \quad P_{\nu_\alpha \rightarrow \nu_\alpha}^{\text{SBL}} = 1 - 4(1 - |U_{\alpha 4}|^2 - |U_{\alpha 5}|^2)(|U_{\alpha 4}|^2 \sin^2 \phi_{41} + |U_{\alpha 5}|^2 \sin^2 \phi_{51}) - 4|U_{\alpha 4}|^2|U_{\alpha 5}|^2 \sin^2 \phi_{54},$$

for $\alpha, \beta = e, \mu$, with

$$(11) \quad \phi_{kj} = \Delta m_{kj}^2 L/4E, \quad \eta = \arg[U_{e4}^* U_{\mu 4} U_{e5} U_{\mu 5}^*].$$

Note the change in sign of the contribution of the CP -violating phase η going from neutrinos to antineutrinos, which allows us to explain the CP -violating difference between MiniBooNE neutrino and antineutrino data.

Figure 5 shows the marginal allowed regions in two-dimensional planes of interesting combinations of the oscillation parameters in our 3+2 global fit of the same set of data used in fig. 4. The best-fit values of the mixing parameters are

$$(12) \quad \Delta m_{41}^2 = 0.90 \text{ eV}^2, \quad |U_{e4}|^2 = 0.017, \quad |U_{\mu 4}|^2 = 0.019,$$

$$(13) \quad \Delta m_{51}^2 = 1.61 \text{ eV}^2, \quad |U_{e5}|^2 = 0.018, \quad |U_{\mu 5}|^2 = 0.0058, \quad \eta = 1.51\pi.$$

The parameter goodness-of-fit obtained with the comparison of the fit of LSND and MiniBooNE antineutrino data and the fit of all other data is 0.24%. This is an improvement with respect to the 0.0016% parameter goodness-of-fit obtained in 3+1 schemes. However, the value of the parameter goodness-of-fit remains low as a consequence of the fact that the $\bar{\nu}_\mu \rightarrow \bar{\nu}_e$ transitions observed in LSND and MiniBooNE must correspond in any neutrino mixing schemes to enough short-baseline disappearance of $\bar{\nu}_e^{(-)}$ and $\bar{\nu}_\mu^{(-)}$ which has not been observed.

The results of our 3+2 global fit are in reasonable agreement with those presented in ref. [32]. There is a discrepancy in the location of the best-fit point in the $\Delta m_{41}^2 - \Delta m_{51}^2$ plane, but we obtain similar regions for the local χ^2 minima. Our allowed regions are larger than those presented in ref. [32]. I think that such difference is probably due to a different treatment of the spectral data of the Bugey-3 reactor experiment [38] which cause the wiggling for $\Delta m^2 \lesssim 1 \text{ eV}^2$ of the disappearance limit in the left panel of fig. 4 and the exclusion curve in the right panel of fig. 4. Such wiggling is wider in fig. 3 of ref. [32], leading to deeper valleys of the χ^2 function and smaller allowed regions.

In conclusion, I think that we are living an exciting time in neutrino physics which may prelude to a transition from the well-established three-neutrino mixing paradigm to a new paradigm of neutrino mixing with sterile neutrinos and possibly other effects (as non-standard interactions and CPT violation) which are very interesting for the exploration of the physics beyond the Standard Model. In order to clarify the validity of the experimental indications in favor of an expansion of neutrino mixing beyond the standard three-neutrino mixing and resolve the tension between the current positive and negative experimental results, new experiments with high sensitivity and low background are needed (see, for example, those proposed in refs. [39-44]).

REFERENCES

- [1] GIUNTI C. and KIM C. W., *Fundamentals of Neutrino Physics and Astrophysics* (Oxford University Press, Oxford, UK) 2007.
- [2] SUPER-KAMIOKANDE, ABE K. *et al.*, *Phys. Rev. D*, **83** (2011) 052010, arXiv:1010.0118.
- [3] SUPER-KAMIOKANDE, ASHIE Y. *et al.*, *Phys. Rev. D*, **71** (2005) 112005, hep-ex/0501064.
- [4] MINOS, ADAMSON P. *et al.*, *Phys. Rev. Lett.*, **106** (2011) 181801, arXiv:1103.0340.
- [5] MINOS, ADAMSON P. *et al.*, *Phys. Rev. Lett.*, **107** (2011) 021801, (2011), arXiv:1104.0344.
- [6] SCHWETZ T., TORTOLA M. and VALLE J. W. F., *New J. Phys.*, **10** (2008) 113011, arXiv:0808.2016.

- [7] MINIBoONE, AGUILAR-AREVALO A. A. *et al.*, *Phys. Rev. Lett.*, **105** (2010) 181801, arXiv:1007.1150.
- [8] LSND, AGUILAR A. *et al.*, *Phys. Rev. D*, **64** (2001) 112007, hep-ex/0104049.
- [9] ALEPH, DELPHI, L3, OPAL, SLD, LEP ELECTROWEAK WORKING GROUP, SLD ELECTROWEAK GROUP, SLD HEAVY FLAVOUR GROUP, SCHAEEL S. *et al.*, *Phys. Rep.*, **427** (2006) 257, hep-ex/0509008.
- [10] CYBURT R. H. *et al.*, *Astropart. Phys.*, **23** (2005) 313, astro-ph/0408033.
- [11] IZOTOV Y. I. and THUAN T. X., *Astrophys. J.*, **710** (2010) L67, arXiv:1001.4440.
- [12] HAMANN J. *et al.*, *Phys. Rev. Lett.*, **105** (2010) 181301, arXiv:1006.5276.
- [13] GIUSARMA E. *et al.*, *Phys. Rev. D*, **83** (2011) 115023, arXiv:1102.4774.
- [14] BEMPORAD C., GRATTA G. and VOGEL P., *Rev. Mod. Phys.*, **74** (2002) 297, hep-ph/0107277.
- [15] MUELLER T. A. *et al.*, *Phys. Rev. C*, **83** (2011) 054615, arXiv:1101.2663.
- [16] MENTION G. *et al.*, *Phys. Rev. D*, **83** (2011) 073006, arXiv:1101.2755.
- [17] MALTONI M. *et al.*, *New J. Phys.*, **6** (2004) 122, hep-ph/0405172.
- [18] CDHSW, DYDAK F. *et al.*, *Phys. Lett. B*, **134** (1984) 281.
- [19] MALTONI M. and SCHWETZ T., *Phys. Rev. D*, **76** (2007) 093005, arXiv:0705.0107.
- [20] MINIBoONE and AGUILAR-AREVALO A. A., *Phys. Rev. Lett.*, **102** (2009) 101802, arXiv:0812.2243.
- [21] GIUNTI C. and LAVEDER M., *Mod. Phys. Lett. A*, **22** (2007) 2499, hep-ph/0610352.
- [22] GIUNTI C. and LAVEDER M., *Phys. Rev. D*, **77** (2008) 093002, arXiv:0707.4593.
- [23] ACERO M. A., GIUNTI C. and LAVEDER M., *Phys. Rev. D*, **78** (2008) 073009, arXiv:0711.4222.
- [24] GIUNTI C. and LAVEDER M., *Phys. Rev. D*, **80** (2009) 013005, arXiv:0902.1992.
- [25] GIUNTI C. and LAVEDER M., *Phys. Rev. D*, **82** (2010) 053005, arXiv:1005.4599.
- [26] GIUNTI C. and LAVEDER M., *Phys. Rev. C*, **83** (2011) 065504, arXiv:1006.3244.
- [27] KARMEN, ARMBRUSTER B. *et al.*, *Phys. Rev. D*, **65** (2002) 112001, hep-ex/0203021.
- [28] NOMAD, ASTIER P. *et al.*, *Phys. Lett. B*, **570** (2003) 19, hep-ex/0306037.
- [29] MALTONI M. and SCHWETZ T., *Phys. Rev. D*, **68** (2003) 033020, hep-ph/0304176.
- [30] AKHMEDOV E. and SCHWETZ T., *JHEP*, **10** (2010) 115, arXiv:1007.4171.
- [31] GIUNTI C. and LAVEDER M., *Phys. Rev. D*, **83** (2011) 053006, arXiv:1012.0267.
- [32] KOPP J., MALTONI M. and SCHWETZ T., *Phys. Rev. Lett.*, **107** (2011) 091801, arXiv:1103.4570.
- [33] MALTONI M. *et al.*, *Nucl. Phys. B*, **643** (2002) 321, hep-ph/0207157.
- [34] SOREL M., CONRAD J. and SHAEVITZ M., *Phys. Rev. D*, **70** (2004) 073004, hep-ph/0305255.
- [35] KARAGIORGI G. *et al.*, *Phys. Rev. D*, **75** (2007) 013011, hep-ph/0609177.
- [36] KARAGIORGI G. *et al.*, *Phys. Rev. D*, **80** (2009) 073001, arXiv:0906.1997.
- [37] GIUNTI C. and LAVEDER M., *Phys. Rev. D*, **82** (2010) 093016, arXiv:1010.1395.
- [38] BUGEY, ACHKAR B. *et al.*, *Nucl. Phys. B*, **434** (1995) 503.
- [39] IANNI A., MONTANINO D. and SCIOSCIA G., *Eur. Phys. J. C*, **8** (1999) 609, hep-ex/9901012.
- [40] BAIBUSSINOV B. *et al.*, (2009), arXiv:0909.0355.
- [41] GAVRIN V. N. *et al.*, (2010), arXiv:1006.2103.
- [42] AGARWALLA S. K. and HUBER P., *Phys. Lett. B*, **696** (2011) 359, arXiv:1007.3228.
- [43] AGARWALLA S. K. and RAGHAVAN R. S., (2010), arXiv:1011.4509.
- [44] VERGADOS J., GIOMATARIS Y. and NOVIKOV Y., *Nucl. Phys. B*, **854** (2012) 54, arXiv:1103.5307.

SESSION III - PHYSICS OF HADRONIC INTERACTIONS

<i>Guido Tonelli</i>	First physics results from the CMS experiment at the LHC
<i>Enrico Scapparini</i>	Early pp physics at ALICE
<i>Evelin Meoni</i>	QCD physics at ATLAS
<i>Juan Rojo</i>	Parton distributions and LHC data
<i>Peter Steinberg</i>	Heavy-ion physics with the ATLAS detector at the LHC
<i>Andrea Dainese</i>	First ALICE results from heavy-ion collisions at the LHC

First physics results from the CMS experiment at the LHC

G. TONELLI

*CERN - Geneva, Switzerland and
INFN, Sezione di Pisa and Università di Pisa - Pisa, Italy*

(ricevuto il 29 Settembre 2011; pubblicato online il 2 Febbraio 2012)

Summary. — Establishing all major SM processes and beginning the searches for new physics was the major goal of the first run of the CERN Large Hadron Collider. The paper describes the first results obtained by the CMS experiment in studying pp collisions at $\sqrt{s} = 7$ TeV. We present first the measurements performed on W , Z and top quark. We then describe the searches for new physics performed by probing any eventual internal structure of quarks, and by looking for new massive gauge bosons, microscopic black holes and particles hinting at large extra dimensions. The first results on the searches for SUSY and Higgs particles at LHC are lastly discussed together with the prospects for the current 2011-12 running period.

PACS 12.38.-t – Quantum chromodynamics.

1. – Introduction

The Large Hadron Collider and its detectors have been designed to discover a large range of signals of new physics: the Higgs Boson and eventual super-symmetric partners of known particles as well as a large set of new massive particles foreseen in many models for new physics including some of the recently proposed extra-dimensional models.

The Compact Muon Solenoid (CMS) is one of the two “general-purpose” detectors of LHC [1]. It is located at the experimental Point 5 of the LHC near Cessy (France). The main distinguishing features of CMS are a large superconducting solenoid magnet, which creates a strong field of 3.8 T, a state-of-the-art silicon tracker, a highly granular crystal electromagnetic calorimeter, fully hermetic hadronic calorimeters and a sophisticated and redundant muon system. The detector has been built thanks to the collective effort of the CMS Collaboration consisting of more than 3170 scientists and engineers from 182 Institutes distributed in 40 countries all over the world.

Prior to collecting pp collisions the detector has been thoroughly calibrated using muons produced in cosmic rays. A large data set of more than 10^9 muons was recorded in successive campaigns of cosmic ray data taking in 2008-9. As a result of these studies it was possible to achieve a good understanding of the initial alignment constants of the major detector components and a detailed map of the magnetic field. They led to an

excellent control of the momentum resolution and absolute scale. The commissioning of the detector was then completed using the first LHC pilot runs at 0.9 and 2.36 TeV collision energies at the end of 2009.

The LHC started 7 TeV operations in spring 2010, at very low luminosity, in the range of $\mathcal{L} = 1 \times 10^{27} \text{ cm}^{-2} \text{ s}^{-1}$, but reached quickly instantaneous luminosities exceeding $\mathcal{L} = 2 \times 10^{32} \text{ cm}^{-2} \text{ s}^{-1}$. In total, an integrated luminosity of 47 pb^{-1} has been delivered by the LHC in 2010. With the LHC running in pp mode CMS has collected 43.2 pb^{-1} of data corresponding to an overall data-taking efficiency of about 92%. The uncertainty in the luminosity determination is estimated to be 4%. The overall operational status of CMS during this data taking was excellent: all sub-systems had a fraction of operational channels exceeding 98%.

2. – Intermediate vector bosons and top quark

The selection of W and Z bosons candidates is particularly important for CMS since their production is a benchmark process at the LHC. The Higgs boson at intermediate or high mass is expected to decay with high branching fractions to pairs of W and Z and, in general, the intermediate vector bosons are among the main sources of background to new physics processes.

W candidate events are characterized by a prompt, energetic ($E_T > 25 \text{ GeV}$), isolated lepton, and significant missing transverse energy. The main backgrounds are QCD multi-jet events and Drell-Yan events in which one lepton fails the selection.

Simple selection cuts lead to the distributions of missing transverse energy that are used to extract the $W \rightarrow l\nu$ event yield. It is worth noticing that at the LHC, due to the quark content of the colliding protons, we expect to measure a production yield for W^+ larger than the corresponding yield for W^- . The $Z \rightarrow l^+l^-$ candidate events are required to have two opposite sign leptons satisfying the same selection criteria used for the $W \rightarrow l\nu$ sample. The inclusive cross section measurements are then extracted from the data using data-driven methods for controlling the lepton efficiency, energy and momentum scale, resolution and all major sources of background.

Figure 1 shows on the left the invariant mass distributions of the di-muon pair in logarithmic scale, to enhance the high purity of the selected sample of Z candidates, while the plot on the right shows the ratio between results and theoretical predictions. It is worth noticing the amazing experimental precision achieved, 1%, and the excellent agreement between data and NNLO calculations performed adopting current parton distribution functions. The largest uncertainty for the cross section measurement comes from the uncertainty in the measurement of the luminosity that, however, cancels out in the ratios [2].

To complete the picture, very recently, we produced the measurement of the lepton charge asymmetry in W decays and the first measurement of the W polarization at a hadron collider. The lepton charge asymmetry in W events has been measured both with electrons and with muons in a large pseudo-rapidity range and for two different thresholds on the minimum transverse momentum of the W (fig. 2, left). The values of the charge asymmetry measured with electrons and muons are in good agreement with each other and the precision of the measurement is such that it is challenging the PDF predictions [3]. The measurement of the W polarization [4] shows that, as expected, both W^+ and W^- , are produced by LHC preferably left-handed (fig. 2, right). These complex and challenging measurements are important benchmarks to prove that precision

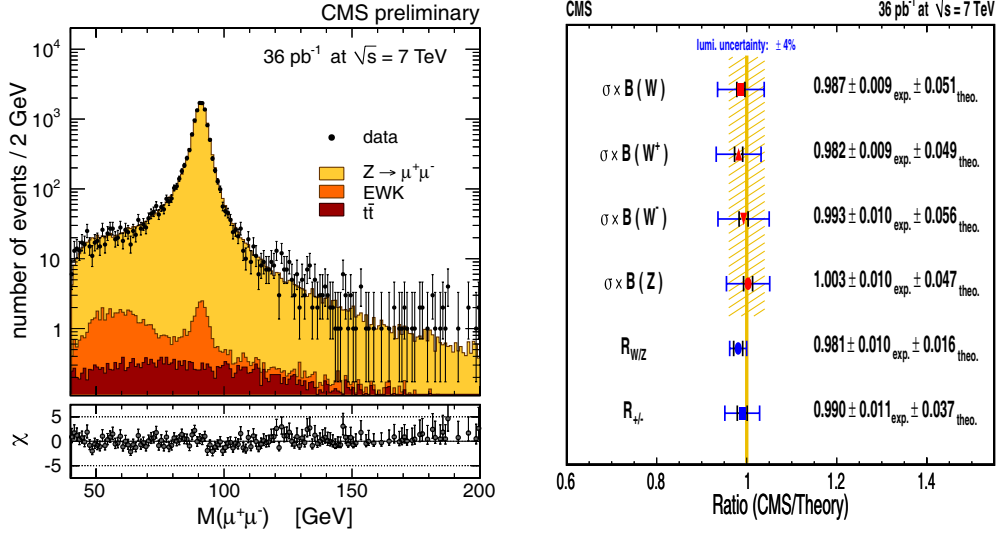


Fig. 1. – Distribution of the di-muon invariant mass of $Z \rightarrow \mu^+\mu^-$ in logarithmic scale (left) and ratio between measurements and theory (right).

electroweak measurements are being already performed at LHC and many others will come as soon as additional data are available.

The selection of top quark candidates is particularly challenging since it requires a complete understanding of all major physics objects as detected by the experiment.

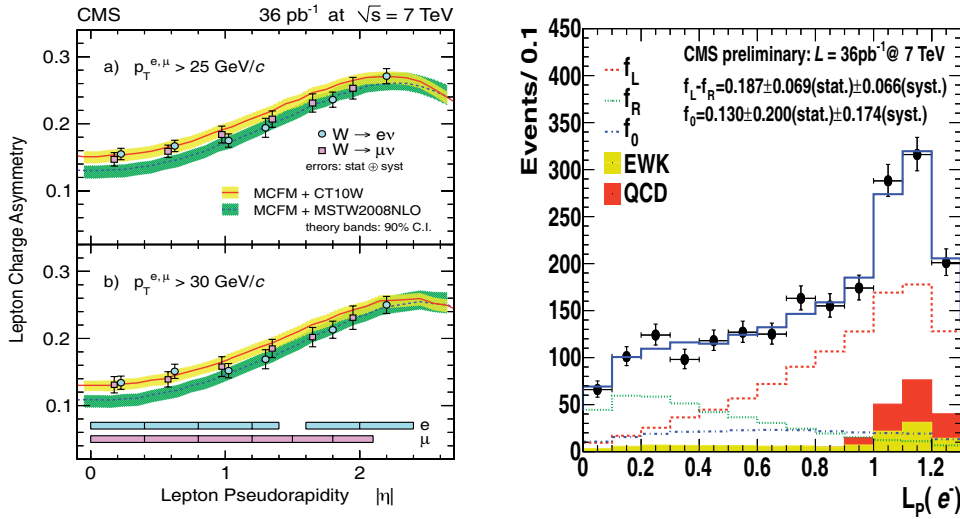


Fig. 2. – Measurement of the lepton charge asymmetry in W events (left) and of the W polarization (right).

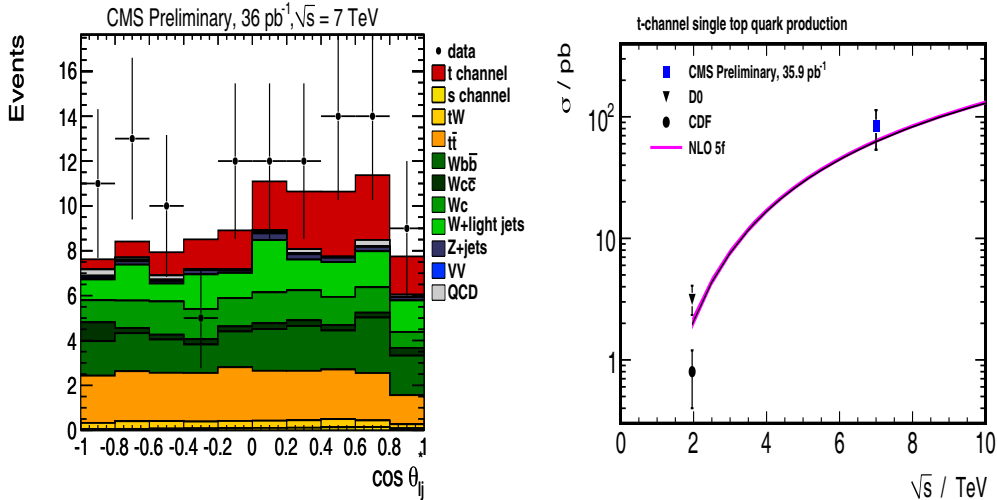


Fig. 3. – Extraction of the single top signal in the t -channel using, as discriminating variable, the angle between the lepton and the jet (left); comparison of the measured cross section at LHC with the NLO theoretical predictions (right).

Searches in CMS for top quark candidates were made looking at channels with high p_T leptons or di-leptons, jets with at least 1 jet b-tagged and missing E_T . With a relatively small data set it was soon possible to identify good event candidates and to collect evidence for top quark production at the LHC in the lepton+jets and di-lepton channels. Going through the full statistics collected so far, we have been able to measure the top pair production cross section using different techniques and various decay channels leading to a combined measurement of the top production cross section at LHC of $\sigma_{t\bar{t}} = 158 \pm 19 \text{ pb}$ [5], value that is in good agreement with the most recent NLO and approximate NNLO predictions. The complete mastering of all tools needed to reconstruct and understand top quarks at LHC has been successfully proven through the first measurement of single top production cross section. The measurement is particularly challenging as a consequence of the tiny cross section expected for the process and for the presence of important sources of background mainly due to W+jets and $t\bar{t}$ events (fig. 3). The fact that using only 36 pb^{-1} of LHC data CMS has been able to measure the single-top production cross section in the t -channel as $\sigma_t = 83 \pm 29.8(\text{stat} + \text{syst}) \pm 3.3(\text{lumi}) \text{ pb}$ [6] is the best evidence for the readiness of the experiment to explore the completely new territory made accessible by the LHC collisions.

3. – Quark compositeness and new heavy bosons

Having fully calibrated the detector response with known SM processes we started a systematic exploration of the new energy regime. The strategy to search for signals of new physics started by looking first at distributions based on very simple, well understood physics objects, like di-jets, di-leptons and di-photons. All these can be considered discovery tools particularly suited to look for signals of quark compositeness, strongly coupling new resonances or heavy exotic particles with significant production

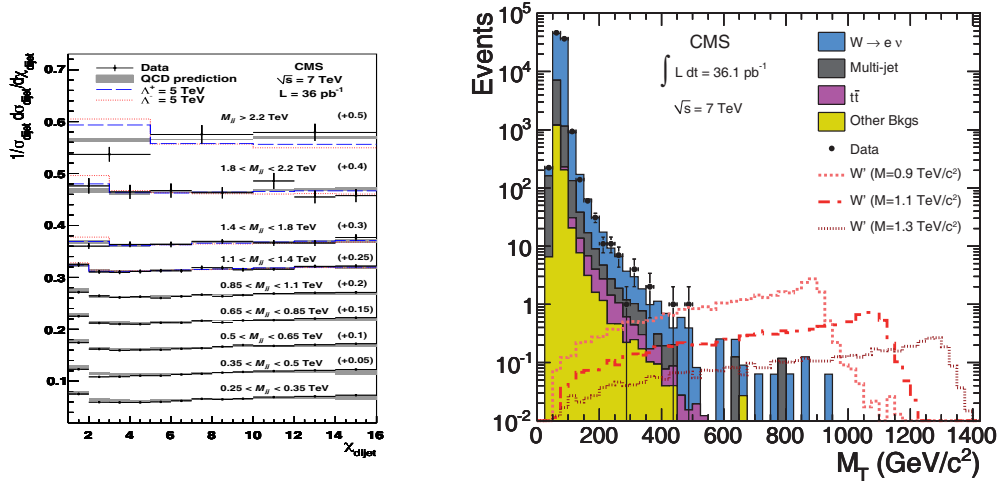


Fig. 4. – Distribution of the angular variable χ in dijet events (left); transverse mass for $W \rightarrow e + \nu$ events in logarithmic scale (right).

cross sections at the LHC. The angular distribution of di-jets is particularly sensitive to the presence of a contact interaction. If the quarks are composite objects high invariant mass di-jets will show significant deviations from the smooth angular behavior predicted by perturbative QCD. The analysis is based on the use of a variable $\chi = e^{|y_1 - y_2|}$ (with y_1 and y_2 being the rapidity of the two jets) which is constructed to be flat if quarks have no internal sub-structure, but very sensitive to any form of Rutherford scattering. Signatures of new physics that might have a more isotropic angular distribution than QCD (*e.g.* quark compositeness) would produce an excess at low values of χ (fig. 4, left). Since we do not observe any anomaly in the di-jet angular distributions it has been relatively straightforward to extract a lower limit (95% C.L.) on the contact interaction scale of $\Lambda = 5.6 \text{ TeV}$ [7]. For CMS, so far, quarks are still point-like objects.

New heavy gauge bosons, generally indicated as Z' and W' , are predicted in various extensions of the Standard Model (SM). The search for a W' is usually performed in the context of the benchmark models where the W' boson is considered a heavy analogue of the SM W boson with the same left-handed fermionic couplings. Thus the W' decay modes and branching fractions are similar to those of the W boson. In this context the search is performed looking for anomalies in the tail of the distribution of the reconstructed transverse mass of the W . An example of this distribution for W decaying to electrons and neutrinos is shown in fig. 4, right, where one can note that events with transverse mass exceeding $400 \text{ GeV}/c^2$ have been collected by CMS. The production of a W' boson would imply an excess of events in the tail of the distribution. Since no excess is visible in our data, we can extract limits on the production of heavy W' vector bosons at the LHC. Assuming standard-model-like couplings and decay branching fractions and combining together the decay modes in electrons and in muons, we can exclude a W' with mass lower than $1.58 \text{ TeV}/c^2$, a value that exceeds the current limits set by the Tevatron experiments [8]. The most stringent limits to date have been obtained also for the search of Z' where the analysis is conceptually similar [9]. The challenge is to study in detail the high mass part of the Z resonance tail looking for any excess that could hint

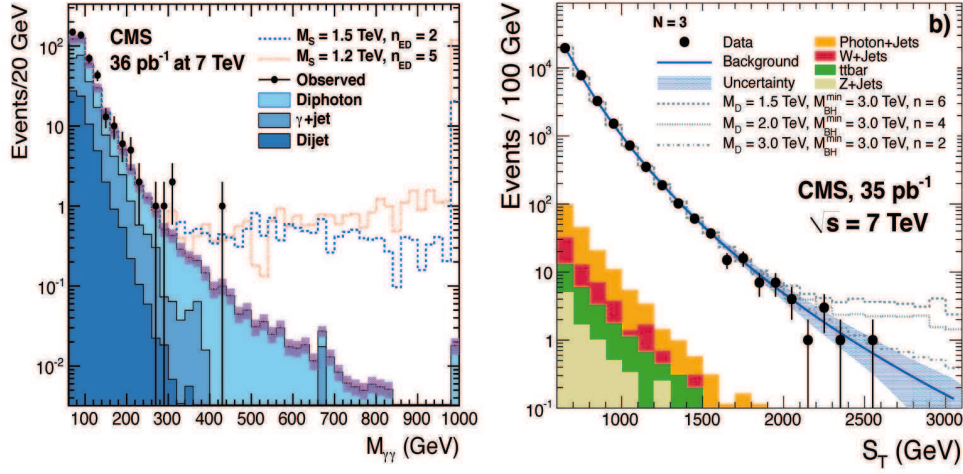


Fig. 5. – Invariant mass distribution of di-photon events with simulation of the excess foreseen in a couple of extra-dimensional models (left). Distribution of the variable S_T and simulation of the excess due to the production of microscopic black holes in different models (right).

at the production of new massive bosons. The most important source of background for both analyses are multi-jet and $t\bar{t}$ events that must be carefully understood to set limits on new phenomena.

Many new limits have been published by CMS in the search for exotic particles, however there is not enough space in this paper to cover all of them. I want to mention briefly only the direct search for large spatial extra-dimensions and the first direct search for signature of microscopic black holes at a particle collider.

4. – Extra-dimensions and microscopic black holes

Compact large extra-dimensions are an intriguing proposed solution to the hierarchy problem of the standard model, which refers to the puzzling fact that the fundamental scale of gravity, $M_{Pl} = 10^{19} \text{ GeV}/c^2$, is so much higher than the electroweak scale $M_{EWSB} = 10^3 \text{ GeV}/c^2$. With such a difference in scales, it is difficult to protect the Higgs mass from radiative corrections without a very high degree of fine-tuning. The original proposal to use extra dimensions to solve the hierarchy problem assumed a scenario where the SM is constrained to the common 3+1 space-time dimensions, while gravity is free to propagate through the entire multidimensional space. Because of this, the gravitational force is effectively diluted, having undergone a Gauss' law reduction in the flux. Phenomenologically, this scenario results in s -channel production of massive Kaluza-Klein (KK) graviton states, which decay into a di-photon final state that can be detected in modern, hermetic detectors like CMS. A search for large extra-dimensions via virtual graviton exchange in the di-photon channel has been performed by CMS looking for an excess of events in the high mass tail of the distribution of the di-photon invariant mass (fig. 5, left). The new limits, obtained in the range of 1.6–2.3 TeV/c^2 , depending on the number of extra-dimensions, can be interpreted as the lower limits on the effective Planck scale, M_D , in these models, and are the most restrictive limits on the existence of large extra-dimensions to date for their number greater than two [10].

Another possible manifestation of the fact that the effective Planck scale, M_D , could be brought to the TeV scale for the presence of compactified extra dimensions could be the production of microscopic black holes. Partons colliding in LHC, once they approach each other to a distance comparable to the size of extra dimensions, could start feeling the full strength of gravity and may collapse into a microscopic black hole. The production cross section can be as high as 100 pb for M_D of 1 TeV/ c^2 . Once produced, the microscopic black holes evaporate almost instantaneously by emitting energetic particles. About three quarters of the emitted particles are expected to be quark and gluons; the rest is accounted for by leptons, photons, W/Z bosons, and possibly Higgs particles. We look therefore for events with high multiplicity of energetic objects. Since the main background comes from copious production of multi-jets that are not well described in QCD predictions, we must use data-driven methods. We have found that a variable, S_T , which is defined as the scalar sum of transverse momenta of all the energetic objects in the event (reconstructed hadronic jets, leptons, photons and missing transverse energy) can be used to describe the multi-jet QCD background (fig. 5, right). The resulting background predictions for the inclusive multiplicities of 3, 4, and 5 or more objects in the final state agree with the observed spectra in the data. As a result, we have been able to exclude black holes with the minimum masses between 3.5 and 4.5 TeV/ c^2 , for the values of M_D in the range of 1.5–3.5 TeV/ c^2 and various other model parameters [11]. These limits are the first direct limits on black hole production at particle colliders and go well beyond potential reach of the Tevatron or cosmic-ray experiments.

5. – Supersymmetry

Supersymmetry is widely considered an attractive theory that is able to solve the hierarchy problem of the Standard Model at the expense of introducing a large number of supersymmetric particles with the same quantum numbers as the SM particles, but differing by half a unit of spin. If R-parity conservation is assumed, supersymmetric particles are produced in pairs and decay to the lightest supersymmetric particle (neutralino or LSP), leading to a characteristic signature of events with large missing transverse energy. The dominant production channels of heavy coloured sparticles at the LHC are squark-squark, squark-gluino and gluino-gluino pair production. Heavy squarks and gluinos decay into quarks, gluons and other SM particles, as well as neutralinos which escape undetected, leading to final states with several hadronic jets and large missing transverse energy.

Just a couple of months after the end of the 2010 data taking CMS performed the first search for SUSY particles at the LHC in events with two or more energetic jets and significant missing transverse energy. Since we were looking for massive objects, events were pre-selected requiring high values of the scalar sum of the transverse energy of jets, $H_T > 350$ GeV, thus ensuring large hadronic activity in the event. The analysis is then based on the use of a very simple variable $\alpha_T = E_{Tj2}/M_T$, where E_{Tj2} is the transverse energy of the less energetic of the two jets in the event and M_T is the transverse mass of the di-jet system. For a perfectly measured di-jet event, with $E_{Tj1} = E_{Tj2}$ and jets back to back in ϕ , and in the limit where the jet momenta are large compared to their masses, the value of α_T is 0.5. In the case of an imbalance in the measured transverse energies of back to back jets, α_T takes on values smaller than 0.5, while for jets that are not back to back, α_T can be greater than 0.5. Values of α_T above 0.5 can occur for QCD multi-jet events, either with multiple jets failing the $E_T > 50$ GeV

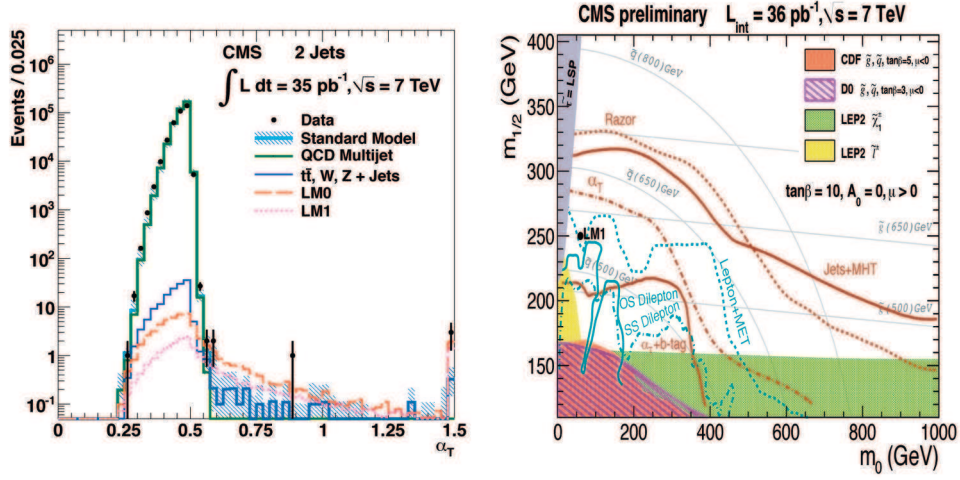


Fig. 6. – Distribution of α_T for di-jet events (left). Exclusion limits on SUSY produced by several different analyses (right).

requirement, or with missing transverse energy arising from jet energy resolution or severe jet energy under-measurements due to detector inefficiencies. On the other hand, events with genuine missing E_T often have much larger values of α_T , resulting in a good separation of signal events from the QCD multi-jet background. As anticipated, these distributions peak at $\alpha_T = 0.5$ for QCD multi-jet events and then fall sharply in the range 0.5 to 0.55, reaching a level 4 to 5 orders of magnitude lower than the peak value (fig. 6, left). Multi-jet events from QCD background are therefore efficiently rejected by requiring α_T to exceed 0.55. A simple generalization of the variable α_T can be used to include final states with more than two jets. A small tail of $t\bar{t}$ and W +jets and Z invisible+jets events survive as a possible contamination to the signal region. Data-driven methods are used to understand all major sources of background. The search for SUSY signals involves looking for an excess of events in the high α_T region. Since no excess has been observed in the full 2010 data set, we have published limits constraining significantly the simplest minimal supersymmetric extensions of the SM [12].

A complex set of additional searches has then been performed using many different topological signatures of SUSY: di-photons and large missing E_T , same sign and opposite sign di-leptons, single leptons and large missing E_T , multi-leptons and fully hadronic final states with large missing E_T . None of these searches produced so far hints of production of SUSY particles at the LHC. Using conservative statistical tools we have extracted limits from the experimental data producing new results exceeding significantly the best measurements performed so far by the Tevatron experiments. Figure 6, right, summarizes the exclusion limits produced by these analyses for a particular choice of SUSY parameters. The highest exclusion limits are obtained using the fully hadronic final states. Based on the results obtained from the analysis of the 2010 data, we can extrapolate that, if supersymmetry is really a symmetry of nature, it will be definitely possible to detect SUSY signals in the 2011-12 LHC data, supposed to be 50-100 times larger with respect to the amount of data so far analyzed.

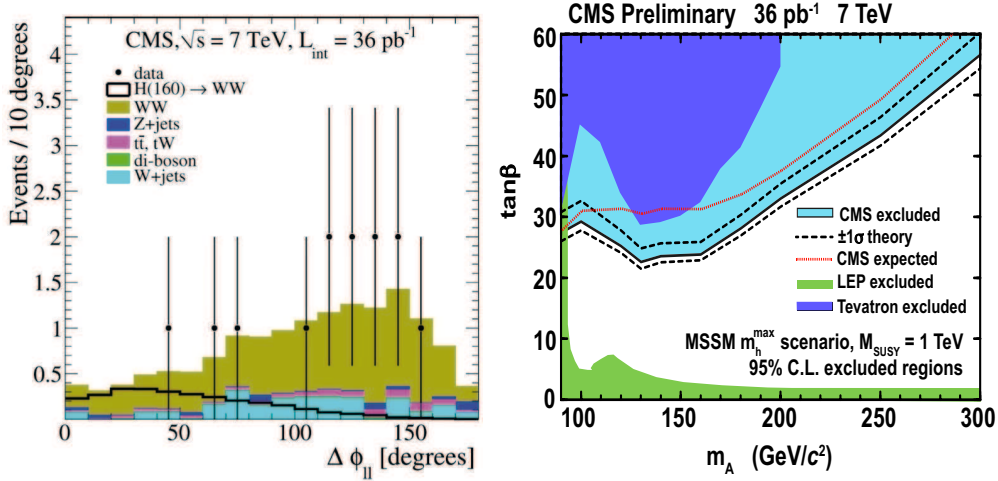


Fig. 7. – Distribution of the opening angle between the two leptons, $\Delta\phi_{ll}$, in WW event candidates (left). Exclusion limits on MSSM neutral Higgs decaying to τ pairs (right).

6. – Higgs boson

The search for the Higgs boson is one of the most ambitious goals of the LHC experiments. The amount of data collected in 2010 was not large enough to perform a complete and exhaustive search that can yield, in general, competitive results with respect to the Tevatron Collider. This has been possible, so far, only for a couple of analyses. One analysis is the search for the SM Higgs in the W^+W^- channel with the Higgs production cross section enhanced by the presence of a fourth generation.

A possible extension of the SM is the addition of a fourth family of fermions. For large lepton and quark masses, this extension has not been excluded by existing constraints. The presence of another family of fermions would produce an enhancement of the dominant gluon fusion cross-section. The irreducible background for $H \rightarrow W^+W^-$ production is the SM non-resonant production of W^+W^- . A good understanding of this process and of its properties is needed anyway since the W^+W^- channel is particularly sensitive in the intermediate mass range (120–200 GeV/c²) and is therefore considered a sort of work-horse for the search of the SM Higgs boson. This is why the search was performed in conjunction with the first measurement of the W^+W^- production cross section at LHC.

W^+W^- candidates are selected in events with two high p_T leptons, electrons or muons and large missing E_T . Leptons originating from $H \rightarrow W^+W^-$ decays tend to have a relatively small opening angle, while those from WW backgrounds are preferentially emitted back-to-back. The opening angle between the two leptons, $\Delta\phi_{ll}$, is therefore a variable providing the best discriminating power between the Higgs boson signal and the majority of the backgrounds in the low mass range. Figure 7, left, shows the distribution of $\Delta\phi_{ll}$, after applying the W^+W^- selections, for a SM Higgs boson signal with $m_H = 160$ GeV/c², and for the major sources of backgrounds. Since no excess above the SM expectations was found in the lower $\Delta\phi_{ll}$ region, upper limits on the Higgs boson production cross section have been derived. In the presence of a sequential fourth family

of fermions with very high masses, a Higgs boson with standard model couplings and a mass between 144 and 207 GeV/ c^2 has been excluded at 95% confidence level [13].

The second analysis yielding new results on Higgs is the search for MSSM Higgs decaying to τ pairs. The minimal supersymmetric extension to the standard model (MSSM) requires the presence of two Higgs doublets. This leads to a more complicated Higgs boson sector, with five massive Higgs bosons: a light neutral scalar (h), two charged scalars (H^\pm), a heavy neutral CP -even state (H) and a neutral CP -odd state (A). The τ pair decays of the neutral Higgs bosons, having a branching ratio of about 10%, serve as the best experimental signature for this search. The b mode, though it has a much larger branching ratio, suffers from an overwhelming background from QCD processes. Three final states where the τ decays leptonically or hadronically are used in our analysis: $e+\tau_h$, $\mu+\tau_h$, and $e\mu$, where we use the symbol τ_h to indicate a reconstructed hadronic decay of a τ . The ee and $\mu\mu$ final states suffer too much background from $Z \rightarrow e^+e^- (\mu^+\mu^-)$ events to be usable. The observed τ pair mass spectrum reveals no evidence for neutral Higgs boson production, and we determine an upper bound on the product of the Higgs boson cross section and τ pair branching ratio. These results, interpreted in the MSSM parameter space, exclude a previously unexplored region reaching as low as $\tan\beta = 23$ at $m_A = 130$ GeV/ c^2 (fig. 7, right) [14]. The results obtained in the searches for the Higgs boson using the 2010 data set bodes well for the current LHC data taking. Assuming that in 2011-12 the LHC will deliver to the experiments an integrated luminosity in a range of 5–10 fb $^{-1}$, as it appears to be possible extrapolating on last year's performance of the machine, we are confident to be able to exclude the SM Higgs boson in the mass range between 120 and 600 GeV/ c^2 , or to discover it with the combination of ATLAS and CMS results.

7. – Conclusion

We have presented the first physics results obtained using pp collisions at 7 TeV. After a few months of data taking we have achieved a good understanding of the detector performance and of the Standard Model properties at 7 TeV. Soon afterwards we have started the systematic exploration of the new energy regime in the quest for signals of new physics. New limits have been produced in many searches: quark compositeness, new vector bosons, extra dimensions. Lastly, the first studies on the searches for SUSY particles and the Higgs boson in LHC data have been presented together with the prospects for the current 2011-12 running period.

* * *

I would like to thank first the LHC accelerator team for achieving an impressive performance of the machine in its first year of running. I am grateful to all colleagues of the CMS Collaboration for their huge collective effort in constructing and running the experiment and analyzing so quickly and so efficiently data collected so recently.

REFERENCES

- [1] THE CMS COLLABORATION, *JINST*, **3** (2008) S08004.
- [2] THE CMS COLLABORATION, *Measurement of Inclusive W and Z Cross Sections in pp Collisions at $\sqrt{s} = 7$ TeV*, CMS PAS EWK-10-005 (2011).
- [3] THE CMS COLLABORATION, *Measurement of the Lepton Charge Asymmetry in Inclusive W Production in pp Collisions at $\sqrt{s} = 7$ TeV*, arXiv:1103.3470, CMS-EWK-10-006 (2011).

- [4] THE CMS COLLABORATION, *Measurement of the Polarization of W Bosons with Large Transverse Momenta in W + jets Events at the LHC*, arXiv:1104.3829, CMS-EWK-10-014 (2011).
- [5] THE CMS COLLABORATION, *Combination of Top Pair Production Cross Sections in pp Collisions at $\sqrt{s} = 7$ TeV and Comparison with Theory*, CMS PAS TOP-11-001 (2011).
- [6] THE CMS COLLABORATION, *Measurement of the t-channel Single Top Quark Production Cross Sections in pp Collisions at $\sqrt{s} = 7$ TeV*, CMS PAS TOP-10-008-001 (2011).
- [7] THE CMS COLLABORATION, *Measurement of Dijet Angular Distributions and Search for Quark Compositeness in pp Collisions at $\sqrt{s} = 7$ TeV*, arXiv:1102.2020, CMS-QCD-10-016 (2011).
- [8] THE CMS COLLABORATION, *Search for a W' Boson Decaying to a Muon and a Neutrino in pp Collisions at $\sqrt{s} = 7$ TeV*, arXiv:1103.0030, CMS-EXO-10-015 (2011).
- [9] THE CMS COLLABORATION, *Search for Resonances in the Dilepton Mass Distribution in pp Collisions at $\sqrt{s} = 7$ TeV*, arXiv:1103.0981, CMS-EXO-10-013 (2011).
- [10] THE CMS COLLABORATION, *Search for Large Extra Dimensions in the Diphoton Final State at the Large Hadron Collider*, arXiv:1103.4279, CMS-EXO-10-026 (2011).
- [11] THE CMS COLLABORATION, *Phys. Lett. B*, **697** (2011) 434.
- [12] THE CMS COLLABORATION, *Phys. Lett. B*, **698** (2011) 196.
- [13] THE CMS COLLABORATION, *Phys. Lett. B*, **699** (2011) 196.
- [14] THE CMS COLLABORATION, *Search for Neutral MSSM Higgs Bosons Decaying to Tau Pairs in pp Collisions at $\sqrt{s} = 7$ TeV*, arXiv:1104.1619, CMS-HIG-10-002 (2011).

Early pp physics at ALICE

E. SCOMPARIN for the ALICE COLLABORATION

INFN, Sezione di Torino - Torino, Italy

(ricevuto il 29 Settembre 2011; pubblicato online il 19 Gennaio 2012)

Summary. — The ALICE experiment, dedicated for heavy-ion collisions at the LHC, is taking data with proton-proton collisions since November 2009. This contribution summarizes the first year of operation and performance of the ALICE detector at the LHC as well as the first results from pp collisions at 0.9 TeV and 7 TeV. In particular, results on global event properties and identified particle spectra, including strangeness, open charm and charmonium production, will be discussed.

PACS 12.38.-t – Quantum chromodynamics.

PACS 12.38.Mh – Quark-gluon plasma.

1. – Introduction

The ALICE detector is very different in both design and purpose from the other experiments at the CERN Large Hadron Collider (LHC). Its main aim is the study of matter under extreme conditions of temperature and pressure, *i.e.* the Quark-Gluon Plasma (QGP), in collisions between heavy ions. With an energy up to almost 30 times higher than that of RHIC, the BNL heavy-ion collider, a very different type of QGP, in terms of initial temperature, lifetime and system volume can be formed at the LHC. Furthermore, for the first time, a conspicuous production of hard signals like jets and heavy quarks which serve as probes to study QGP properties can be observed. Data taking with proton-proton collisions is very important for ALICE, primarily to collect comparison data for the heavy-ion programme. Therefore, our goal in 2010 was to collect about 10^9 Minimum-Bias (MB) pp collisions, to provide sufficient comparison statistics for the first heavy-ion run which took place in November-December 2010. However, given the specific capabilities of the ALICE detector, complementary to those of the other LHC experiments, a number of measurements concerning soft and semi-hard QCD processes are of interest on their own in pp collisions, and are part of the physics programme [1]. More in detail, the large MB pp sample was used to provide a detailed characterization of global event properties over a range of LHC energies, which can be very useful for tuning Monte Carlo generators to better describe the QCD background underlying searches for new physics. Furthermore, results on identified particles, including strange mesons and baryons, open charm and charmonium, were also obtained.

The very first proton-proton collisions in the ALICE intersection region occurred on 23rd November 2009, at a centre-of-mass energy $\sqrt{s} = 0.9$ TeV, during the commissioning of the accelerator. The first few hundreds of recorded pp events served to measure the charged-particle pseudorapidity density in these collisions [2], the first published result obtained with particle collisions at the LHC. At the end of the 2009 commissioning run, the LHC achieved the highest energy of $\sqrt{s} = 2.36$ TeV, at which ALICE collected data on a few 10^4 pp collisions. After the winter shutdown, the LHC running resumed in March 2010 at the collision energy of $\sqrt{s} = 7$ TeV. During 2010, ALICE has collected at this energy more than 8×10^8 MB triggers and about 1.3×10^8 muon triggers, the latter corresponding to an integrated luminosity larger than 100 nb^{-1} . In ALICE, the MB trigger corresponds to the detection of a charged particle in the most central 5 η -units, while a muon trigger requires, in addition, the detection of a particle in the forward muon spectrometer covering the region $2.5 < \eta < 4$.

The first data taking with Pb-Pb collisions took place at the end of 2010. A summary of the first results can be found in [3].

2. – Detector

The ALICE detector consists of a central part, which measures hadrons, electrons and photons, and a forward spectrometer to measure muons. The central part, which covers the pseudorapidity range $|\eta| < 1$ over the full azimuth, is embedded in the large L3 solenoidal magnet supplying a field of 0.5 T. This part consists of: an Inner Tracking System (ITS) of high-resolution silicon detectors; a cylindrical Time-Projection Chamber (TPC); three particle-identification arrays of Time-Of-Flight (TOF), Transition-Radiation-Detector (TRD), and Čerenkov-ring-imaging (called HMPID) counters; two single-arm electromagnetic calorimeters (high resolution PHOS and large acceptance EMCAL). The forward muon spectrometer covering $-4 < \eta < -2.5$ consists of an arrangement of hadron absorbers, a large dipole magnet with a field integral of 3 Tm, and 14 stations of tracking and triggering chambers. Several smaller detectors for triggering and multiplicity measurements (VZERO, T0, FMD, PMD, ZDC) are located at small angles. The main design features include: a robust and redundant, but limited-pseudorapidity-acceptance tracking, designed to cope with the very high particle density in nuclear collisions; a minimum of material in the sensitive tracking volume (10% of radiation length between interaction point and outer radius of the TPC) to reduce multiple scattering; several detector subsystems dedicated to particle identification over a large range in momentum. The layout of the ALICE detector and its eighteen different subsystems are described in detail in [4]. The experiment is essentially fully installed, commissioned and operational. Two subsystems (TRD and EMCAL) which were added more recently in the experiment, had, for the 2010 run, about 40% of their active area installed and will be completed for the next runs. The many years of preparation, analysis tuning with simulations, and detector commissioning with cosmic rays during much of 2008-2009 resulted in having most of the detector components working with collisions rather close to performance specifications. As an example of the performance, the energy-loss distribution in the TPC is shown in fig. 1 (left panel) as a function of momentum, demonstrating the clear separation between particle species reached in the non-relativistic momentum region. After careful calibration with radioactive krypton injected into the gas volume and with cosmic-ray data, the energy loss resolution is about 5–6%, corresponding to design value. To demonstrate, as another example, the TOF performance, in fig. 2 (right panel) the particle velocity β is shown as a function of the rigidity, separately for positive

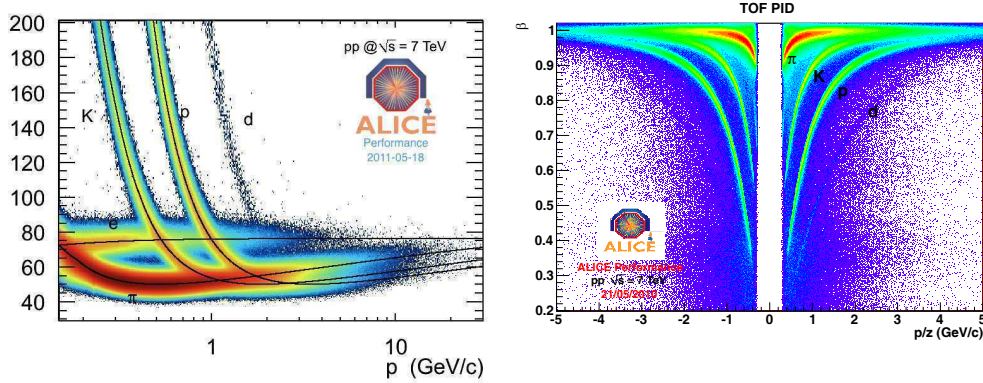


Fig. 1. – Left: dE/dx spectrum *versus* momentum in the ALICE TPC for 7 TeV pp collisions. The lines are a parameterization of the Bethe-Bloch curve. Right: Particle velocity β measured with TOF, as a function of momentum.

and negative charges. The inferred time resolution of the TOF detector is about 90 ps, very close to its design specification.

3. – Physics results

At the time of this conference, a large number of physics results have already been obtained, and only a few of them, for reasons of space, can be shortly summarized in this contribution.

The charged-particle pseudorapidity density $dN_{ch}/d\eta$ as well as the multiplicity distributions were measured at 0.9 TeV, 2.36 TeV and 7 TeV at mid-rapidity [2, 5, 6]. The energy dependence of the multiplicity density, shown in fig. 2 (left panel), is well described

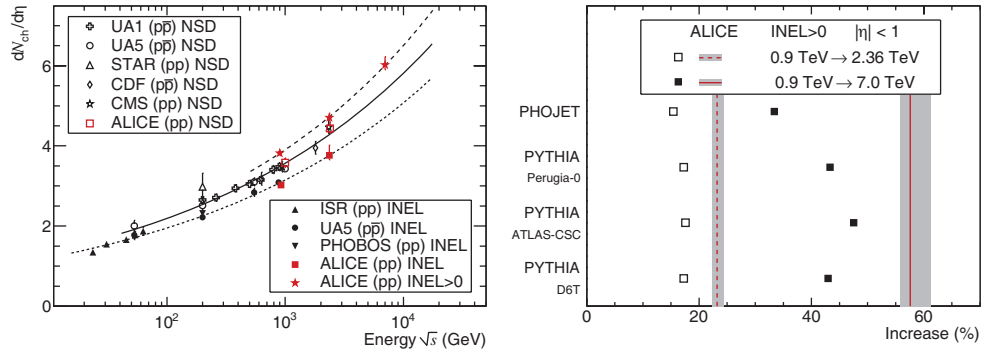


Fig. 2. – Left: Energy dependence of the charged-particle pseudorapidity density in $\eta < 0.5$ for different event classes. The lines indicate the power-law dependence, $s^{0.11}$, for non-single-diffractive events (solid line), for inelastic events (dotted line), and for inelastic events with at least one charged track in $|\eta| < 1$ (dashed line). The references for the data from other experiments can be found in [6]. Right: The relative increase of the charged-particle pseudorapidity density at $\sqrt{s} = 2.36$ TeV (dashed line) and at $\sqrt{s} = 7$ TeV (solid line) with respect to the value at $\sqrt{s} = 0.9$ TeV, compared to model predictions (see [6] for details).

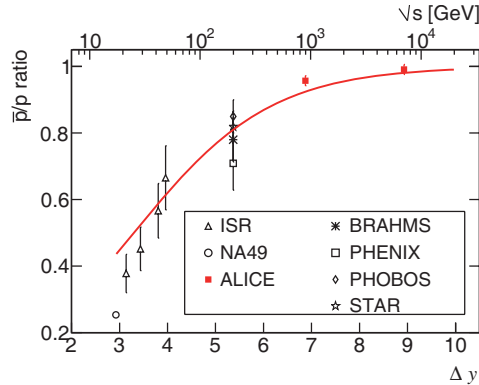


Fig. 3. – Mid-rapidity antiproton-to-proton ratio as a function of the rapidity interval Δy (lower axis) and centre-of-mass energy (upper axis). The line represents a simple calculation of this dependence, assuming Reggeon-like string-junction exchange. The references for the data from other experiments and for models can be found in [8].

by a power law in energy, and this increase is significantly stronger than that predicted by most event generators (fig. 2, right panel). Most of this stronger increase happens in the tail of the multiplicity distribution, *i.e.* for events with much larger than average multiplicity. Likewise, neither the transverse momentum distribution at 0.9 TeV, nor the dependence of average p_T on multiplicity, is well described by various versions of event generators [7], in particular when including low-momentum particles ($p_T < 0.5$ GeV/ c). The shape of the p_T spectra for different multiplicity classes is very similar below 1 GeV/ c (which includes most of the produced particles), whereas the power-law tail of these p_T spectra (above 1 GeV/ c) is significantly steeper for low-multiplicity events than for those with high multiplicities.

The LHC, by far the highest energy proton-proton collider, is well suited to study baryon-number transport over very large rapidity intervals by measuring the antiproton-to-proton ratio at mid-rapidity [8] ($\Delta y = 8.92$ at $\sqrt{s} = 7$ TeV) in order to discriminate between various theoretical models of baryon stopping. An asymmetry in proton-antiproton production at mid-rapidity can be caused by baryon-number transfer from the incoming proton. Baryon number is carried by a non-perturbative configuration of gluon fields called string junction [9], where the three strings coming from the valence quarks of a baryon join. The antiproton-to-proton ratio, shown in fig. 3, is found to be compatible with unity at $\sqrt{s} = 7$ TeV and 4% below 1 at $\sqrt{s} = 0.9$ TeV, with an experimental uncertainty of about 1.4%, dominated by the systematic error. This result favours models which predict a strong suppression of baryon-number transport over large rapidity intervals; they agree very well with standard event generators but not with those which have implemented an enhanced baryon number transport.

Strangeness production has been studied already in the first sample of pp collisions collected at the LHC, at $\sqrt{s} = 0.9$ TeV. The results include yields and transverse momentum spectra of mesons containing strange quarks (K_S^0 , ϕ) and singly/doubly strange baryons (Λ , $\bar{\Lambda}$, $\Xi + \bar{\Xi}$). The results can be compared with predictions for identified particle spectra from QCD-inspired models and provide a baseline for comparisons with both pp measurements at higher energies and heavy-ion collisions. For all species the transverse momentum spectra are found to be slightly harder (*i.e.* they have a slower

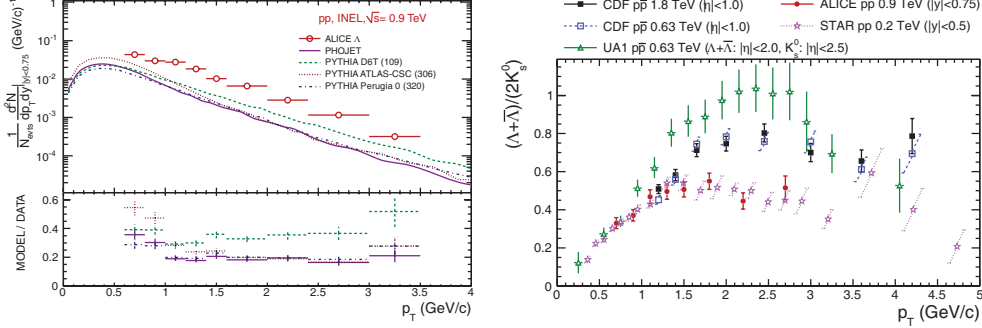


Fig. 4. – Left: Comparison of the transverse momentum differential yield for the Λ particles for pp collisions at $\sqrt{s} = 0.9$ TeV with PHOJET and several PYTHIA tunes. Right: $(\Lambda + \bar{\Lambda})/2K_S^0$ as a function of p_T for different collision energies in pp and $p\bar{p}$ minimum bias events. The ALICE and STAR ratios are feed-down corrected. See [10] for details as well as for references to other experimental results.

decrease with p_T) than the models. As an example, we show in fig. 4 (left) the shape of the p_T spectra for the Λ , compared to PHOJET and to several tunes of PYTHIA. For transverse momenta larger than ~ 1 GeV/c, the strange particle spectra are strongly underestimated by all models, by a factor of ~ 2 for K_S^0 and even ~ 3 for hyperons. The discrepancy is smaller in the case of the ϕ .

The baryon to meson ratio as a function of p_T obtained with the $\Lambda + \bar{\Lambda}$ and K_S^0 spectra measured by ALICE is presented in fig. 4 (right). It includes the $(\Lambda + \bar{\Lambda})/2K_S^0$ ratio in pp collisions at 200 GeV measured by STAR, and the ratios in $p\bar{p}$ collisions at 630 GeV and 1800 GeV computed with the $\Lambda + \bar{\Lambda}$ and K_S^0 spectra published by CDF and UA1. UA1 and CDF Collaborations provide inclusive spectra. The associated ratios are therefore not feed-down corrected, unlike the ALICE and STAR ones. The acceptance windows of these experiments differ significantly: ALICE measures Λ , $\bar{\Lambda}$ and K_S^0 in $|y| < 0.75$, STAR in $|y| < 0.5$, CDF in $|\eta| < 1.0$, whereas UA1 reconstructs $\Lambda + \bar{\Lambda}$ in $|\eta| < 2.0$ and K_S^0 in $|\eta| < 2.5$. The ALICE ratio agrees very well with the STAR results in the measured p_T range, which would suggest little or no energy dependence of $(\Lambda + \bar{\Lambda})/2K_S^0$. A similar conclusion can be drawn when comparing only the ratios measured by CDF at 630 GeV and 1800 GeV, although the ratio found by CDF for $p_T > 1.5$ GeV/c is higher than the one observed with ALICE and STAR. The ratio computed from UA1 spectra however shows a clear disagreement with the other measurements in an intermediate p_T range between $p_T \sim 1.5$ GeV/c and $p_T \sim 3.0$ GeV/c. PYTHIA simulations show that this discrepancy cannot be attributed to the differences in the acceptance or in the colliding system (*i.e.* $p\bar{p}$ instead of pp); effects related to difference between the experiments in acceptance, trigger or feed-down corrections for weak decays might play a role.

The measurement of charm cross sections is needed as baseline data for our heavy-ion programme and it is of interest for comparisons with perturbative QCD calculations. The ALICE detector can measure charm production at midrapidity down to very low momenta using various hadronic decay channels. The very good signal-to-background ratio even at low transverse momenta (down to 2 GeV/c) is a consequence of both the use of particle identification and the excellent performance of the ITS vertex detector, which has reached an impact-parameter resolution of around $80 \mu\text{m}$ at $p_T = 1$ GeV/c.

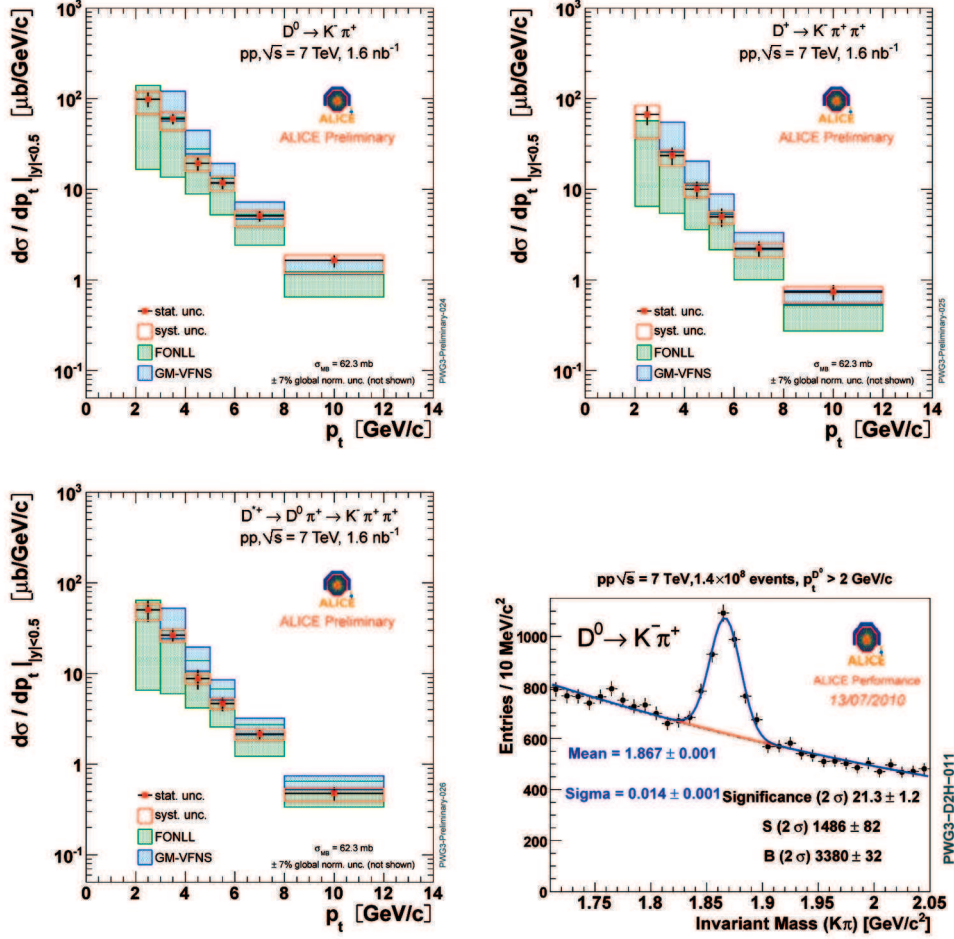


Fig. 5. – D^0 , D^+ , and D^{*+} p_T -differential production cross sections in $|y| < 0.5$ in pp collisions at $\sqrt{s} = 7$ TeV, compared to pQCD calculations. The p_T -integrated $D^0 \rightarrow K^- \pi^+$ signal in the $K\pi$ invariant mass distribution is also shown.

An invariant-mass analysis (see fig. 5 for an example concerning D^0) is then used to extract the raw signal yield, to be then corrected for detector acceptance and for PID, selection and reconstruction efficiency, evaluated from a detailed detector simulation. The contamination of D mesons from B meson decays is estimated to be about 15%, using the beauty production cross section predicted by the FONLL (fixed-order next-to-leading log) calculation [11] and the detector simulation, and it is subtracted from the measured raw p_T spectrum, before applying the efficiency corrections. The D^0 , D^+ , and D^{*+} p_T -differential production cross sections in $|y| < 0.5$ are shown in fig. 5. Theoretical predictions based on pQCD calculations (FONLL [11] and GM-VFNS [12]) are in agreement with the data.

The study of charmonium production plays an essential role in heavy-ion physics since the production of a hot, deconfined medium should lead to a suppression of $c\bar{c}$

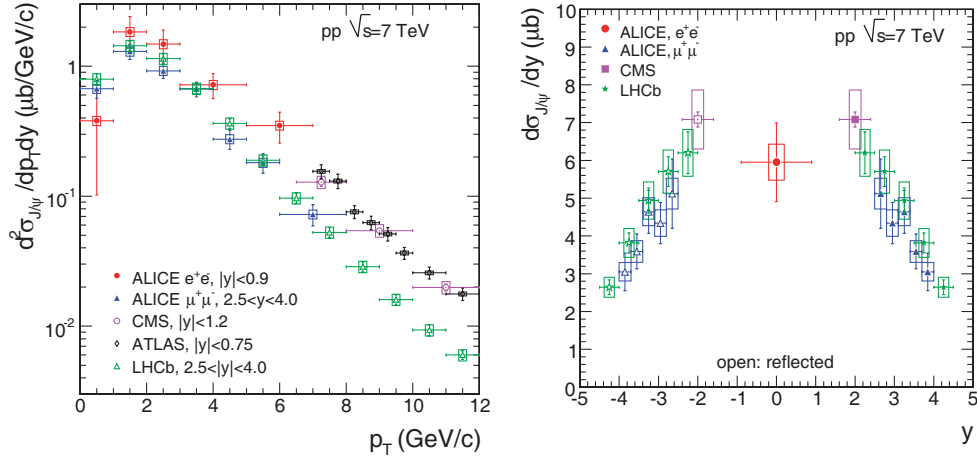


Fig. 6. – Left: $d^2\sigma/dp_T dy$ for J/ψ production in $\sqrt{s} = 7$ TeV pp collisions. The ALICE results are compared to those from the other LHC experiments. Right: $d\sigma/dy$ for J/ψ production in $\sqrt{s} = 7$ TeV pp collision. Results from other experiments are shown when their rapidity coverage extends down to $p_T = 0$. See [13] for details and references to other experimental results.

bound states. A similar effect should also be visible in the bottomonium sector. As for other observables, pp reference data are essential as a baseline, and are useful to constrain theoretical models for hadro-production. In ALICE, J/ψ has been studied [13] over a large y range, including central ($|y| < 0.9$) and forward rapidity ($2.5 < y < 4$), and in both regions the transverse momentum coverage extends down to $p_T = 0$. At central rapidity leptons from the $J/\psi \rightarrow e^+e^-$ decay are identified in the TPC, and the use of TOF and TRD to increase the purity of the signal is currently under study. At forward rapidity, muons from the $J/\psi \rightarrow \mu^+\mu^-$ decay are measured in the forward muon arm. In fig. 6 (left) the J/ψ transverse momentum distributions for pp collisions at $\sqrt{s} = 7$ TeV are shown and compared with results from the other LHC experiments. The ALICE muon measurement and the LHCb result, covering the same y range, are in good agreement, while the ALICE electron result complements the high p_T ATLAS and CMS distributions, reaching $p_T = 0$. In fig. 6 (right) we present $d\sigma/dy$ for ALICE, compared with results from other experiments, quoted when their p_T coverage extends to zero. Also in this case, a good agreement is found. It has to be noted that these results assume that J/ψ production is unpolarized. A direct measurement of J/ψ polarization, through the study of the angular distribution of the decay leptons, is currently underway and is extremely relevant for theory since models are not generally able to reproduce at the same time p_T distributions and polarization.

4. – Conclusions

After nearly twenty years of design, R&D, construction, installation, commissioning and simulations, the ALICE experiment is taking data since LHC started its operation at the end of 2009. Most systems have reached design performance, and several physics results are now available. Even if heavy-ion physics is the main subject, the experiment can also explore the LHC energy territory with pp collisions. The results, which have

been shortly outlined in this contribution, represent a fundamental reference for nuclear collision results [3] but also an interesting testing ground for QCD-related topics, from soft to semi-hard observables.

* * *

The author would like to thank the organizers for the extremely pleasant and fruitful atmosphere of this workshop.

REFERENCES

- [1] ALICE COLLABORATION, *J. Phys. G*, **30** (2004) 1517; **32** (2006) 1295.
- [2] AAMODT K. *et al.* (ALICE COLLABORATION), *Eur. Phys. J. C*, **65** (2010) 111.
- [3] DAINESE A. *et al.* (ALICE COLLABORATION), these proceedings.
- [4] AAMODT K. *et al.* (ALICE COLLABORATION), *J. Instrum.*, **3** (2008) S08002.
- [5] AAMODT K. *et al.* (ALICE COLLABORATION), *Eur. Phys. J. C*, **68** (2010) 89.
- [6] AAMODT K. *et al.* (ALICE COLLABORATION), *Eur. Phys. J. C*, **68** (2010) 345.
- [7] AAMODT K. *et al.* (ALICE COLLABORATION), *Phys. Lett. B*, **693** (2010) 53.
- [8] AAMODT K. *et al.* (ALICE COLLABORATION), *Phys. Rev. Lett.*, **105** (2010) 072002.
- [9] ROSSI G. C. and VENEZIANO G., *Nucl. Phys. B*, **123** (1977) 507.
- [10] AAMODT K. *et al.* (ALICE COLLABORATION), *Eur. Phys. J. C*, **71** (2011) 1594.
- [11] CACCIARI M., GRECO M. and NASON P., *JHEP*, **9805** (1998) 007; private communication.
- [12] KNEHL B. A. *et al.*, *Phys. Rev. Lett.*, **96** (2006) 012001; private communication.
- [13] AAMODT K. *et al.* (ALICE COLLABORATION), *Phys. Lett. B*, **704** (2011) 442, arXiv:1105.0380.

QCD physics at ATLAS

E. MEONI on behalf of the ATLAS COLLABORATION

*Institut de Física d'Altes Energies (IFAE), Edifici Cn
Universitat Autònoma de Barcelona (UAB) - E-08193 Bellaterra (Barcelona), Spain*

(ricevuto il 29 Settembre 2011; pubblicato online il 23 Gennaio 2012)

Summary. — Quantum Chromodynamics (QCD) measurements represent an extensive part of the early physics program of the ATLAS experiment at LHC. In this contribution a selection of the first ATLAS QCD measurements is presented. The results are based on a part of the data sets collected during 2010 at the centre of mass energy of $\sqrt{s} = 7$ TeV. The contribution includes an overview of the underlying event studies. A large number of measurements involving jets is also illustrated. After the investigation of jet shapes, the measurements of the cross section of the inclusive, dijet, multi-jet and bosons plus jets processes are presented. The angular decorrelations results in dijet events are also discussed. Finally the measurement of the prompt photon cross section is shown. The measurements are compared to the predictions from different Monte Carlo (MC) generators implementing leading-order (LO) matrix elements supplemented by parton showers, and to next-to-leading order (NLO) perturbative QCD (pQCD) calculations.

PACS 12.38.-t – Quantum chromodynamics.

1. – Introduction

The LHC started colliding protons at a centre of mass energy of $\sqrt{s} = 7$ TeV early in 2010. The luminosity of the machine has grown roughly exponentially with running time. By the end of the 2010 run, a sample of integrated luminosity around 45 pb^{-1} was collected, at a peak luminosity of around $10^{32} \text{ cm}^{-2} \text{ s}^{-1}$. The ATLAS detector [1] performed well throughout the 2010 run and its response was quickly understood.

The QCD measurements are one of the most important chapters of the ATLAS early physics program. They are interesting in their own right as tests of the phenomenology of the strong interaction at the previously unexplored energy domain probed by the LHC. The hard QCD measurements can be compared with the available NLO pQCD calculations, providing a validation of the theory in the new kinematic regime, whereas deviations from the pQCD predictions could translate into a hint of new physics. In addition the hard QCD processes, mainly constituted by jet physics, form important backgrounds for both Standard Model and Beyond Standard Model physics processes,

therefore a detailed measurement of these processes represents already the first step of the ATLAS discovery program.

In order to perform precise physics measurements or searches for new physics phenomena at hadron colliders, it is essential to have a good understanding not only of the QCD hard scattering process but also of the accompanying beam-beam remnants and the multiple parton interactions, that are the main components of the underlying events. The MC event generators that include LO matrix elements supplemented by parton shower need to be tuned on the data to perform an adequate description of these phenomena. By measuring the observables sensitive to the underlying event, a deeper insight into different contributing processes can be gained and the MC models can be improved.

In this contribution a review of the first QCD measurements is presented including the underlying event results, many hard QCD measurements involving jets and finally prompt photons measurements. Most of the results presented here are based on small data sets ranging from integrated luminosities of 17 nb^{-1} to about 300 nb^{-1} . Although the data sample is modest, the large cross section for QCD processes already allowed significant tests of this phenomenology, with an extension of the kinematical reach beyond the measurements from previous experiments.

2. – The underlying event

The underlying event is defined as everything in the event except the hard scatter itself, so it consists of the accompanying beam-beam remnants and the multiple parton interactions. It also receives contributions from initial and final state parton QCD radiation. The underlying event has been first investigated at ATLAS through the study of the charged particles reconstructed in the Inner Detector [2]. The charged particles in every event are categorized according to their azimuthal angles ϕ . A “toward” region is then defined by the ϕ value of the highest- p_T track, which strongly correlates with the ϕ of the hardest scattering in the event. A “transverse” region is then defined by $60^\circ < |\Delta\phi| < 120^\circ$, with $|\Delta\phi|$ measured relative to the leading track. Little activity associated with the hard scatter is expected in this region and it is thus the most sensitive to underlying event effects. The data are corrected back to the particle level and the distributions are compared with the predictions from different MC models. Figure 1 shows the average number of central charged particles ($|\eta| < 2.5$, $p_T > 0.5 \text{ GeV}$) per event in the transverse region. The level of activity is larger than that predicted by the underlying event model implemented in the different MCs using pre-LHC tunings. An underlying event analysis has also been performed using calorimeter information with similar conclusions [3]. The new tunes of MCs obtained by attempting to fit the charged particle multiplicity distributions in a diffraction limited phase-space, and also using the plateau of the underlying event distributions shown here results in a significant improvement [4].

3. – The jet shapes

Jets are distinctive signature of short-distance (hard) interactions between partons, and probe different aspects of high- p_T physics. Most of the results presented here are based on jets which are reconstructed using the anti- kt algorithm [5] with a distance parameter $R = 0.6$. The inputs to the anti- kt jet algorithm are clusters of calorimeter cells seeded by cells with energy that is significantly above the measured noise [6].

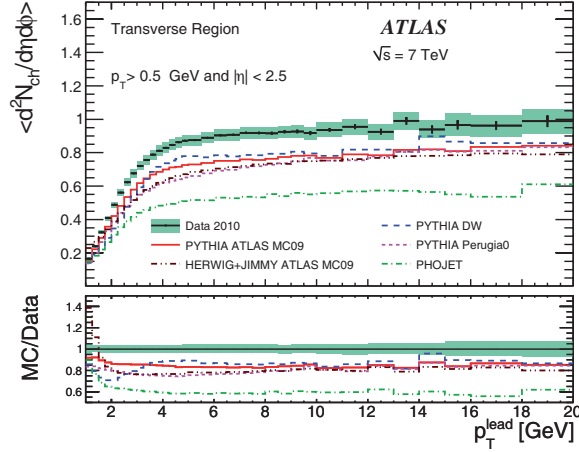


Fig. 1. – The charged particle multiplicity density as a function of the transverse momentum of the leading track restricted to azimuthal angles transverse to the leading particle. Data are compared with MC models.

The measured jet p_T is corrected to the particle level scale using an average correction, computed as a function of jet transverse momentum and pseudorapidity, and extracted from MC simulation. The main systematic uncertainty in the measurements presented here constitutes the jet energy scale uncertainty which, by the time of these studies, is determined to below 7% for central jets above 60 GeV transverse momentum [7].

The jet shapes [8] measurement tests the detailed modelling of jets in the MC generators. The shape of the jet depends on the type of partons (quark or gluon) that give rise to jets in the final state, and is also sensitive to non-perturbative fragmentation effects and underlying event contributions from the interaction between proton remnants. A proper modeling of the soft contributions is crucial for the understanding of jet production in p-p collisions and for the comparison of the jet cross section measurements with pQCD theoretical predictions. The differential jet shape $\rho(r)$ is defined as the average fraction of jet transverse momentum that lies inside an annulus of thickness $\Delta r = 0.1$ around the jet axis, normalized to the thickness. The measurements are carried out in the kinematic region with transverse momentum $30 \text{ GeV} < p_T < 600 \text{ GeV}$ and rapidity in the region $|y| < 2.8$ [9]. Figure 2 shows the measured differential jet shape corrected for detector effects separately for low- p_T (left) and high- p_T jets (right); the data are compared to several leading order QCD matrix element plus parton shower MC predictions, including different sets of tuning parameters. As expected, the measured jets become narrower with increasing jet transverse momentum. The jet shapes predicted by PYTHIA-Perugia2010 [10] provide a reasonable description of the data. HERWIG++ [11] predicts broader jets than the data at low and very high p_T , while ALPGEN [12] and PYTHIA-MC09 tend to produce narrower jets than the data.

4. – The inclusive jet, dijet and multijet cross sections

The first ATLAS inclusive jet and dijet data have been published using a data sample with an integrated luminosity of 17 nb^{-1} [7]. The jet cross section measurements are

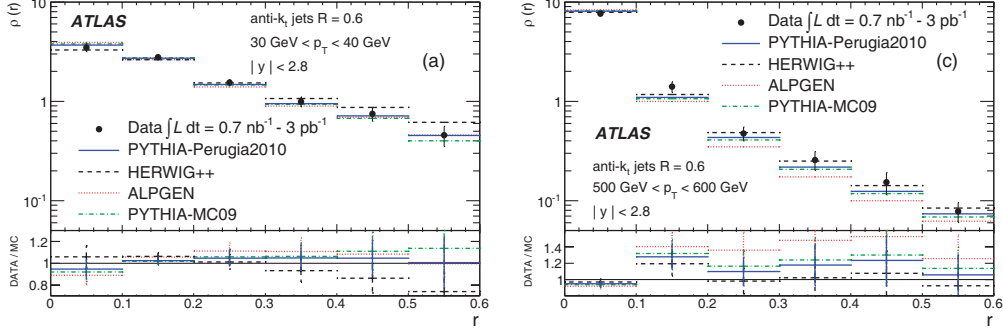


Fig. 2. – The measured differential jet shape, $\rho(r)$, in inclusive jet production for jets with $|y| < 2.8$ and $30 \text{ GeV} < p_T < 40 \text{ GeV}$ (left) and $500 \text{ GeV} < p_T < 600 \text{ GeV}$ (right) is shown in different p_T regions. Data are compared with MC models.

corrected for all experimental effects. They are performed in the kinematic region $p_T > 60 \text{ GeV}$ and $|y| < 2.8$ (in the dijet measurement the second leading jet should have $p_T > 30 \text{ GeV}$). This ensures that jets lie well within the high efficiency plateau region for the triggers used and that the jets are in a region where the jet energy scale is well understood. Figure 3 (left) shows the inclusive jet double-differential cross section measured as a function of the jet p_T in different rapidity regions. Figure 3 (right) shows the dijet differential cross section measured as a function of the invariant mass of the dijet system (m_{12}) binned in the maximum rapidity of the two leading jets. The cross sections extend into previously unmeasured kinematic regimes. For inclusive jets, the p_T

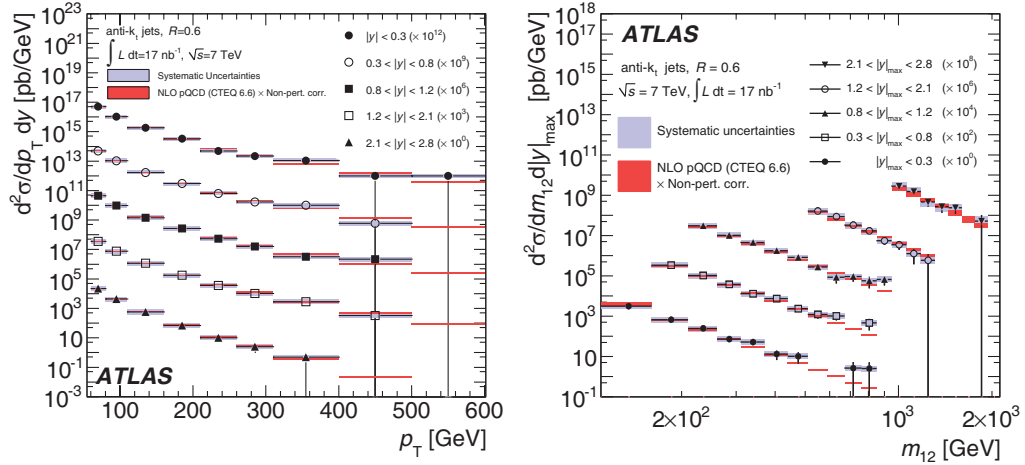


Fig. 3. – The inclusive jet differential cross section as a function of jet p_T in different rapidity regions (left). The dijet double-differential cross section as a function of dijet mass, binned in the maximum rapidity of the two leading jets ($|y|_{max}$) (right). In both cases, the results are shown for jets identified using the anti- kt algorithm with $R = 0.6$. The data are compared to NLO pQCD calculations to which soft QCD corrections have been applied.

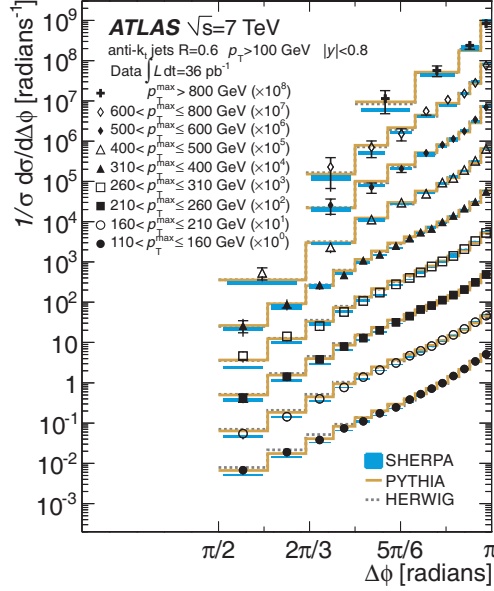


Fig. 4. – The differential cross section $(1/\sigma)(d\sigma/d\Delta\phi)$ binned in nine regions based on the p_T of the leading jet. The data are compared to various MC generators.

distribution extends up to 600 GeV. For dijet events, the dijet mass distribution extends up to nearly 2 TeV. The measurements have been compared to NLO pQCD calculations corrected for non perturbative effects. The theory agrees well with the data.

A particularly challenging class of jet production pertains to the study of events with more than two jets in the final state. Multijet events provide a particularly fertile testing ground for perturbative QCD at high energies. First ATLAS results are shown in [13]. The measurements are well described within uncertainties by the leading order matrix element calculation provided by ALPGEN, and PYTHIA describes the shapes of the distributions adequately.

5. – The dijet azimuthal decorrelation

The measurement of dijet angular decorrelations constitutes a very interesting method to access multi parton production using only the two hardest jets per event. In pure dijet signatures the two jets are back to back in the transverse plane due to energy momentum conservation. These events have small azimuthal decorrelations, $\Delta\phi = \pi$, while $\Delta\phi \ll \pi$ is typical of events with several high- p_T jets. QCD also describes the evolution of the shape of the $\Delta\phi$ distribution, which narrows with increasing leading jet p_T . A detailed understanding of events with large azimuthal decorrelations is important to searches for new physical phenomena with dijet signatures, such as supersymmetric extensions to the Standard Model. Figure 4 shows the measurement of the differential cross section binned in different regions based on the p_T of the leading jet [14]. The data are compared to various MC generators. A reasonable description is given by all MC generators within the measurement uncertainties.

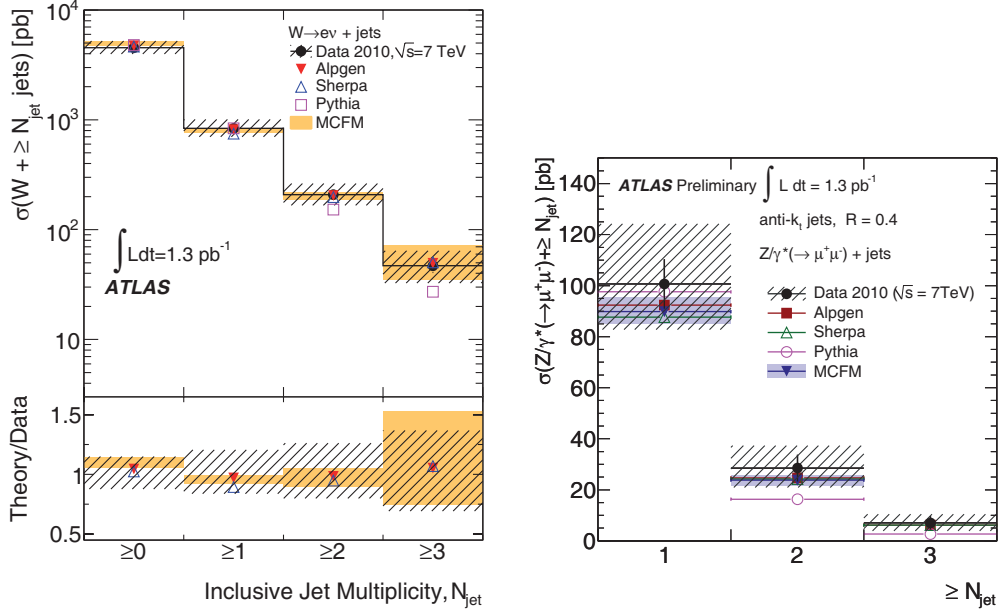


Fig. 5. – The W+jets cross section in the electron decay mode (left) and the Z+jets cross section in the muon decay mode (right) as a function of jet multiplicity. The cross sections are quoted in a limited and well-defined kinematic region, described in the text. Also shown are predictions from PYTHIA, ALPGEN, SHERPA, and MCFM. For the W+jets cross section the ratio of theoretical predictions to data is also shown.

6. – The boson plus jets cross section

The production of jets in association with W or Z bosons forms an important background for both Standard Model and Beyond Standard Model physics processes. A detailed measurement is needed to validate and tune the MCs. The first ATLAS measurement of the inclusive W+jets cross section [15] and of the inclusive Z+jets cross section [16] is based on an integrated luminosity of 1.3 pb^{-1} . Figure 5(left) shows the cross sections in the electron decay mode of the W boson as a function of jet multiplicity; the results have been corrected for all known detector effects and are quoted in a limited and well-defined range of jet and lepton kinematics: $p_T^j > 20 \text{ GeV}$ and $|\eta^j| < 2.8$, $E_T^e > 20 \text{ GeV}$, $|\eta^e| < 2.47$ (excluding $1.37 < |\eta^e| < 1.52$), $p_T^\nu > 25 \text{ GeV}$, $M_T > 40 \text{ GeV}$, $\Delta R^{e,j} > 0.5$, where e , j and ν denote the electron, the jet and the neutrino, respectively. The measured cross sections are compared to particle-level predictions based on perturbative QCD. Next-to-leading order calculations are found in good agreement with the data. Leading-order multi parton event generators, as ALPGEN and SHERPA [17], normalized to the NNLO total cross section, describe the data well for all measured jet multiplicities. PYTHIA underestimates the cross section.

Figure 5(right) shows the first ATLAS total Z+jets cross sections as a function of jet multiplicity, in a similar kinematic region to the W+jets measurement. In this case the data amount is reduced by a factor 10, due to the smaller Z production cross section compared to the W, but the general conclusions are similar to the W+jets measurement within the quite large statistical uncertainty.

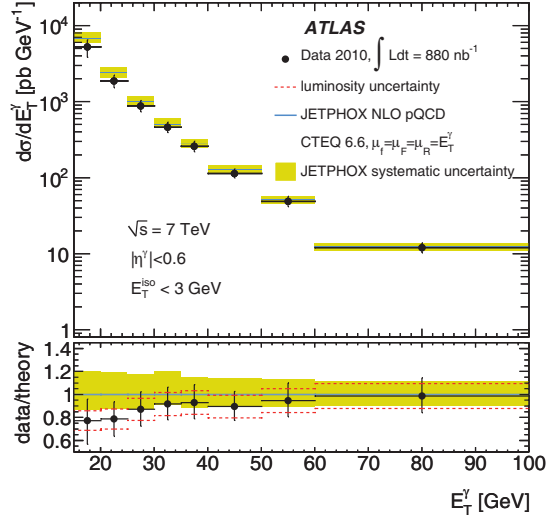


Fig. 6. – The measured and the expected inclusive prompt photon production cross section, for photons with transverse energies above 15 GeV and in the pseudorapidity range $|\eta| < 0.6$.

7. – The prompt photon cross section

The prompt photon production at hadron colliders probes perturbative QCD predictions [18]. They provide a colorless probe of quarks in the hard partonic interaction and the subsequent parton shower. Their production is directly sensitive to the gluon content of the proton through the qg process, which dominates at leading order (LO). The measurement of the prompt photon production cross section can thus be exploited to constrain the gluon density function. The first ATLAS measurement of the inclusive isolated prompt photon cross section is based on an integrated luminosity of 880 nb^{-1} [19]. Figure 6 shows the measured inclusive isolated prompt photon production cross sections as a function of the photon transverse energy in the pseudorapidity range $|\eta^\gamma| < 0.6$ and in the transverse energy range $15 < E_T^\gamma < 100 \text{ GeV}$. The data are compared to NLO pQCD calculations done with JETPHOX [20]. The measured cross section is in agreement with the theoretical predictions for $E_T > 25 \text{ GeV}$.

8. – Conclusions

In this contribution the first QCD measurements in p-p collisions at $\sqrt{s} = 7 \text{ TeV}$ have been presented using the data from the initial data taking phase of the ATLAS experiment at LHC. The data are corrected for detector effects and compared to different leading-order matrix elements plus parton shower MC predictions and to NLO calculations. Properties of hadronic jets have been determined and their cross sections have been measured.

The results for underlying event and jet shapes reported in this paper indicate the potential of these measurements at the LHC to constrain the current phenomenological models for soft gluon radiation, underlying event activity, and non-perturbative fragmentation processes in the final state. The new tunes of the MCs obtained using the

underlying event distributions have been already implemented and show a significant improvements compared to the pre-LHC tunings.

The cross section measurements of the processes presented here show in general a good agreement with NLO QCD calculations and state of the art MC generators, including phase space regions not covered by earlier experiments. This is a decisive test of QCD itself and a very important prerequisite for searches for new physics.

At the time these proceedings are written, preliminary updates of these results with the full 2010 data set have been presented by the Collaboration [21]; the results in general confirm the conclusions of the measurements done with early data.

REFERENCES

- [1] THE ATLAS COLLABORATION, *JINST*, **3** (2008) S08003.
- [2] THE ATLAS COLLABORATION, *Phys. Rev. D*, **83** (2011) 112001, arXiv:1012.0791.
- [3] THE ATLAS COLLABORATION, *Eur. Phys. J. C*, **71** (2011) 1636.
- [4] THE ATLAS COLLABORATION, ATLAS-CONF-2010-031 (<http://cdsweb.cern.ch/record/1277665/files/ATLAS-CONF-2010-031.pdf>).
- [5] CACCIARI M., SALAM G. P. and SOYEZ G., *JHEP*, **04** (2008) 063.
- [6] THE ATLAS COLLABORATION, CERN-PH-EP-2010-034, *Eur. Phys. J. C*, **71** (2011) 1512, arXiv:1009.5908 (2010).
- [7] THE ATLAS COLLABORATION, *Eur. Phys. J. C*, **71** (2011) 1512.
- [8] ELLIS S. D., KUNSZT Z. and SOPER D. E., *Phys. Rev. Lett.*, **69** (1992) 3615; GROSS D. J. and WILCZEK F., *Phys. Rev. D*, **8** (1973) 3633.
- [9] THE ATLAS COLLABORATION, *Phys. Rev. D*, **83** (2011) 052003.
- [10] SJOSTRAND T., MRENN A. S. and SKANDS P. Z., *JHEP*, **05** (2006) 026.
- [11] BAHR M. *et al.*, HERWIG++ PHYSICS and MANUAL, *Eur. Phys. J. C*, **58** (2008) 639; CORCELLA G. *et al.*, *JHEP*, **01** (2001) 010.
- [12] MANGANO M. L. *et al.*, *JHEP*, **07** (2003) 001.
- [13] THE ATLAS COLLABORATION, ATLAS-CONF-2010-084 (<http://cdsweb.cern.ch/record/1298854/files/ATLAS-CONF-2010-084.pdf>).
- [14] THE ATLAS COLLABORATION, *Phys. Rev. Lett.*, **106** (2011) 172002.
- [15] THE ATLAS COLLABORATION, *Phys. Lett. B*, **698** (2011) 325.
- [16] THE ATLAS COLLABORATION, ATLAS-CONF-2011-001 (<http://cdsweb.cern.ch/record/1326324/files/ATLAS-CONF-2011-001.pdf>).
- [17] GLEISBERG T. *et al.*, *JHEP*, **02** (2009) 007, [arXiv:hep-ph/0811.4622].
- [18] ANGELIS A. L. S. *et al.* (CERN-COLUMBIA-OXFORD-ROCKEFELLER), *Phys. Lett. B*, **94** (1980) 106; AURENCHÉ P., BAIER R., FONTANNAZ M. and SCHIFF D., *Nucl. Phys. B*, **297** (1988) 661.
- [19] THE ATLAS COLLABORATION, *Phys. Rev. D*, **83** (2011) 052005.
- [20] CATANI S. *et al.*, *JHEP*, **05** (2002) 028.
- [21] <https://twiki.cern.ch/twiki/bin/view/AtlasPublic:ATLAS-CONF-2011-047> (<http://cdsweb.cern.ch/record/1338578/files/ATLAS-CONF-2011-047.pdf>); ATLAS-CONF-2011-043 (<http://cdsweb.cern.ch/record/1338572/files/ATLAS-CONF-2011-043.pdf>); ATLAS-CONF-2011-060 (<http://cdsweb.cern.ch/record/1344778/files/ATLAS-CONF-2011-060.pdf>); ATLAS-CONF-2011-042 (<http://cdsweb.cern.ch/record/1338571/files/ATLAS-CONF-2011-042.pdf>); ATLAS-CONF-2011-058 (<http://cdsweb.cern.ch/record/1343734/files/ATLAS-CONF-2011-058.pdf>).

Parton distributions and LHC data

J. ROJO

*Dipartimento di Fisica, Università di Milano and INFN, Sezione di Milano
Via Celoria 16, I-20133 Milano, Italy*

(ricevuto il 29 Settembre 2011; pubblicato online il 19 Gennaio 2012)

Summary. — In this contribution we briefly report on the progress and open problems in parton distribution functions (PDFs), with emphasis on their implications for LHC phenomenology. Then we study the impact of the recent ATLAS and CMS W lepton asymmetry data on the NNPDF2.1 parton distributions. We show that these data provide the first constraints on PDFs from LHC measurements.

PACS 12.38.-t – Quantum chromodynamics.
PACS 12.38.Lg – Other nonperturbative calculations.

1. – Progress and open problems in parton distributions

The quantitative control of the Standard Model contribution to collider signal and background processes at the few percent level is a necessary ingredient not only for precision physics, but also for discovery at the LHC. The precision determination of parton distribution functions (PDFs) is essential in order to achieve this level of theoretical accuracy.

There has been substantial progress in PDF analysis in the last years, and it is thus impossible to review it in detail in this contribution. A recent concise report of the status of the field can be found in ref. [1], while more detailed reviews can be found in refs. [2-5]. In this contribution we restrict ourselves to highlight some important topics in PDF determinations. First of all, we will sketch the current status of PDF fits and discuss some of the open problems in the field. Then we will discuss how the ATLAS and CMS measurements of the W lepton asymmetry data provide the first constraints on PDFs from the LHC, thus paving the way for PDFs based on LHC data.

PDF analysis have entered the era in which they can be considered as a quantitative science. An ideal PDF determination should satisfy several important requirements [2]. These include being based on a dataset which is as wide as possible, in order to ensure that all relevant experimental information is retained, to use a sufficiently general and unbiased parton parametrization and to provide statistically consistent confidence levels for PDF uncertainties. Moreover, such ideal set should include heavy quark mass effects through a GM-VFN scheme [6] and be based on computations performed at the highest

TABLE I. – Summary of the features of the most updated PDF sets from each group. The CT10, MSTW08 and NNPDF2.1 sets include data from a wide variety of physical processes and are thus called global PDF sets. See text for more details.

	Ref	Dataset	Parametrization	PDF uncertainties
ABKM09	[14]	DIS+DY	Polynomial	Hessian, standard tol.
CT10	[15]	DIS+DY+W/Z+jet	Polynomial	Hessian, dyn. tol.
HERAPDF1.0	[16]	DIS	Polynomial	Hessian, standard tol.
JR08	[17]	DIS+DY+jet	Polynomial	Hessian, fixed tol.
MSTW08	[18]	DIS+DY+W/Z+jet	Polynomial	Hessian, dyn. tol.
NNPDF2.1	[12]	DIS+DY+W/Z+jet	Neural Nets	Monte Carlo

	PT order	Heavy Quarks	Strong coupling
ABKM09	NLO/NNLO	FFNS	Fitted
CT10	NLO	S-ACOT- χ	Fixed + range of values
HERAPDF1.0	NLO	TR	Fixed
JR08	NLO/NNLO	FFNS	Fitted
MSTW08	LO/NLO/NNLO	TR	Fitted + range of values
NNPDF2.1	NLO	FONLL-A	Fixed + range of values

available perturbative order. Finally, PDF sets should be provided for a variety of values of α_s , reasonably thinly spaced, similarly for the heavy quark masses, and should include an estimate of uncertainties related to the truncation of the perturbative expansion. While for each of these aspects there has been sizable progress in the recent years, still no PDF sets fulfill all these conditions.

One important development in PDFs in the recent years has been the NNPDF approach [7-11]. Thanks to a combination of Monte Carlo techniques and the use of artificial neural networks, the NNPDF approach avoids some of the drawbacks of the standard approach like the bias due to the arbitrary choice of input functional forms or the use of linear approximations for PDF uncertainty estimation. The most updated NNPDF set is NNPDF2.1 [12], an unbiased NLO global fit of all relevant hard scattering data based on the FONLL-A GM-VFN scheme [13].

Several groups provide regular updates of their PDF sets: in alphabetic order these are ABKM, CT, HERAPDF, JR, MSTW and NNPDF. In table I we summarize some of the features of the most updated PDF sets from each collaboration. We consider only those sets available in the LHAPDF library. We compare the dataset, parametrization, method to estimate PDF uncertainties, perturbative order at which PDFs are available, the theoretical schemes adopted to include heavy quark mass effects and the treatment of the strong coupling α_s . More details on each of these issues can be found in refs. [2, 4, 5], as well as in the original publications of each group.

The main difference arises from the data sets used in each of the various analysis. The CT10, MSTW08 and NNPDF2.1 sets include data from a wide variety of physical

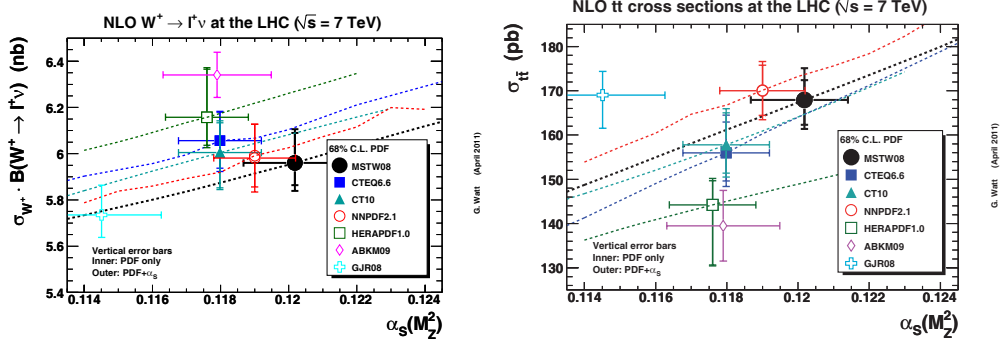


Fig. 1. – Comparison of the NLO total cross sections for W^+ and $t\bar{t}$ production and their combined PDF+ α_s uncertainties at the LHC 7 TeV between the most updated PDF sets of each group. Plots from G. Watt.

processes and are thus called *global* PDF sets. Other PDF sets use more restrictive subsets, like ABKM09, which excludes Tevatron jet and weak vector production data and HERAPDF1.0, that is based solely on HERA data.

PDFs are typically parametrized with relatively simple functional forms like $q(x, Q_0^2) \sim x^a(1-x)^b P(x, c, d, \dots)$ with P a polynomial that interpolates between the small- and large- x regions. These unjustified theoretical assumptions introduce a potentially large functional form bias in PDF determinations. The NNPDF approach bypasses this problem using neural networks as universal unbiased interpolants. Related techniques for general PDF parametrizations like Chebishev polynomials have also been discussed in the literature [19, 20].

PDF uncertainties are estimated by all groups (but NNPDF) using the Hessian method. However, different choices for the tolerance $T = \sqrt{\Delta\chi^2}$ adopted to define 1-sigma PDF uncertainties are used. For example, while HERAPDF1.0 and ABKM08 are based on a textbook tolerance $\Delta\chi^2 = 1$, MSTW08 and CT10 adopt a dynamical tolerance criterion that results in tolerances $\Delta\chi^2 \geq 1$, which are moreover different for each eigenvector direction. The need for large tolerances has been suggested to partly arise when restrictive input functional forms are used [20]. NNPDF, on the other hand, is based on the Monte Carlo approach, that is, a sampling in the space of experimental data, that allows an exact uncertainty propagation from data to PDFs and from these to physical observables.

Recently, a detailed benchmarking of the predictions for relevant LHC observables from modern NLO PDF sets was performed in the context of the PDF4LHC working group [5]. In fig. 1 we compare the NLO predictions for different PDF sets for two important LHC observables, the total W^+ and $t\bar{t}$ cross sections. One of the conclusions from that study is that the agreement between *global* PDF sets is reasonable for most LHC processes, much better than for sets based on restrictive datasets. However, it was also clear that even within global sets there are important discrepancies whose origin needs still to be understood, related for example to the large- x gluon and to strangeness. Another recent benchmark study, this time at NNLO, was presented in [21].

The PDF4LHC exercise allowed to elucidate differences and similarities between PDF sets. In particular it showed that the most important source of difference between sets is the choice of fitted data. This study was the basis of the PDF4LHC recommendation [22],

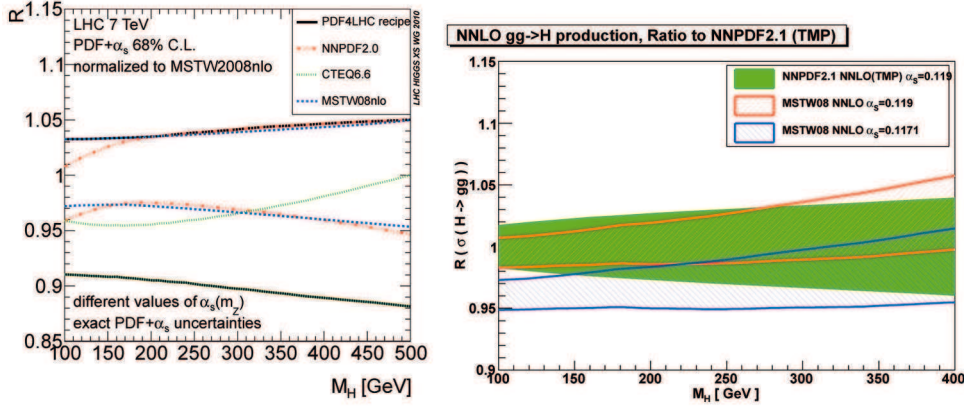


Fig. 2. – Left plot: Comparison of the NLO Higgs production cross section with the combined PDF+ α_s uncertainties from NNPDF2.0, MSTW08 and CTEQ6.6, and the resulting PDF4LHC recipe [22] envelope, from ref. [1]. Right plot: comparison of the MSTW08 and the preliminary NNPDF2.1 NNLO predictions for the NNLO Higgs production cross section. For the MSTW08 prediction two values of α_s have been used.

that suggests to take the envelope of the combined PDF+ α_s uncertainties from the three global PDF sets, CT10, MSTW08 and NNPDF2.1, to estimate the PDF+ α_s uncertainty on LHC processes. The PDF4LHC has been adopted by ATLAS and CMS in those analysis sensitive to PDFs, and in particular the LHC Higgs cross section working group [1] uses the PDF4LHC recipe to estimate the combined PDF+ α_s uncertainty in their theoretical predictions, see fig. 2. The same recipe has been used to derive the most updated Tevatron Higgs exclusion limits [23].

Let us now turn to discuss some open problems in PDF fits: the treatment of α_s , Higgs production at hadron colliders and deviations from DGLAP in HERA data. The treatment of the strong coupling in PDF fits is a source of differences between sets, as summarized in table I. Some groups, like MSTW or ABKM, determine α_s simultaneously with the PDFs, while others, like CT or NNPDF, take for α_s a fixed value close to the PDG average [24], $\alpha_s(M_Z) = 0.1184 \pm 0.0007$ in the latest update. Differences between PDF sets are reduced when a common value of α_s is used, as shown also in the comparison plots of fig. 1.

Let us emphasize that the choice of fixing α_s to the PDG value in the reference PDF set is not necessarily related to the sensitivity of a given PDF analysis to α_s . Rather, it reflects the idea than the average of α_s from a wide range of processes, including some like τ decays unrelated to the proton structure, is necessarily more accurate than the determination from a single PDF fit. For example, NNPDF [25] has recently performed a NLO determinations of the strong coupling, finding good consistency with the PDG value: $\alpha_s(M_Z) = 0.1191 \pm 0.0006$, where the uncertainty is purely statistical.

The treatment of α_s is closely related to one of the most important process at the LHC, the Higgs production cross section in its dominant production channel of gluon fusion. This process is very sensitive to α_s [26], since the partonic cross section depends as $\mathcal{O}(\alpha_s^2)$ already at leading order, and has received a lot of attention recently due to claims that theoretical uncertainties were being underestimated. Preliminary NNLO results from NNPDF, shown in fig. 2, suggest a reasonable agreement with the MSTW08

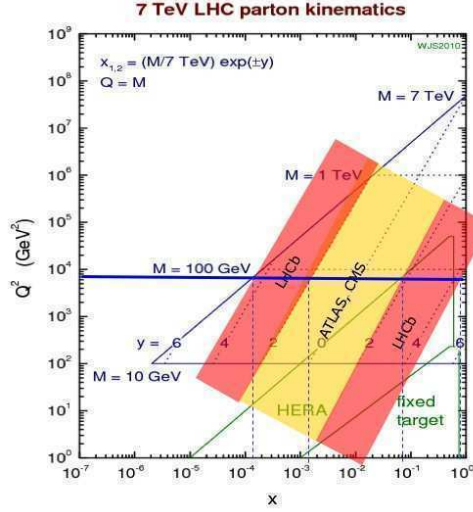


Fig. 3. – The kinematic coverage in the (x, Q^2) plane for W production at the LHC in the central (ATLAS and CMS) and forward (LHCb) regions.

NNLO prediction, as was already the case at NLO, thus confirming the PDF4LHC recipe estimates. It is also clear how the use of a common value of α_s improves further the agreement between the two sets.

Another open problem in PDF determinations are the potential departures from fixed-order DGLAP evolution in small- x and Q^2 HERA data. The analysis of refs. [27, 28] found evidence for deviations from NLO DGLAP in the small- x combined HERA-I data, consistent with small- x resummation and non-linear dynamics but not with NNLO corrections. This effect has been confirmed by the HERAPDF analysis, which also finds a worse fit quality at NNLO for the small- x data. A related CT10 [29] analysis found some hints as well but it was restricted to the use of few functional forms for the small- x PDFs. If deviations from DGLAP for low- x HERA data are confirmed, this suggests that small- x resummation [30] is a necessary ingredient in order to use all the potential of HERA data for precision LHC physics.

2. – Constraining PDFs with LHC W asymmetry data

We now turn to discuss the first constraints on PDFs from LHC data, provided by the ATLAS [31] and CMS [32] measurements of the leptonic W asymmetry⁽¹⁾. As is well known, W production at hadron colliders is sensitive to the light quark and antiquark PDFs at medium and small- x . The kinematic coverage of W production at the LHC is summarized in fig. 3. We have studied the impact of the W asymmetry data using the Bayesian reweighting method of ref. [33]. Bayesian reweighting is a powerful technique to efficiently determine the impact of new data into PDFs without the need of refitting. This method also allows to determine the internal consistency of the data sets and their compatibility with the global fit.

⁽¹⁾ There exist as well preliminary data from LHCb that will be sensitive to even smaller and larger values of x , see fig. 3.

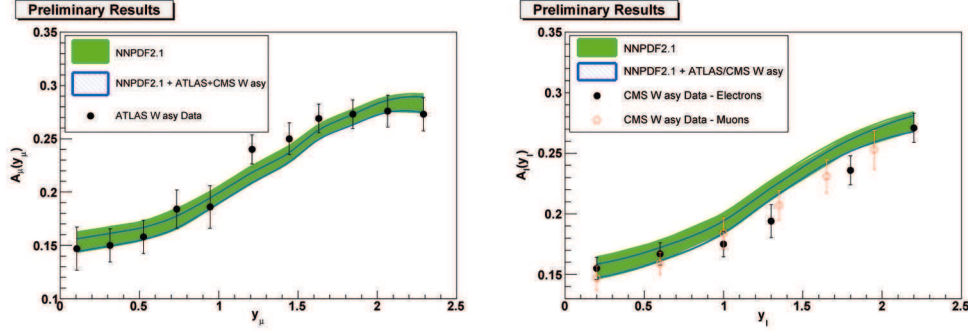


Fig. 4. – The ATLAS and CMS W lepton asymmetry data compared to the NNPDF2.1 predictions before and after reweighting.

A detailed discussion of the impact of LHC data on NNPDF will be presented elsewhere. In this contribution we restrict ourselves to some selected preliminary results. We will show results for the impact of the combined ATLAS and CMS data. In the case of CMS we consider the more inclusive dataset (with the cut in lepton transverse momentum of $p_t^l \geq 25$ GeV) and both electrons and muons. For ATLAS only the muon asymmetry has been presented. The theoretical predictions have been computed with the DYNLO generator [34] at NLO accuracy for NNPDF2.1. The kinematic cuts are the same as in the respective experimental analyses.

In fig. 4 we compare the ATLAS and CMS lepton asymmetry data with the NNPDF2.1 predictions before and after including the effect of these data sets. We notice that the data is already nicely consistent with the NNPDF2.1 prediction within the respective uncertainties. After including the LHC measurements, one finds that the W asymmetry data constraints the PDF uncertainties and leads to an even better agreement with the data. A more detailed statistical analysis confirms that the ATLAS and CMS data are consistent between them and with the experiments included in the global PDF analysis. After reweighting, the χ^2 per data point of the combined CMS and ATLAS data is ~ 1 .

Next, in fig. 5 we show the constraints on the PDFs provided by the combined ATLAS and CMS W asymmetry data. We find that the PDF uncertainties are reduced for

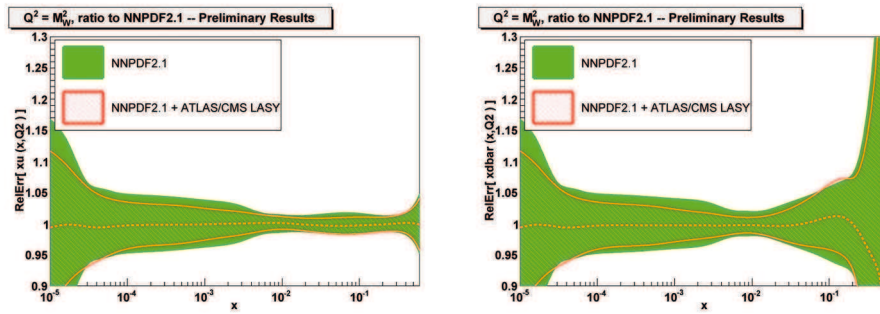


Fig. 5. – The impact of the ATLAS and CMS lepton asymmetry data on the relative uncertainty of the light quark and antiquark NNPDF2.1 PDFs.

medium- and small- x light quark and antiquarks, by a factor that can be as large as $\sim 30\text{--}40\%$. The impact on other PDFs is smaller. The central PDF prediction is almost unaffected by the LHC data, confirming further the consistency of the W asymmetry measurements with the global fit. At large- x the constraints are weaker, as expected from the kinematic coverage shown in fig. 3. Upcoming measurements of this asymmetry by LHCb might help in reducing PDF uncertainties in the large- x region.

Note that these preliminary results have been derived from a sample of only $N_{\text{rep}} = 100$ Monte Carlo replicas. This means that there can be non-negligible fluctuations and explains why PDF uncertainties are apparently reduced even at very small x , outside the kinematic coverage of the ATLAS and CMS data.

To summarize, we have shown that the W lepton asymmetry is the first dataset from the LHC that has the precision to constrain PDFs and thus improve the accuracy of Standard Model computations for LHC processes. We have quantified this impact on the light quark and antiquark PDFs, and found that PDF uncertainties can be reduced by factors up to $\sim 40\%$ at medium and small x . More constraints on PDFs should soon be available from upcoming LHC measurements.

3. – Outlook

In this contribution we have briefly reviewed recent developments and open problems related to PDFs, with emphasis on their implications for the LHC physics program. While our understanding of the proton structure has seen a huge progress in the recent years, there are still open questions that need to be answered, and that are important to improve even further the accuracy of theoretical predictions at the LHC. We have also presented preliminary results on the impact of the LHC W lepton asymmetry data on the NNPDF2.1 set. We have shown that these data provide the first constraints on PDFs from LHC measurements, in particular they help to pin down with better accuracy the medium- and small- x light quarks and antiquarks.

In the medium term, LHC measurements will provide very important constraints on most PDF combinations. This will allow parton distributions to be derived solely from collider data: HERA, Tevatron and the LHC. Collider data is more robust theoretically and experimentally than low-energy fixed target data, that now provide basic constraints in global PDF analysis. In order to achieve this program, several measurements will be provided by the LHC: Z -boson rapidity distributions, low mass Drell-Yan differential distributions, high- E_T jets and photons, and W/Z production in association with heavy quarks. The increased experimental and theoretical accuracy on PDFs determined this way will provide a solid ground for precision Standard Model predictions and searches for new physics at the LHC.

* * *

I would like to thank the La Thuile 2011 organizers for their kind invitation to present this review. I thank all the members of the NNPDF Collaboration for endless discussions on PDFs, specially S. FORTE. I thank G. WATT for providing the plots in fig. 1.

REFERENCES

- [1] DITTMAYER S. *et al.* (LHC HIGGS CROSS SECTION WORKING GROUP), arXiv:1101.0593 [hep-ph].
- [2] FORTE S., *Acta Phys. Polon. B*, **41** (2010) 2859, arXiv:1011.5247 [hep-ph].

- [3] CAMPBELL J. M., HUSTON J. W. and STIRLING W. J., *Rep. Prog. Phys.*, **70** (2007) 89, arXiv:hep-ph/0611148.
- [4] DE ROECK A. and THORNE R. S., arXiv:1103.0555 [hep-ph].
- [5] ALEKHIN S. *et al.*, arXiv:1101.0536 [hep-ph].
- [6] ROJO J. *et al.*, Sect. 22 in ANDERSEN J. R. *et al.* (SM and NLO MULTILEG WORKING GROUP), arXiv:1003.1241 [hep-ph].
- [7] DEL DEBBIO L., FORTE S., LATORRE J. I., PICCIONE A. and ROJO J. (NNPDF COLLABORATION), *JHEP*, **03** (2005) 080, arXiv:hep-ph/0501067.
- [8] DEL DEBBIO L., FORTE S., LATORRE J. I., PICCIONE A. and ROJO J. (NNPDF COLLABORATION), *JHEP*, **03** (2007) 039, arXiv:hep-ph/0701127.
- [9] BALL R. D. *et al.* (NNPDF COLLABORATION), *Nucl. Phys. B*, **809** (2009) 1 Erratum: **816** (2009) 293, arXiv:0808.1231 [hep-ph].
- [10] BALL R. D. *et al.* (THE NNPDF COLLABORATION), *Nucl. Phys. B*, **823** (2009) 195, arXiv:0906.1958 [hep-ph].
- [11] BALL R. D., DEL DEBBIO L., FORTE S., GUFFANTI A., LATORRE J. I., ROJO J. and UBIALI M., *Nucl. Phys. B*, **838** (2010) 136, arXiv:1002.4407 [hep-ph].
- [12] BALL R. D. *et al.*, *Nucl. Phys. B*, **849** (2011) 296, arXiv:1101.1300 [hep-ph].
- [13] FORTE S., LAENEN E., NASON P. and ROJO J., *Nucl. Phys. B*, **834** (2010) 116, arXiv:1001.2312 [hep-ph].
- [14] ALEKHIN S., BLUMLEIN J., KLEIN S. and MOCH S., *Phys. Rev. D*, **81** (2010) 014032, arXiv:0908.2766 [hep-ph].
- [15] LAI H. L., GUZZI M., HUSTON J., LI Z., NADOLSKY P. M., PUMPLIN J. and YUAN C. P., *Phys. Rev. D*, **82** (2010) 074024, arXiv:1007.2241 [hep-ph].
- [16] AARON F. D. *et al.* (H1 AND ZEUS COLLABORATION), *JHEP*, **01** (2010) 109, arXiv:0911.0884 [hep-ex].
- [17] JIMENEZ-DELGADO P. and REYA E., *Phys. Rev. D*, **79** (2009) 074023 [arXiv:0810.4274 [hep-ph]].
- [18] MARTIN A. D., STIRLING W. J., THORNE R. S. and WATT G., *Eur. Phys. J. C*, **63** (2009) 189, arXiv:0901.0002 [hep-ph].
- [19] GLAZOV A., MOCH S. and RADESCU V., *Phys. Lett. B*, **695** (2011) 238, arXiv:1009.6170 [hep-ph].
- [20] PUMPLIN J., *Phys. Rev. D*, **82** (2010) 114020, arXiv:0909.5176 [hep-ph].
- [21] ALEKHIN S., BLUMLEIN J., JIMENEZ-DELGADO P., MOCH S. and REYA E., *Phys. Lett. B*, **697** (2011) 127, arXiv:1011.6259 [hep-ph].
- [22] BOTJE M. *et al.*, arXiv:1101.0538 [hep-ph].
- [23] AALTONEN T. *et al.* (CDF and D0 COLLABORATION), arXiv:1103.3233 [hep-ex].
- [24] NAKAMURA K. *et al.* (PARTICLE DATA GROUP), *J. Phys. G*, **37** (2010) 075021.
- [25] LIONETTI S. *et al.*, arXiv:1103.2369 [hep-ph].
- [26] DEMARTIN F., FORTE S., MARIANI E., ROJO J. and VICINI A., *Phys. Rev. D*, **82** (2010) 014002, arXiv:1004.0962 [hep-ph].
- [27] CAOLA F., FORTE S. and ROJO J., *Phys. Lett. B*, **686** (2010) 127, arXiv:0910.3143 [hep-ph].
- [28] CAOLA F., FORTE S. and ROJO J., *Nucl. Phys. A*, **854** (2011) 32, arXiv:1007.5405 [hep-ph].
- [29] LAI H. L., HUSTON J., LI Z., NADOLSKY P., PUMPLIN J., STUMP D. and YUAN C. P., *Phys. Rev. D*, **82** (2010) 054021, arXiv:1004.4624 [hep-ph].
- [30] FORTE S., ALTARELLI G. and BALL R. D., *Nucl. Phys. Proc. Suppl.*, **191** (2009) 64, arXiv:0901.1294 [hep-ph].
- [31] AAD G. *et al.* (ATLAS COLLABORATION), arXiv:1103.2929 [hep-ex].
- [32] CHATRCHYAN S. *et al.* (CMS COLLABORATION), *JHEP*, **04** (2011) 050, arXiv:1103.3470 [hep-ex].
- [33] BALL R. D. *et al.* (THE NNPDF COLLABORATION), *Nucl. Phys. B*, **849** (2011) 112, arXiv:1012.0836 [hep-ph].
- [34] CATANI S., CIERI L., FERRERA G., DE FLORIAN D. and GRAZZINI M., *Phys. Rev. Lett.*, **103** (2009) 082001, arXiv:0903.2120 [hep-ph].

Heavy-ion physics with the ATLAS detector at the LHC

P. STEINBERG for the ATLAS COLLABORATION

Brookhaven National Laboratory - Upton, NY, USA

(ricevuto il 29 Settembre 2011; pubblicato online il 23 Gennaio 2012)

Summary. — First results on jet, J/ψ and Z production are presented from the first lead-lead run at the LHC, using the ATLAS detector. The transverse energies of opposed dijets are observed to show greater asymmetry with increasing event centrality, something not observed in proton-proton collisions. This may point to an interpretation in terms of strong jet energy loss in a hot, dense medium. Also, using the ATLAS muon spectrometer, a centrality-dependent suppression has been observed in the yield of J/ψ mesons. It is found to be qualitatively similar to the trends observed at previous, lower-energy experiments. The relative yields of Z bosons as a function of centrality are also presented, although the low statistics precludes any strong conclusions. These results provide a first look at the modification of high- p_T processes in heavy-ion collisions at the highest-available beam energy.

PACS 25.75.-q – Relativistic heavy-ion collisions.

1. – Heavy-ion physics with the ATLAS detector at the LHC

Collisions of heavy ions at ultra-relativistic energies are expected to produce an evanescent hot, dense state, with temperatures exceeding several trillion kelvins, in which the relevant degrees of freedom are not hadrons, but quarks and gluons. The ATLAS detector [1], a schematic diagram of which is shown in fig. 1, is a powerful tool for studying lead-lead collisions at the LHC energy of $\sqrt{s_{NN}} = 2.76$ TeV in the nucleon-nucleon center-of-mass frame. The Inner Detector measures charged-particle tracks for $|\eta| < 2.5$, the longitudinally segmented calorimeter provides electromagnetic and hadronic energy measurements for $|\eta| < 4.9$ and the Muon Spectrometer identifies and measures muons for $|\eta| < 2.7$.

2. – Jet quenching

In the hot, dense medium, high-energy quarks and gluons are expected to transfer energy to the medium by multiple interactions with the ambient plasma. There is a rich theoretical literature on in-medium QCD energy loss extending back to Bjorken, who proposed to look for “jet quenching” in proton-proton collisions [2]. This work also

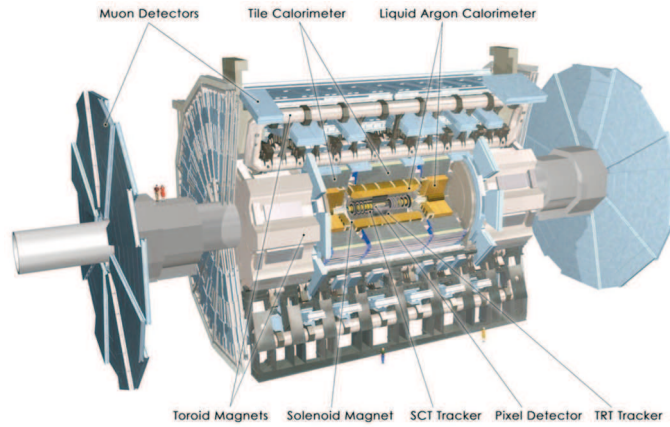


Fig. 1. – Schematic diagram of the ATLAS detector, showing the three main subsystems: the Inner Detector ($|\eta| < 2.5$), the Calorimeter ($|\eta| < 4.9$) and the Muon Spectrometer ($|\eta| < 2.7$).

suggested the observation of highly unbalanced dijets when one jet is produced at the periphery of the collision. For comprehensive reviews of recent theoretical work in this area, see refs. [3, 4].

The first LHC result on jet quenching was published by ATLAS shortly after the start of the 2010 heavy ion run [5]. To look for jet quenching, the jet energy imbalance is expressed in terms of the asymmetry A_J ,

$$(1) \quad A_J = \frac{E_{T1} - E_{T2}}{E_{T1} + E_{T2}}, \quad \Delta\phi > \frac{\pi}{2},$$

where the first jet is required to have a transverse energy $E_{T1} > 100$ GeV, and the second jet is the highest-transverse-energy jet in the opposite hemisphere with $E_{T2} > 25$ GeV. Focusing on the highest-transverse-energy pair of jets in events where those jets have an azimuthal angle separation, $\Delta\phi = |\phi_1 - \phi_2| > \pi/2$ reduces contributions from multijet final states. The average contribution of the underlying event energy is subtracted when deriving the individual jet transverse energies. The event selection is chosen such that the first jet has nearly 100% reconstruction efficiency and the second jet is typically (but not always) above the distribution of background fluctuations and the intrinsic soft jets associated with the collision. Dijet events are expected to have A_J peaked near zero, albeit with large deviations arising from a variety of effects. Energy loss of one or both jets in the medium would be expected to lead to much stronger deviations in the reconstructed energy balance.

The primary event triggers were based on coincidence signals from two sets of Minimum Bias Trigger Scintillator (MBTS) detectors, positioned at $z = \pm 3.56$ m, covering the full azimuth in the range $2.09 < |\eta| < 3.84$, as well as the Zero-Degree Calorimeters (ZDCs). These triggers have a large overlap and are close to fully efficient for the events studied here. In the offline analysis, events are required to have a time difference between the two sets of MBTS counters of $\Delta t < 3$ ns and a reconstructed vertex to efficiently reject beam-halo backgrounds. The primary vertex is derived from the reconstructed tracks in the Inner Detector (ID), which covers $|\eta| < 2.5$ with silicon pixel and strip detectors

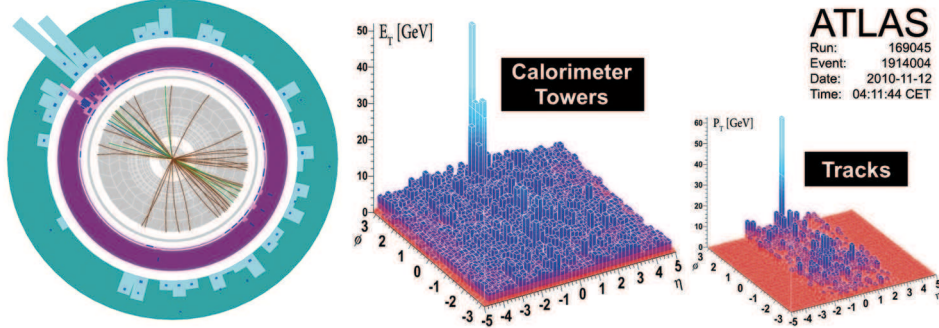


Fig. 2. – Event display of a highly asymmetric dijet event, with one jet with $E_T > 100$ GeV and no evident recoiling jet, and with high-energy calorimeter cell deposits distributed over a wide azimuthal region. By selecting tracks with $p_T > 2.6$ GeV and applying cell thresholds in the calorimeters ($E_T > 700$ MeV in the electromagnetic calorimeter, and $E > 1$ GeV in the hadronic calorimeter) the recoil can be seen dispersed widely over azimuth.

surrounded by straw tubes. These event selection criteria have been estimated to accept about 98% of the total lead-lead inelastic cross section.

Event centrality is characterized using the total transverse energy (ΣE_T) deposited in the Forward Calorimeters (FCal) covering $3.2 < |\eta| < 4.9$. Bins are defined in centrality according to fractions of the total lead-lead cross section selected by the trigger and are expressed in terms of percentiles (0–10%, 10–20%, 20–40% and 40–100%) with the 0–10% bin containing the most central events. Previous heavy ion experiments have shown a clear correlation of the ΣE_T with the geometry of the overlap region of the colliding nuclei and, correspondingly, the total event multiplicity. This is verified by the observation of a tight correlation between the transverse energy emitted near mid-rapidity and that measured at forward angles. Ultimately, the forward ΣE_T is used for this analysis to avoid any bias on the centrality measurement due to the presence of jets.

Jets have been reconstructed using the infrared-safe anti- k_t jet clustering algorithm [6] with the radius parameter $R = 0.4$. The inputs to this algorithm are towers of calorimeter cells of size $\Delta\eta \times \Delta\phi = 0.1 \times 0.1$ with the input cells weighted using energy-density-dependent factors (the so-called “H1 weights”) to correct for calorimeter non-compensation and other energy losses. Jet four-momenta are constructed by the vectorial addition of cells, treating each cell as an (E, \vec{p}) four-vector with zero mass.

After event selection, the requirement of a leading jet with $E_T > 100$ GeV and $|\eta| < 2.8$ yields a sample of 1693 events. A striking feature of this sample is the appearance of events with only one high- E_T jet clearly visible in the calorimeter, and no high- E_T jet opposite to it in azimuth. Such an event is shown in fig. 2. The calorimeter E_T and the sum of charged particle p_T are shown in regions of $\Delta\eta \times \Delta\phi = 0.1 \times 0.1$. Inspection of this event shows a highly-asymmetric pair of jets with the particle and energy flow recoiling against the leading jet being widely distributed in azimuth. The lead-lead data are also compared with a sample of 17 nb^{-1} of proton-proton collision data [7], which yields 6732 events.

To quantify the transverse energy balance between jets, we calculate the dijet asymmetry, A_J between the highest E_T (leading) jet and the highest E_T jet in the opposite hemisphere (second jet). This is done for each centrality bin. The second jet is required

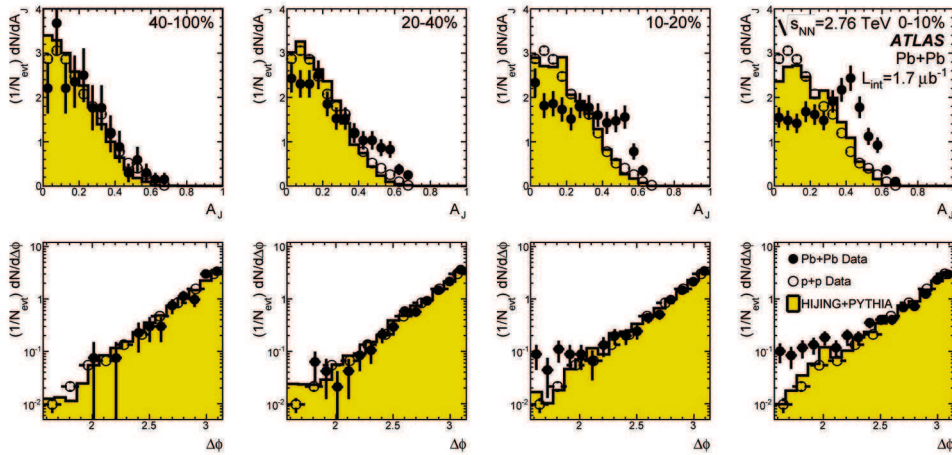


Fig. 3. – Top: Dijet asymmetry distributions for data (points) and unquenched HIJING with superimposed PYTHIA dijets (solid yellow histograms), as a function of collision centrality (left to right from peripheral to central events). Proton-proton data from $\sqrt{s} = 7$ TeV, analyzed with the same jet selection, is shown as open circles. Bottom: Distribution of $\Delta\phi$, the azimuthal angle between the two jets, for data and HIJING+PYTHIA, also as a function of centrality.

to have $E_T > 25$ GeV in order to discriminate against background from the underlying event. It is found that around 5% of the jet selected events in the 40% most-central collisions have no second jet satisfying these cuts, while the more peripheral samples generally always have a dijet pair.

The dijet asymmetry and $\Delta\phi$ distributions are shown in four centrality bins in fig. 3, where they are compared with proton-proton data and with fully reconstructed simulated HIJING [8] events embedded with PYTHIA [9] dijets (the latter to illustrate the magnitude of instrumental effects). The dijet asymmetry in peripheral lead-lead events is similar to that in both proton-proton and simulated events. As the events become more central, the lead-lead data distributions show an increased rate of highly asymmetric dijet events. The asymmetry distribution broadens; the mean shifts to higher values; the peak at zero asymmetry is no longer visible; and for the most central events a small (and not very significant) peak can be seen at higher asymmetry values. It is notable that the $\Delta\phi$ distributions show that the leading and second jets are primarily back-to-back in all centrality bins, although a noticeable tail develops for the most central events at large angles relative to the recoil direction.

Numerous studies have been performed to verify that the events with large asymmetry are not produced by backgrounds or detector effects. Detector effects primarily include readout errors and local acceptance loss due to dead channels and detector cracks. All of the jet events in this sample were checked, and no events were flagged as problematic. Furthermore, the highly-asymmetric dijets were not found to populate any specific region of the calorimeter, indicating that no substantial fraction of produced energy was lost in an inefficient or uncovered region. Asymmetric jet events were found to be uncorrelated with the presence of high energy muons or missing energy (*e.g.*, from W decays). Ultimately, the asymmetry appears to be a robust result, confirmed recently by other LHC experiments (*e.g.*, ref. [10]), and turns out to be the first indication that jet quenching can be observed at the jet level, rather than just the hadron level.

3. – J/Ψ suppression and Z observation

The measurement of quarkonia production in ultra-relativistic heavy-ion collisions provides a potentially powerful tool for studying the properties of hot and dense matter created in these collisions. If deconfined matter is formed, then color screening is expected to prevent the formation of quarkonium states when the screening length becomes shorter than the quarkonium size [11]. As this length is directly related to the temperature, a measurement of a suppressed quarkonium yield may provide direct experimental sensitivity to the temperature of the medium created in high energy nuclear collisions [12]. The interpretation of J/ψ suppression in terms of color screening is generally complicated by the quantitative agreement between the overall levels of J/ψ suppression measured by the NA50 experiment at the CERN SPS [13] ($\sqrt{s_{NN}} = 17.3$ GeV) and the PHENIX experiment at RHIC [14] ($\sqrt{s_{NN}} = 200$ GeV). Data from proton-nucleus and deuteron-gold collisions also show decreased rates of J/ψ production [15], indicating that mechanisms unrelated to color screening may also be relevant. Finally, there exist proposals for J/ψ enhancement at high energies from charm quark recombination [16]. Measurements at higher energies, with concomitantly higher temperatures and heavy quark production rates, are clearly needed to address these debates with new experimental input. The production of Z bosons, only available in heavy-ion collisions at LHC energies, can serve as a reference process for J/ψ production, since Z 's are not expected to be affected by the hot, dense medium, although modifications to the nuclear parton distribution functions must be considered [17]. The first measurement of both J/ψ and Z bosons were published by ATLAS in ref. [18].

In ATLAS, muons are measured by combining independent measurements of the muon trajectories from the Inner Detector (ID) and the Muon Spectrometer (MS). The Inner Detector volume is immersed in a 2 T field and measures the trajectories of charged particles in the pseudorapidity region $|\eta| < 2.5$. A charged particle typically traverses three layers of silicon pixel detectors, eight silicon strip sensors (SCT detector) arranged in four layers of double-sided modules, and a transition radiation tracker composed of straw tubes (the latter being excluded from the present analysis). The MS surrounds the calorimeters and provides tracking for muons with $|\eta| < 2.7$ and triggering in the range $|\eta| < 2.4$. Muon momentum determination is based on three stations of precision drift chambers that measure the trajectory of each muon in a toroidal magnetic field produced by three air-core toroids. In order to reach the MS, muons have to cross the electromagnetic and hadronic calorimeters, losing typically 3 to 5 GeV of energy, depending on the muon pseudorapidity. The calorimeters efficiently absorb the copious charged and neutral hadrons produced in lead-lead collisions, keeping the muon spectrometer occupancy low.

The same conventions for collision centrality are used as described previously. The centrality dependence of the muon detection efficiency is parameterized as a function of the total number of hits per unit of pseudorapidity detected in the first pixel layer. This is strongly correlated with ΣE_T^{FCal} , but gives a more direct measure of the ID occupancy. The full data sample is divided into four bins of collision centrality, 40–80%, 20–40%, 10–20%, and 0–10%. The most peripheral 20% of collisions are excluded from this analysis due to larger systematic uncertainties in estimating the number of binary nucleon-nucleon collisions in these events, which are derived using a Monte Carlo Glauber calculation [19, 20].

The $J/\psi \rightarrow \mu^+\mu^-$ reconstruction efficiency is obtained from the MC samples as a function of centrality. The inefficiency gradually increases from peripheral to central collisions, due primarily to an occupancy-induced inefficiency in the ID tracking.

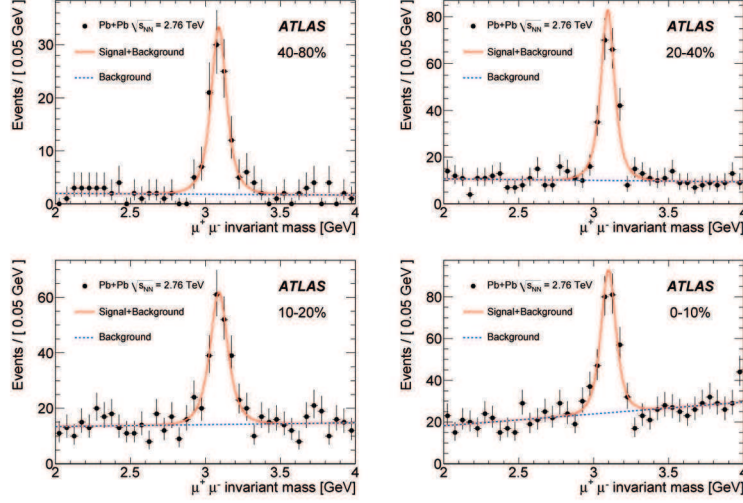


Fig. 4. – Oppositely charged dimuon invariant-mass spectra in the four considered centrality bins from most peripheral (40–80%) to most central (0–10%). The J/ψ yields in each centrality bin are obtained using a sideband technique. The fits shown here are used only as a cross-check.

The oppositely charged dimuon invariant mass spectra in the J/ψ region after the selection are shown in fig. 4. The number of $J/\psi \rightarrow \mu^+\mu^-$ decays is then found by a sideband technique, with the signal mass window from 2.95–3.25 GeV. and the background sidebands defined in 2.4–2.8 GeV and 3.4–3.8 GeV. To determine the uncertainties related to the signal extraction, an alternative method based on a maximum-likelihood fit with the mass resolution left as a free parameter is used as a cross check. With the chosen transverse momentum cuts on the decay muons, 80% of the reconstructed J/ψ have $p_T > 6.5$ GeV.

The measured J/ψ yields at different centralities are corrected by the reconstruction efficiency ϵ_c for $J/\psi \rightarrow \mu^+\mu^-$, derived from MC and parameterized in each centrality bin, and the width of the centrality bin, W_c , which represents a well-defined fraction of the minimum bias events. The corrected yield of J/ψ mesons is given by

$$(2) \quad N_c^{\text{corr}}(J/\psi \rightarrow \mu^+\mu^-) = \frac{N_c^{\text{meas}}(J/\psi \rightarrow \mu^+\mu^-)_c}{\epsilon(J/\psi)_c \cdot W_c}.$$

The “relative yield” is defined by normalizing to the yield found in the most peripheral 40–80% centrality bin: $R_c = N_c^{\text{corr}}/N_{40-80\%}^{\text{corr}}$. Note that the uncertainties in the 40–80% bin are not propagated into this ratio for the more central bins. Finally, the “normalized yield” is defined by scaling the relative yield by the ratio R_{coll} which is the mean number of binary collisions $N_{\text{coll},c}$ in each centrality bin divided by that for the most peripheral (40–80%) bin: $R_{cp} = R_c/R_{\text{coll}}$. The total systematic uncertainties on the ratios R_{coll} are evaluated by combining the variations of the various parameters going into the Glauber calculation (radius, skin depth, nucleon-nucleon cross section, and the fraction of the minimum-bias cross section sampled by the trigger and event selection) in quadrature.

The relative J/ψ yields after normalization and efficiency corrections as in equation (2), R_c , are compared to the expected R_{coll} values in the left panel of fig. 5. The yield

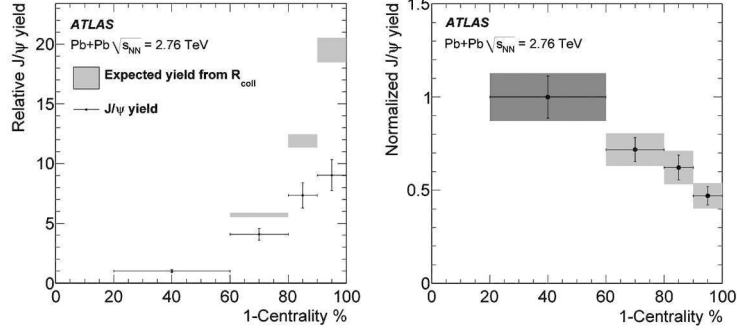


Fig. 5. – Left: Relative J/ψ yield as a function of centrality normalized to the most peripheral bin (black dots with errors). The expected relative yields from the (normalized) number of binary collisions (R_{coll}) are also shown (boxes, reflecting 1σ systematic uncertainties). Right: Value of R_{cp} , as described in the text, as a function of centrality. The statistical errors are shown as vertical bars while the grey boxes also include the combined systematic errors. The uncertainties for the most peripheral bin are not propagated into the more central ones.

errors are computed by adding the statistical and systematic uncertainties in quadrature. A clear difference is observed as a function of centrality between the measured relative J/ψ yield and the prediction based on R_{coll} , indicating a deviation from the simplest expectation based on QCD factorization. The ratio of these two values, R_{cp} , is shown as a function of centrality in the right panel of fig. 5. The data points are not consistent with a fit to a constant value giving a $P(\chi^2, N_{\text{DOF}})$ value of 0.11% with three degrees of freedom. Instead, a significant decrease of R_{cp} as a function of centrality is observed.

Z candidates are selected by requiring a pair of oppositely charged muons with $p_T > 20$ GeV and $|\eta| < 2.5$ [21]. We apply an additional cosmic ray rejection cut on the sum of the pseudorapidities of the two muons, $|\eta_1 + \eta_2| > 0.01$. The invariant mass distribution of the selected pairs is shown in the left panel of fig. 6. With this selection, 38 Z candidates

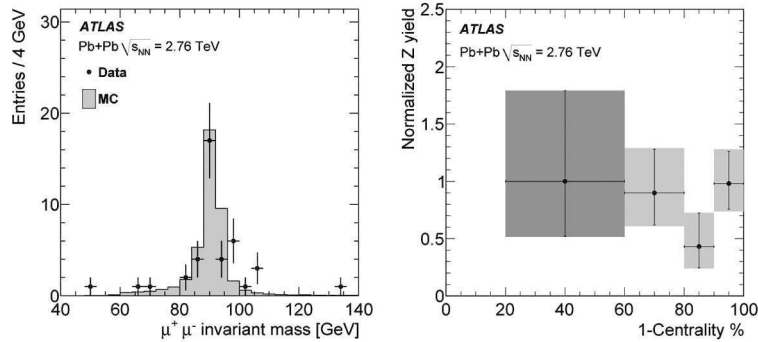


Fig. 6. – The dimuon invariant mass (left) after the selection described in the text. The value of R_{cp} (right) computed with the 38 selected Z candidates. The statistical errors are shown as vertical bars while the grey boxes also include the combined systematic errors. The darker box indicates that the 40–80% bin is used to set the scale for all bins, but the uncertainties in this bin are not propagated into the more central ones.

are retained in the signal mass window of 66 to 116 GeV. The background after this selection is expected to be below 2%, and is not corrected for in the result.

The R_{cp} variable for the Z candidates is computed in the same way as for the J/ψ sample. The same systematic uncertainties as for the J/ψ results have been applied to the Z relative yield measurements. Several cross-checks have been performed to support this approach. In addition to the tracks reconstructed with the combined ID and MS information, tracks reconstructed by the MS alone have been checked, and only one additional candidate was found. In the Z mass window, no candidate was found using same-charge muon pairs. Cosmic rays were rejected by studies of the transverse impact parameter distributions.

The measured Z yields are displayed in the right panel of fig. 6, normalized to the yield in the most peripheral bin and to the number of binary collisions (R_{cp}). The Z yields appear to be compatible with a linear scaling with the number of binary collisions, although the low statistics preclude drawing any strong conclusions.

4. – Conclusions and outlook

The first results from the ATLAS detector using data from the LHC heavy-ion run are presented. The first published observations of strong dijet asymmetry clearly confirm previous reports of jet quenching in heavy ion collisions using high-momentum hadrons, but show that the suppression can be seen at the jet level. A systematic suppression of high-momentum J/ψ mesons near mid-rapidity is also observed, with a centrality dependence similar to that seen for inclusive J/ψ at lower energies. The first observation of Z bosons show no strong deviations from the expected scaling with the number of binary collisions, but the low statistics preclude strong conclusions.

* * *

The author would like to thank the La Thuile organizers for the invitation, the ATLAS Collaboration for providing an excellent environment to do heavy-ion physics, and the LHC team for superlative performance of the machine during the first lead-lead run.

REFERENCES

- [1] AAD G. *et al.* (ATLAS COLLABORATION), *JINST*, **3** (2008) S08003.
- [2] BJORKEN J. D., FERMILAB-PUB-82-059-THY (1982).
- [3] WIEDEMANN U. A., arXiv:0908.2306 [hep-ph].
- [4] MAJUMDER A. and VAN LEEUWEN M., arXiv:1002.2206 [hep-ph].
- [5] AAD G. *et al.* (ATLAS COLLABORATION), *Phys. Rev. Lett.*, **105** (2010) 252303.
- [6] CACCIARI M., SALAM G. P. and SOYEZ G., *JHEP*, **0804** (2008) 63.
- [7] AAD G. *et al.* (ATLAS COLLABORATION), *Eur. Phys. J. C*, **71** (2011) 1512.
- [8] WANG X.-N. and GYULASSY M., *Phys. Rev. D*, **44** (1991) 3501.
- [9] SJOSTRAND T., MRENNA S. and SKANDS P. Z., *JHEP*, **0605** (2006) 26.
- [10] CHATRCHYAN S. *et al.* (CMS COLLABORATION), arXiv:1102.1957 [nucl-ex].
- [11] MATSUI T. and SATZ H., *Phys. Lett. B*, **178** (1986) 416.
- [12] MOCSY A. and PETRECKZY P., *Phys. Rev. Lett.*, **99** (2007) 211602.
- [13] ALESSANDRO B. *et al.* (NA50 COLLABORATION), *Eur. Phys. J. C*, **39** (2005) 335-345.
- [14] ADARE A. *et al.* (PHENIX COLLABORATION), *Phys. Rev. Lett.*, **98** (2007) 232301.

- [15] BADIER J. *et al.* (NA3 COLLABORATION), *Z. Phys. C*, **20** (1983) 101; ABREU M. C. *et al.* (NA38 COLLABORATION), *Phys. Lett. B*, **444** (1998) 516; LEITCH M. J. *et al.* (FNAL E866 COLLABORATION), *Phys. Rev. Lett.*, **84** (2000) 3256; ALESSANDRO B. *et al.* (NA50 COLLABORATION), *Eur. Phys. J. C*, **33** (2004) 31; ALESSANDRO B. *et al.* (NA50 COLLABORATION), *Eur. Phys. J. C*, **48** (2006) 329; ABT I. *et al.* (HERA-B COLLABORATION), *Eur. Phys. J. C*, **60** (2009) 525; ADARE A. *et al.* (PHENIX COLLABORATION), *Phys. Rev. Lett.* **107** (2011) 142301.
- [16] THEWS R. L. and MANGANO M. L., *Phys. Rev. C*, **73** (2006) 014904.
- [17] VOGT R., *Phys. Rev. C*, **64** (2001) 044901.
- [18] AAD G. *et al.* (THE ATLAS COLLABORATION), *Phys. Lett. B*, **697** (2011) 294.
- [19] ALVER B., BAKER M., LOIZIDES C. *et al.*, arXiv:0805.4411 [nucl-ex].
- [20] MILLER M. L., REYGERS K., SANDERS S. J. *et al.*, *Annu. Rev. Nucl. Part. Sci.*, **57** (2007) 205.
- [21] AAD G. *et al.* (ATLAS COLLABORATION), *JHEP*, **1012** (2010) 60.

First ALICE results from heavy-ion collisions at the LHC

A. DAINESE(*) for the ALICE COLLABORATION

INFN, Sezione di Padova - Padova, Italy

(ricevuto il 29 Settembre 2011; pubblicato online il 25 Gennaio 2012)

Summary. — The ALICE detector recorded Pb-Pb collisions at $\sqrt{s_{\text{NN}}} = 2.76$ TeV at the LHC in November-December 2010. We present the results of the measurements that provide a first characterization of the hot and dense state of strongly interacting matter produced in heavy-ion collisions at these energies. In particular, we describe the measurements of the particle multiplicity, collective flow, Bose-Einstein correlations, high-momentum suppression, and their dependence on the collision centrality. These observables are related to the energy density, the size, the viscosity, and the opacity of the system. Finally, we give an outlook on the upcoming results, with emphasis on heavy flavour production.

PACS 24.85.+p – Quarks, gluons, and QCD in nuclear reactions.

PACS 25.75.-q – Relativistic heavy-ion collisions.

PACS 25.75.Ag – Global features in relativistic heavy ion collisions.

1. – Introduction

The ALICE experiment [1] studies nucleus-nucleus and proton-proton collisions at the Large Hadron Collider, with the main goal of investigating the properties of the high-density state of QCD matter that is expected to be formed in Pb-Pb collisions [2,3]. According to lattice QCD calculations, under the conditions of high-energy density and temperature reached in these collisions, the phase transition to a Quark-Gluon Plasma (QGP) would occur, colour confinement of quarks and gluons into hadrons would be removed and chiral symmetry would be restored (see, *e.g.* [4]).

The ALICE detector was designed in order to provide tracking and particle identification over a large range of momenta (from tens of MeV/ c to over 100 GeV/ c), low material budget and excellent vertexing capabilities. These features have been tailored to reach a detailed characterization of the state of matter produced in Pb-Pb collisions, with particular attention to global event properties and hard probes.

(*) E-mail: andrea.dainese@pd.infn.it

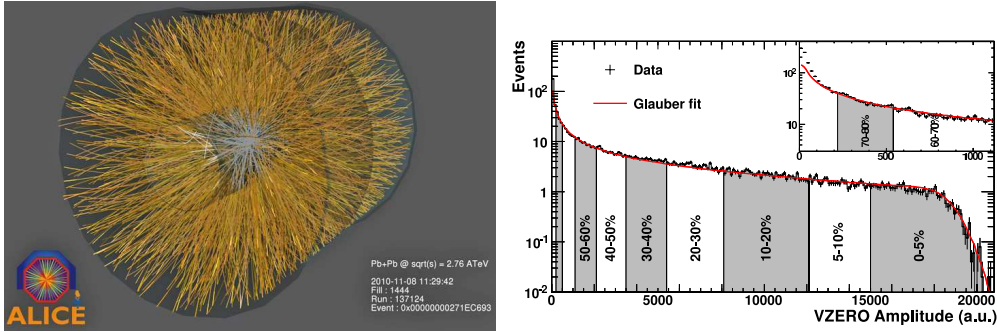


Fig. 1. – Left: tracks reconstructed in the ALICE Time Projection Chamber and Inner Tracking System in one of the first Pb-Pb collisions recorded by the detector. Right: distribution of the summed amplitudes in the VZERO scintillator tiles (histogram); inset shows the low amplitude part of the distribution; the curve shows the result of the Glauber model fit to the measurement. The vertical lines separate the centrality classes used in the analysis [6].

The experiment has collected the first Pb-Pb data in November-December 2010 at a centre-of-mass energy $\sqrt{s_{NN}} = 2.76$ TeV per nucleon-nucleon collision (see fig. 1, left). With a fourteen-fold increase with respect to nucleus-nucleus collisions at the RHIC collider (Au-Au at $\sqrt{s_{NN}} = 200$ GeV), this constitutes the largest energy increase in the history of heavy-ion physics and, as such, it opens new exciting scenarios for the study of high-density QCD matter. During the Pb-Pb run and shortly after it, the first results on the characterization of this state of matter were obtained [5-9]. These results are summarized in the present report.

In sect. 2, the ALICE experimental setup is briefly described, with emphasis on the detectors that were used for the results presented here, along with the data collection and collision centrality determination. The most fundamental measurement that characterizes the inclusive particle production is reported in sect. 3: the charged particle multiplicity density [5] and its dependence on the collision centrality [6]. This measurement provides information on the energy density of the system and, via comparison with models, on the gluon dynamics in the high-energy colliding nuclei. In sect. 4 the elliptic flow measurement is described, compared to lower-energy data, and related to the hydro-dynamical properties of the produced system [7]. In sect. 5 the measurement of the Bose-Einstein two-pion correlation, that allows to characterize the spatial extension of the particle emitting source, is described [8]. The study of the suppression of the charged particle production at large momentum, via the so-called nuclear modification factor, is presented in sect. 6. Finally, in sect. 7, an outlook is given on the ongoing analyses, which will provide further insight on the QCD medium properties.

2. – ALICE detector, Pb-Pb data sample, and collision-centrality determination

The ALICE apparatus is described in [1]. It consists of two main parts: a central detector, placed inside a solenoidal magnet providing a field of up to 0.5 T, where charged and neutral particles are reconstructed and identified in the pseudorapidity range $|\eta| < 0.9$, and a forward muon spectrometer covering the range $-4 < \eta < -2.5$. The apparatus is completed by a set of smaller detectors in the forward areas, for triggering, charged particle and photon counting, and event classification.

The main results presented in this report were obtained using the following ALICE detectors: the VZERO scintillators, the Inner Tracking System (ITS), the Time Projection Chamber (TPC).

The two forward scintillator hodoscopes (VZERO) are segmented into 32 scintillator counters each, arranged in four rings around the beam pipe. They cover the pseudorapidity ranges $2.8 < \eta < 5.1$ and $-3.7 < \eta < -1.7$, respectively. The ITS is composed of high-resolution silicon tracking detectors, arranged in six cylindrical layers at radial distances to the beam line from 3.9 to 43 cm. Three different technologies are employed: Silicon Pixel Detectors (SPD) for the two innermost layers, Silicon Drift Detector (SDD) for the two intermediate layers, and Silicon Strip Detector (SSD) for the two outermost layers. The TPC is a large cylindrical drift detector with cathode pad readout multi-wire proportional chambers at the two edges. The active volume is $85 < r < 247$ cm and $-250 < z < 250$ cm in the radial and longitudinal directions, respectively.

All data presented in this report were collected with a magnetic field of 0.5 T and a minimum-bias trigger requiring at least two out of these three conditions: a hit in the SPD, a hit in the forward rapidity VZERO counters, or a hit in the backward rapidity VZERO counters. This request selects about 98% of the Pb-Pb inelastic cross section. The instantaneous luminosity was typically of the order of 10^{25} cm⁻² s⁻¹ during the Pb-Pb run and a total statistics of about 30 million minimum-bias triggers was recorded, in addition to high-multiplicity and ultra-peripheral collision triggers.

Nucleus-nucleus collisions are classified according to their centrality, which measures the number of nucleons that undergo inelastic scattering (number of participants, N_{part}), and is related to the initial extension of the system produced in the collision. Several experimental observables, mainly measures of the number of particles produced in the collisions, can be used to categorize the events in centrality classes. Figure 1 (right) shows the distribution of the observable that was used for the first analyses of Pb-Pb data collected in 2010 [6]: the sum of amplitudes in the VZERO scintillator detector, the response of which is proportional to the event multiplicity. The distribution is fit using the Glauber model [10] to describe the collision geometry and a Negative Binomial Distribution (NBD) to describe particle production [11]. In addition to the two parameters of the NBD, there is one free parameter that controls the power law dependence of particle production on the number of participating nucleons (N_{part}). The fit is restricted to amplitudes above a value corresponding to 88% of the hadronic cross section. In this region the trigger and event selection are fully efficient, and the contamination by electromagnetic processes is negligible. Centrality classes are determined by integrating the measured distribution above the cut, as shown in fig. 1 (right).

3. – Charged-particle multiplicity and its collision-centrality dependence: a high-density system from gluon-saturated colliding nuclei

The multiplicity of charged particles per unit of pseudo-rapidity (η) at central rapidity is measured using the Silicon Pixel Detector, the innermost sub-detector of the Inner Tracking System, made of two layers with radii of 3.9 and 7.6 cm, and with acceptances $|\eta| < 2.0$ and $|\eta| < 1.4$, respectively. Tracklet candidates are formed using information on the position of the primary vertex, reconstructed with the same detector, and of hits on the two layers. In particular, a tracklet is defined by a pair of hits, one on each layer, selected on the basis of their polar and azimuthal angles, so that the resulting tracklet points to the primary vertex. The cut imposed on the azimuthal angle efficiently selects charged particles with transverse momentum (p_t) above 50 MeV/c. Particles

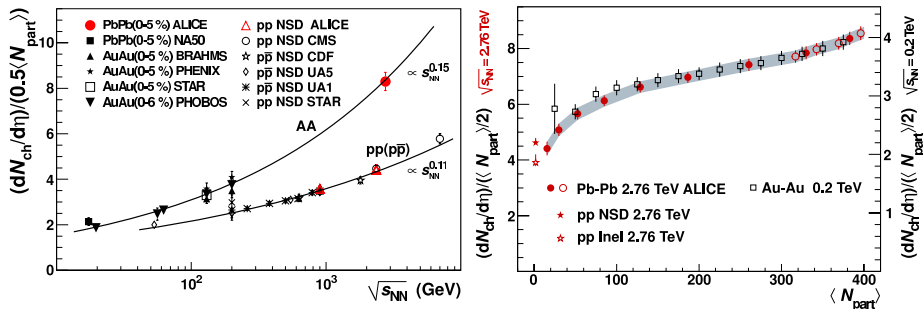


Fig. 2. – Charged-particle multiplicity. Left: $dN_{ch}/d\eta$ per participant pair for central nucleus-nucleus and non-single diffractive pp ($p\bar{p}$) collisions, as a function of $\sqrt{s_{NN}}$ ([5] and references therein). Right: the same observable as a function of collision centrality for nucleus-nucleus collisions at $\sqrt{s_{NN}} = 2.76$ [6] and 0.2 TeV [12] (scaled up by a factor 2.1).

below 50 MeV/c are mostly absorbed by material. The charged-particle pseudo-rapidity density $dN_{ch}/d\eta$ is obtained from the number of tracklets within $|\eta| < 0.5$, corrected for acceptance, efficiency and background contamination. The background is estimated from the data and from simulations with three different methods [5].

In the 5% most central Pb-Pb collisions, we measured a density of primary charged particles at mid-rapidity $dN_{ch}/d\eta = 1584 \pm 4(\text{stat.}) \pm 76(\text{sys.})$ [5]. Normalizing per participant pair (using N_{part} from the Glauber model fit), we obtained $dN_{ch}/d\eta/(0.5\langle N_{part} \rangle) = 8.3 \pm 0.4(\text{sys.})$ with negligible statistical error. In fig. 2 (left), this value is compared to the measurements for Au-Au and Pb-Pb, and non-single diffractive (NSD) pp and $p\bar{p}$ collisions over a wide range of collision energies. It is interesting to note that the energy dependence is steeper for heavy-ion collisions than for pp collisions. A significant increase, by a factor 2.1, in the pseudo-rapidity density is observed at $\sqrt{s_{NN}} = 2.76$ TeV for Pb-Pb compared to $\sqrt{s_{NN}} = 200$ GeV for Au-Au. Bjorken's estimation of the initial energy density in the system formed in the collisions reads: $\epsilon = \text{Energy}/\text{Volume} = dN/dy \cdot \langle m_t \rangle / (\tau_0 A)$, where dN/dy and $\langle m_t \rangle$ are the rapidity density and the average transverse mass of the produced particles, τ_0 is the formation time of the system, and A is the mass number of the colliding nuclei, which estimates the transverse area of the nuclear overlap for central collisions. This relation and our measurement suggest that the energy density of the system produced at LHC energies is at least a factor of 3 larger than at RHIC energies, considering the 2.1-fold larger multiplicity and the fact that the formation time τ_0 is expected to be shorter by a factor of about two with respect to RHIC energies. Figure 2 (right) shows the centrality dependence of the charged multiplicity per participant pair [6], compared to the corresponding RHIC measurement [12], scaled by a factor 2.1. The trend is very similar at the two energies and the mild increase in semi-central to central collisions is found to be better described by models that include a mechanism to tame the increase with centrality in the number of scattering centres. This suggests a certain degree of saturation in the phase-space of small x (fractional momentum) gluons in the initial state of the collision.

4. – Elliptic flow: the perfect liquid at the LHC

One of the experimental observables that is sensitive to the properties of high-density QCD matter is the azimuthal distribution of particles in the plane perpendicular to the

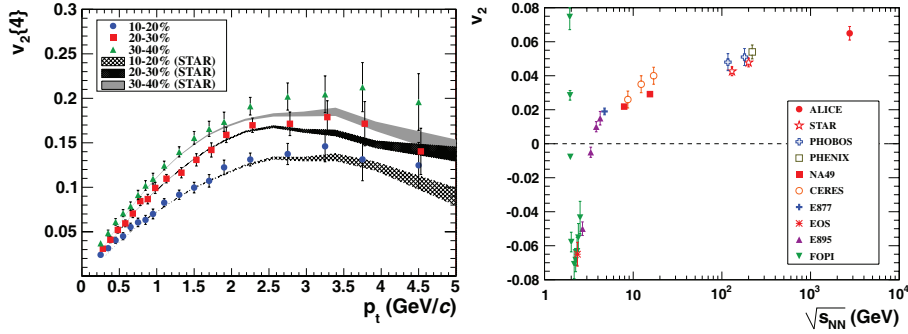


Fig. 3. – Elliptic flow. Left: $v_2\{4\}(p_t)$ for various centralities compared to STAR measurements. Right: integrated elliptic flow at 2.76 TeV in Pb-Pb 20–30% centrality class compared with results from lower energies taken at similar centralities ([7] and references therein).

beam direction. In non-central collisions, the geometrical overlap region and therefore the initial matter distribution is anisotropic (almond shaped). If the matter is interacting, this spatial asymmetry is converted via multiple collisions into an anisotropic momentum distribution. This anisotropy is quantified via the elliptic flow coefficient, v_2 , defined as the second moment of the final state hadron azimuthal distribution, $dN/d\phi$, with respect to the reaction plane, which contains the centres of the colliding nuclei and the beam line. The elliptic flow is a response of the dense system to the initial conditions and therefore it is sensitive to the early and hot, strongly interacting phase of the evolution. The large elliptic flow measured for Au-Au collisions at RHIC is well reproduced by models based on relativistic hydrodynamics with a QGP equation of state and small, but non-zero, viscosity.

The first results on the elliptic flow in Pb-Pb collisions at the LHC were obtained using charged particle tracks reconstructed in the TPC and in the ITS. The tracks were required to have at least 70 reconstructed space points out of the maximum 159 in the TPC and a χ^2 per TPC cluster ≤ 4 (with two degrees of freedom per cluster). Additionally, at least two of the six ITS layers must have a hit associated with the track, including at least one of the two pixel layers. A selection based on the distance of closest approach to the primary vertex was used to reject a large fraction of the tracks produced by secondary particles, from decays and interactions in the detector material. The p_t -differential flow was measured for different event centralities using various analysis techniques [7], based on multi-particle cumulants ($v_2\{2\}$ and $v_2\{4\}$). Figure 3 (left) presents $v_2(p_t)$ obtained with the 4-particle cumulant method for three different centralities, compared to STAR measurements at RHIC. The transverse momentum dependence is qualitatively similar for all three centrality classes. The observed similarity at RHIC and the LHC of the p_t -differential elliptic flow at low p_t is consistent with predictions of hydrodynamic models. The integrated elliptic flow measured in the 20–30% centrality class is compared to results from lower energies in fig. 3 (right). The figure shows that there is a continuous increase in the magnitude of the elliptic flow for this centrality region from RHIC to LHC energies. We find that the integrated elliptic flow increases by about 30% from $\sqrt{s_{NN}} = 200$ GeV at RHIC to 2.76 TeV. This increase is higher than current predictions from ideal hydrodynamic models. The hydrodynamic models which incorporate viscous corrections and certain hybrid models do allow for such an increase.

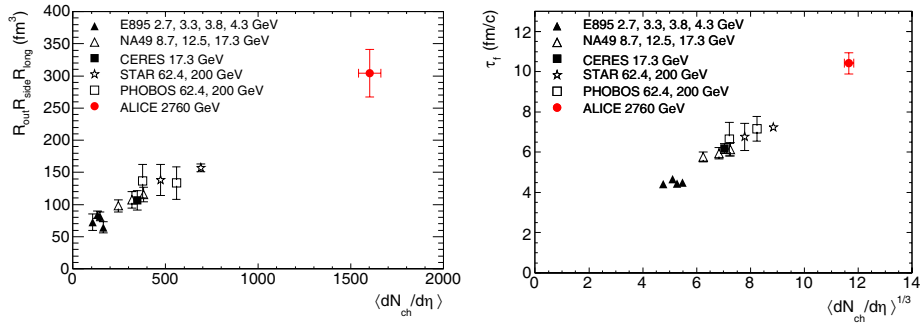


Fig. 4. – (Colour on-line) Femtoscopic measurements. Product of the three pion HBT radii (left) and decoupling time extracted from R_{long} (right). The ALICE results (red filled dots) are compared to those obtained for central gold and lead collisions at lower energies at the AGS, SPS, and RHIC. See [8] and references therein.

In these models the increase is due to the reduced importance of viscous corrections at LHC energies. This is a first indication that the high-density QCD matter produced in Pb-Pb collisions at the LHC resembles closely a perfect liquid, with viscosity close to zero.

5. – Femtoscopic study: a larger and longer-lived particle-emitting source

The Bose-Einstein enhancement of identical-pion pairs at low relative momentum allows to assess the spatial scale of the emitting source in e^+e^- , hadron-hadron, lepton-hadron, and heavy-ion collisions. Especially in the latter case, this technique, known as Hanbury Brown-Twiss (HBT) interferometry and being a special case of femtoscopic, has been developed into a precision tool to probe the dynamically generated geometry of the emitting system. See [8] for more details and references.

The first measurement of the HBT radii for Pb-Pb collisions at the LHC [8] was carried out using pion tracks, reconstructed in the TPC and ITS (similar selection cuts as for the flow analysis) and identified using the TPC specific energy deposit dE/dx . The details on the construction of the two-pion correlation functions and their analysis are described in [8]. Figure 4 (left) shows the dependence on charged particle multiplicity of the product of the three HBT radii ($R_{\text{out}} \cdot R_{\text{long}} \cdot R_{\text{side}}$), extracted as the Gaussian widths of the correlation function in three perpendicular directions. This product is connected to the volume of the homogeneity region. In central Pb-Pb collisions at $\sqrt{s_{\text{NN}}} = 2.76$ TeV we measured a product of about 300 fm^3 , about two times larger than at RHIC energy.

Within hydrodynamic scenarios, the decoupling time for hadrons at mid-rapidity can be estimated as follows: the size of the homogeneity region is inversely proportional to the velocity gradient of the expanding system; the longitudinal velocity gradient in a high-energy nuclear collision decreases with time as $1/\tau$; therefore, the magnitude of R_{long} (longitudinal HBT radius) is proportional to the total duration of the longitudinal expansion, *i.e.* to the decoupling time of the system. The decoupling times extracted from this fit to the ALICE radii and to the values published at lower energies are shown in fig. 4 (right). As can be seen, τ_f scales with the cube root of the charged-particle multiplicity and reaches 10–11 fm/c in central Pb-Pb collisions at the LHC.

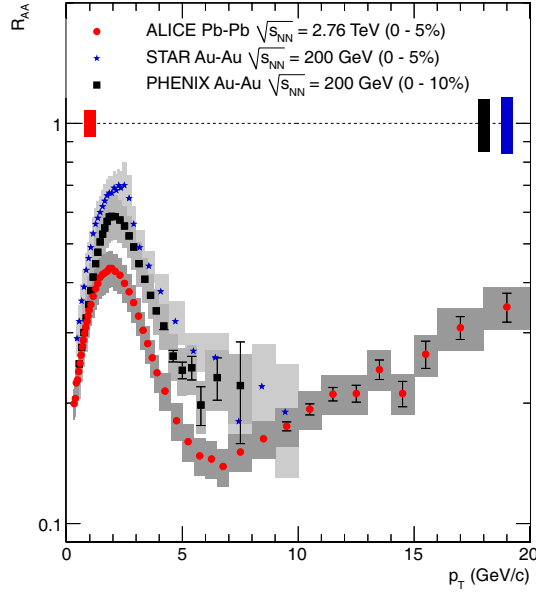


Fig. 5. – Nuclear modification factor R_{AA} for charged hadrons in central Pb-Pb collisions at the LHC, compared to measurements at $\sqrt{s_{NN}} = 200$ GeV by the PHENIX and STAR experiments. See [9] and references therein.

6. – Suppression of high- p_t charged-particle production: an intriguing pattern

One of the most awaited for measurements in heavy-ion collisions at the LHC is certainly the nuclear modification factor of charged hadrons, which ten years ago at RHIC yielded the first indication of the jet quenching phenomenon, now commonly attributed to parton energy loss in hot and dense QCD matter. This observable is defined as $R_{AA}(p_t) = (dN_{AA}/dp_t)/(1/\langle N_{coll} \rangle dN_{pp}/dp_t)$, that is, the ratio of the p_t spectrum measured in nucleus-nucleus to that expected on the basis of the proton-proton spectrum scaled by the number N_{coll} of binary nucleon-nucleon collisions in the nucleus-nucleus collision (as calculated in the Glauber model). At RHIC energies, the R_{AA} factor was measured to be of about 0.2 and roughly independent of p_t in the range 5–15 GeV/c, *i.e.* a factor of five suppression in high- p_t particle production with respect to pp collisions.

The charged particles R_{AA} was measured by ALICE out to $p_t = 20$ GeV/c after a few days of the end of the Pb-Pb run [9]. Charged particle tracks were reconstructed using information from the TPC and ITS detector systems in the region $|\eta| < 0.8$. The primary track selection described in sect. 4 was applied. When R_{AA} was first evaluated, no measured pp reference at $\sqrt{s} = 2.76$ TeV existed⁽¹⁾. As explained in [9], a reference was constructed by interpolating the ALICE measurements at $\sqrt{s} = 0.9$ and 7 TeV. Figure 5 shows the nuclear modification factor R_{AA} of charged hadrons for central Pb-Pb collisions, compared to the same measurement by the PHENIX and STAR experiments at RHIC. In central collisions at the LHC, R_{AA} exhibits a very strong suppression, reaching a minimum of ≈ 0.14 at $p_t = 6$ –7 GeV/c. Despite the much flatter p_t spectrum

⁽¹⁾ The LHC was run with pp collisions at this energy later, in March 2011.

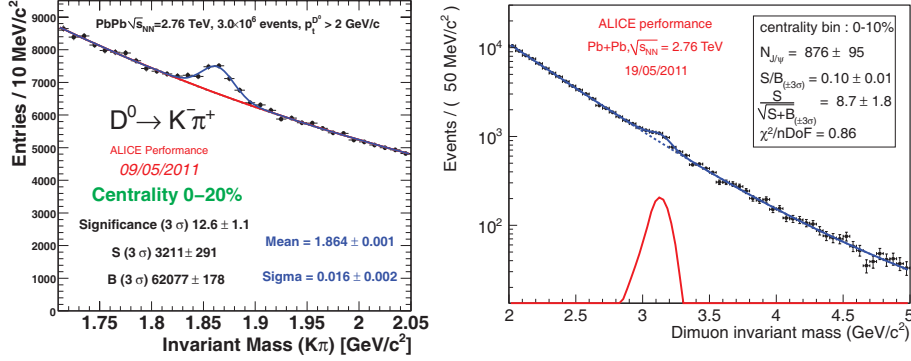


Fig. 6. – Signals of charm particles in central Pb-Pb collisions at the LHC. Left: $D^0 \rightarrow K^- \pi^+$ at central rapidity ($|y| < 0.8$). Right: $J/\psi \rightarrow \mu^+ \mu^-$ at forward rapidity ($2.5 < y < 4$).

in pp at the LHC, the nuclear modification factor at $p_t = 6-7$ GeV/c is smaller than at RHIC. This suggests an enhanced energy loss at LHC and therefore a denser medium. A significant rise by about a factor of two is observed for $7 < p_t < 20$ GeV/c. This pattern is very intriguing, because it suggests that very high momentum partons may lose only a small fraction of their energy in the medium and, thus, be sensitive probes of its properties.

7. – Ongoing analyses

Several measurements of strange and heavy-flavour particle production have been carried out, as well as studies of jet production and jet-like particle correlations [13]. As examples of the ALICE detector performance in Pb-Pb collisions, we report in fig. 6 the invariant mass distributions showing the signal of $D^0 \rightarrow K^- \pi^+$ decays selected using displaced decay vertices at central rapidity and $J/\psi \rightarrow \mu^+ \mu^-$ decays in the forward muon spectrometer.

8. – Conclusions

We have presented the first ALICE physics results from Pb-Pb collisions at the LHC.

- The highest ever reached charged-particle multiplicity was measured, suggesting that a system with an energy density at least three times higher than at RHIC energies is produced.
- The volume of the particle emitting source is found to be twice larger than at RHIC energies.
- The collision-centrality dependence of the particle multiplicity tends to flatten towards most central collisions, suggesting that some kind of saturation mechanism is at play for the initial-state gluon fields in the colliding nuclei.
- The produced hadrons exhibit a strong collective flow, in agreement with the hydrodynamic models in which the system expands similarly to a liquid with very small viscosity.

- High-momentum particle production shows a suppression by a factor of 5–7, close to that observed at lower energy in the same momentum range, suggesting that the medium opaqueness to hard partons is higher at the LHC.

The study of these observables for many species of identified particles (baryons, strange, heavy-flavour particles, charmonia) is well advanced and opens the path for a detailed characterization of the Quark-Gluon Plasma state produced in the highest-energy nuclear collisions at the LHC.

REFERENCES

- [1] AAMODT K. *et al.* (ALICE COLLABORATION), *J. Instrum.*, **3** (2008) S08002.
- [2] ALESSANDRO B. *et al.* (ALICE COLLABORATION), *J. Phys. G*, **32** (2006) 1295.
- [3] CARMINATI F. *et al.* (ALICE COLLABORATION), *J. Phys. G*, **30** (2004) 1517.
- [4] KARSCH F., *Nucl. Phys. A*, **698** (2002) 199.
- [5] AAMODT K. *et al.* (ALICE COLLABORATION), *Phys. Rev. Lett.*, **105** (2010) 252301, arXiv:1011.3916 [nucl-ex].
- [6] AAMODT K. *et al.* (ALICE COLLABORATION), *Phys. Rev. Lett.*, **106** (2011) 032301, arXiv:1012.1657 [nucl-ex].
- [7] AAMODT K. *et al.* (ALICE COLLABORATION), *Phys. Rev. Lett.*, **105** (2010) 252302, arXiv:1011.3914 [nucl-ex].
- [8] AAMODT K. *et al.* (ALICE COLLABORATION), *Phys. Lett. B*, **696** (2011) 328, arXiv:1012.4035 [nucl-ex].
- [9] AAMODT K. *et al.* (ALICE COLLABORATION), *Phys. Lett. B*, **696** (2011) 30, arXiv:1012.1004 [nucl-ex].
- [10] ALVER B. *et al.*, (2008) arXiv:0805.4411 [nucl-ex].
- [11] MILLER M. L. *et al.*, *Annu. Rev. Nucl. Part. Sci.*, **57** (2007) 205, arXiv:0701025[nucl-ex].
- [12] ADLER S. S. *et al.* (PHENIX COLLABORATION), *Phys. Rev. C*, **71** (2005) 034908, arXiv:0409015 [nucl-ex].
- [13] *XXII International Conference on Ultra-relativistic Nucleus–Nucleus Collisions (Quark Matter) Annecy (France), May 23–28, 2011*, <http://qm2011.in2p3.fr>.

SESSION IV - FLAVOUR PHYSICS, CP VIOLATION AND RARE DECAYS

<i>Vincent Tisserand</i>	Recent results from BABAR
<i>Jonathan Lewis</i>	CP violation and suppressed B_s decays at CDF
<i>Chih-Hsiang Cheng</i>	Charmless B decays in B -factories
<i>Andreas Crivellin</i>	Chiral enhancement in the MSSM — An overview
<i>Victor Novikov</i>	Comments on CPT
<i>David Straub</i>	New physics searches in flavour physics
<i>Spasimir Balev</i>	New results on K physics from NA48 and NA62 experiments
<i>Salvatore Fiore</i>	The KLOE-2 project at the DAΦNE accelerator upgraded in luminosity
<i>Marjorie Corcoran</i>	CP violation and rare B_s decays at the Tevatron
<i>Olivier Leroy</i>	Prospects for CP violation in $B_s^0 \rightarrow J/\psi\phi$ from first LHCb data

Recent results from BABAR

V. TISSERAND on behalf of the BABAR COLLABORATION

*Laboratoire d'Annecy-le-Vieux de Physique des Particules (LAPP), Université de Savoie
CNRS/IN2P3, F-74941 Annecy-Le-Vieux, France*

(ricevuto il 29 Settembre 2011; pubblicato online il 19 Gennaio 2012)

Summary. — We present recent results on bottomonium spectroscopy, rare neutral D mesons decays, and semi-leptonic B_s mesons decays. They are based on datasets collected at the $\Upsilon(2S)$, $\Upsilon(3S)$, and $\Upsilon(4S)$ resonances and slightly below and above (up to twice the Λ_b mass) by the BABAR detector at the PEP-II storage rings at SLAC from year 2000 to 2008. All the results presented here are preliminary. A search of $\eta_b(1S)$ and $\eta_b(2S)$ quarkonia is performed in radiative transitions using an experimental technique employing converted γ rays in the $\Upsilon(2S)$ and $\Upsilon(3S)$ decays. The $h_b(1P)$ state is searched in the $\Upsilon(3S) \rightarrow h_b(1P)\pi^0/\pi^+\pi^-$ decays, and an evidence of signal is seen in the channel with a neutral pion. A search of the rare FCNC $D^0 \rightarrow \gamma\gamma$ decay is presented and the channel $D^0 \rightarrow \pi^0\pi^0$ is accurately measured. Finally, we present a study of the semi-leptonic branching ratio of the B_s mesons and of the f_s fraction, the production of B_s mesons. It is based on the very last BABAR dataset collected in 2008 and corresponding to an energy scan above the $\Upsilon(4S)$ resonances performed at PEP-II.

PACS 14.40.Pq – Heavy quarkonia.

PACS 14.40.Lb – Charmed mesons.

PACS 13.20.He – Decays of bottom mesons.

1. – Bottomonium spectroscopy

1.1. Introduction. – The bottomonium spectroscopy bellow the $B\bar{B}$ mass threshold is somewhat richer than in the case of charmonium state [1, 2], bellow the $D\bar{D}$ mass threshold. The measurement of the bottomonium mass states and of the branching ratios (\mathcal{B}) are important tests of the heavy $q\bar{q}$ potential models and set constrains on lattice QCD, as well as on theories such as pNRQCD. Hadronic transitions probe non-perturbative QCD. While bottomonium states with quantum numbers $L = 0, 1$ and $S = 1$ have been observed and abundantly studied since 1977, not all the predicted states are yet observed. In particular no spin singlet have been observed until 2008 [3]. The first D -wave state $\Upsilon(1D_{J=2})$ has only been observed in 2004 by CLEO, in the transition $\gamma\gamma\Upsilon(1S)$ and latter on in 2010 by BABAR, in the channel $\pi^+\pi^-\Upsilon(1S)$ [4].

At the end of its operation in 2008, the BABAR experiment collected large datasets of approximately 120M $\Upsilon(3S)$ and 100M $\Upsilon(2S)$ events, creating renewed possibilities for probes on bottomonium system. We present herein a study of the $\Upsilon(2S)$ and

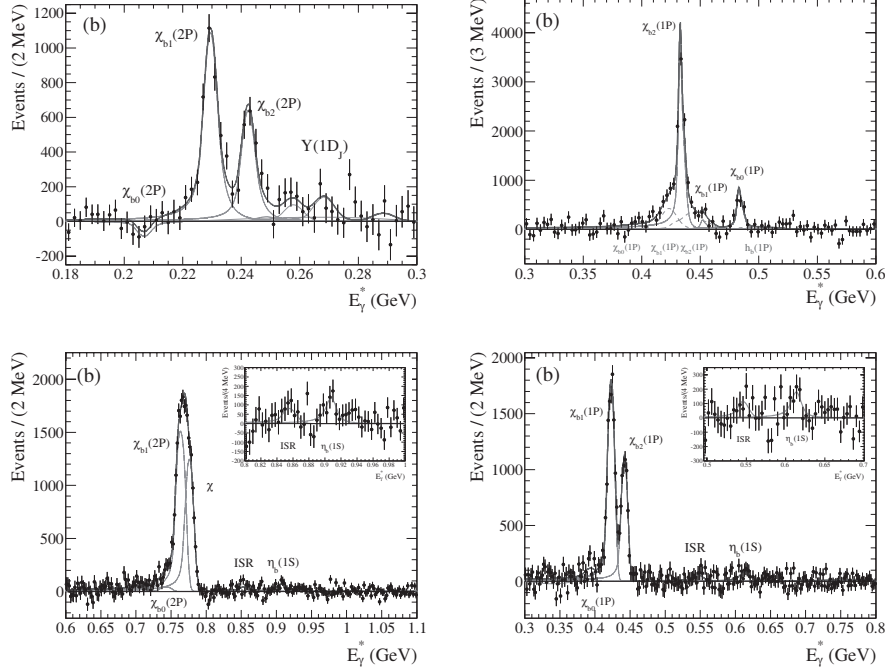


Fig. 1. – Fit to the E_γ^* spectrum in the $\Upsilon(3S)$ and $\Upsilon(2S)$ data. $\Upsilon(3S)$ top left: [180, 300] MeV, top right: [300, 600] MeV, and [600, 1100] MeV. $\Upsilon(2S)$ bottom right: [300, 800] MeV.

$\Upsilon(3S)$ inclusive converted photon spectrum, and the search for the $h_b(1P)$ state in both $\Upsilon(3S) \rightarrow \pi^0 h_b(1P)[\eta_b(1S)\gamma]$ and $\pi^+\pi^- h_b(1P)$.

1.2. Radiative transitions using converted γ rays. – Following the success encountered in the observation of the $\eta_b(1S)$ state in radiative decays of the $\Upsilon(3S)$ and $\Upsilon(2S)$ events [3], the BABAR Collaboration has recently developed a technique to study the inclusive converted photon spectrum of these events. The details of the analysis can be found in ref. [5] (see also references therein for previous and alternate measurements). The monochromatic γ rays radiated in the bottomonium transitions are reconstructed through the converted e^+e^- pair produced in the material of the Silicon Vertex Tracker (SVT) [6] and whose charged track trajectories are bent in the magnetic field of the axial 1.5 T solenoid. This technique improves substantially the mass spectrum resolution (E_γ^*) with respect to the photons reconstructed in the Electro-Magnetic Calorimeter (EMC) (typically from 25 down to 5 MeV/ c^2). This accurate measurement helps to resolve overlapping resonances γ rays. The price to pay is a relatively lower efficiency ($\sim 1/20$) as the material budget of the BABAR tracking system is quite limited [6].

The various monochromatic γ rays are studied with χ^2 fits to the recoil E_γ^* spectrum in the $\Upsilon(3S)$ and $\Upsilon(2S)$ events after subtraction of the combinatoric background. The γ spectra presented in fig. 1 display the rich phenomenology accessible. In these spectra we study the decays: $\Upsilon(3S)/\Upsilon(2S) \rightarrow \gamma\eta_b(1S)$ and possibly $\Upsilon(3S) \rightarrow \gamma\eta_b(2S)$. It offers an alternate search for the states $\eta_b(1S, 2S)$ and possibly a more accurate mass measurement. In addition to the combinatoric background coming from $e^+e^-(\sqrt{s} = m_{\Upsilon(nS)}) \rightarrow \gamma_{ISR}\Upsilon(1S)$

transitions can more easily be unfolded and also one can study accurately the decays: $\chi_{bJ}(1P, 2P) \rightarrow \gamma\Upsilon(1S)$, $\chi_{bJ}(2P) \rightarrow \gamma\Upsilon(2S)$, and $\Upsilon(3S) \rightarrow \gamma\chi_{bJ}(1P)$. The recoil E_γ^* spectra are divided in 4 energy ranges; for $\Upsilon(3S)$ “low”: [180, 300] MeV, “medium”: [300, 600] MeV, and “high”: [600, 1100] MeV and for $\Upsilon(2S)$: [300, 800] MeV.

In the “low” $\Upsilon(3S)$ region we observe the transitions $\chi_{b1,2}(2P) \rightarrow \gamma\Upsilon(2S)$ with more than 12 and 8 statistical standard deviations, while the $\chi_{b0}(2P) \rightarrow \gamma\Upsilon(2S)$ is not seen. It is consistent with previous works by CLEO and CUSB (1992) (see refs. in [5]) and our measurements are more precise.

In the “medium” $\Upsilon(3S)$ region we observe the transitions $\Upsilon(3S) \rightarrow \gamma\chi_{b0,2}(1P)$ with more than 7 and 15 statistical standard deviations, while the $\Upsilon(3S) \rightarrow \gamma\chi_{b1}(1P)$ is not seen. This work is in agreement with recent measurements performed by CLEO [7]. An upper limit $\mathcal{B}(\Upsilon(3S) \rightarrow \gamma\eta_b(2S)) < 1.9 \times 10^{-3}$ is set at 90% CL, for a scan of the resonance in the narrow range: $335 < E_\gamma^* < 375$ MeV.

In the “high” $\Upsilon(3S)$ region we observe the transitions $\chi_{b1,2}(2P) \rightarrow \gamma\Upsilon(1S)$ with a much better accuracy than CLEO and CUSB, and confirm an absence of observation of the $\chi_{b0}(2P) \rightarrow \gamma\Upsilon(1S)$. For the $\eta_b(1S)$ state a 2.9 statistical standard deviation signal is seen (respectively 2.7 when including systematic uncertainties that are dominated by width assumption for the signal). The fitted mass of the quarkonium state is $(9403.6 \pm 2.8 \pm 0.9)$ MeV/ c^2 and is inconsistent with the PDG average by about 3.1σ deviations [2]. The measured $\mathcal{B}(\Upsilon(3S) \rightarrow \gamma\eta_b(1S)) = (5.9 \pm 1.6_{-1.6}^{+1.4}) \times 10^{-4}$ is however consistent with previous measurements [3].

Finally, for the $\Upsilon(2S)$ data spectrum one observes the transitions $\chi_{b1,2}(1P) \rightarrow \gamma\Upsilon(1S)$ with a much better accuracy than CLEO and CUSB, and confirms an absence of observation of the $\chi_{b0}(1P) \rightarrow \gamma\Upsilon(1S)$. For the $\eta_b(1S)$ state a non significant 1.7 statistical standard deviation signal when including systematic uncertainties is obtained (2.5σ for statistics only). The fitted mass of the quarkonium state is nevertheless fairly consistent with the PDG average [2]. One sets the upper limit: $\mathcal{B}(\Upsilon(2S) \rightarrow \gamma\eta_b(1S)) < 0.22\%$ at 90% of CL.

The results of that analysis [5] are the best $\mathcal{B}(\chi_{bJ}(nP) \rightarrow \gamma\Upsilon(1S, 2S))$ available measurements and in good agreement with theory predictions [8]. We have the most accurate measurements of the transitions $\Upsilon(3S) \rightarrow \gamma\chi_{b0,2}(1P)$ and we don’t observe the $\chi_{b1}(1P)$. This is inconsistent with any theory prediction but this is in good agreement with CLEO [7]. Unfortunately very few concluding informations are derived for the $\eta_b(1S, 2S)$ states as initially hoped.

1.3. Search for $\Upsilon(3S) \rightarrow \pi^0 h_b(1P)$ and $\pi^+\pi^- h_b(1P)$ transitions. – The $h_b(1P)$ bottomonium state is the axial vector partner of the three *P-wave* $\chi_{bJ}(1P)$ states and its mass is expected to be at the center of gravity of their masses: $m_{h_b(1P)} = \Sigma_J[(2J+1) \times m_{\chi_{bJ}(1P)}] / \Sigma_J(2J+1) = (9900 \pm \mathcal{O}(3))$ MeV/ c^2 .

The predicted production mechanisms in $\Upsilon(3S)$ decays are $\mathcal{B}(\Upsilon(3S) \rightarrow \pi^0 h_b(1P)) \sim 10^{-3}$ and $\mathcal{B}(\Upsilon(3S) \rightarrow \pi^+\pi^- h_b(1P)) \sim 10^{-5} - 10^{-3}$. Such predictions lead to a relative ratio of branching ratios of the 2 decay modes ($\pi^0/\pi^+\pi^-$) ranging from 5 to 20% [9]. The $\Upsilon(3S) \rightarrow \gamma h_b(1P)$ decay is forbidden by *C*-parity.

The expected $h_b(1P)$ decay width is less than 1 MeV. The particle decays to 3 gluons ($\sim 57\%$) or to 2 gluons plus a photon ($\sim 2\%$), and for 40–50% of the time, to $\gamma\eta_b(1P)$. The latter mode offer an experimental signature that helps to reduce the background and that can be compared to the technique that was employed by CLEO in 2005 and latter on by BES in 2010 to observe the charmonium state h_c in the decay $\psi(2S) \rightarrow \pi^0 h_c[\gamma\eta_c]$. More recently CLEO-c [10] measured the decay $e^+e^- \rightarrow \pi^+\pi^- h_c$.

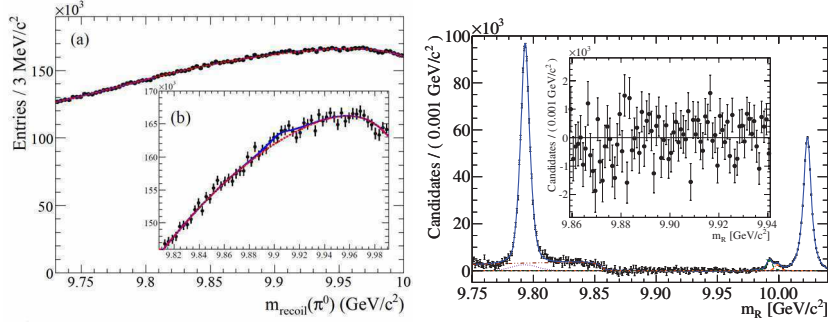


Fig. 2. – Fitted recoil mass spectra for $\Upsilon(3S) \rightarrow \pi^0 h_b(1P)$ (left) and $\Upsilon(3S) \rightarrow \pi^+ \pi^- h_b(1P)$ (right). The right-hand side plot is displayed after that the fitted combinatoric background has been subtracted.

The existing information for the branching ratios are: $\mathcal{B}(\Upsilon(3S) \rightarrow \pi^+ \pi^- h_b(1P)) < 1.8 \times 10^{-3}$ and $\mathcal{B}(\Upsilon(3S) \rightarrow \pi^0 h_b(1P)) < 2.7 \times 10^{-3}$ at 90% CL [2]. At this conference R. Mizuk [11], for the BELLE Collaboration, has presented the first observation of the $h_b(1P)$ and $h_b(2P)$ states in $\Upsilon(5S) \rightarrow \pi^+ \pi^- h_b(1P, 2P)$ transitions.

We perform the search in the 2 channels $\Upsilon(3S) \rightarrow \pi^0 h_b(1P)$ [12] and $\Upsilon(3S) \rightarrow \pi^+ \pi^- h_b(1P)$ [13].

The $\Upsilon(3S) \rightarrow \pi^0 h_b(1P)$ channel is reconstructed by requiring a photon with an energy E_γ^* consistent with the transition $h_b(1P) \rightarrow \gamma \eta_b(1P)$ ([420, 540] MeV). Additional selection criteria are applied. They are based on the number of tracks, event shape, and we veto photons matching π^0 . The global signal efficiency is about 16%. The number of signal event is extracted from fits to the distribution of the mass recoiling against the pion system in the $\Upsilon(3S)$ rest frame and in a mass region near the predicted $h_b(1P)$ mass (9.9 GeV/c²). The recoil mass window comprises 90 bins of 3 MeV/c² width each. Very precise fits to photon pairs are performed and account for accurate effects from re-weighted Monte Carlo simulation to data (the signal region is excluded in the procedure). The average reduced χ^2 of the fit presented in fig. 2 (left) is 0.98 ± 0.03 .

The fit to the recoil mass spectrum yields $9145 \pm 2804 \pm 1082$ signal events. This is an evidence for the signal at the level of 3.0 standard deviations and this number includes all the sources of uncertainties (statistical and systematic). The systematic uncertainties are dominated by the background and signal line shape models and the $m(\gamma\gamma)$ fits. The above signal significance is slightly higher (3.2σ) when the systematic uncertainties contributions are omitted. The mass of the $h_b(1P)$ signal is $(9902 \pm 4 \pm 1)$ MeV/c² and is fully compatible with an expected value as the centre of gravity of the $\chi_{bJ}(1P)$ states.

When assuming $\mathcal{B}(h_b(1P) \rightarrow \gamma \eta_b(1P)) = (45 \pm 5)\%$, we measure $\mathcal{B}(\Upsilon(3S) \rightarrow \pi^0 h_b(1P)) = (3.7 \pm 1.1 \pm 0.4) \times 10^{-4}$. We also set the upper limit to be 5.8×10^{-4} at 90% CL. It is fully consistent with the prediction by Voloshin [9] and coherent the previous limits.

The $\Upsilon(3S) \rightarrow \pi^+ \pi^- h_b(1P)$ channel is reconstructed by requiring a pair of positively-charged track as the dipion pair. Additional criteria are applied. They are based on the event energy and shape, the number of tracks, and we also veto mainly $K_S^0 \rightarrow \pi^+ \pi^-$ decays and we reduce the also less worrying baryon decay $\Lambda \rightarrow p \pi^-$ and converted γ to a $e^+ e^-$ pair. The global signal efficiency is about 42%. Here also a search of a signal peak near 9.9 GeV/c² is performed by fitting the recoil mass against the dipion system.

The signal resolution is expected to be of the order of $9 \text{ MeV}/c^2$.

The fit of the subtracted combinatoric background spectrum is displayed in fig. 2 (right). A 1D χ^2 fit is performed to extract the signal and it comprises 7 components: the $h_b(1P)$ signal, the $\Upsilon(3S) \rightarrow \pi^+\pi^-\Upsilon(2S)$ transition at the $\Upsilon(2S)$ mass, the $\Upsilon(2S) \rightarrow \pi\pi\Upsilon(1S)$ contribution slightly below $9.8 \text{ GeV}/c^2$, the $\chi_{b1,2}(2P) \rightarrow \pi^+\pi^-\chi_{b1,2}(1P)$, the remaining $K_S^0 \rightarrow \pi^+\pi^-$ pollution, and the non-peaking background (including ISR $e^+e^- \rightarrow \pi^+\pi^-\Upsilon(1S)$). No signal is seen. The fit yields a negative number of signal events: -1106 ± 2432 (statistical uncertainty only is included here). This leads to the upper limit: $\mathcal{B}(\Upsilon(3S) \rightarrow \pi^+\pi^-h_b(1P)) < 1.2 \times 10^{-4}$ at 90% CL. The maximum significance over the scanned range is 2 standard deviations at most. The systematic uncertainties are dominated by the decay knowledge in the simulation for the charmless mesons and by the continuum model and residual K_S^0 and ISR backgrounds.

We also extract the branching ratios of the transitions $\Upsilon(3S) \rightarrow X(\chi_{bJ}(2P) \rightarrow \pi^+\pi^-\chi_{bJ'}(1P))$, where $J = J'$ and are equal to 1 or 2. We measure: $\mathcal{B}(J = J' = 1 \text{ or } 2) = (1.16 \pm 0.07 \pm 0.12) \times 10^{-3}$ or $(0.64 \pm 0.05 \pm 0.08) \times 10^{-3}$. And we improve the PDG [2] accuracy for the $\mathcal{B}(\Upsilon(3S) \rightarrow \pi^+\pi^-\Upsilon(2S))$ and $\mathcal{B}(\Upsilon(3S) \rightarrow X(\Upsilon(2S) \rightarrow \pi^+\pi^-\Upsilon(1S)))$ decays. We measure respectively: $(3.00 \pm 0.02 \pm 0.14)\%$ and $(1.78 \pm 0.02 \pm 0.11)\%$.

Finally it is possible to estimate the ratio of branching ratios $\mathcal{B}(\Upsilon(3S) \rightarrow \pi^0 h_b(1P))$ over $\mathcal{B}(\Upsilon(3S) \rightarrow \pi^+\pi^-h_b(1P))$ from the above measurements. It is higher than 3.7–5.8 and so far consistent with predictions from theory [9].

2. – Rare $D^0 \rightarrow \gamma\gamma$ and $D^0 \rightarrow \pi^0\pi^0$ decays

In the Standard Model (SM) Flavor Changing Neutral Currents (FCNC) are forbidden at tree level. These decays are allowed at higher order and have been measured in kaons and B mesons. For charm mesons the low mass of the down-type companion quark introduces a large suppression at the 1-loop level from the GIM mechanism. So far no FCNC decays of charm mesons have been observed. The search of rare charmed meson decay such as $D^0 \rightarrow \gamma\gamma$ is one possible way to perform that search.

In the SM the process $D^0 \rightarrow \gamma\gamma$ is dominated by long distance effects [14]. At short range mainly 2-loops contribute and the branching ratio \mathcal{B} of $D^0 \rightarrow \gamma\gamma$ is expected to be of the order of 3×10^{-11} . This is several orders of magnitude below the sensitivity of current experiments. But in fact, the transition $D^0 \rightarrow \gamma\gamma$ is dominated by Vector Meson Dominance processes (VMD), so that the value of $\mathcal{B}(D^0 \rightarrow \gamma\gamma)$ is enhanced to $(3.5_{-2.6}^{+4.0}) \times 10^{-8}$. This larger value is confirmed in the $HQ\chi PT$ computations that predict $\mathcal{B}(D^0 \rightarrow \gamma\gamma) = (1.0 \pm 0.5) \times 10^{-8}$.

Such small values are anyhow still a bit far away from experimental capacities. But possible large enhancements arising from long distance New Physics (NP) effects are such that they can lead to values as large as 6×10^{-6} for $\mathcal{B}(D^0 \rightarrow \gamma\gamma)$. This is in fact within the reach of present experiments at B-factories. Such effects may for example originate from gluino-exchange within the MSSM framework [15].

The BABAR experiment with about 470 fb^{-1} of data collected near the $\Upsilon(4S)$ resonance has such a discovery potential. This integrated luminosity corresponds to more than 610×10^6 $c\bar{c}$ quark pairs. The search of the process $D^0 \rightarrow \gamma\gamma$ is therefore an appealing, even difficult, mode for NP search. BABAR has effected such an analysis.

The existing upper limit on $\mathcal{B}(D^0 \rightarrow \gamma\gamma)$ is 2.7×10^{-5} at 90% CL [2] and was obtained by the CLEO experiment [16]. The measurement of that branching ratio is normalized to the abundant, pure and precisely measured channel $D^0 \rightarrow K_S^0\pi^0$, whose branching ratio is equal to $(1.22 \pm 0.5) \times 10^{-2}$ [2]. When employing that technique some systematic

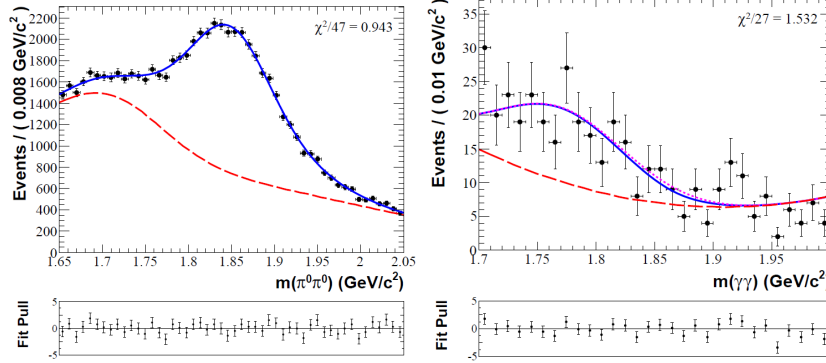


Fig. 3. – (Colour online) Fitted mass spectra of the $D^0 \rightarrow \pi^0\pi^0$ (left) and $D^0 \rightarrow \gamma\gamma$ (right) signals. The dots with error bars are the data. On top we superimpose with the long dashed red curve the fitted combinatorial background component, the signal is shown with the solid blue line. In the case of the $\gamma\gamma$ analysis the signal is fitted together with the $D^0 \rightarrow \pi^0\pi^0$ background component which results in a negative signal (small dash purple curve). The fit is determined from unbinned maximum likelihood but the χ^2 value is determined from binned data and is provided as goodness-of-fit measure. The pull distributions show the differences between the data and the solid blue curve above with values and uncertainties normalized to the Poisson statistics.

uncertainties cancel in the ratio of branching ratio.

The largest background for $D^0 \rightarrow \gamma\gamma$ channel is the decay mode $D^0 \rightarrow \pi^0\pi^0$. Is presently measured \mathcal{B} is equal to $(8.0 \pm 0.8) \times 10^{-4}$ [2]. We also perform similarly the measurement of that latter channel using the normalization technique to the $D^0 \rightarrow K_S^0\pi^0$. Doing that measurement at the same time allows to have a better handling of the $D^0 \rightarrow \pi^0\pi^0$ background for the search of the $D^0 \rightarrow \gamma\gamma$ mode. The main backgrounds for $D^0 \rightarrow \pi^0\pi^0$ are the modes $D^0 \rightarrow K^0/\bar{K}^0\pi^0$ and $K^-\pi^+\pi^0$.

In order to remove $B\bar{B}$ backgrounds, we use $D^{*+} \rightarrow D^0\pi^+$ tagged events and require $P_{D^*} > 2.4 - 2.85 \text{ GeV}/c^2$. We remove QED background by requiring at least 4 tracks or neutrals within the BABAR detector acceptance. The channels $D^{*0} \rightarrow D^0\pi^0/\gamma$ are the largest backgrounds for the normalization channel $D^0 \rightarrow K_S^0\pi^0$. Finally in the case of the $\gamma\gamma$ analysis, we perform a veto against photons that can be associated to another photon in the event to build a π^0 candidate. Such a veto is 66% efficient on D^0 signal and removes 95% of the photons originated from π^0 .

For the $D^0 \rightarrow \pi^0\pi^0$ analysis the selection efficiencies of the $D^0 \rightarrow \pi^0\pi^0$ signal is 15.2% and it is 12.0% for the normalization channel $D^0 \rightarrow K_S^0\pi^0$. For the $D^0 \rightarrow \gamma\gamma$ analysis the selection efficiencies of the $D^0 \rightarrow \gamma\gamma$ signal is 6.1% and it is 7.6% for the normalization channel $D^0 \rightarrow K_S^0\pi^0$.

Figure 3 shows the fitted spectra of the $D^0 \rightarrow \pi^0\pi^0$ (left) and $D^0 \rightarrow \gamma\gamma$ (right) signals.

The $\pi^0\pi^0$ analysis fitted yield is 26010 ± 304 signal events, while for the normalization channel $K_S^0\pi^0$ the yield is 103859 ± 392 events. This corresponds to $\mathcal{B}(D^0 \rightarrow \pi^0\pi^0) = (8.4 \pm 0.1 \pm 0.4 \pm 0.3) \times 10^{-4}$, where the third uncertainty is related to uncertainty on the world average for $\mathcal{B}(D^0 \rightarrow K_S^0\pi^0)$ [2]. This measurement is 40% more accurate than the present world average value.

For the $\gamma\gamma$ analysis the fit yields a negative number: -6 ± 15 events. It corresponds to an upper limit of 25.1 events at 90% CL. This number converts into an upper limit,

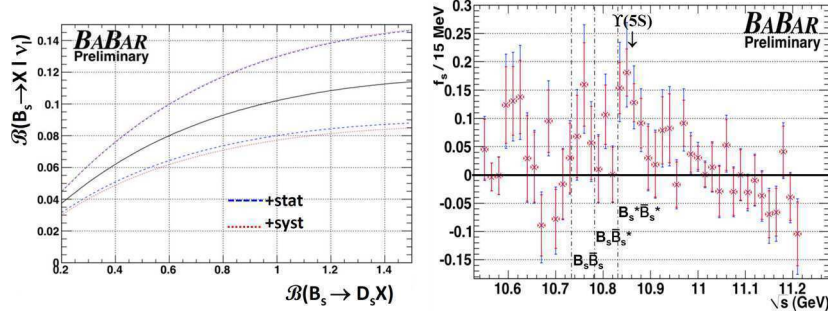


Fig. 4. – Fitted value of $\mathcal{B}(B_s)_{SL}$ with respect to $\mathcal{B}(B_s \rightarrow D_s X)$ (left) and of f_s versus the value of the center-of-mass energy of the 2008 BABAR scan (right) [20]. The statistical and additional systematic uncertainties are plotted separately.

computed from pseudo Monte Carlo experiments. That computation includes systematic uncertainties. We set the upper limit: $\mathcal{B}(D^0 \rightarrow \gamma\gamma) < 2.4 \times 10^{-6}$ at 90% CL ($< 2.06 \times 10^{-6}$ without systematic uncertainties). Such a value is already constraining specific NP models [15]. It is an order of magnitude lower than the existing best world limit [16].

3. – Semi-leptonic branching ratio of the B_s mesons and the fraction f_s above the $\Upsilon(4S)$ resonance

As opposed to the semi-leptonic $\mathcal{B}(B_{u,d} \rightarrow X l^- \bar{\nu}_l)$, that are well known and equal to $(10.33\text{--}10.99 \pm 0.28)\%$, the existing measurements of the semi-leptonic branching ratio in B_s decays are still inaccurate [2]. It is expected to be from 1.5 to 3% lower than that of B_d [17]. Its world average is $(7.9 \pm 2.4)\%$, from LEP experiment at the Z^0 and they include the information on the fraction $P(b \rightarrow B_s) = (10.5 \pm 0.9)\%$. The alternate measurement $(10.2 \pm 0.8 \pm 0.9)\%$ is from the $\Upsilon(5S)$ data collected by the BELLE experiment [18]. The LHCb experiment has yet already started to contribute by providing measures of ratios of specific semi-exclusive decays to total inclusive semi-leptonic B_s decay [19].

Recently the BABAR Collaboration has performed the measurement of $\mathcal{B}(B_s \rightarrow X l^- \bar{\nu}_l)$ ($\mathcal{B}(B_s)_{SL}$) and of f_s , the fraction of $B_s^{(*)}$ mesons produced above the $\Upsilon(4S)$ resonance. For this we use 4.1 fb^{-1} of data from a final energy scan performed in the last period of the data taking in 2008 [20]. In that energy scan, data were collected every 5 MeV above the $\Upsilon(4S)$ resonance, from which 3.15 fb^{-1} was taken in the range $[2m_{B_s}, 2m_{\Lambda_B}]$.

These 2 measurements are based on the counting of the yield of produced ϕ mesons and of ϕ mesons produced in correlation with a high-momentum lepton. Such signatures are more abundant in B_s decays than in $B_{u,d}$ decays. As a function of the center of mass energy in the scan, one can unfold the 2 parameters $\mathcal{B}(B_s)_{SL}$ and f_s from the 3 observables: the number of produced B hadrons, the ϕ mesons inclusive rate, and the rate of ϕ mesons produced in correlation with a high-momentum lepton.

The light $q\bar{q}$ ($q = u, s, c$) pair of quarks contribution are subtracted by using data collected 40 MeV below the $\Upsilon(4S)$ resonance. The $B_{u,d}$ contributions are computed from data collected at the $\Upsilon(4S)$ resonance. Many quantities derived from the PDG [2] such as $\mathcal{B}(B_s \rightarrow D_s X)$, $\mathcal{B}(D_s \rightarrow X l^- \bar{\nu}_l)$, $\mathcal{B}(D_s \rightarrow \phi X)$, $\mathcal{B}(D_s \rightarrow \phi X l^- \bar{\nu}_l)$ (...) are exploited in the computation of $\mathcal{B}(B_s)_{SL}$ and f_s from the above enumerated 3 observables. The input $\mathcal{B}(B_s \rightarrow D_s X)$ is from far the less accurately known of the various input parameters. Its

present world average is $(93 \pm 25)\%$.

Figure 4 displays the fitted value of $\mathcal{B}(B_s)_{SL}$ with respect to $\mathcal{B}(B_s \rightarrow D_s X)$ (left) and of f_s versus the value of the center-of-mass energy of the 2008 PEP-II scan (right). We measure $\mathcal{B}(B_s)_{SL} = (9.9^{+2.6}_{-2.1}(\text{stat.})^{+1.3}_{-2.0}(\text{syst.}))\%$. This branching ratio is consistent with previously mentioned measurements. The values of f_s for bins near the $\Upsilon(5S)$ resonance are fully compatible with those obtained by BELLE: $(18.0 \pm 1.3 \pm 3.2)\%$ and CLEO: $(16.8 \pm 2.6^{+6.7}_{-3.4})\%$ in 2007 [21].

* * *

I would like to thank my BABAR colleagues for their help in the preparation of that presentation and their many useful comments and inputs during our discussions.

REFERENCES

- [1] EICHTEN E. *et al.*, *Rev. Mod. Phys.*, **80** (2008) 1161.
- [2] NAKAMURA K. *et al.* (PARTICLE DATA GROUP), *J. Phys. G*, **37** (2010) 07502.
- [3] AUBERT B. *et al.* (THE BABAR COLLABORATION), *Phys. Rev. Lett.*, **101** (2008) 071801; *Phys. Rev. Lett.*, **103** (2009) 161801; BONVICINI G. *et al.* (THE CLEO COLLABORATION), *Phys. Rev. D*, **81** (2010) 031104(R).
- [4] BONVICINI G. *et al.* (THE CLEO COLLABORATION), *Phys. Rev. D*, **70** (2004) 032001; DEL AMO SANCHEZ P. *et al.* (THE BABAR COLLABORATION), *Phys. Rev. D*, **82** (2010) 111102(R).
- [5] LEES J.-P. *et al.* (THE BABAR COLLABORATION), *Phys. Rev. D*, **84** (2011) 072002, arXiv:1104.5254 (2011).
- [6] AUBERT B. *et al.* (THE BABAR COLLABORATION), *Nucl. Instrum. Methods Phys. Res. A*, **479** (2002) 1.
- [7] KORNICER M. *et al.* (THE CLEO COLLABORATION), *Phys. Rev. D*, **83** (2011) 054003.
- [8] KWONG W. and ROSNER J. L., *Phys. Rev. D*, **38** (1988) 279.
- [9] TUAN Y.-P. *et al.*, *Phys. Rev. D*, **37** (1988) 1210, GODFREY S. and ROSNER J. L., *Phys. Rev. D*, **66** (2002) 014012; GODFREY S., *J. Phys. Conf. Ser.*, **9** (2005) 123; VOLOSHIN M. B., *Sov. J. Nucl. Phys.*, **43** (1986) 1011.
- [10] MITCHELL R. E. (FOR THE CLEO-C COLLABORATION), at CHARM 2010, arXiv:1102.3424 (2011).
- [11] MIZUK R. (FOR THE BELLE COLLABORATION), at La Thuile 2011, arXiv:1103.3419 (2011).
- [12] LEES J.-P. *et al.* (THE BABAR COLLABORATION), *Phys. Rev. D*, **84** (2011) 091101(R), arXiv:1102.4565 (2011).
- [13] LEES J.-P. *et al.* (THE BABAR COLLABORATION), *Phys. Rev. D.*, **84** (2011) 011104, arXiv:1105.4234 (2011).
- [14] BURDMAN G. *et al.*, *Phys. Rev. D*, **66** (2002) 014009; FAJFER S., SINGER P. and ZUPAN J., *Phys. Rev. D*, **64** (2001) 074008.
- [15] PRELOWSEK S. and WYLER D., *Phys. Lett. B*, **500** (2001) 304.
- [16] COAN T. E. *et al.* (THE CLEO COLLABORATION), *Phys. Rev. Lett.*, **90** (2003) 101801; RUBIN P. *et al.* (THE CLEO COLLABORATION), *Phys. Rev. Lett.*, **96** (2006) 081802; MENDEZ H. *et al.* (THE CLEO COLLABORATION), *Phys. Rev. D*, **81** (2010) 052013.
- [17] BIGI I. I., MANNEL T. and URALTSEV N., arXiv:1105.4574 (2011).
- [18] DRUTSKOY A. (FOR THE BELLE COLLABORATION), at EPS07 and LP07, arXiv:0710.2548 (2007).
- [19] AAJJ R. *et al.* (THE LHCb COLLABORATION), *Phys. Lett. B*, **698** (2011) 14.
- [20] AUBERT B. *et al.* (THE BABAR COLLABORATION), *Phys. Rev. Lett.*, **101** (2008) 012001.
- [21] DRUTSKOY A. *et al.* (THE BELLE COLLABORATION), *Phys. Rev. Lett.*, **98** (2007) 052001; HUANG G. S. *et al.* (THE CLEO COLLABORATION), *Phys. Rev. D*, **75** (2007) 012002.

CP violation and suppressed B_s decays at CDF

J. D. LEWIS

Fermi National Accelerator Laboratory - Batavia, IL, USA

(ricevuto il 29 Settembre 2011; pubblicato online il 26 Gennaio 2012)

Summary. — The study of heavy-quark decays continues to have wide interest as a possible avenue for the discovery of physics beyond the standard model. With data samples as large as 6 fb^{-1} , the CDF Collaboration is exploring new channels that will extend the reach of measurements in probing the CKM mechanism of *CP* violation. Several new measurements are presented.

PACS 12.15.Ff – Quark and lepton masses and mixing.

PACS 14.40.Lb – Charmed mesons ($|C| > 0$, $B = 0$).

PACS 14.40.Nd – Bottom mesons ($|B| > 0$).

1. – Measurement of the branching fraction of $B_s^0 \rightarrow J/\psi f_0(980)$

Because the standard model phase is predicted to be small in B_s mixing [1], the study of B_s decays remains an important avenue to search for indications of new physics. Thus far measurements have been restricted to the decay mode $B_s^0 \rightarrow J/\psi \phi$, $\phi \rightarrow K^+ K^-$ [2,3] which not only requires tagging the flavor of the b quark at production, but also requires an angular analysis to disentangle the contributions of the *CP* even and odd contributions in the decay to two vector mesons. These fits over decay-time and angular variables can also yield measurements of the difference in the lifetimes of the two B_s eigenstates. The decay mode $B_s^0 \rightarrow J/\psi f_0(980)$ provides new information in several important ways [4]. Because the f_0 is a scalar, this decay mode can be used to study *CP* violation without the need of an angular analysis. Also, the suppressed decay $B_s^0 \rightarrow J/\psi f_0(980)$, $f_0(980) \rightarrow K^+ K^-$ may yield an *S*-wave contribution that would pollute the fit in $J/\psi \phi$ analysis. Finally, as a pure *CP* = -1 decay, $B_s^0 \rightarrow J/\psi f_0(980)$ can provide a direct measurement of $1/\Gamma_H$, the lifetime of the heavier B_s mass eigenstate.

A convenient way to normalize the branching fraction is to measure it relative to the more copious $B_s^0 \rightarrow J/\psi \phi$ decay mode:

$$(1) \quad R_{f_0/\phi} = \frac{\mathcal{B}(B_s^0 \rightarrow J/\psi f_0(980))}{\mathcal{B}(B_s^0 \rightarrow J/\psi \phi)} \frac{\mathcal{B}(f_0(980) \rightarrow \pi^+ \pi^-)}{\mathcal{B}(\phi \rightarrow K^+ K^-)},$$

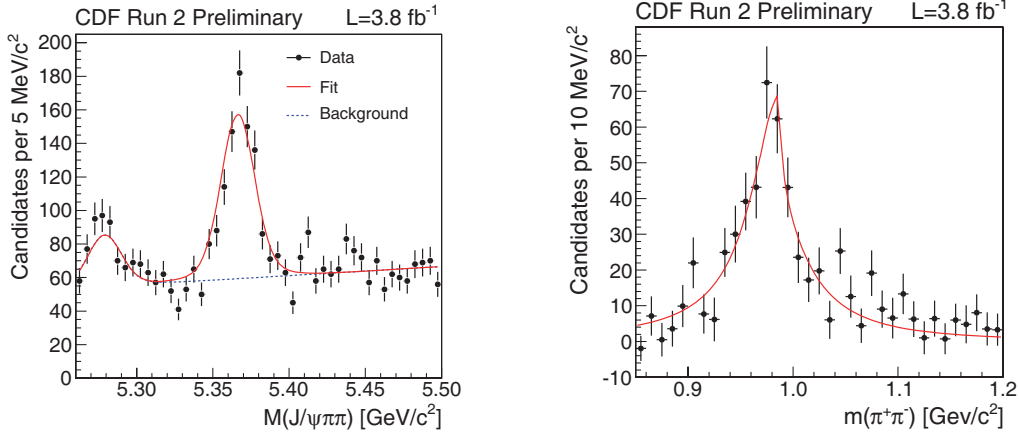


Fig. 1. – Fit of the mass distribution for the yield of $B_s^0 \rightarrow J/\psi f_0(980), f_0 \rightarrow \pi^+ \pi^-$.

which is predicted to be in the range 0.1 to 0.5 [4-6]. LHCb has recently reported the first observation of this decay mode with a significance exceeding 12σ and measured $R_{f_0/\phi} = 0.252^{+0.046+0.027}_{-0.032-0.033}$ [7]. Belle has also observed the decay in data taken at the $\Upsilon(5S)$ resonance at found $\mathcal{B}(B_s^0 \rightarrow J/\psi f_0(980), f_0 \rightarrow \pi^+ \pi^-) = (1.16^{+0.31+0.15+0.26}_{-0.19-0.17-0.18}) \times 10^{-4}$ [8].

CDF has searched for the $B_s^0 \rightarrow J/\psi f_0(980), f_0 \rightarrow \pi^+ \pi^-$ in 3.8 fb^{-1} of $p\bar{p}$ collision data and has measured $R_{f_0/\phi}$ with substantially improved precision [9]. The analysis begins with a sample of pairs of opposite-charge muon candidates found in the pseudorapidity range $|\eta| < 1$ with transverse momentum $p_T > 1.5 \text{ GeV}/c$ that are selected by the trigger if they have masses in the range $2.7 < M_{\mu\mu} < 4 \text{ GeV}/c^2$. In a kinematic fit, the pairs are required to originate from a common point and to have a mass consistent with a J/ψ . These J/ψ candidates are then combined with two additional charged-particle tracks that are assumed to be pions. The pion pair must have a mass in the range $0.85 < M_{\pi\pi} < 1.2 \text{ GeV}/c^2$ to be considered as an f_0 candidate, and a kinematic fit of the B candidate is performed. A neural network algorithm (NN) is used to purify the sample. The quantities used include kinematic variables, the displacement and quality of the reconstructed decay point, and quality of the muon identification. Monte Carlo (MC) simulations of $J/\psi f_0(980)$ events are used for the signal in the NN training, while the background is taken from events in the data with a B_s candidate mass in the range $5.45\text{--}5.55 \text{ GeV}/c^2$. The normalization $B_s^0 \rightarrow J/\psi \phi$ sample is identified in a similar way with the substitution of a pair of tracks assumed to be kaons instead of pions. The mass of the KK pair is required to be within $10 \text{ MeV}/c^2$ of the ϕ pole mass. The same NN selection is used for the normalization and signal modes, and the relative efficiency is determined in simulations. In the simulation of the signal, the dipion mass spectrum is modeled using a Flatté distribution using parameters measured by BES [10].

The yield is found using an unbinned maximum likelihood fit for the B candidate mass in the range 5.26 to $5.5 \text{ GeV}/c^2$ which avoids physics backgrounds such as improperly reconstructed $B^0 \rightarrow J/\psi K^{*0}$. Physics backgrounds such as $J/\psi \rho$ decays are included in the fit. The signal shape is two Gaussians with parameters determined in simulations. The mass distribution with a projection of the fit is shown in fig. 1. The yield is 571 ± 37 events in the signal and 2302 ± 49 in the normalization channel. Figure 1 also shows

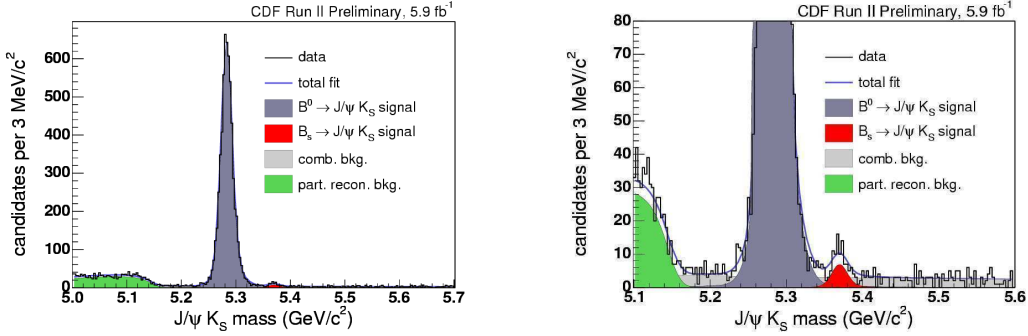


Fig. 2. – Fit of the mass distribution for the yield of $B_s^0 \rightarrow J/\psi K_S^0, K_S^0 \rightarrow \pi^+\pi^-$. The full distribution showing the dominant B^0 peak is shown on the left, while in the zoomed-in view on the right, the B_s^0 signal is visible.

the dipion mass distribution when selecting events consistent with the B_s mass and performing a sideband subtraction. A fit to the Flatté distribution is overlaid, showing that the signal is quite consistent with the f_0 hypothesis. Projections of the helicity angle of the $J/\psi \rightarrow \mu^+\mu^-$ and $f_0 \rightarrow \pi^+\pi^-$ are also consistent with the decay of a pseudoscalar to a vector and a scalar particle. The principal systematic uncertainties are from the relative efficiency, the shape of the background, and the mass resolution scale. When all uncertainties are included the ratio of branching fractions is: $R_{f_0/\phi} = 0.292 \pm 0.020 \pm 0.017$.

2. – Measurement of the branching fraction of $B_s^0 \rightarrow J/\psi K_S^0$

The decay $B_s^0 \rightarrow J/\psi K_S^0$ is also a CP -odd final state and thus has much the same interest as $J/\psi f_0$. However, the former is Cabibbo suppressed; therefore, one expects a ratio of branching fractions

$$(2) \quad R_{K_S^0} = \frac{\mathcal{B}(B_s^0 \rightarrow J/\psi K_S^0)}{\mathcal{B}(B^0 \rightarrow J/\psi K_S^0)} \simeq 0.05.$$

CDF has observed this decay mode [11] in a 5.9fb^{-1} data sample. The principal differences in the experimental technique compared to the $J/\psi f_0$ search are that reconstruction must account for the $K_S^0 \rightarrow \pi^+\pi^-$ decay length, the signal sample is a tail on the mass distribution of the normalization sample, and the relative yield is derived in a single mass fit. The combinatorial background is again suppressed using a NN with a Monte Carlo simulation for the signal sample and data from the upper sideband as the background sample for the training. The MC is also used to derive a signal shape distribution for the fit where the mass peak and a width scale factor are set by the dominant B^0 mode, and the B_s peak uses the same shape parameters with the known [12] mass splitting (see fig. 2).

A binned log-likelihood fit including the combinatorial backgrounds and background from partially reconstructed b hadrons yields $64 \pm 14 B_s^0 \rightarrow J/\psi K_S^0$ decays. To determine the significance, the null hypothesis is tested with the fit repeated without a B_s contribution. The difference in $-2\ln\mathcal{L}$ is interpreted as $\Delta\chi^2$ yielding a probability of background fluctuation of 4×10^{-13} or a significance of 7.2σ . The ratio of yields

$N(B_s^0 \rightarrow J/\psi K_S^0)/N(B^0 \rightarrow J/\psi K_S^0) = 0.0108 \pm 0.0019$ can be multiplied by the ratio of efficiencies found from the MC and the ratio of production abundances of B_s^0 and B^0 to result in $R_{K_S^0} = 0.041 \pm 0.007(\text{stat.}) \pm 0.004(\text{syst.}) \pm 0.005(\text{frag.})$, in good agreement with expectations.

3. – Measurement of the time-integrated mixing parameter $\bar{\chi}$

The measurement in the previous section has a large uncertainty from the fragmentation fraction f_s/f_d , the ratio of production fractions of B_s^0 and B^0 mesons. Several different types of measurements can contribute to the extraction of f_s/f_d : in semileptonic decays, one can assume $SU(3)$ (*e.g.*, $\Gamma(B^+ \rightarrow \bar{D}^0 \mu^+ \nu) = \Gamma(B^0 \rightarrow D^- \mu^+ \nu) = \Gamma(B_s^0 \rightarrow D_s^- \mu^+ \nu)$), and use the yields in various partially reconstructed decay modes to extract the production fractions; with theoretical input on the ratios of branching fractions of decays with similar topology, the yields in exclusive hadronic decays can be used; and the time-average mixing parameter $\bar{\chi} = f_d \chi_d + f_s \chi_s$ provides additional constraints since the mixing parameter χ_d is known from the B factories at the $\Upsilon(4S)$ and $\chi_s \simeq 0.5$ since B_s mixing is nearly maximal.

There is significant tension in existing measurements of $\bar{\chi}$ and f_s/f_d , with the LEP average of $\bar{\chi} = 0.1259 \pm 0.0042$ [13] and a recent measurement from D0 of $\bar{\chi} = 0.132 \pm 0.007 \pm 0.024$ [14], while CDF in Run 1A found $\bar{\chi} = 0.152 \pm 0.007 \pm 0.011$. Similarly, the averages for the relative fractions [15] are $f_s/f_d = 0.363 \pm 0.047$ from Tevatron measurements and $f_s/f_d = 0.256 \pm 0.024$ for measurements taken at the Z . While this difference could be an indication of a difference in the fragmentation properties of b quarks in the two environments, precise measurements from the Tevatron are required to understand if the difference is significant.

$\bar{\chi}$ is measured from the ratio of same-sign to opposite-sign dileptons

$$(3) \quad R = \frac{N(\ell^+ \ell^+) + N(\ell^- \ell^-)}{N(\ell^+ \ell^-)}$$

after correcting for other sources of dileptons such as fakes, charmonium, and sequential $b \rightarrow c \rightarrow \ell$ decays. The new CDF measurement [16] uses a 1.4 fb^{-1} sample of dimuons with $p_T > 3 \text{ GeV}/c$ and $|\eta| < 0.6$ that have traversed about 8 hadronic interaction lengths of material. In addition, to exclude pairs from a single B decay, the pair mass is required to exceed $5 \text{ GeV}/c^2$. Muons can come from several sources: bottom hadron decays, charm hadron decays, or fakes. The fakes in turn can be from prompt particles or from heavy-flavor decays. The different sources can be distinguished statistically on the basis of the impact parameter distribution of the muons. This method has been used previously to measure the correlated $b\bar{b}$ cross section [17]. The analysis uses a two-dimensional binned fit to the distribution of the impact parameters of the two muons. The templates are derived from MC as are constraints on heavy-flavor fakes ($b, c \rightarrow K\pi \rightarrow \mu$). The fake rates for kaons and pions to yield reconstructed muons are derived from $D^0 \rightarrow K^- \pi^+$ decays in an independently triggered data sample.

The event selection for this analysis is significantly more stringent than for the Run 1 measurement with tight cuts on the quality of the track reconstruction in the silicon detector, including the requirement of a hit in the innermost layer which is 1.7 cm from the beam. This last requirement removes a background of tracks with large impact parameter that was not accounted for in earlier fits using the template method. Figure 3 shows projections of the fits onto a single axis for the $\mu^+ \mu^-$, $\mu^+ \mu^+$, and $\mu^- \mu^-$ samples. The raw

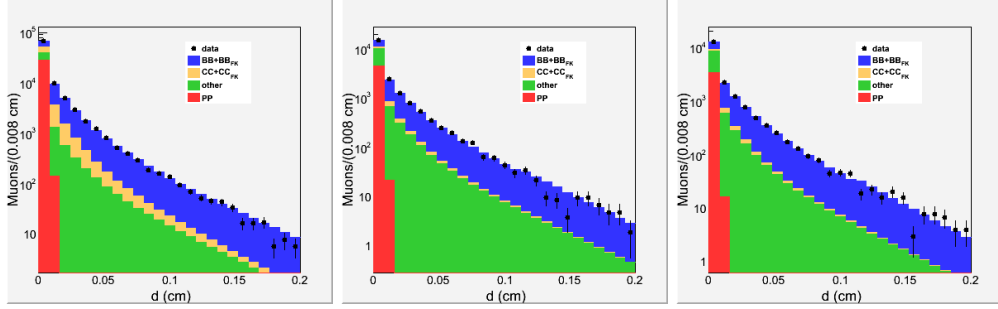


Fig. 3. – Fit of templates to the two-dimensional impact parameter distributions for $\mu^+\mu^-$ (left), $\mu^+\mu^+$ (center), and $\mu^-\mu^-$ (right) events.

value of the asymmetry is $R_{\mu\mu,raw} = 0.472 \pm 0.011 \pm 0.007$ where the dominant systematic uncertainty is due to the fake muon contributions. There are many sources of like-sign dimuons in the $b\bar{b} \rightarrow \mu\mu$ sample including b semileptonic decay, $b \rightarrow c \rightarrow \mu$ sequential decays, $b \rightarrow \psi \rightarrow \mu\mu$ decays, and hadron fakes. Only the first component should be included in the determination of $\bar{\chi}$. MC results are used to correct for the other contributions to yield the final result $\bar{\chi} = 0.126 \pm 0.008$. The systematic uncertainty on the indirect muon contributions in b decays is included in the total uncertainty. This result is now quite close to the LEP and D0 values. While this may hint that the fragmentation process may not be very different in the two environments, better determination of the b baryon fraction will be required to make a definitive statement.

4. – Measurement of branching fractions and CP asymmetries in $B^\pm \rightarrow D^0 h^\pm$ decays

The CKM angle $\gamma = \arg(-V_{ud}V_{ub}^*/V_{cd}V_{cb}^*)$ is the least well-known element of the unitarity triangle and is challenging to determine from experiment. The ADS method [18] is one of several techniques that have been proposed. It takes advantage of the interference between two doubly Cabibbo-suppressed decay chains. In one, a color-allowed $b \rightarrow c + \bar{u}s(d)$ decay is followed by a doubly Cabibbo-suppressed $D^0 \rightarrow K^+\pi^-$ decay, and in the other, a color-suppressed $b \rightarrow u + \bar{c}s(d)$ transition is followed by a Cabibbo-favored $\bar{D}^0 \rightarrow K^+\pi^-$ decay. There are two ADS observables:

$$(4) \quad R_{ADS} = \frac{\mathcal{B}(B^- \rightarrow [K^+\pi^-]_{D^0} K^-) + \mathcal{B}(B^+ \rightarrow [K^-\pi^+]_{D^0} K^+)}{\mathcal{B}(B^- \rightarrow [K^-\pi^+]_{D^0} K^-) + \mathcal{B}(B^+ \rightarrow [K^+\pi^-]_{D^0} K^+)},$$

$$(5) \quad A_{ADS} = \frac{\mathcal{B}(B^- \rightarrow [K^+\pi^-]_{D^0} K^-) - \mathcal{B}(B^+ \rightarrow [K^-\pi^+]_{D^0} K^+)}{\mathcal{B}(B^- \rightarrow [K^+\pi^-]_{D^0} K^-) + \mathcal{B}(B^+ \rightarrow [K^-\pi^+]_{D^0} K^+)}.$$

R_{ADS} is the ratio of fraction of doubly-Cabibbo-suppressed (DCS) decays to Cabibbo-favored (CF) decays, and A_{ADS} is the asymmetry between B^+ and B^- for decays in the DCS modes. The relationship between γ and the observables can be found in ref. [18]. Similar observables are defined with a pion in the final state instead of the kaon.

The CDF analysis [19] uses 5fb^{-1} of data collected with the displaced secondary vertex trigger. The selection is optimized using the CF hypothesis to minimize combinatorial background using cuts on kinematics, candidate isolation, and decay lengths.

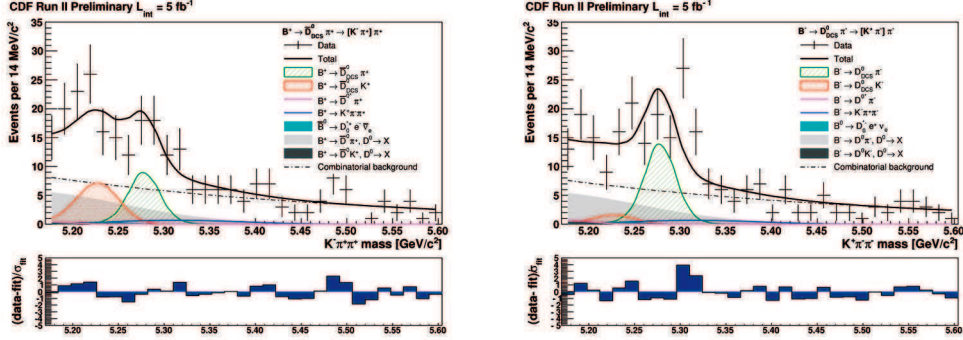


Fig. 4. – Mass distributions of DCS decays $B^+ \rightarrow [K^- \pi^+]_{D^0} h^+$ (left) and $B^- \rightarrow [K^+ \pi^-]_{D^0} h^-$ (right). The curves show projections of the fit that include $D^0 K$ and $D^0 \pi$ signal contribution as well as backgrounds from random combinations and physics sources such as partially reconstructed B decays.

Candidates that are consistent with a D^0 reconstructed both in the CF and DCS mode are rejected. Specific ionization (dE/dx) is used to reject $D^0 \rightarrow \pi^+ \pi^-$ decays. Events are reconstructed according to both the CF and DCS $B^- \rightarrow D^0 \pi^-$ hypotheses. The sample also includes $B^- \rightarrow D^0 K^-$ decays which will populate a secondary peak in the mass distribution shifted below the B mass. The numbers of CF and DCS events in the B^+ and B^- samples are determined in a joint fit over the CF and DCS sets of candidates that includes the candidate ($K\pi\pi$) mass as well as dE/dx to distinguish between $D^0 K$ and $D^0 \pi$ decays. Figure 4 shows the DCS mass distributions with projections of the fit overlaid. The signal shape is common to CF and DCS candidates so there is little uncertainty in the shape for the DCS candidates. The fit includes contributions from combinatorial backgrounds as well as partially reconstructed B decays and other physics backgrounds. The ADS observables are determined directly from the yields after including a small correction for the difference in nuclear interaction probabilities for K^+ and K^- . The observed values are

$$(6) \quad R_{ADS}(K) = 0.022 \pm 0.008 \pm 0.008,$$

$$(7) \quad R_{ADS}(\pi) = 0.0041 \pm 0.0008 \pm 0.0004,$$

$$(8) \quad A_{ADS}(K) = -0.63 \pm 0.40 \pm 0.23,$$

$$(9) \quad A_{ADS}(\pi) = 0.22 \pm 0.18 \pm 0.06.$$

The systematic uncertainties arise from the fit model, physics background, and dE/dx model. These are the first measurements of ADS observables at a hadron collider, and they are consistent and competitive with measurements from Belle [20] and BaBar [21].

5. – Measurement of CP violation in $D^0 \rightarrow \pi^+ \pi^-$ and $D^0 \rightarrow K^+ K^-$ decays

The time-integrated CP -violating asymmetry in the Cabibbo-suppressed decays $D^0 \rightarrow \pi^+ \pi^-$ and $D^0 \rightarrow K^+ K^-$ offers a strong probe for physics beyond the standard model. The B decays $B^0 \rightarrow K^+ K^-$ and $\pi^+ \pi^-$ have large asymmetries because the $b \rightarrow u$ transition as a complex CKM phase at order λ^3 ; however, charm transitions are real up to $O(\lambda^5)$. Therefore, a significant asymmetry would be the result of a new process. The

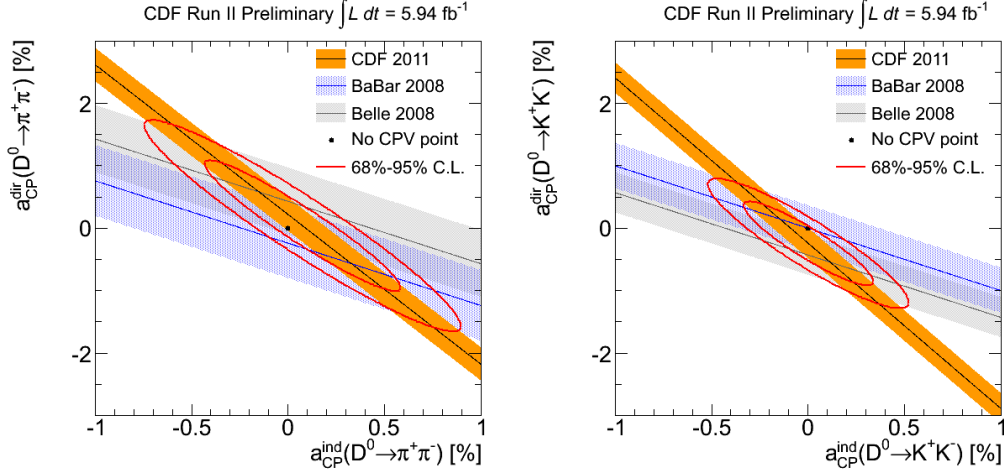


Fig. 5. – Allowed region for a_{CP}^{Indirect} and a_{CP}^{Direct} from CDF for $D^0 \rightarrow \pi^+\pi^-$ (left) and $D^0 \rightarrow K^+K^-$ (right) decays shown in comparison to results from Belle and BaBar. The ellipses show the 68% and 95% CL allowed regions from combining the result.

asymmetry is the difference between the rates of decay of D^0 mesons to a particular final state compared to that for a \bar{D}^0 to the same final state:

$$(10) \quad A_{CP}(D^0 \rightarrow h^+h^-) = \frac{\Gamma(D^0 \rightarrow h^+h^-) - \Gamma(\bar{D}^0 \rightarrow h^+h^-)}{\Gamma(D^0 \rightarrow h^+h^-) + \Gamma(\bar{D}^0 \rightarrow h^+h^-)}.$$

Both direct CP violation and mixing-induced CP violation are possible. Because charm mixing is slow, to first order the time-integrated asymmetry can be expressed as

$$(11) \quad A_{CP} = a_{CP}^{\text{Direct}} + \int_0^\infty A_{CP}(t)D(t)dt \approx a_{CP}^{\text{Direct}} + a_{CP}^{\text{Indirect}} \frac{\langle t \rangle}{\tau},$$

where $D(t)$ is the observed distribution of proper decay times. Therefore, experiments that are sensitive to different regions of proper decay time will have differing sensitivity to the direct and indirect components.

In a 5.9 fb^{-1} sample collected with a displaced-decay trigger, CDF has measured asymmetries in both the KK and $\pi\pi$ channels [22]. The flavor of the D^0 at production is tagged using $D^{*+} \rightarrow D^0\pi^+$ decays where the charge of the pion tags the flavor: π^+ for D^0 and π^- for \bar{D}^0 . The observed asymmetry for D^* -tagged h^+h^- events is $A_{obs}(h^+h^-, \pi_S) = A_{CP}(h^+h^-) + \delta(\pi_S)$ where A_{obs} is the observed asymmetry, A_{CP} is the true asymmetry, and $\delta(\pi_S)$ is the detection asymmetry for the tagging soft pion. That detector asymmetry can be found from events with a D^* tag and Cabibbo-favored $D^0 \rightarrow K^-\pi^+$ decays where the flavor of the decay is known: $A_{obs}(K^-\pi^+, \pi_S) = A_{CP}(K^-\pi^+) + \delta(K^-\pi^+) + \delta(\pi_S)$ which also includes intrinsic and detector asymmetries from the D decay mode. These in turn can be measured from inclusive $D^0 \rightarrow K^-\pi^+$ decays where the asymmetry is $A_{obs}(K^-\pi^+) = A_{CP}(K^-\pi^+) + \delta(K^-\pi^+)$. These three equations are solved to find

$$(12) \quad A_{CP}(h^+h^-) = A_{obs}(h^+h^-, \pi_S) - A_{obs}(K^-\pi^+, \pi_S) + A_{obs}(K^-\pi^+).$$

This method relies on several fairly weak assumptions. First, it is assumed that there is no production asymmetry for D^{*+} and D^{*-} which should be the case for the charge symmetric $p\bar{p}$ initial state. The soft pion efficiency is assumed to be independent of the D decay mode, and there is assumed to be no variation in acceptance as a function of rapidity. Both of these latter assumptions are verified with data. Fits to the mass distributions give yields of $106421 \pm 361 \pi^+\pi^-\pi_S^+$, $110447 \pm 368 \pi^+\pi^-\pi_S^-$, $232520 \pm 759 K^+K^-\pi_S^+$, and $243575 \pm 778 K^+K^-\pi_S^-$ events. The measured asymmetries are

$$(13) \quad A_{CP}(D^0 \rightarrow \pi^+\pi^-) = +0.22 \pm 0.24 \pm 0.11\%,$$

$$(14) \quad A_{CP}(D^0 \rightarrow K^+K^-) = -0.24 \pm 0.22 \pm 0.10\%,$$

where the dominant systematic uncertainty comes from allowing changes in the signal shape for the oppositely tagged samples. As described in eq. (11), these asymmetries depend on the actual experiment and correspond to a joint limit in the $(a_{CP}^{\text{Indirect}}, a_{CP}^{\text{Direct}})$ plane. Those limits are shown in fig. 5 along with limits from Belle [23] and BaBar [24]. The CDF limits are the most stringent to date. The slopes CDF and B -factory measurements are different as a result of the different lifetime distributions of the samples, thus the results can be combined to yield the elliptical limit regions shown on the figure. All of the results are consistent with the point showing no CP violation.

REFERENCES

- [1] GROSSMAN Y., NIR Y. and RAZ G., *Phys. Rev. Lett.*, **97** (2006) 151801.
- [2] AALTONEN T. *et al.* (CDF COLLABORATION), *Phys. Rev. Lett.*, **100** (2008) 161802.
- [3] ABAZOV V. M. *et al.* (D0 COLLABORATION), *Phys. Rev. Lett.*, **101** (2008) 241801.
- [4] STONE S. and ZHANG L., *Phys. Rev. D*, **79** (2009) 074024.
- [5] ECKLUND K. *et al.* (CLEO COLLABORATION), *Phys. Rev. D*, **80** (2009) 052009.
- [6] COLANGELO P., DE FAZIO F. and WANG W., *Phys. Rev. D*, **81** (2010) 074001 and arXiv:1009.4612 [hep-ph].
- [7] AAIJ R. *et al.* (LHCb COLLABORATION), *Phys. Lett. B*, **698** (2011) 115.
- [8] LI J. *et al.* (BELLE COLLABORATION), *Phys. Rev. Lett.*, **106** (2011) 121802.
- [9] AALTONEN T. *et al.* (CDF COLLABORATION), arXiv:1106.3682v2 [hep-ph].
- [10] ABLIKIM M. *et al.* (BES COLLABORATION), *Phys. Lett. B*, **607** (2005) 243.
- [11] AALTONEN T. *et al.* (CDF COLLABORATION), *Phys. Rev. D*, **83** (2011) 052012.
- [12] NAKAMURA K. *et al.*, *J. Phys. G*, **37** (2010) 075021.
- [13] THE ALEPH COLLABORATION, THE DELPHI COLLABORATION, THE L3 COLLABORATION, THE OPAL COLLABORATION, THE SLD COLLABORATION, THE LEP ELECTROWEAK WORKING GROUP, THE SLD ELECTROWEAK and THE HEAVY FLAVOUR GROUPS, *Phys. Rep.*, **427** (2006) 257.
- [14] ABAZOV V. M. *et al.* (D0 COLLABORATION), *Phys. Rev. D*, **74** (2006) 092001.
- [15] ASNER D. *et al.*, arXiv:1010.1589v3 [hep-ph].
- [16] For details see <http://www-cdf.fnal.gov/physics/new/bottom/110127.blessed-chibar/cdf10335.ps>.
- [17] AALTONEN T. *et al.* (CDF COLLABORATION), *Phys. Rev. D*, **77** (2008) 072004.
- [18] ATWOOD D., DUNIETZ I. and SONI A., *Phys. Rev. Lett.*, **78** (1997) 3257 and *Phys. Rev. D*, **63** (2001) 036005.
- [19] AALTONEN T. *et al.* (CDF COLLABORATION), arXiv:1108.5765v2 [hep-ph].
- [20] HORII Y. *et al.* (BELLE COLLABORATION), *Phys. Rev. Lett.*, **106** (2011) 231803.
- [21] DEL AMO SANCHEZ P. *et al.* (BABAR COLLABORATION), *Phys. Rev. D*, **82** (2010) 072006.
- [22] AALTONEN T. *et al.* (CDF COLLABORATION), arXiv:1111.5023v1 [hep-ph].
- [23] STARIC M. *et al.* (BELLE COLLABORATION), *Phys. Lett. B*, **670** (2008) 190.
- [24] AUBERT B. *et al.* (BABAR COLLABORATION), *Phys. Rev. Lett.*, **100** (2008) 061803.

Charmless B decays in B -factories

C. H. CHENG

California Institute of Technology - 1200 East California Boulevard, Pasadena, CA 91125, USA

(ricevuto il 29 Settembre 2011; pubblicato online il 24 Gennaio 2012)

Summary. — In this paper we present recent results of charmless hadronic B decays from the two B -factories, $BABAR$ at SLAC, USA, and Belle at KEK, Japan. They include partial branching fractions of inclusive charmless B decays to K^+ , K^0 , and π^+ , branching fractions and polarizations of $B^+ \rightarrow \rho^0 K^{*+}$, $f_0 K^{*+}$, and $B^0 \rightarrow K^{*0} \bar{K}^{*0}$, and branching fractions, CP asymmetries and angular distributions in $B \rightarrow \phi\phi K$ decays.

PACS 14.40.Nd – Bottom mesons ($|B| > 0$).

PACS 13.20.He – Decays of bottom mesons.

1. – Introduction

The dominating processes in B meson decays are through tree-level $b \rightarrow cW^*$, leaving a charm meson in the final states. In charmless hadronic B decays, other types of diagrams, such as $b \rightarrow s$ penguin diagrams are enhanced. These processes allow studies of short- and long-distance QCD effects, CP -violating asymmetries, hadronic phases, and searching for evidence for physics beyond the Standard Model.

To date, approximately one hundred charmless hadronic B decay modes have been measured with more than four-sigma significance. The majority of them are from $BABAR$ collaboration at SLAC in the United States and Belle collaboration at KEK in Japan, both of which started operation in 1999 and ended in 2008 and 2010, respectively. The branching fractions of these decay modes range from a few times 10^{-5} down to 10^{-6} [1]. Several other charmless channels are also searched and the upper limits of the branching fractions are well below 10^{-6} .

Both B -factories, $BABAR$ and Belle, spent most of their operation time on the $\Upsilon(4S)$ resonance and recorded a wealth of B meson decay data through $e^+e^- \rightarrow \Upsilon(4S) \rightarrow B\bar{B}$ processes. $BABAR$ and Belle collected approximately 430 fb^{-1} and 710 fb^{-1} of data on $\Upsilon(4S)$, respectively, which corresponds to a total of more than 1.2×10^9 $B\bar{B}$ pairs. Approximately 10% of the time they operated at about 40 MeV below the $\Upsilon(4S)$ resonance to study non- B background. They also operated at other Υ resonances and scanned over an energy range above $\Upsilon(4S)$ to higher than known resonances.

The common analysis technique amongst the analyses presented in the paper is to fully reconstruct a B meson in an event by combining all decay products of a B meson and exploiting the kinematic properties to separate signal from background. The most useful variables are energy-substituted (or beam energy-constrained) mass $m_{ES} = \sqrt{E_{\text{beam}}^{*2} - p_B^{*2}}$ and $\Delta E = E_B^* - E_{\text{beam}}^*$, where the asterisk denotes the quantities evaluated in the center-of-mass (c.m.) frame, (E_B, p_B) are the energy and momentum of the reconstructed B candidate. The m_{ES} and ΔE distributions for the B signal peak at the B meson mass and zero, respectively, and have a width of approximate 3 MeV and 30 MeV, respectively. The width of ΔE varies in a wide range depending on the number of neutral particles in the final state. The dominant background comes from continuum events $e^+e^- \rightarrow q\bar{q}$, where q stands for light quarks u, d, s , or c . The topology of the continuum events is much more jet-like than the $B\bar{B}$ events because light quarks carries much higher momentum than the B mesons. We exploit the event shape variables to build Fisher discriminant or other more sophisticated multivariate classifiers to separate signal from background. Finally, it is important to separate kaons from pions in many final states we study. Both B -factories utilize the Cherenkov radiation as the major tools to distinguish kaons from pions. The specific ionization in the tracking devices also plays a roll in particle identification.

2. – Inclusive charmless B decays to K^+ , K^0 , and π^+

In the standard model (SM) the inclusive branching fraction of B mesons decaying to charmless final states is of the order of 2% [2]. Particles associated with physics beyond the SM, such as supersymmetric partners of SM particles, could enter the loop in $b \rightarrow s$ and $b \rightarrow d$ diagrams and enhance the inclusive $b \rightarrow sg$ (g denoting a gluon) branching fraction [3, 4]. Furthermore, semi-inclusive processes are usually affected by smaller hadronic uncertainties than those that arise in calculations for exclusive final states, therefore these decays can be sensitive to non-perturbative amplitudes, such as charming penguins [5].

The signature of the inclusive charmless B decays is the presence of a light meson (K^+ , K_S^0 , or π^+) with momentum beyond the kinematic endpoint for B decays to charmed mesons. To suppress the overwhelming background from continuum events, one B meson is fully reconstructed through the decay modes $B \rightarrow D^{(*)}Y^\pm$, where Y^\pm is a combination of hadrons containing one, three, or five charged kaons or pions, up to two neutral pions, and at most two $K_S^0 \rightarrow \pi^+\pi^-$. After applying selections in m_{ES} , ΔE , and event shape variables, and fitting to m_{ES} and Fisher discriminant, 2×10^6 $B\bar{B}$ events are reconstructed by BABAR from a data set of 383×10^6 $B\bar{B}$ pairs.

From the remaining particles that does not belong to the fully reconstructed B , events that contains candidates consistent with a charm meson are rejected, and only events that contains a K^+ , K_S^0 or π^+ with a momentum p^* in the recoiled frame greater than 1.8 GeV are retained. Event yields are extracted from a maximum likelihood fit to three variables, m_{ES} , Fisher, and p^* . The probability density function (PDF) includes signal, $q\bar{q}$, and $b \rightarrow c$ background components. An iterative fitting procedure is used to determine the background shapes, using events with $p^* > 1.8$ GeV, and the signal yields at higher momentum, as shown in fig. 1. The charge CP asymmetry is also measured. The main systematic uncertainty sources include the number of fully reconstructed B candidates, efficiency estimations, PDF shapes, and $b \rightarrow c$ background yield extrapolation.

The fitted results to the high p^* region are shown in table I. The partial branching fraction above $p^* > 2.34$ GeV is in the range $2\text{--}4 \times 10^{-4}$. This results are in agree-

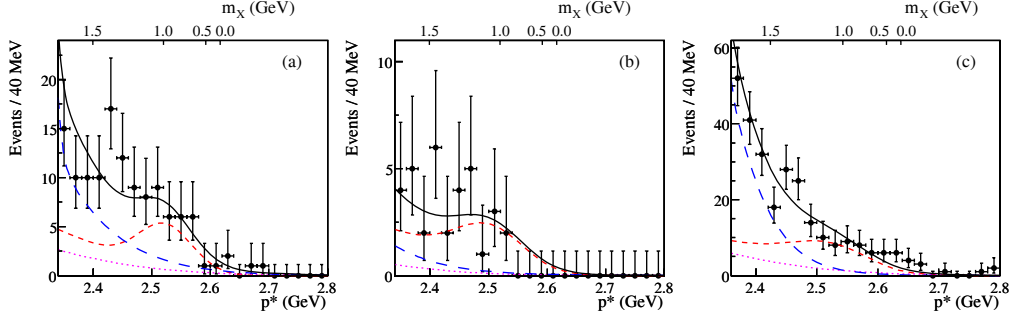


Fig. 1. – (Color online) Projection plots at high p^* for (a) K^+ , (b) K_S^0 , and (c) π^+ samples [6]. The solid curves are the total fit function, the (red) dashed lines are the signal component, the (blue) long dashed are the $b \rightarrow c$ background and the (magenta) dotted are $q\bar{q}$. A likelihood cut is applied to suppress the background. The scale on the upper border of the plots indicates the mass of the system recoiling against the light hadron.

ment with the estimates of the sums of known exclusive branching fractions of charmless two- and three-body B decays. On the other hand, predictions based on SCET [5] underestimate the measurements, and substantial non-perturbative charming penguin contributions or large higher-order corrections may be needed.

3. – $B^+ \rightarrow \rho^0 K^{*+}$ and $f_0 K^{*+}$

QCD factorization models predict a large longitudinal polarization fraction f_L , of order $(1 - 4m_V^2/m_B^2) \sim 0.9$, for B to two vector particles (VV) [7]. However, several measurements of penguin dominated VV final states give $f_L \sim 0.5$ [8]. Many literatures attempt to understand the low f_L values within or beyond the SM [9].

In this section, the branching fractions, polarizations, and direct CP asymmetries of the decay modes $B^+ \rightarrow \rho^0 K^{*+}$ (892) and $f_0(980) K^{*+}$ measured by $BABAR$ are summarized [10]. The measurements are based on a data sample of $(467 \pm 5) \times 10^6$ $B\bar{B}$ pairs, and an additional 44 fb^{-1} of data collected 40 MeV below the $\Upsilon(4S)$ is used for background studies.

The $B^+ \rightarrow \rho^0 K^{*+}$ and $f_0 K^{*+}$ candidates are reconstructed through the decays of ρ^0 or $f_0 \rightarrow \pi^+\pi^-$, $K^{*+} \rightarrow K_S^0\pi^+$ or $K^{*+} \rightarrow K^+\pi^0$, with $K_S^0 \rightarrow \pi^+\pi^-$ and $\pi^0 \rightarrow \gamma\gamma$. The differential decay rate for $B^+ \rightarrow \rho^0 K^{*+}$, after integrating over the angle between

TABLE I. – Summary of the fit results of inclusive charmless B decays [6].

	$B \rightarrow K^+ X$	$B \rightarrow K^0 X$	$B \rightarrow \pi^+ X$
Signal yield (events)	54_{-10}^{+11}	32 ± 7	107_{-14}^{+15}
Significance (σ)	2.9	3.8	6.7
$\mathcal{B}(\times 10^{-6})_{p^* > 2.34 \text{ GeV}}$	$119_{-29}^{+32} \pm 37$	$195_{-45}^{+51} \pm 50$	$372_{-47}^{+50} \pm 59$
A_{CP}	$0.57 \pm 0.24 \pm 0.05$	–	$0.10 \pm 0.16 \pm 0.05$

the decay planes of the vectors is proportional to

$$(1) \quad \frac{1 - f_L}{4} \sin^2 \theta_{K^{*+}} \sin^2 \theta_{\rho^0} + f_L \cos^2 \theta_{K^{*+}} \cos^2 \theta_{\rho^0},$$

where $\theta_{K^{*+}}(\theta_{\rho^0})$ are helicity angle of the K^{*+} (ρ^0). The direct CP asymmetry A_{CP} is defined as $(\Gamma^- - \Gamma^+)/(\Gamma^- + \Gamma^+)$, where $\Gamma^\pm = \Gamma(B^\pm \rightarrow f^\pm)$.

Events with $0.792 < m_{K\pi} < 0.992$ GeV, $0.52 < m_{\pi^+\pi^-} < 1.05$ GeV, $|\Delta E| < 10$ MeV and $5.225 < m_{ES} < 5.289$ GeV are retained for further fit. If the final tracks can be combined to form a D candidates, the candidate is rejected. To avoid the region where the efficiency falls off rapidly, K^{*+} and ρ^0 candidates need to satisfy $\cos \theta_{K^{*+}} < 0.92$ and $|\cos \theta_{\rho^0}| < 0.95$, respectively. Finally a neural network discriminant is used to provide additional separation between signal and $q\bar{q}$ background.

An extended likelihood function is used to simultaneously fit branching fractions, f_L of $B^+ \rightarrow K^{*+}\rho^0$ and A_{CP} . The PDF uses seven variables: m_{ES} , ΔE , neural network output, $m_{\pi^+\pi^-}$, $m_{K\pi}$, $\cos \theta_{\pi^+\pi^-}$, and $\cos \theta_{K\pi}$. In the end, BABAR observes $B^+ \rightarrow \rho^0 K^{*+}$ with a significance of 5.3σ , and measures branching fraction $\mathcal{B}(B^+ \rightarrow \rho^0 K^{*+}) = (4.6 \pm 1.0 \pm 0.4) \times 10^{-6}$, the longitudinal polarization $f_L = 0.78 \pm 0.12 \pm 0.03$, and $A_{CP} = 0.31 \pm 0.13 \pm 0.03$. They also measure $\mathcal{B}(B^+ \rightarrow f_0(980)K^{*+}) \times \mathcal{B}(f_0(980) \rightarrow \pi^+\pi^-) = (4.2 \pm 0.6 \pm 0.3) \times 10^{-6}$, and $A_{CP} = -0.15 \pm 0.12 \pm 0.03$.

It is interesting to compare f_L of the three charge combinations of $B \rightarrow \rho K^*$: $f_L(K^{*+}\rho^0) = 0.78 \pm 0.12 \pm 0.03$ [10], $f_L(K^{*0}\rho^0) = 0.57 \pm 0.09 \pm 0.08$ [11], $f_L(K^{*0}\rho^+|BABAR) = 0.52 \pm 0.10 \pm 0.04$ [11], and $f_L(K^{*0}\rho^+|Belle) = 0.43 \pm 0.11^{+0.05}_{-0.02}$ [12]. $B^+ \rightarrow K^{*0}\rho^+$ is a pure penguin process, $B^0 \rightarrow K^{*0}\rho^0$ is penguin plus color-suppressed $\bar{b} \rightarrow \bar{u}u\bar{s}$ tree, and $B^+ \rightarrow K^{*+}\rho^0$ is penguin plus color-allowed $\bar{b} \rightarrow \bar{u}u\bar{s}$ tree. The trend of their f_L is consistent with other observations that penguin dominated processes have $f_L \sim 0.5$ and tree dominated processes have $f_L \sim 0.9$.

4. $B^0 \rightarrow K^{*0}\bar{K}^{*0}$ and $K^{*0}K^{*0}$

The decay $B^0 \rightarrow K^{*0}\bar{K}^{*0}$ is a pure $b \rightarrow d$ penguin process to two vector particles. It should have a similar longitudinal polarization fraction f_L as $b \rightarrow s$ penguin processes under U-spin symmetry. Studying this decay mode may provide insight into the polarization puzzle in $b \rightarrow s$ penguin dominated processes as described in the previous section, and test factorization models. If sufficient signal events are observed, a time-dependent angular analysis of $B^0 \rightarrow K^{*0}\bar{K}^{*0}$ can distinguish between penguin annihilation and rescattering as mechanisms for the value of f_L in penguin-dominated $B \rightarrow VV$ [13]. $B \rightarrow K^{*0}K^{*0}$ is highly suppressed in the SM, and could appear via an intermediate heavy boson beyond the SM.

BABAR uses a data sample consisting of 383×10^6 $B\bar{B}$ pairs, and Belle uses 657×10^6 . The analysis is very similar to that of $B \rightarrow \rho K^*$ described in the previous section. The angular distribution is identical to equation 1 after substituting ρ^0 with K^{*0} . The K^{*0} is reconstructed from $K^{*0} \rightarrow K^+\pi^-$, where the charge of K identifies the flavor of K^* . BABAR selects only $0.792 < m_{K\pi} < 1.025$ GeV, while Belle keeps a larger range of $[0.7, 1.7]$ GeV to study other resonances that contributes to $B \rightarrow K^+\pi^- K^-\pi^+$ decays.

Events are vetoed if $K\pi\pi$ can be combined to form a D^- meson candidate, or if $K\pi$ can be combined to form a ϕ meson candidate when the kaon mass is assigned to the pion candidate. To suppress the dominant $q\bar{q}$ continuum background, both experiments exploit event shape variables, B candidate flight direction, and flavor tagging information.

TABLE II. – Branching fractions of $B \rightarrow K^{*0}\bar{K}^{*0}$ and $K^{*0}K^{*0}$, and polarization of $K^{*0}\bar{K}^{*0}$.

	$\mathcal{B}(K^{*0}\bar{K}^{*0})$ (10^{-6})	$f_L(K^{*0}\bar{K}^{*0})$	$\mathcal{B}(K^{*0}K^{*0})$ (10^{-6})
BABAR [14]	$1.28^{+0.35}_{-0.30} \pm 0.11$	$0.80^{+0.10}_{-0.12} \pm 0.06$	< 0.41 at 90% C.L.
Belle [15]	$0.26^{+0.33+0.10}_{-0.29-0.08}$ (< 0.8 at 90% C.L.)	—	< 0.2 at 90% C.L.

Both experiments use an extended unbinned maximum-likelihood fit to extract signal yields and polarization simultaneously. *BABAR* uses seven variables in their PDF: m_{ES} , ΔE , Fisher discriminant, and invariant masses and helicity angles of the two K^* candidates. Belle uses the product of two two-dimensional functions of $(m_{ES}, \Delta E)$ and of the two K^* candidates invariant masses. Belle fits higher K^* resonances and K^* (892) simultaneously, while *BABAR* fits for K^{*0} (1430) contribution separately and extrapolate its contribution to K^* (892) region.

The results from both experiments are summarized in table II. The projection plots, after cutting on likelihood ratios to enhance signal component, are shown in figs. 2, 3. *BABAR* observes $B \rightarrow K^{*0}\bar{K}^{*0}$ with a significance of 6σ , while Belle's central value is roughly 2σ below that of *BABAR*, and sets an upper limit below *BABAR*'s central value.

5. – $B \rightarrow \phi\phi K$

The three-body $B \rightarrow \phi\phi K$ decay is a penguin $b \rightarrow s\bar{s}s$ transition. This final state can also occur through the tree-level decay $B \rightarrow \eta_c K$, followed by $\eta_c \rightarrow \phi\phi$. The tree and penguin amplitudes may interfere at the region where the invariant mass $m_{\phi\phi}$ is near η_c mass. Within the SM, the relative weak phase between these two amplitudes is very close to zero, so no CP asymmetry is expected. However, new physics contributions to the penguin loop in $B \rightarrow \phi\phi K$ decay could introduce a non-zero relative CP -violating phase and produce a significant direct CP asymmetry [16].

The analysis techniques are very similar between Belle and *BABAR*. Both $B^+ \rightarrow \phi\phi K^+$ and $B^0 \rightarrow \phi\phi K^0$ are studied. In addition to $q\bar{q}$ continuum background, possible background sources from B decays include $B \rightarrow \phi K^+ K^- K$, $B \rightarrow 5K$, $B \rightarrow f_0\phi K$, and $B \rightarrow f_0 K^+ K^- K$. These backgrounds can be distinguished on the $m_{(KK)_1} - m_{(KK)_2}$

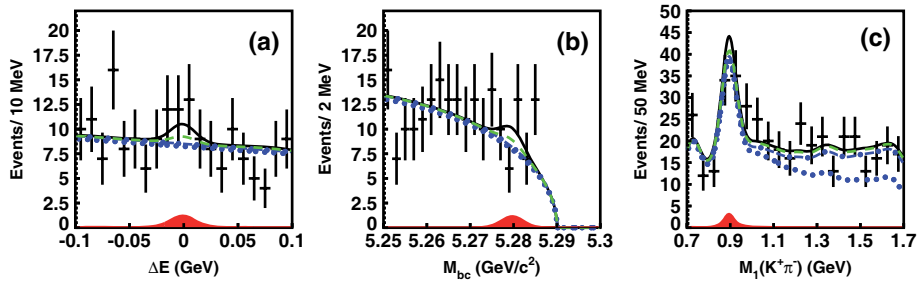


Fig. 2. – [Belle] Projections of the four-dimensional fit onto (a) ΔE , (b) m_{ES} , and (c) $m_{K^+\pi^-}$ and for $B^0 \rightarrow K^{*0}\bar{K}^{*0}$ candidates. The thick solid curve shows the overall fit result; the solid shaded region represents the signal component; and the dotted, dot-dashed and dashed curves represent continuum background, $b \rightarrow c$ background, and charmless B decay background, respectively [15].

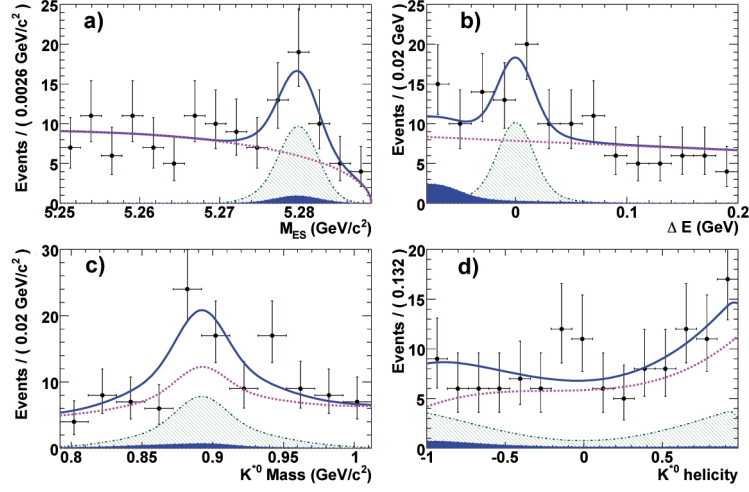


Fig. 3. – [BABAR] Projections of the fit onto (a) m_{ES} , (b) ΔE , (c) K^{*0} mass, and (d) cosine of K^{*0} helicity angle for $B^0 \rightarrow K^{*0} \bar{K}^{*0}$. The solid line shows signal-plus-background; the dashed line is the continuum background; the hatched region is the signal; and the shaded region is the $B\bar{B}$ background [14].

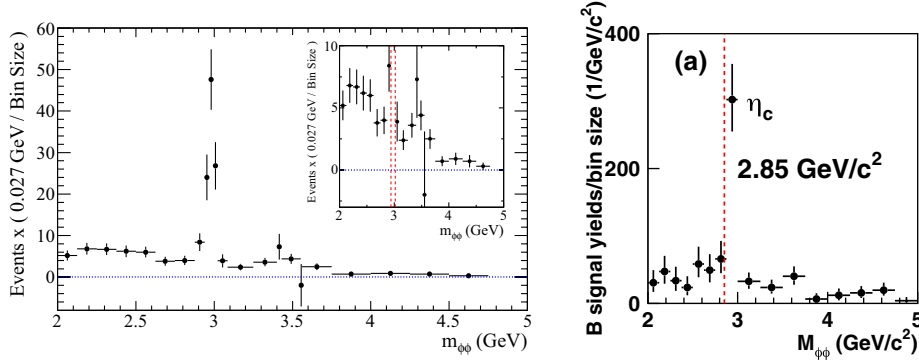


Fig. 4. – Fitted $B^+ \rightarrow \phi\phi K^+$ yield as a function of $m_{\phi\phi}$. Left is from BABAR [18]; right is from Belle [17]. The inset in the left plot is the same data with an extended vertical range.

TABLE III. – Partial branching fraction of $B \rightarrow \phi\phi K$ and direct CP asymmetry in $B^+ \rightarrow \phi\phi K^+$.

Partial BF (10^{-6}) ($m_{\phi\phi} < 2.85$ GeV)		$\mathcal{B}(B^+ \rightarrow \phi\phi K^+)$	$\mathcal{B}(B^0 \rightarrow \phi\phi K^0)$
BABAR [18]		$5.6 \pm 0.5 \pm 0.3$	$4.5 \pm 0.8 \pm 0.3$
Belle [17]		$3.2^{+0.6}_{-0.5} \pm 0.3$	$2.3^{+1.0}_{-0.7} \pm 0.2$
CP Asymmetry	$m_{\phi\phi} < 2.85$ GeV	2.94–2.98 GeV	2.98–3.02 GeV
BABAR [18]	$-0.10 \pm 0.08 \pm 0.02$	$-0.10 \pm 0.15 \pm 0.02$	$-0.08 \pm 0.14 \pm 0.02$
Belle [17]	$0.01^{+0.19}_{-0.16} \pm 0.02$	$0.15^{+0.16}_{-0.17} \pm 0.02$	

plane where the two KK pairs form the two ϕ candidates. Events are retained if the invariant masses of the ϕ candidates are below 1.2 GeV.

Event yields are obtained by fitting with a likelihood function of m_{ES} and ΔE ($BABAR$ uses Fisher and two KK pair masses as well). Figure 4 shows event yields in slices of $m_{\phi\phi}$. Belle and $BABAR$ find 34 ± 6 (7 ± 3) and 178 ± 15 (40 ± 7) signal events, respectively, for $B^+ \rightarrow \phi\phi K^+$ ($B^0 \rightarrow \phi\phi K^0$) signal events below $m_{\phi\phi} < 2.85$ GeV. The partial branching fractions and direct CP asymmetry in regions of $m_{\phi\phi}$ are summarized in table III. The CP asymmetry is consistent with zero, and no large deviation from the SM is found.

$BABAR$ also analyzes the angular distributions to investigate the spin components of the $\phi\phi$ system below and within the η_c resonance in $B^+ \rightarrow \phi\phi K^+$. They find that below η_c the distributions are more consistent with $J^P = 0^+$ than 0^- , while within η_c region they are all consistent with $J^P = 0^-$.

6. – Conclusions

Charmless B decays provide a rich program in heavy flavor phenomenology and new physics search. Both B -factories continue to produce new results after the end of data taking. Partial branching fractions and CP asymmetries of inclusive $B \rightarrow XK$, $X\pi$ and $B \rightarrow \phi\phi K$ show no evidence of new physics. More B to vector-vector final states ($\rho^0 K^{*+}$ and $K^{*0} \bar{K}^{*0}$) are studied, and more information is added to the understanding of polarization puzzle.

REFERENCES

- [1] ASNER D. *et al.* (HFAG), “Averages of b-hadron, c-hadron, and tau-lepton Properties”, arXiv:1010.1589 (2010).
- [2] GREUB C. and LINIGER P., *Phys. Rev. D*, **63** (2001) 054025.
- [3] BIGI I. *et al.*, *Phys. Lett. B*, **323** (1994) 408.
- [4] GOKSU A., ILTAN E. O. and SOLMAZ L., *Phys. Rev. D*, **64** (2001) 054006.
- [5] CHAY J., KIM C., LEIBOVICH A. K. and ZUPAN J., *Phys. Rev. D*, **76** (2007) 094031.
- [6] DEL AMO SANCHEZ P. *et al.* (THE BABAR COLLABORATION), *Phys. Rev. D*, **83** (2011) 031103(R).
- [7] ALI A. *et al.*, *Z. Phys. C*, **1** (1979) 269; SUZUKI M., *Phys. Rev. D*, **66** (2002) 054018.
- [8] CHEN K.-F. *et al.* (BELLE COLLABORATION), *Phys. Rev. Lett.*, **94** (2005) 221804; AUBERT B. *et al.* (BABAR COLLABORATION), *Phys. Rev. Lett.*, **98** (2007) 051801; AUBERT B. *et al.* (BABAR COLLABORATION), *Phys. Rev. Lett.*, **99** (2007) 201802.
- [9] KAGAN A., *Phys. Lett. B*, **601** (2004) 151; BAUER C. *et al.*, *Phys. Rev. D*, **70** (2004) 054015; COLANGELO P. *et al.*, *Phys. Lett. B*, **597** (2004) 291; LADISA M. *et al.*, *Phys. Rev. D*, **70** (2004) 114025; LI H.-N. and MISHIMA S., *Phys. Rev. D*, **71** (2005) 054025; BENEKE M. *et al.*, *Phys. Rev. Lett.*, **96** (2006) 141801.
- [10] DEL AMO SANCHEZ P. *et al.* (THE BABAR COLLABORATION), *Phys. Rev. D*, **83** (2011) 051101(R).
- [11] AUBERT B. *et al.* (THE BABAR COLLABORATION), *Phys. Rev. Lett.*, **97** (2006) 201801.
- [12] ZHANG J. *et al.* (THE BELLE COLLABORATION), *Phys. Rev. Lett.*, **95** (2005) 141801.
- [13] DATTA A. *et al.*, *Phys. Rev. D*, **76** (2007) 034015.
- [14] AUBERT B. *et al.* (THE BABAR COLLABORATION), *Phys. Rev. Lett.*, **100** (2008) 081801.
- [15] CHIANG C.-C. *et al.* (THE BELLE COLLABORATION), *Phys. Rev. D*, **81** (2010) 071101(R).
- [16] HAZUMI M., *Phys. Lett. B*, **583** (2004) 285.
- [17] SHEN Y.-T. *et al.* (THE BELLE COLLABORATION), arXiv:0802.1547v1 (2008).
- [18] LEES J. P. *et al.* (THE BABAR COLLABORATION), *Phys. Rev. D*, **84** (2011) 012001.

Chiral enhancement in the MSSM — An overview

A. CRIVELLIN

*Albert Einstein Center for Fundamental Physics, Institute for Theoretical Physics
University of Bern - CH-3012 Bern, Switzerland*

(ricevuto il 29 Settembre 2011; pubblicato online il 19 Gennaio 2012)

Summary. — In this article I review the origin and the effects of chirally enhanced loop-corrections in the MSSM based on previous papers. Chiral enhancement is related to fermion-Higgs couplings (or self-energies when the Higgs field is replaced by its vev). I describe the resummation of these chirally-enhanced corrections to all orders in perturbation theory and the calculation of the effective fermion-Higgs and gaugino (higgsino)-fermion vertices. As an application a model with radiative flavor-violation is discussed which can solve the SUSY- CP and the SUSY-flavor problem while it is still capable of explaining the observed deviation from the SM in the $B_s - \bar{B}_s$ mixing phase.

PACS 14.65.Fy – Bottom quarks.

PACS 14.80.Da – Supersymmetric Higgs bosons.

PACS 14.80.Ly – Supersymmetric partners of known particles.

1. – Introduction

In this article I summarize recent progress in the field of chirally enhanced self-energies in the MSSM done in collaboration with Jennifer Girrbach, Lars Hofer, Ulrich Nierste, Janusz Rosiek and Dominik Scherer. The discussion will skip the technical aspects and subtleties and instead focus on the essential features. The interested reader is referred to refs. [1-3] for a detailed discussion.

In the standard model chirality violation is suppressed by small Yukawa couplings (except for the top quark). However, the MSSM does not necessarily possess the same suppression effects since the bottom Yukawa coupling can be big at large of $\tan\beta = v_u/v_d$ and also the trilinear A -terms do not necessarily respect the hierarchy of the Yukawa couplings. Thus, chirality-flipping self-energies can be enhanced either by a factor of $\tan\beta$ [4] or by a ratio $A_{ij}^q/(vY_{ij}^q)$. This enhancement can compensate for the loop suppression leading to corrections which are of the same order as the corresponding physical quantities, *i.e.* of order one. These large corrections must be taken into account to all orders in perturbation theory (sect. 3) leading to effective fermion-gaugino and fermion-Higgs couplings (see sect. 4).

It is even possible that light-fermion masses and the CKM elements are entirely due to radiative corrections involving the trilinear A -terms [5]. Such a model of radiative flavor-violation can solve the SUSY- CP [6] and the SUSY-flavor problem while still leading to interesting effects in flavor-observables (see sect. 5).

2. – Self-energies

One can decompose any fermion self-energy into chirality-flipping and chirality-conserving parts in the following way:

$$(1) \quad \Sigma_{ji}^f(p) = \left(\Sigma_{ji}^{f LR}(p^2) + \not{p} \Sigma_{ji}^{f RR}(p^2) \right) P_R + \left(\Sigma_{ji}^{f RL}(p^2) + \not{p} \Sigma_{ji}^{f LL}(p^2) \right) P_L.$$

Here i and j are flavor indices running from 1 to 3. Since the SUSY particles are known to be much heavier than the SM fermions it is possible to expand in the external momentum. For our purpose it is even sufficient to work in the limit $\not{p} = 0$ in which only the chirality-flipping parts $\Sigma_{ji}^{f LR}(0) = \Sigma_{ij}^{f RL*}(0)$ remain. It is well known that in the MSSM these self-energies can be enhanced either by a factor $\tan \beta$ [4] or by a factor $A_{ij}^f / (Y_{ij}^f M_{\text{SUSY}})$ [2] which compensates for the loop-suppression and leads to order one corrections. The chirality-changing part of the fermion self-energy (at $\not{p} = 0$, involving sfermions and gauginos (higgsions)) can be written as

$$(2) \quad \Sigma_{ji}^{f \tilde{\lambda} LR} = \frac{-1}{16\pi^2} \sum_{s=1}^6 \sum_{I=1}^N m_{\tilde{\lambda}_I} \Gamma_{f_j \tilde{f}_s}^{\tilde{\lambda}_I L*} \Gamma_{f_i \tilde{f}_s}^{\tilde{\lambda}_I R} B_0 \left(m_{\tilde{\lambda}_I}^2, m_{\tilde{f}_s}^2 \right).$$

Here $\tilde{\lambda}$ stands for the SUSY fermions (\tilde{g} , $\tilde{\chi}^0$, $\tilde{\chi}^\pm$) and N denotes their corresponding number (2 for charginos, 4 for neutralinos and 8 for gluinos). The coupling coefficients $\Gamma_{f_i \tilde{f}_s}^{\tilde{\lambda}_I L(R)}$ and the loop functions B_0 are defined in the appendix of ref. [1].

The couplings $\Gamma_{f_i \tilde{f}_s}^{\tilde{\lambda}_I L(R)}$ in eq. (2) involve the corresponding sfermion mixing matrices W^f which diagonalize the sfermion mass matrices: $W_{s't'}^{f*}(M_{\tilde{f}}^2)_{s't} W_{t't}^f = m_{\tilde{f}_s}^2 \delta_{st}$. In the case of neutralino-quark-squark and chargino-quark-squark vertices they also depend on Yukawa couplings and CKM elements.

An interesting feature of the self-energies in eq. (2) is that they are finite and that they do not vanish in the limit of infinitely heavy SUSY masses. We refer to this approximation in which only such non-decoupling terms for the self-energies are kept as “the decoupling limit”. Note, however, that we do not integrate out the SUSY particles but rather keep them as dynamical degrees of freedom.

Let us take a closer look at the quark self-energy with squarks and gluinos as virtual particles⁽¹⁾. To leading order in v/M_{SUSY} , the self-energy is proportional to one chirality flipping element $\Delta_{jk}^{q LR}$ of the squark mass matrix:

$$(3) \quad \Sigma_{fi}^{q \tilde{g} LR} = \frac{2\alpha_s}{3\pi} m_{\tilde{g}} \sum_{j,k,j',f'=1}^3 \sum_{s,t=1}^6 \Lambda_{s fj}^{q LL} \Delta_{jk}^{q LR} \Lambda_{t ki}^{q RR} C_0 \left(m_{\tilde{g}}^2, m_{\tilde{q}_L}^2, m_{\tilde{q}_R}^2 \right).$$

⁽¹⁾ The gluino contribution is the dominant one in the flavor-conserving case. In the presence of non-minimal sources of flavor-violation it is also usually the dominant one.

Here the off-diagonal elements of the sfermion mass matrices are given by

$$(4) \quad \begin{aligned} \Delta_{ij}^{uLR} &= -v_u A_{ij}^u - v_d A_{ij}^{\prime u} - v_d \mu Y^{u_i} \delta_{ij}, \\ \Delta_{ij}^{d,\ell LR} &= -v_d A_{ij}^{d,\ell} - v_u A_{ij}^{\prime d,\ell} - v_u \mu Y^{d_i,\ell} \delta_{ij}, \end{aligned}$$

and the matrices $\Lambda_{sij}^{fLL,RR} = W_{i+3,s}^{f*} W_{js}^f$ take into account the flavor changes due to bilinear terms. Note that in the decoupling limit W_{st}^f depends only on the bilinear terms.

For equal SUSY masses we can give a simple approximate formula for the self-energy in eq. (3):

$$(5) \quad \Sigma_{fi}^{d\tilde{g}LR} = \frac{-1}{100} v_d (A_{fi}^d / M_{\text{SUSY}} + Y^{d_i} \tan \beta \delta_{fi}),$$

$$(6) \quad \Sigma_{fi}^{u\tilde{g}LR} = \frac{-1}{100} v_u (A_{fi}^u / M_{\text{SUSY}} + Y^{u_i} \cot \beta \delta_{fi}).$$

Thus, generic A^d -terms which are of the order M_{SUSY} lead to self-energies which are approximately $v_d/100$. The part of eq. (6) containing Y^b is of the order of 2 GeV for $\tan \beta \approx 50$. In the case of up-quarks, only the part of the self-energy proportional to A^u can be important: it is of the order of 1.5 GeV for $A^u \approx M_{\text{SUSY}}$.

According to eq. (4) and eq. (6) the quark self-energy with a gluino as virtual particle can be divided into a part linear in a Yukawa coupling and a part linear in an A -term. Such a decomposition is possible for all self-energies (in the decoupling limit) because either a Yukawa coupling or a trilinear A -term is needed in order flip the chirality. Thus, we can also decompose the chargino self-energies (we do not consider the neutralino self-energy here, because it is usually subleading) in an analogous way. In the flavor changing case we also have to distinguish whether the flavor-change is due to a CKM element or not which is important when we consider later the CKM renormalization. Thus we decompose the down-quark self-energy as follows:

$$(7) \quad \begin{aligned} \Sigma_{ii}^{dLR} &= \Sigma_{ii}^{dLR} + v_u Y^{d_i} \epsilon_i^d, \\ \Sigma_{fi}^{dLR} &= \Sigma_{fi}^{dLR} + m_{d_3} V_{3f}^{(0)*} \epsilon_{FC}^d \delta_{i3} \quad \text{for } f \neq i. \end{aligned}$$

Here ϵ_i^d is the part of the flavor-conserving down-quark self-energy proportional to Y^{d_i} divided by $v_u Y^{d_i}$, Σ_{fi}^{dLR} is the sum of all self-energies where the flavor-change is not due to CKM elements and ϵ_{FC}^d arises from the part of the chargino self-energy where the flavor change comes from a CKM element:

$$(8) \quad \epsilon_{FC}^d = \frac{-1}{16\pi^2} \mu \frac{Y^{d_3}}{m_{d_3}} \sum_{m,n=1}^3 Y^{u_3*} \Lambda_{m33}^{qLL} \Delta_{33}^{uLR*} \Lambda_{n33}^{uRR} C_0 \left(|\mu|^2, m_{\tilde{q}_m^L}^2, m_{\tilde{u}_n^R}^2 \right).$$

For the discussion of the effective Higgs vertices we also need a decomposition of Σ_{ji}^{fLR} into its holomorphic and non-holomorphic parts. Here non-holomorphic means that the loop-induced coupling is to the other Higgs doublet than the one involved in the Yukawa-term of the superpotential, *i.e.* for down-quarks the self-energy involves v_u and for up-quarks the self-energy contains v_d . In the decoupling limit all enhanced holomorphic

self-energies are proportional to A -terms and we denote the sum as Σ_{jiA}^{fLR} , while the non-holomorphic part is denoted as $\Sigma_{ji}^{\prime fLR}$:

$$(9) \quad \Sigma_{ji}^{fLR} = \Sigma_{jiA}^{fLR} + \Sigma_{ji}^{\prime fLR}.$$

3. – Renormalization

Chirally enhanced self-energies modify the relation between the bare Yukawa couplings $Y^{qi} \equiv Y^{q_i}$ and the corresponding physical fermion masses m_{f_i} . For quarks we have the relation

$$(10) \quad m_{q_i} = v_q Y^{q_i} + \Sigma_{ii}^{qLR} \quad (q = u, d).$$

Equation (10) implicitly determines the bare Yukawa couplings Y^{qi} for a given set of SUSY parameters. In the up-quark sector the enhanced terms in the self-energy Σ_{ii}^{uLR} are independent of Y^{u_i} . Therefore eq. (10) is easily solved for Y^{u_i} and one finds

$$(11) \quad Y^{u_i} = (m_{u_i} - \Sigma_{ii}^{uLR}) / v_u.$$

In the down-quark sector we have terms proportional to one power of Y^{d_i} at most (in the decoupling limit) and by solving eq. (10) we recover the well-known resummation formula [7] with an extra correction due to the A -terms [8]⁽²⁾:

$$(12) \quad Y^{d_i} = \frac{m_{d_i} - \Sigma_{ii}^{dLR}}{v_d (1 + \tan \beta \epsilon_i^d)}$$

The flavor-changing self-energies Σ_{fi}^{qLR} induce wave function rotations $\psi_i^{fL,R} \rightarrow U_{ij}^{qL,R} \psi_j^{qL,R}$ in the flavor space which have to be applied to all external fermion fields. At the two-loop level U_{fi}^{qL} is given by

$$(13) \quad U^{qL} = \begin{pmatrix} 1 - \frac{1}{2} |\sigma_{12}^q|^2 & \sigma_{12}^q + \frac{m_{q1}}{m_{q2}} \sigma_{21}^{q*} & \sigma_{13}^q + \frac{m_{q1}}{m_{q3}} \sigma_{31}^{q*} \\ -\sigma_{12}^{q*} - \frac{m_{q1}}{m_{f2}} \sigma_{21}^q & 1 - \frac{1}{2} |\sigma_{12}^q|^2 & \sigma_{23}^q + \frac{m_{f2}}{m_{q3}} \sigma_{32}^{q*} \\ -\sigma_{13}^{q*} - \frac{m_{q1}}{m_{q3}} \sigma_{31}^q + \sigma_{12}^{q*} \sigma_{23}^{q*} & -\sigma_{23}^{q*} - \frac{m_{q2}}{m_{q3}} \sigma_{32}^q & 1 \end{pmatrix},$$

where we have neglected terms which are quadratic or of higher order in small quark mass ratios and we have defined the abbreviation $\sigma_{fi}^q = \Sigma_{fi}^q / m_{q_{\max(f,i)}}$. The corresponding expressions for U^{fR} is obtained from the one for U^{qL} by replacing $\sigma_{ji}^q \rightarrow \sigma_{ij}^{q*}$. The rotations in eq. (13) also renormalize the CKM matrix. The bare CKM matrix $V^{(0)}$, which arises because of the misalignment between the bare Yukawa couplings, is now determined through the physical one by

$$(14) \quad V^{(0)} = U^{uL} V U^{dL\dagger}.$$

⁽²⁾ This equation can be directly transferred to the lepton sector by replacing fermion index d for ℓ , except for the vev.

This equation can be solved analytically by exploiting the CKM hierarchy. First one calculates the effects of $\Sigma_{f_i \text{CKM}}^{dLR}$ which lead to an additive change in the CKM elements. Then the self-energies containing CKM elements lead to a scaling of new CKM elements $\tilde{V}_{13}, \tilde{V}_{23}, \tilde{V}_{31}, \tilde{V}_{32}$ elements by a factor $1/(1 - \epsilon_{FC}^d)$ (similar to eq. (12)).

4. – Effective vertices

4.1. Higgs vertices. – The effective Higgs vertices are most easily obtained in an effective field theory approach [9] which is an excellent approximation to the full theory. In addition to the flavor-diagonal holomorphic couplings of quarks to the Higgs fields flavor-changing couplings to both Higgs doublets are induced via loops. The resulting effective Yukawa-Lagrangian is that of a general 2HDM of type III and is given (in the super-CKM basis) by

$$(15) \quad \begin{aligned} \mathcal{L}_Y^{eff} = & \bar{Q}_{fL}^a \left[(Y^{d_i} \delta_{fi} + E_{fi}^d) \epsilon_{ab} H_d^b - E_{fi}^d H_u^{a*} \right] d_{iR} \\ & - \bar{Q}_{fL}^a \left[(Y^{u_i} \delta_{fi} + E_{fi}^u) \epsilon_{ab} H_u^b + E_{fi}^u H_d^{a*} \right] d_{iR}. \end{aligned}$$

Here a and b denote $SU(2)_L$ - indices and ϵ_{ab} is the two-dimensional antisymmetric tensor with $\epsilon_{12} = 1$. The loop-induced couplings $E^{(\prime)q}$ are given by

$$(16) \quad E_{ij}^d = \frac{\Sigma_{ijA}^{dLR}}{v_d}, \quad E_{ij}^{\prime d} = \frac{\Sigma_{ij}^{\prime dLR}}{v_u}, \quad E_{ij}^u = \frac{\Sigma_{ijA}^{uLR}}{v_u}, \quad E_{ij}^{\prime u} = \frac{\Sigma_{ij}^{\prime uLR}}{v_d}.$$

Diagonalizing the effective quark mass matrices (after electroweak symmetry breaking) and decomposing the Higgs fields into their physical components leads to the following effective neutral Higgs couplings:

$$(17) \quad \begin{aligned} \Gamma_{u_f u_i}^{H_u^0 LR eff} &= x_u^k \left(\frac{m_{u_i}}{v_u} \delta_{fi} - \tilde{E}_{fi}^{\prime u} \cot \beta \right) + x_d^{k*} \tilde{E}_{fi}^{\prime u}, \\ \Gamma_{d_f d_i}^{H_d^0 LR eff} &= x_d^k \left(\frac{m_{d_i}}{v_d} \delta_{fi} - \tilde{E}_{fi}^{\prime d} \tan \beta \right) + x_u^{k*} \tilde{E}_{fi}^{\prime d}, \end{aligned}$$

with

$$(18) \quad \begin{aligned} \tilde{E}_{fi}^{\prime q} &= U_{jf}^{qL*} E_{jk}^{\prime q} U_{ki}^{qR} \approx E_{fi}^{\prime q} - \Delta E_{fi}^{\prime q}, \\ \Delta E^{\prime q} &= \begin{pmatrix} 0 & \sigma_{12}^q E_{22}^{\prime q} & (\sigma_{13}^q - \sigma_{12}^q \sigma_{23}^q) E_{33}^{\prime q} + \sigma_{12}^q E_{23}^{\prime q} \\ E_{22}^{\prime q} \sigma_{21}^q & 0 & \sigma_{23}^q E_{33}^{\prime q} \\ E_{33}^{\prime q} (\sigma_{31}^q - \sigma_{32}^q \sigma_{21}^q) + E_{32}^{\prime q} \sigma_{21}^q & E_{33}^{\prime q} \sigma_{32}^q & 0 \end{pmatrix}. \end{aligned}$$

The new term $\Delta E^{\prime q}$ is especially interesting: it contains a non-holomorphic flavor-conserving part which multiplies a flavor-changing holomorphic term. In this way the holomorphic A -terms can lead to flavor-changing neutral Higgs couplings. The origin of this term can be understood in the following way: Even though the couplings E_{ij}^d are holomorphic, they lead to an additional rotation (if E_{ij}^d is flavor non-diagonal) which is needed to diagonalize the effective quark mass matrix. These rotations then lead to off-diagonal neutral Higgs couplings even if $E_{ij}^{\prime d}$ is flavor conserving. This effect will allow us to explain the B_s mixing in our model with radiative flavor violation.

4'2. *Gaugino (higgsino)-fermion-vertices.* – Effective gaugino (higgsino)-fermion-vertices which include the chirally enhanced corrections are obtained by inserting the bare values for the Yukawa couplings and the CKM elements into the corresponding Feynman rules and applying the wave function rotations in eq. (13) to all external fermion fields. Since the genuine vertex corrections are not enhanced, these vertices then include all chirally enhanced effects.

5. – Radiative flavor violation

The smallness of the off-diagonal CKM elements and the Yukawa couplings of the first two generations suggests the idea that these quantities might be due to radiative corrections, *i.e.* they are zero at tree-level. Indeed, as we have seen previously, the self-energies involving the trilinear A -terms lead to order one effects in the renormalization of the CKM elements and the light fermion masses and it is possible that they are generated by the self-energy radiative corrections [5]. From eq. (6) we see that this is the case if the A -terms are of the same order as the other SUSY parameters.

However, the third generation fermion masses are too heavy to be loop generated (without unnaturally large values for the A -terms which would violate vacuum stability [10]) and the successful bottom-tau (top-bottom) Yukawa coupling unification in SU(5) (SO(10)) GUTs suggests to keep the third generation fermion masses. Thus we assume the following structure for the Yukawa couplings of the MSSM superpotential:

$$(19) \quad Y_{ij}^f = Y^{f3} \delta_{i3} \delta_{j3}, \quad V_{ij}^{(0)} = \delta_{ij}.$$

This means that (in the language of [11]) the global $[U(3)]^5$ flavor symmetry of the gauge sector is broken down to $[U(2)]^5 \times [U(1)]^2$ by the Yukawa couplings of the third generation. Here the five $U(2)$ factors correspond to rotations of the left-handed doublets and the right-handed singlets of the first two generation fermions in flavor space, respectively.

Let us first consider the quark sector. Here we demand that the light quark masses and the off-diagonal CKM elements are generated by gluino self-energies. Regarding only the first two generations, no direction in flavor space is singled out by the Yukawa term in the superpotential and the Cabibbo angle is generated by a misalignment between A^u and A^d ⁽³⁾. Regarding the third generation, the situation is different because their non-zero Yukawa couplings fix the quark-field rotations involving the third generation. Thus $V_{ub,cb,ts,td}$ are generated by a misalignment between the A^u , A^d and the third generation Yukawa couplings. We will consider the two limiting cases in which the CKM elements arise only from a mismatch between $(A^d) A^u$ and $(Y^d) Y^d$ which we call CKM generation in the down (up) sector for obvious reasons. This means we require

$$(20) \quad \Sigma_{23}^{dLR} = m_b V_{cb} \approx -m_b V_{ts}^*, \quad \Sigma_{13}^{dLR} = m_b V_{ub},$$

$$(21) \quad \text{or } \Sigma_{23}^{uLR} = -m_t V_{cb} \approx m_t V_{ts}^*, \quad \Sigma_{13}^{uLR} = m_t V_{td}^*.$$

If the CKM matrix is generated in the down-sector the most stringent constraint stems from an enhancement of $b \rightarrow s\gamma$ due to the off-diagonal element Δ_{23}^{dLR} in the squark mass matrix. The resulting bounds on the squark and gluino mass are shown

⁽³⁾ This also implies that the quark-squark gluino vertex is flavor-diagonal for transitions between the first two generations in the super-CKM basis.

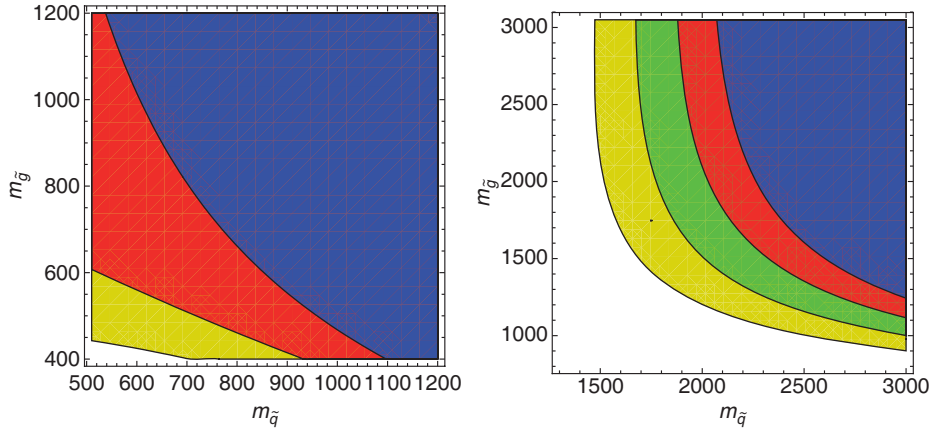


Fig. 1. – (Colour on-line) Left: Allowed regions in the $m_{\tilde{g}}-m_{\tilde{q}}$ plane. Constraint from $b \rightarrow s\gamma$ assuming that the CKM matrix is generated in the down sector. We demand that the gluino contributions should not exceed the SM one. Yellow (lightest): $\mu \tan \beta = 30$ TeV, red: $\mu \tan \beta = 0$ TeV and blue (darkest): $\mu \tan \beta = -30$ TeV. Right: Allowed regions in the $m_{\tilde{g}}-m_{\tilde{q}}$ plane. Constraints from Kaon mixing for different values of M_2 assuming that the CKM matrix is generated in the up sector. Yellow (lightest): $M_2 = 1000$ GeV, green: $M_2 = 750$ GeV, red: $M_2 = 500$ GeV and blue: $M_2 = 250$ GeV.

in the left plot of fig. 1. In addition flavor-changing neutral Higgs coupling are induced according to eq. (17) which gives an additional contribution to $B_s \rightarrow \mu^+ \mu^-$. Also B_s mixing can be affected but because it is protected by a Peccei-Quinn symmetry a double Higgs penguins contributes only if also Σ_{23}^{dRL} is non-zero (see right plot in fig. 3).

In the case of CKM matrix generation in the up-sector, the most stringent constraints stem from ϵ_K (see right plot of fig. 1) which receives additional contributions via a chargino box diagram involving the double mass insertion $\delta_{23}^{uLR} \delta_{13}^{uLR}$. At the same time the rare Kaon decays $K^+ \rightarrow \pi^+ \nu \bar{\nu}$ and $K_L \rightarrow \pi^0 \nu \bar{\nu}$ receive sizable corrections (see fig. 2) which is very interesting for NA62.

Radiative mass generation is also possible in the lepton sector. Here the anomalous magnetic moment of the muon probes the soft muon Yukawa coupling because it gets an additive contribution which depends only on the SUSY scale. If one demands that SM contribution plus the supersymmetric one is within the 2σ region of the experimental measurement the smuon mass must lie between 600 GeV and 2200 GeV for $M_1 < 1$ TeV if its Yukawa coupling is loop-generated (see left plot of fig. 3). If a smuon is found to be lighter, the observed muon mass cannot entirely stem from the soft SUSY-breaking sector and consequently the muon must have a nonzero Yukawa coupling y_μ in the superpotential.

6. – Conclusions

In the MSSM self-energies can be chirally enhanced by a factor $\tan \beta$ or by a factor $A_{ij}^q / (v Y_{ij}^q)$ which can compensate for the loop-suppression. This leads to order one corrections which must be taken into account to all orders in perturbation theory. This goal can be achieved by using effective vertices which include these corrections. The trilinear A -terms can even entirely generate the light fermion masses and the off-diagonal CKM

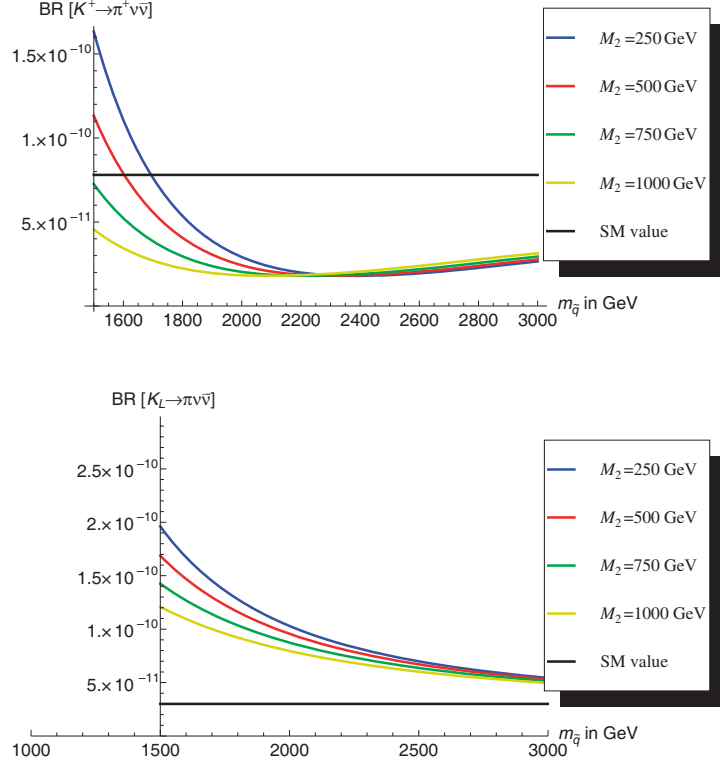


Fig. 2. – Predicted branching ratio for the rare Kaon decay $K_L \rightarrow \pi^0 \nu \bar{\nu}$ (left) and $K^+ \rightarrow \pi^+ \nu \bar{\nu}$ (right) assuming that the CKM matrix is generated in the up-sector for $m_{\bar{q}} = m_{\bar{g}}$.

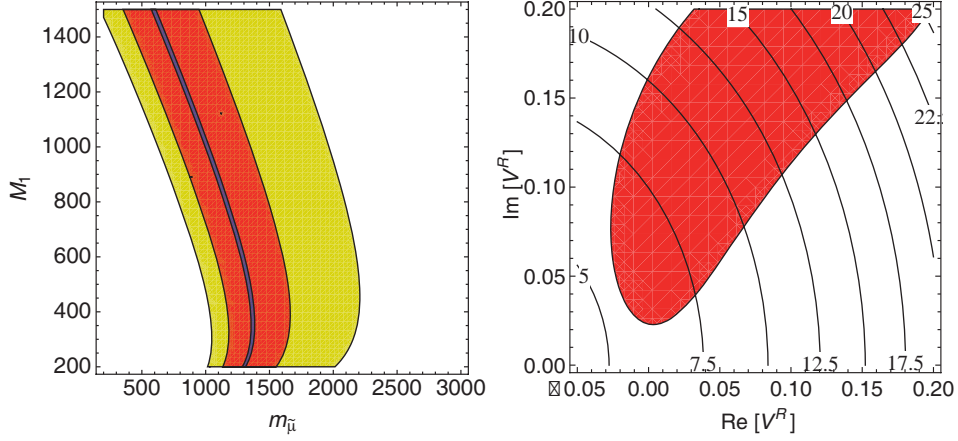


Fig. 3. – Left: Allowed region in the M_1 - $m_{\bar{\mu}}$ plane assuming that the muon Yukawa coupling is generated radiatively by $v_d A_{22}^\ell$ and/or $v_u A_{22}^{\ell'}$. Here $m_{\bar{\mu}}$ is the lighter smuon mass. Yellow (lightest): $a_\mu \pm 2\sigma$, red: $a_\mu \pm 1\sigma$, blue (darkest): a_μ . Right: correlations between $B_s \rightarrow \mu^+ \mu^-$ and $B_s - \bar{B}_s$ mixing for $\epsilon_b = 0.0075$, $m_H = 400$ GeV and $\tan \beta = 12$ in the complex $V_R = \Sigma_{23}^{dRL}/m_{d_3}$ plane. Red: Allowed region from $B_s - \bar{B}_s$ mixing (95% confidence level). The contour lines show $\text{Br}[B_s \rightarrow \mu^+ \mu^-] \times 10^9$.

elements via radiative corrections. Such a model of radiative flavor violation can both solve the SUSY CP problem and is consistent with FCNC constraints for SUSY masses of the order of 1 TeV. In addition in the case of CKM generation in the down-sector $B_s \rightarrow \mu^+\mu^-$ and $B_s - \bar{B}_s$ mixing receive additional contributions via Higgs penguins which and can even generate a sizable phase in B_s mixing. In the case of CKM generation in the up sector the branching ratio of the rare Kaon decays $K^+ \rightarrow \pi^+\nu\bar{\nu}$ and $K_L \rightarrow \pi^0\nu\bar{\nu}$ can be enhanced compared to the SM prediction.

* * *

I thank the organizers, especially GINO ISIDORI, for the invitation to the “La Thuille conference”. This work is supported by the Swiss National Foundation. I am grateful to LARS HOFER and LORENZO MERCOLLI for proofreading the manuscript. The Albert Einstein Center for Fundamental Physics is supported by the “Innovations- und Kooperationsprojekt C-13 of the Schweizerische Universitätskonferenz SUK/CRUS”.

REFERENCES

- [1] CRIVELLIN A., *Phys. Rev. D*, **83** (2011) 056001 [arXiv:1012.4840 [hep-ph]]; CRIVELLIN A., HOFER L. and ROSIEK J., arXiv:1103.4272 [hep-ph].
- [2] CRIVELLIN A. and NIERSTE U., *Phys. Rev. D*, **79** (2009) 035018 [arXiv:0810.1613 [hep-ph]]; CRIVELLIN A. and NIERSTE U., *Phys. Rev. D*, **81** (2010) 095007 [arXiv:0908.4404 [hep-ph]]; CRIVELLIN A. and GIRRBACH J., *Phys. Rev. D*, **81** (2010) 076001 [arXiv:1002.0227 [hep-ph]]; HOFER L., NIERSTE U. and SCHERER D., *JHEP*, **10** (2009) 081 [arXiv:0907.5408 [hep-ph]]. GIRRBACH J., MERTENS S., NIERSTE U. and WIESENFELDT S., *JHEP*, **05** (2010) 026 [arXiv:0910.2663 [hep-ph]].
- [3] CRIVELLIN A., GIRRBACH J. and NIERSTE U., *Phys. Rev. D*, **83** (2011) 055009 [arXiv:1010.4485 [hep-ph]]; CRIVELLIN A., HOFER L., NIERSTE U. and SCHERER D., [arXiv:1105.2818 [hep-ph]].
- [4] HALL L. J., RATAZZI R. and SARID U., *Phys. Rev. D*, **50** (1994) 7048 [arXiv:hep-ph/9306309].
- [5] BUCHMULLER W. and WYLER D., *Phys. Lett. B*, **121** (1983) 321.
- [6] BORZUMATI F., FARRAR G. R., POLONSKY N. and THOMAS S. D., *Nucl. Phys. B*, **555** (1999) 53 [arXiv:hep-ph/9902443].
- [7] CARENA M. S., GARCIA D., NIERSTE U. and WAGNER C. E. M., *Nucl. Phys. B*, **577** (2000) 88 [arXiv:hep-ph/9912516].
- [8] GUASCH J., HAFLIGER P. and SPIRA M., *Phys. Rev. D*, **68** (2003) 115001 [arXiv:hep-ph/0305101].
- [9] ISIDORI G. and RETICO A., *JHEP*, **09** (2002) 063 [arXiv:hep-ph/0208159].
- [10] CASAS J. A., LLEYDA A. and MUNOZ C., *Nucl. Phys. B*, **471** (1996) 3 [arXiv:hep-ph/9507294]; PARK J. H., *Phys. Rev. D*, **83** (2011) 055015 [arXiv:1011.4939 [hep-ph]].
- [11] D’AMBROSIO G., GIUDICE G. F., ISIDORI G. and STRUMIA A., *Nucl. Phys. B*, **645** (2002) 155 [arXiv:hep-ph/0207036]; CHIVUKULA R. S. and GEORGI H., *Phys. Lett. B*, **188** (1987) 99.

Comments on CPT (*)

V. NOVIKOV

ITEP - Moscow, Russia

(ricevuto il 29 Settembre 2011; pubblicato online il 26 Gennaio 2012)

Summary. — We present a class of interacting nonlocal quantum field theories, in which the CPT invariance is violated while the Lorentz invariance is not. This result rules out a previous claim in the literature that the CPT violation implies the violation of Lorentz invariance.

PACS 11.10.-z – Field theory.

PACS 11.30.Er – Charge conjugation, parity, time reversal, and other discrete symmetries.

1. – Introduction

Lorentz symmetry and the CPT invariance are two of the most respectable symmetries in Nature. The individual symmetries C , P and T have been observed to be violated. The combined product — CPT — remarkably remains as an exact symmetry.

2. – A brief history of CPT

As far as I know, J. Schwinger was the first one who mentioned the CPT theorem in his paper in 1951. He considered CPT theorem as a rather self-evident statement. The first Proof of CPT was done by Lüders [2], by Pauli [3] and by John Bell (but I have never seen his paper) within the Hamiltonian formulation of quantum field theory with local and Lorentz-invariant interaction. Later Jost [4] gave a General Proof of CPT within the axiomatic formulation of quantum field theory. The great deal was that the “local commutativity” condition was relaxed to “weak local commutativity”.

Lorentz symmetry has been an essential ingredient of the proof, both in the Hamiltonian QFT and in the axiomatic QFT. The main idea was that the reflection of all 4 axes is equivalent to the rotation for Euclidean space with even dimensions. Lorentz boost

(*) This talk is based on the paper the author has written in collaboration with Sasha Dolgov, Masud Chaichian and Anca Tureanu [1].

in Minkowsky space-time is more or less equivalent to rotation in Euclidean time. The problem was in accurate continuation of Minkowsky space to Euclidean one.

Violation of Lorentz symmetry and *CPT* was considered in the literature for decades. A long list of references includes the great names of Coleman, Glashow, Okun, Colladay, Kostelecky, Cohen, Lehner.

It is important to clarify the relation between *CPT* and Lorentz invariance. Does the violation of any of the symmetries automatically imply the violation of the other one? This issue has recently become a topical one due to the growing phenomenological importance of *CPT*-violating scenarios in neutrino physics and in cosmology.

The first phenomenological consideration was made by Murayama and Yanagida [5]. They introduced a *CPT*-violating quantum field theory with a mass difference between neutrino and antineutrino. Later Barenboim *et al.* [6] and then Greenberg [7] investigated theoretical aspects of this assumption. Greenberg conclusion is: *CPT* violation implies violation of Lorentz invariance.

The dispute on the validity of the theorem is the subject of this talk.

3. – *CPT*-violating free-field model

To formulate the *CPT*-violating free-field model we use commutation relations for particle $a(p), a^+(p')$ with mass m ; Bose commutation relations for antiparticle $b(p), b^+(p')$ with mass \tilde{m} and the considered Hamiltonian as a sum over free oscillators.

Greenberg arguments were that the propagator of free particles is not Lorentz covariant, unless the masses of particle and antiparticle coincide. The theory is nonlocal and acausal: the $\Delta(x, y)$ -function, *i.e.* the commutator of two fields, does not vanish for space-like separation, unless the two masses are the same, thus violating the Lorentz invariance. These arguments support a general “theorem” that interacting fields that violate *CPT* symmetry necessarily violate Lorentz invariance.

I would like to point out that such theory can not be considered as a quantum field theory. There are no differential equations of motion. Canonical conjugate momenta do not exist and, as a result, there are no canonical equal-time commutation relations “Free fields” separated by a space-like distance do not commute. They do not anticommute as well. One has no rule whether to apply commutation or anticommutation relations in quantizing the fields! There does not exist any reasonable field theory formulation of a model where particle and antiparticle have different masses.

4. – *CPT*-violating, Lorentz-invariant nonlocal model

We propose a model which preserves Lorentz invariance and breaks the *CPT* symmetry through a (nonlocal) interaction.

In this model the free-field theory is a local one. Nonlocal field theories appear, in general, as effective field theories of a larger theory.

Consider a field theory with nonlocal interaction Hamiltonian of the type

$$(1) \quad \mathcal{H}_{int}(x) = g \int d^4y \phi^*(x) \phi(x) \phi^*(x) \theta(x_0 - y_0) \theta((x - y)^2) \phi(y) + \text{h.c.},$$

where $\phi(x)$ is a Lorentz-scalar field and θ is the Heaviside step function, with values 0 or 1, for its negative and positive argument, respectively. The combination $\theta(x_0 - y_0) \theta((x - y)^2)$ ensures the Lorentz invariance, *i.e.* invariance under the proper orthochronous Lorentz

transformations, since the order of the times x_0 and y_0 remains unchanged for time-like intervals, while for space-like distances the interaction vanishes.

Also, the same combination makes the nonlocal interaction causal at the tree level, which dictates that there is no interaction when the fields are separated by space-like distances and thus there is a maximum speed of $c = 1$ for the propagation of information.

On the other hand, it is clear that C and P invariance are trivially satisfied in (1), while T invariance is broken due to the presence of $\theta(x_0 - y_0)$ in the integrand.

One can always insert into the Hamiltonian (1), without changing its symmetry properties, a weight function or form factor $F((x - y)^2)$, for instance of a Gaussian type:

$$(2) \quad F = \exp\left(-\frac{(x - y)^2}{l^2}\right),$$

with l being a nonlocality length in the considered theory. Such a weight function would smear out the interaction and would guarantee the desired behaviour of the integrand in (1); in the limit of fundamental length $l \rightarrow 0$ in (2), the Hamiltonian (1) would correspond to a local, CPT - and Lorentz-invariant theory.

A weight function such as (2) would make the acausality of the model (see the next section) restricted only to very small distances, of the order of l . The latter could be looked upon as being a characteristic parameter relating the effective field theory to its parent one, for instance the radius of a compactified dimension when the parent theory is a higher-dimensional one. Furthermore, with such a weight function, the interaction vanishes at infinite $(x - y)^2$ separations and thus one can envisage the existence of in- and out-fields.

There exists a whole class of such CPT -violating, Lorentz-invariant field theories involving different, scalar, spinor or higher-spin interacting fields. Typical simplest examples are

$$(3) \quad \begin{aligned} H_{int}(x) &= g_1 \int d^4y \phi_1^*(x) \phi_1(x) \theta(x_0 - y_0) \theta((x - y)^2) \phi_2(y) + \text{h.c.}, \\ H_{int}(x) &= g_2 \int d^4y \bar{\psi}(x) \psi(x) \theta(x_0 - y_0) \theta((x - y)^2) \phi(y) + \text{h.c.}, \\ H_{int}(x) &= g_3 \int d^4y \phi(x) \theta(x_0 - y_0) \theta((x - y)^2) \phi^2(y) + \text{h.c.} \end{aligned}$$

5. – Quantum theory of nonlocal interaction

The S -matrix in the interaction picture is obtained as solution of the Lorentz-covariant Tomonaga-Schwinger equation:

$$(4) \quad i \frac{\delta}{\delta \sigma(x)} \Psi[\sigma] = H_{int}(x) \Psi[\sigma],$$

with σ a space-like hypersurface, and the boundary condition

$$(5) \quad \Psi[\sigma_0] = \Psi,$$

where H_{int} is for instance the Hamiltonian (3) with the fields in the interaction picture. Then eq. (4) with the boundary condition (5) represents a well-posed Cauchy problem.

The existence of a unique solution for the Tomonaga-Schwinger equation is ensured if the integrability condition

$$(6) \quad \frac{\delta^2 \Psi[\sigma]}{\delta \sigma(x) \delta \sigma(x')} - \frac{\delta^2 \Psi[\sigma]}{\delta \sigma(x') \delta \sigma(x)} = 0,$$

with x and x' on the surface σ , is satisfied. The integrability condition (6), inserted into (4), requires that the commutator of the interaction Hamiltonian densities vanishes at space-like separation:

$$(7) \quad [\mathcal{H}_{int}(x), \mathcal{H}_{int}(y)] = 0, \quad \text{for } (x - y)^2 < 0.$$

Since in the interaction picture the field operators satisfy free-field equations, they automatically satisfy Lorentz-invariant commutation rules. The Lorentz-invariant commutation relations are such that (7) is fulfilled only when x and y are space-like separated, $(x - y)^2 < 0$, *i.e.* when σ is a space-like surface. As a result, the integrability condition (7) is equivalent to the microcausality condition for local relativistic QFT. When the surfaces σ are hyperplanes of constant time, the Tomonaga-Schwinger equations reduce to the single-time Schrödinger equation. Inserting the expression (3) into (7), we have

$$(8) \quad [\mathcal{H}_{int}(x), \mathcal{H}_{int}(y)] = \int d^4 a d^4 b \theta((x - a)^2) \theta(x^0 - a^0) \theta((y - b)^2) \theta(y^0 - b^0) \times [\phi(x) \phi^2(a) + \text{h.c.}, \phi(y) \phi^2(b) + \text{h.c.}].$$

The commutator on the r.h.s. will open up into a sum of products of field at the points x , y , a , b , multiplied by commutators of free fields like $[\phi(x), \phi(y)]$, $[\phi(x), \phi(b)]$, $[\phi(a), \phi(y)]$, $[\phi(a), \phi(b)]$. In order for the commutator (8) to vanish, all the coefficients of the products of fields in the expansion have to vanish, since the fields at different space-time points are independent. Clearly, the terms with the coefficient $\Delta(x - y) = [\phi(x), \phi(y)]$ vanish for $(x - y)^2 < 0$. However, the commutator (8) does not vanish for $(x - y)^2 < 0$. In order to show this, it is enough to show that one independent product of fields has nonzero coefficient. Let us consider the products which contain the fields $\phi(x)$, $\phi(y)$, $\phi(a)$, $\phi(b)$

A straightforward calculation shows that the terms containing these fields are:

$$(9) \quad \int d^4 a d^4 b \theta((x - a)^2) \theta(x^0 - a^0) \theta((y - b)^2) \theta(y^0 - b^0) \times 2\Delta(a - b) \{\phi(a), \phi(b)\} \phi(x) \phi(y) + \text{h.c.}$$

A closer study of the expression (9) shows that it does not vanish at space-like distances between x and y and thus the causality condition (7) is not satisfied.

This, in turn, implies that the field operators in the Heisenberg picture, $\Phi_H(x)$ and $\Phi_H(y)$, do not satisfy the locality condition

$$(10) \quad [\Phi_H(x), \Phi_H(y)] = 0, \quad \text{for } (x - y)^2 < 0,$$

when the quantum corrections are taken into account. This is in accord with the requirement of locality condition (10) for the validity of *CPT* theorem both in the Hamiltonian

proof (Luders, Pauli) and in the axiomatic one (Jost, Bogoliubov), taking into account that there is no example of a QFT, which satisfies the weak local commutativity condition (WLC) but not the local commutativity (LC).

6. – Conclusions

Let me summarize the results. We have presented a very simple class of interacting nonlocal quantum field theories, which violate *CPT* invariance and preserve Lorentz invariance. This result invalidates a general claim made previously by Greenberg, that “*CPT* violation implies violation of Lorentz invariance”. Violation of Lorentz invariance does not necessarily lead to *CPT* violation.

We hope that we have made a step in the right direction.

* * *

I would like to thank the organizers of La Thuile conference, particularly M. GRECO, for their warm hospitality and for the excellent conference. This research was partly supported by RFBR grant 11-02-00441.

REFERENCES

- [1] CHAICHIAN M., DOLGOV A. D., NOVIKOV V. A. and TUREANU A., *Phys. Lett. B*, **699** (2011) 177.
- [2] LÜDERS G., *Mat.-Fis. Medd.*, **28** (1954) 5.
- [3] PAULI W., *Phys. Rev.*, **58** (1940) 716; PAULI W., in *Niels Bohr and the development of physics* (Pergamon Press, London) 1955.
- [4] JOST R., *Helv. Phys. Acta*, **30** (1957) 409.
- [5] MURAYAMA H. and YANAGIDA T., *Phys. Lett. B*, **520** (2001) 263.
- [6] BARENBOIM G., BORISSOV L., LYKKEN J.D. and SMIRNOV A. Y., *JHEP*, **0210** (2002) 001; BARENBOIM G., BORISSOV L. and LYKKEN J. D., *Phys. Lett. B*, **534** (2002) 106.
- [7] GREENBERG O. W., *Phys. Rev. Lett.*, **89** (2002) 231602.

New physics searches in flavour physics

D. M. STRAUB

Scuola Normale Superiore and INFN, Sezione di Pisa - Piazza dei Cavalieri 7, 56126 Pisa, Italy

(ricevuto il 29 Settembre 2011; pubblicato online il 24 Gennaio 2012)

Summary. — The origin of flavour and CP violation is among the most important open questions in particle physics. Imminent results from the LHC as well as planned dedicated flavour physics experiments might help to shed light on this puzzle. This talk concentrates on the NP sensitivity of the rare B decays $B_{s,d} \rightarrow \mu^+ \mu^-$ and $B \rightarrow K^* \mu^- \mu^-$ and of the CP -violating phase in B_s mixing. A brief summary of a supersymmetric model with interesting signatures in the flavour sector is presented.

PACS 12.60.-i – Models beyond the standard model.

PACS 13.20.He – Decays of bottom mesons.

1. – Introduction

The tremendous progress in experimental flavour physics facilitated by the B factories, the Tevatron and other experiments shows that the CKM picture of flavour and CP violation describes the data well, both for tree and loop-induced processes. Since the Standard Model (SM) is only an effective theory valid up to some energy scale Λ , which is yet to be determined but is expected to lie in the TeV region from naturalness considerations, this success is a challenge for theories of new physics (NP). Assuming generic flavour and CP -violating couplings, the bounds on Λ from $\Delta F = 2$ processes exceed 10000 TeV [1]. On the other hand, given that a theoretical understanding of the hierarchical structure of quark masses and CKM mixings is still lacking, this paradox might simply indicate that the flavour structure of NP is related to the SM one. If in fact the Yukawa couplings, already present in the SM, are the *only* sources of breaking of the flavour symmetry, theories with this property of Minimal Flavour Violation (MFV, [2,3]) can have TeV-scale dynamics without being in conflict with observations [4].

Then again, MFV might well be too restrictive an assumption. Concrete models aiming to explain the origin of flavour often bring about a certain amount of non-minimal flavour violation (see, *e.g.*, [5-8]). Furthermore, the MFV principle does not preclude the presence of flavour-blind CP -violating phases [9,10]. Therefore, testing whether indeed the Yukawa couplings are the only source of flavour breaking and testing whether indeed the CKM phase is the only source of CP breaking are among the major goals of flavour physics in this decade.

TABLE I. – SM predictions and 95% CL experimental upper bounds on the $B_q \rightarrow \mu^+ \mu^-$ branching ratios [11, 12].

Observable	SM prediction	Experimental bound
$\text{BR}(B_s \rightarrow \mu^+ \mu^-)$	$(3.2 \pm 0.2) \times 10^{-9}$	$< 43 \times 10^{-9}$
$\text{BR}(B_d \rightarrow \mu^+ \mu^-)$	$(0.10 \pm 0.01) \times 10^{-9}$	$< 7.6 \times 10^{-9}$

The experimental prospects for progress in this direction are excellent, in view of planned dedicated flavour physics experiments like the Super B factories and searches for electric dipole moments (EDMs) or rare K decays; Moreover, in the near future, important results on $b \rightarrow s$ transitions are expected from the LHC. Sections. **2-4** will therefore discuss three particularly promising probes of NP at the LHC: the rare leptonic decays $B_{s,d} \rightarrow \mu^+ \mu^-$, CP violation in B_s mixing, and angular observables in the $B \rightarrow K^* \mu^+ \mu^-$ decay. Section **5** contains a brief summary of a model leading to interesting signatures in precision flavour experiments: supersymmetry with hierarchical squark masses, effective MFV and flavour-blind phases.

2. – $B_{s,d} \rightarrow \mu^+ \mu^-$

The decays $B_{s,d} \rightarrow \mu^+ \mu^-$ are strongly helicity suppressed in the SM and have not been experimentally observed yet; the current upper bounds still lie one/two orders of magnitude above the SM predictions (see table I) but will be improved in the near future by the Tevatron and LHC experiments.

Concerning NP effects in $B_s \rightarrow \mu^+ \mu^-$, in models where only the SM Wilson coefficient C_{10} receives NP contributions, an order-of-magnitude enhancement of the branching ratio is disfavoured due to constraints from inclusive and exclusive $b \rightarrow s \ell^+ \ell^-$ transitions on C_{10} . In that case, $\text{BR}(B_s \rightarrow \mu^+ \mu^-) \lesssim 10^{-8}$ [13].

Much larger enhancements are possible in principle in models with contributions to the scalar and/or pseudoscalar Wilson coefficients $C_{S,P}$. In two-Higgs-doublet models, a neutral Higgs penguin contributes to the branching fraction with an enhancement factor of $\tan \beta^4$, where $\tan \beta$ is the ratio of Higgs VEVs. In the MSSM, this dependence is even $\tan \beta^6$. Consequently, an upper bound $\text{BR}(B_s \rightarrow \mu^+ \mu^-) < 10^{-8}$ would already constrain numerous well-motivated NP scenarios, such as SUSY GUTs with a unification of Yukawa couplings [14]⁽¹⁾.

An important test of MFV is represented by the measurement of the ratio of the two $B_q \rightarrow \mu^+ \mu^-$ branching ratios. In MFV (as defined in [3]), it is simply given by

$$(1) \quad \frac{\text{BR}(B_s \rightarrow \mu^+ \mu^-)}{\text{BR}(B_d \rightarrow \mu^+ \mu^-)} = \frac{\tau_{B_s} f_{B_s}^2 m_{B_s}}{\tau_{B_d} f_{B_d}^2 m_{B_d}} \left| \frac{V_{ts}}{V_{td}} \right|^2.$$

While a simultaneous enhancement over the SM satisfying (1) would be a strong indication in favour of MFV, a non-SM effect incompatible with (1) would immediately rule out MFV. Figure 1 (for details see [16]) shows possible values of this ratio attained in

⁽¹⁾ On the other hand, even within the MFV MSSM very large $\tan \beta$ would remain a valid possibility if the trilinear couplings are small, such as in gauge mediation scenarios [15].

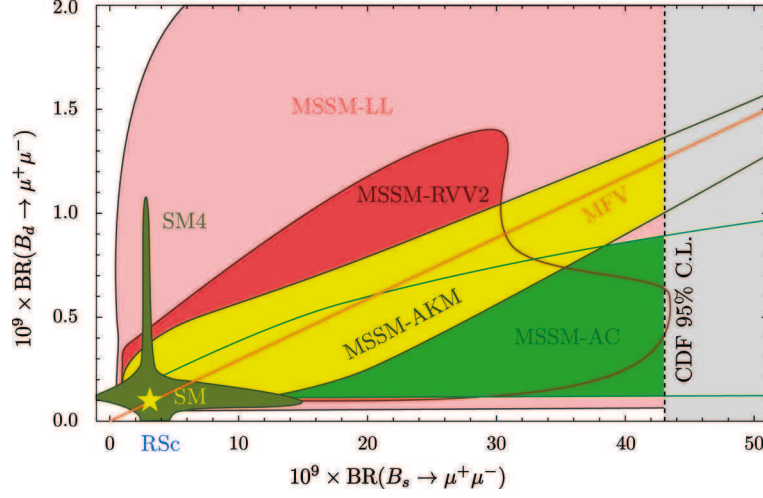


Fig. 1. – Correlation between the branching ratios of $B_s \rightarrow \mu^+\mu^-$ and $B_d \rightarrow \mu^+\mu^-$ in MFV, the SM4 and four SUSY flavour models. The gray area is ruled out experimentally. The SM point is marked by a star. Taken from [16].

several non-MFV models: four SUSY flavour models studied in [5] and the SM with 4 generations [12]. This highlights the power of the correlation between $B_s \rightarrow \mu^+\mu^-$ and $B_d \rightarrow \mu^+\mu^-$ to discriminate between different NP models.

3. – CP violation in B_s mixing

In the SM, CP violation in B_s mixing is a small effect since the relevant combination of CKM elements has an accidentally small phase,

$$(2) \quad \phi_s \equiv \arg(M_{12}) = 2\beta_s \equiv 2 \arg \left(-\frac{V_{ts}^* V_{tb}}{V_{cs}^* V_{cb}} \right) \approx -0.04.$$

Recently however, two experimental hints for a possibly large non-SM contribution to ϕ_s have emerged. One concerns the mixing-induced CP asymmetry $S_{\psi\phi}$ extracted from the time-dependent CP asymmetry in $B_s \rightarrow J/\psi\phi$ decays,

$$(3) \quad A_{\text{CP}}^s(\psi\phi, t) \equiv \frac{\Gamma(\bar{B}_s(t) \rightarrow \psi\phi) - \Gamma(B_s(t) \rightarrow \psi\phi)}{\Gamma(\bar{B}_s(t) \rightarrow \psi\phi) + \Gamma(B_s(t) \rightarrow \psi\phi)} \approx S_{\psi\phi} \sin(\Delta M_s t),$$

where $S_{\psi\phi} = -\sin \phi_s$. The other concerns the charge asymmetry A_{SL} in dimuon events at D0, which can be related to the semileptonic CP asymmetries in flavour-specific B_d and B_s decays, $a_{\text{SL}}^{d,s}$, as [17]

$$(4) \quad A_{\text{SL}} \approx (a_{\text{SL}}^d + a_{\text{SL}}^s) / 2,$$

with $O(10\%)$ uncertainties on the coefficients on the right-hand side of (4).

While 2009 results on $S_{\psi\phi}$ showed a discrepancy with the SM somewhere in the ballpark of 3 standard deviations [18], 2010 updates seem to be in agreement with the

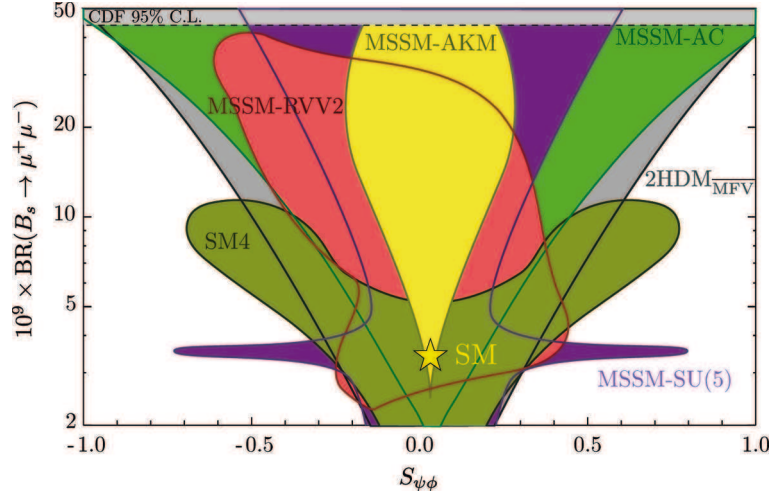


Fig. 2. – Correlation between the branching ratio of $B_s \rightarrow \mu^+ \mu^-$ and the mixing-induced CP asymmetry $S_{\psi\phi}$ in the SM4, the two-Higgs doublet model with flavour blind phases and three SUSY flavour models. The SM point is marked by a star.

SM at the 1σ level [19, 20], although no combination has been performed yet. The D0 result on A_{SL} deviates by 3.2σ from the SM [21], interestingly pointing in the same direction as the possible effect in $S_{\psi\phi}$ ⁽²⁾.

If these hints turn out to be genuine signals of NP in B_s mixing, it would have far-reaching consequences, in particular for theories with MFV. If a theory satisfying MFV does not have any source of CP violation beyond the CKM phase, a sizable B_s mixing phase cannot be generated. Even if the MFV theory has flavour-blind phases, this is nontrivial. While a two-Higgs doublet model with MFV and flavour-blind phases can generate a sizable ϕ_s [23, 24], this possibility is precluded in the MSSM by the impact of constraints like $B \rightarrow X_s \gamma$ and $B_s \rightarrow \mu^+ \mu^-$ [5]. A confirmation of ϕ_s deviating significantly from the value in (2) would thus immediately rule out many well-motivated theories, including the MFV MSSM.

Another interesting tool to discriminate between NP models is the correlation between $S_{\psi\phi}$ and the branching ratio of $B_s \rightarrow \mu^+ \mu^-$. In many models, sizable deviations from the SM prediction for ϕ_s are tied to the presence of scalar currents, which can also affect $B_s \rightarrow \mu^+ \mu^-$. This is the case *e.g.* for the two-Higgs doublet model with MFV and flavour-blind phases ($2HDM_{MFV}$) or for the SUSY flavour model of Agashe and Carone (AC, [25]). As shown in fig. 2, sizable $S_{\psi\phi}$ implies a sizable enhancement of $BR(B_s \rightarrow \mu^+ \mu^-)$ in these models, while the converse is obviously not true. In the SM4, on the other hand, even the converse statement is true: If $B_s \rightarrow \mu^+ \mu^-$ is found with a rate significantly enhanced with respect to the SM, this model unambiguously predicts a sizable deviation also in $S_{\psi\phi}$. In yet other models, like in the $SU(5)$ model of [26], both observables can be enhanced independently of each other, but a simultaneous enhancement is unlikely.

⁽²⁾ After this talk was given, preliminary data on $B_s \rightarrow J/\psi\phi$ from the LHCb experiment were presented [22] also showing a preference for an effect in the same direction, although still with a small significance.

4. $B \rightarrow K^* \mu^+ \mu^-$

The exclusive decay $\bar{B} \rightarrow \bar{K}^{*0}(\rightarrow K^- \pi^+) \mu^+ \mu^-$ gives access to many observables potentially sensitive to NP [27-31, 13]; since it is a “self-tagging” decay, it also allows a straightforward measurement of CP asymmetries.

The decay poses several theoretical challenges. In addition to calculating the 7 $B \rightarrow K^*$ form factors, one has to estimate non-factorizable strong interaction effects. At intermediate values of the dilepton invariant mass squared q^2 , resonant charmonium production leads to a breakdown of quark-hadron duality. The most studied region is the low q^2 region, where QCD factorization can be used to calculate non-factorizable corrections [32, 33] and light-cone sum rules to calculate the form factors [34, 30]. The high- q^2 region above the charmonium resonances has recently attracted increasing attention [13, 35]. While QCD factorization and LCSR methods are not applicable in this kinematical domain, a local operator product expansion in powers of $1/\sqrt{q^2}$ allows a systematic calculation of the observables [36, 35]. In [35], it has been argued that, in contrast to the low- q^2 region, non-perturbative corrections *not* accounted for by the form factors are small (see also [37]).

A complete set of observables accessible in the angular distribution of the decay and its CP -conjugate is given by the 9 CP -averaged angular coefficients S_i and the 9 CP asymmetries A_i , defined in terms of the angular coefficients I_i, \bar{I}_i as [30]

$$(5) \quad S_i = (I_i + \bar{I}_i) \left/ \frac{d(\Gamma + \bar{\Gamma})}{dq^2} \right., \quad A_i = (I_i - \bar{I}_i) \left/ \frac{d(\Gamma + \bar{\Gamma})}{dq^2} \right..$$

Not all of the S_i and A_i are both theoretically interesting and experimentally promising. In addition, at B factories, at the Tevatron and at the early LHC, statistics is quite limited so a full angular analysis is not possible and it might be easier to consider one- or two-dimensional angular distributions depending on a limited set of observables.

In addition to the observables⁽³⁾ which have already been studied by BaBar [39], Belle [40] and CDF [41]—the differential branching ratio, the forward-backward asymmetry and the K^* longitudinal polarization fraction—two observables sensitive to NP that could be extracted from a one-dimensional angular distribution are the CP -averaged S_3 and the CP -asymmetry A_9 . While they are both negligibly small in the SM, they could be nonzero in NP models with right-handed currents [27, 30].

Two additional observables could be extracted from a two-dimensional angular distribution and might be accessible even during the early LHC running: the CP -averaged observable S_5 and the CP -asymmetry A_7 . In [31], it has been shown that even with an integrated luminosity of only 2 fb^{-1} , LHCb can measure S_5 with a precision that already allows to probe certain NP scenarios. Since A_7 is accessible from the same angular distribution, the naive expectation is that the sensitivity should be comparable. Just as A_9 , A_7 is a T-odd CP asymmetry, meaning that it is not suppressed by small strong phases [28]. Sizable effects in A_7 of up to 20% are expected in well-motivated NP scenarios like the one discussed in the next section.

⁽³⁾ See [38] for a dictionary between different notations for the $B \rightarrow K^* \mu^+ \mu^-$ observables.

5. – CP violation in supersymmetry with effective MFV

As mentioned in the introduction, the MFV principle provides a symmetry argument to explain the absence of any evidence for flavour violation beyond the SM, but does not address the absence of signals of CP violation beyond the CKM phase, *e.g.* in EDMs.

In supersymmetry, a different way to address the flavour problem is to assume a strong hierarchy between the squarks of the first two *versus* the ones of the third generation: the heaviness of the former helps evading the strong bounds from K physics, while the lightness of the latter preserves the SUSY solution to the gauge hierarchy problem. For a generic flavour structure of the soft SUSY breaking terms, this hypothesis is however by far insufficient to ensure the absence of excessive flavour violation and needs to be extended by some amount of flavour alignment (see [42] and references therein).

In ref. [43], the hierarchical sfermion idea was combined with a specific flavour symmetry-breaking pattern inspired by MFV. The starting point is a global flavour symmetry in the quark sector of the form

$$(6) \quad G_F = U(1)_{\tilde{B}_1} \otimes U(1)_{\tilde{B}_2} \otimes U(1)_{\tilde{B}_3} \otimes U(3)_{d_R},$$

where \tilde{B}_i acts like baryon number, but only for the right-handed up-type and the left-handed (s)quark fields. G_F is subsequently broken down to baryon number by a single spurion, the down-type Yukawa coupling Y_d . As a consequence, it was shown in [43] that the theory is essentially MFV-like at low energies (therefore the name “Effective MFV”), with the most significant constraint coming from CP violation in neutral kaon mixing.

Interestingly, hierarchical sfermions also ameliorate the SUSY CP problem compared to MFV since the one-loop contributions to the experimentally accessible EDMs involve the superpartners of first generation fermions. Therefore, in ref. [44] the Effective MFV (EMFV) framework was analyzed allowing all the CP violating phases not forbidden by the flavour symmetry. With hierarchical squark masses, the usual argument that flavour blind phases need to be tiny to meet the EDM bounds does not apply in EMFV.

The main results of [44] can be summarized as follows.

- The one-loop contributions to the EDMs are under control if the first generation up-squark and sneutrino masses fulfill the following bounds,

$$(7) \quad m_{\tilde{u}} > 2.7 \text{ TeV} \times (\sin \phi_\mu \tan \beta)^{\frac{1}{2}}, \quad m_{\tilde{\nu}} > 4.0 \text{ TeV} \times (\sin \phi_\mu \tan \beta)^{\frac{1}{2}}.$$

- Two-loop contributions from Barr-Zee-type diagrams not suppressed by first- or second-generation sfermion masses give contributions to the electron EDM that are in the ballpark of the experimental bound in the case of a sizable phase in the μ term, and are usually below it if the stop trilinear coupling (but not μ) is complex.
- Even if the EDMs are under control, potentially visible effects can arise in CP asymmetries in B physics, induced by one-loop contributions involving third generation sfermions to the magnetic and chromomagnetic $b \rightarrow s$ dipole operators.

As an example for the possible effects in B physics, fig. 3 shows the correlation between the mixing-induced CP asymmetry in $B \rightarrow \eta' K_S$ and the angular CP asymmetry A_7 (integrated in the low q^2 range) in $B \rightarrow K^* \mu^+ \mu^-$ discussed in sect. 4 for two scenarios: first, assuming an arbitrary phase of the μ term, second, assuming an arbitrary phase

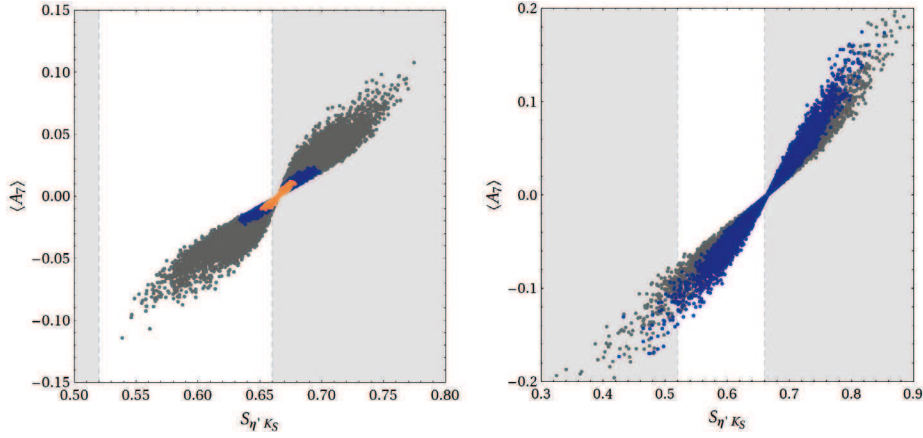


Fig. 3. – Correlation between the mixing-induced CP asymmetry in $B \rightarrow \eta' K_S$ and the angular CP asymmetry $\langle A_7 \rangle$ in $B \rightarrow K^* \mu^+ \mu^-$ in two scenarios with a complex μ term (left) or complex A_t term (right). The gray points are allowed by all constraints except d_e , while the blue points are compatible with all constraints. The orange points in the left-hand plot have $|\sin \phi_\mu| < 0.2$.

for the stop trilinear coupling. In particular in the second scenario, sizable effects in the CP asymmetries can be generated without violating the EDM bounds⁽⁴⁾.

This study provides an example of a model with interesting signatures in flavour physics observables and also highlights the importance of dedicated flavour physics experiments, like EDM searches or Super B factories, as complements to the LHC. The results are applicable to all MSSM scenarios with hierarchical sfermions (see, *e.g.*, [8]), with possible additional effects in the presence of non-minimal flavour violation.

6. – Conclusions

The LHC era is in full swing, also in flavour physics. Imminent results on decays like $B_s \rightarrow \mu^+ \mu^-$ or $B \rightarrow K^* \mu^+ \mu^-$ and on CP violation in B_s mixing discussed in this talk will help shed light on the question whether there is new physics at the TeV scale, and subsequently whether the Yukawa couplings are the only source of breaking of the flavour and CP symmetries, as in the SM.

Supersymmetry with hierarchical squark masses, combined with Effective MFV [43, 44], can solve the SUSY flavour *and* CP problems and leads to potentially visible effects in CP asymmetries in B physics, without violating EDM bounds.

* * *

I thank the organizers for their invitation to this wonderful conference and WOLFGANG ALTMANNSHOFER for useful comments on the manuscript. This work was supported by the EU ITN “Unification in the LHC Era”, contract PITN-GA-2009-237920 (UNILHC).

⁽⁴⁾ The signals in flavour physics arising in this second scenario are very similar to the effects in the MFV MSSM with a complex A_t term and a real μ term [45, 5]. Of course, the two setups are easily distinguishable on the basis of their different spectrum.

REFERENCES

- [1] ISIDORI G., NIR Y. and PEREZ G., arXiv:1002.0900 [hep-ph].
- [2] BURAS A. J. *et al.*, *Phys. Lett. B*, **500** (2001) 161.
- [3] D'AMBROSIO G. *et al.*, *Nucl. Phys. B*, **645** (2002) 155.
- [4] HURTH T., ISIDORI G., KAMENIK J. F. and MESCIA F., *Nucl. Phys. B*, **808** (2009) 326.
- [5] ALTMANNSHOFER W. *et al.*, *Nucl. Phys. B*, **830** (2010) 17.
- [6] GRINSTEIN B., REDI M. and VILLADORO G., *JHEP*, **11** (2010) 067.
- [7] BURAS A. J., GROJEAN C., POKORSKI S. and ZIEGLER R., arXiv:1105.3725 [hep-ph].
- [8] BARBIERI R., ISIDORI G., JONES-PEREZ J., LODONE P. and STRAUB D. M., arXiv:1105.2296 [hep-ph].
- [9] MERCOLLI L. and SMITH C., *Nucl. Phys. B*, **817** (2009) 1.
- [10] PARADISI P. and STRAUB D. M., *Phys. Lett. B*, **684** (2010) 147.
- [11] CDF COLLABORATION, CDF Public Note 9892.
- [12] BURAS A. J. *et al.*, *JHEP*, **09** (2010) 106.
- [13] BOBETH C., HILLER G. and VAN DYK D., *JHEP*, **07** (2010) 098.
- [14] ALTMANNSHOFER W. *et al.*, *Phys. Lett. B*, **668** (2008) 385.
- [15] ALTMANNSHOFER W. and STRAUB D. M., *JHEP*, **09** (2010) 078.
- [16] STRAUB D. M., arXiv:1012.3893 [hep-ph].
- [17] GROSSMAN Y., NIR Y. and RAZ G., *Phys. Rev. Lett.*, **97** (2006) 151801.
- [18] PUNZI G., *PoSE*, **PS-HEP2009** (2009) 022, LENZ A. *et al.*, *Phys. Rev. D*, **83** (2011) 036004, ASNER D. *et al.*, arXiv:1010.1589 [hep-ex].
- [19] CDF COLLABORATION, CDF Public Note 10206.
- [20] D0 COLLABORATION, D0 Conference Note 6098.
- [21] ABAZOV V. M. *et al.*, *Phys. Rev. D*, **82** (2010) 032001.
- [22] UWER U., talk given at the *13th International Conference on B-Physics at Hadron Machines, April 4 2011, Amsterdam*.
- [23] KAGAN A. L., PEREZ G., VOLANSKY T. and ZUPAN J., *Phys. Rev. D*, **80** (2009) 076002.
- [24] BURAS A. J., CARLUCCI M. V., GORI S. and ISIDORI G., *JHEP*, **10** (2010) 009.
- [25] AGASHE K. and CARONE C. D., *Phys. Rev. D*, **68** (2003) 035017.
- [26] BURAS A. J., NAGAI M. and PARADISI P., *JHEP*, **05** (2011) 005.
- [27] LUNGI E. and MATIAS J., *JHEP*, **04** (2007) 058.
- [28] BOBETH C., HILLER G. and PIRANISHVILI G., *JHEP*, **07** (2008) 106.
- [29] EGEDE U. *et al.*, *JHEP*, **11** (2008) 032.
- [30] ALTMANNSHOFER W. *et al.*, *JHEP*, **01** (2009) 019.
- [31] BHARUCHA A. and REECE W., *Eur. Phys. J. C*, **69** (2010) 623.
- [32] BENEKE M., FELDMANN T. and SEIDEL D., *Nucl. Phys. B*, **612** (2001) 25.
- [33] BENEKE M., FELDMANN T. and SEIDEL D., *Eur. Phys. J. C*, **41** (2005) 173.
- [34] BALL P. and ZWICKY R., *Phys. Rev. D*, **71** (2005) 014029.
- [35] BEYLICH M., BUCHALLA G. and FELDMANN T., *Eur. Phys. J. C*, **71** (2011) 1635.
- [36] GRINSTEIN B. and PIRJOL D., *Phys. Rev. D*, **70** (2004) 114005.
- [37] KHODJAMIRIAN A. *et al.*, *JHEP*, **09** (2010) 089.
- [38] STRAUB D. M., arXiv:1105.4719v1 [hep-ph].
- [39] AUBERT B. *et al.*, *Phys. Rev. D*, **79** (2009) 031102.
- [40] WEI J. T. *et al.*, *Phys. Rev. Lett.*, **103** (2009) 171801.
- [41] AALTONEN T. *et al.*, *Phys. Rev. Lett.*, **106** (2011) 161801.
- [42] GIUDICE G. F., NARDECCHIA M. and ROMANINO A., *Nucl. Phys. B*, **813** (2009) 156.
- [43] BARBIERI R. *et al.*, *JHEP*, **12** (2010) 070.
- [44] BARBIERI R., LODONE P. and STRAUB D. M., *JHEP*, **05** (2011) 049.
- [45] ALTMANNSHOFER W., BURAS A. J. and PARADISI P., *Phys. Lett. B*, **669** (2008) 239.

New results on K physics from NA48 and NA62 experiments

S. BALEV

European Organization for Nuclear Research, CERN - CH-1211 Geneve 23, Switzerland

(ricevuto il 29 Settembre 2011; pubblicato online il 25 Gennaio 2012)

Summary. — Several analyses from the experiments NA48 and NA62 are presented in this paper, including new measurements with $K^\pm \rightarrow \pi^\pm \mu^+ \mu^-$ decays, $K_{\mu 3}^\pm$ form factors, branching fraction of $K^\pm \rightarrow \pi^+ \pi^- e^\pm \nu$, and precise LFV test with K_{l2} decays.

PACS 13.20.Eb – Decays of K mesons.

PACS 12.15.Hh – Determination of Cabibbo-Kobayashi & Maskawa (CKM) matrix elements.

PACS 11.30.Fs – Global symmetries (*e.g.*, baryon number, lepton number).

1. – Introduction

During 2003 and 2004 the experiment NA48/2 collected a large sample of simultaneously recorded K^+ and K^- decays in order to search for direct CP violation in three-pion final state [1]. Many other precise studies were performed on this multipurpose data-set, taking advantage of the highly symmetric experimental conditions. Sections. 3, 4 and 5 briefly discuss several of the most recent NA48/2 measurements. In 2007 started the data taking for the first phase of the experiment NA62⁽¹⁾, dedicated to precise LFV test with K_{l2} decays (sect. 6).

2. – Experimental setup

The beam line of NA48/2 and the first phase of NA62 experiment is designed to deliver simultaneously K^+ and K^- , produced on a beryllium target from SPS primary protons⁽²⁾. The beams of 60 ± 3 GeV/ c (74 ± 2 GeV/ c) momentum for NA48/2 (NA62) are selected by a system of magnetic elements. After final cleaning and collimation the two beams enter the 114 m long decay volume. The momenta of the charged decay products are measured by a magnetic spectrometer consisting of four drift chambers (DCH) and

⁽¹⁾ The future program of the experiment, now in advanced stage of construction, is dedicated to 10% measurement of the ultra-rare decay $K^+ \rightarrow \pi^+ \nu \bar{\nu}$ [2].

⁽²⁾ More detailed description and schematic view of the beam line can be found in [1].

a dipole magnet. The resolution of the spectrometer is $\sigma(p)/p = 1.0\% \oplus 0.044\%p$ for NA48/2 and $\sigma(p)/p = 0.5\% \oplus 0.009\%p$ for NA62 (p in GeV/ c). A scintillator hodoscope, located after the spectrometer, sends fast trigger signals from charged particles and measures their time with a resolution of 150 ps. The electromagnetic energy of particles is measured by a liquid krypton calorimeter (LKr), a quasi-homogeneous ionisation chamber with an active volume of 10 m³, 27 X_0 deep and segmented transversely into 13248 cells (2×2 cm² each). The energy resolution is $\sigma(E)/E = 0.032/\sqrt{E} \oplus 0.09/E \oplus 0.0042$ and the spatial resolution in the transverse coordinates x and y for a single electromagnetic shower is $\sigma_x = \sigma_y = 0.42/\sqrt{E} \oplus 0.06$ cm (E in GeV). A muon detector, composed of three planes of plastic scintillator strips, is used for muon identification. A beam pipe traversing the centres of the detectors allows undecayed beam particles and muons from decays of beam pions to continue their path in vacuum. A detailed description of the detector setup can be found in [3].

3. – $K_{\mu 3}^{\pm}$ form factors

3.1. Introduction. – The K_{l3} decays provide the cleanest and most accurate way to access the $|V_{us}|$ element of CKM-matrix. They are described by two form factors $f_{\pm}(t)$, functions of the 4-momentum transfer to the lepton system (t):

$$M = \frac{G_F}{2} V_{us} [f_+(t)(P_K - P_{\pi})^{\mu} \bar{u}_l \gamma_{\mu} (1 - \gamma_5) u_{\nu} + f_-(t) m_l \bar{u}_l (1 + \gamma_5) u_{\nu}]$$

The form factor $f_-(t)$ can be measured with $K_{\mu 3}$ only (and not with $K_{e 3}$ due to $m_e \ll M_K$). A linear combination of the two form factors can be defined: $f_0(t) = f_+(t) + t f_-(t)/(m_K^2 - m_{\pi}^2)$, with $f_+(0) = f_0(0)$ by construction. $f_+(0)$ is not measurable directly and the form factors are normalised to it: $\bar{f}_+(t) = f_+(t)/f_+(0)$ and $\bar{f}_0(t) = f_0(t)/f_+(0)$. Various parametrisations of the form factors are discussed in subsect. 3.3.

3.2. Event selection and analysis. – In order to reconstruct the $K_{\mu 3}$ candidates, it is required the presence of a single track with momentum above 10 GeV/ c and with a hit in the muon detector associated with it. The ratio of the energy deposit associated with the track in LKr (E) and the measured momentum by the spectrometer (p) should be $E/p < 0.2$, consistent with muon hypothesis⁽³⁾. The two photons from π^0 decays are identified as clusters of deposited energy in LKr, away from any other activity in the detector and not associated with tracks. The invariant mass of di-photon system ($m_{\gamma\gamma}$) is calculated assuming a position of the decay vertex, defined by the closest approach of the muon candidate to the nominal beam axis. It is required that $|m_{\gamma\gamma} - m_{\pi^0}| < 10$ MeV/ c^2 . The missing mass in $K_{\mu 3}^{\pm}$ hypothesis $m_{miss}^2 = (P_K - P_{\mu} - P_{\pi^0})^2$ should satisfy the condition $|m_{miss}^2| < 10$ MeV/ c^2 . A cut in $(M_{\pi^{\pm}\pi^0}, P_{\pi^{\pm}}^t)$ space, where $M_{\pi^{\pm}\pi^0}$ is the invariant mass of the final state particles in π^{\pm} hypothesis for the track and $P_{\pi^0}^t$ is the transverse momentum of π^0 , is used to suppress the dominant $K_{\pi^{\pm}\pi^0}^{\pm}$ background to 0.6%. The background contribution from $K_{\pi^{\pm}\pi^0\pi^0}^{\pm}$ is 0.14%. The total amount of selected $K_{\mu 3}^{\pm}$ candidates is $3.4 \cdot 10^6$.

The form factors parameters are extracted by a fit to the Dalitz plot, after background subtraction and acceptance correction. The radiative effects are simulated according to [4], changing the Dalitz plot slope by $\sim 1\%$.

⁽³⁾ The notation E/p is used with the same meaning in all the other sections of the paper.

3.3. Results. – Several parametrisations of the form factors has been studied. For the pole parametrisation $\bar{f}_{+,0}(t) = m_{V,S}^2/(m_{V,S}^2 - t)$ which describes exchange of K^* resonances with spin-parity $1^-(0^+)$ and mass $m_V(m_S)$, the following values for the free parameters were found: $m_V = 836 \pm 7_{\text{stat}} \pm 9_{\text{syst}}$ MeV/ c^2 ; $m_S = 1210 \pm 25_{\text{stat}} \pm 10_{\text{syst}}$ MeV/ c^2 . The parametrisation based on dispersive approach [5]:

$$\bar{f}_+(t) = \exp \left[\frac{t}{m_\pi^2} (\Lambda_+ + H(t)) \right], \quad \bar{f}_0(t) = \exp \left[\frac{t}{\Delta_{K\pi}} (\ln C + G(t)) \right]$$

gives the following results for the free parameters: $\Lambda_+ = (28.5 \pm 0.6_{\text{stat}} \pm 0.7_{\text{syst}} \pm 0.5_{\text{theor}}) \cdot 10^{-3}$ and $\ln C = (188.8 \pm 7.1_{\text{stat}} \pm 3.7_{\text{syst}} \pm 5.0_{\text{th}}) \cdot 10^{-3}$.

The slope parameters in the linear and quadratic expansion of the form factors in terms of t :

$$\bar{f}_{+,0}(t) = 1 + \lambda_{+,0} \frac{t}{m_\pi^2}, \quad \bar{f}_{+,0}(t) = 1 + \lambda'_{+,0} \frac{t}{m_\pi^2} + \frac{1}{2} \lambda''_{+,0} \left(\frac{t}{m_\pi^2} \right)^2,$$

are found to be: $\lambda'_+ = (30.3 \pm 2.7_{\text{stat}} \pm 1.4_{\text{syst}}) \cdot 10^{-3}$, $\lambda''_+ = (1.0 \pm 1.0_{\text{stat}} \pm 0.7_{\text{syst}}) \cdot 10^{-3}$ and $\lambda_0 = (15.6 \pm 1.2_{\text{stat}} \pm 0.9_{\text{syst}}) \cdot 10^{-3}$ (there is no sensitivity to λ''_0). The above preliminary results are very competitive with the measurements by other experiments and for the first time use $K_{\mu 3}^+$ decays.

4. – New results with $K^\pm \rightarrow \pi^\pm \mu^+ \mu^-$

The FCNC decay $K^\pm \rightarrow \pi^\pm \mu^+ \mu^-$ (denoted $K_{\pi\mu\mu}^\pm$) is induced at 1-loop in SM and its rate is dominated by long-distance contributions, involving one-photon exchange. During the 2003–2004 run the experiment NA48/2 collected a sample of 3120 $K_{\pi\mu\mu}^\pm$ decays, ~ 4.5 times larger than the total world sample, which allowed form factor, rate and asymmetry measurements with improved precision.

In the selection of this decay a presence of three tracks is required, forming a vertex in the decay volume, with only one pion candidate with $E/p < 0.8$. The other two tracks should carry opposite charges and be both consistent with the muon hypothesis (associated hits in the muon detector and $E/p < 0.2$). The invariant mass of the final state is required to be consistent with the nominal kaon mass within ± 8 MeV/ c^2 . The main source of background is $K^\pm \rightarrow \pi^\pm \pi^+ \pi^-$ (denoted $K_{3\pi^\pm}^\pm$) with $\pi \rightarrow \mu$ decay or mis-identification. This background is estimated to be $(3.3 \pm 0.5_{\text{stat}} \pm 0.5_{\text{syst}})\%$ from the forbidden “wrong sign” evens $\pi^\mp \mu^\pm \mu^\pm$.

The $K_{\pi\mu\mu}^\pm$ decay is sensitive to a single form factor $W(z)$, where $Z = (M_{\mu\mu}/M_K)^2$ [6]. The results within various models are summarised in table I: 1) Linear: $W(z) = G_F M_K^2 f_0 (1 + z\delta)$; 2) NLO ChPT [7]; 3) combined framework of ChPT and large- N_c QCD [8]; 4) ChPT parametrisation involving meson masses [9].

The branching ratio of $K^\pm \rightarrow \pi^\pm \mu^+ \mu^-$ is measured to be $(9.62 \pm 0.21_{\text{stat}} \pm 0.11_{\text{syst}} \pm 0.07_{\text{ext}}) \cdot 10^{-8}$, where the external error is related to the precision of the branching fraction of the normalisation mode $K_{3\pi^\pm}^\pm$. Having a measurement for both kaon charges, we put a limit on the charge asymmetry $|\Delta(K_{\pi\mu\mu}^\pm)| < 2.9 \times 10^{-2}$ at 90% CL. A new limit on forward-backward asymmetry is set: $|A_{FB}| < 2.3 \times 10^{-2}$ at 90% CL. Finally 52 “wrong sign” events are observed in the signal region with the expected background of (52.6 ± 19.8) estimated from MC simulation, leading to an upper limit of the $BR(K^\pm \rightarrow \pi^\mp \mu^\pm \mu^\pm) < 1.1 \cdot 10^{-9}$ at 90% CL. Full details about the selection procedure, the analysis technique and discussion of the above results can be found in [10].

TABLE I. – The measured model parameters, their correlation coefficients, χ^2/ndf of the fits, and the model-independent BR.

Model (1)	$\rho(f_0 , \delta) = -0.993$				$\chi^2/\text{ndf} = 12.0/15$		
$ f_0 =$	0.470	$\pm 0.039_{\text{stat.}}$	$\pm 0.006_{\text{syst.}}$	$\pm 0.002_{\text{ext.}}$	$=$	0.470	± 0.040
$\delta =$	3.11	$\pm 0.56_{\text{stat.}}$	$\pm 0.11_{\text{syst.}}$	$=$	$=$	3.11	± 0.57
Model (2)	$\rho(a_+, b_+) = -0.976$				$\chi^2/\text{ndf} = 14.8/15$		
$a_+ =$	-0.575	$\pm 0.038_{\text{stat.}}$	$\pm 0.006_{\text{syst.}}$	$\pm 0.002_{\text{ext.}}$	$=$	-0.575	± 0.039
$b_+ =$	-0.813	$\pm 0.142_{\text{stat.}}$	$\pm 0.028_{\text{syst.}}$	$\pm 0.005_{\text{ext.}}$	$=$	-0.813	± 0.145
Model (3)	$\rho(\tilde{w}, \beta) = 0.999$				$\chi^2/\text{ndf} = 13.7/15$		
$\tilde{w} =$	0.064	$\pm 0.014_{\text{stat.}}$	$\pm 0.003_{\text{syst.}}$	$=$	$=$	0.064	± 0.014
$\beta =$	3.77	$\pm 0.61_{\text{stat.}}$	$\pm 0.12_{\text{syst.}}$	$\pm 0.02_{\text{ext.}}$	$=$	3.77	± 0.62
Model (4)	$\rho(M_a, M_\rho) = 0.999$				$\chi^2/\text{ndf} = 15.4/15$		
$M_a/(\text{GeV}/c^2) =$	0.993	$\pm 0.083_{\text{stat.}}$	$\pm 0.016_{\text{syst.}}$	$\pm 0.001_{\text{ext.}}$	$=$	0.993	± 0.085
$M_\rho/(\text{GeV}/c^2) =$	0.721	$\pm 0.027_{\text{stat.}}$	$\pm 0.005_{\text{syst.}}$	$\pm 0.001_{\text{ext.}}$	$=$	0.721	± 0.028
$\text{BR} \times 10^8 =$	9.62	$\pm 0.21_{\text{stat.}}$	$\pm 0.11_{\text{syst.}}$	$\pm 0.07_{\text{ext.}}$	$=$	9.62	± 0.25

5. – Measurement of $K^\pm \rightarrow \pi^+\pi^-e^\pm\nu$ branching fraction

5.1. Introduction. – The semileptonic $K^\pm \rightarrow \pi^+\pi^-e^\pm\nu$ decay (denoted K_{e4}^{+-}) is one of the richest kaon decays, providing possibility for precise tests of ChPT. The hadronic part of the matrix element can be described in terms of two axial (F and G) and one vector (H) complex form factors [11]. Their expansions into partial s and p waves are further developed in Taylor series in $q^2 = M_{\pi\pi}^2/4m_{\pi^\pm}^2 - 1$ and $M_{e\nu}^2/4m_{\pi^\pm}^2$, where $M_{\pi\pi}$ and $M_{e\nu}$ are the invariant masses of the di-pion and di-lepton systems, respectively. This allows to determine the form factor parameters from the experimental data: $F = F_s e^{i\delta_s} + F_p \cos\theta_\pi e^{i\delta_p}$, $G = G_p e^{i\delta_g}$, $H = H_p e^{i\delta_h}$, where $F_s = f_s + f'_s q^2 + f''_s q^4 + f'_e M_{e\nu}^2/4m_\pi^2$, $F_p = f_p + f'_p q^2$, $G_p = g_p + g'_p q^2$, $H_p = h_p + h'_p q^2$.

Recently NA48/2 published a precise measurement of the relative form factors of K_{e4}^{+-} decays (normalised to f_s) and $\pi\pi$ -scattering lengths [12]. In order to access the absolute form factors with high precision, a new measurement of the decay probability (which is proportional to f_s^2) was performed by NA48/2.

5.2. K_{e4}^{+-} selection and background estimation. – Since the kaon flux is not measured, the branching ratio of K_{e4}^{+-} is calculated by normalising to the most suitable decay: $K_{3\pi^\pm}^\pm$. It is not only topologically similar, but its branching ratio is known with relatively good precision of 0.72% [13]. The selection procedures for the two decay modes share significant common part, which allows to minimise various systematic effects. The presence of three reconstructed tracks in the spectrometer forming a good vertex within the decay volume is required. No hits in the muon detector should be associated with the tracks. For K_{e4}^{+-} one of the tracks is required to be an electron candidate ($E/p > 0.9$). Additional π -e separation is achieved by using a highly efficient linear discriminant variable, which takes into account the shower shape and its relative position with respect to the corresponding track. The two other tracks (opposite charges) are required to have

$E/p < 0.8$ consistent with pion hypothesis. A cut in the $(M_{3\pi}, p^t)$ space is used in order to suppress the background from $K_{3\pi^\pm}^\pm$, where $M_{3\pi}$ is the invariant mass of the three tracks in pion hypothesis and p^t is the transverse momentum of the system. Additional cuts are applied against $K_{\pi\pi^0\pi^0}$ and $K_{\pi\pi^0}$ with Dalitz decays of π^0 . Fixing the kaon mass and the direction of the beam at their nominal values, the four-momentum conservation leads to a quadratic equation for the kaon momentum p_K due to the undetected neutrino. If solution in the range (54-66) GeV/c exists, the event is kept and the closest solution to the nominal beam momentum (60 GeV/c) is assigned to p_K . The three tracks in the $K_{3\pi}$ selection are required to have $E/p < 0.8$ and invariant mass consistent with m_K within ± 12 MeV/c².

A total of $1.11 \cdot 10^6$ events passes the full K_{e4}^{+-} selection ($7.12 \cdot 10^5$ K^+ and $3.97 \cdot 10^5$ K^-). The number of selected $K_{3\pi^\pm}^\pm$ decays for normalisation is $1.9 \cdot 10^9$.

The main source of background in K_{e4}^{+-} sample is coming from $K_{3\pi^\pm}^\pm$ decays with a pion misidentified as an electron, or with $\pi \rightarrow e$ decay. Since the $K^\pm \rightarrow e^\mp \pi^\pm \pi^\pm$ decay is suppressed by a factor of 10^{-10} due to $\Delta S = \Delta Q$ rule, counting these ‘‘wrong sign’’ events gives direct access to the expected $K_{3\pi^\pm}^\pm$ contamination (divided by 2) in K_{e4}^{+-} sample. With the described selection, the background is at the level of 0.95%. This estimation is confirmed by Monte Carlo simulation with 15% precision. The other components of the background are negligible.

5.3. Branching ratio calculation, systematic uncertainties and results. – The branching ratio of K_{e4}^{+-} is calculated as

$$BR(K_{e4}^{+-}) = \frac{N_{K_{e4}} - 2 \cdot N_{WS}}{N_{K_{3\pi}}} \cdot \frac{A_{K_{3\pi}}}{A_{K_{e4}}} \cdot \frac{\epsilon_{K_{3\pi}}}{\epsilon_{K_{e4}}} \cdot BR(K_{3\pi}),$$

where $N_{K_{e4}}$ and $N_{K_{3\pi}}$ are the number of selected signal and normalisation candidates, and N_{WS} is the number of ‘‘wrong sign’’ events. The acceptances for both modes $A_{K_{e4}} = 18.22\%$ and $A_{K_{3\pi}} = 24.18\%$ are calculated using the detailed MC simulation of the experimental setup, based on Geant3. The trigger efficiencies for both modes are measured on control samples and found to be $\epsilon_{K_{e4}} = 98.3\%$ and $\epsilon_{K_{3\pi}} = 97.5\%$. Finally $BR(K_{3\pi}) = (5.59 \pm 0.04)\%$ is the branching ratio of $K_{3\pi^\pm}^\pm$ decay mode [13], determining the external error of the result.

The following relative systematic uncertainties for $BR(K_{e4}^{+-})$ are considered: 0.18% from acceptance estimation and beam geometry; 0.16% from the performance of the muon vetoing; 0.15% from accidental activity in the detectors; 0.14% from the background estimation; 0.09% from particle identification; 0.08% from the simulation of the radiative effects. The total relative systematic error is 0.35%.

The preliminary result on the total data set is $BR(K_{e4}^{+-}) = (4.279 \pm 0.004_{\text{stat}} \pm 0.005_{\text{trig}} \pm 0.015_{\text{syst}} \pm 0.031_{\text{ext}}) \cdot 10^{-5} = (4.279 \pm 0.035) \cdot 10^{-5}$ (including the radiative K_{e4}^{+-} decays). The trigger error is related to the limited control sample used for efficiency measurement. The total error is three times smaller than the current world average [13]. The branching ratios for both positive and negative kaons are compatible: $BR(K_{e4}^+) = (4.277 \pm 0.009) \cdot 10^{-5}$ and $BR(K_{e4}^-) = (4.283 \pm 0.012) \cdot 10^{-5}$ (only the combined statistical and trigger error is quoted). This is the first measurement performed for negative kaons. The ratio of the decay probabilities for K_{e4}^{+-} and $K_{3\pi}$ is $(7.654 \pm 0.030) \cdot 10^{-4}$, where the quoted total error is 5 times smaller than the world average. An estimation of the absolute form factors using the new branching fraction measurement is in progress.

6. – Lepton flavour violation test with NA62

6.1. Introduction. – The ratio of kaon leptonic decay rates $R_K = \Gamma(K_{e2}^\pm)/\Gamma(K_{\mu2}^\pm)$ is known in the SM with excellent precision due to cancellation of the hadronic effects: $R_K^{SM} = (m_e/m_\mu)^2 (\frac{m_K^2 - m_e^2}{m_K^2 - m_\mu^2})^2 (1 + \delta R_{QED}) = (2.477 \pm 0.001) \times 10^{-5}$ [14], where $\delta R_{QED} = (-3.78 \pm 0.04)\%$ is a correction due to the inner bremsstrahlung (IB) $K_{l2\gamma}$ process which is included by definition into R_K ⁽⁴⁾. Being helicity suppressed due to $V - A$ structure of the charged weak current, R_K is sensitive to non-SM effects. In particular MSSM allows non-vanishing $e - \tau$ mixing, mediated by H^+ , which can lead to few percent enhancement of R_K [15].

The present world average of $R_K = (2.493 \pm 0.031) \times 10^{-5}$ is dominated by the recent KLOE final result [16]. The NA62 experiment collected data during 2007 and 2008 aiming to reach accuracy of $\sim 0.4\%$. The final result on partial data set is presented here.

6.2. Analysis strategy. – Due to the topological similarity of K_{e2} and $K_{\mu2}$ decays a large part of the selection conditions are common for both decays. We require the presence of single reconstructed charged track with momentum $13 \text{ GeV}/c < p < 65 \text{ GeV}/c$ (the lower limit is due to the 10 GeV LKr energy deposit requirement in K_{e2} trigger). The track extrapolated to DCH, LKr and HOD should be within their geometrical acceptances. The CDA between the charged track and the nominal kaon beam axis should be less than 1.5 cm. The event is rejected if a cluster in the LKr with energy larger than 2 GeV and not associated with track is present, in order to suppress the background from other kaon decays.

A kinematical separation between K_{e2} and $K_{\mu2}$ for low track momenta is possible, based on the reconstructed missing mass, assuming the track to be an electron or a muon: $M_{\text{miss}}^2(l) = (P_K - P_l)^2$, where P_l ($l = e, \mu$) is the four-momentum of the lepton. Since the kaon four-momentum P_K is not measured directly in every event, its average is monitored in each SPS spill with fully reconstructed $K^\pm \rightarrow 3\pi^\pm$ decays. A cut $M_1^2 < M_{\text{miss}}^2(e) < M_2^2$ is applied to select K_{e2} candidates, and $M_1^2 < M_{\text{miss}}^2(\mu) < M_2^2$ for $K_{\mu2}$ ones, where M_1^2 and M_2^2 vary from 0.010 to 0.016 $(\text{GeV}/c^2)^2$ for different track momenta, depending on M_{miss} resolution. Particle identification is based on the ratio E/p . Particles with $0.95 < E/p < 1.1$ for $p > 25 \text{ GeV}/c$ and $0.90 < E/p < 1.1$ otherwise⁽⁵⁾, are identified as electrons, while particles with $E/p < 0.85$ as muons.

The analysis is based on counting the number of reconstructed K_{e2} and $K_{\mu2}$ candidates with the selection described above. Since the decays are collected simultaneously, the result does not depend on kaon flux measurement and the systematic effects due to the detector efficiency cancel to first order. To take into account the momentum dependence of signal acceptance and background level, the measurement is performed independently in bins of reconstructed lepton momentum. The ratio R_K in each bin is computed as

$$(1) \quad R_K = \frac{1}{D} \cdot \frac{N(K_{e2}) - N_B(K_{e2})}{N(K_{\mu2}) - N_B(K_{\mu2})} \cdot \frac{f_\mu \times A(K_{\mu2}) \times \epsilon(K_{\mu2})}{f_e \times A(K_{e2}) \times \epsilon(K_{e2})} \cdot \frac{1}{f_{\text{LKr}}},$$

⁽⁴⁾ Unlike the structure dependent (SD) $K_{l2\gamma}$.

⁽⁵⁾ The background to K_{e2} is concentrated in the region $p > 25 \text{ GeV}/c$, hence the need of tighter electron ID.

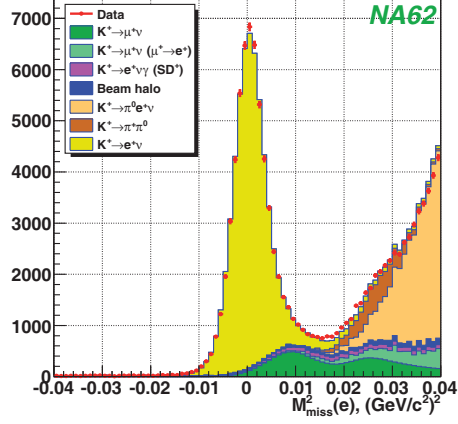


Fig. 1. – $M_{\text{miss}}^2(e)$ distributions for K_{e2} candidates and for various backgrounds.

where $N(K_{l2})$ are the numbers of selected K_{l2} candidates ($l = e, \mu$), $N_B(K_{l2})$ are numbers of background events, f_l are efficiencies of electron and muon identification criteria, $A(K_{l2})$ are geometrical acceptances, $\epsilon(K_{l2})$ are trigger efficiencies, f_{LKr} is the global efficiency of the LKr readout, and $D = 150$ is the downscaling factor of the $K_{\mu 2}$ trigger. In order to compute $A(K_{l2})$, a detailed Geant3-based Monte-Carlo simulation is employed.

6.3. Backgrounds. – $N_B(K_{e2})$ in (1) is dominated by $K_{\mu 2}$ events with track misidentified as electron, mainly in case of high energetic bremsstrahlung after the magnetic spectrometer, when the photon takes more than 95% of muon's energy. The probability for such process is measured directly by clean sample of muons passing $\sim 10X_0$ of lead (Pb) before hitting the LKr. A Geant4 simulation is used to evaluate the Pb correction to the probability for muon misidentification which occurs via two principal mechanisms: 1) muon energy loss in Pb by ionisation, dominating at low momenta; 2) bremsstrahlung in the last radiation lengths of Pb increasing the probability for high track momenta. The background is evaluated to be $(6.11 \pm 0.22)\%$.

Since the incoming kaon track is not measured and the signature of K_{l2} decays is a single reconstructed track, the background from beam halo should be considered. The performance of the muon sweeping system results in lower background in K_{e2}^+ sample ($\sim 1\%$) than in K_{e2}^- sample ($\sim 20\%$), therefore $\sim 90\%$ of data were collected with the K^+ beam only, and small fractions were recorded with simultaneous beams and K^- beam only. The halo background in K_{e2}^+ was measured to be $(1.16 \pm 0.06)\%$ from data, collected without K^+ beam.

The other backgrounds considered are: $(0.27 \pm 0.04)\%$ from $K_{\mu 2}$ with subsequent $\mu \rightarrow e$ decay⁽⁶⁾; $(1.07 \pm 0.05)\%$ from $K_{e2\gamma}(\text{SD})$ ⁽⁷⁾; 0.05% for both K_{e3} and $K_{2\pi}$ decays.

The number of K_{e2} candidates is 59813 before background subtraction. The $M_{\text{miss}}^2(e)$ distribution of data events and backgrounds are presented in fig. 1.

⁽⁶⁾ This background is suppressed according to Michel distribution, as muons from $K_{\mu 2}$ decays are fully polarised.

⁽⁷⁾ The recent KLOE measurement [16] is used for this estimation.

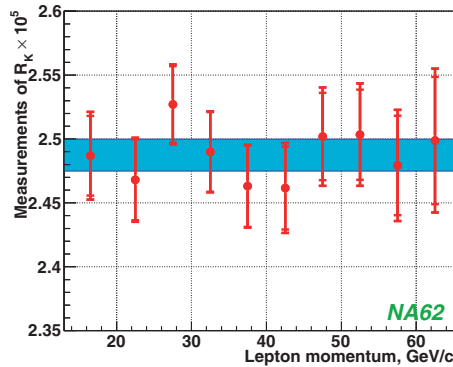


Fig. 2. – R_K measurement in lepton momentum bins. The shaded area indicates the average R_K and its total uncertainty.

6.4. Systematic uncertainties and results. – The electron identification efficiency is measured directly as a function of track momentum and its impact point at LKr using electrons from K_{e3} decays. The average f_e is $(99.27 \pm 0.05)\%$ (f_μ is negligible). The geometric acceptance correction $A(K_{\mu 2})/A(K_{e 2})$ is known with permille precision and depends on the radiative $K_{e 2\gamma}$ (IB) decays, simulated following [17] with higher order corrections according to [18]. The trigger efficiency correction $\epsilon(K_{e 2})/\epsilon(K_{\mu 2}) \approx 99.6\%$ is significant only in the first analysis bin $13 < p < 20$ GeV/c and accounts for the difference in the trigger conditions, namely the requirement of $E > 10$ GeV energy deposited in LKr for $K_{e 2}$ only. Additional small systematic uncertainty arises due to the global LKr readout efficiency, measured to be $(99.80 \pm 0.01)\%$.

The independent measurements of R_K in track momentum bins are presented in fig. 2. The final NA62 result, based on 40% of the accumulated statistics is $R_K = (2.487 \pm 0.011_{\text{stat}} \pm 0.007_{\text{syst}}) \times 10^{-5} = (2.487 \pm 0.013) \times 10^{-5}$, consistent with SM expectation. The analysis of the whole data set will allow to reach uncertainty of 0.4%.

REFERENCES

- [1] BATLEY J. R. *et al.*, *Eur. Phys. J. C*, **52** (2007) 875.
- [2] *Proposal to measure the Rare Decay at the CERN SPS*, CERN-SPSC-2005-013.
- [3] FANTI V. *et al.*, *Nucl. Instrum. Methods A*, **574** (2007) 433.
- [4] GATTI C., *Eur. Phys. J. C*, **45** (2006) 417.
- [5] BERNARD V., *Phys. Rev. D*, **80** (2009) 034034.
- [6] ECKER G. *et al.*, *Nucl. Phys. B*, **291** (1987) 692.
- [7] D’AMBROSIO G. *et al.*, *JHEP*, **08** (1998) 4.
- [8] FRIOT S. *et al.*, *Phys. Lett. B*, **595** (2004) 301.
- [9] DUBNICKOVÁ A. Z. *et al.*, *Phys. Part. Nucl. Lett.*, **5** (2008) 76.
- [10] BATLEY J. R. *et al.*, *Phys. Lett. B*, **697** (2011) 107.
- [11] BIJNENS J. *et al.*, *2nd DAΦNE Physics Handbook* (INFN-LNF, Frascati) 1995, p. 315.
- [12] BATLEY J. R. *et al.*, *Eur. Phys. J. C*, **70** (2010) 635.
- [13] NAKAMURA K. *et al.*, *J. Phys. G*, **37** (2010) 075021.
- [14] CIRIGLIANO V. and ROSELL I., *Phys. Rev. Lett.*, **99** (2007) 231801.
- [15] MASIERO A., PARADISI P. and PETRONZIO R., *Phys. Rev. D*, **74** (2006) 011701.
- [16] AMBROSINO F. *et al.*, *Eur. Phys. J. C*, **64** (2009) 627; **65** (2010) 703(E).
- [17] BIJNENS J., ECKER G. and GASSER J., *Nucl. Phys. B*, **396** (1993) 81.
- [18] WEINBERG S., *Phys. Rev.*, **140** (1965) B516; GATTI C., *Eur. Phys. J. C*, **45** (2006) 417.

The KLOE-2 project at the DAΦNE accelerator upgraded in luminosity

S. FIORE(*) on behalf of the KLOE-2 COLLABORATION

*Dipartimento di Fisica, Sapienza Università di Roma, Italy and
INFN, Sezione di Roma - p.le Aldo Moro 2, 00185 Roma, Italy*

(ricevuto il 29 Settembre 2011; pubblicato online il 26 Gennaio 2012)

Summary. — The KLOE-2 experiment is going to start a new data taking campaign at the upgraded DAΦNE collider. Highlights on the main physics results of KLOE will be presented, followed by present and future detector upgrades and estimates of their impact on the physics program.

PACS 03.65.Yz – Decoherence; open systems; quantum statistical methods.

PACS 12.15.Hh – Determination of Cabibbo-Kobayashi & Maskawa (CKM) matrix elements.

PACS 13.20.-v – Leptonic, semileptonic, and radiative decays of mesons.

1. – Introduction

The KLOE experiment has taken data at the Frascati ϕ factory DAΦNE, an $e^+ e^-$ collider running at $\sqrt{s} \sim 1020$ MeV (ϕ mass) with beams colliding with a crossing angle of $(\pi - 0.025)$ rad. KLOE is a multipurpose detector, mainly consisting of a large cylindrical drift chamber with an inner radius of 25 cm and an outer radius of 2 m, surrounded by a lead-scintillating fibers electromagnetic calorimeter. Both are immersed in the 0.52 T field of a superconducting solenoid. Peculiar to KLOE is the spherical, 10 cm radius, beam pipe which allows K_S^0 mesons produced in ϕ decays to move in vacuum before decaying. Details of the detector can be found in refs. [1-5]. From 2000 to 2006, KLOE has acquired 2.5 fb^{-1} of data at the $\phi(1020)$ peak, plus additional 250 pb^{-1} off the ϕ peak, mostly at 1000 MeV.

The ϕ meson predominantly decays into charged and neutral kaons, thus allowing KLOE to make precision studies in the fields of flavor physics and low energy QCD. The latter can also be addressed using ϕ meson radiative decays into scalar or pseudoscalar particles. Test of discrete symmetries conservation can be performed using several different methods. More details can be found in ref. [6]. Some of the main KLOE physics

(*) E-mail: salvatore.fiore@roma1.infn.it

results will be discussed in the following, and their possible improvements thanks to the new KLOE-2 run with detector upgrades will be discussed [7].

2. – CKM Unitarity and lepton universality

Purely leptonic and semileptonic decays of K mesons ($K \rightarrow \ell\nu$, $K \rightarrow \pi\ell\nu$, $\ell = e, \mu$) are mediated in the Standard Model (SM) by tree-level W-boson exchange. Gauge coupling universality and three-generation quark mixing imply that semileptonic processes such as $d^i \rightarrow u^j\ell\nu$ are governed by the effective Fermi constant $G_{ij} = G_\mu V_{ij}$, where G_μ is the muon decay constant, and V_{ij} are the elements of the unitary Cabibbo-Kobayashi Maskawa (CKM) matrix. This implies the universality relations: i) in the SM the effective semileptonic constant G_{ij} does not depend on the lepton flavor (*lepton universality*); ii) if one extracts V_{ij} from different semileptonic transitions assuming quark-lepton gauge universality (*i.e.* normalizing the decay rates with G_μ), the CKM unitarity condition $\sum_j |V_{ij}|^2 = 1$ should be verified.

Precision tests of the universality relations probe physics beyond the SM and are sensitive to several SM extensions [8-11]. After four years of data analysis, KLOE has produced the most comprehensive set of results from a single experiment, measuring the main BRs of K_L [12], K^\pm [13-15] and K_S [16, 17] (unique to KLOE), including semileptonic and two-body decays; lifetime measurements for K_L [18] and K^\pm [19]; form factor slopes from the analysis of $K_L e3$ [20] and $K_L \mu3$ [21, 22]. A value of $|V_{us}| \times f_+(0) = 0.2157(6)$ has been obtained [23] using the K_S lifetime from PDG [24] as the only non-KLOE input, since at that time the new KLOE measurement of K_S lifetime [25] was not published. This result is compatible with the world-averaged value, with the same precision. These data together with the value of $|V_{us}|/|V_{ud}|$ from the KLOE measurement of the $K^\pm \rightarrow \mu^\pm\nu(\gamma)$ branching ratio [14] and the extraction of $|V_{ud}|$ from superallowed nuclear β decays, provide the basis for testing the unitarity of the quark-flavor mixing matrix: $1 - |V_{ud}|^2 - |V_{us}|^2 = 9(8) \times 10^{-4}$ [23]. Both more statistics and improvements on signal selection are needed to improve the related lifetimes and branching ratios measurements, and reach better sensitivity on unitarity tests.

3. – CPT symmetry and quantum mechanics

A unique feature of the ϕ -factory is the production of neutral kaon pairs in a pure quantum state. This state exhibits maximal entanglement which has been observed in the $\phi \rightarrow K_S K_L \rightarrow \pi^+\pi^-\pi^+\pi^-$ [26] by the KLOE collaboration in year 2005. Since then, more data (a total of 1.7 fb^{-1}) and improvements in the analysis procedure have brought to the results on several decoherence and *CPT*-violating parameters. Different hypotheses on decoherence and *CPT*-violating phenomena are expressed by different modifications of the function:

$$I(\pi^+\pi^-, \pi^+\pi^-; \Delta t) \propto e^{-\Gamma_L \Delta t} + e^{-\Gamma_S \Delta t} - 2e^{-\frac{(\Gamma_S + \Gamma_L)}{2} \Delta t} \cos(\Delta m \Delta t),$$

where Δt is the absolute value of the time difference of the two $\pi^+\pi^-$ decays. The modified expressions have been then used to obtain the best values of the QM- and *CPT*-violating parameters ($\zeta_{K_S K_L}$, $\zeta_{K^0 \bar{K}^0}$, γ , $\Re\omega$, $\Im\omega$, Δa_X , Δa_Y , Δa_Z) [26, 27]. In general all decoherence effects show a deviation from the quantum mechanical prediction $I(\pi^+\pi^-, \pi^+\pi^-; \Delta t = 0) = 0$. Hence the reconstruction of events in the region $\Delta t \approx 0$,

i.e., with vertices close to the IP, is crucial for precise determination of the parameters related to CPT violation and to decoherence.

4. – Low-energy QCD

4.1. $K_S \rightarrow \gamma\gamma$. – A precise measurement of the $K_S \rightarrow \gamma\gamma$ decay rate is an important test of Chiral Perturbation Theory (ChPT) predictions. The decay amplitude of $K_S \rightarrow \gamma\gamma$ has been evaluated at leading order of ChPT [28], $\mathcal{O}(p^4)$, providing a precise estimate of $\mathcal{B}(K_S \rightarrow \gamma\gamma) = 2.1 \times 10^{-6}$, with 3% uncertainty. This estimate is $\sim 30\%$ lower with respect to the latest determination from NA48 [29], thus suggesting relevant contributions from higher order corrections. KLOE measured the $K_S \rightarrow \gamma\gamma$ rate using 1.9 fb^{-1} of integrated luminosity, obtaining [30]

$$(1) \quad \mathcal{B}(K_S \rightarrow \gamma\gamma) = (2.26 \pm 0.12_{\text{stat}} \pm 0.06_{\text{syst}}) \times 10^{-6},$$

which differs by 3σ from the previous best determination. Our result is also consistent with $\mathcal{O}(p^4)$ ChPT prediction. The background composition is dominated by $K_S \rightarrow 2\pi^0$, with two photons pointing the beam pipe region being undetected by the EMC.

4.2. η pseudoscalar meson. – CP violation in flavor-conserving processes can be tested in the η decays to final states that are, as in the K_L case: $\eta \rightarrow \pi\pi$, $\eta \rightarrow \pi^0 e^+ e^-$ and $\eta \rightarrow \pi^+ \pi^- e^+ e^-$ decay. In the latter, CP violation could manifest in the angular asymmetry between the $\pi^+ \pi^-$ and $e^+ e^-$ decay planes. The $\eta \rightarrow \pi^+ \pi^- e^+ e^-$ decay has been studied with KLOE [31], which measured an asymmetry A_ϕ in the angle between the $\pi\pi$ and ee decay planes consistent with zero with 3% accuracy, while theoretical predictions allow this quantity to be up to 2%. The largest contribution to the uncertainty of this measurement comes from the statistical error.

5. – $\gamma\gamma$ physics: a challenge for KLOE-2

The term “ $\gamma\gamma$ physics” (or “two-photon physics”) stands for the study of the reaction

$$e^+ e^- \rightarrow e^+ e^- \gamma^* \gamma^* \rightarrow e^+ e^- + X,$$

where X is some arbitrary final state with $J^{PC} = 0^{\pm+}, 2^{\pm+}$, not directly coupled to one photon ($J^{PC} = 1^{--}$) [32]. The cross section of these processes, of $\mathcal{O}(\alpha^4)$, depends on the logarithm of the center of mass energy \sqrt{s} , so that, for \sqrt{s} greater than a few GeV they dominate hadronic production at $e^+ e^-$ colliders. The cross section $\sigma(\gamma\gamma \rightarrow X)$ was studied at $e^+ e^-$ colliders, from PETRA to CESR to LEP, over the years. However, the experimental situation in the low-energy region, $m_\pi \leq W_{\gamma\gamma} \leq 700 \text{ MeV}$, [33] is unsatisfactory since it is affected by large statistical and systematic uncertainties, due to small data samples and large background contributions, very small detection efficiency and particle identification ambiguities for low-mass hadronic systems. Recently the KLOE collaboration started $\gamma\gamma$ physics analysis, using its off-peak data sample. In fact, a huge source of background while running on the peak of the ϕ resonance, comes from ϕ decays, so that we need to perform background suppression adding the information coming from a tagger system with an efficient detection of scattered electrons. Figure 1 shows the flux function multiplied by an integrated luminosity $L_{ee} = 1 \text{ fb}^{-1}$, as a function of the $\gamma\gamma$ invariant mass for three different center-of-mass energies. This plot demonstrates

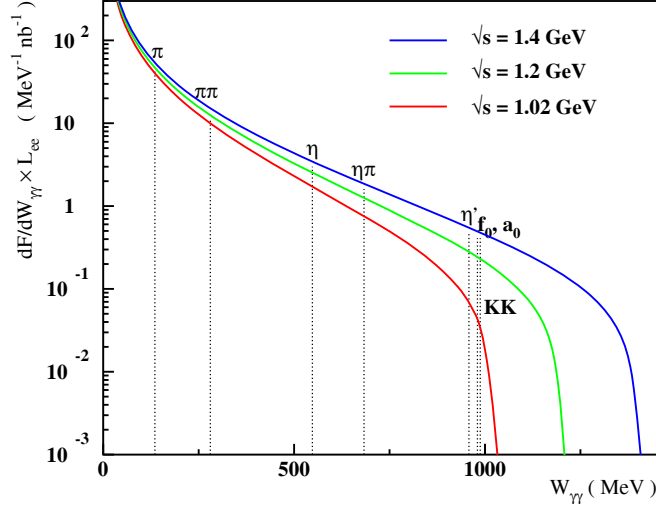


Fig. 1. – Differential $\gamma\gamma$ flux function as a function of the center-of-mass energy.

the feasibility of the detection of the final states $\pi^+\pi^-$, $\pi^0\pi^0$, $\pi^0\eta$ whose cross-sections are of the order of or larger than 1 nb [34–38], and the identification of the resonances produced in these channels, among which the controversial σ meson. Single pseudoscalar ($X = \pi^0$, η or η') production is also accessible and would improve the determination of the two-photon decay widths of these mesons, relevant for the measurement of the transition form factors $\mathcal{F}_{X\gamma^*\gamma^*}(q_1^2, q_2^2)$ as a function of the momentum of the virtual photons, q_1^2 and q_2^2 . The interest in such form factors is rising in connection with the theoretical evaluation of the hadronic light-by-light contribution to the muon magnetic anomaly.

6. – KLOE-2 detector upgrades

During year 2008 the Accelerator Division of the Frascati Laboratory has tested a new interaction scheme on the DAΦNE ϕ -factory collider, with the goal of reaching a peak luminosity of $5 \times 10^{32} \text{ cm}^{-2} \text{ s}^{-1}$, a factor of three larger than what previously obtained. The test has been successful [39,40], and the commissioning of DAΦNE for the approved KLOE-2 run [41] has started in 2011. For this new run [42], upgrades have also been proposed and realized for the detector.

A tagging system has been installed along the beam line to detect the scattered electrons/positrons from $\gamma\gamma$ interactions. The electron tagger is essential to study $\gamma\gamma$ physics while running at $\sqrt{s} = M_\phi$, in order to reduce the large background from ϕ decays. Leptons from $\gamma\gamma$ interactions, with $E < 510 \text{ MeV}$, follow a path through the machine optics different from the orbit of the circulating beams. For this reason we have built two different detectors in different regions on both sides of the interaction point (IP): the Low Energy Tagger (LET) to detect leptons with energy between 150 and 400 MeV and the High Energy Tagger (HET) for those with energy greater than 420 MeV.

The LET region is one meter from the IP, inside the KLOE-2 magnetic field. In this region the correlation between the energy and the position of the leptons is weak. For this reason the LET detector is made by two LYSO crystal calorimeters, read out by Silicon Photomultipliers able to measure the electron/positron energy with a resolution

better than 10% over the range [150–400] MeV [43]. The LET has been installed in June 2010, and after a commissioning phase is ready to take data.

The HET detector consists in a couple of hodoscopes, located just at the exit of each of the first bending dipoles after the interaction point. Each hodoscope is made of plastic scintillators read out by photomultipliers [44]. In this position the off-momentum electrons or positrons escaping from the beam-pipe show a clear correlation between energy and deviation from the nominal orbit. Therefore the energy of the particles can be obtained from the measurement of the displacement with respect to the machine orbit using a position detector. The beam pipe has been modified on this purpose and is ready to host two HET stations, which are going to be installed before the end of 2011.

In a second phase, three additional detectors will be added to KLOE-2. A light-material internal tracker (IT) will be installed in the region between the beam pipe and the drift chamber inner wall to improve charged vertex resolution by a factor ≈ 3 , and to increase the acceptance for low p_T tracks [45]. It will be made of four coaxial cylindrical layers, each of them being a Triple-GEM foil detector. This allows the detector to have a total thickness of 0.015 radiation lengths. The IT will be the first cylindrical GEM detector ever built, and required a long dedicated R&D study [46]. Crystal calorimeters (CCALT) will cover the low θ -angle region, aiming at increasing acceptance for very forward electrons and photons down to 8° . These calorimeters will be made of LYSO crystals read out by Silicon Photomultipliers, exploiting the technological development already done for the LET [47]. A new tile calorimeter (QCALT) will be used to instrument the DAΦNE focusing system for the detection of photons coming from K_L decays in the drift chamber. This calorimeter will cover the beam pipe and quadrupoles with a sampling structure of Tungsten and scintillating tiles [48]. Implementation of the second phase is planned for the year 2012. The total integrated luminosity collected by KLOE-2 at the end of the two phases, from here on referred as step-0 and step-1, will be 5 fb^{-1} and 20 fb^{-1} , respectively.

7. – Improving KLOE physics results with KLOE-2

7.1. CKM Unitarity and lepton universality. – KLOE-2 can significantly improve the accuracy on the measurement of K_L , K^\pm lifetimes and K_{Se3} branching ratio with respect to present world average [49] with data from KLOE-2/step-0. The present 0.23% fractional uncertainty on $|V_{us}| \times f_+(0)$ can be reduced to 0.14% using KLOE present data set together with the KLOE-2/step-0 statistics. The world-average uncertainties on phase space integrals and K_L semileptonic BRs [49] have been used in table I to summarize the expected accuracy on $|V_{us}| \times f_+(0)$ for each decay mode and with the contributions from branching ratio, lifetime, $SU(2)$ -breaking and long-distance EM corrections, and phase space integral. Statistical uncertainties on the measurement of BRs and lifetimes have been obtained scaling to the total sample of 7.5 fb^{-1} of integrated luminosity available at the completion of KLOE-2/step-0. The estimate of systematic errors is rather conservative, being based on KLOE published analyses without including any improvement from the detector upgrade.

7.2. CPT symmetry and quantum mechanics. – As already stated, the vertex resolution for K_S decays affects the $I(\pi^+\pi^-, \pi^+\pi^-; \Delta t)$ distribution both reducing the sensitivity of the fit and introducing systematic uncertainties, as shown in fig. 2. The improvement on vertex resolution made through the insertion of the IT will lead to an increase of the experimental sensitivity on the decoherence parameters by a factor of two.

TABLE I. – KLOE-2/step-0 prospects on $|V_{us}| \times f_+(0)$ extracted from K_{l3} decay rates; the fractional accuracy on partial contributions from branching fraction (\mathcal{B}), lifetime (τ), $SU(2)$ and EM corrections (δ) and phase-space integral (I_{Kl}) are also shown.

Mode	$\delta V_{us} \times f_+(0)$ (%)	\mathcal{B}	τ	δ	I_{Kl}
$K_L e3$	0.21	0.09	0.13	0.11	0.09
$K_L \mu3$	0.25	0.10	0.13	0.11	0.15
$K_S e3$	0.33	0.30	0.03	0.11	0.09
$K^\pm e3$	0.37	0.25	0.05	0.25	0.09
$K^\pm \mu3$	0.40	0.27	0.05	0.25	0.15

7.3. $K_S \rightarrow \gamma\gamma$. – KLOE-2 will improve both sample statistics and data quality, the latter thanks to the CCALT crystal calorimeters, that will increase the rejection of $K_S \rightarrow \pi^0\pi^0$ with photons at low polar angle. The KLOE-2 measurement can clarify the disagreement between KLOE and NA48 [50,51] and help settling the $\mathcal{O}(p^6)$ contributions to the amplitude $A(K_L \rightarrow \pi^0\gamma\gamma)$, related by chiral symmetry to the $K_S \rightarrow \gamma\gamma$ terms only [52].

7.4. η pseudoscalar meson. – The $\eta \rightarrow \pi^+\pi^-e^+e^-$ decay plane asymmetry measurement by KLOE is limited by the statistical uncertainties. In KLOE the minimal transverse momentum of reconstructed tracks, $P_{T\min}$, is 23 MeV. It limits the selection efficiency to $\sim 8\%$. The installation of the inner tracker, in the second phase of the KLOE-2 experiment, would reduce $P_{T\min}$ to 16 MeV improving at the same time the tracking resolution [31]. With a sample of 20 fb^{-1} and the acceptance increase, KLOE-2 could measure the asymmetry A_ϕ with a statistical precision better than 1%.

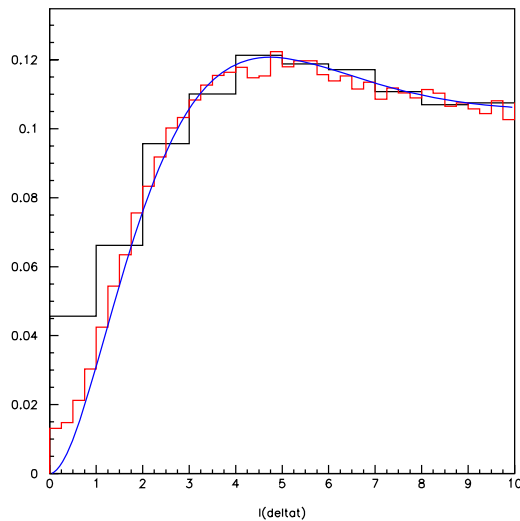


Fig. 2. – Monte Carlo simulation of the $I(\pi^+\pi^-, \pi^+\pi^-; \Delta t)$ as a function of $|\Delta t|$ (in τ_S units) with the present KLOE resolution $\sigma_{\Delta t} \approx \tau_S$ (histogram with large bins), with an improved resolution $\sigma_{\Delta t} \approx 0.3\tau_S$ (histogram with small bins), and in the ideal case (solid line).

REFERENCES

- [1] ADINOLFI M. *et al.*, *Nucl. Instrum. Methods A*, **488** (2002) 51.
- [2] ADINOLFI M. *et al.*, *Nucl. Instrum. Methods A*, **482** (2002) 364.
- [3] ADINOLFI M. *et al.* (KLOE COLLABORATION), *Nucl. Instrum. Methods A*, **492** (2002) 134.
- [4] ADINOLFI M. *et al.*, *Nucl. Instrum. Methods A*, **483** (2002) 649.
- [5] ALOISIO A. *et al.*, *Nucl. Instrum. Methods A*, **516** (2004) 288.
- [6] BOSSI F., DE LUCIA E., LEE-FRANZINI J., MISCETTI S. and PALUTAN M. (KLOE COLLABORATION), *Riv. Nuovo Cimento*, **31** (2008) 531, [arXiv:0811.1929](#).
- [7] AMELINO-CAMELIA G. *et al.*, *Eur. Phys. J. C*, **68** (2010) 619.
- [8] MARCIANO W. J. and SIRLIN A., *Phys. Rev. D*, **35** (1987) 1672.
- [9] HAGIWARA K., MATSUMOTO S. and YAMADA Y., *Phys. Rev. Lett.*, **75** (1995) 3605.
- [10] KURYLOV A. and RAMSEY-MUSOLF M. J., *Phys. Rev. Lett.*, **88** (2002) 071804, [hep-ph/0109222](#).
- [11] CIRIGLIANO V., JENKINS J. and GONZALEZ-ALONSO M., *Nucl. Phys. B*, **830** (2010) 95, [0908.1754](#).
- [12] AMBROSINO F. *et al.* (KLOE COLLABORATION), *Phys. Lett. B*, **632** (2006) 43, [hep-ex/0508027](#).
- [13] AMBROSINO F. *et al.* (KLOE COLLABORATION), *JHEP*, **02** (2008) 098, [arXiv:0712.3841](#).
- [14] AMBROSINO F. *et al.* (KLOE COLLABORATION), *Phys. Lett. B*, **632** (2006) 76, [hep-ex/0509045](#).
- [15] AMBROSINO F. *et al.* (KLOE COLLABORATION), *Phys. Lett. B*, **666** (2008) 305, [arXiv:0804.4577](#).
- [16] AMBROSINO F. *et al.* (KLOE COLLABORATION), *Phys. Lett. B*, **636** (2006) 173, [hep-ex/0601026](#).
- [17] AMBROSINO F. *et al.* (KLOE COLLABORATION), *Eur. Phys. J. C*, **48** (2006) 767, [hep-ex/0601025](#).
- [18] AMBROSINO F. *et al.* (KLOE COLLABORATION), *Phys. Lett. B*, **626** (2005) 15, [hep-ex/0507088](#).
- [19] AMBROSINO F. *et al.* (KLOE COLLABORATION), *JHEP*, **01** (2008) 073, [arXiv:0712.1112](#).
- [20] AMBROSINO F. *et al.* (KLOE COLLABORATION), *Phys. Lett. B*, **636** (2006) 166, [hep-ex/0601038](#).
- [21] AMBROSINO F. *et al.* (KLOE COLLABORATION), *JHEP*, **12** (2007) 105, [arXiv:0710.4470](#).
- [22] TESTA M. *et al.* (KLOE COLLABORATION) (2008), [arXiv:0805.1969](#).
- [23] AMBROSINO F. *et al.* (KLOE COLLABORATION), *JHEP*, **04** (2008) 059, [arXiv:0802.3009](#).
- [24] AMSLER C. *et al.* (PARTICLE DATA GROUP), *Phys. Lett. B*, **667** (2008) 1.
- [25] AMBROSINO F. *et al.* (KLOE COLLABORATION), *Eur. Phys. J. C*, **71** (2011) 1604.
- [26] AMBROSINO F. *et al.* (KLOE COLLABORATION), *Phys. Lett. B*, **642** (2006) 315, [hep-ex/0607027](#).
- [27] DI DOMENICO A. *et al.* (KLOE COLLABORATION), *J. Phys. Conf. Ser.*, **171** (2009) 012008.
- [28] D'AMBROSIO G. and ESPRIN D., *Phys. Lett. B*, **175** (1986) 237.
- [29] LAI A. *et al.* (NA48 COLLABORATION), *Phys. Lett. B*, **551** (2003) 7.
- [30] AMBROSINO F. *et al.* (KLOE COLLABORATION), *JHEP*, **05** (2008) 51.
- [31] AMBROSINO F. *et al.* (KLOE COLLABORATION), *Phys. Lett. B*, **675** (2009) 283, [arXiv:0812.4830](#).
- [32] PENNINGTON M. R., [arXiv:hep-ph/0511146](#) and references therein.
- [33] MARSISKE H. *et al.* (CRYSTAL BALL COLLABORATION), *Phys. Rev. D*, **41** (1990) 3324.
- [34] BOYER J. *et al.*, *Phys. Rev. D*, **42** (1990) 1350.
- [35] MARSISKE H. *et al.* (CRYSTAL BALL COLLABORATION), *Phys. Rev. D*, **41** (1990) 3324.
- [36] OEST T. *et al.* (JADE COLLABORATION), *Z. Phys. C*, **47** (1990) 343.
- [37] MORI T. *et al.* (BELLE COLLABORATION), *Phys. Rev. D*, **75** (2007) 051101, [hep-ex/0610038](#).
- [38] UEHARA S. *et al.* (BELLE COLLABORATION), *Phys. Rev. D*, **78** (2008) 052004, [arXiv:0810.0655](#).
- [39] MILARDI C. *et al.*, *ICFA Beam Dyn. Newslett.*, **48** (2009) 23.

- [40] ZOBOV M. *et al.*, *ICFA Beam Dyn. Newslett.*, **48** (2009) 34.
- [41] BECK R. *et al.* (KLOE-2 COLLABORATION) (2006), KLOE-2 Public Documents - K2PD-1, <http://www.lnf.infn.it/kloe2/>.
- [42] BECK R. *et al.* (KLOE-2 COLLABORATION) (2007), Letter of Intent for the KLOE-2 Roll-in, LNF-07/19(IR).
- [43] BABUSCI D. *et al.*, *Nucl. Instrum. Methods A*, **617** (2010) 81.
- [44] ARCHILLI F. *et al.*, *Nucl. Instrum. Methods A*, **617** (2010) 266.
- [45] ARCHILLI F. *et al.* (KLOE-2 COLLABORATION), [arXiv:1002.2572](https://arxiv.org/abs/1002.2572) (2010).
- [46] BALLA A. *et al.*, *Nucl. Instrum. Methods A*, **628** (2011) 194.
- [47] HAPPACHER F. *et al.*, *Nucl. Phys. B Proc. Suppl.*, **197** (2009) 215.
- [48] CORDELLI M. *et al.*, *Nucl. Instrum. Methods A*, **617** (2010) 105.
- [49] ANTONELLI M. *et al.* (FLAVIANET WORKING GROUP ON KAON DECAYS), [arXiv:0801.1817](https://arxiv.org/abs/0801.1817) (2008).
- [50] LAI A. *et al.* (NA48 COLLABORATION), *Phys. Lett. B*, **551** (2003) 7, [hep-ex/0210053](https://arxiv.org/abs/hep-ex/0210053).
- [51] AMBROSINO F. *et al.* (KLOE COLLABORATION), *JHEP*, **05** (2008) 051, [arXiv:0712.1744](https://arxiv.org/abs/0712.1744).
- [52] BUCHALLA G., D'AMBROSIO G. and ISIDORI G., *Nucl. Phys. B*, **672** (2003) 387, [hep-ph/0308008](https://arxiv.org/abs/hep-ph/0308008).

CP violation and rare B_s decays at the Tevatron

M. D. CORCORAN for the CDF and D0 COLLABORATIONS

Rice University, USA

(ricevuto il 29 Settembre 2011; pubblicato online il 26 Gennaio 2012)

Summary. — This note gives updates on three results from the Fermilab Tevatron $p\bar{p}$ collider operating at $\sqrt{s} = 1.96$ TeV. The results presented include: the D0 dimuon charge asymmetry; the measurement of the *CP*-violating phase ϕ_s in the decay $B_s \rightarrow J/\psi\phi$ from both CDF and D0; and the most recent results from both CDF and D0 on the search for the ultra-rare decay $B_s \rightarrow \mu^+\mu^-$.

PACS 11.30.Er – Charge conjugation, parity, time reversal, and other discrete symmetries.

PACS 13.20.He – Leptonic, semileptonic, and radiative decays of mesons: Decays of bottom mesons.

PACS 13.25.Hw – Hadronic decays of mesons: Decays of bottom mesons.

1. – Introduction

CP violation was first observed in the K^0/\bar{K}^0 system in 1964 [1]. In 1967 Andrei Sakharov showed that *CP* violation is a necessary ingredient in the generation of the matter-antimatter asymmetry of the universe [2]. In the standard model (SM), *CP* violation arises from the complex phase in the CKM matrix, but the amount of *CP* violation from this source is too small by many orders of magnitude to account for the observed asymmetry. So we have a long-standing puzzle as to the origin of the missing *CP* violation.

Neutral mesons such as K^0 , D^0 , B_d^0 and B_s^0 can mix through double W-exchange (the “box diagram”), as shown in fig. 1. Asymmetric mixing, which is both *CP* and *T* violating, occurs when the rate of (for example) $B_s \rightarrow \bar{B}_s$ is not equal to the rate $\bar{B}_s \rightarrow B_s$. The solution to the time-dependent Schroedinger equation in this case yields two mass eigenstates which are not *CP* eigenstates and which have different masses (usually referred to as “heavy” and “light”) and different lifetimes. *CP* violation can also arise from interference of the decay and mixing amplitudes through phases, or directly through the decay amplitudes.

The neutral Kaon system has been well studied for many years, and the B_d system has been extensively studied at the B-factories, resulting in stringent constraints on the

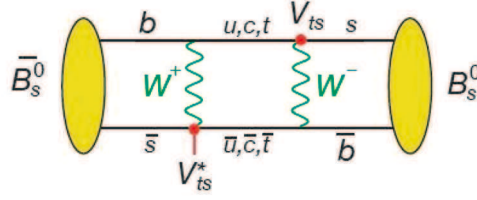


Fig. 1. – Box diagram for B_s mixing.

CKM matrix elements and therefore on CP -violating parameters in the B_s system. Any deviation from the SM expectations would be an indication of new physics.

The physics parameters related to B_s mixing are: Δm_s , the mass difference between the light and heavy eigenstates (well-measured by CDF to be $17.77 \pm 0.12 \text{ ps}^{-1}$ [3]); $\Delta\Gamma$, the lifetime difference between the light and heavy eigenstates; and ϕ_s , the phase between the decay and mixing amplitudes. The SM expectation for $\Delta\Gamma$ is 0.096 ± 0.0014 , and the SM expectation for ϕ_s is 0.0042 ± 0.0014 . The small expected value of ϕ_s makes its measurement especially interesting in the search for new physics. One can write $\phi_s = \phi_s^{SM} + \phi_s^{NP}$, where SM refers to the standard model contribution, and NP refers to a possible new phenomena contribution.

The decay $B_s \rightarrow J/\psi\phi$ can occur directly, or the B_s meson could first mix and then decay: $B_s \rightarrow \bar{B}_s \rightarrow J/\psi\phi$. Interference between these two processes is characterized by the phase β_s which in the SM is related to the CKM matrix elements by $\beta_s^{SM} = \text{arg}[-V_{ts}V_{tb}^*/V_{cs}V_{cb}^*]$. The SM expectation for this quantity is small, with $\beta_s^{SM} = 0.038 \pm 0.002$. Note that D0 uses the quantity $\phi_s^{J/\psi\phi} = -2\beta_s$. If new physics enters B_s mixing and $B_s \rightarrow J/\psi\phi$ the same way, we would have $\phi_s^{J/\psi\phi} = -2\beta_s + \phi_s^{NP}$, with ϕ_s^{NP} the same for B_s mixing and for $B_s \rightarrow J/\psi\phi$.

Decays which are heavily suppressed in the SM are another excellent place to search for new physics. The decay $B_s \rightarrow \mu\mu$ is highly suppressed in the SM since it is a flavor changing neutral current which is also helicity suppressed. Many scenarios of physics beyond the SM, in particular Supersymmetry, produce enhancements of this process by large factors, which makes this rare decay a promising place to search for new processes.

2. – Dimuon charge asymmetry

The D0 collaboration has measured the like-sign dimuon charge asymmetry from B decays, defined as

$$A_{sl}^b = \frac{N_b^{++} - N_b^{--}}{N_b^{++} + N_b^{--}},$$

where $N_b^{++}(N_b^{--})$ refers to the number of events from B/\bar{B} meson decays with two positive (negative) muons. B/\bar{B} meson decays can lead to muons of the same charge if one of the mesons mixes and they both undergo semileptonic decays to muons. Only if the rate of $B \rightarrow \bar{B}$ is not equal to the rate of $\bar{B} \rightarrow B$ will A_{sl}^b be nonzero. Therefore this asymmetry directly measures CP -violating effects. The SM expectation for this quantity is $A_{sl}^b(SM) = (-2.8_{-0.6}^{+0.5}) \times 10^{-4}$, below the sensitivity of the D0 experiment.

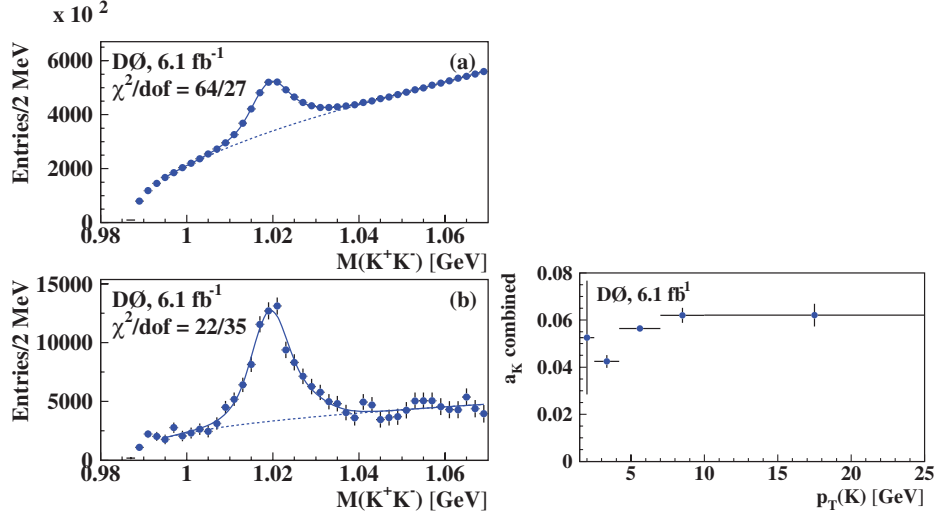


Fig. 2. – K^+K^- mass distributions. (a) The sum of $K^+ \rightarrow \mu^+$ and $K^- \rightarrow \mu^-$, with the ϕ peak clearly visible. (b) The difference $K^+ \rightarrow \mu^+ - K^- \rightarrow \mu^-$. The excess of positive muons is due to the larger interaction cross section for K^- , resulting in an overall charge asymmetry. The right plot shows the combined K asymmetry as determined from $\phi \rightarrow KK$ and $K^{0*} \rightarrow K\pi$ decays.

DØ also measures the single-muon charge asymmetry a_{sl}^b , defined as

$$a_{sl}^b = \frac{\Gamma(\bar{B} \rightarrow \mu^+ X) - \Gamma(B \rightarrow \mu^- X)}{\Gamma(\bar{B} \rightarrow \mu^+ X) + \Gamma(B \rightarrow \mu^- X)},$$

which can be shown to be equal to A_{sl}^b . There are thus two independent measurements of the same quantity. The final result will take advantage of the fact that many of the systematic errors of these two measurements are highly correlated, allowing some cancellation.

In this measurement, no distinction is made between B_d and B_s mesons, so the measured quantity is a linear combination of the asymmetries from B_d (a_{sl}^d) and B_s (a_{sl}^s). The coefficients of the linear combination are known from other measurements at B factories and at the Tevatron. The analysis selects well-identified muons to define the inclusive muon sample (1.5×10^9 events) and the like-sign dimuon sample (3.7×10^6 events). The data sample corresponds to 6.1 fb^{-1} of recorded luminosity.

After initial selection, corrections are made for backgrounds from hadrons that fake muons and for detector-related asymmetries. These corrections are determined almost completely from the data. Then corrections are made for non-B contributions and non-oscillating contributions to the inclusive and dimuon samples. The final step uses the two independent measurements of A_{sl}^b to cancel some systematics.

The most significant source of background is due to $K \rightarrow \mu\nu$ decays which have an asymmetry due to the larger cross section for K^- interactions in matter compared to K^+ . Processes such as $K^- p \rightarrow \Lambda\pi^0$ are possible for the K^- but not K^+ . Therefore more K^- mesons interact with the detector material and do not survive long enough to decay, leading to a significant positive charge asymmetry that must be measured and corrected for. This background is measured from the data in two ways: from $\phi \rightarrow KK$ and from

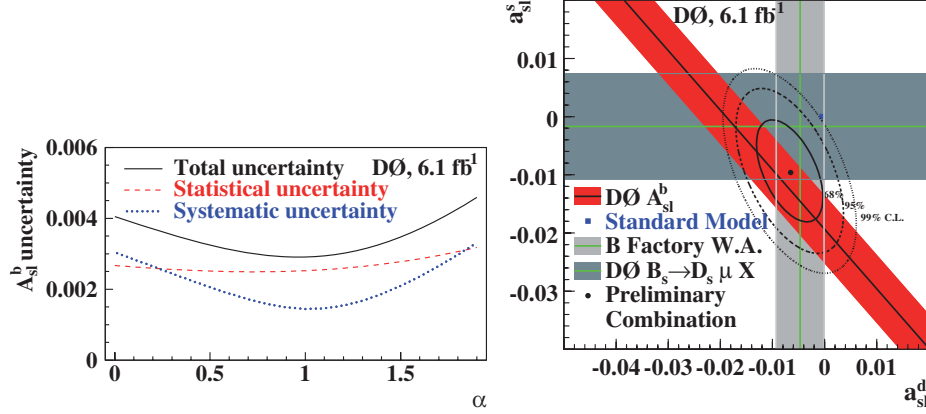


Fig. 3. – The left plot shows the error on A_{sl}^b as a function of the combination parameter α . The value of α is chosen to minimize the overall error. The right figure shows the two-dimensional plot of the semileptonic charge asymmetries a_{sl}^d vs. a_{sl}^s . The diagonal band is the result of this measurement. The vertical band is the world average measurement of a_{sl}^d from B-factories. The horizontal band is an independent measurement of a_{sl}^s from D0. The solid circle is the combination of these three measurements, and the square point is the SM expectation.

$K^{0*} \rightarrow K\pi$. Figure 2 shows the $\phi \rightarrow KK$ signal for events in which one of the K 's has faked a muon. The top-left plot (a) shows the sum of positive and negative muons, while the bottom-left plot (b) shows the difference of positive and negative muons. There is a significant asymmetry as expected. The K asymmetry is also measured using $K^* \rightarrow K\pi$, yielding consistent results. The right plot in fig. 2 shows the overall K asymmetry as determined from both decay modes. There are also fake muons from π decay and proton punchthrough. These asymmetries are measured using $K_s \rightarrow \pi\pi$ and $\Lambda \rightarrow p\pi$ and are much smaller than the K asymmetry.

In addition to the asymmetry from $K \rightarrow \mu$ decays, the fraction of muons due to K^* decay must be determined. This fraction is determined from the data using K^* decays. Then Monte Carlo ratios of K/π and K/p are used to determine the π and proton fraction of fake muons.

An important feature of the D0 detector is the periodic changing of the magnet polarities for both the solenoid and toroid. Detector-related asymmetries are nearly completely canceled out when the different magnet polarities are combined. Any residual asymmetries are measured from $J/\psi \rightarrow \mu\mu$ decays and corrected for.

The final result is obtained by combining the uncorrected asymmetries A (from the dimuon sample) and a (from the inclusive muon sample) $A' = A - \alpha a$, where α is a parameter which is varied to minimize the final error. Figure 3 shows the total uncertainty as a function of the parameter α . The result is $A_{sl}^b = [-0.957 \pm 0.251(\text{stat}) \pm 0.146(\text{syst})]\%$ while the SM expectation is $A_{sl}^b(\text{SM}) = [0.023_{-0.006}^{+0.005}]\%$. Figure 3 also shows the final result plotted in the a_{sl}^d vs. a_{sl}^s plane along with the world average results for a_{sl}^d from the B factories and a_{sl}^s from the D0 measurement of $B_s \rightarrow D_s \mu X$. The SM expectation is shown as the square point, and the solid dot is the combination of the three measurements. This result has a 3.2 standard deviation discrepancy with the SM expectation. Many cross checks have been carried out and are detailed in the publications [4]. An update of this result with more data, improved background determinations, and varying impact parameter bins is underway.

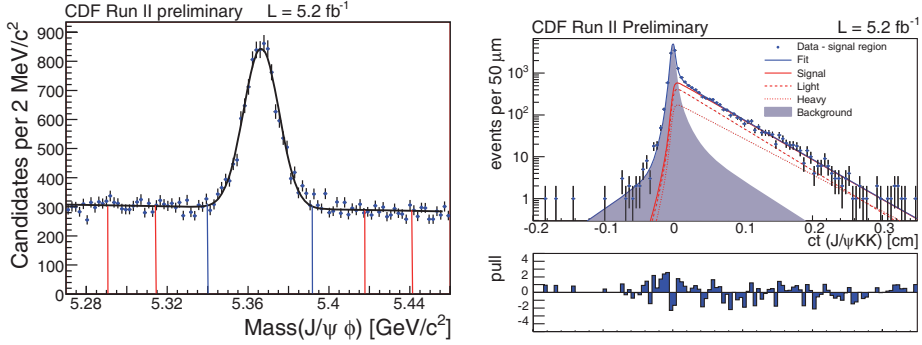


Fig. 4. – The left plot shows the $\mu\mu KK$ mass distribution for events entering into the fit. The right plot shows the lifetime distribution.

3. – $B_s \rightarrow J/\psi\phi$

The decay $B_s \rightarrow J/\psi\phi$ is of special interest since previously a CDF/D0 combination showed a 2.1σ discrepancy with the SM for the phase $\phi_s^{J/\psi\phi} \approx -2\beta_s$ [5]. CDF and D0 both have recent updates to this analysis. This decay is complicated since it is a scalar meson decaying into two vector particles. The final state particles are detected in the decays $J/\psi \rightarrow \mu\mu$ and $\phi \rightarrow KK$. The relative orbital angular momentum of the J/ψ and ϕ can take on values $l = 0, 1, 2$, and therefore decay is described by three complex amplitudes. The fits to the lifetime distributions require of order 30 parameters including background, so care must be taken to ensure stability. Both experiments do unbinned maximum-likelihood fits. The recent CDF result [6] is based on 5.2 fb^{-1} of integrated luminosity. Figure 4 shows the mass and lifetime distributions for events entering into the fit. As can be seen in the figure, the fit includes both heavy and light eigenstates with different lifetimes. The two-dimensional likelihood contours of the phase β_s vs. the lifetime difference between the two mass eigenstates, $\Delta\Gamma$, are shown in fig. 5 along with

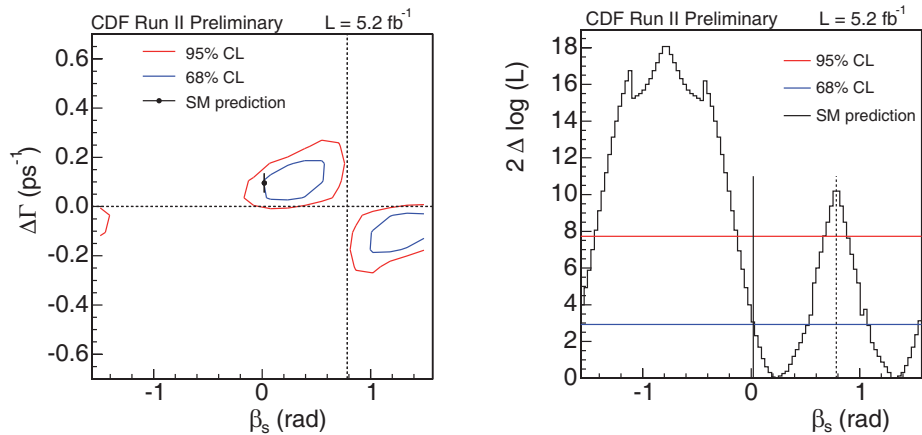


Fig. 5. – The left plot shows the CDF two-dimensional plot of the 68% and 95% confidence level contours in the β_s vs. $\Delta\Gamma$ plane. The right plot shows the one-dimensional projection of β_s .

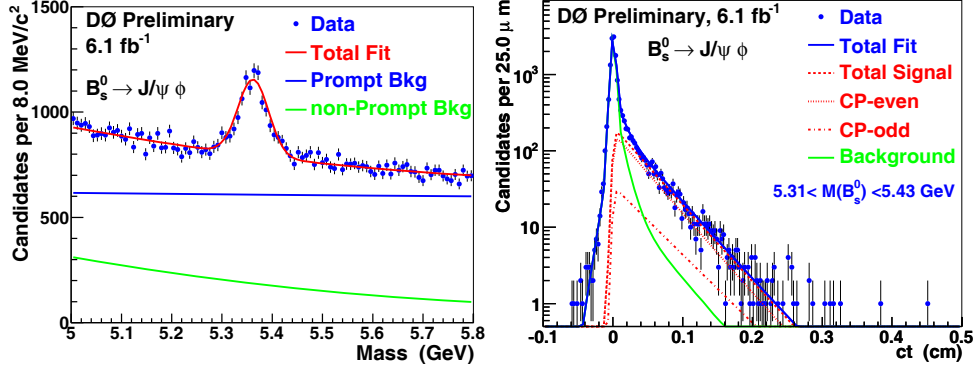


Fig. 6. – D0 mass and lifetime distributions for $B_s \rightarrow J/\psi\phi$.

the one-dimensional projection of β_s . The SM expectation is shown as the black point. The CDF result agrees with the SM within one standard deviation.

D0 also has presented a new preliminary result for this decay mode [7]. The analysis technique is similar to CDF's, with a maximum-likelihood fit being done to about 30 parameters. Figure 6 shows the D0 mass and lifetime distributions with the fit results. The D0 fits have constrained the strong phases δ_1 and δ_2 to values near the $B^0 \rightarrow J/\psi K^*$ values measured by B-factories. Gronau and Rosner [8] have argued that the strong phases should be similar for B_s and B_d decays. The D0 result for the two-dimensional likelihood contours for $\phi_s^{J/\psi\phi}$ vs. $\Delta\Gamma$ and the one-dimensional projection for $\phi_s^{J/\psi\phi}$ are shown in fig. 7. The 68% and 95% CL bands from the same-sign dimuon charge asymmetry result are shown in the left plot. The D0 one-dimensional projection deviates from the SM value by about two standard deviations. The situation therefore remains somewhat murky, with CDF's most recent result in agreement with the SM, while the D0 result still deviates from the SM by about the same amount as the earlier result. Both experiments agree that there can be significant variation of results from experiment to experiment, or for different subsets of the data within the same experiment. For

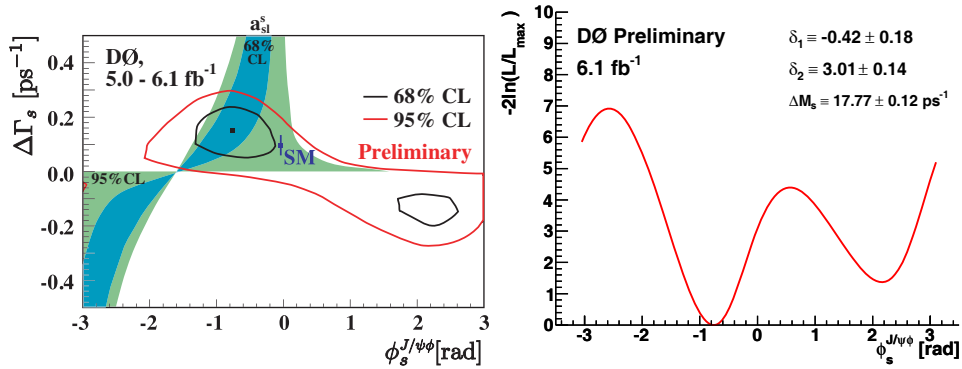


Fig. 7. – D0 likelihood contours for $\phi_s^{J/\psi\phi}$ vs. $\Delta\Gamma$ (left). The 68% and 95% CL bands from the dimuon charge asymmetry result are also shown. The right plot shows the one-dimensional projection of $\phi_s^{J/\psi\phi}$.

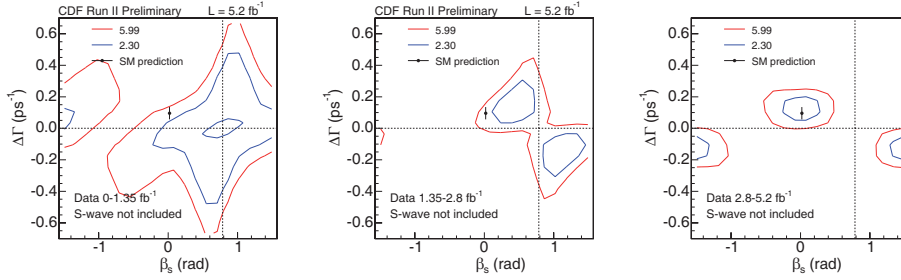


Fig. 8. – CDF likelihood contours for three different data-taking periods.

example, fig. 8 shows CDF results divided into three data-taking periods of about the same integrated luminosity. Although the detector and analysis techniques are the same, the results vary significantly for the three periods. Both CDF and D0 are working on further updates of this analysis.

4. – $B_s \rightarrow \mu^+ \mu^-$

The SM expected branching ratio is $(3.6 \pm 0.3) \times 10^{-9}$ [9]. The most recent CDF branching ratio limit [10] at the 95% CL is 43×10^{-9} (33×10^{-9}) for the observed (expected) limit.

D0 has a recent update on this measurement [11] based on 6.1 fb^{-1} of recorded luminosity. The analysis uses a Bayesian neural network (BNN) with six variables to separate signal from background. The variables that were found to have the best signal/background separation power were: the minimum muon impact parameter; dimuon

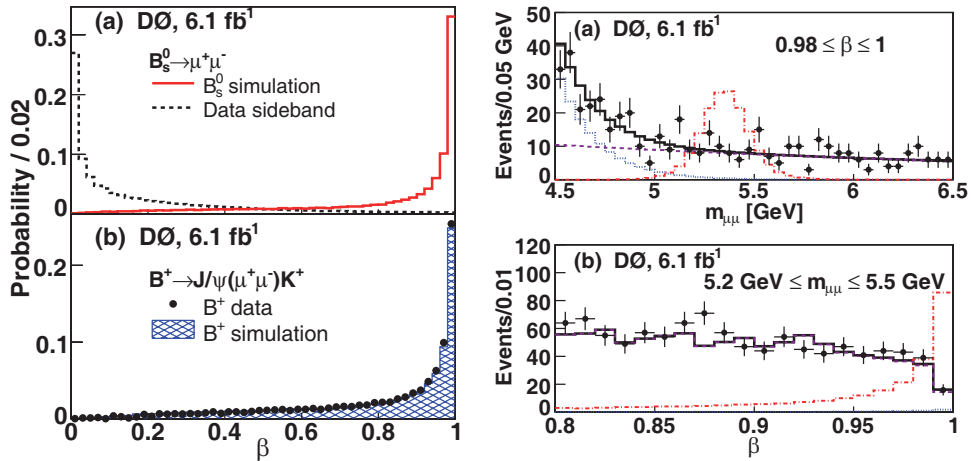


Fig. 9. – D0 search for $B_s \rightarrow \mu\mu$. The top left plot shows the output of the BNN for signal Monte Carlo and data sideband backgrounds. The bottom left shows the BNN output for the normalization mode. The right plot shows the projections of the dimuon mass and BNN output parameter β for the most sensitive bin of BNN output. The dot-dash curve shows a simulated signal at $100\times$ the SM expectation.

vertex χ^2 ; the decay length significance; the angle between the dimuon momentum vector and the vector from the primary vertex to the secondary vertex (the “pointing angle”); and the minimum muon transverse momentum. Monte Carlo studies indicate that the most serious background is due to production of a $b\bar{b}$ pair, both of with decay semileptonically. Signal Monte Carlo and data sidebands are used to train the BNN. Figure 9 shows the output of the BNN for signal Monte Carlo and data sidebands. This figure also shows the selection for the normalization mode $B^\pm \rightarrow J/\psi K^\pm$. The final limit is calculated in bins of $\mu\mu$ mass and β , the output of the BNN. Figure 9 shows the projection in dimuon mass and β for the most sensitive bin in β . The dot-dashed curve represents a signal $100\times$ the SM expectation. There is no evidence of a signal, and D0 sets a branching ratio limit at the 95% CL of 51×10^{-9} (38×10^{-9}) for the observed (expected) limit. Both experiments are working on an update to this measurement.

5. – Conclusion

The D0 like-sign dimuon charge asymmetry exhibits a 3.2σ discrepancy with the SM. An update on this result, including an impact parameter study and more data, should be available soon. This result challenges the SM, and it is important to have this result verified (or not) by another experiment.

The decay $B_s \rightarrow J/\psi\phi$ has been studied by both CDF and D0. Extracting the physics parameters requires a complicated fit of 30+ parameters. The current situation is unclear, with CDF’s most recent result in agreement with the SM, and D0’s result still about two standard deviations away from the SM expectation. But within errors the two experiments are in agreement.

Both CDF and D0 have presented branching ratio limits for the ultra-rare decay $B_s \rightarrow \mu\mu$ which are about 10 times the SM expectation. Both CDF and D0 are continuing to push the branching ratio limits on this mode.

REFERENCES

- [1] CHRISTIANSEN J. H., CRONIN J. W., FITCH V. L. and TURLAY R., *Phys. Rev. Lett.*, **13** (1964) 138.
- [2] SAKHAROV A. D., *JETP*, **5** (1967) 24.
- [3] ABULENCIA A. *et al.*, *Phys. Rev. Lett.*, **97** (2006) 242003.
- [4] ABAZOV V. *et al.*, *Phys. Rev. D*, **82** (2010) 032001; ABAOV V. *et al.*, *Phys. Rev. Lett.*, **105** (2010) 081801.
- [5] CDF and D0 COLLABORATIONS, Combination of D0 and CDF Results on $\Delta\Gamma$ and the CP -Violating Phase $\beta_s^{J/\psi\phi}$, CDF/PHYS/BOTTOM/CDFR/9787 and D0 Note 5928-CONF, 2009.
- [6] CDF COLLABORATION, “An Updated Measurement of the CP Violating Phase $\beta_s^{J/\psi\phi}$ in $B_s^0 \rightarrow J/\psi\phi$ Decays using 5.2fb^{-1} of Integrated Luminosity”, CDF/ANAL/BOTTOM/PUBLIC/10206 (2010).
- [7] D0 COLLABORATION, “Updated Measurement of the CP -Violating Phase $\phi_s^{J/\psi\phi}$ Using the Flavor-tagged Decay $B_s \rightarrow J/\psi\phi$ ”, D0 Note 6098-CONF (2010).
- [8] GRONAU M. and ROSNER J. L., *Phys. Lett. B*, **669** (2008) 321.
- [9] BURAS A. J., *Prog. Theor. Phys.*, **122** (2009) 145.
- [10] CDF COLLABORATION, “Search for $B_s^0 \rightarrow \mu^+\mu^-$ and $B_d^0 \rightarrow \mu^+\mu^-$ Decays on 3.7fb^{-1} of $p\bar{p}$ Collisions with CDF II”, CDF Public Note 9892.
- [11] ABAZOV V. *et al.*, *Phys. Lett. B*, **693** (2010) 539.

Prospects for CP violation in $B_s^0 \rightarrow J/\psi\phi$ from first LHCb data

OLIVIER LEROY on behalf of the LHCb COLLABORATION

CPPM, Aix-Marseille Université IN2P3 CNRS - Aix-Marseille, France

(ricevuto il 29 Settembre 2011; pubblicato online il 26 Gennaio 2012)

Summary. —

The determination of the CP -violating phase in $B_s^0 \rightarrow J/\psi\phi$ decays is one of the key goals of the LHCb experiment. Its value is predicted to be very small in the Standard Model but can be significantly enhanced in many models of New Physics. The steps towards a precise determination of this phase with a flavour-tagged, time-dependent angular analysis of the decay $B_s^0 \rightarrow J/\psi\phi$ are reviewed and first studies performed with data collected in 2010 at LHC in pp collisions at 7 TeV center-of-mass energy are presented for the first time. In particular, we report the first LHCb measurements of lifetime in the channels $B^+ \rightarrow J/\psi K^+$, $B^0 \rightarrow J/\psi K^{*0}$, $B^0 \rightarrow J/\psi K_S^0$, $B_s^0 \rightarrow J/\psi\phi$, $\Lambda_b \rightarrow J/\psi\Lambda$; the polarization amplitudes in $B^0 \rightarrow J/\psi K^{*0}$ and $B_s^0 \rightarrow J/\psi\phi$; the width and mass differences of the B_s^0 mass eigenstates, $\Delta\Gamma_s$ and Δm_s . The data sample used corresponds to an integrated luminosity of 36pb^{-1} .

PACS 12.15.Hh – Determination of Cabibbo-Kobayashi & Maskawa (CKM) matrix elements.

1. – Introduction

The interference between B_s^0 decays to $J/\psi\phi$ either directly or via $B_s^0\text{-}\bar{B}_s^0$ oscillation gives rise to a CP -violating phase $\phi_s^{J/\psi\phi}$. In the Standard Model, this phase is predicted to be $\simeq -2\beta_s$, where $\beta_s = \arg(-V_{ts}V_{tb}^*/V_{cs}V_{cb}^*)$. The indirect determination via global fits to experimental data gives $2\beta_s = (0.0363 \pm 0.0017)$ rad [1], within the Standard Model. The direct measurement of this phase is one of the key goals of the LHCb experiment. Indeed, $\phi_s^{J/\psi\phi}$ is one of the CP observables with the smallest theoretical uncertainty in the Standard Model, and New Physics could significantly modify this prediction, if new particles contribute with a new phase to the $B_s^0\text{-}\bar{B}_s^0$ box diagram. Both CDF and DØ have reported constraints on $\phi_s^{J/\psi\phi}$ with large uncertainties [2, 3].

In this document, we present the steps towards a measurement of $\phi_s^{J/\psi\phi}$ at LHCb and give the first preliminary results obtained with the 2010 data. The CP -violation phase will be extracted from a tagged time-dependent angular analysis of $B_s^0 \rightarrow J/\psi\phi$ decays. Therefore, the following steps are required:

- in sect. 2, we present the selection and lifetime of $B_s^0 \rightarrow J/\psi(\mu\mu)\phi(KK)$ channel, together with other $b \rightarrow J/\psi(\mu\mu)X$ control channels;

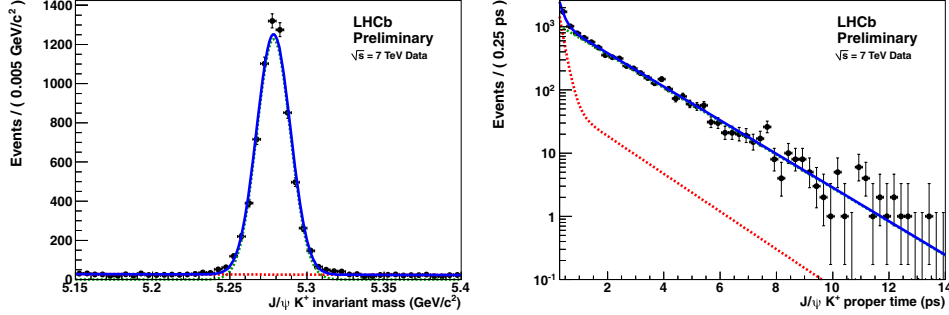


Fig. 1. – B^+ mass (left) and proper time (right) projections of the two-dimensional fit to the $B^+ \rightarrow J/\psi K^+$ candidates with $t > 0.3$ ps. The total fit is represented by the blue solid line, the signal contribution by the green dashed line and the background contribution by the red dashed line. The mass range for the fit is $m \in [5.15, 5.40]$ GeV/c^2 .

- in sect. **3**, we report on the untagged angular analysis of $B_s^0 \rightarrow J/\psi \phi$, together with the control channel $B^0 \rightarrow J/\psi K^{*0}$;
- the tagging of the B_s^0 flavour at production is discussed in sect. **4**, together with the measurement of Δm_d and Δm_s ;
- other channels can be used to measure the mixing-induced CP violation in B_s^0 -decays amongst which the $B_s^0 \rightarrow J/\psi f_0$ channel. The first observation of this decay is reported in Sect. **5**.

2. – Selections and lifetime measurement

The trigger and selection of $B_s^0 \rightarrow J/\psi(\mu\mu)\phi(KK)$ and control channels are described in [4]. The measurement of $\phi_s^{J/\psi\phi}$ requires a good understanding of detector effects such as the proper time acceptance and resolution, angular acceptance, mistag fraction and background. The strategy is to trigger and select several $b \rightarrow J/\psi X$ decay modes in a similar way and use them as control channels to calibrate the detector and validate the analysis procedures used when studying $B_s^0 \rightarrow J/\psi\phi$.

The b-hadron lifetimes are extracted from a maximum-likelihood fit to the proper time distributions of the fully reconstructed candidates. In order to avoid as much as possible a proper time dependent efficiency both the trigger and the offline selection are chosen to be lifetime unbiased: the selections avoid cutting on variables that are correlated with the b-hadron proper time, such as impact parameters of final state particles with respect to the primary vertex. The only exception is a cut on proper time $t > 0.3$ ps which allows to remove the huge prompt background dominated by combinations of tracks originating from the primary vertex.

The reconstructed mass and proper time projections of $B^+ \rightarrow J/\psi K^+$, $B^0 \rightarrow J/\psi K^{*0}$, $B^0 \rightarrow J/\psi K_S^0$, $B_s^0 \rightarrow J/\psi\phi$ and $\Lambda_b \rightarrow J/\psi\Lambda$ are shown in figs. 1 to 5. The extracted lifetimes and the signal yields in the proper time range $t \in [0.3, 14]$ ps are shown in table I. They are compatible with the PDG values [5]. The proper time resolution measured in $B_s^0 \rightarrow J/\psi\phi$ event is 50 fs. The systematics uncertainties are given in table II and detailed in [4].

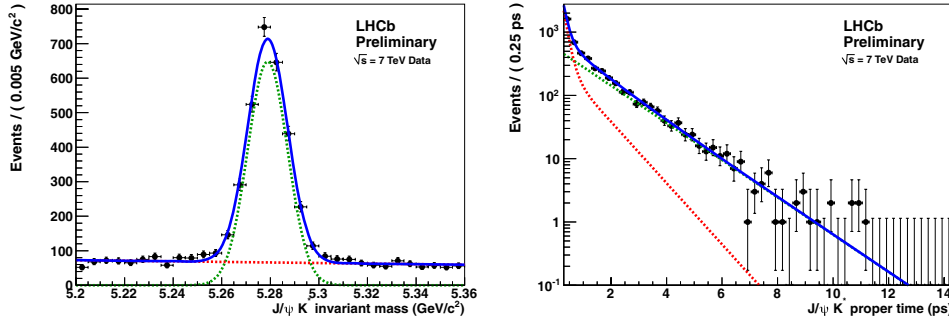


Fig. 2. – B^0 mass (left) and proper time (right) projections of the two-dimensional fit to the $B^0 \rightarrow J/\psi K^0$ candidates with $t > 0.3$ ps. The total fit is represented by the blue solid line, the signal contribution by the green dashed line and the background contribution by the red dashed line. The mass range for the fit is $m \in [5.20, 5.36]$ GeV/c^2 .

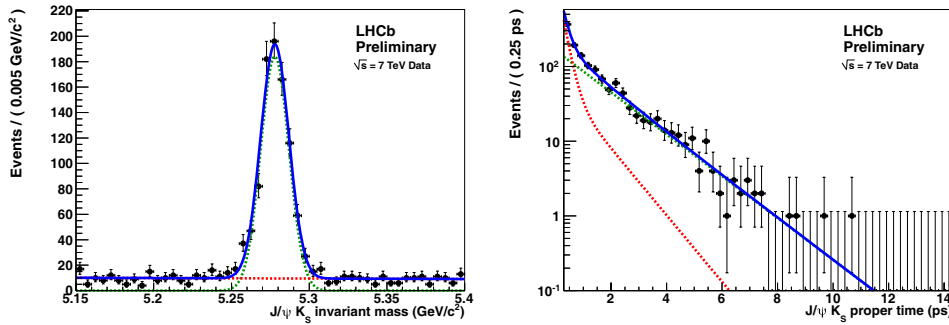


Fig. 3. – B^0 mass (left) and proper time (right) projections of the two-dimensional fit to the $B^0 \rightarrow J/\psi K_S^0$ candidates with $t > 0.3$ ps. The total fit is represented by the blue solid line, the signal contribution by the green dashed line and the background contribution by the red dashed line. The mass range for the fit is $m \in [5.15, 5.40]$ GeV/c^2 .

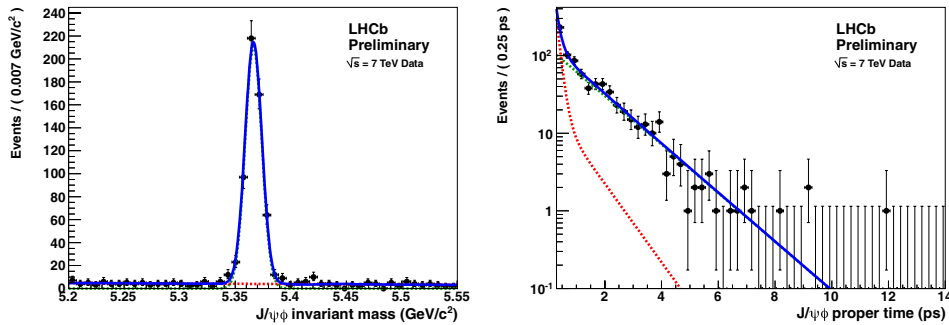


Fig. 4. – B_s^0 mass (left) and proper time (right) projections of the two-dimensional fit to the $B_s^0 \rightarrow J/\psi\phi$ candidates with $t > 0.3$ ps. The total fit is represented by the blue solid line, the signal contribution by the green dashed line and the background contribution by the red dashed line. The mass range for the fit is $m \in [5.20, 5.55]$ GeV/c^2 .

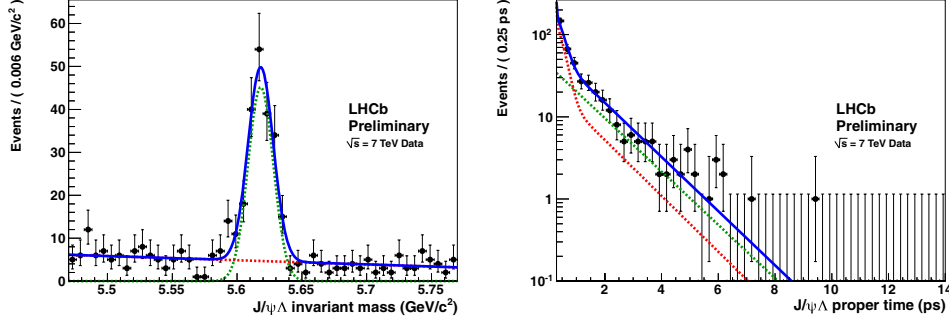


Fig. 5. – Λ_b mass (left) and proper time (right) projections of the two-dimensional fit to the $\Lambda_b \rightarrow J/\psi\Lambda$ candidates with $t > 0.3$ ps. The total fit is represented by the blue solid line, the signal contribution by the green dashed line and the background contribution by the red dashed line. The mass range for the fit is $m \in [5.47, 5.77] \text{ GeV}/c^2$.

TABLE I. – Signal event yields and lifetimes extracted from the likelihood fits to the candidates with proper time $t \in [0.3, 14]$ ps. A single exponential is used to fit the proper time distribution.

Channel	Lifetime (ps)	Yield
$B^+ \rightarrow J/\psi K^+$	$1.689 \pm 0.022(\text{stat.}) \pm 0.047(\text{syst.})$	6741 ± 85
$B^0 \rightarrow J/\psi K^{*0}$	$1.512 \pm 0.032(\text{stat.}) \pm 0.042(\text{syst.})$	2668 ± 58
$B^0 \rightarrow J/\psi K_S^0$	$1.558 \pm 0.056(\text{stat.}) \pm 0.022(\text{syst.})$	838 ± 31
$B_s^0 \rightarrow J/\psi \phi$	$1.447 \pm 0.064(\text{stat.}) \pm 0.056(\text{syst.})$	570 ± 24
$\Lambda_b \rightarrow J/\psi \Lambda$	$1.353 \pm 0.108(\text{stat.}) \pm 0.035(\text{syst.})$	187 ± 16

TABLE II. – Systematic uncertainties in the lifetime measurements (ps).

	$B^+ \rightarrow J/\psi K^+$	$B^0 \rightarrow J/\psi K^{*0}$	$B_s^0 \rightarrow J/\psi \phi$	$B^0 \rightarrow J/\psi K_S^0$	$\Lambda_b \rightarrow J/\psi \Lambda$
Signal mass model	0.002	0.002	0.010	0.014	0.012
Signal time model	0.043	0.038	0.040	0.015	0.022
Bkg. mass model	0.009	0.020	0.005	0.008	0.023
Bkg. time model	0.003	0.006	0.003	0.006	0.006
Time resol. model	0.005	0.005	0.005	0.005	0.005
Momentum scale	0.001	0.001	0.001	0.001	0.001
Decay length scale	0.001	0.001	0.001	0.001	0.001
Quadratic sum	0.047	0.042	0.056	0.022	0.035

3. – Untagged angular analysis of $B^0 \rightarrow J/\psi K^{*0}$ and $B_s^0 \rightarrow J/\psi \phi$

The decays $B_s^0 \rightarrow J/\psi \phi$ and $B^0 \rightarrow J/\psi K^{*0}$ are both pseudo-scalar to vector-vector transitions. Both decays are described by three time-dependent decay amplitudes corresponding to transitions in which the J/ψ and ϕ (or K^{*0}) have a relative orbital momentum

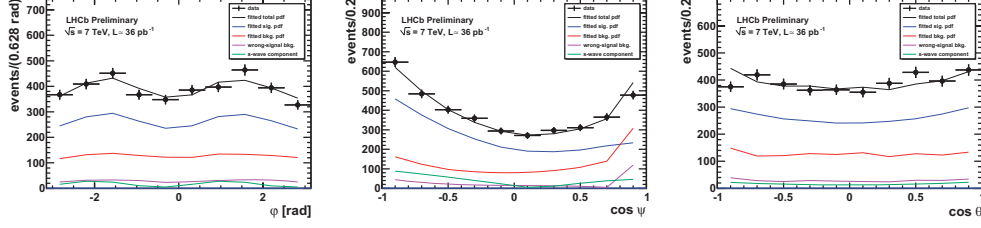


Fig. 6. – Fitted PDF with S -wave included projected on the transversity angles compared to the data distributions for the selected $B^0 \rightarrow J/\psi K^{*0}$ candidates. Shown are the total PDF, the PDFs for signal (blue), S -wave (green), total background (red) and wrong-signal (purple).

L of 0, 1, or 2. In the transversity formalism [6], the initial amplitudes at time $t = 0$, $A_0(0)$ and $A_{\parallel}(0)$ describe the decays with $L = 0, 2$ while $A_{\perp}(0)$ describes the $L = 1$ final states. The arguments of these complex amplitudes are strong phases denoted δ_0 , δ_{\parallel} and δ_{\perp} . The measurement of the polarization amplitudes and strong phases using untagged events is presented in [7]. For the $B^0 \rightarrow J/\psi K^{*0}$ channel, we find:

$$\begin{aligned} |A_{\parallel}(0)|^2 &= 0.252 \pm 0.020 \pm 0.016, \\ |A_{\perp}(0)|^2 &= 0.178 \pm 0.022 \pm 0.017, \\ \delta_{\parallel} &= -2.87 \pm 0.11 \pm 0.10, \\ \delta_{\perp} &= 3.02 \pm 0.10 \pm 0.07. \end{aligned}$$

The first error is the statistical uncertainty from the 5-dimensional fit (mass, proper time and 3 angles). The second error is the systematic uncertainty, details of which are given in [7]. The 1-dimensional projections of the 5-dimensional fit function are compared to the measured data in fig. 6.

For the $B_s^0 \rightarrow J/\psi\phi$ channel, assuming $\phi_s^{J/\psi\phi} = 0$, we measure:

$$\begin{aligned} \Gamma_s &= 0.680 \pm 0.034 \pm 0.027 \text{ ps}^{-1}, \\ \Delta\Gamma_s &= 0.084 \pm 0.112 \pm 0.021 \text{ ps}^{-1}, \\ |A_{\perp}(0)|^2 &= 0.279 \pm 0.057 \pm 0.014, \\ |A_0(0)|^2 &= 0.532 \pm 0.040 \pm 0.028, \\ \cos \delta_{\parallel} &= -1.24 \pm 0.27 \pm 0.09, \end{aligned}$$

where the first error is the statistical error from the fit and the second error is the systematic uncertainty detailed in table III. The 1-dimensional projections of the 5-dimensional fit function are compared to the measured data in fig. 7.

4. – Flavour tagging and measurement of Δm_s using $B_s^0 \rightarrow D_s^-(3)\pi^+$

The tagging of the initial B -flavour in LHCb is a key step towards the measurement of $\phi_s^{J/\psi\phi}$. It is described in [8]. The algorithm exploits charged tracks originating from the b -hadron opposite to the signal B -meson (kaon, muon, electron and vertex charge) and also tracks close to the signal B -meson (same-side tagging). The algorithm is optimized using $B^0 \rightarrow D^{*-}\mu^+\nu_{\mu}$ and $B^+ \rightarrow J/\psi K^+$ events and calibrated using $B^+ \rightarrow J/\psi K^+$, $B^0 \rightarrow J/\psi K^{*0}$

TABLE III. – *Systematic uncertainties assigned to the extracted physics parameters of the decay $B_s^0 \rightarrow J/\psi\phi$.*

Systematic effect	$\Gamma_s[\text{ps}^{-1}]$	$\Delta\Gamma_s[\text{ps}^{-1}]$	$ A_{\perp}(0) ^2$	$ A_{\parallel}(0) ^2$	$\cos\delta_{\parallel}$
Proper time resolution	0.0001	–	–	–	–
Angular acceptance	–	–	–	0.0007	–
Acceptance parametrisation	0.0002	0.001	0.0017	0.0013	–
Proper time acceptance	0.0272	0.001	0.0003	0.0002	–
S -wave treatment	0.003	0.003	0.013	0.028	0.09
Background treatment	0.0002	0.02	0.0016	0.0012	–
Mass model	0.0004	0.004	0.0032	0.0006	–
Total (quadratic sum)	0.0274	0.0206	0.0136	0.0281	0.09

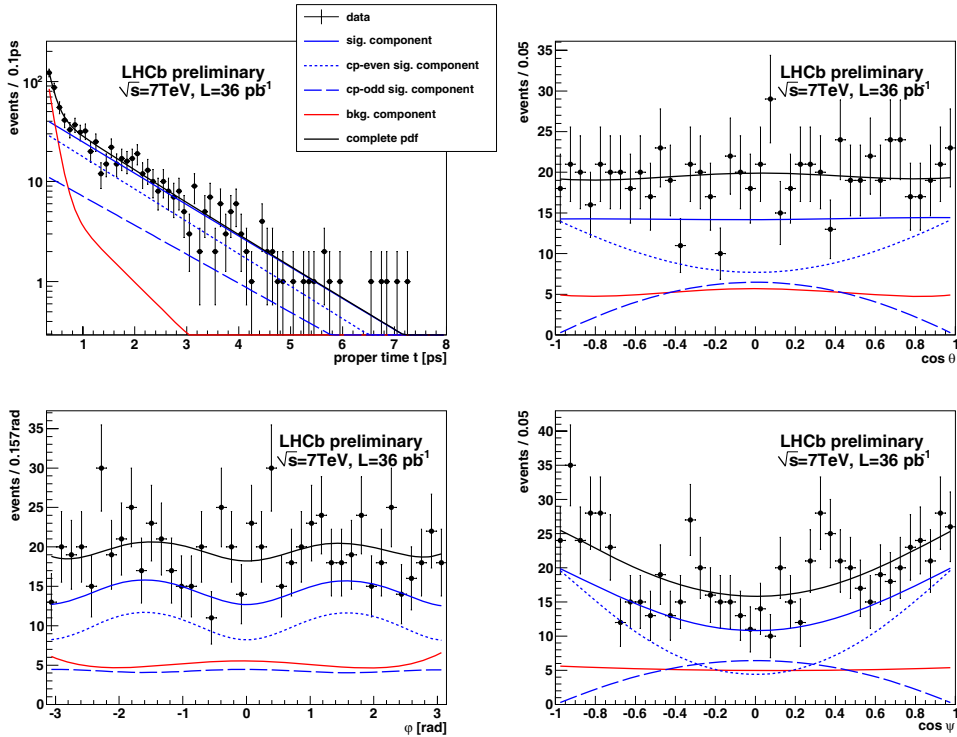


Fig. 7. – Fitted PDF projected on the lifetime and the transversity angles compared to the data distributions for the selected $B_s^0 \rightarrow J/\psi\phi$ candidates. Shown are the total PDF, the PDFs for signal, the PDFs for the CP-even and CP-odd signal components and the total background PDF.

TABLE IV. – Number of B_s^0 signal candidates used in the Δm_s measurement.

Decay mode	# signal candidates
$B_s \rightarrow D_s^- (\phi\pi^-)\pi^+$	515 ± 25
$B_s \rightarrow D_s^- (K^*K)\pi^+$	338 ± 27
$B_s \rightarrow D_s^- (K^+K^-\pi^-)\pi^+$	283 ± 27
$B_s \rightarrow D_s^- (K^+K^-\pi^-)3\pi$	245 ± 46

events. In [9], the calibration is cross-checked using $B^0 \rightarrow K^+\pi^-$ events and the $B^0\text{-}\bar{B}^0$ mixing frequency is measured to be

$$\Delta m_d = 0.499 \pm 0.032 \text{ (stat.)} \pm 0.003 \text{ (syst.) ps}^{-1}.$$

An additional crucial test is performed in [10], by measuring the $B_s^0\text{-}\bar{B}_s^0$ mixing frequency using $B_s^0 \rightarrow D_s^-(3)\pi^+$ events. In that case, only opposite side tagging is used. The effective tagging efficiency is $(3.8 \pm 2.1)\%$. Using the events sample given in table IV, we measure:

$$\Delta m_s = 17.63 \pm 0.11 \text{ (stat.)} \pm 0.04 \text{ (syst.) ps}^{-1},$$

which is compatible and competitive with the world best measurement [11]. The details of the systematics uncertainties are given in [10]. The likelihood profile as a function of the mixing frequency Δm_s is shown in fig. 8. The statistical significance of the signal is evaluated by comparing the likelihood value at the measured Δm_s value of 17.63 ps^{-1} with the likelihood value obtained on the same sample in the limit of infinitely high mixing frequency. We find a significance of 4.6σ for the observed mixing signal. The statistical size of the sample is not large enough to illustrate the oscillation pattern of the time dependent asymmetry. However we can more clearly observe the oscillation if we plot the asymmetry as a function of the proper time modulo $\frac{2\pi}{\Delta m_s}$ (fig. 9). Additionally we provide an amplitude scan in fig. 9, with all details given in [10].

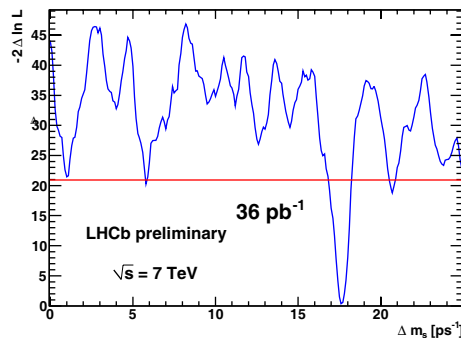


Fig. 8. – Likelihood scan for Δm_s in the range from $[0.0, 25.0] \text{ ps}^{-1}$. The line at 20.94 indicates the likelihood value evaluated in the limit of infinite mixing frequency.

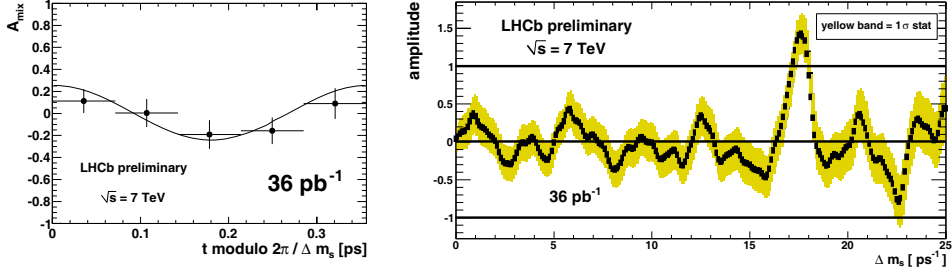


Fig. 9. – Left: Mixing asymmetry for signal B_s^0 candidates as a function of proper time modulo $\frac{2\pi}{\Delta m_s}$. The fitted signal asymmetry is superimposed. Right: Fitted amplitude as a function of Δm_s . See the text for further explanation.

5. – First observation of $B_s^0 \rightarrow J/\psi f_0$

When LHCb will have accumulated more data, the measurement of ϕ_s will not only be done in $B_s^0 \rightarrow J/\psi \phi$, but also in other similar channels. One of them, $B_s^0 \rightarrow J/\psi f_0$, has been observed for the first time in LHCb [12]. The $J/\psi \pi^+ \pi^-$ and $\pi^+ \pi^-$ invariant masses are shown in fig. 10. We measure

$$R_{f_0/\phi} \equiv \frac{\Gamma(B_s^0 \rightarrow J/\psi f_0, f_0 \rightarrow \pi^+ \pi^-)}{\Gamma(B_s^0 \rightarrow J/\psi \phi, \phi \rightarrow K^+ K^-)} = 0.252_{-0.032}^{+0.046+0.027}.$$

Despite a smaller branching ratio, with respect to $B_s^0 \rightarrow J/\psi \phi$, the fact that $J/\psi f_0$ is a pure CP-odd final state makes the measurement of ϕ_s simpler, since no angular analysis is required.

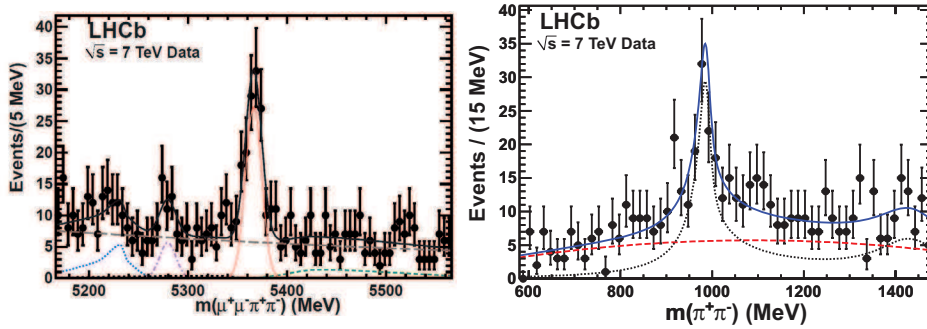


Fig. 10. – Left: The invariant mass of $J/\psi \pi^+ \pi^-$ combinations when the $\pi^+ \pi^-$ pair is required to be within ± 90 MeV of the $f_0(980)$ mass. The data have been fit with a signal Gaussian and several background functions. The thin (red) solid curve shows the signal, the long-dashed (brown) curve the combinatorial background, the dashed (green) curve the $B^+ \rightarrow J/\psi K^+ (\pi^+)$ background, the dotted (blue) curve the $B^0 \rightarrow J/\psi K^{*0}$ background, the dash-dot curve (purple) the $B^0 \rightarrow J/\psi \pi^+ \pi^-$ background, the barely visible dotted curve (black) the sum of $B_s^0 \rightarrow J/\psi \eta'$ and $J/\psi \phi$ backgrounds, and the thick-solid (black) curve the total. Right: The invariant mass of $\pi^+ \pi^-$ combinations when the $J/\psi \pi^+ \pi^-$ combination is required to be within ± 30 MeV of the B_s^0 mass. The dashed curve is the like-sign background that is taken from the data both in shape and absolute normalization. The dotted curve is the result of the fit described in [12].

6. – Epilogue

While completing these proceedings LHCb has released its first preliminary results on $\phi_s^{J/\psi\phi}$ [13]. The dataset was too small to calibrate the same-side tagger; the opposite side tagger has a measured effective efficiency of $2.2 \pm 0.4\%$. Although it was not possible to give a point estimate contours in the ϕ_s - $\Delta\Gamma_s$ space could be calculated.

7. – Conclusions

The $B_s^0 \rightarrow J/\psi\phi$ channel will allow LHCb to probe possible New Physics effects in the B_s^0 - \bar{B}_s^0 box diagram. We have presented, for the first time at this conference, the preliminary results needed for a $\phi_s^{J/\psi\phi}$ measurement, obtained with the data taken in 2010. The data sample used corresponds to an integrated luminosity of 35 pb^{-1} . We have measured the lifetime of $B^+ \rightarrow J/\psi K^+$, $B^0 \rightarrow J/\psi K^{*0}$, $B^0 \rightarrow J/\psi K_s^0$, $B_s^0 \rightarrow J/\psi\phi$, $\Lambda_b \rightarrow J/\psi\Lambda$, the polarization amplitudes in $B^0 \rightarrow J/\psi K^{*0}$ and $B_s^0 \rightarrow J/\psi\phi$, the width and mass differences of the B_s^0 mass eigenstates, $\Delta\Gamma_s$ and Δm_s . In particular, we measure: $\Delta m_s = 17.73 \pm 0.11$ (stat.) ± 0.04 (syst.) ps^{-1} . With the data currently being taken in 2011, we expect to obtain this year the world best measurement of $\phi_s^{J/\psi\phi}$.

* * *

I wish to thank the organizers of the “Rencontres de Physique de la vallee d’Aoste”, for the very nice atmosphere during the conference in La Thuile, and all my LHCb colleagues who make possible the first presentation of these 17 new beautiful results.

REFERENCES

- [1] CHARLES J. *et al.* (CKMFITTER GROUP), *Eur. Phys. J. C*, **41** (2005) 1-131, hep-ph/0406184, updated results and plots available at <http://ckmfitter.in2p3.fr/>.
- [2] THE CDF COLLABORATION, public note CDF/ANAL/BOTTOM/PUBLIC/10206 (2010).
- [3] THE D0 COLLABORATION, D0 Conference note 6098-CONF (2010).
- [4] THE LHCb COLLABORATION, “ b -hadron lifetime measurements with exclusive $b \rightarrow J/\psi X$ decays reconstructed in the 2010 data”, LHCb-CONF-2011-001.
- [5] NAKAMURA K. *et al.* (PARTICLE DATA GROUP), *J. Phys. G*, **37** (2010) 075021.
- [6] THE LHCb COLLABORATION, “Roadmap for selected key measurements of LHCb.”, LHCb-PUB-2009-029, arXiv:0912.4179.
- [7] THE LHCb COLLABORATION, “Untagged angular analysis of $B^0 \rightarrow J/\psi K^{*0}$ and $B_s^0 \rightarrow J/\psi\phi$ decays”, LHCb-CONF-2011-002.
- [8] THE LHCb COLLABORATION, “Optimization and Calibration of the Tagging performances using 2010 data”, LHCb-CONF-2011-003.
- [9] THE LHCb COLLABORATION, “Measurement of ΔM_d in $B^0 \rightarrow D\pi$ ”, LHCb-CONF-2011-010.
- [10] THE LHCb COLLABORATION, “Measurement of ΔM_s and calibration and tuning of the Same-Side Tagging algorithm with $B_s^0 \rightarrow D_s\pi$ decays using the 2010 data sample”, LHCb-CONF-2011-005.
- [11] ABULENCIA A. *et al.* (CDF COLLABORATION), *Phys. Rev. Lett.*, **97** (2006) 242003.
- [12] LHCb COLLABORATION, “First observation of $B_s^0 \rightarrow J/\psi f^0(980)$ decays”, PLB... 2011.
- [13] THE LHCb COLLABORATION, “Tagged time-dependent angular analysis of $B_s^0 \rightarrow J/\psi\phi$ decays with the 2010 LHCb data”, LHCb-CONF-2011-006.

SESSION V - ELECTROWEAK AND TOP PHYSICS

<i>Jadranka Sekaric</i>	Electroweak physics at the Tevatron
<i>Rikard Sandström</i>	Electroweak and Top physics at ATLAS
<i>Michele De Gruttola</i>	Measurement of W, Z and Top properties with CMS
<i>Hyun Su Lee</i>	Top physics at Tevatron
<i>Dante Amidei</i>	Forward-backward asymmetry in $t\bar{t}$ production

Electroweak physics at the Tevatron

J. SEKARIC for the CDF and DØ COLLABORATIONS

Department of Physics and Astronomy, University of Kansas - Lawrence, KS 66045, USA

(ricevuto il 29 Settembre 2011; pubblicato online il 17 Gennaio 2012)

Summary. — The most recent Electroweak results from the Tevatron are presented. The importance of precise Standard Model measurements in the Higgs sector, quantum chromodynamics and searches for new physics is emphasized. Analyzed data correspond to $1\text{--}7\text{ fb}^{-1}$ of integrated luminosity recorded by the CDF and DØ detectors at the Tevatron Collider at $\sqrt{s} = 1.96\text{ TeV}$ during the period between 2002 and 2010.

PACS 12.15.Ji – Applications of electroweak models to specific processes.

PACS 13.85.Qk – Inclusive production with identified leptons, photons, or other nonhadronic particles.

PACS 14.70.Fm – W bosons.

PACS 14.70.Hp – Z bosons.

1. – Introduction

The main goal of the Electroweak (EW) physics is to probe the mechanism of the EW symmetry breaking. An important aspect of these studies is related to precise measurements of the Standard Model (SM) parameters and tests of the $SU(2) \times U(1)$ gauge symmetry. Deviations from the SM may be indicative of new physics. Thus, the interplay between the tests of the “standard” physics and searches for a “non-standard” physics is an important aspect of the EW measurements. The observables commonly used in these measurements are cross sections, gauge boson couplings, differential distributions, asymmetries, etc. Besides, many EW processes represent a non-negligible background in a Higgs boson and top quark production, and production of supersymmetric particles. Therefore, the complete and detailed understanding of EW processes is a mandatory precondition for early discoveries of very small new physics signals. Furthermore, several EW analyses represent a proving ground for analysis techniques and statistical treatments used in the Tevatron Higgs searches.

2. – Single-boson production

Measurements of gauge boson properties such as mass, differential distributions and production asymmetries represent an important input to theoretical predictions which will provide a better description of Tevatron data and increase sensitivity to new physics signals.

Precise measurements of the W boson mass are important, because they restrict the phase space of the so far unseen SM Higgs and set indirect constraints on new physics via EW radiative corrections. At the Tevatron, the W boson mass is measured using three kinematic variables: lepton transverse momentum, p_T^l (where $l = e, \mu$), imbalance in transverse energy arising from the neutrino, p_T^ν (often referred as to missing E_T), and the W boson transverse mass defined as $M_T = \sqrt{2p_T^l p_T^\nu (1 - \cos \Delta\phi)}$, where $\Delta\phi$ is the opening angle between the electron (muon) and neutrino momenta in the plane transverse to the beam. Correct modeling of the hadronic recoil from the QCD radiation is highly important for W mass measurement as it balances the boson's p_T . CDF selects events with $p_T^l > 18$ (30) GeV/ c in the electron (muon) channel, missing $E_T > 30$ GeV and $|\vec{u}| < 15$ GeV/ c in 0.2 fb^{-1} of integrated luminosity using both the electron and muon channel. DØ selects events with $p_T^l > 25$ GeV/ c , missing $E_T > 25$ GeV and $|\vec{u}| < 15$ GeV/ c in 1.0 fb^{-1} of integrated luminosity using only the electron channel. Both experiments use all three reconstructed variables to measure the W boson mass. CDF measures q W mass of 80.413 ± 0.034 (stat) ± 0.034 (syst) GeV/ c^2 [1]. DØ measures the W mass to be 80.401 ± 0.021 (stat) ± 0.038 (syst) GeV/ c^2 [2] which represents the most precise single W mass measurement to date. Using the same data DØ extracts the width of the W boson to be $\Gamma_W = 2.028 \pm 0.039$ (stat) ± 0.061 (syst) GeV using M_T distribution [3].

The production of single W bosons in $p\bar{p}$ collisions also provides information on the momentum fraction dependence of the u and d quark parton distribution functions (PDF) within the proton. The boost along the z -axis in the direction of more energetic parton causes an asymmetry in the W boson and charged lepton production. After data has been corrected for detector effects, efficiencies, charge mis-identification, etc, the asymmetry A is measured as a function of rapidity y_W of the W boson or pseudorapidity η_l of charged lepton, and transverse momentum. Current results on lepton charge asymmetry from 1 fb^{-1} of CDF integrated luminosity, electron charge asymmetry from 0.75 fb^{-1} of DØ integrated luminosity [4] and muon charge asymmetry from 5 fb^{-1} of DØ integrated luminosity [5], show mutual disagreement when split in different lepton p_T bins. In addition, both CDF and DØ lepton charge asymmetries do not agree with CTEQ6.6 PDF prediction when split into p_T bins while W boson asymmetry measured by CDF agrees well with higher-order predictions [6].

The study of Z boson kinematic distributions is yet another test that contributes to the tuning of theoretical QCD predictions. Distributions such as transverse momentum, rapidity and ϕ_η^* of dilepton pairs are studied at the Tevatron.

The differential cross section as a function of the dimuon p_T distribution has been studied with 1 fb^{-1} of integrated luminosity recorded at DØ. Unfolded data normalized to the PYTHIA Perugia 6 prediction is compared to other generators as shown in fig. 1. In the low p_T region (Z $p_T < 30$ GeV) the resummation describes data well while the high Z $p_T > 30$ GeV region shows the best shape agreement with higher-order perturbative QCD but with an offset in normalization. Since the p_T distribution is sensitive to resolution effects, the ϕ_η^* distribution based exclusively on angular resolution is an excellent place to probe QCD predictions with higher precision. It is defined as $\phi_\eta^* = \tan(\phi_{acop}/2) \sin(\theta)_\eta^*$ where ϕ_{acop} is the acoplanarity angle $\phi_{acop} = \pi - \Delta\phi_{ll}$ and $\Delta\phi_{ll}$ is the difference in azimuthal angle ϕ between the two leptons. The variable $(\theta)_\eta^*$ is defined as $(\theta)_\eta^* = a \cos[\tanh(\eta^- - \eta^+)/2]$ where η^- and η^+ are the pseudorapidities of the negatively and positively charged lepton, respectively. As presented in fig. 2 where the ratio of the corrected distribution $(1/\sigma) \times (d\sigma/d\phi_\eta^*)$ to RESBOS is shown for three different rapidity

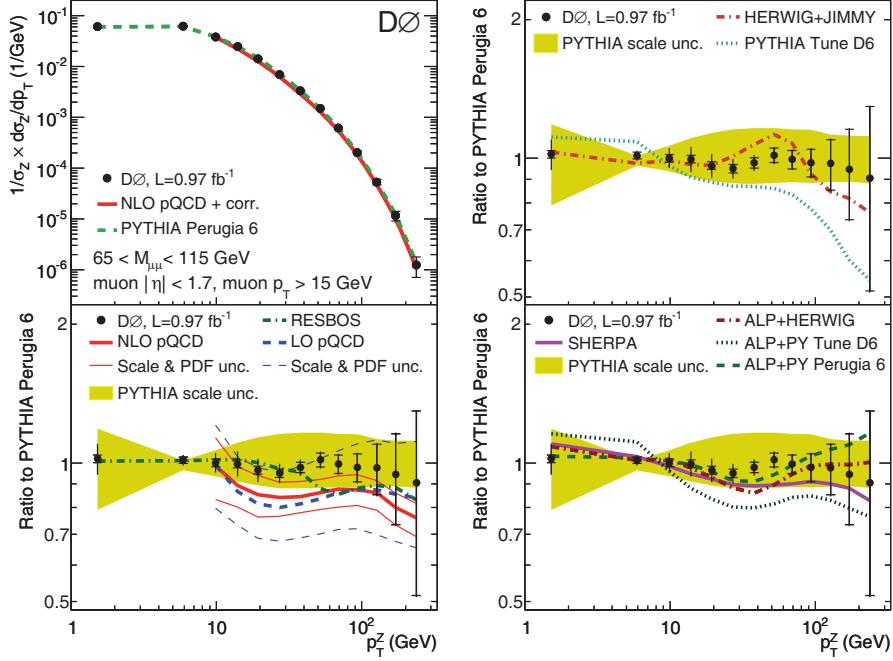


Fig. 1. – The normalized differential cross section and its ratio relative to PYTHIA Perugia 6 in bins of $Z p_t$ for $Z/\gamma^*(\rightarrow \mu\mu) + X$ events. The data are shown with statistical and systematic uncertainties. The distribution is compared to different generators and NLO predictions.

regions, predictions from RESBOS fail to describe the detailed shape of the data, and a prediction that includes the effect of small- x broadening is disfavored.

The CDF experiment performs a measurement of $d\sigma/dy$ selecting $Z/\gamma^* \rightarrow e^+e^-$ events in the mass range of 66 to 116 GeV/ c^2 using data of 2.1 fb $^{-1}$ of integrated luminosity. The comparison of unfolded data to different QCD predictions shows a good agreement as presented in fig. 3. The measured cross section for Z production of $\sigma_Z \times BR(Z \rightarrow e^+e^-) = 256.6 \pm 15.5$ (stat + syst) pb is in good agreement with higher order QCD predictions. In addition, the selected data is used to extract p_T dependent angular coefficients, A_0, A_2, A_3 and A_4 . The p_T dependence of A_0 and A_2 is found to be in agreement with the predictions of perturbative QCD, confirming the Lam-Tung relation which implies that the spin of the gluon is 1 if $A_0 = A_2$. The values of A_3 and A_4 are in agreement with the predictions of all QCD models [7]. The measured A_4 is used to extract $\sin^2 \theta_W = 0.2329 \pm 0.0008_{-0.0009}^{+0.0010}$ (QCD) as shown in fig. 3.

3. – Diboson production

As an important production mechanism for understanding the EW symmetry breaking, diboson physics focuses on precise measurements of the cross section and the trilinear gauge boson couplings (TGCs) [8]. Besides, the most precise knowledge of these processes and their proper modeling is highly valuable in many searches for new physics which may exist at some energy scale Λ . The quantity Λ is physically interpreted as the mass scale where the new phenomenon responsible for the anomalous couplings is directly observable.

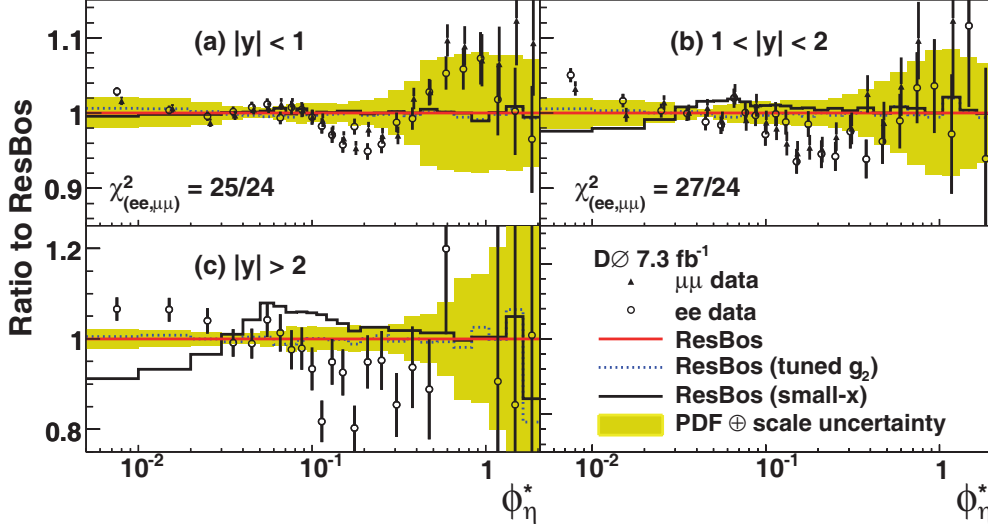


Fig. 2. – Ratio of $(1/\sigma) \times (d\sigma/d\phi_\eta^*)$ to RESBOS in different Z rapidity bins. The yellow band around the RESBOS prediction represents the quadrature sum of uncertainty due to CTEQ6.6 PDFs and the uncertainty due to the QCD scale. Comparisons to the RESBOS predictions when g_2 is set to 0.66 GeV^2 (dotted blue line) and to the small- x broadening (solid black line) are shown as well.

The $Z\gamma \rightarrow l^+l^-\gamma$ ($l = e, \mu$) and $Z\gamma \rightarrow \nu\bar{\nu}\gamma$ events selected from the CDF data of 5 fb^{-1} of integrated luminosity have a photon with transverse energy $E_T > 50 \text{ GeV}$ which is spatially separated from a lepton by $\Delta R_{l\gamma} > 0.7$. Charged leptons are required to have $p_T > 20 \text{ GeV}/c$ ($E_T > 20 \text{ GeV}$) for one muon (electron) candidate and $p_T > 10 \text{ GeV}/c$ ($E_T > 10 \text{ GeV}$) for the other. The three-body mass cut of 100 GeV is applied to separate

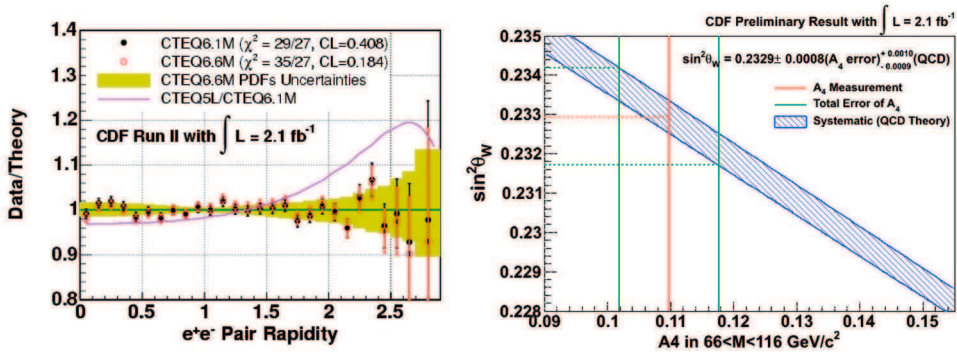


Fig. 3. – (Colour on-line) Left: Ratio of data to theory prediction for $(1/\sigma) \times (d\sigma/dy)$. The prediction uses PYTHIA MC with NLO CTEQ6.1M and CTEQ6.6M PDFs. Right: The value of $\sin^2 \theta_W$ as a function of A_4 . Measured values of $\sin^2 \theta_W$ and A_4 are shown in red, and the blue band corresponds to different QCD predictions. The green lines represent the total uncertainty from measurement of A_4 .

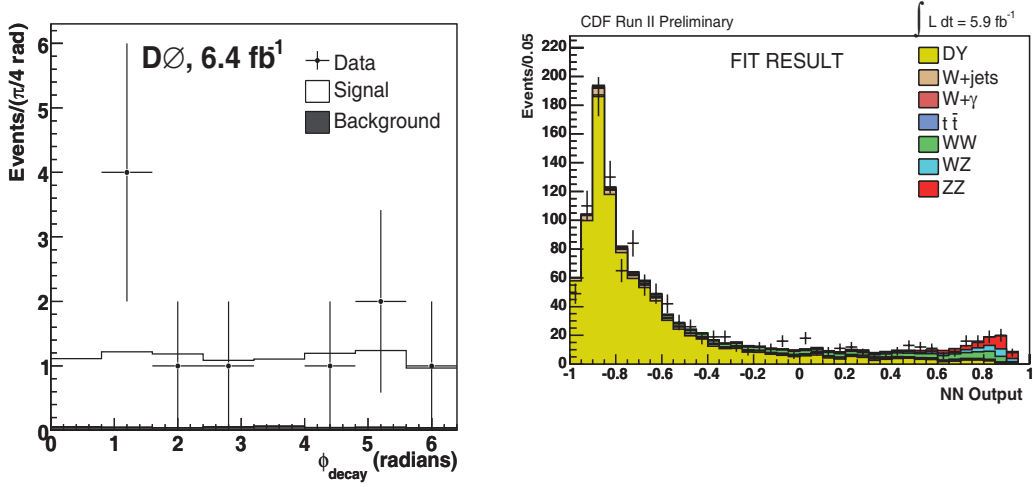


Fig. 4. – Left: The azimuthal angle decay distribution of the Z/γ^* candidates selected in the $ZZ \rightarrow \bar{l}l'\bar{l}'$ analysis, compared to the expected signal and background. Right: The Neural Network output used in the fit to the data to measure the ZZ cross section.

events which originate from the final-state radiation. Photon E_T spectra from $l^+l^-\gamma$ and $\nu\bar{\nu}\gamma$ candidate events are combined and used to set the limits on $Z\gamma\gamma/ZZ\gamma$ TGCs. The one-dimensional 95% CL limits on $h_{3,4}^{\gamma,Z}$ at $\Lambda = 1.5$ TeV are $-0.017 < h_3^{Z,\gamma} < 0.016$, $-0.0006 < h_4^Z < 0.0005$ and $|h_4^\gamma| < 0.0006$. They are the most restrictive limits on these couplings to date [9].

The ϕ_{decay} distribution of ten $ZZ \rightarrow \bar{l}l'\bar{l}'$ ($l, l' = e, \mu$) candidate events observed in $D\bar{O}$ data of 6.4fb^{-1} of integrated luminosity with a significance of 6 standard deviations are shown in fig. 4. The ϕ_{decay} distribution is sensitive to different

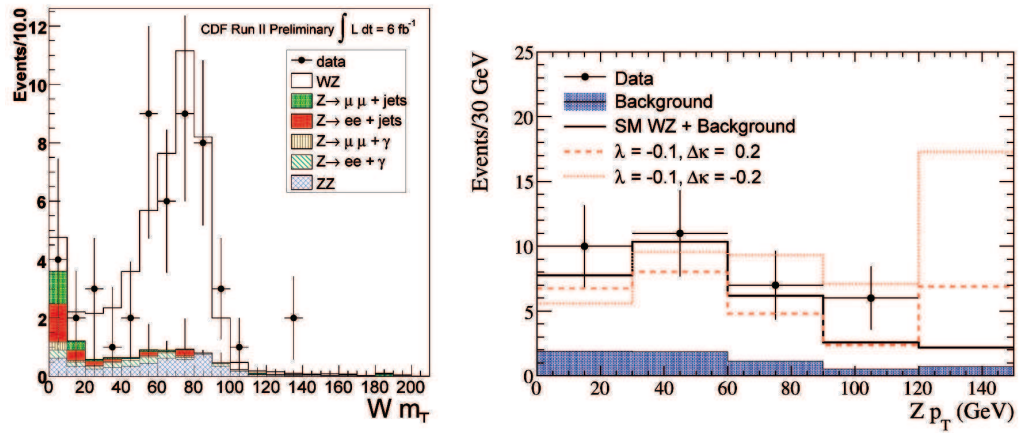


Fig. 5. – Left: Transverse mass of W bosons in WZ candidates. Right: Comparison of the Z boson p_T spectrum from data, total background, the SM WZ signal+total background and two TGC models.

scalar models arising from new physics [10]. The measured cross section is $\sigma_{ZZ} = 1.24_{-0.37}^{+0.47}$ (stat) ± 0.11 (syst) ± 0.08 (lumi) pb and it represents the most precise σ_{ZZ} measurement at a hadron collider to date [11]. The $ZZ \rightarrow l\bar{l}\nu\bar{\nu}$ ($l = e, \mu$) events selected from data of 5.9 fb^{-1} of integrated luminosity at CDF were used to measure the cross section of $\sigma_{ZZ} = 1.45_{-0.51}^{+0.60}$ (stat + syst) pb [12]. The Neural Network output shown in fig. 4 is used in analysis to separate ZZ events from the most dominant Drell-Yan background. The measured ZZ cross sections are in agreement with the SM prediction.

The most precise measurement of the $WZ \rightarrow l\nu ll$ cross section has been recently performed by the CDF Collaboration. The analysis selects events with missing $E_T > 25 \text{ GeV}$ and leptons of $p_T > 15 \text{ GeV}/c$ where two leptons are of the same flavour, opposite charge and lie in the mass window $(m_{ll} - M_Z) < 15 \text{ GeV}/c^2$. After the final selection 50 candidate events are selected with expected background of 11.2 ± 1.63 events. The WZ cross section, measured relative to the Z cross section is $\sigma_{WZ}/\sigma_Z = [5.5 \pm 0.8$ (stat) ± 0.5 (syst)] $\cdot 10^{-4}$. Using a next-to-NLO calculation of the $\sigma_Z \cdot \text{BR}(Z \rightarrow ll) = (251.3 \pm 5)$ pb gives the cross section of $\sigma_{WZ} = 4.1 \pm 0.6$ (stat) ± 0.4 (syst) pb [13]. The DØ Collaboration measures the σ_{WZ} cross section selecting events in the same final states, requiring lepton candidates with $p_T > 15 \text{ GeV}/c$ and missing $E_T > 20 \text{ GeV}$. The selection yields 34 WZ candidate events with an estimated 23.3 ± 1.5 signal, and 6.0 ± 0.6 background events. The measured cross section of $\sigma_{WZ} = 3.90_{-0.85}^{+1.01}$ (stat + syst) ± 0.31 (lumi) pb.

In addition, $Z p_T$ spectrum shown in fig. 5 is used to set the limits on WWZ TGCs. The one-dimensional 95% CL limits on $\Delta\kappa_Z, \lambda_Z$ and Δg_1^Z at $\Lambda = 2.0 \text{ TeV}$ are $-0.376 < \Delta\kappa_Z < 0.686$, $-0.075 < \lambda_Z < 0.093$ and $-0.053 < \Delta g_1^Z < 0.156$. They are the best limits on these couplings to date as measured from direct WZ production [14].

4. – Summary

The most recent EW results from CDF and DØ Collaborations using Tevatron data of $1\text{--}7 \text{ fb}^{-1}$ of integrated luminosity have been presented. The W mass, cross sections and TGCs are measured with the best precision to date at a hadron collider. Observations are in agreement with the SM predictions though some discrepancies with theoretical predictions have been observed.

REFERENCES

- [1] AALTONEN T. *et al.* (CDF COLLABORATION), *Phys. Rev. Lett.*, **99** (2007) 151801.
- [2] ABAZOV V. *et al.* (D0 COLLABORATION), *Phys. Rev. Lett.*, **103** (2009) 141801.
- [3] ABAZOV V. *et al.* (D0 COLLABORATION), *Phys. Rev. Lett.*, **103** (2009) 231802.
- [4] ABAZOV V. *et al.* (D0 COLLABORATION), *Phys. Rev. Lett.*, **101** (2008) 211801.
- [5] ABAZOV V. *et al.* (D0 COLLABORATION), D0 Note 5976-CONF (2009).
- [6] AALTONEN T. *et al.* (CDF COLLABORATION), *Phys. Rev. Lett.*, **102** (2009) 181801.
- [7] AALTONEN T. *et al.* (CDF COLLABORATION), *Phys. Rev. Lett.*, **106** (2011) 241801, arXiv:1103.5699v3 [hep-ex] (2011).
- [8] HAGIWARA K., WOODSIDE J. and ZEPPENFELD D., *Phys. Rev. D*, **41** (1990) 2113.
- [9] AALTONEN T. *et al.* (CDF COLLABORATION), *Phys. Rev. Lett.*, **107** (2011) 051802, arXiv:1103.2990v1 [hep-ex] (2011).
- [10] CAO Q. *et al.*, *Phys. Rev. D*, **81** (2010) 015010.
- [11] ABAZOV V. *et al.* (D0 COLLABORATION), *Phys. Rev. D*, **84** (2011) 011103, arXiv:1104.3078v1 [hep-ex] (2011).
- [12] AALTONEN T. *et al.* (CDF COLLABORATION), CDF Note 10358 (2010).
- [13] AALTONEN T. *et al.* (CDF COLLABORATION), CDF Note 10238 (2010).
- [14] ABAZOV V. *et al.* (D0 COLLABORATION), *Phys. Lett. B*, **695** (2011) 67.

Electroweak and Top physics at ATLAS

A. R. SANDSTRÖM on behalf of the ATLAS COLLABORATION

*Max-Planck-Institut für Physik, (Werner-Heisenberg-Institut) - Föhringer Ring 6,
80805 München, Germany*
*Nikhef National Institute for Subatomic Physics, and University of Amsterdam
Science Park 105, 1098 XG Amsterdam, The Netherlands*

(ricevuto il 29 Settembre 2011; pubblicato online il 19 Gennaio 2012)

Summary. — The observations of electroweak boson (W, Z) and top quark pair ($t\bar{t}$) production are among the key milestones for the early LHC physics programme. Production of $t\bar{t}$, W and Z in association with jets are important backgrounds in various searches for physics beyond the Standard Model, and new physics may also give rise to additional production mechanisms or modification of the decay channels. This note summarizes the electroweak and top physics performed in ATLAS with $\sqrt{s} = 7$ TeV proton-proton collisions during 2010 and compares the observations with theoretical predictions.

PACS 14.65.Ha – Top quarks.

PACS 14.70.Fm – W bosons.

PACS 14.70.Hp – Z bosons.

1. – Introduction

The ATLAS experiment [1] at the Large Hadron Collider recorded more than 40 pb^{-1} at $\sqrt{s} = 7$ TeV proton-proton collisions during 2010. This note summarizes some of the tests of the Standard Model that were performed with integrated luminosity ranging from 0.3 to 31 pb^{-1} . The note first covers the results using electroweak bosons before presenting results using top quarks.

2. – Electroweak results

2.1. W/Z cross section. – At hadron colliders, the W and Z bosons can most easily be detected via their leptonic decay mode. The ATLAS experiment observed $W \rightarrow e\nu$, $W \rightarrow \mu\nu$, $Z \rightarrow ee$, and $Z \rightarrow \mu\mu$ candidates produced from the $\sqrt{s} = 7$ TeV proton-proton collisions of the LHC [2]. The measurements are based on data corresponding to an integrated luminosity of approximately 0.3 pb^{-1} . The absolute luminosity was calibrated using beam separation scans, yielding a total systematic uncertainty of $\pm 11\%$ [3], dominated by the measurement of the LHC beam currents.

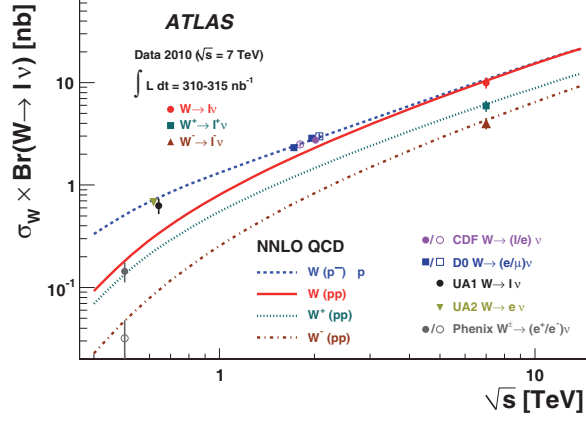


Fig. 1. – The measured values of $\sigma_W \times \text{BR}(W \rightarrow l\nu)$ for W^+ , W^- and for their sum compared to the theoretical predictions based on NNLO QCD calculations. Results are shown for the combined electron-muon results. The predictions are shown for both proton-proton (W^+ , W^- and their sum) and proton-antiproton colliders (W) as a function of \sqrt{s} . In addition, previous measurements at proton-antiproton and proton-proton colliders are shown. The data points at the various energies are staggered to improve readability. The CDF and D0 measurements are shown for both Tevatron collider energies, $\sqrt{s} = 1.8 \text{ TeV}$ and $\sqrt{s} = 1.96 \text{ TeV}$. All data points are displayed with their total uncertainty. The theoretical uncertainties are not shown [2].

Muons are required to have at least one combined muon track with $p_T > 20 \text{ GeV}$ and p_T measured by the muon spectrometer (MS) alone greater than $p_T^{\text{MS}} > 10 \text{ GeV}$, within the range $|\eta_\mu| < 2.4$. Electron tracks are required to have $E_T > 20 \text{ GeV}$ and $|\eta| < 2.47$ where candidates in the calorimeter transition region $1.37 < |\eta| < 1.52$ are excluded. $Z \rightarrow ll$ candidates are required to have two leptons of the same flavour and opposite charge. W candidates are selected by requiring one lepton and missing transverse energy $E_T^{\text{miss}} > 25 \text{ GeV}$. Furthermore, a transverse mass requirement $m_T > 40 \text{ GeV}$ is imposed on W candidates, where

$$(1) \quad m_T = \sqrt{2p_T^l p_T^\nu (1 - \cos(\phi^l - \phi^\nu))},$$

and where the highest p_T lepton is used and the (x, y) components of the neutrino momentum are inferred from the corresponding E_T^{miss} components.

The $W \rightarrow l\nu$ analysis resulted in a total of 1069 candidates pass all requirements in the electron channel and 1181 candidates in the muon channel. The $Z \rightarrow ll$ found a total of 70 candidates pass all requirements in the electron channel and 109 candidates in the muon channel, within the invariant mass window $66 < m_{ll} < 116 \text{ GeV}$. After correcting for acceptance and inefficiencies these observations lead to the measured cross sections

$$(2) \quad \sigma_W \times \text{BR}(W \rightarrow l\nu) = 9.96 \pm 0.23(\text{stat}) \pm 0.50(\text{syst}) \pm 1.10(\text{lumi}) \text{ nb},$$

$$(3) \quad \sigma_{Z/\gamma^*} \times \text{BR}(Z/\gamma^* \rightarrow ll) = 0.82 \pm 0.06(\text{stat}) \pm 0.05(\text{syst}) \pm 0.09(\text{lumi}) \text{ nb}.$$

These results are shown in figs. 1 and 2, together with results at lower center-of-mass energies. Theoretical predictions, based on NNLO QCD calculations, are in good agreement with these measurements.

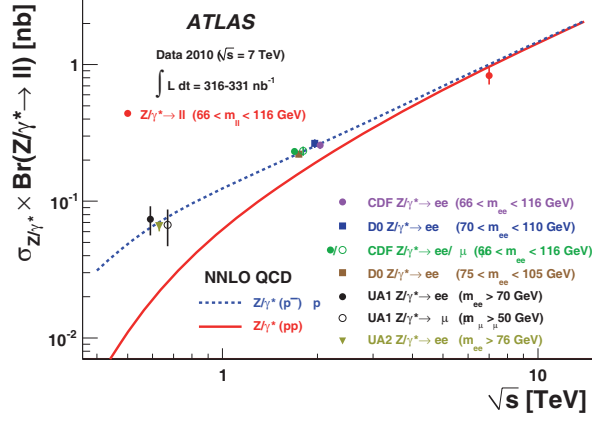


Fig. 2. – The measured value of $\sigma_Z/\gamma^* \times \text{BR}(Z/\gamma^* \rightarrow ll)$ where the electron and muon channels have been combined, compared to the theoretical predictions based on NNLO QCD calculations. The predictions are shown for both proton-proton and proton-antiproton colliders as a function of \sqrt{s} . In addition, previous measurements at proton-antiproton and proton-proton colliders are shown. The data points at the various energies are staggered to improve readability. The CDF and D0 measurements are shown for both Tevatron collider energies, $\sqrt{s} = 1.8 \text{ TeV}$ and $\sqrt{s} = 1.96 \text{ TeV}$. All data points are displayed with their total uncertainty. The theoretical uncertainties are not shown [2].

The measurement of the ratio of the W to Z cross sections times branching ratios constitutes an important test of the Standard Model. It can be measured with a higher relative precision than the individual cross sections since both experimental and theoretical uncertainties partially cancel. The observed ratio is

$$(4) \quad R_{W/Z} = 11.7 \pm 0.9(\text{stat}) \pm 0.4(\text{syst}),$$

whereas the theoretical prediction is $R_{W/Z} = 10.840 \pm 0.054$ [4, 5].

2.2. W charge asymmetry. – The measurement of the charge asymmetry of leptons originating from the decay of singly produced W bosons at pp , $p\bar{p}$ and ep colliders provides important information about the proton structure as described by parton distribution functions (PDFs). The W boson charge asymmetry is mainly sensitive to valence quark distributions via the dominant production process $u\bar{d}(\bar{u}d) \rightarrow W^{+(-)}$ and provides complementary information to that obtained from measurements of inclusive deep inelastic scattering cross sections at the HERA electron-proton collider [6].

The ATLAS experiment has measured the muon charge asymmetry from the decay of W^\pm bosons in pp collisions at a centre-of-mass energy of $\sqrt{s} = 7 \text{ TeV}$ at the LHC [7]. The asymmetry varies significantly as a function of the pseudorapidity. The muon charge asymmetry A_μ is defined from the cross sections for $W \rightarrow \mu\nu$ production $d\sigma_{W\mu^\pm}/d\eta_\mu$ as

$$(5) \quad A_\mu = \frac{d\sigma_{W\mu^+}/d\eta_\mu - d\sigma_{W\mu^-}/d\eta_\mu}{d\sigma_{W\mu^+}/d\eta_\mu + d\sigma_{W\mu^-}/d\eta_\mu},$$

where the cross sections include the event kinematical cuts used to select $W \rightarrow \mu\nu$

events. Systematic effects on the W -production cross section measurements are typically the same for positive and negative muons, mostly canceling in the asymmetry. The results presented are based on data collected in 2010 with an integrated luminosity of 31 pb^{-1} . The W candidate events were selected with the same kinematical cuts as in the $W \rightarrow l\nu$ analysis described above.

The W yield is corrected for reconstruction inefficiencies by correction factors corresponding to the ratio of reconstructed over generated events in the simulated W sample, satisfying all kinematic requirements of the event selection. No extrapolation to the full phase space is attempted in order to reduce the dependence on theoretical predictions.

The main backgrounds to $W \rightarrow \mu\nu$ arise from heavy flavour decays in multijet events and from the electro-weak background from $W \rightarrow \tau\nu$ with a semi-muonic tau decay, $Z \rightarrow \mu\mu$ where one muon is not reconstructed and produces fake $E_{\text{T}}^{\text{miss}}$, and $Z \rightarrow \tau\tau$ with a semi-muonic tau decay, as well as semileptonic $t\bar{t}$ decays in the muon channel. The $W \rightarrow \tau\nu$ contribution is treated as a background.

The dominant sources of systematic uncertainty on the asymmetry come from the trigger and reconstruction efficiencies. There is a loss of trigger efficiency in the low pseudorapidity region due to reduced geometric acceptance, resulting in a larger statistical error. As a result, the trigger systematic uncertainty on the asymmetry is largest in the low pseudorapidity bins (6–7% for central $|\eta_{\mu}|$ and 2–3% for forward $|\eta_{\mu}|$). Similarly, the uncertainty associated with the reconstruction efficiency is in average 1–2% but can be up to 7% in certain detector regions. The systematic uncertainties due to the QCD background is 1–2% and arise primarily from the uncertainty on the isolation efficiency for muons in QCD events. The combination of the other backgrounds results in an uncertainty on the asymmetry of less than 1%. The impact of using an NLO MC using the CTEQ 6.6 [8] PDF rather than PYTHIA with MRST LO PDF [5] in the correction factor calculation has been evaluated and an additional systematic uncertainty of about 3% is included to account for the theoretical modelling.

The measured differential muon charge asymmetry in eleven bins of muon absolute pseudorapidity is shown in fig. 3. The statistical and systematic uncertainties per $|\eta_{\mu}|$ bin are included and contribute comparably to the total uncertainty. Figure 3 also show expectations for the muon asymmetry from W predictions at NLO with different PDF sets: CTEQ 6.6, HERA 1.0 [6] and MSTW 2008 [9]; all predictions are presented with 90% confidence level error bands. While the predictions with different PDF sets differ within their respective uncertainty bands, they follow the same global trend. The measured asymmetry agrees with this expectation. As demonstrated graphically in fig. 3, all PDF sets are compatible with the data.

3. – Top cross section

In the Standard Model (SM) the $t\bar{t}$ production cross section in pp collisions is calculated to be $164.6^{+11.4}_{-15.7} \text{ pb}$ [10] at a centre of mass energy $\sqrt{s} = 7 \text{ TeV}$ assuming a top mass of 172.5 GeV , and top quarks are predicted to decay to a W boson and a b -quark ($t \rightarrow Wb$) nearly 100% of the time. Events with a $t\bar{t}$ pair can be classified as “single-lepton”, “dilepton”, or “all hadronic” by the decays of the two W bosons: a pair of quarks ($W \rightarrow q\bar{q}$) or a lepton-neutrino pair ($W \rightarrow \ell\nu$), where ℓ refers to a lepton. The production of $t\bar{t}$ at the LHC is dominated by gg fusion.

The results described in this note are based on reconstructed electrons and muons and include small contributions from leptonically decaying tau leptons. The single-lepton

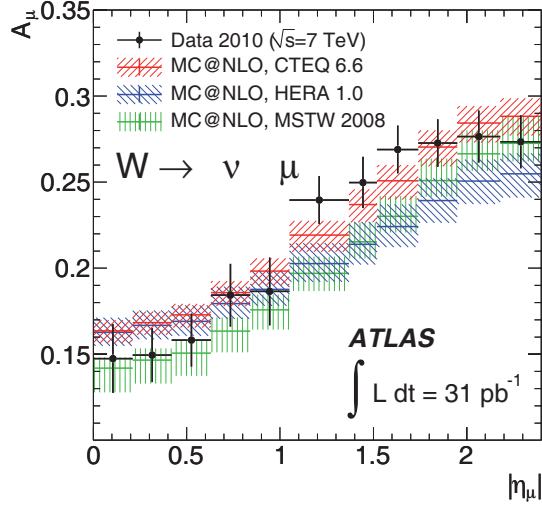


Fig. 3. – The muon charge asymmetry from W -boson decays in bins of absolute pseudorapidity. The kinematic requirements applied are muon $p_T > 20$ GeV, neutrino $p_T > 25$ GeV and $m_T > 40$ GeV. The data points (shown with error bars including the statistical and systematic uncertainties) are compared to MC@NLO predictions with different PDF sets. The PDF uncertainty bands are described in the text and include experimental uncertainties as well as model and parametrization uncertainties [7].

mode, with a branching ratio⁽¹⁾ of 37.9% (combining e and μ channels), and the dilepton mode, with a branching ratio of 6.5% (combining ee , $\mu\mu$ and $e\mu$ channels), both give rise to final states with at least one lepton, missing transverse energy and jets, some with b flavour. The cross section measurements in both modes are based on a straightforward counting method using 2.9 pb^{-1} of integrated luminosity. The number of signal events is obtained in a signal enriched sample after background subtraction. The main background contributions are determined using data-driven methods, since the theoretical uncertainties on the normalisation of these backgrounds are relatively large.

3.1. Single-lepton channel. – The single lepton $t\bar{t}$ final state is characterized by an isolated lepton with relatively high p_T and missing transverse energy corresponding to the neutrino from the W leptonic decay, two b quark jets and two light jets from the hadronic W decay. Events with at least four jets with $p_T > 25$ GeV, where at least one of the jets with is tagged as a b -jet, and exactly one reconstructed lepton (electron or muon) with $p_T > 20$ GeV and $E_T^{\text{miss}} > 20$ GeV and $E_T^{\text{miss}} + m_T(W) > 60$ GeV where considered as $t\bar{t}$ signal candidates. Muon tracks and jets are reconstructed within the geometrical acceptance of the inner detector, $|\eta| < 2.5$. Electrons are selected using the same pseudorapidity regions as used in the W/Z cross section measurements.

For the QCD multi-jet and W + jets backgrounds, data-driven estimates are used, while for the expected background from Z +jets and single-top production, simulation

⁽¹⁾ The quoted branching ratios also include small contributions from leptonically decaying tau leptons.

estimates are used. The $W + \text{jet}$ background is estimated from the measurement of fraction the of $W + 2$ jets that are b -tagged. The fraction of the $W + 4$ jets events that are b -tagged is obtained by a theoretical correction factor for differences in the event flavour composition for the different jet multiplicities. This fraction together with the fact that the ratio of $W + n + 1$ jets to $W + n$ jets is approximately constant as a function of n [11] is used to estimate the background passing the b -tagged $W + 4$ jets requirement.

The QCD multi-jet background in the muon channel was estimated by using non-isolated muons. $Z \rightarrow \mu\mu$ events were used to estimate the fraction of muons from W decays that pass into the signal region from this control region. The fraction of muons from QCD multi-jet events that pass into the signal region was estimated using two regions which are enriched with muons from QCD processes. In the electron channel the QCD multi-jet background was estimated by template fitting E_T^{miss} where the template for the background was extracted from two QCD-dominated control regions.

The electron channel yields 17 events passing all cuts, while for muons 20 events are observed. Of these 37 events 12.2 ± 3.9 are estimated to be background, thereby yielding an estimated $24.8 \pm 6.1(\text{stat}) \pm 3.9(\text{syst})$ single lepton $t\bar{t}$ events.

3.2. Dilepton channel. – The dilepton $t\bar{t}$ final state is characterized by two isolated leptons with relatively high p_T , missing transverse energy corresponding to the neutrinos from the W leptonic decays, and two b quark jets. Events with at least two jets with $p_T > 20$ GeV, and exactly two oppositely charged leptons (electron or muon) with $p_T > 20$ GeV were considered as $t\bar{t}$ signal candidates. The pseudorapidity regions where leptons and jets are considered are the same as in the single lepton analysis described above. In addition, to suppress background from $Z + \text{jets}$ and QCD multi-jet events in the ee channel, the missing transverse energy must satisfy $E_T^{\text{miss}} > 40$ GeV, and the invariant mass of the two leptons must differ by at least 5 GeV from the Z boson mass, *i.e.* $|m_{ee} - m_Z| > 5$ GeV. For the muon channel, the corresponding requirements are $E_T^{\text{miss}} > 30$ GeV and $|m_{\mu\mu} - m_Z| > 10$ GeV. Events in the $e\mu$ -channel are required to have a the scalar sum of the transverse energies of the two leptons and all selected jets larger than 150 GeV.

A total of 9 events (2 ee , 3 $\mu\mu$ and 4 $e\mu$) passed the selection. For the ee and $\mu\mu$ channels the $Z + \text{jets}$ is the largest background. It was estimated by a Z enriched control region scaled by the fraction of simulation events in the control region that passes into the signal region.

3.3. Combination of subchannels. – The combined measurement of the $t\bar{t}$ production cross-section is based on a likelihood fit in which the number of expected events is modeled as

$$(6) \quad N^{\text{exp}}(\sigma_{t\bar{t}}, \alpha_j) = L \cdot \epsilon_{t\bar{t}}(\alpha_j) \cdot \sigma_{t\bar{t}} + \sum_{bkg} L \cdot \epsilon_{bkg}(\alpha_j) \cdot \sigma_{bkg}(\alpha_j) + N_{DD}(\alpha_j),$$

where L is the integrated luminosity, $\epsilon_{t\bar{t}}$ is the signal acceptance, ϵ_{bkg} , σ_{bkg} are the efficiency and cross section for backgrounds as obtained from MC simulation respectively, and N_{DD} is the number of expected events from data-driven estimates. The acceptance and background estimates depend on sources of systematic uncertainty labelled as α_j .

Table I lists the cross sections and signal significance for the single-lepton, dilepton and the combined channels with the corresponding statistical and systematic uncertainties extracted from the likelihood fit. By combining all five channels, the background-only hypothesis is excluded at a significance of 4.8σ obtained with the approximate method

TABLE I. – Summary of $t\bar{t}$ cross-section and signal significance calculated by combining the single-lepton and dilepton channels individually and for all channels combined.

	Cross section [pb]	Signal significance [σ]
Single-lepton channels	$142 \pm 34^{+50}_{-31}$	4.0
Dilepton channels	$151^{+78}_{-62} \text{ }^{+37}_{-24}$	2.8
All channels	$145 \pm 31^{+42}_{-27}$	4.8

of [12]. These results have been cross checked with two independent fit based methods, and the results are consistent.

Figure 4 shows the ATLAS and CMS measurements together with previous Tevatron measurements. The measured $t\bar{t}$ cross-section is in good agreement with the measurement in the dilepton channel by CMS [15], as well as with approximate NNLO top quark cross section calculation [13].

4. – Summary and conclusion

The ATLAS Collaboration presents first measurements of the $W \rightarrow l\nu$ and $Z \rightarrow l\nu$ production cross sections in proton-proton collisions at $\sqrt{s} = 7$ TeV with an integrated luminosity of approximately 320 nb^{-1} . Theoretical predictions, based on NNLO QCD calculations, are in good agreement with all measurements.

The measurement of the W charge asymmetry in pp collisions at $\sqrt{s} = 7$ TeV performed in the $W \rightarrow \mu\nu$ decay mode using 31 pb^{-1} of data is expected to contribute to

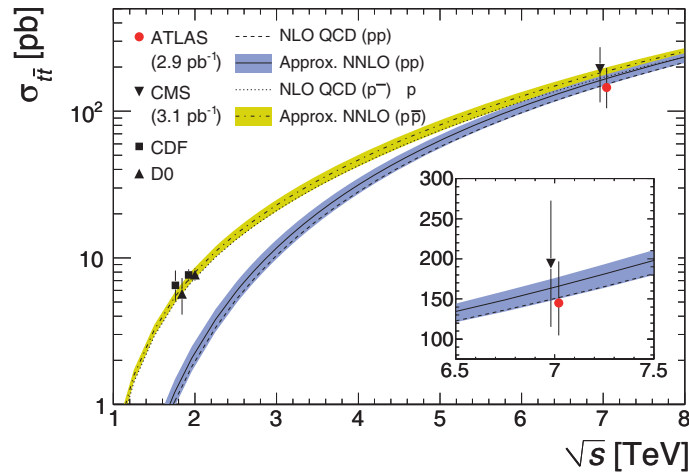


Fig. 4. – Top quark pair-production cross section at hadron colliders as measured by CDF and D0 at Tevatron, CMS and ATLAS (this measurement). The theoretical predictions for proton-proton and proton-antiproton collisions include the scale and PDF uncertainties, obtained using the HATHOR tool [13] with the CTEQ6.6 PDFs and assume a top-quark mass of 172.5 GeV [14].

the determination of the next generation of PDF sets, helping reduce PDF uncertainties, particularly the shapes of the valence quark distributions in the low- x region.

The ATLAS Collaboration measured the $t\bar{t}$ production cross section to be

$$(7) \quad 145 \pm 31_{-27}^{+42} \text{ pb}$$

with 2.9 pb^{-1} of proton-proton data at $\sqrt{s} = 7 \text{ TeV}$ using both single lepton and dilepton decay channels. This result is in good agreement with expectations and the CMS result.

REFERENCES

- [1] ATLAS COLLABORATION, *JINST*, **3** (2008) S08003.
- [2] ATLAS COLLABORATION, *JHEP*, **12** (2010) 060, arXiv:1010.2130.
- [3] ATLAS COLLABORATION, “Luminosity determination using the atlas detector,” Technical Report ATLAS-CONF-2010-060, CERN, Geneva, July 2010.
- [4] ANASTASIOU C., DIXON L., MELNIKOV K. and PETRIELLO F., *Phys. Rev. D*, **69** (2004) 094008.
- [5] SHERSTNEV A. and THORNE R. S., *Eur. Phys. J. C*, **55** (2008) 553.
- [6] H1 and ZEUS COLLABORATIONS, *JHEP*, **01** (2010) 109, arXiv:0911.0884.
- [7] ATLAS COLLABORATION (AAD *et al.*), *Phys. Lett. B*, **701** (2011) 31, arXiv:1103.2929.
- [8] PUMPLIN J. *et al.*, *JHEP*, **07** (2002) 012, arXiv:hep-ph/0201195.
- [9] MARTIN A. D., STIRLING W. J., THORNE R. S. and WATT G., *Eur. Phys. J. C*, **63** (2009) 189.
- [10] MOCH S. and UWER P., *Phys. Rev. D*, **78** (2008) 034003.
- [11] BERGER C., BERN Z., DIXON L. J., CORDERO F., FORDE D. *et al.*, *Phys. Rev. Lett.*, **106** (2011) 092001, arXiv:1009.2338.
- [12] COWAN G., CRANMER K., GROSS E. and VITELLS O., *Eur. Phys. J. C*, **71** (2011) 1554, arXiv:1007.1727.
- [13] ALIEV M., LACKER H., LANGENFELD U., MOCH S., UWER P. *et al.*, *Comput. Phys. Commun.*, **182** (2011) 1034, arXiv:1007.1327.
- [14] ATLAS COLLABORATION, *Eur. Phys. J. C*, **71** (2011) 1577, arXiv:1012.1792.
- [15] KHACHATRYAN V. *et al.*, *Phys. Lett. B*, **695** (2011) 424, arXiv:1010.5994.

Measurement of W , Z and Top properties with CMS

M. DE GRUTTOLA on behalf of the CMS COLLABORATION

*University of Florida, Institute for High Energy Physics and Astrophysics
Department of Physics - Gainesville, FL, USA and
Fermi National Accelerator Laboratory - Batavia IL, USA*

(ricevuto il 29 Settembre 2011; pubblicato online il 19 Gennaio 2012)

Summary. — We present several measurements in the domain of electroweak and top physics in proton-proton collisions at the LHC at a centre-of-mass energy of 7 TeV. We use data collected with the CMS experiment during the year 2010, and amounting up to a total integrated luminosity of 36 pb^{-1} . Measurements include total cross section productions, asymmetries, top mass measurements and focus on final states with the presence of charged leptons. The results are compared with theory predictions.

PACS 14.70.Fm – W bosons.
PACS 14.70.Hp – Z bosons.
PACS 14.65.Ha – Top quarks.

1. – Introduction

Electroweak (EWK) and top quark measurements are important benchmark process at hadron colliders: the inclusive Z and W cross section are among the first measurement to be performed at LHC, top-quark processes can now be studied extensively in multi-TeV proton-proton collisions, and we can already provide new insights into parton distribution functions with precision measurement of the lepton charge asymmetry.

CMS can extend these measurements to significantly higher energies than the past measurements with LEP and Tevatron, namely, with pp collisions at a center-of-mass energy of 7 TeV provided by the Large Hadron Collider (LHC). The data were collected in 2010, by the Compact Muon Solenoid (CMS) experiment, and correspond to an integrated luminosity of about 36 pb^{-1} . The skeleton of this article is the following: after a first introduction of the CMS detector, we first present the inclusive Z and W cross section measurement, describing also in detail the lepton and missing energy identification and reconstruction in CMS. We then describe the lepton charge asymmetry using W decay identified events, which is among the most outstanding precision EWK measurement performed with CMS data in 2010. Finally we enter in the great domain of top physics study: we describe the top cross section measurement and properties with

leptons in the final state and the first result obtained by the CMS Collaboration for the measurement of the top quark mass.

2. – The CMS detector

A detailed description of the CMS experiment can be found elsewhere [1]. The central feature of the CMS apparatus is a superconducting solenoid, of 6 m internal diameter, 13 m in length, providing an axial field of 3.8 T. Within the field volume are the silicon pixel and strip tracker, the crystal electromagnetic calorimeter (ECAL) and the brass/scintillator hadron calorimeter (HCAL). Muons are measured in gas-ionization detectors embedded in the steel return yoke of the solenoid. The most relevant sub-detectors for this measurement are the ECAL, the muon system, and the tracking system. The electromagnetic calorimeter consists of nearly 76000 lead tungstate crystals which provide coverage in pseudorapidity $|\eta| < 1.479$ in the barrel region and $1.479 < |\eta| < 3.0$ in two endcap regions. A preshower detector consisting of two planes of silicon sensors interleaved with a total of $3X_0$ of lead is located in front of the ECAL endcaps. The ECAL has an ultimate energy resolution of better than 0.5% for unconverted photons with transverse energies above 100 GeV. The electron energy resolution is 3% or better for the range of electron energies relevant for this analysis. Muons are measured in the pseudorapidity range $|\eta| < 2.4$, with detection planes made of three technologies: drift tubes, cathode strip chambers, and resistive plate chambers. Matching the muons to the tracks measured in the silicon tracker results in a transverse momentum resolution of about 2% in the relevant muon p_T range.

CMS uses a right-handed coordinate system, with the origin at the nominal interaction point, the x -axis pointing to the center of the LHC, the y -axis pointing up (perpendicular to the LHC plane), and the z -axis along the anticlockwise-beam direction. The polar angle, θ , is measured from the positive z -axis and the azimuthal angle, ϕ , is measured in the x - y plane. The pseudorapidity is given by $\eta = -\ln(\tan(\theta/2))$.

3. – Electroweak measurement

3.1. W and Z production cross section. – The dominant production mechanism for electroweak gauge bosons W and Z in pp collisions is the weak Drell-Yan production process [2], where a quark and an antiquark annihilate to form a vector boson: the reaction $pp \rightarrow W + X$ is dominated by $\bar{u}d \rightarrow W^+$ and $\bar{d}u \rightarrow W^-$ while the $pp \rightarrow Z + X$ is dominated by $\bar{u}u, \bar{d}d \rightarrow Z$. We present here a measurement of W and the Z production cross sections and their ratios with the full luminosity recorded by CMS at LHC in 2010 corresponding to 36 pb^{-1} .

3.1.1. Selection. Events with high- E_T electrons are selected online when they pass an unrescaled L1 trigger filter that requires a coarse-granularity region of the ECAL to have $E_T > 5$ or 8 GeV depending on the run period. They subsequently must pass an unrescaled HLT filter that requires an ECAL cluster with E_T well below the offline E_T threshold of 25 GeV, using the full granularity of the ECAL and E_T measurements corrected using offline calibration [3]. Events with high- p_T muon are selected online by the unrescaled single-muon trigger. The energy threshold at the L1 is 7 GeV. The p_T threshold at the HLT level depends on the run period and has been 9 GeV for the first 7.5 pb^{-1} of collected data and 15 GeV for the remaining 28.4 pb^{-1} .

$W \rightarrow ln$ events are characterized by a prompt, energetic and isolated lepton, and significant missing energy (\cancel{E}_T). No cut on \cancel{E}_T is applied. Rather, the \cancel{E}_T is used as the main discriminant variable against backgrounds from QCD events.

The Z boson decays to leptons (electrons or muons) are selected based on two energetic and isolated leptons. The reconstructed di-lepton invariant mass is required to lie within a mass window consistent with the known Z boson mass.

Electrons are identified offline as clusters of ECAL energy deposits matched to tracks from the silicon tracker. The ECAL clusters must fall in the ECAL fiducial volume of $|\eta| < 1.44$ for EB clusters or $1.57 < |\eta| < 2.5$ for EE clusters. We select events with one or two electrons having $E_T > 25$ GeV for the $W \rightarrow e\nu$ or the $Z \rightarrow ee$ analysis respectively. The electron selection criteria were obtained by optimizing signal and background levels according to simulation-based studies, for more details see [4].

Muons candidates are first reconstructed separately in the central tracker (referred to simply as “tracks”) and in the muon detector (“stand-alone muons”). Stand-alone muons are then matched and combined with tracker tracks to form “global muons”. Another independent algorithm proceeds from the inner tracker outwards matching muon chambers hits, and produce “tracker muons”. We require that global and stand-alone muon candidates must have at least one good muon chamber hit. Tracker muons must match to at least two muon stations. Tracks, global and tracker muons must have more than 10 hits in the inner tracker, of which at least one in the pixel detector, and the impact parameter in the transverse plane, d_{xy} , calculated with respect to the beam spot, must be smaller than 2 mm. More details and studies on muon identification can be found in ref. [5].

$W \rightarrow \mu\nu$ candidate events must have a muon candidate in the fiducial volume $|\eta| < 2.1$ with $p_T > 25$ GeV. We require the muon to be isolated. For $Z \rightarrow \mu\mu$ we require two opposite charge muons with the same identification cuts but with $p_T > 20$ GeV. The efficiencies for the isolation and identification cuts are obtained with the “Tag and Probe” [4] technique applied on both data and simulation, and correcting the simulation for the residual efficiency ratio.

3.1.2. Results. The signal and background yields are obtained by fitting the \cancel{E}_T distribution for $W \rightarrow e\nu$ and $W \rightarrow \mu\nu$. An accurate \cancel{E}_T measurement is essential for distinguishing a signal from QCD multi-jet production backgrounds. We profit from the application of the particle flow (PF) algorithm [6], which provides superior \cancel{E}_T reconstruction performance. The final plots for the W candidate selection and signal fit are reported in fig. 1. The inclusive $Z \rightarrow ll$ yield can be obtained counting the number of selected candidates after subtracting the residual background, correcting for the estimated lepton selection efficiencies. The final plots are reported below in fig. 2. Note that the background is so tiny with the given selection cuts that it is not visible in linear scale.

The largest uncertainty for the cross section measurement comes from the knowledge of the integrated luminosity [7, 8] which amounts to 4%. Besides luminosity, the main source of systematic uncertainty comes from lepton efficiency correction factors obtained from the tag-and-probe method. Table I shows a summary of the systematic uncertainties for the W and Z cross section measurements. For all measurements we present results for electrons and muons combined, assuming lepton universality in W and Z decays.

We measure the following cross sections for inclusive W production:

$$(1) \quad \sigma(pp \rightarrow WX) \times \text{BF}(W \rightarrow \ell\nu) = 10.31 \pm 0.02(\text{stat.}) \pm 0.09(\text{syst.}) \pm 0.10(\text{th.}) \pm 0.41(\text{lumi.}) \text{ nb.}$$

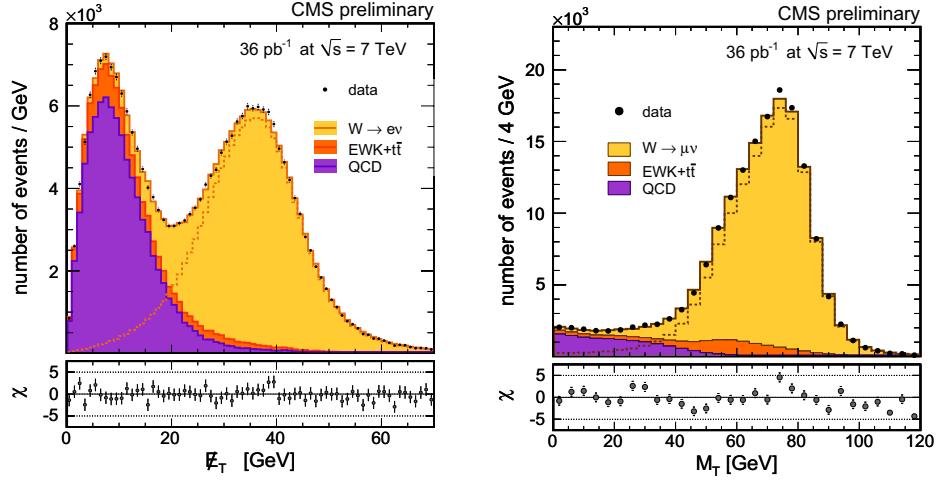


Fig. 1. – (Colour on-line) Left: result of fixed shape template fit on \cancel{E}_T for all $W \rightarrow e\nu$ candidates. Right: Total M_T spectrum and fitted contributions for $W \rightarrow \mu\nu$ candidate events. Signal from the different processes are shown stacked, W signal (light yellow histogram), other EWK processes (medium orange histogram), and QCD background (dark purple histogram).

The NNLO prediction is 10.44 ± 0.52 nb. The results for charge-specific W production are

$$(2) \quad \sigma(pp \rightarrow W^+ X) \times \text{BF}(W^+ \rightarrow \ell^+ \nu) = 6.04 \pm 0.02(\text{stat.}) \pm 0.06(\text{syst.}) \pm 0.08(\text{th.}) \pm 0.24(\text{lumi.}) \text{ nb};$$

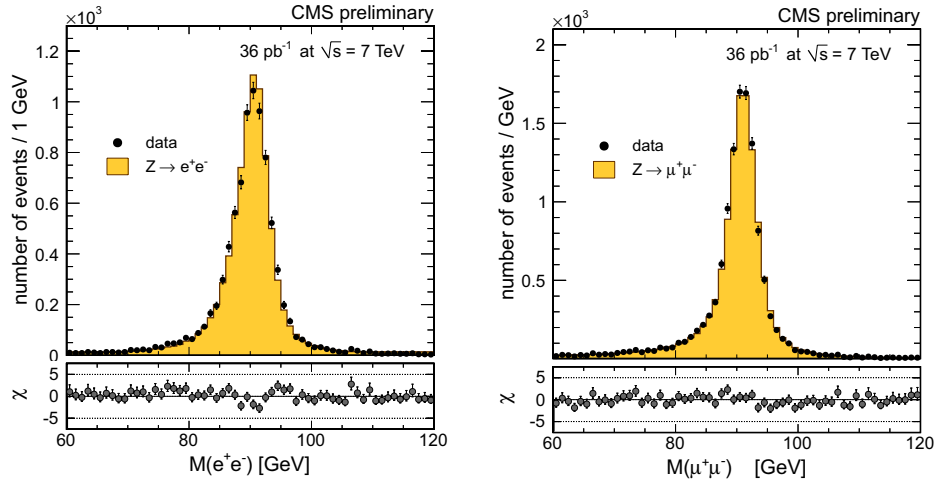


Fig. 2. – Left: $Z \rightarrow ee$ signal in linear after applying energy scale correction factors. Right: Distribution of the di-muon invariant mass of $Z \rightarrow \mu\mu$ “golden” candidates for data (dots) and for Monte Carlo (histogram) signal and background events.

TABLE I. – *Systematic uncertainties in percent for all inclusive W and Z cross sections. “n/a” means the source does not apply. A common luminosity uncertainty of 4% applies to all channels.*

Source	$W \rightarrow e\nu$	$W \rightarrow \mu\nu$	$Z \rightarrow ee$	$Z \rightarrow \mu\mu$
Lepton reconstruction & identification	1.3	0.9	1.8	n/a
Trigger pre-firing	n/a	0.5	n/a	0.5
Momentum scale & resolution	0.5 xspace	0.22	0.12	0.35
\cancel{E}_T scale & resolution	0.3	0.2	n/a	n/a
Background subtraction/modeling	0.35	0.4	0.14	0.28
Trigger changes throughout 2010	n/a	n/a	n/a	0.1
Total experimental	1.5	1.1	1.8	0.7
PDF uncertainty for acceptance	0.6	0.8	0.9	1.1
Other theoretical uncertainties	0.7	0.8	1.4	1.6
Total theoretical	0.9	1.1	1.6	1.9
Total	1.7	1.6	2.4	2.0

and

$$(3) \quad \sigma(pp \rightarrow W^- X) \times \text{BF}(W^- \rightarrow \ell^- \bar{\nu}) = 4.26 \pm 0.01(\text{stat.}) \pm 0.04(\text{syst.}) \pm 0.07(\text{th.}) \pm 0.17(\text{lumi.}) \text{ nb.}$$

The NNLO predictions for these cross sections are 6.15 ± 0.29 nb for W^+ and 4.29 ± 0.23 nb for W^- . We also measure the following cross sections for Z production:

$$(4) \quad \sigma(pp \rightarrow ZX) \times \text{BF}(Z \rightarrow \ell^+ \ell^-) = 0.975 \pm 0.007(\text{stat.}) \pm 0.007(\text{syst.}) \pm 0.018(\text{th.}) \pm 0.039(\text{lumi.}) \text{ nb.}$$

The reported Z cross sections pertain to the invariant mass range $60 < m_{\ell^+ \ell^-} < 120$ GeV, and are corrected for the kinematic acceptance but not for γ^* exchange. The NNLO prediction for Z production is 0.97 ± 0.04 nb.

The ratio of cross sections for W and Z production is

$$\frac{\sigma_W}{\sigma_Z} = \frac{N_W}{N_Z} \frac{\epsilon_Z}{\epsilon_W} \frac{A_Z}{A_W},$$

where A_Z and A_W are the acceptances for Z and W selections, respectively. The uncertainty from A_Z/A_W is determined from Monte Carlo generator studies to be 1.5%. The two different decay channels are combined by assuming fully correlated uncertainty for the acceptance factor, with other uncertainties assumed uncorrelated. This results in the measurements

$$(5) \quad \frac{\sigma(pp \rightarrow WX) \times \text{BF}(W \rightarrow \ell\nu)}{\sigma(pp \rightarrow ZX) \times \text{BF}(Z \rightarrow \ell^+ \ell^-)} = 10.54 \pm 0.07(\text{stat.}) \pm 0.08(\text{syst.}) \pm 0.16(\text{th.}).$$

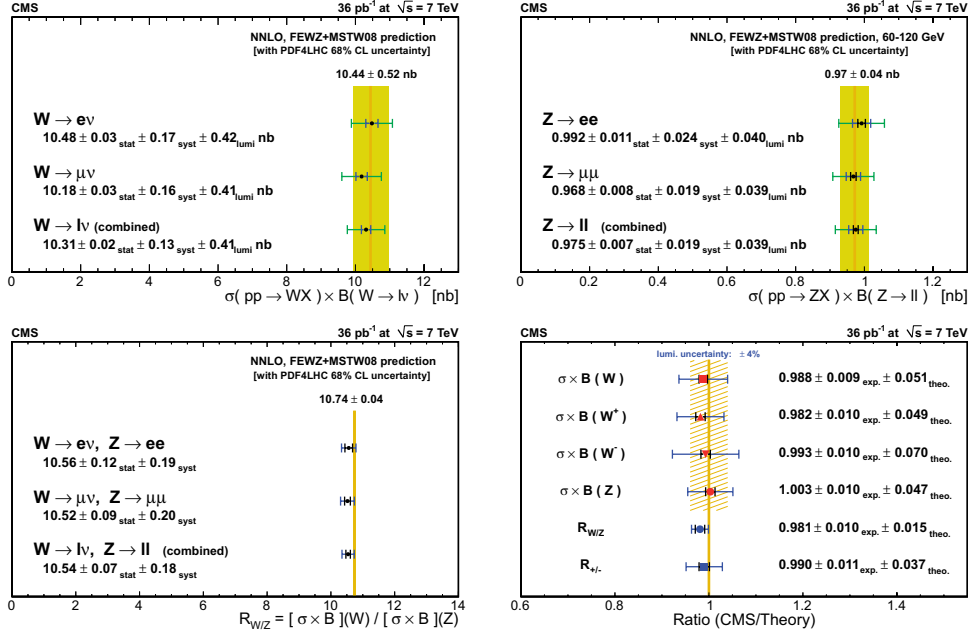


Fig. 3. – Summary of results for W and Z production, W/Z ratio and ratios of CMS measurements to the theoretical values.

The NNLO prediction for this ratio is 10.74 ± 0.04 , in good agreement with our measurement. The cross section ratios of W^+ and W^- are given by

$$\frac{\sigma_{W^+}}{\sigma_{W^-}} = \frac{N_{W^+}}{N_{W^-}} \frac{\epsilon_{W^-}}{\epsilon_{W^+}} \frac{A_{W^-}}{A_{W^+}},$$

where A_{W^+} and A_{W^-} are the acceptances for W^+ and W^- , respectively. The uncertainty from A_{W^-}/A_{W^+} is determined from Monte Carlo generator studies to be 2%. The two different decay channels are combined by assuming fully correlated uncertainty for the acceptance factor, with other uncertainties assumed uncorrelated. This results in the measurements

$$(6) \quad \frac{\sigma(pp \rightarrow W^+ X) \times \text{BF}(W^+ \rightarrow \ell^+ \nu)}{\sigma(pp \rightarrow W^- X) \times \text{BF}(W^- \rightarrow \ell^- \bar{\nu})} = 1.421 \pm 0.006(\text{stat.}) \pm 0.014(\text{syst.}) \pm 0.029(\text{th.}).$$

The NNLO prediction is 1.43 ± 0.04 , which agrees with the measured values. Summaries of the measurements are given in figs. 3, illustrating the good agreement of our measurements with theoretical predictions computed at the NNLO QCD level with modern NLO PDF sets, as well as the consistency in the measurements in the electron and muon channels. The ratios of our measurements to the theoretical predictions are also reported on the figure.

3.2. W asymmetries. – For lack of space we cannot show all the measurements performed by CMS in 2010 involving W and Z bosons properties. Among all we chose to show a measurement of the lepton charge asymmetry in inclusive $pp \rightarrow WX$ production [9]. This high precision measurement of the lepton charge asymmetry, performed in both the $W \rightarrow e\nu$ and $W \rightarrow \mu\nu$ channels, provides new insights into parton distribution functions. In pp collisions, W bosons are produced primarily via the processes $u\bar{d} \rightarrow W^+$ and $d\bar{u} \rightarrow W^-$. The first quark is a valence quark from one of the protons, and the second one is a sea antiquark from the other proton. Due to the presence of two valence u quarks in the proton, there is an overall excess of W^+ over W^- bosons. Measurement of this production asymmetry between W^+ and W^- bosons as a function of boson rapidity can provide new insights on the u/d ratio and the sea antiquark densities in the ranges of the Björken parameter x [10] probed in pp collisions at $\sqrt{s} = 7$ TeV. However, due to the presence of neutrinos in leptonic W decays the boson rapidity is not directly accessible. The experimentally accessible quantity is the lepton charge asymmetry, defined to be

$$\mathcal{A}(\eta) = \frac{d\sigma/d\eta(W^+ \rightarrow \ell^+\nu) - d\sigma/d\eta(W^- \rightarrow \ell^-\bar{\nu})}{d\sigma/d\eta(W^+ \rightarrow \ell^+\nu) + d\sigma/d\eta(W^- \rightarrow \ell^-\bar{\nu})},$$

where ℓ is the daughter charged lepton, η is the charged lepton pseudorapidity, and $d\sigma/d\eta$ is the differential cross section for charged leptons from W boson decays. The lepton charge asymmetry can be used to test SM predictions with high precision. Due to the $V-A$ structure of the W boson couplings to fermions, theoretical predictions of the charge asymmetry depend on the transverse momentum (p_T) threshold applied on the daughter leptons. For this reason, we measure $\mathcal{A}(\eta)$ for two different charged lepton p_T (p_T^ℓ) thresholds, 25 GeV and 30 GeV. For this measurement the same lepton identification cuts and trigger described in the previous section has been used, and the same strategy to select W candidates in the inclusive cross section analysis. QCD background is obtained from data using a binned extended maximum likelihood fits performed over the \cancel{E}_T distribution, while the shape for Drell-Yan and other electroweak background are obtained from simulation. Figure 4 shows a comparison of these asymmetries to predictions from the MSTW2008NLO PDF model [11] and the CT10W PDF model [12]. CMS data suggest a flatter pseudorapidity dependence of the asymmetry than the PDF models studied.

4. – The top physics

At the LHC, the $t\bar{t}$ production mechanism is expected to be dominated by a gluon fusion process, whereas at the Tevatron, top-quark pairs are predominantly produced through quark-antiquark annihilation. Measurements of top quark production at the LHC are therefore important new tests of our understanding of the $t\bar{t}$ production mechanism. These measurements are also crucial components in the LHC physics program, since many signatures of new physics models accessible at the LHC either suffer from top-quark production as a significant background or contain top quarks themselves.

4.1. Top cross section measurement. – The cross section for top quark-antiquark pair production has been measured in proton-proton collisions at $\sqrt{s} = 7$ TeV in the data sample corresponding to 36 pb^{-1} of integrated luminosity collected by the CMS experiment. In the standard model, a top quark decays nearly 100% of the time to a W boson and a b quark. The decay of a $t\bar{t}$ pair is categorized by the decay of the

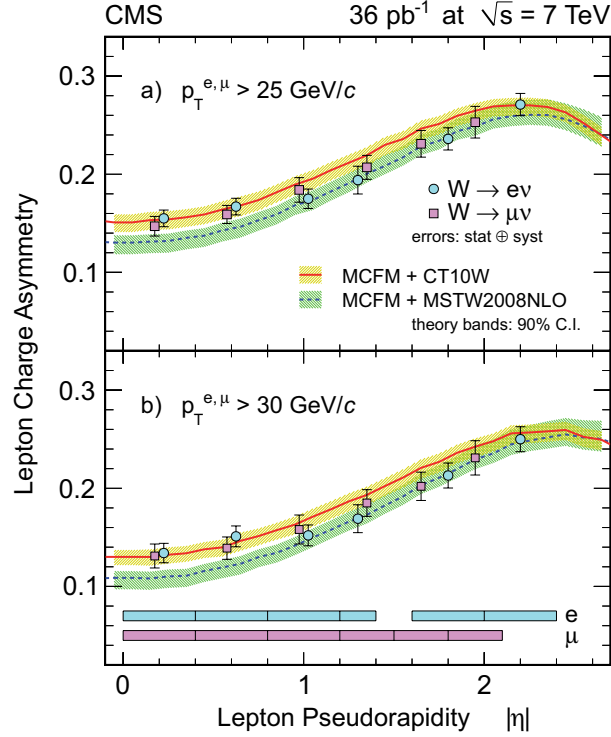


Fig. 4. – Comparison of the measured lepton charge asymmetry to different PDF models for a) lepton $p_T^l > 25 \text{ GeV}/c$ and b) lepton $p_T^l > 30 \text{ GeV}/c$. The error bars include both statistical and systematic uncertainties. The PDF uncertainty band is corresponding to the 90% confidence interval (CI). The bin width for each data point is shown by the filled bars in fig. b). The data points are placed at the centers of pseudorapidity bins, except that for display purposes the first three data points are shifted $+0.025$ (-0.025) for electron (muon).

W bosons produced by the pair. Thus the channel in which both W bosons decay to leptons is referred to as the “dilepton” channel, and the channel in which one W decays to leptons and the other to quark jets is the “lepton+jets” channel. The channel in which both W bosons decay to jets is called the “all hadronic” channel. CMS has performed the measurements on both dileptons [13] and leptons+jets sample [14]. Here we report the search in events with two energetic leptons (electrons or muons) in the final state. Presence of the b quark jets in the top-quark decays is tested with a selection requiring jets identified as coming from the b quarks. Results of the measurement in events with and without b quark identification are compared and combined. For simplicity we will only show plots and yields for events without an explicit b -tag requirement. Lepton reconstruction and identification for this analyses are identical to the one described before. We rely on single muon and electron trigger. In the event selection for the electron+jets channel, at least one electron with transverse energy greater than 30 GeV and $|\eta|$ less than 2.5 is required, while muons in the muons+jets sample must have $p_T > 20 \text{ GeV}$ and $|\eta| < 2.1$. Selected jets are required to have a jet-energy-scale-corrected $p_T > 30 \text{ GeV}$, $|\eta| < 2.4$, and must be separated by $\Delta R > 0.3$ from isolated electrons and $\Delta R > 0.1$

TABLE II. – Expected signal and background contributions compared to the number of events observed in data passing full selection with at least two jets and without a b -tagging requirement. Contributions from Drell-Yan and events with non- W/Z leptons are estimated from data and are quoted with statistical and systematic uncertainties combined. All other contributions are estimated from simulation.

Source	e^+e^-	$\mu^+\mu^-$	$e\mu$
Dilepton $t\bar{t}$	$14.6 \pm 1.2 \pm 2.3$	$18.3 \pm 1.4 \pm 2.8$	$52.5 \pm 3.3 \pm 8.1$
VV	0.3 ± 0.1	0.3 ± 0.1	0.9 ± 0.3
Single top - tW	0.6 ± 0.2	0.7 ± 0.2	1.9 ± 0.6
Drell-Yan $\tau\tau$	0.6 ± 0.2	0.5 ± 0.2	2.5 ± 0.9
Drell-Yan $e^-e^-, \mu^+\mu^-$	3.0 ± 1.8	7.4 ± 4.1	N/A
Non- W/Z leptons	1.1 ± 1.4	0.6 ± 1.1	1.4 ± 1.6
Total backgrounds	5.5 ± 2.3	9.5 ± 4.3	6.7 ± 2.0
Data	23	28	60

from isolated muons. There is a requirement of $\cancel{E}_T > 30$ GeV for the e^+e^- and $\mu^+\mu^-$ channels, while no \cancel{E}_T requirement for the $e\mu$ sample.

A summary of the expected number of signal and background events is compared with the number of events observed in data in table II for events selected with at least two jets. Good agreement is observed between the expectations and the number of events in data in all channels. The background and signal expectations compared to the number of events in data separately in events with a different jet multiplicity are shown in fig. 5 for events without a b -tagging requirement. The $t\bar{t}$ production cross section is measured using

$$\sigma(pp \rightarrow t\bar{t}) = \frac{N - B}{AL},$$

where N is the number of observed events; B is the number of estimated background events for data whenever possible; A is the total acceptance relative to all produced $t\bar{t}$ events, including the branching ratio to leptons, the geometric acceptance, and the event selection efficiency already corrected for differences between data and simulation; and L is the integrated luminosity.

The measurements in the three final states (e^+e^- , $\mu^+\mu^-$, $e\mu$) and with and without b -tag requirements can be combined assuming they all correspond to the same physical quantity of the total top-quark pair production cross section. The combination of measurements in all three dilepton final states is found to be

$$(7) \quad 168 \pm 18(\text{stat.}) \pm 14(\text{syst.}) \pm 7(\text{lum.}) \text{ pb.}$$

4.2. *Top mass.* – Many methods have been developed for measuring the top quark mass m_{top} in the dilepton channel. The Matrix Weighting Technique (MWT) [15] has been the first approach, other approaches were also been developed, for example the fully

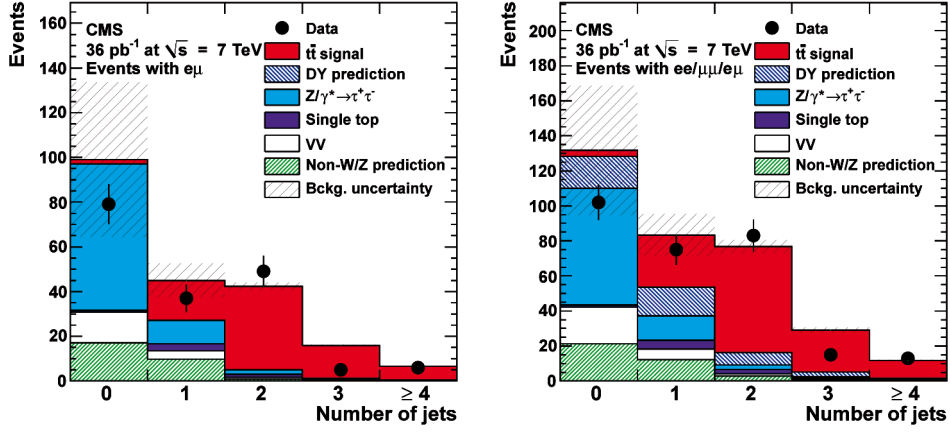


Fig. 5. – Jet multiplicity for events passing full dilepton selection criteria without b -tagging, less the requirement on the number of jets compared to signal expectations from simulation, Drell-Yan and non- W/Z lepton backgrounds estimated in data, and remaining backgrounds estimated from simulation. The total uncertainty on the background contribution is displayed by the shaded area. The distributions are for $e\mu$ and all final-states combined.

kinematic method (KIN) [16]. The average of the measurements in the dilepton channel is $m_{top} = 171.1 \pm 2.5 \text{ GeV}/c$ by Tevatron [17].

The reconstruction of m_{top} from dilepton events leads to an under-constrained system, since the dilepton channel contains at least two neutrinos in the final state. For each $t\bar{t}$ event, the kinematic properties are fully specified by 24 variables, which are the four-

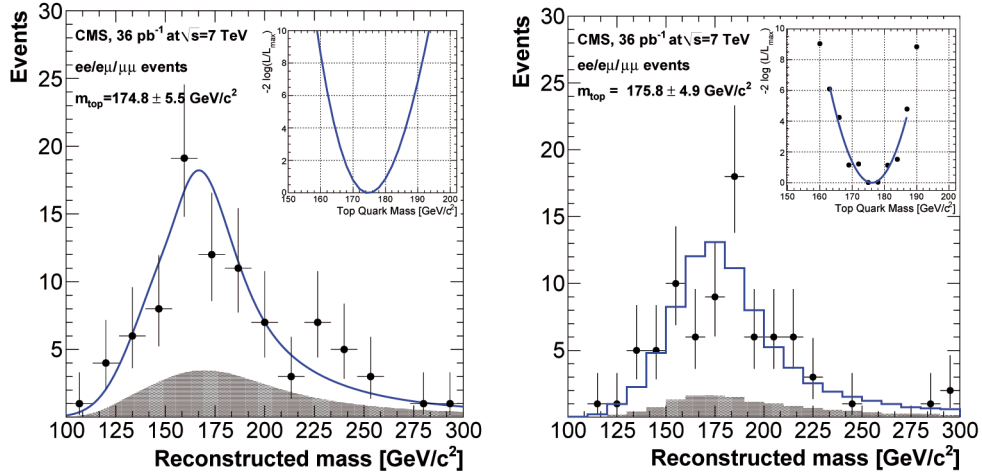


Fig. 6. – Reconstructed mass distribution for the $t\bar{t}$ dilepton events, for the KIN (left) and MWT (right) methods. Also shown is the background shape (shaded) and the sum of background plus MC simulations for $m_{top} = 172.5 \text{ GeV}/c^2$. The inset shows the likelihood fit used to determine the top mass.

momenta of the 6 particles in the final state. Of the 24 free parameters, 23 are known from different sources: 14 are measured (the three-momenta of the jets and leptons, and the two components of the \cancel{E}_T) and 9 are constrained. The system can be constrained by imposing the W boson mass to its measured value (2 constraints), by setting the top and anti-top quark masses to be the same (1), and the masses of the 6 final state particles to the values used in the simulation (6). This still leaves one free parameter that must be constrained by using some hypothesis that depends on the method employed.

A subset of the events selected for measuring the top quark pair production cross section is used to determine m_{top} . In the fully kinematic method KINb, the kinematic equations describing the $t\bar{t}$ system are solved many times per event for each lepton-jet combination. In the analytical matrix weighting technique, the mass of the top quark is used to fully constrain the $t\bar{t}$ system. For a given top quark mass hypothesis, the constraints and the measured observables restrict the transverse momenta of the neutrinos to lie on ellipses in the p_x - p_y plane. If we assume that the measured missing transverse energy is solely due to the neutrinos, the two ellipses constraining the transverse momenta of the neutrinos can be obtained, and the intersections of the ellipses provide the solutions that fulfil the constraints.

The top quark mass is estimated with a likelihood unbinned fit of the experimental mass distribution with the signal and background components, which maximizes the probability that the data are described by a mixture of signal and background events for both the methods. Figure 6 shows the reconstructed top quark mass in the data. The combination of the two measurements yields

$$(8) \quad m_{top} = 175.5 \pm 4.6(\text{stat.}) \pm 4.6(\text{syst.}) \text{ GeV}/c^2.$$

This CMS result is the first measurement of the top quark mass that not performed at the Tevatron.

REFERENCES

- [1] CMS COLLABORATION, *JINST*, **03** (2008) S08004.
- [2] DRELL S. D. and YAN T. M., *Phys. Rev. Lett.*, **25** (1970) 316, doi:10.1103/PhysRevLett.25.316.
- [3] CMS COLLABORATION, *Electromagnetic calorimeter calibration with 7 TeV data*, CMS Physics Analysis Summary CMS-PAS-EGM-10-003 (2010).
- [4] CMS COLLABORATION, *Measurements of Inclusive W and Z Cross Sections in pp Collisions at $\sqrt{s}=7$ TeV*, CMS Physics Analysis Summary CMS-PAS-EWK-10-005 (2010).
- [5] CMS COLLABORATION, *Performance of CMS muon identification in pp collisions at $\sqrt{s}=7$ TeV*, CMS PAS MUO-2010-002 (2010).
- [6] CMS COLLABORATION, *Particle-flow commissioning with muons and electrons from J/Psi and W events at 7 TeV*, CMS PAS PFT-2010-003 (2010).
- [7] CMS COLLABORATION, *Measurement of CMS luminosity*, CMS PAS EWK-2010-004 (2010).
- [8] CMS COLLABORATION, *Absolute luminosity normalization*, CMS DPS 2011-002 (2011).
- [9] CMS COLLABORATION, *Measurement of the Lepton Charge Asymmetry in Inclusive W Production in pp Collisions at $\sqrt{s} = 7$ TeV*, arXiv:1103.3470v1 [hep-ex] 17 Mar 2011, *JHEP*, **04** (2011) 50.
- [10] BJORKEN J. D. and PASCHOS E. A., *Phys. Rev.*, **185** (1969) 1975, doi:10.1103/PhysRev.185.1975.
- [11] MARTIN A. D., STIRLING W. J., THORNE R. S. *et al.*, *Eur. Phys. J. C*, **63** (2009) 189, arXiv:0901.0002, doi:10.1140/epjc/s10052-009-1072-5.

- [12] LAI H.-L. *et al.*, *Phys. Rev. D*, **82** (2010) 074024, arXiv:1007.2241, doi:10.1103/PhysRevD.82.074024.
- [13] CMS COLLABORATION, *Measurement of the $t\bar{t}$ production cross section and the top quark mass in the dilepton channel in pp collisions at $\sqrt{s} = 7$ TeV*, arXiv:1105.5661v1 [hep-ex] 27 May 2011, *JHEP*, **07** (2011) 49.
- [14] CMS COLLABORATION, *Measurement of the $t\bar{t}$ Production Cross Section in pp Collisions at $\sqrt{s} = 7$ TeV using the Kinematic Properties of Events with Leptons and Jets*, arXiv:1106.0902v1 [hep-ex] 5 June 2011, *Eur. Phys. J. C*, **71** (2011) 1721.
- [15] D0 COLLABORATION, *Phys. Rev. Lett.*, **80** (1998) 2063, arXiv:hep-ex/9706014, doi:10.1103/PhysRevLett.80.2063.
- [16] CDF COLLABORATION, *Phys. Rev. D*, **73** (2006) 112006, arXiv:hep-ex/0602008, doi:10.1103/PhysRevD.73.112006.
- [17] CDF and D0 COLLABORATION, *Combination of CDF and D0 results on the mass of the top quark* (2010) arXiv:1007.3178v1 [hep-ex].

Top physics at Tevatron

HYUN SU LEE on behalf of the CDF and D0 COLLABORATIONS

University of Chicago - Chicago, IL, USA

(ricevuto il 29 Settembre 2011; pubblicato online il 25 Gennaio 2012)

Summary. — The top quark, discovered in 1995 at the Fermilab Tevatron collider from CDF and D0 experiments, remains by far the most interesting particle to test standard model. Having data collected more than 7 fb^{-1} of integrated luminosity of $p\bar{p}$ collision, both experiments have been studied the top quark in all the possible directions. In this article, we present the recent measurements of the top quark properties including the mass, width, spin correlation, and W helicity as well as new particle searches using $t\bar{t}$ signature.

PACS 14.65.Ha – Top quarks.

1. – Introduction

The top quark, observed by both the CDF and D0 experiments in 1995 [1], is by far the heaviest known elementary particle and its mass is almost 40 times heavier than its isospin partner, the bottom (b) quark [2]. Due to the heavy mass, the top quark plays an important role in electroweak radiative corrections relating the top quark mass (M_{top}) and the W boson mass to the mass of the predicted Higgs boson [3,4]. The lifetime of top quark is about 20 times shorter than the timescale for strong interactions, and therefore it does not form hadrons, giving us a unique opportunity to study a “bare” quark.

Top quarks at the Tevatron are predominantly produced in pairs, and decay almost always to a W boson and a b quark in the standard model (SM). The topology of $t\bar{t}$ events depends on the different decay of the two W bosons. In the dilepton channel, each W boson decay to charged lepton (electron and muon) and neutrino. Events in this channel thus contain two leptons, two b -quark jets, and two undetected neutrinos. Because of the presence of two leptons, this channel has the lowest background. However the dilepton channel has the smallest branching fraction. In the all-jets channel, each W boson decays to two jets so that this channel contains two b quark jets and four light quark jets. This channel has the largest branching fraction but also the largest background from QCD multijet production. The lepton+jets channel has one W boson decaying leptonically and the other hadronically so that we have one charged lepton, two b -quark jets, two light quark jets, and one undetected neutrino. Because of the relatively large branching fraction with manageable backgrounds, lepton+jets channel is considered as the “golden

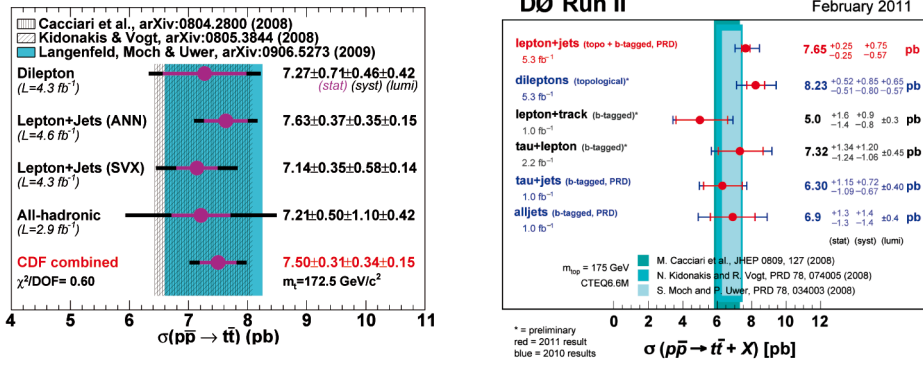


Fig. 1. – Summary of the top quark pair production cross section measurement from CDF (left) and D0 (right) are shown. The results are compared with various NLO calculations.

channel” in the top quark studies. By this reason, the most results presented here use the lepton+jets final state.

2. – Top quark pair production cross section measurement

The top quark pair production cross section at the Tevatron is calculated within the SM to be $7.5^{+0.72}_{-0.63}$ pb for $M_{\text{top}} = 172.5 \text{ GeV}/c^2$ in the next leading order (NLO) calculation [5]. Deviations of the measurements from this value indicate non-perturbative effects, or new production mechanism beyond the SM. Both CDF and D0 have very precise measurements in the lepton+jets channel using neural network technique [6, 7] taking advantages of the different kinematics between the signal and backgrounds. Since a large uncertainty of the luminosity determination (about 6%), CDF Collaboration employed the ratio measurement of $t\bar{t}$ to Z -boson ($\sigma_{t\bar{t}}/\sigma_Z$) converting to $t\bar{t}$ cross section with the theoretical Z boson cross section. With this approach, we obtained the most accurate $t\bar{t}$ cross section measurement at the Tevatron as 7.70 ± 0.52 pb [6] which is less than 7% relative precision. Figure 1 shows a summary of CDF and D0 $t\bar{t}$ cross section measurements obtained using various different decay channels and techniques. All measurements are excellently agreed with the SM predictions.

2.1. Boosted top search. – If the top quark is highly boosted, it would appear as a jet with structure. CDF Collaboration has studied very high p_T ($p_T > 400 \text{ GeV}/c$) jets and isolates the top quark signal region using jet mass ($130 \text{ GeV}/c^2 < m_{\text{jet}} < 210 \text{ GeV}/c^2$). Because of the dominant QCD multijet production and low cross section of the boosted top production, we just set the upper limit of $\sigma_{t\bar{t}}^{\text{boost}} < 40 \text{ fb}$ at 95% CL [8].

3. – Top quark mass and t - \bar{t} mass difference

The mass of the top quark is very important to estimate the SM Higgs boson because precise top and W boson masses measurements can predict the mass of the Higgs boson either SM or beyond SM. Since the discovery of the top quark, both the CDF and D0 experiments have been improving the precision of the M_{top} measurement [9].

For the M_{top} measurements, two primary techniques have been established. The template method (TM) uses the distributions of variables (templates) which are strongly

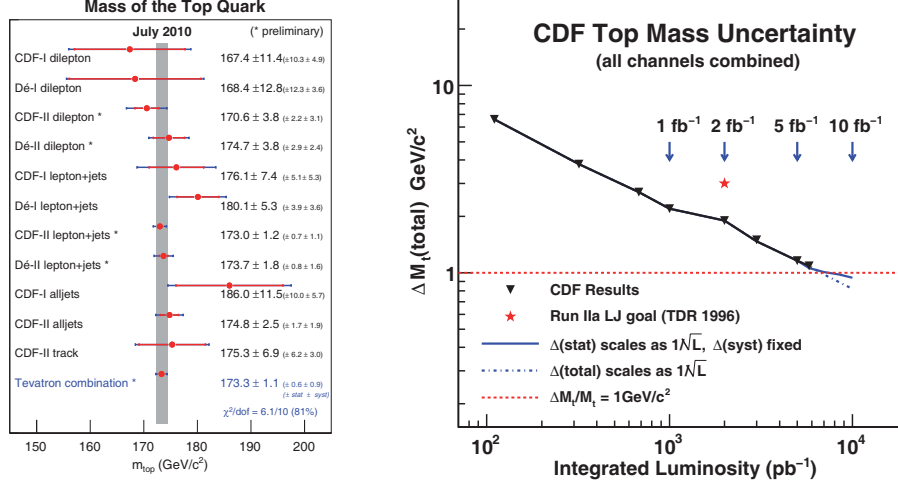


Fig. 2. – Left: Summary of the Tevatron top quark mass measurements and its combination. Right: CDF prediction of M_{top} precision by scaling using increased luminosity (solid line) and plus possible improvement (dashed line).

correlated with the top quark mass and JES. In the building of a probability, only a few variables (usually less than two) are used, for instance reconstructed top quark mass and dijet mass of hadronic decay W boson in the lepton+jets channel. The Matrix Element Method (ME) uses event's probability to be a combination of signals and background. ME exploits all the information in the event by using a leading-order matrix element calculation convoluted with parton distribution function and transfer functions (TFs) making connection between detector response and parton level particle. Because we can use all the information of $t\bar{t}$ production and decay in principle, ME usually provides better precision of M_{top} than TM. Both techniques employ likelihood to compare data to the modeling of signals and background to extract M_{top} .

CDF and D0 experiments have performed the M_{top} measurements in the various final states with different techniques. In the lepton+jets and all-jets channels the uncertainty from jet energy scale (JES) can be reduced by using the reconstructed dijet mass from hadronically decaying W boson with *in situ* calibration of JES. To date the most precise measurement has been performed by CDF Collaboration using lepton+jets channel with ME. We found $M_{\text{top}} = 173.0 \pm 1.2 \text{ GeV}/c^2$ using 5.6 fb^{-1} of the data [10]. D0 carried out the most precise M_{top} measurement in the dilepton channel using TM. We built templates of the reconstructed top quark mass distributions and extract $M_{\text{top}} = 173.3 \pm 3.2 \text{ GeV}/c^2$ using 5.3 fb^{-1} data [11]. Figure 2 (left) shows the summary of the M_{top} measurements and the combination of the Tevatron M_{top} measurements [9]. The precision, $\Delta M_{\text{top}}/M_{\text{top}} \sim 0.6\%$, is already surpassed the prediction of RunII experiments and close to the $1 \text{ GeV}/c^2$. We predict to reach less than $1 \text{ GeV}/c^2$ precision by end of RunII with approximately 10 fb^{-1} data as shown in fig. 2 (right).

The precision determination of M_{top} allows us to measure the mass difference between top quark and anti-top quark to a few GeV. In the CPT theorem, which is fundamental to any local Lorentz-invariant quantum field theory, the quark mass should be the same as its anti-quark partner. Despite the fact that no violations have ever been observed in

the meson and baryon sectors, it is important to test CPT violation in all sectors such as quarks and high mass particles.

D0 Collaboration has a first direct measurement of top quark and antitop quark mass difference (δM_{top}) in the lepton+jets channel using the ME. In the matrix element calculation, one assumes SM-like $t\bar{t}$ production and decay, where identical particle and antiparticle masses are assumed for b quarks and W bosons but not for top quarks. Using 1 fb^{-1} of $p\bar{p}$ collision data, we measure $\delta M_{\text{top}} = 3.8 \pm 3.7\text{ GeV}/c^2$ [12]. CDF Collaboration measures the mass difference using the TM. We reconstruct the mass difference using modified kinematic fitter allowing mass difference between hadronic top quark and leptonic top quark. Using 5.6 fb^{-1} of $p\bar{p}$ collisions, we measure $\delta M_{\text{top}} = -3.3 \pm 1.7\text{ GeV}/c^2$ [13]. It is consistent with CPT symmetry at a 2σ level. This is the most precise measurement of a quark and anti-quark mass difference.

4. – Study of other top properties

We have studied the top quark properties in various different ways using its unique characteristics. Since top quarks decay before hadronization, information of the top quarks is carried by the decay products. Therefore, we can directly determine the properties of the top quark.

Because of the short lifetime, a direct determination of the top quark lifetime is extremely hard. However, we can calculate it from the decay width. CDF Collaboration has a direct measurement of the top quark width (Γ_{top}) using 4.3 fb^{-1} of $p\bar{p}$ collision. The M_{top} and the mass of W boson that decays hadronically are reconstructed for each event and compared with templates of different Γ_{top} and deviations from nominal jet energy scale (Δ_{JES}) to perform a simultaneous fit for both parameters, where Δ_{JES} is used for the *in situ* calibration of the jet energy scale. By applying a Feldman-Cousins approach, we establish an upper limit at 95% confidence level of $\Gamma_{\text{top}} < 7.6\text{ GeV}$ and a two-sided 68% CL interval of $0.3\text{ GeV} < \Gamma_{\text{top}} < 4.4\text{ GeV}$ [14]. D0 Collaboration has an indirect determination of Γ_{top} using single top t -channel cross section and $t \rightarrow Wb/t \rightarrow Wq$ fraction measurements. The Γ_{top} is calculated with quantum mechanical relation, $\Gamma_{\text{top}} = \frac{\sigma(t \rightarrow ch)}{Br(t \rightarrow bW)} \cdot \frac{Br(t \rightarrow bW)_{\text{SM}}}{\sigma(t \rightarrow ch)_{\text{SM}}}$. The result, $\Gamma_{\text{top}} = 1.99_{-0.55}^{+0.65}\text{ GeV}$, is the most precise determination of the top quark width using experimental data sample and consistent with SM [15].

The $t\bar{t}$ spin correlation is predicted by the SM and a potentially sensitive discriminant of new physics coupled to the top quark. The spin state is observable in angular correlations among the quark decay products. In the dilepton channel, we used the angular correlation between two leptons and measured consistent results with SM from both CDF [16] and D0 [17] Collaborations. CDF Collaboration has a new measurement using lepton+jets channel by introducing new technique which separate the down-type (d or s) quark of hadronic decay W boson. Using the correlation between lepton and down-type quark we measure the spin correlation coefficient $\kappa = 0.72 \pm 0.62 \pm 0.26$ using 5.3 fb^{-1} data. It is consistent with SM ($\kappa_{\text{SM}} = 0.78$) [18].

The SM predicts that the top quark decays almost entirely to a W boson and a bottom quark, and that the Wtb vertex is a $V - A$ charged weak current interaction. A consequence of this is that approximately 70% of the top quark decay longitudinally, 30% of the top quarks have left handed polarization ($f_0 = 70\%$, $f_- = 30\%$, $f_+ = 0\%$) [19]. Any new particles involved in the same decay topologies and non-standard coupling could create a different mixture of polarized W bosons. Therefore, a measurement of this fraction

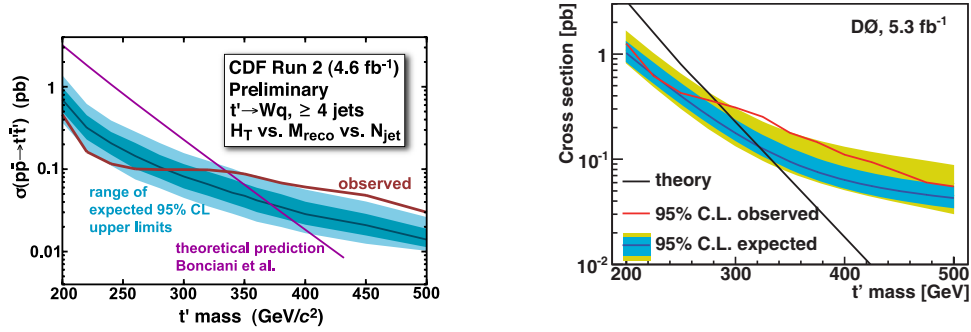


Fig. 3. – 95% CL limits of t' pair production cross section measured by CDF (left) and D0 (right) overlaid predicted cross section.

is a test of the $V - A$ nature of the Wtb vertex. D0 Collaboration uses both lepton+jets and dilepton channel simultaneously with 4.3 fb^{-1} data and extracts $f_+ = 0.02 \pm 0.05$ and $f_0 = 0.06 \pm 0.01$ with the simultaneous fit of the two variables [20]. This is consistent with SM at the 98% CL. CDF Collaboration has results in both lepton+jets [21] and dilepton channels [22] which are also consistent with SM.

Several exotic physics models, such as SUSY and two Higgs doublet, predict flavor-changing neutral current (FCNC) in the top decay. In the SM, this decay mode is highly suppressed so, any signals from FCNC decay chain indicate an evidence of new physics. FCNC decay of top quark ($t \rightarrow Zq$) predict different final state of $t\bar{t}$ with SM decays. D0 Collaboration uses trilepton final state ($Z \rightarrow ll$ and $W \rightarrow l\nu$) using 4.1 fb^{-1} data. Based on the data which is consistent with null signal of FCNC decay, we set the upper limit of FCNC branching fraction as $Br(t \rightarrow Zq) < 3.3\%$ at 95% CL [23]. CDF Collaboration has a dilepton channel ($Z \rightarrow ll$ and $W \rightarrow qq$) analysis using 1.9 fb^{-1} and set the 95% CL upper limit of 3.7% [24].

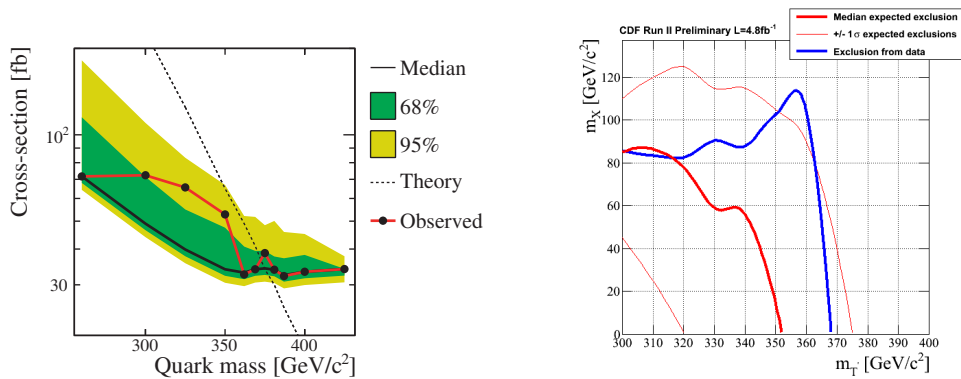


Fig. 4. – 95% CL limits of b' pair production cross section as a function of b' masses (left) and of t' pair production cross section in the two dimensional space of t' and invisible particle masses (right).

5. – New physics particle searches

The electroweak precision measurements did not prohibit the fourth generation of quarks such as t' (top-like quark) and b' (bottom like quark). CDF and D0 Collaborations have been searching the fourth generation t' in a decay mode of $t' \rightarrow Wq$ which was preferred in case of a small mass splitting between t' and b' . We use the reconstructed t' mass and H_T to isolate signals. As one can see in fig. 3, both experiments have approximately 2σ access in the t' mass around $350 \text{ GeV}/c^2$ [25, 26]. This is interesting access of signal and might be figured out with larger data sample of 10 fb^{-1} at the end of Run II in both experiments.

CDF Collaboration has searched the b' in a decay mode of $b' \rightarrow tW$. We expect very energetic and large jet multiplicity signature from $b'\bar{b}'$ decay. We use H_T categorized by jet multiplicity to extract signal. Data consisted with null signal set the lower limit of $M_{b'} > 385 \text{ GeV}/c^2$ as one can see in fig. 4 (left) [27].

A more exotic model predicts t' decay into tX where X is invisible particle of the dark matter candidate. CDF Collaborations has searched pair productions of t' decaying into t and invisible. Taking advantage of large missing energy from signal, we extract the exotic t' signal from data which is consistent with null signal. We then set the 95% CL limit of parameter space as shown in fig. 4 (right) [28].

6. – Conclusion

The CDF and D0 Collaborations have performed a robust set of analyses using many techniques and improvements to have better understand the top quark nature. As a result, we determine the M_{top} with $\Delta M_{\text{top}}/M_{\text{top}}$ less than 0.7% and $\Delta\sigma_{t\bar{t}}/\sigma_{t\bar{t}}$ less than 7% precisions. By end of Run II, we expect $\sim 12 \text{ fb}^{-1}$ of data delivered to both experiments by the Tevatron which could be almost a double the data sample used in this report. An ultimate precision of about M_{top} less than $1 \text{ GeV}/c^2$ will be possible. The other top properties and new particle searches, which are mostly limited by statistics, have been significantly improved and we may have surprising results.

* * *

I would like to thank for the CDF and D0 colleagues for their efforts to carry out these challenging physics analyses. I also thank for the conference organizers for a very rich week of physics.

REFERENCES

- [1] ABE F. *et al.* (CDF COLLABORATION), *Phys. Rev. Lett.*, **74** (1995) 2626; ABACHI S. *et al.* (D0 COLLABORATION), *Phys. Rev. Lett.*, **74** (1995) 2632.
- [2] NAKAMURA K. *et al.* (PARTICLE DATA GROUP), *J. Phys. G*, **37** (2010) 075021.
- [3] ALEPH, CDF, D0, DELPHI, L3, OPAL, SLD, THE LEP ELECTROWEAK WORKING GROUP, THE TEVATRON ELECTROWEAK WORKING GROUP, and THE SLD ELECTROWEAK and HEAVY FLAVOR WORKING GROUPS, arXiv:1012.2367v2.
- [4] FLÄCHER H. *et al.*, *Eur. Phys. J. C*, **60** (2009) 543.
- [5] MOCH S. and UWER P., *Nucl. Phys. Proc. Suppl.*, **183** (2008) 75.
- [6] AALTONEN T. *et al.* (CDF COLLABORATION), *Phys. Rev. Lett.*, **105** (2010) 012001.
- [7] ABAZOV V. *et al.* (D0 COLLABORATION), arXiv:1101.0124.
- [8] (CDF COLLABORATION), CDF conference note 10234.

- [9] THE TEVATRON ELECTROWEAK WORKING GROUP (CDF AND D0 COLLABORATIONS), FERMILAB-TM-2466-E, arXiv:1007.3178.
- [10] AALTONEN T. *et al.* (CDF COLLABORATION), *Phys. Rev. Lett.*, **105** (2010) 252001.
- [11] (D0 COLLABORATION), D0 conference note 6104.
- [12] ABAZOV V. *et al.* (D0 COLLABORATION), *Phys. Rev. Lett.*, **103** (2009) 132001.
- [13] AALTONEN T. *et al.* (CDF COLLABORATION), *Phys. Rev. Lett.*, **106** (2011) 152001.
- [14] AALTONEN T. *et al.* (CDF COLLABORATION), *Phys. Rev. Lett.*, **105** (2010) 232003.
- [15] ABAZOV V. *et al.* (D0 COLLABORATION), *Phys. Rev. Lett.*, **106** (2010) 022001.
- [16] (CDF COLLABORATION), CDF conference note 9824.
- [17] ABAZOV V. *et al.* (D0 COLLABORATION), arXiv:1103.1871.
- [18] AALTONEN T. *et al.* (CDF COLLABORATION), *Phys. Rev. D*, **83** (2011) 031104.
- [19] AGUILAR-SAAVEDRA J. *et al.*, *Eur. Phys. J. C*, **50** (2007) 519.
- [20] ABAZOV V. *et al.* (D0 COLLABORATION), *Phys. Rev. D*, **83** (2011) 032009.
- [21] AALTONEN T. *et al.* (CDF COLLABORATION), *Phys. Rev. Lett.*, **105** (2010) 042002.
- [22] (CDF COLLABORATION), CDF conference note 10333.
- [23] ABAZOV V. *et al.* (D0 COLLABORATION), arXiv:1103.4574.
- [24] AALTONEN T. *et al.* (CDF COLLABORATION), *Phys. Rev. Lett.*, **101** (2008) 192002.
- [25] (CDF COLLABORATION), CDF conference note 10110.
- [26] ABAZOV V. *et al.* (D0 COLLABORATION), arXiv:1104.4522.
- [27] AALTONEN T. *et al.* (CDF COLLABORATION), *Phys. Rev. Lett.*, **106** (2011) 141803.
- [28] AALTONEN T. *et al.* (CDF COLLABORATION), arXiv:1103.2482.

Forward-backward asymmetry in $t\bar{t}$ production

D. AMIDEI on behalf of the CDF COLLABORATION

University of Michigan - Ann Arbor, MI, USA

(ricevuto il 29 Settembre 2011; pubblicato online il 2 Febbraio 2012)

Summary. — We present new measurements of the forward-backward asymmetry in $t\bar{t}$ production, performed with 5 fb^{-1} of Tevatron $p\bar{p}$ collisions at center of mass energy 1.96 TeV, recorded and analyzed at CDF. Significant inclusive asymmetries are observed in both the lepton+jets and the dilepton decay modes of the $t\bar{t}$ pair. In the dilepton mode, the asymmetry is observed in the reconstructed top rapidity, and in the lepton rapidity difference which is independent of any top reconstruction. In the lepton plus jets sample, the full reconstruction of the top kinematics is used to measure the dependence of the asymmetry on the rapidity difference Δy and the invariant mass $M_{t\bar{t}}$ of the $t\bar{t}$ system, and the asymmetry is found to be most significant at large rapidity and mass.

PACS 14.65.Ha – Top quarks.

1. – Introduction

Top quark pair production is a test of QCD at large momentum transfer. This strong process is symmetric at leading order (LO), but has a small charge asymmetry (O(6%)) arising at order α_s^3 [1]. The top quark production angle or rapidity is measured in reconstructed lepton+jets events and used to calculate the simple asymmetry $A_{\text{FB}} = \frac{F-B}{F+B}$ which is corrected for backgrounds, acceptance and resolution effects to yield a “parton-level” asymmetry to be compared to theory.

In 2008 CDF and D0 published asymmetry measurements in the lepton+jets mode with $1\text{--}2\text{ fb}^{-1}$ that both found large positive asymmetries with large uncertainties [2]. CDF has recently completed a new series of measurements in which we update the sample to 5.3 fb^{-1} and explore both the lepton+jets and dilepton decay modes, and the charge, rapidity, and mass dependence of the asymmetry [3, 4].

These measurements have stimulated a number of models for new interactions in the top sector [5]. In one class of theories the gluon interferes with new axial s -channel objects arising from an extended strong gauge group or extra dimensions. Consistency with the measured top cross section and $M_{t\bar{t}}$ distribution requires masses greater than $\sim 2\text{ TeV}/c^2$. Another broad class of theories posits potentially light t -channel objects with non-standard u - t or d - t flavor couplings, with the asymmetry then arising from dominance

of the flavor-change into the forward Rutherford peak. Although the asymmetry itself is challenging to observe in the pp collisions of the LHC, many of these theories predict other new phenomena that can be detected at the Tevatron and LHC.

2. – Inclusive measurement in lepton+jets mode

We select 1260 “lepton+jets” events with a central e or μ with $p_T > 20$ GeV, $\cancel{E}_T > 20$ GeV, four or more jets with $E_T > 20$ GeV, and at least one secondary vertex “ b -tag”. Non- $t\bar{t}$ background shapes and normalizations are understood in precision $t\bar{t}$ cross-section measurements [6] which predict 283 ± 91 non- $t\bar{t}$ events. The $t\bar{t}$ kinematics are reconstructed with a χ^2 -based comparison of the jet-parton matching and neutrino solutions along with the constraints that $M_W = 80.4$ GeV/ c^2 , $M_t = 172.5$ GeV/ c^2 , and b -tagged jets are matched to b -partons.

We measure the frame-independent rapidity difference of the leptonic and hadronic top decay systems, Δy_{lh} . When weighted by the lepton charge q , this gives the top-antitop rapidity difference: $q\Delta y_{lh} = q(y_l - y_h) = y_t - y_{\bar{t}} = \Delta y$. In the limit of small $t\bar{t}$ system p_T this is simply related to the top quark rapidity in the $t\bar{t}$ rest frame: $y_t^{t\bar{t}} = \frac{1}{2}\Delta y$. The total asymmetry in the $t\bar{t}$ rest frame is

$$(1) \quad A^{t\bar{t}} = \frac{N(\Delta y > 0) - N(\Delta y < 0)}{N(\Delta y > 0) + N(\Delta y < 0)}.$$

In QCD at NLO, a small charge asymmetry arises from the interference of $q\bar{q}$ processes behaving differently under charge conjugation. We use MCFM to predict a parton-level asymmetry of 0.058 ± 0.009 . We also use the event generator MC@NLO with the CDF detector simulation and standard non- $t\bar{t}$ background models to predict a “data-level” asymmetry of 0.017 ± 0.004 . (MCFM and MC@NLO calculations include 15% scale dependence uncertainty.) The data-level prediction is less than the statistical error of the current data set, so PYTHIA remains a good approximation of the standard model. To test our methods in the presence of large asymmetries we developed a simple coloron model with MADGRAPH and the CDF simulation, tuning the octet mass and couplings to produce an inclusive asymmetry similar to the data while minimizing the impact on $M_{t\bar{t}}$ and the $t\bar{t}$ cross-section.

The left plot in fig. 1 shows the distribution Δy in the data compared to Monte Carlo predictions. In the data, $A^{t\bar{t}} = 0.057 \pm 0.028$. The Δy_{lh} asymmetries in the separate lepton-charge species (not shown) are $A_+^{t\bar{t}} = 0.067 \pm 0.040$ and $A_-^{t\bar{t}} = -0.048 \pm 0.039$. With large errors, these are equal in magnitude and opposite in sign, as expected for a CP conserving charge asymmetry.

The Δy distribution can be corrected to the $t\bar{t}$ “signal-level” by subtracting backgrounds. Further correcting the signal for selection, acceptance, and resolution distortions provides “parton-level” measurements that can be compared to theoretical predictions. The correction is a simple linear unfold of Δy using a response matrix based on Pythia, and tested on an alternate Pythia sample, MC@NLO, and the color octet models. The raw and corrected asymmetries are shown in table I. At all levels the asymmetry exceeds the prediction with modest significance. The signal level is consistent with the value of 0.08 ± 0.04 recently reported by D0 [7]. The corrected $q\Delta y$ distribution can be used to calculate a crude rapidity dependent asymmetry in two bins of $q\Delta y$. In the $t\bar{t}$ rest frame we measure fully corrected asymmetries of $A^{t\bar{t}}(|\Delta y| < 1.0) = 0.026 \pm 0.118$

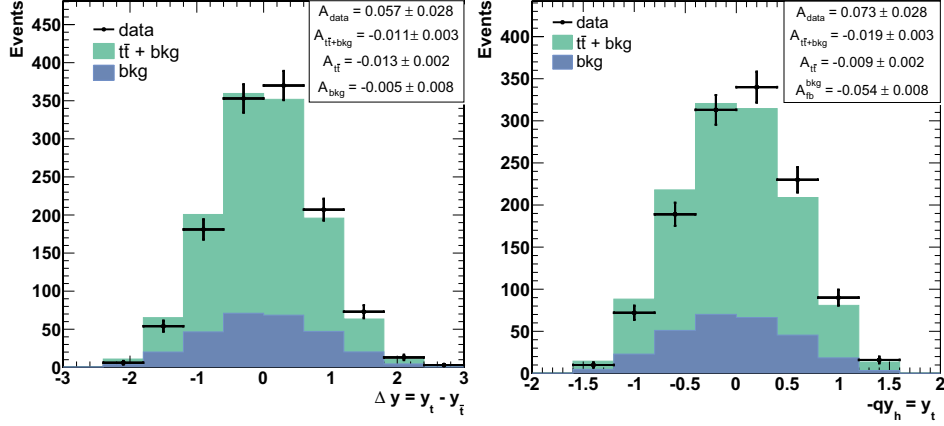


Fig. 1. – Charge-weighted rapidities and asymmetries in data and models. Left: Δy . Right: $-qy_h$.

and $A^{t\bar{t}}(|\Delta y| \geq 1.0) = 0.611 \pm 0.256$, compared with MCFM predictions of 0.039 ± 0.006 and 0.123 ± 0.008 for these Δy regions respectively.

3. – Asymmetry in dilepton mode

CDF has recently measured the inclusive $t\bar{t}$ forward-backward asymmetry in the dilepton decay mode [4]. We select 334 events with two opposite sign central leptons (e or μ) with $p_T > 20$ GeV and mass inconsistent with a Z -boson $m_{ll} = [75, 105]$ GeV/ c^2 , $\cancel{E}_T > 25$ GeV, two or more jets with $E_T > 20$ GeV, and total scalar energy $H_t > 200$ GeV. The non- $t\bar{t}$ background is estimated to be 87 ± 17 events.

The difference of the lepton pseudo-rapidities $\Delta\eta = \eta_+ - \eta_-$, is correlated with Δy and has none of the multijet, \cancel{E}_T , and b -tagging vagaries of the lepton+jets sample. We define the inclusive asymmetry

$$(2) \quad A^{\Delta\eta} = \frac{N(\Delta\eta > 0) - N(\Delta\eta < 0)}{N(\Delta\eta > 0) + N(\Delta\eta < 0)}.$$

The $A^{\Delta\eta}$ measurement is tested in large Z -boson samples as a function of associated jet multiplicity and yields the expected electroweak asymmetries with very good

TABLE I. – Summary of lepton+jet asymmetries $A^{t\bar{t}}$ at data, signal, and parton level.

Sample	Level	$A^{t\bar{t}}$
data	data	0.057 ± 0.028
MC@NLO	$t\bar{t}+\text{bkg}$	0.017 ± 0.004
data	signal	0.075 ± 0.037
MC@NLO	$t\bar{t}$	0.024 ± 0.005
data	parton	0.158 ± 0.074
MCFM	parton	0.058 ± 0.009

TABLE II. – Asymmetries $A^{\Delta\eta}$ in the dilepton selection. Statistical errors only.

Selection	= 0 jets	= 1 jet	≥ 2 jets
reco data	-0.038 ± 0.047	0.040 ± 0.057	0.138 ± 0.054
MC@NLO	-0.026 ± 0.037	-0.009 ± 0.053	-0.022 ± 0.022

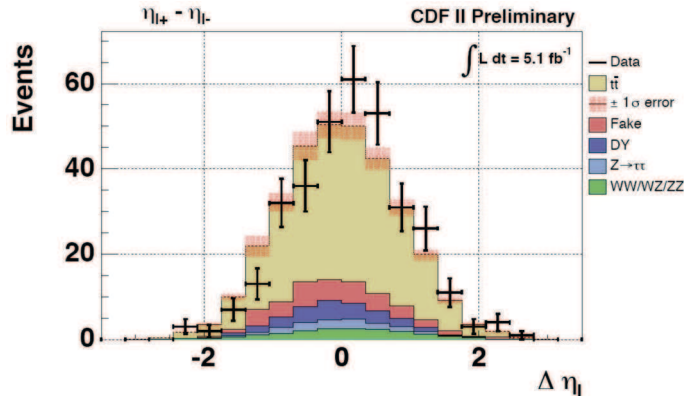
precision. With the top like selection including Z -veto and missing E_T , we measure in $\Delta\eta$ while controlling the multiplicity of jets. Events with 0 jets are dominated by W -pair production, while those with 1 jet are a mix of WW , Drell-Yan, $Z \rightarrow \tau\tau$, and $W+$ jets with a fake lepton. Events with 2 jets are the $t\bar{t}$ selection. $A^{\Delta\eta}$ for each category, along with the prediction, are shown in table II. The background dominated 0 and 1 jet events have small asymmetries consistent with prediction (and 0), while the $t\bar{t}$ dominated 2 jet sample shows a significant positive asymmetry. The $\Delta\eta$ distribution in the 2 jet sample is shown in fig. 2.

A simple transformation to the parton-level value is derived based on the minimal assumption that $A(\Delta y)$ is proportional to Δy . The reconstructed parton level asymmetry is found to be $A^{t\bar{t}} = 0.475 \pm 0.114$. The asymmetry is positive by $\sim 3\sigma$, like the lepton+jets sample. The asymmetries of the dilepton and lepton plus jets samples differ by 1.7σ

4. – Mass dependence in lepton+jets mode

We generally expect the $M_{t\bar{t}}$ dependence to contain information on the fundamental asymmetry mechanism. The NLO QCD asymmetry grows linearly to 15% at $M_{t\bar{t}} \sim 800 \text{ GeV}/c^2$ and other models predict alternative mass dependences [5]. Using the full reconstruction in the lepton+jets sample, a mass-dependent asymmetry $A^{t\bar{t}}(M_{t\bar{t}})$ is found by dividing the data into bins of mass $M_{t\bar{t},i}$ and examining the Δy distribution in each:

$$(3) \quad A^{t\bar{t}}(M_{t\bar{t},i}) = \frac{N(\Delta y > 0, M_{t\bar{t},i}) - N(\Delta y < 0, M_{t\bar{t},i})}{N(\Delta y > 0, M_{t\bar{t},i}) + N(\Delta y < 0, M_{t\bar{t},i})}.$$

Fig. 2. – $\Delta\eta$ distribution in the 2-jet top selection. $A^{\Delta\eta} = 0.138 \pm 0.054$.

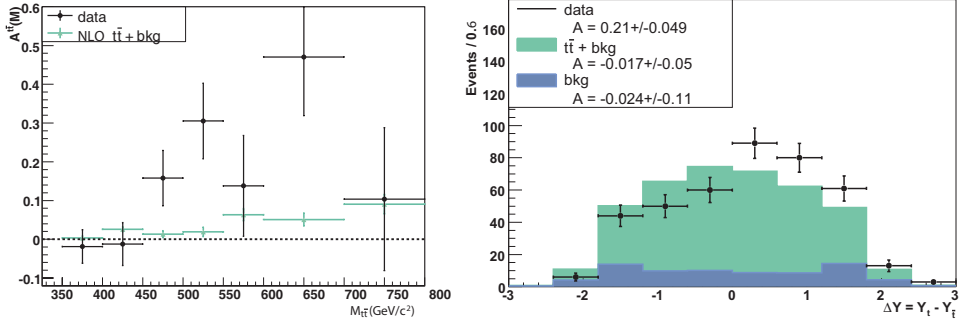


Fig. 3. – Left: Asymmetry Δy in bins of $M_{t\bar{t}}$, compared to the prediction of MC@NLO $t\bar{t}$ + backgrounds. Statistical errors only. The last bin includes all $M_{t\bar{t}} \geq 700 \text{ GeV}/c^2$. Right: Δy for events with $M_{t\bar{t}} > 450 \text{ GeV}/c^2$

The measured $A^{t\bar{t}}(M_{t\bar{t},i})$ is shown on the left in fig. 3, compared to the prediction (MC@NLO + bkg). At high mass the asymmetry is consistently above the prediction. To quantify $A^{t\bar{t}}(M_{t\bar{t}})$ in a simple, statistically robust way, we use a compact representation of $A^{t\bar{t}}(M_{t\bar{t},i})$ into just two $M_{t\bar{t}}$ bins, below and above a given mass boundary. In the color-octet samples, which have $A^{t\bar{t}}(M_{t\bar{t},i})$ distributions that are comparable to the data, the significance of the asymmetry at high mass is maximized when the bin division is at $M_{t\bar{t}} = 450 \text{ GeV}/c^2$, and we adopt this boundary.

The first lines of table III show the high and low mass asymmetries and the MC@NLO prediction. At low mass the asymmetry is consistent with zero. At high mass the reconstructed asymmetry $A^{t\bar{t}} = 0.210 \pm 0.049$ is more than three standard deviations above the prediction. The right panel in fig. 3 shows the Δy distribution for the $M_{t\bar{t}} > 450 \text{ GeV}/c^2$.

The asymmetries in Δy_{lh} for separate lepton charge species are given in the bottom part of table III. Under the interchange of lepton charge, the asymmetry at high mass is reversed in a manner consistent with CP conservation. This argues against a false positive arising in event selection or $t\bar{t}$ reconstruction, as neither contains information on the lepton charge.

5. – Asymmetry in the laboratory frame

The well-measured rapidity of the hadronic top decay system y_h , multiplied by the opposite of the lepton charge, yields the top rapidity in the laboratory frame. The

TABLE III. – Asymmetries at the data-level in the $l\bar{t}$ jets sample. Data has statistical errors only.

Selection	All $M_{t\bar{t}}$	$M_{t\bar{t}} < 450 \text{ GeV}/c^2$	$M_{t\bar{t}} \geq 450 \text{ GeV}/c^2$
reco data	0.057 ± 0.028	-0.016 ± 0.034	0.210 ± 0.049
MC@NLO	0.017 ± 0.004	0.012 ± 0.006	0.030 ± 0.007
A_{lh}^+	0.067 ± 0.040	-0.013 ± 0.050	0.210 ± 0.066
A_{lh}^-	-0.048 ± 0.039	0.020 ± 0.047	-0.210 ± 0.071

TABLE IV. – Reconstruction level asymmetries $A^{\text{P}\bar{\text{P}}}$ in the laboratory frame. Data has statistical errors only.

Selection	All $M_{t\bar{t}}$	$M_{t\bar{t}} < 450 \text{ GeV}/c^2$	$M_{t\bar{t}} \geq 450 \text{ GeV}/c^2$
data reco	0.073 ± 0.028	0.059 ± 0.034	0.103 ± 0.049
MC@NLO +bkg	0.001 ± 0.003	-0.008 ± 0.005	0.022 ± 0.007
A_h^+	-0.070 ± 0.040	-0.028 ± 0.050	-0.148 ± 0.066
A_h^-	0.076 ± 0.039	0.085 ± 0.047	0.053 ± 0.072

inclusive $-qy_h$ distribution is shown in the right plot of fig. 1 and the data level asymmetries are shown in table IV. Because the backgrounds in the lab frame enter with a negative asymmetry, the predicted lab frame asymmetry is $A^{\text{P}\bar{\text{P}}} \sim 0$. The measurement is 2.6σ above that prediction. The NLO effect predicts that $A^{\text{P}\bar{\text{P}}} < A^{t\bar{t}}$, which is not seen in the inclusive measurement, although the uncertainty is large. At high mass, the ratio $A^{\text{P}\bar{\text{P}}}/A^{t\bar{t}} = 0.49 \pm 0.23$ is less than the MC@NLO prediction of 0.74, but the uncertainty is again large. With improved precision, the ratio $A^{\text{P}\bar{\text{P}}}/A^{t\bar{t}}$ may provide discrimination between NLO QCD and other models for the asymmetry.

6. – Conclusion

A significant forward-backward asymmetry is measured in inclusive $t\bar{t}$ production in two different decay modes. In the lepton+jets mode, there is evidence that the asymmetry arises from the small population of events at large Δy and $M_{t\bar{t}}$, and a suggestion that asymmetries in the lab frame and $t\bar{t}$ frame contain independent information. If the asymmetry is real it could be evidence for new interactions in the top sector or unexpected behavior of QCD at higher order.

* * *

We thank the organizers for including this special talk and also for a stimulating and enjoyable conference. We acknowledge the assistance of T. TAIT with the MADGRAPH model of the color octet.

REFERENCES

- [1] ALMEIDA L., STERMAN G. and VOGELSANG W., *Phys. Rev. D*, **78** (2008) 014008; ANTUNANO O., KUHN J. and RODRIGO G., *Phys. Rev. D*, **77** (2008) 014003; BOWEN M., ELLIS S. and RAINWATER D., *Phys. Rev. D*, **73** (2006) 014008.
- [2] ABAZOV V. *et al.* (D0 COLLABORATION), *Phys. Rev. Lett.*, **100** (2008) 142002; AALTONEN T. *et al.* (CDF COLLABORATION), *Phys. Rev. Lett.*, **101** (2008) 202001.
- [3] AALTONEN T. *et al.* (CDF COLLABORATION), arXiv:1101.0034, submitted to *Phys. Rev. D*.
- [4] <http://www-cdf.fnal.gov/physics/new/top/2011/D11Afb/cdfpubnote.pdf>.
- [5] GRESHAM M., KIM I. and ZUREK K., arXiv:1102.0018; CAO Q., MCKEEN D., ROSNER J., SHAUGHNESSY G. and WAGNER C., *Phys. Rev. D*, **81** (2010) 114004.
- [6] AALTONEN T. *et al.* (CDF COLLABORATION), *Phys. Rev. Lett.*, **105** (2010) 012001; ACOSTA D. *et al.* (CDF COLLABORATION), *Phys. Rev. D*, **71** (2005) 052003.
- [7] <http://www-d0.fnal.gov/Run2Physics/WWW/results/prelim/TOP/T90/>.

SESSION VI - HIGGS SEARCHES, HOT TOPICS

<i>Wei-Ming Yao</i>	Search for the low mass Higgs boson at the Tevatron
<i>Marc Buehler</i>	Search for a high mass SM Higgs boson at the Tevatron
<i>Abdelhak Djouadi</i>	The Tevatron Higgs exclusion limits and theoretical uncertainties
<i>Michele Redi</i>	The non-standard model Higgs
<i>Mikhail Vysotsky</i>	Coulomb law and energy levels in a superstrong magnetic field

Search for the low mass Higgs boson at the Tevatron

WEI-MING YAO for the CDF and DØ COLLABORATION

*Lawrence Berkeley National Lab, MS-50B-5239 - One Cyclotron Rd, Berkeley
CA 94720, USA*

(ricevuto il 29 Settembre 2011; pubblicato online il 25 Gennaio 2012)

Summary. — We present the recent results on the search for the low mass Higgs boson at the Tevatron by the CDF and DØ Collaborations. With up to 5.9 fb^{-1} of data analyzed at CDF and up to 6.7 fb^{-1} at DØ, the 95% C.L. upper limits on Higgs boson production are factors of 1.56 times the values of the standard model cross section for a Higgs boson mass of $m_H = 115 \text{ GeV}/c^2$.

PACS 14.80.Bn – Standard-model Higgs bosons.

1. – Introduction

The Higgs boson is the last unobserved particle postulated in the standard model, and could help explain the origin of mass in the universe. A longstanding key objective in observing the Higgs boson is to probe the mechanism of electroweak symmetry breaking. The direct search from LEP and global fit of precision electroweak data constrain the Higgs mass between $114.4 \text{ GeV}/c^2$ and $186 \text{ GeV}/c^2$ at 95% C.L., which therefore places the SM Higgs boson within the Tevatron's reach. With a full dataset and improved analysis the Tevatron could add crucial information about $H \rightarrow b\bar{b}$, which is more difficult to detect at LHC. Not seeing a low mass Higgs guarantees that there might be new physics waiting to be found at LHC. Of course, it would be exciting if we started to see something soon. We need to measure as many of its properties as possible since any new physics may influence the Higgs boson's production and decays.

The Tevatron is doing very well and has delivered more than 10 fb^{-1} data, with the record luminosity exceeding $4.1 \times 10^{32} \text{ cm}^{-2} \text{ s}^{-1}$. Additional 2 fb^{-1} data is expected by the end of FY2011, which gives a final dataset close to 12 fb^{-1} . In this report, we present the recent results from the direct searches for the low mass SM Higgs boson at the Tevatron [1]. Most results presented are based on 6 fb^{-1} data and major improvements in the low mass searches are expected to be completed in the summer of 2011.

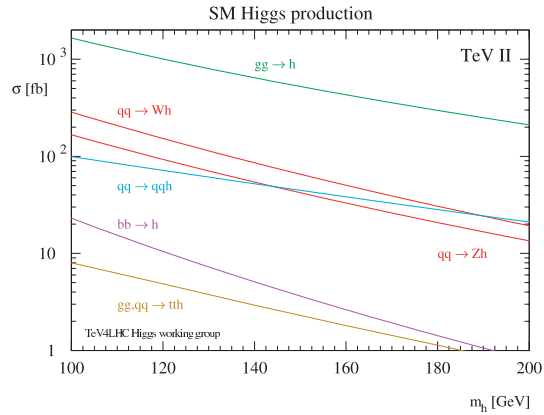


Fig. 1. – SM Higgs production cross sections for $p\bar{p}$ collisions at the Tevatron as a function of the Higgs boson mass.

2. – Search strategies and analysis techniques

The dominant Higgs production processes from $p\bar{p}$ collisions at the Tevatron are gluon-gluon fusion and associated production with either a W or Z boson. The cross sections for the production of SM Higgs bosons are summarized in fig. 1, and the branching fractions for the most relevant decay modes of the SM Higgs boson are shown in fig. 2 as a function of the Higgs boson mass between 100 and 200 GeV/c^2 . For Higgs masses above 135 GeV/c^2 , the Higgs boson will decay predominantly into WW^* which will be covered elsewhere [2]. For Higgs masses below 135 GeV/c^2 , the Higgs boson predominantly decays into $b\bar{b}$, which makes the associated production with W and Z semileptonic decay most assessible at the Tevatron while the direct production $gg \rightarrow H \rightarrow b\bar{b}$ is limited by the multi-jet QCD background. The detection of $H \rightarrow b\bar{b}$ is difficult at LHC due to a large $t\bar{t}$ background and it needs to rely on $H \rightarrow \gamma\gamma$ instead [3].

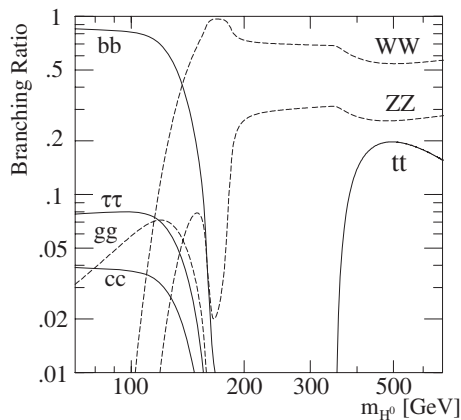


Fig. 2. – Branching fractions for the main decay of the SM Higgs boson as a function of the Higgs boson mass.

For the low mass Higgs boson signatures we look for a dijet mass resonance from the Higgs boson decay associated with the W or Z boson, where the W decays into $l\nu$ and $Z \rightarrow \nu\bar{\nu}, l^+l^-$, which gives final states of either $l\nu b\bar{b}$, $\nu\bar{\nu}b\bar{b}$, or $l^+l^-b\bar{b}$. Just to set the scale on how rare these processes are, we would expect 30 $WH \rightarrow l\nu b\bar{b}$ events, 15 $ZH \rightarrow \nu\bar{\nu}b\bar{b}$ events, 5 $ZH \rightarrow l^+l^-b\bar{b}$ events, respectively, per fb^{-1} per experiment for Higgs mass at 115 GeV before any detector acceptances. At the same time, the backgrounds are $W + \text{jets}$, $t\bar{t}$, single top, and diboson, and are copiously produced at a rate many orders of magnitude greater. The challenge is to separate the small signal from the huge background using multivariate analysis techniques. Recent observations of single top [4, 5] and diboson [6, 7] provide solid evidence that these advanced tools do work.

The strategies we employed for the low mass Higgs search are quite similar for the corresponding CDF and DØ analyses. The primary gains in recent years are mainly from improved signal acceptance, more triggers, loose lepton identification, better b -tagging, improved dijet mass resolution, and advanced analysis techniques, which we will go over in some detail. These are essential for the low mass Higgs searches.

The first thing we can do to improve the acceptance is to improve lepton identification and corresponding triggers. For example, selecting high- P_T leptons with multivariate lepton identification could gain 20% more Z 's than a simple cut-based selection. We also gain lepton acceptance by including the loose muon as an isolated track from $\cancel{E}_T + \text{jets}$ triggers.

Identifying b -quark jets is another way to reduce backgrounds that do not contain heavy flavor content. The typical b -tag efficiency is between 50 and 70% for the b -jets, with the mistag rate ranging between 1 and 6% for the light flavor jets. Requiring b -tagging for both jets would significantly reduce the background from both charm and mistags in the $W + \text{jets}$.

We can also improve the dijet mass by combining the calorimeter and tracking information with a neural network [8]. The new b -jet neural network correction improves the dijet mass resolution from 15% to 11% for the mass ranges we are interested in.

Finally, we could be more aggressive by employing advanced multivariate techniques to suppress the background since we know exactly what we are looking for. For example, the leading order matrix element (ME) is used to calculate event probabilities based on a set of observed inputs and likelihood ratios with respect to other backgrounds. Alternatively, these inputs could be fed into an artificial neural network (NN) or boosted decision tree (BDT) to find a discriminant variable. A typical improvement of using the advanced multivariate techniques is about 25% with respect to using a single variable, such as dijet mass.

3. – Highlights of the low mass searches

We will describe the searches performed by the CDF and DØ Collaborations for the low mass Higgs boson in some detail.

3.1. Search for $WH \rightarrow l\nu b\bar{b}$. – One of the gold channels for the low mass Higgs boson search is the Higgs production association with a W boson, where the W decays semileptonically and the Higgs boson decays into $b\bar{b}$ [9, 10]. We select events with one isolated high P_T lepton (electron, muon, or isolated track), and two jets, with one or more b -tagged jets, identified as containing a weakly decaying B hadron. Selected events must also have a significant imbalance in transverse momentum as missing transverse

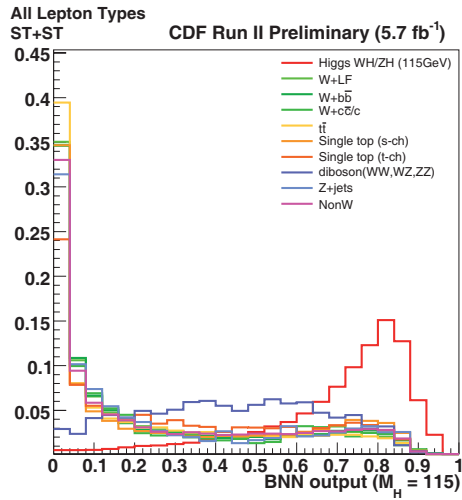


Fig. 3. – The Bayesian Neural Network Output is shown from the CDF $WH \rightarrow l\nu b\bar{b}$ analysis.

energy or \cancel{E}_T . Events with more than one isolated lepton are vetoed. For multivariate discriminants, CDF and DØ use slightly different multivariate techniques. CDF trained a Bayesian neural network discriminant (BNN) at each Higgs mass in $W + 2$ jets, separately for each lepton and b -tagging category, while for the three jet sample a ME discriminant is used. DØ trained the Random Forest Decision (RFD) discriminant separately for both $W + 2$ and 3 jets for each Higgs mass.

Figure 3 shows the BNN output in double tight tagged $W + 2$ jet at CDF and fig. 4 shows the RFD output in double tagged $W + 2$ jets from DØ. Both data are consistent with the background expectations. The expected Higgs signals are also shown, but rescaled by a large factor.

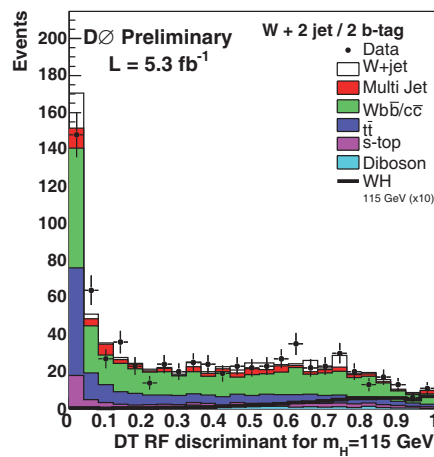


Fig. 4. – The boosted decision tree discriminant distribution is shown from the DØ $WH \rightarrow l\nu b\bar{b}$ analysis.

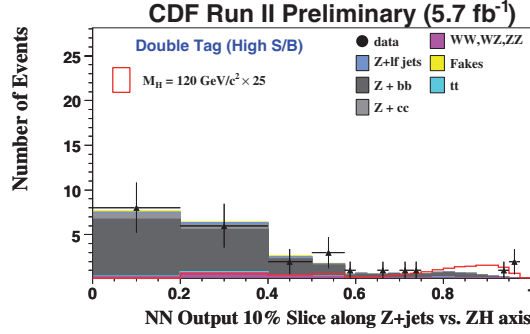


Fig. 5. – The Neural Network Output is shown from the CDF $ZH \rightarrow l^+l^-b\bar{b}$ analysis.

Since there is no excess of signal observed in the data, we can set an upper limit at 95% C.L. on the Higgs production cross section times branching ratio with respect to the SM predictions as a function of Higgs mass. For $m_H = 115 \text{ GeV}/c^2$, CDF set an observed (expected) limit at 3.3 (3.1) \times SM while DØ set a limit at 4.1 (4.8) \times SM. We are not yet competitive for a single channel, and we need to combine all other channels and both CDF and DØ results together.

3.2. Search for $ZH \rightarrow l^+l^-b\bar{b}$. – Another interesting channel to pursue in the search for the Higgs boson is the Higgs production associated with a Z boson, where the Z boson decays into a charged lepton pair and the Higgs boson decays into $b\bar{b}$ [11,12]. This channel has a low event yield due to a small branching fraction of $Z \rightarrow e^+e^-, \mu^+\mu^-$, but it provides a clean signature. We select two high P_T leptons from $Z+2\text{jet}$. DØ’s $ZH \rightarrow l^+l^-b\bar{b}$ analyses separate events into non-overlapping samples of events with one and two b -tags. CDF separates events into single tag, double tag, and loose double tag samples. To increase signal acceptance DØ has loosened the selection criteria for one of the leptons to include either an isolated track not reconstructed in the muon detector or an electron from the inter-cryostat region. CDF has added additional sub-channels for candidate events with two loose muon candidates selected using a neural network discriminant. For the DØ analysis the random forests of decision trees provide the final variables for setting limits, while CDF utilizes outputs of two-dimensional neural networks. These networks incorporate likelihoods based on event probabilities, which are obtained from ME calculations as additional inputs.

Figure 5 shows the NN output 10% slice along $Z+\text{jets}$ vs. ZH in double tags from CDF. Figure 6 shows the RFD output in double tags from DØ. Again, the data agree quite well with the background expectation. CDF has a few candidates that are very Higgs-like, but it is not statistically significant yet. CDF is able to set an observed limit at 95% C.L. at $6.5 \times$ SM while at $8.0 \times$ SM for DØ with comparable expected sensitivity to $6 \times$ SM for $m_H = 115 \text{ GeV}/c^2$.

3.3. Search for $VH \rightarrow \nu\bar{\nu}b\bar{b}$. – We also have looked for the Higgs boson in the ZH channel where the Z decays into two neutrinos, or WH where the lepton from the W decay is undetected [13,14]. The channel has a large signal rate, and it has a large QCD multijet background as well. However, the final state is relatively clean, containing two b -jets and large \cancel{E}_T . We require $\cancel{E}_T > 50 \text{ GeV}$ and two b -tagged jets. Both CDF and DØ analyses use a track-based missing transverse momentum calculation as

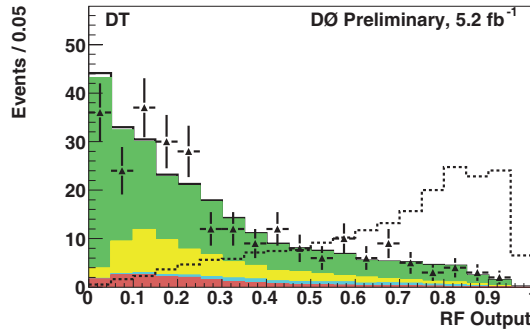


Fig. 6. – The boosted decision tree discriminant distribution is shown from the DØ $ZH \rightarrow l^+l^-b\bar{b}$ analysis.

a discriminant against false \cancel{E}_T . In addition both CDF and DØ utilize multivariate techniques, a boosted decision tree at DØ and a neural network at CDF, to further discriminate against the multi-jet background. Figure 7 shows the boosted decision tree discriminant distribution used by DØ for rejecting multi-jet QCD backgrounds before b -tagging.

The final discriminant is obtained by combining dijet mass, track \cancel{E}_T and other kinematic variables, shown in fig. 8. Again there is no Higgs signal observed. CDF set an observed limit at 95% C.L. at $2.3 \times \text{SM}$, compared to $4.0 \times \text{SM}$ expected. DØ set an observed limit at $3.4 \times \text{SM}$ with $4.2 \times \text{SM}$ expected for Higgs mass at $115 \text{ GeV}/c^2$.

3.4. Other searches. – Due to time constraints, we did not get a chance to show the results from other searches that are still one order of magnitude away from the SM predictions. They are $VH \rightarrow jjb\bar{b}$, ttH , $H \rightarrow \tau^+\tau^-$, and $H \rightarrow \gamma\gamma$. For more information, you are welcome to check out CDF and DØ public web pages at

- <http://www-cdf.fnal.gov/physics/new/hdg/Results.html>
- <http://www-d0.fnal.gov/Run2Physics/ResultsWinter2011.html>.

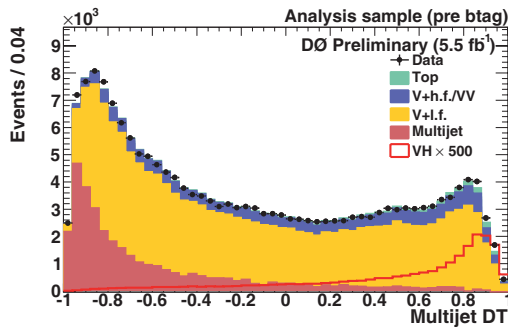


Fig. 7. – The boosted decision tree discriminant distribution for rejecting multi-jet QCD background used by the DØ $ZH \rightarrow \nu\bar{\nu}b\bar{b}$ analysis.

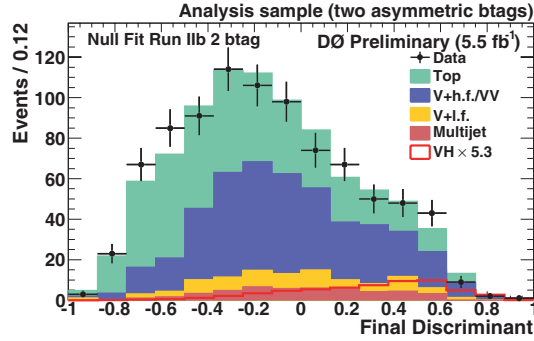


Fig. 8. – The boosted decision tree discriminant distribution is shown from the $D\bar{0} ZH \rightarrow \nu\bar{\nu}b\bar{b}$ analysis.

4. – The Tevatron combination

We performed two types of combinations, using Bayesian and Modified Frequentist (CL_s) approaches [1], which yield results that agree within 10% to gain confidence that the final result does not depend on the details of the statistical method. Both methods rely on distributions of final discriminants, not just on event counts, for their likelihood calculations. Systematic uncertainties are treated as nuisance parameters with truncated Gaussian distributions.

The combinations of results of each single experiment, as used in the Tevatron combination, yield the following ratios of 95% C.L. observed (expected) limits to the SM cross section: 1.79 (1.90) for CDF and 2.52 (2.36) for $D\bar{0}$ at $m_H = 115 \text{ GeV}/c^2$. Figure 9 shows the Tevatron combination after combining CDF and $D\bar{0}$ together. We start to exclude the Higgs mass at the low end between $100 < m_H < 109 \text{ GeV}/c^2$. We obtain the observed limit of 1.56 with expected 1.45 for $m_H = 115 \text{ GeV}/c^2$. The observed and median expected ratios are listed for the tested Higgs boson masses in table I for $m_H \leq 150 \text{ GeV}/c^2$, as obtained by the Bayesian and the CL_s methods.

The combined results we presented significantly extend the individual limits of each collaboration and those obtained in our previous combination. The sensitivity of our

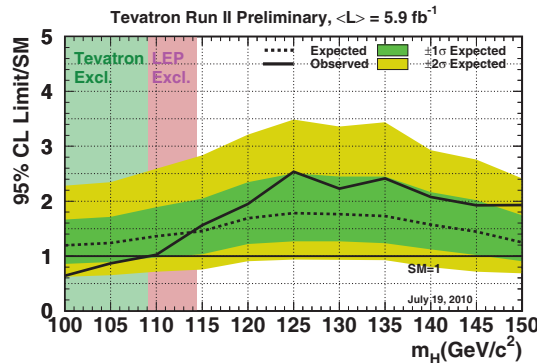


Fig. 9. – The Tevatron combination of Higgs limit for the Higgs mass below 150 GeV.

TABLE I. – Ratios of expected and observed 95% C.L. limit to the SM prediction for the combined CDF and DØ data as a function of the Higgs mass, obtained with the Bayesian and the CL_s method.

Bayesian	100	110	115	120	130	140	150
Expected	1.20	1.36	1.45	1.69	1.76	1.57	1.25
Observed	0.64	1.02	1.56	1.95	2.23	2.07	1.93
CL_s	100	110	115	120	130	140	150
Expected	1.17	1.36	1.50	1.66	1.78	1.56	1.20
Observed	0.61	1.06	1.64	2.05	2.38	2.07	1.79

combined search is expected to improve significantly in the future as more data are added and future improvements are made to our analysis techniques. We may start to see some deviation between the observed and expected limits if the Higgs boson does exist somewhere in the low mass range. In order to test that, we did the exercise of injecting a standard model Higgs boson signal at $m_H = 115 \text{ GeV}/c^2$ in several CDF low mass channels. The new exclusion limit is shown in fig. 10, which jumps up like it had a 1σ fluctuation on a rather large mass range, over the limits where the Higgs signal is absent. The effect would be more pronounced with more channels including DØ's.

5. – Future prospects

Figure 11 shows the higgs sensitivity obtained over time from CDF, which improves better than $1/\sqrt{L}$. The sensitivity has been improved more than a factor of 2 since 2005. The shaded band is what we expected with future improvements. Figure 12 shows the luminosity required to achieve the expected number of sigma as a function of the Higgs boson mass. With 10 fb^{-1} data, the Tevatron could exclude a significant fraction of the low mass Higgs allowed region.

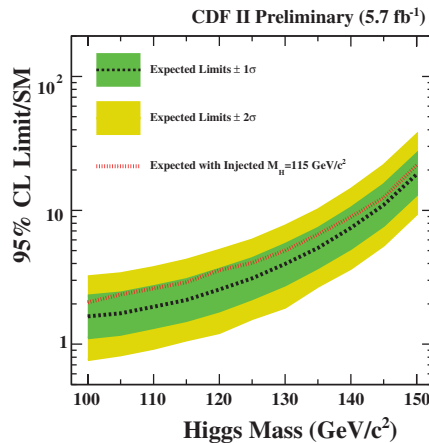


Fig. 10. – The CDF VH limit by injecting the SM Higgs signal.

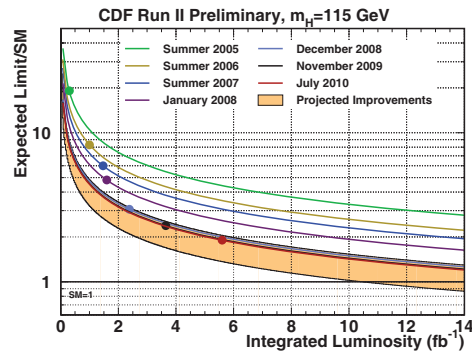


Fig. 11. – The Higgs sensitivity obtained over time from CDF, which improves better than $1/\sqrt{L}$.

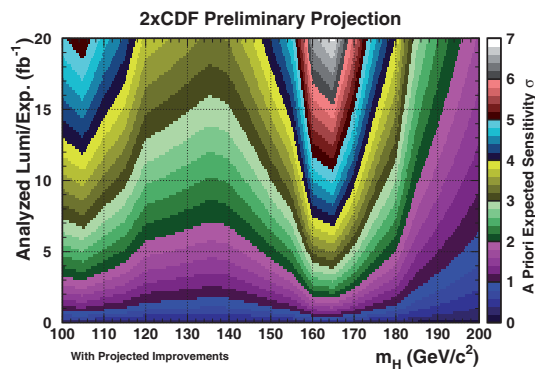


Fig. 12. – The Tevatron luminosity required to achieve certain Higgs sensitivity as a function of the Higgs mass.

6. – Conclusion

We present the recent results of searches for a low mass standard model Higgs boson by the CDF and D0 experiments at the Tevatron $p\bar{p}$ collider at $\sqrt{s} = 1.96$ TeV. The data correspond to an integrated total luminosity up to 5.9 (CDF) and 6.7 (D0) fb^{-1} of $p\bar{p}$ collisions. No excess is observed above background expectation, and resulting limits on Higgs boson production are a factor of 1.56 times the value of the SM cross section for a Higgs boson mass of $m_H = 115 \text{ GeV}/c^2$.

The Tevatron is doing remarkably well and has delivered an integrated luminosity of more than 10 fb^{-1} . Both CDF and D0 continue to add additional Higgs sensitivity with “no channel too small” strategies. With a 10 fb^{-1} analyzable dataset and improved analysis, the Tevatron could exclude a significant fraction of the low mass Higgs allowed region by the winter of 2012. Unfortunately, the Tevatron is scheduled to shutdown at the end of FY2011, but the ideas and techniques developed at the Tevatron will certainly benefit LHC.

* * *

We would like to thank the organizers of *Les XXV Rencontres de Physique de la Vallée d’Aoste* for a wonderful conference with excellent presentations and to thank the

CDF and DØ Collaborations for the results presented at this conference. Special thanks go to J. YAO, A. WARBURTON, C. GROUP, and E. JAMES for their useful comments.

REFERENCES

- [1] CDF and DØ COLLABORATION, *Combined CDF and DØ Upper Limits on Standard Model Higgs-Boson Production with up to 6.7fb^{-1} of Data*, arXiv:1007.4587v1 (2010).
- [2] BUEHLER M., *Search for a High Mass SM Higgs Boson at the Tevatron*, these proceedings.
- [3] ATLAS COLLABORATION, *ATLAS: Detector and physics performance technical design report*, Vol. **2**, CERN-LHCC-99-15.
- [4] CDF COLLABORATION, *Phys. Rev. D*, **82** (2010) 112005.
- [5] DØ COLLABORATION, *Phys. Rev. Lett.*, **103** (2009) 092001.
- [6] CDF COLLABORATION, *Phys. Rev. Lett.*, **104** (2010) 101801.
- [7] DØ COLLABORATION, *Phys. Rev. Lett.*, **102** (2009) 161801.
- [8] AALTONEN T., BUZATU A., KILMINSTER B., NAGAI Y. and YAO W., *Improved b-jet Energy Correction for $H \rightarrow b\bar{b}$ Searches at CDF*, submitted to *Nucl. Instrum. Methods*.
- [9] CDF COLLABORATION, *Search for Standard Model Higgs boson production in association with a W boson using Neural Network techniques with 5.7fb^{-1}* , CDF Conference Note 10239 (2010); *Search for Standard Model Higgs boson production in association with a W boson using Matrix Elements techniques with 5.7fb^{-1}* , CDF Conference Note 10217 (2010).
- [10] DØ COLLABORATION, *Search for WH associated production with 5.3fb^{-1} of Tevatron data*, DØ Conference Note 6092 (2010).
- [11] CDF COLLABORATION, *A Search for Standard Model Higgs boson production in the process $ZH \rightarrow l^+l^-b\bar{b}$ using 5.7fb^{-1} of CDF II Data*, CDF Conference Note 10235 (2010). *A Search for the Standard Model Higgs boson in the process $ZH \rightarrow l^+l^-b\bar{b}$ using a loosened muon selection*, CDF Conference Note 10221 (2010).
- [12] DØ COLLABORATION, *A Search for $ZH \rightarrow l^+l^-b\bar{b}$ Production in 6.2fb^{-1} of data with the DØ detector in $p\bar{p}$ collisions at $\sqrt{s} = 1.96\text{TeV}$* , DØ Conference Note 6089 (2010).
- [13] CDF COLLABORATION, *Search for the Standard Model Higgs boson in the \cancel{E}_T plus jets sample*, CDF Conference Note 10212 (2010).
- [14] DØ COLLABORATION, *Phys. Rev. Lett.*, **104** (2010) 071801.

Search for a high mass SM Higgs boson at the Tevatron

M. BUEHLER on behalf of the CDF and DØ COLLABORATIONS

*University of Virginia, Physics Department - 382 McCormick Rd, Charlottesville
VA 22904-4714, USA*

(ricevuto il 29 Settembre 2011; pubblicato online il 24 Gennaio 2012)

Summary. — The Higgs mechanism accommodates the observed breaking of electroweak symmetry in the standard model (SM). In addition to generating masses for the electroweak W and Z bosons, as well as for fermions, the theory predicts a new scalar Higgs boson with well-determined couplings, but unknown mass. Confirmation of the existence and properties of the Higgs boson would be a key step in elucidating the origins of electroweak symmetry breaking. This paper summarizes the status of the search for a high mass ($m_H > 135$ GeV) SM Higgs boson at Fermilab's Tevatron $p\bar{p}$ accelerator. In the absence of a Higgs signal the Tevatron excludes at the 95% C.L. the production of a SM Higgs boson in the mass range of 158–175 GeV.

PACS 13.85.Rm – Limits on production of particles.

PACS 14.80.Bn – Standard-model Higgs bosons.

1. – High mass searches

No single Higgs search channel has reached SM sensitivity yet. Therefore, all feasible production and decay modes need to be explored and combined. Since $\frac{S}{\sqrt{B}}$ ratios are generally very low, it is impossible to perform traditional cut-based analyses. Instead, Multivariate Analysis Techniques (MVA) are required for signal extraction. This includes Matrix Element (ME) calculations, Neural Networks (NN) and Boosted Decision Trees (BDT) [1].

The main Higgs production mode at the Tevatron is through the gluon fusion process ($gg \rightarrow H$). Associated production ($q\bar{q} \rightarrow VH$) and vector boson fusion ($q\bar{q} \rightarrow q\bar{q}H$) contribute to a lesser degree:

- $\sigma(gg \rightarrow H) = 0.2\text{--}1$ pb
- $\sigma(q\bar{q} \rightarrow VH) = 0.01\text{--}0.3$ pb
- $\sigma(q\bar{q} \rightarrow q\bar{q}H) = 0.01\text{--}0.1$ pb.

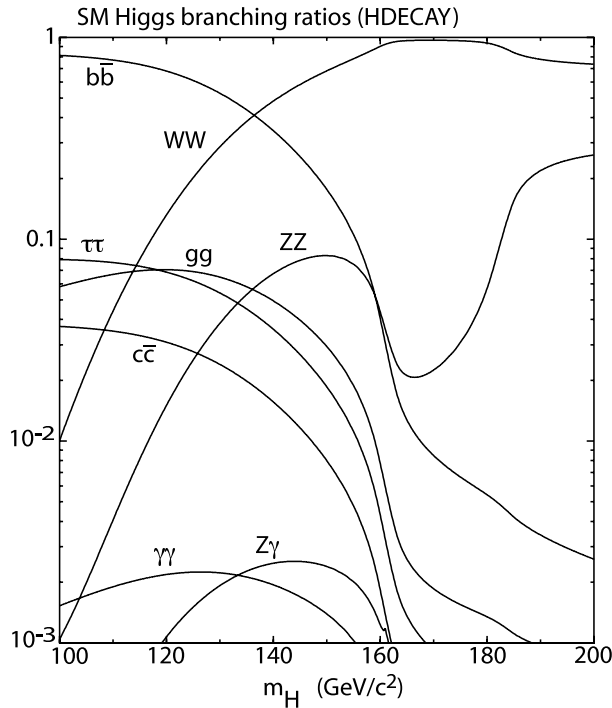


Fig. 1. – SM Higgs boson branching fractions as a function of the Higgs mass.

Figure 1 illustrates that for $m_H > 135$ GeV the Higgs boson predominantly decays into pairs of W vector bosons ($H \rightarrow WW$), which makes this decay mode the preferred mode for high mass SM Higgs searches at the Tevatron. The case where both W vector bosons decay leptonically presents the most sensitive final state ($H \rightarrow WW \rightarrow l\nu l\nu$). More recently, the “semi-leptonical” final state has been incorporated ($H \rightarrow WW \rightarrow l\nu qq$).

The overall strategy of the Tevatron Higgs program is to create as many analysis sub-channels as allowed by statistics, in order to tune multivariate discriminants on different mixes of signal and background contributions. The following chapter gives an overview of the high mass Tevatron Higgs search program.

1.1. $gg \rightarrow H \rightarrow WW \rightarrow l\nu l\nu$. – This channel yields a final state with two oppositely charged leptons (e, μ) and a large amount of missing transverse energy (MET) in the calorimeter. Additionally, one can take advantage of spin correlations. Due to the scalar nature of the Higgs boson, di-lepton pairs from signal tend to be more aligned, while dilepton pairs from SM backgrounds are emitted back-to-back. Background from non-resonant W pair production can be suppressed in this way (fig. 2).

Backgrounds from Drell-Yan processes ($Z \rightarrow ll$) can be suppressed by cutting on MET (fig. 3).

1.1.1. CDF Searches. Based on a 5.9 fb^{-1} data set, this analysis is split into 4 sub-channels:

- By requiring no jets in the final state, the main background is due to WW pairs (fig. 4). This sub-channel uses a likelihood ratio based on ME calculations as an additional MVA input.

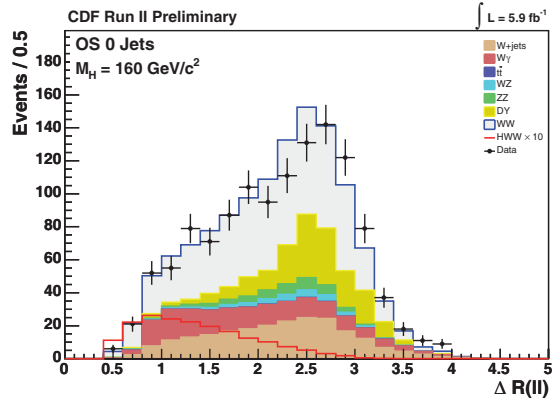


Fig. 2. – ΔR between the two leptons.

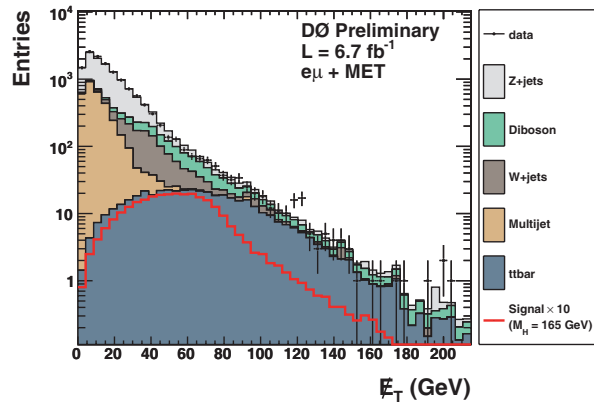


Fig. 3. – Missing transverse energy (MET).

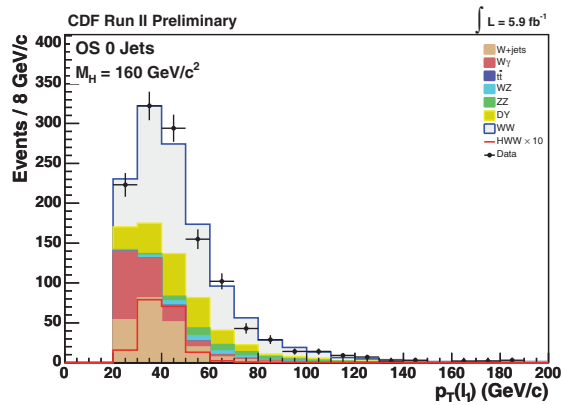


Fig. 4. – Transverse momentum of the leading lepton in the 0 jet sample.

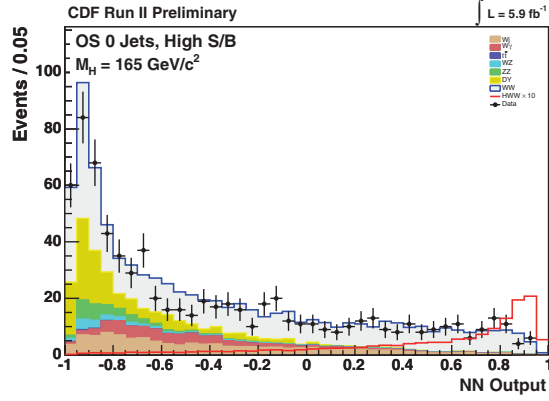


Fig. 5. – NN output for the 0 jet sample.

- By requiring one jet in the final state, the main background is due to Drell-Yan pairs. This sub-channel gains an additional $\approx 20\%$ in signal from associated production and vector boson fusion processes.
- By requiring at least two jets in the final state, the main background is due to top pair production. This background is suppressed by requiring a tight secondary vertex b -tag.
- Additional signal acceptance is recovered by creating a separate sub-channel for events with low di-lepton invariant mass ($M_{ll} < 16$ GeV). In this case the dominant background is due to $W\gamma$ events.

NNs are used to extract the signal. Separate NNs are trained for each sub-channel and each Higgs mass hypothesis. Figure 5 shows the NN distributions for the 0 jet sample.

1.1.2. DØ Searches. Various sub-channels are created by separating lepton final states and jet multiplicities:

- Using 6.7fb^{-1} of data the $H \rightarrow WW \rightarrow e\nu\mu\nu$ analysis is further split into sub-channels by jet multiplicity (0 jets, 1 jet, ≥ 2 jets). $Z \rightarrow \tau\tau$ backgrounds dominate in the 0 jets and 1 jet sub-channels, while $t\bar{t}$ dominates in the ≥ 2 jets case.
- Using 5.4fb^{-1} of data the $H \rightarrow WW \rightarrow l\nu l\nu$ analysis is further split into sub-channels by lepton flavor (ee -channel and $\mu\mu$ -channel). $Z \rightarrow ll$ and $W + \text{jets}$ backgrounds dominate.

Depending on the final-state lepton flavor composition different instrumental and physics backgrounds as well as lepton momentum resolutions come into play. Therefore, separate MVAs are trained for the ee , $\mu\mu$ and $e\mu$ sub-channels. In case of the ee and $\mu\mu$ sub-channels NNs are used for signal extraction (fig. 6). The $e\mu$ sub-channel uses a BDT (fig. 7).

1.2. Same-sign lepton and trilepton searches. – Events with same-sign leptons ($WH \rightarrow WWW \rightarrow l^{+(-)}l^{+(-)} + X$) and three leptons ($VH \rightarrow VWW \rightarrow lll + X$) in the final state originating from associated production processes are examined in a separate analysis effort.

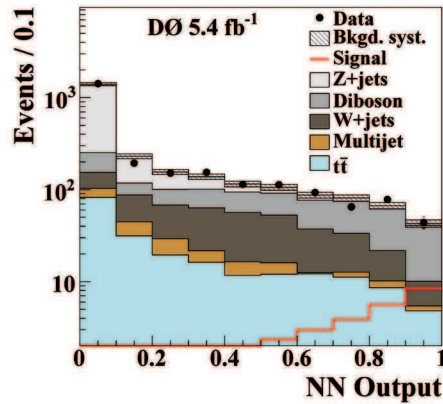


Fig. 6. – NN output for the $l\nu l\nu$ sample ($l = e, \mu$).

1.2.1. CDF Searches. Based on a 5.9 fb^{-1} data set both same-sign and tripleton final states are considered.

The tripleton final states are further split. A sample with same-flavor, opposite-sign dilepton pairs (“inside of Z peak”) enhances sensitivity to ZH production, while a sample with same-flavor, same-sign dilepton pairs (“outside of Z peak”) enhances sensitivity to WH production. NNs are used for signal extraction.

1.2.2. $D\emptyset$ Searches. Based on a 5.4 fb^{-1} data set same-sign lepton final states are considered.

This analysis is further divided into sub-channels based on lepton flavors ($ee, e\mu, \mu\mu$). Charge flip backgrounds are dominating, requiring good lepton charge ID. A BDT is used for signal extraction.

1.3. *Hadronic tau channel.* – Based on a 5.9 fb^{-1} data set hadronic taus in the final state are considered ($H \rightarrow WW \rightarrow l\nu\tau_{had}\nu$).

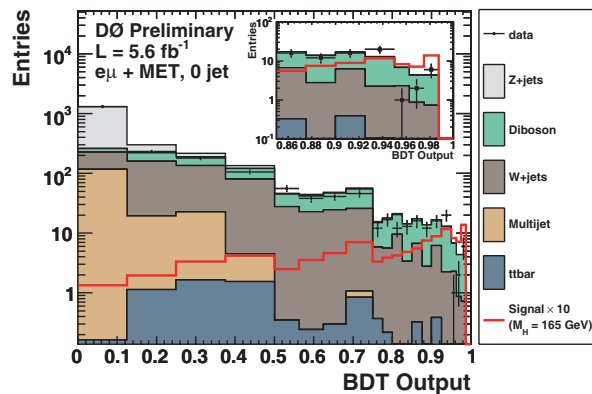


Fig. 7. – Boosted Decision Tree (BDT) output for $e\nu\mu\nu$ sub-channel.

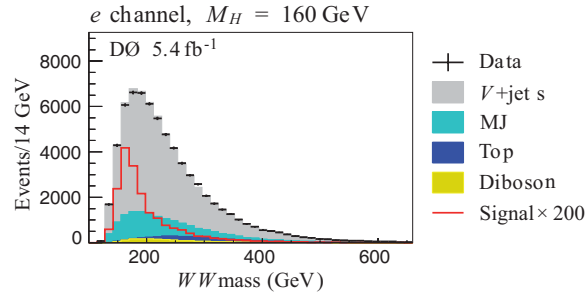
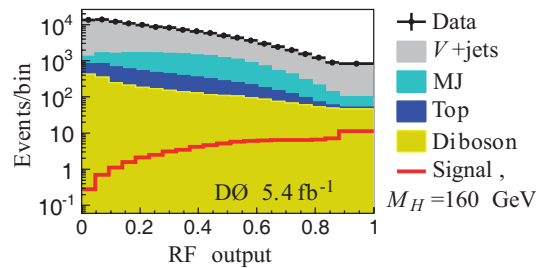
Fig. 8. – WW invariant mass.

Fig. 9. – Random Forest output.

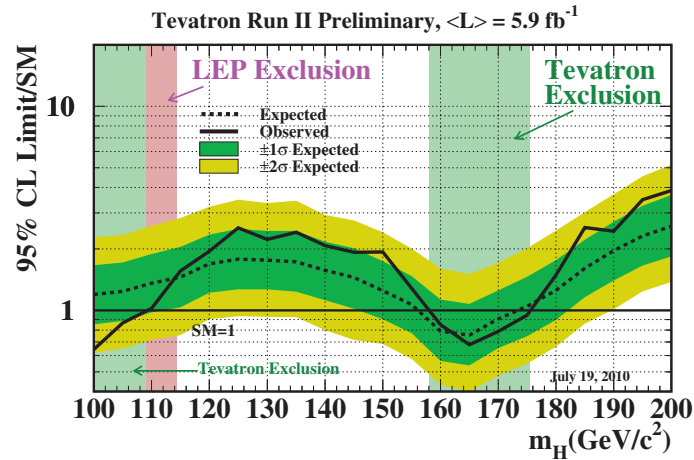


Fig. 10. – Observed and expected (median, for the background-only hypothesis) 95% C.L. upper limits on the ratios to the SM cross section, as functions of the Higgs boson mass for the combined CDF and DZero analyses. The limits are expressed as a multiple of the SM prediction for test masses (every $5 \text{ GeV}/c^2$) for which both experiments have performed dedicated searches in different channels. The points are joined by straight lines for better readability. The band indicate the 68% and 95% probability regions where the limits can fluctuate, in the absence of signal. The limits displayed in this figure are obtained using a Bayesian calculation.

1.4. *Semi-leptonic channel.* – Based on a 5.4 fb^{-1} data set events with semi-leptonic final states are considered ($H \rightarrow WW \rightarrow lvqq$) [2].

This analysis is split into two sub-channels by lepton flavor (e, μ). The large branching

fraction of hadronic W decays increases $\sigma \times \text{BR}$ by ≈ 6 . However, large backgrounds mainly from $W + \text{jets}$ events require a good background model. By imposing a constraint on the W mass it is possible to reconstruct the z -component of the neutrino momentum (p_z). This allows to reconstruct the Higgs mass for $m_H > 160 \text{ GeV}$ (fig. 8). A Random Forest is used for signal extraction (fig. 9).

2. – Combination and limits

No significant excess of signal-like events is observed in any of the aforementioned search channels. Therefore, MVA outputs are used to set exclusion limits at the 95% C.L. [3]. Combining results from both low mass and high mass SM Higgs searches, fig. 10, shows the combined Tevatron exclusion limits. The production of a SM Higgs boson is excluded at the 95% C.L. in the mass range of 158–175 GeV.

3. – Summary and outlook

The Tevatron limits presented so far are based on $\approx 6 \text{ fb}^{-1}$ of data. When Tevatron data taking has ended 10 fb^{-1} will be available for analysis. With this data set it will be possible to have $> 2.4\sigma$ expected sensitivity for Higgs masses of 100–200 GeV, and 3σ expected sensitivity for $m_H = 115 \text{ GeV}$.

$gg \rightarrow H$ cross sections for this measurements are obtained from ref. [4] and ref. [5]. For more details concerning ingredients for the Tevatron Higgs search limits see ref. [6] and ref. [7].

REFERENCES

- [1] BREIMAN L., *Machine Learning*, **45** (2001) 5.
- [2] DØCOLLABORATION, *Phys. Rev. Lett.*, **106** (2011) 171802.
- [3] CDF COLLABORATION, DØCOLLABORATION, TEVATRON NEW PHYSICS AND HIGGS WORKING GROUP, arXiv:1007.4587 [hep-ex].
- [4] DE FLORIAN D. and GRAZZINI M., arXiv:0901.2427 [hep-ph].
- [5] ANASTASIOU C., BOUGHEZAL R. and PETRIELLO F., arXiv:0811.3458 [hep-ph].
- [6] http://tevnpwg.fnal.gov/results/SMHPubWinter2010/gghtheoryreplies_may2010.html
- [7] http://tevnpwg.fnal.gov/results/SM_Higgs_Summer_10/addendumresponse_oct2010.html

The Tevatron Higgs exclusion limits and theoretical uncertainties

A. DJOUADI

*Laboratoire de Physique Théorique, Université Paris-Sud and CNRS - F-91405 Orsay, France
Theory Unit, Department of Physics, CERN - CH-1211 Geneva 23, Switzerland*

(ricevuto il 29 Settembre 2011; pubblicato online il 24 Gennaio 2012)

Summary. — We discuss the exclusion limits set by the CDF and D0 experiments on the Higgs sector from their Higgs boson searches at the Tevatron in the light of large theoretical uncertainties that affect the signal (and background) production cross sections. In the context of the Standard Model, when the theoretical uncertainties stemming from strong (and to a much lesser extent, electroweak) interaction effects are consistently taken into account, the sensitivity of the two experiments becomes significantly lower and the currently excluded Higgs mass range could be entirely reopened. In the Minimal Supersymmetric extension of the Standard Model where the Higgs sector is enlarged to contain two doublet scalar fields, including the theoretical uncertainties will also significantly loosen the constraints obtained at the Tevatron on the supersymmetric Higgs sector parameter space.

PACS 14.80.Bn – Standard-model Higgs bosons.

1. – Introduction

The search for the Higgs bosons, the remnants of the spontaneous breaking of the electroweak symmetry that is at the origin of the elementary particle masses, is the main goal of present high-energy colliders. While a single Higgs boson is predicted in the Standard Model (SM), the minimal realization of the symmetry breaking with only one Higgs doublet field [1], the Higgs sector is extended in supersymmetric theories [2], that are widely considered to be the most attractive extensions of the SM as they stabilize the hierarchy between the electroweak and Planck scales induced by the large radiative corrections to the Higgs boson mass. In the minimal extension, the Minimal Supersymmetric Standard Model (MSSM) [2], two Higgs doublet fields are required, leading to the existence of five Higgs particles: two CP-even h and H , a CP-odd A and two charged H^\pm particles [3, 4]. With its successful operation in the last years, the Tevatron $p\bar{p}$ collider has now collected a substantial amount of integrated luminosity which allows the CDF and D0 experiments to be sensitive to these Higgs particles and (for the moment) to set exclusion limits on their masses.

At the Tevatron, the main search channel for the SM Higgs boson is the top and bottom quark loop mediated gluon-gluon fusion mechanism⁽¹⁾ $gg \rightarrow H$ with the Higgs boson decaying into WW pairs which lead to the clean $\ell\nu\ell\bar{\nu}$ final states with $\ell = e, \mu$. Strong constraints beyond the well established LEP bounds [5] have been recently set by the CDF and D0 collaborations on the Higgs mass and the range $M_H = 158\text{--}175\text{ GeV}$ has been excluded at the 95% confidence level (CL) [6].

Nevertheless, this exclusion limit relies crucially on the theoretical predictions for the cross sections of both the Higgs signal and the relevant SM backgrounds which, as is well known, are affected by significant uncertainties. In recent studies [7, 8], it has been re-emphasized that this is indeed the case for the main Higgs search channel at the Tevatron: adding all sources of theoretical uncertainties in a consistent manner, one obtains an overall uncertainty of about $\pm 40\%$ on the $gg \rightarrow H \rightarrow \ell\nu\ell\bar{\nu}$ signal⁽²⁾. This is much larger than the uncertainty assumed in the CDF/D0 analysis, *i.e.* 10% for D0 and 20% for CDF, thus casting some doubts on the resulting exclusion limit.

In this talk, we confront the Tevatron exclusion Higgs limit with the theoretical uncertainties that affect the signal and background rates. We show that when they are included, the sensitivity of the CDF/D0 experiments is significantly lower than the currently quoted one. We find the necessary luminosity that is required to recover the current sensitivities to be substantially higher than the present luminosity. In the case of the MSSM, we also consider the two main production and detection channels: gluon-gluon and bottom quark fusion leading to Higgs bosons (with possibly large rates as a result of enhanced Higgs- $b\bar{b}$ couplings) which subsequently decay into tau leptons, $gg, b\bar{b} \rightarrow \text{Higgs} \rightarrow \tau^+\tau^-$ and show that the theoretical uncertainties will also significantly loosen the constraints obtained on the supersymmetric Higgs sector at the Tevatron.

2. – Theoretical uncertainties

We start by summarizing the impact of the theoretical uncertainties on the $gg \rightarrow H$ signal cross section [10] in the SM which has a threefold problem. First, the perturbative QCD corrections to the cross section turned out to be extremely large: the K -factor defined as the ratio of the higher order to the leading order (LO) cross sections, is about a factor of 2 at next-to-leading order (NLO) and about a factor of 3 at next-to-next-to-leading order (NNLO). It is clear that it is this exceptionally large K -factor which presently allows sensitivity to the Higgs at the Tevatron. Nevertheless, the K -factor is so large that one may question the reliability of the perturbative series and the possibility of still large higher order contributions beyond NNLO cannot be excluded.

The effects of the unknown contributions are usually estimated from the variation of the cross section with the (renormalisation μ_R and factorisation μ_F) scale at which the process is evaluated. Starting from a median scale μ_0 which is taken to be $\mu_R = \mu_F = \mu_0 = \frac{1}{2}M_H$ in the $gg \rightarrow H$ process, the current convention is to vary these two scales within the range $\mu_0/\kappa \leq \mu_R, \mu_F \leq \kappa\mu_0$ with the choice $\kappa = 2$. However, as the QCD corrections are so large in the present case, it is wise to extend the domain of scale

⁽¹⁾ The subleading Higgs-strahlung processes $q\bar{q} \rightarrow WH, ZH$ add a little to the sensitivity, in particular at low Higgs masses; they will not be discussed here.

⁽²⁾ There are also uncertainties on the Higgs decay branching ratios, but they are very small in the excluded M_H range; see ref. [9].

variation and adopt instead a value $\kappa = 3$. This is the choice made in ref. [7] which resulted in an $\mathcal{O}(20\%)$ scale uncertainty⁽³⁾ on $\sigma_{gg \rightarrow H}^{\text{NNLO}}$.

Another problem that is specific to the $gg \rightarrow H$ process is that, already at LO, it occurs at the one-loop level with the additional complication of having to account for the finite mass of the loop particle. This renders the NLO calculation extremely complicated and the NNLO calculation a formidable task. Luckily, one can work in an effective field theory (EFT) approach in which the heavy loop particles are integrated out, making the calculation of the contributions beyond NLO possible. While this approach is justified for the dominant top quark contribution for $M_H \lesssim 2m_t$, it is not valid for the b -quark loop and for those involving the electroweak gauge bosons [12]. The uncertainties induced by the use of the EFT approach at NNLO are estimated to be of $\mathcal{O}(5\%)$ [7].

A third problem is due to the presently not satisfactory determination of the parton distribution functions (PDFs). Indeed, in this gg initiated process, the gluon densities are poorly constrained, in particular in the high Bjorken- x regime which is relevant for the Tevatron. Furthermore, since $\sigma_{gg \rightarrow H}^{\text{LO}} \propto \alpha_s^2$ and receives large contributions at $\mathcal{O}(\geq \alpha_s^3)$, a small change of α_s leads to a large variation of $\sigma_{gg \rightarrow H}^{\text{NNLO}}$. Related to that is the significant difference between the world average α_s value and the one from deep-inelastic scattering (DIS) data used in the PDFs [13]. There is a statistical method to estimate the PDF uncertainties by allowing a 1σ (or more) excursion of the experimental data that are used to perform the global fits. In addition, the MSTW collaboration [14] provides a scheme that allows for a combined evaluation of the PDF uncertainties and the (experimental and theoretical) ones on α_s . In ref. [7], the combined 90% CL PDF + $\Delta^{\text{exp}}\alpha_s + \Delta^{\text{th}}\alpha_s$ uncertainty on $\sigma_{gg \rightarrow H}^{\text{NNLO}}$ at the Tevatron, was found to be of order 15%. However, this method does not account for the theoretical assumptions that enter into the parametrization of the PDFs. A way to access this theoretical uncertainty is to compare the results for the central values of the cross section with the best-fit PDFs when using different parameterizations.

On the left-hand side of fig. 1 are displayed the values of $\sigma_{gg \rightarrow H}^{\text{NNLO}}$ obtained when using the gluon densities that are predicted by the four PDF sets that have parameterizations at NNLO: MSTW [14], JR [15], ABKM [16] and HERAPDF [17]. As can be seen, there is a very large spread in the four predictions, in particular at large M_H where the poorly constrained gluon densities at high- x are involved. The largest rate is obtained with MSTW, but the cross section using the ABKM⁽⁴⁾ set is $\approx 25\%$ – 30% lower than that [18].

A related issue, which is of utmost importance, is the way these various uncertainties should be combined. The CDF and D0 experiments simply add in quadrature the uncertainties from the scale variation and the PDF uncertainties obtained through the Hessian method (and ignore the smaller EFT uncertainty) and they obtain an overall uncertainty of order 20% on the inclusive cross section. We believe (see also ref. [19]) that this procedure has no justification⁽⁵⁾. Indeed, the uncertainties associated to the PDFs

⁽³⁾ See also ref. [11] for another reason to increase the scale uncertainty to 20%.

⁽⁴⁾ In an earlier version of ref. [8], an error resulted in a HERAPDF prediction that was $\approx 40\%$ lower than that of MSTW. We thank Graham Watt for pointing to us the problem.

⁽⁵⁾ There were some responses to the addendum of ref. [7] from CDF and D0 on the tevnp.hwg.fnal.gov web site. While many comments were made on secondary and/or agreed points, the main issue (which explains the difference between our results) is the way to combine the scale and PDF uncertainties, and it was not really addressed.

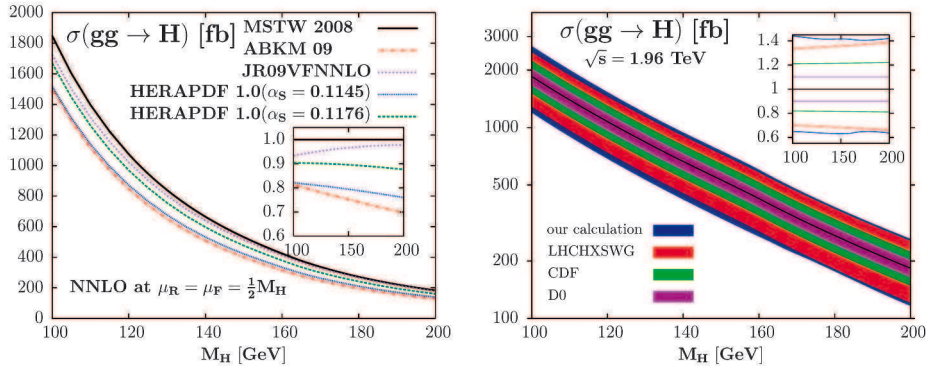


Fig. 1. – Left: the $gg \rightarrow H$ cross section as a function of M_H when the four NNLO PDF sets, MSTW, ABKM, JR and HERAPDF, are used; in the inserts, shown are the deviations with respect to the central MSTW value. Right: $\sigma_{gg \rightarrow H}^{\text{NNLO}}$ at the Tevatron using the MSTW PDFs, with the uncertainty band when all theoretical uncertainties are added as in ref. [7] (BD); it is compared the uncertainties quoted by the CDF and D0 experiments [6] as well as the uncertainty when the LHC procedure [20] is adopted; in the insert, the relative size of the uncertainties compared to the central value are shown.

in a given scheme should be viewed as purely theoretical uncertainties (due to the theoretical assumptions in the parameterization) despite of the fact that they are presented as the 1σ or more departure from the central values of the data included in the PDF fits. In some sense, they should be equivalent to the spread that one observes when comparing different parameterizations of the PDFs. Thus, the PDF uncertainties should be considered as having no statistical ground (or a flat prior in statistical language), and thus, combined linearly with the uncertainties from the scale variation and the EFT approach, which are pure theoretical errors. This is the procedure recommended, for instance, by the LHC Higgs cross section working group [20]. Another, almost equivalent, procedure has been proposed in ref. [7]: one applies the combined PDF- α_s uncertainties directly on the maximal/minimal cross sections with respect to scale variation⁽⁶⁾, and then adds linearly the small uncertainty from the EFT approach. This last procedure, that we have used here, provides an overall uncertainty that is similar (but slightly smaller) to that obtained with the linear sum of all uncertainties.

The overall theoretical uncertainty on $\sigma_{gg \rightarrow H}^{\text{NNLO}}$ that is obtained this way, using MSTW PDFs, is shown on the right-hand side of fig. 2. In the mass range $M_H \approx 160$ GeV with almost the best sensitivity, one obtains a $\approx +41\%$, -37% total uncertainty, to be compared to the $\approx 10\%$ and $\approx 20\%$ uncertainties assumed, respectively, by the CDF and D0 collaborations. We also show for comparison, the result obtained when one adds linearly, *i.e.* as recommended by the LHC Higgs cross section working group, the uncertainties from scale ($+20\%$, -17% on the sum of the jet cross sections⁽⁷⁾) and PDFs

⁽⁶⁾ A similar procedure has also been advocated in ref. [21] for top quark pair production.

⁽⁷⁾ An additional uncertainty of $\approx 7.5\%$ from jet acceptance is introduced when considering the Higgs+jet cross sections. We will consider it to be experimental and, when added in quadrature to others, will have little impact.

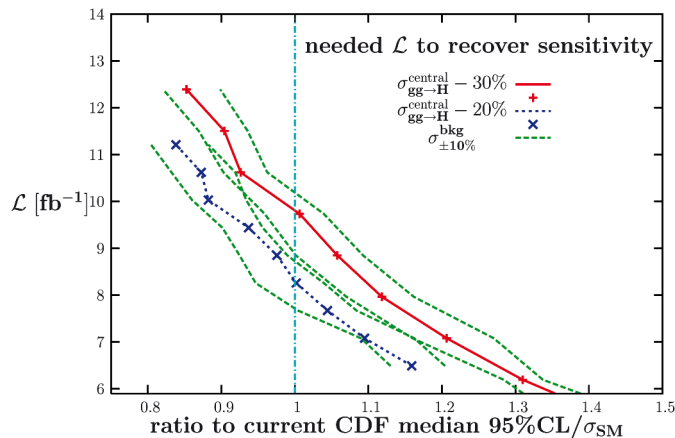


Fig. 2. – The luminosity needed by the CDF experiment to recover the current sensitivity (with 5.9 fb^{-1} data) when the $gg \rightarrow H \rightarrow \ell\nu\nu$ signal rate is lowered by 20 and 30% and with a $\pm 10\%$ change in the $p\bar{p} \rightarrow WW$ dominant background.

(+16%, –15% when the MSTW 68% CL PDF + $\Delta^{\text{exp}}\alpha_s$ error is multiplied by a factor of two following the PDF4LHC recommendation), leading to a total of $\approx +36\%$, –32% for $M_H \approx 160 \text{ GeV}$. Thus, the uncertainty that we assume is comparable to the one obtained using the LHC procedure [20], the difference being simply due to the additional $\mathcal{O}(5\%)$ uncertainty from the use of the EFT approach that we also include.

3. – Emulation of the Tevatron limit

Let us now come to the discussion of the Higgs Tevatron exclusion limit in the light of these theoretical uncertainties. We base our exploration on a CDF study [22] which provides us with all the necessary details. In the analysis of the $gg \rightarrow H \rightarrow WW \rightarrow \ell\nu\nu$ signal, the cross section has been broken into the three pieces which yield different final state signal topologies, namely $\ell\nu\nu + 0$ jet, $\ell\nu\nu + 1$ jet and $\ell\nu\nu + 2$ jets or more. These channels which represent, respectively, $\approx 60\%$, $\approx 30\%$ and $\approx 10\%$ of the total $\sigma_{gg \rightarrow H}^{\text{NNLO}}$ [19], have been studied separately (other channels are irrelevant in practice). Our main goal is to estimate the necessary relative variation of the integrated luminosity needed to reproduce the currently quoted sensitivity of the CDF collaboration, if the normalization of the Higgs signal cross section (as well as the corresponding backgrounds) is different from the one assumed to obtain the results. Our approach consists of the following.

First, we try to reproduce as closely as possible the CDF results using the information given in ref. [22] for a mass $M_H = 160 \text{ GeV}$, for which the sensitivity is almost the best (we will assume that the results are similar in the entire excluded mass range $M_H \approx 158\text{--}175 \text{ GeV}$). Then, we consider scenarios in which the *normalisation* of the Higgs production cross section is reduced. We estimate the *relative variation* of the sensitivity and increase the integrated luminosity until we recover our initial sensitivity. Finally, we assume that the obtained relative variations of the sensitivity as well as the required luminosity to reproduce the initial sensitivity, would be the same for the CDF experiment.

To be as close as possible to the CDF analysis and results [22], we considered their neural network outputs for all the search channels (each one for the signals, backgrounds and

data) to build the background only and the background plus signal hypotheses, implemented them in the program `MCLimit` [23] and used a ratio of log-likelihood “à la LEP” as a test-statistic for which we combined the above channels; this provided the 95% CL/ σ_{SM} sensitivity limit on the Higgs boson at the considered mass of $M_H = 160$ GeV. We obtain median expected and expected 95% CL/ σ_{SM} limits that are satisfactorily close to the those in the CDF analysis.

We consider two scenarios in which the $gg \rightarrow H \rightarrow WW \rightarrow \ell\nu\nu$ signal cross section has been reduced by 20% and 30%. The first one is to account for the difference between the quadratic and (almost) linear ways of combining the individual uncertainties. The second scenario, would be simply to adopt the normalisation obtained using the ABKM PDFs which gives a $\approx 30\%$ reduction of $\sigma_{gg \rightarrow H}^{\text{NNLO}}$. In both cases, the remaining $\approx 20\%$ uncertainty due to scale variation and the EFT will correspond to the overall theoretical uncertainty that has been assumed in the Tevatron analysis.

In each case, the expected signals and the corresponding backgrounds at the Tevatron have been multiplied by a luminosity factor that has been varied. For each value of the luminosity factor, the corresponding median expected 95% CL/ σ_{SM} has been estimated and normalized to the initial sensitivity $S_0 = 1.35$ obtained above. The results are reported in fig. 2 where the Tevatron luminosity is shown as a function of the obtained normalised sensitivity. One sees that if $\sigma_{gg \rightarrow H}^{\text{NNLO}}$ is lowered by 20%, a luminosity of $\approx 8 \text{ fb}^{-1}$, compared to 5.9 fb^{-1} used in [22] would be required for the same analysis to obtain the current sensitivity. If the rate is lower by 40% (as it was the case with our incorrect HERAPDF cross section), the required luminosity should increase to $\approx 13 \text{ fb}^{-1}$, *i.e.* more than a factor of two, to obtain the present CDF sensitivity.

As an additional exercise, we also analyzed the impact of changing the normalization of the background rate by $\pm 10\%$ simultaneously with lowering the signal rate (the correlation between signal and background is implicitly taken into account as we use the results of [22]; we assume though that it is almost the same when another PDF set is adopted). Indeed, it is clear that one should equally consider the same uncertainties in the cross sections of the backgrounds, the by far largest one being $p\bar{p} \rightarrow W^+W^-$. We have evaluated it and found that the uncertainty, when evaluated according to ref. [7], is $\approx 10\%$ larger than what CDF/D0 assume. In addition, if we adopt the ABKM set, one would obtain a rate that is $\approx 10\%$ higher than with MSTW [18]. We will thus consider that $\sigma(p\bar{p} \rightarrow W^+W^-)$ can be $\approx 10\%$ larger/lower than assumed by CDF/D0 and we will consider a third scenario in which the normalization of the $p\bar{p} \rightarrow WW$ background is changed by $\pm 10\%$.

From fig. 2, one clearly sees that increasing/decreasing the background will degrade/improve the sensitivity and a $\approx 10\%$ higher/lower luminosity would be required to recover the sensitivity. Hence, the reduction of the signal by 30% and the increase of the background by 10%, as would be the case if the ABKM PDFs were used for their normalization, would reopen a large part of the mass range $M_H = 158\text{--}175$ GeV excluded by the CDF/D0 analysis with 12.6 fb^{-1} combined data. Hence, we face the uncomfortable situation in which the Higgs exclusion limit depends on the considered PDF.

4. – The case of the MSSM

While a single Higgs boson is predicted in the SM, the Higgs sector is extended in supersymmetric theories [2] to contain five Higgs particles: two [3, 4]. Two parameters are needed to describe the Higgs sector at tree-level: the mass M_A of the pseudoscalar boson and the ratio of vacuum expectation values of the two Higgs fields, $\tan\beta$, that is

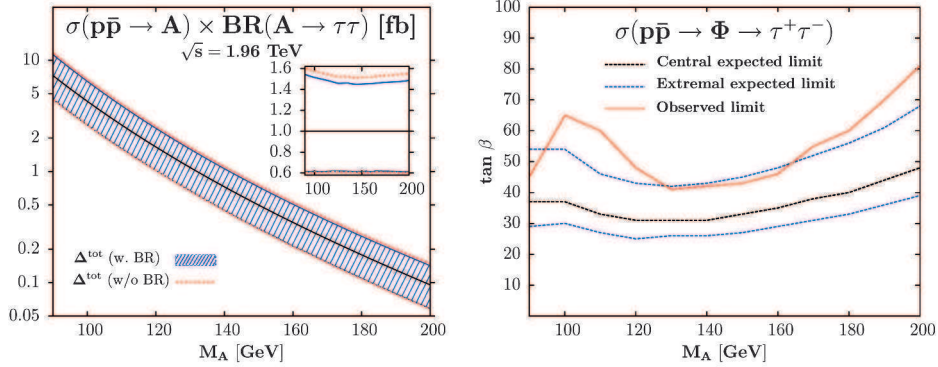


Fig. 3. – Left: $\sigma(p\bar{p} \rightarrow A) \times \text{BR}(A \rightarrow \tau^+\tau^-)$ as a function of M_A at the Tevatron, together with the associated overall theoretical uncertainty. Right: contours for the expected $\sigma(p\bar{p} \rightarrow \Phi \rightarrow \tau^+\tau^-)$ rate at the Tevatron in the $[M_A, \tan\beta]$ plane with the associated theory uncertainties, confronted to the 95% CL exclusion limit.

expected to lie in the range $1 \lesssim \tan\beta \lesssim 50$. At high $\tan\beta$ values, $\tan\beta \gtrsim 10$, one of the neutral CP-even states has almost exactly the properties of the SM Higgs particle: its couplings to fermions and gauge bosons are the same, but its mass is restricted to values $M_H^{\text{max}} \approx 110\text{--}135$ GeV depending on some SUSY parameters that enter the radiative corrections [4]. The other CP-even and the CP-odd states, that we will denote collectively by $\Phi = A, H(h)$, are then almost degenerate in mass and have the same properties: no couplings to gauge bosons, while the couplings to isospin down-type (up-type) quarks and charged leptons are (inversely) proportional to $\tan\beta$.

Thus, for $\tan\beta \gtrsim 10$, the Φ boson couplings to bottom quarks and τ -leptons are strongly enhanced while those to top quarks are suppressed. As a result, the phenomenology of these states becomes rather simple. To a very good approximation, the Φ bosons decay almost exclusively into $b\bar{b}$ and $\tau^+\tau^-$ pairs with branching ratios of, respectively, $\approx 90\%$ and $\approx 10\%$, while the other decay channels are suppressed to a negligible level [24]. The main production mechanisms for these particles are those processes which involve the couplings to bottom quarks. At hadron colliders, these are the gluon-gluon fusion mechanism, $gg \rightarrow \Phi$, which dominantly proceeds through b -quark triangular loops [25] and bottom-quark fusion, $b\bar{b} \rightarrow \Phi$ [26], in which the bottom quarks are directly taken from the protons in a five active flavor scheme. The latter process is similar to the channel $p\bar{p} \rightarrow b\bar{b}\Phi$ when no b -quarks are detected in the final state [27].

In ref. [28], we have updated the cross sections for the production of the MSSM CP-odd like Higgs bosons Φ at the Tevatron in the processes $gg \rightarrow \Phi$ and $b\bar{b} \rightarrow \Phi$ and found smaller rates in the high Higgs mass range compared to those assumed by the Tevatron experiments [29]. We have then evaluated the associated theoretical uncertainties, including also the ones in the $\Phi \rightarrow \tau^+\tau^-$ branching fractions, and find that they are very large; see the left-hand side of fig. 3. These uncertainties, together with the correct normalization, affect significantly the exclusion limits set on the MSSM parameter space from the negative Higgs searches in the channel $p\bar{p} \rightarrow \Phi \rightarrow \tau^+\tau^-$ at the Tevatron.

To visualize the impact of these theoretical uncertainties on the MSSM $[M_A, \tan\beta]$ parameter space that is probed when searching experimentally for the $p\bar{p} \rightarrow \Phi \rightarrow \tau^+\tau^-$ channel, we show on the right-hand side of fig. 3 the contour of the cross section times

branching ratio in this plane, together with the contours when the uncertainties are included. We apply the model independent 95% CL expected and observed limits from the CDF/D0 analysis [29]. However, rather than applying the limits on the central $\sigma \times \text{BR}$ rate, we apply them on the minimal one when the theory uncertainty is included. Indeed, since the latter has a flat prior, the minimal $\sigma \times \text{BR}$ value is as respectable and likely as the central value. One observes then that only values $\tan\beta \gtrsim 50$ are excluded in the mass ranges, $M_{\Phi} \approx 95\text{--}125$ GeV and $M_{\Phi} \gtrsim 165$ GeV. In the intermediate range $M_{\Phi} \approx 125\text{--}165$ GeV, the exclusion limit is $\tan\beta \gtrsim 40\text{--}45$, to be contrasted with the values $\tan\beta \gtrsim 30$ excluded in the CDF/D0 analysis. Hence, the inclusion of the theory uncertainties has a drastic impact on the allowed $[M_A, \tan\beta]$ parameter space.

* * *

I thank the organisers of the special Rencontres de la Vallée d'Aoste for their very kind invitation and for the perfect organisation, with a nice and stimulating atmosphere. I would also like to wish a happy birthday to Mario Greco, with the hope that he will still organise as many Rencontres as did in the past. We acknowledge the project ANR CPV-LFV-LHC NT09-508531 (FR) for support.

REFERENCES

- [1] HIGGS P., *Phys. Lett.*, **12** (1964) 132; ENGLERT F. and BROUT R., *Phys. Rev. Lett.*, **13** (1964) 321.
- [2] For a review see, DREES M., GODBOLE R. and ROY P., *Theory and Phenomenology of Sparticles* (World Scientific) 2004.
- [3] GUNION J., HABER H., KANE G. and DAWSON S., *The Higgs Hunter's Guide* (Addison-Wesley, Reading) 1990.
- [4] For recent reviews, see: DJOUADI A., *Phys. Rep.*, **457** (2008) 1; **459** (2008) 1.
- [5] THE LEP COLLABORATIONS, *Phys. Lett. B*, **565** (2003) 61.
- [6] THE CDF and D0 COLLABORATIONS, *Phys. Rev. Lett.*, **104** (2010) 061802; updated in arXiv:1007.4587 [hep-ex].
- [7] BAGLIO J. and DJOUADI A., *JHEP*, **1010** (2010) 064.
- [8] BAGLIO J., DJOUADI A., FERRAG S. and GODBOLE R., *Phys. Lett. B*, **699** (2011) 368; arXiv:1101.1832 [hep-ph] and erratum to appear.
- [9] BAGLIO J. and DJOUADI A., *JHEP*, **1103** (2011) 055.
- [10] GEORGI H. *et al.*, *Phys. Rev. Lett.*, **40** (1978) 692; DJOUADI A., SPIRA M. and ZERWAS P., *Phys. Lett. B*, **264** (1991) 440; DAWSON S., *Nucl. Phys. B*, **359** (1991) 283; SPIRA M. *et al.*, *Nucl. Phys. B*, **453** (1995) 17; HARLANDER R. V. and KILGORE W., *Phys. Rev. Lett.*, **88** (2002) 201801; ANASTASIOU C. and MELNIKOV K., *Nucl. Phys. B*, **646** (2002) 220; RAVINDRAN V., SMITH J. and VAN NEERVEN W. L., *Nucl. Phys. B*, **665** (2003) 325; CATANI S. *et al.*, *JHEP*, **0307** (2003) 028.
- [11] BERGER C. F. *et al.*, arXiv:1012:4480 [hep-ph].
- [12] ACTIS S. *et al.*, *Nucl. Phys. B*, **811** (2009) 182; ANASTASIOU C. *et al.*, *JHEP*, **0904** (2009) 003.
- [13] NAKAMURA K. *et al.*, *J. Phys. G*, **37** (2010) 075021.
- [14] MARTIN A.D., STIRLING W., THORNE R. and WATT G., *Eur. Phys. J. C*, **63** (2009) 189; *Eur. Phys. J. C*, **64** (2009) 653.
- [15] JIMENEZ-DELGADO P. and REYA E., *Phys. Rev. D*, **80** (2009) 114011.
- [16] ALEKHIN S. *et al.*, *Phys. Rev. D*, **81** (2010) 014032.
- [17] See www.desy.de/h1zeus/combined_results.
- [18] ALEKHIN S. *et al.*, arXiv:1011.6259 [hep-ph].
- [19] ANASTASIOU C. *et al.*, *JHEP*, **0908** (2009) 099.
- [20] DITTMAYER S. *et al.*, *Handbook of LHC Higgs cross sections*, arXiv:1101.0593 [hep-ph].

- [21] CACCIARI M., FRIXIONE S., MANGANO M., NASON P. and RIDOLFI G., *JHEP*, **0809** (2008) 127.
- [22] THE CDF COLLABORATION, CDF note 10232 (16/08/2010).
- [23] JUNK T., *Nucl. Instrum. Methods A*, **434** (1999) 435.
- [24] DJOUADI A., KALINOWSKI J. and SPIRA M., *Comput. Phys. Commun.*, **108** (1998) 56.
- [25] SPIRA M. *et al.*, *Phys. Lett. B*, **318** (1993) 347; SPIRA M., *Fortschr. Phys.*, **46** (1998) 203; hep-ph/9510347.
- [26] HARLANDER R. and KILGORE W., *Phys. Rev. D*, **68** (2003) 013001.
- [27] DITTMAIER S., KRAMER M. and SPIRA M., *Phys. Rev. D*, **70** (2004) 074010; DAWSON S. *et al.*, *Phys. Rev. D*, **69** (2004) 074027.
- [28] BAGLIO J. and DJOUADI A., *Phys. Lett. B*, **699** (2011) 372; arXiv:1103.6247 [hep-ph].
- [29] THE CDF/D0 TEVNPHWG, arXiv:1003.3363 [hep-ex].

The non-standard model Higgs

M. REDI

*INFN - 50019 Sesto Fiorentino, Firenze, Italy and
CERN, Theory Division - CH-1211, Geneva 23, Switzerland*

(ricevuto il 29 Settembre 2011; pubblicato online il 25 Gennaio 2012)

Summary. — This is the write-up of the talk presented at the XXV Rencontres de Physique de La Valle d'Aoste (La Thuile), aimed to introduce the ideas of Composite Higgs Models to an experimental audience. We review the basic features of theories where the Higgs is a composite state and its phenomenological consequences at LHC. We also emphasize the possibility of a heavy Higgs which could provide a first experimental hint on this type of models.

PACS 12.60.-i – Models beyond the standard model.

1. – Introduction

When these proceedings are published the LHC will have hopefully found evidence of the elusive Higgs boson, the only missing piece of the Standard Model (SM). Confirming or rejecting the SM will however likely require significant more work. In this talk I will review Composite Higgs Models (CHM) which are a realistic possibility for the physics beyond the Standard Model. In this scenarios the Higgs boson is a Goldstone boson (GB) of some strongly coupled dynamics, generalizing technicolor ideas. The presence of a physical Higgs allows to obtain models which are in reasonable agreement with experimental data and could be soon tested at the LHC.

2. – Weak or strong dynamics?

The basic question that the LHC will answer is whether the breaking of electro-weak symmetry is due to weak or strong dynamics. In the SM the first option is realized and electro-weak symmetry is broken spontaneously by a scalar doublet of hypercharge 1/2 which acquires a VEV,

$$(1) \quad H(x) = U(x) \begin{pmatrix} 0 \\ v + h(x) \end{pmatrix}, \quad v = 174 \text{ GeV}.$$

$U(x)$ is an $SU(2)$ matrix and h a real scalar. $U(x)$ describes the 3 GBs associated to the breaking: these degrees of freedom are the longitudinal polarization of W and Z and effectively they have been already discovered since we have measured their masses. One important feature is that the Higgs Lagrangian has an approximate global symmetry $SO(4) \sim SU(2)_L \otimes SU(2)_R$ broken spontaneously to $SU(2)_{L+R}$ by the Higgs VEV. This symmetry, known as “custodial”, guarantees the correct ratio of W and Z masses at tree level and is the starting point of any successful theory of electro-weak symmetry breaking. The real scalar $h(x)$ describes the physical Higgs and is the only missing piece within the SM. If the SM is correct the only unknown is the Higgs mass, or equivalently quartic coupling,

$$(2) \quad m_h = \sqrt{\lambda} v.$$

In principle a physical Higgs is not needed to break the electro-weak symmetry. In this case the scattering amplitudes of longitudinal gauge bosons become strongly coupled near the electro-weak scale,

$$(3) \quad A(W_L^+ W_L^- \rightarrow W_L^+ W_L^-) = \frac{1}{2v^2}(s+t),$$

and perturbative unitarity is lost around $\Lambda \sim 2 \text{ TeV}$. This simply indicates that new physics must appear below λ but does not require necessarily a Higgs particle.

Indeed electro-weak symmetry breaking without a Higgs is already realized in nature once. In QCD with two massless flavors electro-weak symmetry is broken by the chiral condensate

$$(4) \quad \langle 0 | \bar{\Psi}_L^i \Psi_R^j + \bar{\Psi}_R^i \Psi_L^j | 0 \rangle = \Lambda_{QCD}^3 \delta_{ij} \longrightarrow \frac{SU(2)_L \otimes SU(2)_R}{SU(2)_{L+R}}.$$

Famously the pions are the GB associated to the spontaneous breaking of chiral symmetry and they would become longitudinal polarizations of W and Z in the absence of other effects. The mass would be only $m_W \simeq g f_\pi \simeq 30 \text{ MeV}$. This clearly does not work phenomenologically but the new strong interaction with the appropriate scale,

$$(5) \quad f = \sqrt{2} v,$$

could very well break the electro-weak symmetry and reproduce, because of the unbroken $SU(2)_{L+R}$ symmetry, the known masses of W and Z bosons. This is the idea of technicolor. In this case the longitudinal polarizations of W and Z are the technipions associated to the chiral symmetry breaking of the technicolor theory. Their scattering, as the one pions, is unitary because they are composite objects made of constituents (techniquarks). There is no analog of the Higgs particle but we expect, in analogy with QCD, techni-resonances of various spin which may also partially unitarize scattering of W and Z .

We emphasize that this is the only truly satisfactory explanation of the separation of fundamental scales that we are aware of. Starting from order one gauge couplings at a high scale, perhaps the Planck scale $M_p = 10^{19} \text{ GeV}$, the coupling grows in the infrared due to the logarithmic running becoming non-perturbative at an exponentially smaller scale. When this happens, similarly to QCD, we expect confinement to take place and a mass gap to be generated. This phenomenon, known as dimensional transmutation,

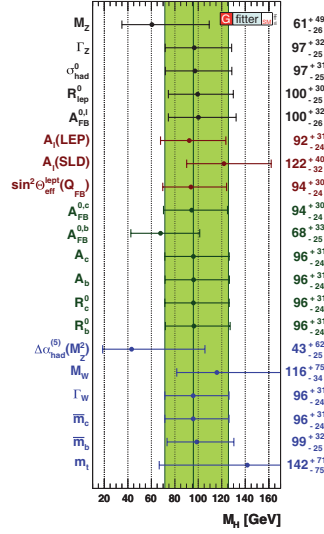


Fig. 1. – Central value of the Higgs mass removing different observables [1].

explains dynamically why the proton is so much lighter than M_p so that there is no hierarchy problem in QCD. It is natural to suspect that a similar mechanism might be at work for the electro-weak scale.

Sadly, at least the simplest versions of technicolor are ruled out: precision electro-weak measurements are problematic and even worse the standard realization of fermion masses generically leads to unacceptably large flavor changing neutral currents which are excluded by experiments by many orders of magnitude.

The situation is very different in the SM. Due to the presence of the physical Higgs there are new diagrams contributing to the scattering of longitudinal gauge bosons. For example one finds,

$$(6) \quad A(W_L^+ W_L^- \rightarrow W_L^+ W_L^-) = \frac{1}{2v^2} \left[s - \frac{s^2}{s - m_h^2} + (s \rightarrow t) \right],$$

so that the amplitude does not grow indefinitely at high energies and the theory remains weakly coupled above the electro-weak scale. Indeed, due to the fact that the theory is renormalizable, it can mathematically be consistent up to very large energies with no need for new physics.

However the SM has without doubts its weaknesses: hierarchy problem, dark matter, origin of flavor and CP violation, etc. Moreover while the SM fits the data extremely well it does not explain why electro-weak symmetry breaking happens. Of these arguments only the first clearly requires new physic at the weak scale. This might be taken as a theoretical prejudice by some so it is worth having a look at the data. The SM model provides a reasonable fit though not perfect. Statistically the probability of the fit is 15% but if only observables most directly related to the Higgs are included this drops to just 2%. In particular the b asymmetry, which is 3σ away from the SM value (the largest deviation), is necessary to pull up the central preferred value of the Higgs mass, in any case below the LEP exclusion limit, see fig. 1. This situation can only be improved with new physics in the TeV range.

3. – Composite Higgs

The idea of a composite Higgs is a natural extension of technicolor theories first studied by Georgi and Kaplan in the '80s and recently revived, see [2] for nice review and references therein. Among the states of the strong sector there could be a scalar doublet which plays the role of the Higgs. This relieves the SM naturalness problem because quadratic divergences of the Higgs mass are physically cut off by the compositeness scale. For example the top quadratic divergence

$$(7) \quad \delta m_h^2 \sim \frac{3y_t^2}{4\pi^2} m_\rho^2.$$

As a consequence the electro-weak scale can be natural if m_ρ is not too large. Conceptually composite Higgs is similar to technicolor since m_ρ can be generated by dimensional transmutation but the presence of a physical Higgs allows to improve significantly the phenomenology as we will see.

This picture is particularly compelling when the Higgs is an approximate Goldstone boson (GB) as it is massless at leading order and its existence is guaranteed by the symmetries. In the simplest realization the strong sector has a global symmetry $SO(5)$ broken spontaneously to $SO(4) \sim SU(2)_L \otimes SU(2)_R$ [3]. This delivers precisely 4 GBs with the quantum numbers of the Higgs doublet and custodially symmetric interactions. Other patterns of symmetry breaking can also be considered [4],

$$(8) \quad \frac{SO(6)}{SO(4) \otimes U(1)}, \quad \frac{SU(5)}{SU(4) \otimes U(1)}, \quad \frac{SU(5)}{SO(5)}, \quad + \dots,$$

leading to an extended Higgs sector. The interaction of GBs are determined by the symmetries and by their decay constant f (analogous to the one of the pions) which is related to the compositeness scale by

$$(9) \quad m_\rho = g_\rho f,$$

g_ρ being the coupling of the strong sector.

The Higgs cannot be an exact GB. In general GBs shift under the *spontaneously* broken symmetries and this symmetry is certainly not respected in the SM, being *explicitly* broken by the SM Yukawas, gauge couplings and by the Higgs potential. The general picture in these models is the following [6]: there is a strong sector which delivers various resonances among which GBs with quantum numbers of the Higgs. At the level of the strong sector the Higgs doublet might be an exact GB in which case it is massless. One important ingredient of modern constructions is the mechanism of partial compositeness. The SM fermions and gauge fields are mostly elementary states⁽¹⁾ which mix with states of the strong sector as allowed by the SM gauge symmetry. This generates Yukawas,

$$(10) \quad y \sim \frac{\lambda_L \lambda_R}{g_\rho}.$$

⁽¹⁾ For the top quark its large mass requires that at least one of the chiralities must be strongly composite, in certain cases it can even be part of the strong sector.

The mixings break explicitly the global symmetry of the strong sector that guarantees the Higgs to be massless. As a consequence a potential is generated at loop level. The main contribution to the potential is normally associated to the top which breaks the global symmetry most strongly but one should keep in mind that other contributions to the potential, not associated to SM interactions, may exist.

Phenomenologically there are two main differences with respect to old technicolor theories which make these models phenomenologically appealing. First, the scale of new resonances m_ρ is not directly linked to the electro-weak VEV. If $m_\rho \gg v$ the composite Higgs approaches the SM Higgs allowing to successfully reproduce all the successes of the SM. In practice however the scale m_ρ should not be very large if the theory shall remain natural (at most few TeV). Secondly, contrary to technicolor, the SM flavor structure is generated by the mixings and this greatly reduces flavor problems. Indeed flavor changing neutral currents turn out to be proportional to the mixing SM fermions which are small for the light generations.

With some caveats a reasonable phenomenology can be imagined with a scale of compositeness of around 3 TeV. Overall the models are far from perfect but the general picture is compelling and worth taking seriously.

4. – Signatures

In the LHC era the relevant question is whether CHM can be distinguished from an elementary SM Higgs. In CHM, as in technicolor, we expect the existence of resonances whose mass roughly determines the compositeness scale. As a consequence at least some of these resonances are expected to be seen, even though this may require high energy and luminosity.

One robust feature is the presence of spin 1 resonances (electro-weak and gluonic) and spin 1/2 resonances of SM fermions. The latter are required by the mechanism of partial compositeness. An important experimental feature, at least in standard scenarios, is that the new resonances are mostly coupled to third generation quarks and to the Higgs, so they will decay into these states.

The main production mechanism of spin 1 resonances is through mixing of SM gauge bosons to composite spin 1 resonances. Colored spin 1/2 resonances could either be produced in pairs through the strong interactions or singly produced through weak-interactions. In certain cases the mass of these states could be lower than the overall dynamical scale making their discovery less challenging.

The other crucial experimental difference of CHM relative to the SM are the modified couplings. The coupling of the Higgs to gauge and matter fields can be parametrized as,

$$(11) \quad \begin{aligned} g_{hW^+W^-} &= i\sqrt{2}\frac{m_W^2}{v} a, \\ g_{h^2W^+W^-} &= i\frac{m_W^2}{2v^2} b, \\ g_{hf\bar{f}} &= -i\frac{m_f}{\sqrt{2}v} c. \end{aligned}$$

The SM model predicts $a = b = c = 1$. This choice also guarantees that the theory remains perturbative, since the Higgs exactly unitarizes WW scattering and the theory is renormalizable.

This does not hold in CHM because the SM vertices are corrected, proportionally to v^2/f^2 to leading order. These corrections are moreover calculable, depending on the symmetry structure and representations of the theory. Measuring deviations from $a = b = c = 1$ would directly test the idea of a composite Higgs. In particular, WW scattering is only partially unitarized and, as in technicolor, new strong interactions are necessary, even though at a higher energy scale. Moreover production and decay of the Higgs will be modified. Practically however, unless $f \sim v$ these deviations from SM couplings will be very hard to be seen at the LHC and will likely require precision measurements at the linear collider.

There might be however a short-cut. The experimental success of the SM requires the Higgs to be light, most likely below 200 GeV. A discovery of a heavy Higgs would immediately rule out the SM and would require new physics at a relatively low scale in order to reproduce precision tests.

In CHM there is no *a priori* reason why the Higgs should be light. Indeed if the Higgs mass is natural a heavy Higgs is favored. Consider the quadratic divergences associated to the top (7). The fine tuning required to have a mass m_h can be estimated as,

$$(12) \quad \text{tuning} \equiv \frac{m_h^2}{\delta m_h^2} \approx \left(\frac{4m_h}{m_\rho} \right)^2.$$

Phenomenologically the compositeness scale m_ρ should be at least 3 TeV so that the tuning is already few percent. A small fine tuning can be achieved if the Higgs is somewhat heavy. Alternatively the top quadratic divergences should be cut off at a lower scale which can be realized in specific models but is not generic.

One can see that the Higgs is naturally heavy if the coupling of the strong sector is large. There can be in general several contributions to the potential [6]. One unavoidable contribution is due to the Yukawa couplings, the top being the largest. The GB nature of the Higgs allows to estimate the potential to all orders in the Higgs as

$$(13) \quad N_c \frac{y_t^2}{8\pi^2} \times \frac{m_\rho^4}{g_\rho^2} \times \hat{V}_{yuk}(H/f),$$

where $N_c = 3$ is the number of colors. This can be obtained by naturalness matching with the quadratic term (7). In absence of tuning \hat{V} will have no hierarchies and the natural VEV of H is f . In practice one accepts a modest fine tuning of the quadratic terms so that $f > v$. This implies that one can expand the potential to quartic order to determine the Higgs VEV. Extracting the quartic from the potential one obtains the estimate

$$(14) \quad m_h^2 \sim N_c \left(\frac{g_\rho}{4\pi} \right)^2 y_t^2 v^2.$$

For large g_ρ the Higgs can already be above 200 GeV. Depending on the model even larger contributions to the potential may exist, generating an heavier Higgs. For example Higgs dependent kinetic terms by naturalness generate contributions to the potential

$$(15) \quad N_c \frac{\lambda_{L,R}^2}{16\pi^2} \times \frac{m_\rho^4}{g_\rho^2} \times \hat{V}_{kin}(H/f)$$

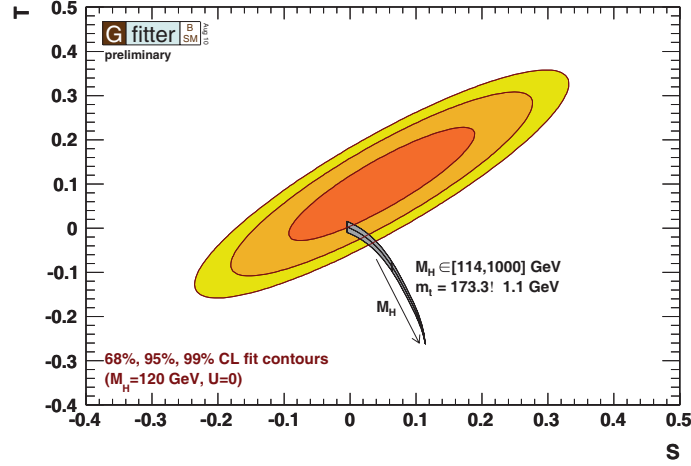


Fig. 2. – Standard Model S and T plane [1]. Large Higgs mass quickly drives the SM out of the allowed region.

which can be larger than the previous if $\lambda_L > y_t$. In this case one finds

$$(16) \quad m_h^2 \sim N_c \left(\frac{g_\rho}{4\pi} \right)^2 y_t g_\rho v^2,$$

which is easily above 200 GeV.

Inserting the Higgs mass in (12) we obtain,

$$(17) \quad \text{tuning} \sim \frac{v^2}{f^2},$$

which shows that the tuning is controlled by f (smaller than m_ρ at strong coupling), despite the fact that physically that loops are cut off at m_ρ . This is consistent with the fact that the Higgs is heavy.

As shown in fig. 2, in the SM a heavy Higgs is ruled out by the data. While the contribution to S of a heavy Higgs is relatively small, the negative contribution to T drives quickly the SM outside of the allowed region. Within the SM this strongly favors the presence of a light a Higgs which must be lighter than 158 GeV at 2σ CL (225 GeV at 3σ CL). As a consequence a heavy Higgs must be accompanied by positive contributions to T which can only arise in the presence of new physics around the TeV scale⁽²⁾.

The correction to T is even more necessary in CHM for two reasons. First with $m_\rho \sim 3$ TeV we expect (positive) contributions to the S parameter of the order of the experimental uncertainty. Moreover the modified couplings of the Higgs to W bosons gives an extra-negative contributions to the T parameter [7]. Depending on the mass of the Higgs a positive contribution to T in the range 0.2–.04 is typically necessary to agree with precision electro-weak tests.

⁽²⁾ Yet, this new physics might be beyond the experimental reach of LHC.

Sizable contributions to T can certainly arise from the next states of theory around the scale m_ρ . In particular the mixing of quark doublets with singlets of the strong sector can give a large positive contribution if it dominates. Whether the required contribution to T is obtained remains model dependent but it is conceivable.

To summarize, our point of view is that a heavy Higgs does not worsen significantly the status of electro-weak precision tests in CHM while it is suggested by naturalness of the electro-weak scale, improving the little hierarchy problem between m_ρ and v . Finding a heavy Higgs at the LHC would immediately rule out the SM and provide a significant hint for compositeness. This an exciting possibility because LHC should be able to discover a Higgs up to 500 GeV in the near future. Moreover the decay into longitudinal W and Z , which is the main decay channel of a heavy SM Higgs, would be modified (reduced), so that measuring mass and width could allow to see deviations from the SM. If a light Higgs is found distinguishing the SM from CHMs will require much more refined tests or production of resonances at LHC14 with high luminosity.

5. – Conclusions

Finding something like the Higgs in the present LHC run is quite likely. Distinguishing the SM Higgs from a composite Higgs will take energy (14 TeV) and time (hundreds of fb^{-1} of luminosity). Unless it is heavy. In this case the SM will be ruled out with 7 TeV center-of-mass energy by 2012 and differences with SM predictions could be seen even with relatively low luminosity. We have emphasized that in CHM the Higgs can be naturally heavy. If this is realized, the discovery of CHM might be around the corner.

* * *

I would like to thank R. CONTINO, J. MRAZEK, A. POMAROL, R. RATTAZZI, J. SERRA, G. VILLADORO, A. WEILER and A. WULZER for numerous discussions on composite Higgs models and related subjects.

REFERENCES

- [1] HOECKER A. (GFITTER COLLABORATION), *Status of the global electroweak fit of the Standard Model, PoS, EPS-HEP2009* (2009) 366 [arXiv:0909.0961 [hep-ph]].
- [2] CONTINO R., *The Higgs as a Composite Nambu-Goldstone Boson* [arXiv:1005.4269 [hep-ph]].
- [3] AGASHE K., CONTINO R. and POMAROL A., *Nucl. Phys. B*, **719** (2005) 165 [hep-ph/0412089].
- [4] MRAZEK J., POMAROL A., RATTAZZI R., REDI M., SERRA J. and WULZER A., *The Other Natural Two Higgs Doublet Model* [arXiv:1105.5403 [hep-ph]].
- [5] CONTINO R., GROJEAN C., MORETTI M., PICCININI F. and RATTAZZI R., *JHEP*, **05** (2010) 089 [arXiv:1002.1011 [hep-ph]].
- [6] GIUDICE G. F., GROJEAN C., POMAROL A. and RATTAZZI R., *JHEP*, **06** (2007) 045 [hep-ph/0703164].
- [7] BARBIERI R., BELLAZZINI B., RYCHKOV V. S. and VARAGNOLO A., *Phys. Rev. D*, **76** (2007) 115008 [arXiv:0706.0432 [hep-ph]].

Coulomb law and energy levels in a superstrong magnetic field

M. I. VYSOTSKY

Institute of Theoretical and Experimental Physics - Moscow, Russia

(ricevuto il 29 Settembre 2011; pubblicato online il 24 Gennaio 2012)

Summary. — The analytical expression for the Coulomb potential in the presence of a superstrong magnetic field is derived. The structure of hydrogen levels originating from LLL is analyzed.

PACS 11.10.Kk – Field theories in dimensions other than four.

PACS 30.31.J- – Relativistic and quantum electrodynamics (QED) effects in atoms, molecules, and ions.

1. – Introduction

The long awaited discovery of Higgs boson is planned during the next two years at LHC. For the first time what is called now the Higgs phenomenon was used in the Ginzburg-Landau phenomenological theory of superconductivity to expel the magnetic field from a superconductor.

Quite unexpectedly in the superstrong magnetic field a photon also gets a (quasi) mass. In this talk we have discussed this phenomenon and how it affects the atomic energy levels. The talk is based on papers [1].

In what follows the strong magnetic field is $B > m_e^2 e^3$; the superstrong magnetic field is $B > m_e^2/e^3$; the critical magnetic field is $B_{cr} = m_e^2/e$ and we use Gauss units: $e^2 = \alpha = 1/137$.

The Landau radius of an electron orbit in the magnetic field B is $a_H = 1/\sqrt{eB}$ and it is much smaller than the Bohr atomic radius for $B \gg e^3 m_e^2$. For such strong B electrons on Landau levels feel a weak Coulomb potential moving along the magnetic field. In [2] a numerical solution of the Schrödinger equation for a hydrogen atom in strong B was performed. According to this solution the ground level goes to $-\infty$ when B goes to $+\infty$. However, the photon mass leads to the Coulomb potential screening and the ground level remains finite at $B \rightarrow \infty$ [3]. Since the electron at the ground Landau level moves freely along the magnetic field, the problem resembles $D = 2$ QED and we will start our discussion from this theory.

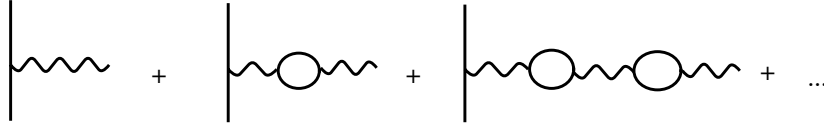


Fig. 1. – Modification of the Coulomb potential due to the dressing of the photon propagator.

2. – $D = 2$ QED: screening of Φ

The following equation for an electric potential of the point-like charge holds; see fig. 1:

$$(1) \quad \Phi(\bar{k}) \equiv A_0(\bar{k}) = \frac{4\pi g}{\bar{k}^2}; \quad \Phi \equiv \mathbf{A}_0 = D_{00} + D_{00}\Pi_{00}D_{00} + \dots$$

Summing the series we get

$$(2) \quad \Phi(k) = -\frac{4\pi g}{k^2 + \Pi(k^2)}, \quad \Pi_{\mu\nu} \equiv \left(g_{\mu\nu} - \frac{k_\mu k_\nu}{k^2} \right) \Pi(k^2),$$

$$(3) \quad \Pi(k^2) = 4g^2 \left[\frac{1}{\sqrt{t(1+t)}} \ln(\sqrt{1+t} + \sqrt{t}) - 1 \right] \equiv -4g^2 P(t),$$

where $t \equiv -k^2/4m^2$, $[g] = \text{mass}$.

Taking $k = (0, k_\parallel)$, $k^2 = -k_\parallel^2$ for the Coulomb potential in the coordinate representation, we get

$$(4) \quad \Phi(z) = 4\pi g \int_{-\infty}^{\infty} \frac{e^{ik_\parallel z} dk_\parallel / 2\pi}{k_\parallel^2 + 4g^2 P(k_\parallel^2/4m^2)},$$

and the potential energy for the charges $+g$ and $-g$ is finally $V(z) = -g\Phi(z)$.

The asymptotics of $P(t)$ are

$$(5) \quad P(t) = \begin{cases} \frac{2}{3}t, & t \ll 1, \\ 1, & t \gg 1. \end{cases}$$

Let us take as an interpolating formula for $P(t)$ the following expression:

$$(6) \quad \bar{P}(t) = \frac{2t}{3 + 2t}.$$

The accuracy of this approximation is not worse than 10% for the whole interval of t

variation, $0 < t < \infty$. Substituting an interpolating formula in (4) we get

$$\begin{aligned}
 (7) \quad \Phi &= 4\pi g \int_{-\infty}^{\infty} \frac{e^{ik_{\parallel}z} dk_{\parallel} / 2\pi}{k_{\parallel}^2 + 4g^2(k_{\parallel}^2/2m^2)/(3 + k_{\parallel}^2/2m^2)} \\
 &= \frac{4\pi g}{1 + 2g^2/3m^2} \int_{-\infty}^{\infty} \left[\frac{1}{k_{\parallel}^2} + \frac{2g^2/3m^2}{k_{\parallel}^2 + 6m^2 + 4g^2} \right] e^{ik_{\parallel}z} \frac{dk_{\parallel}}{2\pi} \\
 &= \frac{4\pi g}{1 + 2g^2/3m^2} \left[-\frac{1}{2}|z| + \frac{g^2/3m^2}{\sqrt{6m^2 + 4g^2}} \exp\left(-\sqrt{6m^2 + 4g^2}|z|\right) \right].
 \end{aligned}$$

In the case of heavy fermions ($m \gg g$) the potential is given by the tree level expression; the corrections are suppressed as g^2/m^2 .

In the case of light fermions ($m \ll g$)

$$(8) \quad \Phi(z)|_{m \ll g} = \begin{cases} \pi e^{-2g|z|}, & z \ll \frac{1}{g} \ln\left(\frac{g}{m}\right), \\ -2\pi g \left(\frac{3m^2}{2g^2}\right) |z|, & z \gg \frac{1}{g} \ln\left(\frac{g}{m}\right), \end{cases}$$

$m = 0$ corresponds to the Schwinger model; the photon gets a mass.

Light fermions make the transition from $m > g$ to $m = 0$ continuous.

3. - $D = 4$ QED

In order to find the potential of a point-like charge we need an expression for P in strong B . One starts from the electron propagator G in strong B . The solutions of the Dirac equation in the homogeneous constant in time B are known, so one can write the spectral representation of the electron Green function. The denominators contain $k^2 - m^2 - 2neB$, and for $B \gg m^2/e$ and $k_{\parallel}^2 \ll eB$ in sum over levels the lowest Landau level (LLL, $n = 0$) dominates. In the coordinate representation a transverse part of LLL wave function is $\Psi \sim \exp((-x^2 - y^2)eB)$ which in the momentum representation gives $\Psi \sim \exp((-k_x^2 - k_y^2)/eB)$ (we suppose that B is directed along the z -axis).

Substituting the electron Green functions we get the expression for the polarization operator in superstrong B .

For $B \gg B_{cr}$, $k_{\parallel}^2 \ll eB$ the following expression is valid [4]:

$$\begin{aligned}
 (9) \quad \Pi_{\mu\nu} &\sim e^2 eB \int \frac{dq_x dq_y}{eB} \exp\left(-\frac{q_x^2 + q_y^2}{eB}\right) \\
 &* \exp\left(-\frac{(q+k)_x^2 + (q+k)_y^2}{eB}\right) dq_0 dq_z \gamma_{\mu} \frac{1}{\hat{q}_{0,z} - m} (1 - i\gamma_1 \gamma_2) \gamma_{\nu} \\
 &* \frac{1}{\hat{q}_{0,z} + \hat{k}_{0,z} - m} (1 - i\gamma_1 \gamma_2) = e^3 B * \exp\left(-\frac{k_{\perp}^2}{2eB}\right) * \Pi_{\mu\nu}^{(2)}(k_{\parallel} \equiv k_z).
 \end{aligned}$$

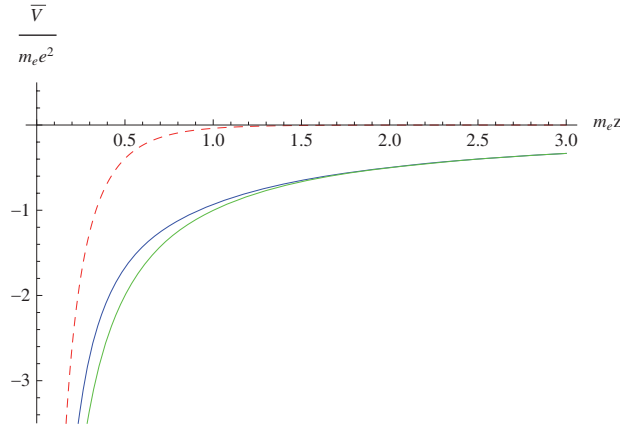


Fig. 2. – (Colour on-line) A modified Coulomb potential at $B = 10^{17}$ G (blue, dark solid) and its long distance (green, pale solid) and short distance (red, dashed) asymptotics.

With the help of it, the following result was obtained in [1]:

$$(10) \quad \Phi(k) = \frac{4\pi e}{k_{\parallel}^2 + k_{\perp}^2 + \frac{2e^3 B}{\pi} \exp\left(-\frac{k_{\perp}^2}{2eB}\right) P\left(\frac{k_{\parallel}^2}{4m^2}\right)},$$

$$(11) \quad \Phi(z) = 4\pi e \int \frac{e^{ik_{\parallel}z} dk_{\parallel} d^2 k_{\perp} / (2\pi)^3}{k_{\parallel}^2 + k_{\perp}^2 + \frac{2e^3 B}{\pi} \exp(-k_{\perp}^2 / (2eB)) (k_{\parallel}^2 / 2m_e^2) / (3 + k_{\parallel}^2 / 2m_e^2)}$$

$$= \frac{e}{|z|} \left[1 - e^{-\sqrt{6m_e^2}|z|} + e^{-\sqrt{(2/\pi)e^3 B + 6m_e^2}|z|} \right].$$

For the magnetic fields $B \ll 3\pi m^2 / e^3$ the potential is Coulomb up to small power suppressed terms:

$$(12) \quad \Phi(z) \Big|_{e^3 B \ll m_e^2} = \frac{e}{|z|} \left[1 + O\left(\frac{e^3 B}{m_e^2}\right) \right],$$

in full accordance with the $D = 2$ case, $e^3 B \rightarrow g^2$.

In the opposite case of the superstrong magnetic fields $B \gg 3\pi m_e^2 / e^3$ we get

$$(13) \quad \Phi(z) = \begin{cases} \frac{e}{|z|} e^{(-\sqrt{(2/\pi)e^3 B}|z|)}, & \frac{1}{\sqrt{(2/\pi)e^3 B}} \ln\left(\sqrt{\frac{e^3 B}{3\pi m_e^2}}\right) > |z| > \frac{1}{\sqrt{eB}}, \\ \frac{e}{|z|} (1 - e^{(-\sqrt{6m_e^2}|z|)}), & \frac{1}{m} > |z| > \frac{1}{\sqrt{(2/\pi)e^3 B}} \ln\left(\sqrt{\frac{e^3 B}{3\pi m_e^2}}\right), \\ \frac{e}{|z|}, & |z| > \frac{1}{m}, \end{cases}$$

$$(14) \quad \bar{V}(z) = -e\Phi(z).$$

In fig. 2 the plot of a Coulomb potential modified by the superstrong B as well as its short- and long-distance asymptotics are presented.

4. – Electron in the magnetic field

The spectrum of the Dirac equation in the homogeneous magnetic field constant in time is given by [5]

$$(15) \quad \varepsilon_n^2 = m_e^2 + p_z^2 + (2n + 1 + \sigma_z)eB,$$

$n = 0, 1, 2, 3, \dots; \quad \sigma_z = \pm 1.$

For $B > B_{cr} \equiv m_e^2/e$ the electrons are relativistic with only one exception: the electrons from the lowest Landau level (LLL, $n = 0, \quad \sigma_z = -1$) can be nonrelativistic. In what follows we will find the spectrum of electrons from LLL in the screened Coulomb field of the proton.

The spectrum of the Schrödinger equation in cylindrical coordinates (ρ, z) is [6]

$$(16) \quad E_{p_z n_\rho m \sigma_z} = \left(n_\rho + \frac{|m| + m + 1 + \sigma_z}{2} \right) \frac{eB}{m_e} + \frac{p_z^2}{2m_e},$$

LLL: $n_\rho = 0, \sigma_z = -1, m = 0, -1, -2, \dots,$

$$(17) \quad R_{0m}(\rho) = \left[\pi (2a_H^2)^{1+|m|} (|m|!) \right]^{-1/2} \rho^{|m|} e^{(im\varphi - \rho^2/(4a_H^2))}.$$

Now we should take into account the electric potential of the atomic nuclei situated at $\rho = z = 0$. For $a_H \ll a_B$ the adiabatic approximation is applicable and the wave function in the following form should be looked for:

$$(18) \quad \Psi_{n0m-1} = R_{0m}(\rho)\chi_n(z),$$

where $\chi_n(z)$ is the solution of the Schrödinger equation for electron motion along the magnetic field

$$(19) \quad \left[-\frac{1}{2m} \frac{d^2}{dz^2} + U_{eff}(z) \right] \chi_n(z) = E_n \chi_n(z).$$

Without screening the effective potential is given by the following formula:

$$(20) \quad U_{eff}(z) = -e^2 \int \frac{|R_{0m}(\rho)|^2}{\sqrt{\rho^2 + z^2}} d^2\rho,$$

For $|z| \gg a_H$ the effective potential equals the Coulomb one

$$(21) \quad U_{eff}(z)|_{z \gg a_H} = -\frac{e^2}{|z|}$$

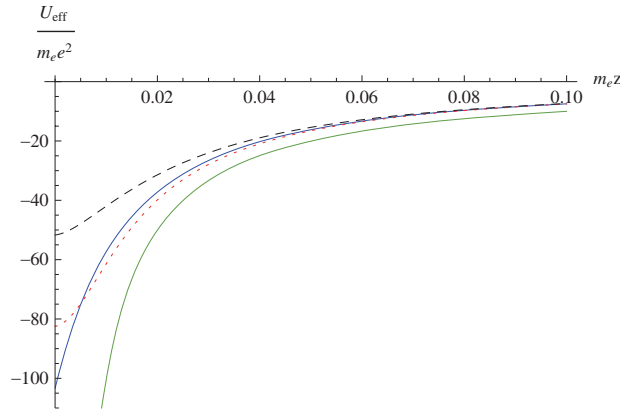


Fig. 3. – (Colour on-line) Effective potential with screening for $m = 0$ (dark solid (blue) curve) and $m = -1$ (long-dashed curve), (24); simplified potential (short-dashed (red) curve) (25). The curves correspond to $B = 3 \times 10^{17}$ G. The Coulomb potential (pale solid (green)) is also shown.

and it is regular at $z = 0$

$$(22) \quad U_{eff}(0) \sim -\frac{e^2}{|a_H|}.$$

Since $U_{eff}(z) = U_{eff}(-z)$, the wave functions are odd or even under the reflection $z \rightarrow -z$; the ground states (for $m = 0, -1, -2, \dots$) are described by the even wave functions. The energies of the odd states are

$$(23) \quad E_{\text{odd}} = -\frac{m_e e^4}{2n^2} + O\left(\frac{m_e^2 e^3}{B}\right), \quad n = 1, 2, \dots$$

So, for the superstrong magnetic fields $B > m_e^2/e^3$ they coincide with the Balmer series.

5. – Energies of even states: screening

When screening is taken into account the expression for the effective potential transforms into [1]

$$(24) \quad \tilde{U}_{eff}(z) = -e^2 \int \frac{|R_{0m}(\vec{\rho})|^2}{\sqrt{\rho^2 + z^2}} d^2\rho \left[1 - e^{-\sqrt{6m_e^2} z} + e^{-\sqrt{(2/\pi)e^3 B + 6m_e^2} z} \right].$$

For $m = 0$ the following simplified formula can be used:

$$(25) \quad U_{simpl}(z) = -e^2 \frac{1}{\sqrt{a_H^2 + z^2}} \left[1 - e^{-\sqrt{6m_e^2} z} + e^{-\sqrt{(2/\pi)e^3 B + 6m_e^2} z} \right].$$

In fig. 3 the plots of the effective potentials for $m = 0$ and $m = -1$ are presented.

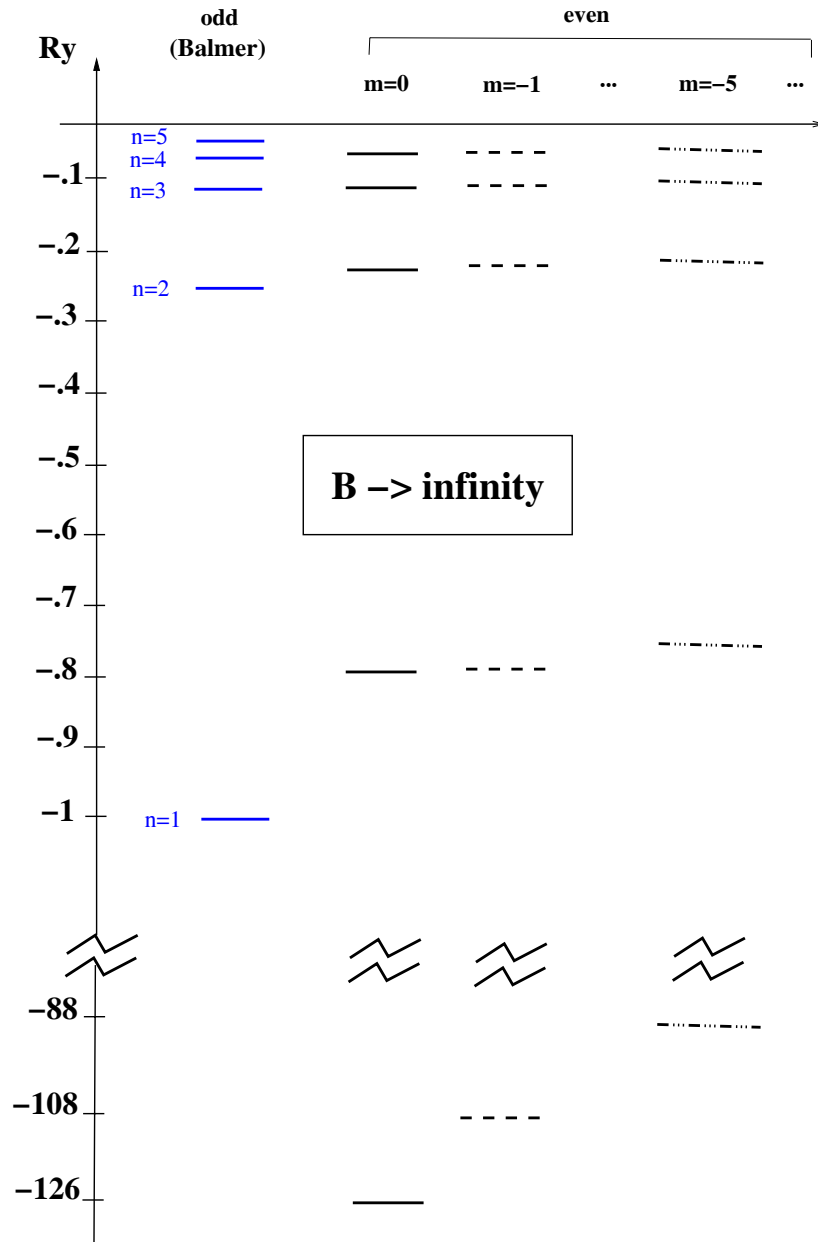


Fig. 4. – Spectrum of the hydrogen levels in the limit of the infinite magnetic field. Energies are given in Rydberg units, $Ry \equiv 13.6 \text{ eV}$.

6. – Karnakov-Popov equation

It provides a several percent accuracy for the energies of even states for $H > 10^3$ ($H \equiv B/(m_e^2 e^3)$), see [7].

The main idea is to integrate the Shrödinger equation with the effective potential from $x = 0$ till $x = z$, where $a_H \ll z \ll a_B$ and to equate the obtained expression for $\chi'(z)$ to the logarithmic derivative of Whittaker function—the solution of Shrödinger equation with Coulomb potential, which exponentially decreases at $z \gg a_B$

$$(26) \quad \begin{aligned} 2 \ln \left(\frac{z}{a_H} \right) + \ln 2 - \psi(1 + |m|) + O(a_H/z) = \\ 2 \ln \left(\frac{z}{a_B} \right) + \lambda + 2 \ln \lambda + 2\psi \left(1 - \frac{1}{\lambda} \right) + 4\gamma + 2 \ln 2 + O(z/a_B), \end{aligned}$$

where $\psi(x)$ is the logarithmic derivative of the gamma-function and

$$(27) \quad E = -(m_e e^4 / 2) \lambda^2.$$

The modified KP equation, which takes screening into account, looks like [1]

$$(28) \quad \ln \left(\frac{H}{1 + \frac{e^6}{3\pi} H} \right) = \lambda + 2 \ln \lambda + 2\psi \left(1 - \frac{1}{\lambda} \right) + \ln 2 + 4\gamma + \psi(1 + |m|).$$

The spectrum of the hydrogen atom in the limit $H \rightarrow \infty$ is shown in fig. 4.

7. – Conclusions

- Atomic energies at superstrong B is the only known (for me) case when the radiative “correction” determines the energy of states.
- The analytical expression for the charged particle electric potential in $d = 1$ is given; for $m < g$ screening takes place at all distances.
- The analytical expression for the charged particle electric potential at superstrong B in $d = 3$ is found; screening takes place at the distances $|z| < 1/m_e$.
- An algebraic formula for the energy levels of a hydrogen atom originating from the lowest Landau level in superstrong B has been obtained.

* * *

I am very grateful to the conference organizers and to M. GRECO in particular for the warm hospitality at La Thuile. This work was partially supported by the grants RFFI 11-02-00441, N-Sh 4172.2010.2 and the contract 02.740.11.5158 of the Ministry of Education and Science of the RF.

REFERENCES

- [1] VYSOTSKY M. I., *JETP Lett.*, **92** (2010) 15; MACHET B. and VYSOTSKY M. I., *Phys. Rev. D*, **83** (2011) 025022.
- [2] ELLIOTT R. J. and LOUDON R., *J. Phys. Chem. Solids*, **15** (1960) 196.
- [3] SHABAD A. E. and USOV V. V., *Phys. Rev. Lett.*, **98** (2009) 180403; *Phys. Rev. D*, **77** (2008) 025001.
- [4] SKOBELEV V. V., *Izv. Vyssh. Uchebn. Zaved., Fiz.*, **10** (1975) 142 (*Sov. Phys. J.*, **18** (1975) 1481); LOSKUTOV YU. M. and SKOBELEV V. V., *Phys. Lett. A*, **56** (1976) 151.
- [5] AKHIEZER A. I. and BERESTETSKII V. B., *Quantum Electrodynamics* (Interscience publishers, New York, London, Sydney) 1965, p. 121.
- [6] LANDAU L. D. and LIFSHITZ E. M., *Quantum Mechanics: Non-Relativistic Theory*, 3rd edition (Pergamon, New York) 1991, Sec. 112, problem 1.
- [7] KARNAKOV B. M. and POPOV V. S., *Zh. Eksp. Teor. Fiz.*, **124** (2003) 996 (*J. Exp. Theor. Phys.*, **97** (2003) 890).

SESSION VII - SEARCHING FOR NEW PHYSICS

- Luca Galli* $\mu^+ \rightarrow e^+ \gamma$ search with the MEG experiment: Results and perspectives
- Gaia Lanfranchi* Search for the rare decays $B_s^0 \rightarrow \mu^+ \mu^-$ and $B^0 \rightarrow \mu^+ \mu^-$ with the LHCb experiment
- Paride Paradisi* Theoretical review on lepton flavour violation
- Simona Rolli* Search for New Physics at the Fermilab Tevatron $p\bar{p}$ collider
- Henning Flächer* Searches for New Physics at CMS
- Marco Nardecchia* Working Technicolor at the LHC

$\mu^+ \rightarrow e^+ \gamma$ search with the MEG experiment: Results and perspectives

L. GALLI on behalf of the MEG COLLABORATION

INFN, Sezione di Pisa - Pisa, Italy

(ricevuto il 29 Settembre 2011; pubblicato online il 24 Gennaio 2012)

Summary. — I present the preliminary results of the data collected by the MEG detector at the Paul Scherrer Institute in 2009 in search of the lepton flavour violating decay $\mu^+ \rightarrow e^+ \gamma$ with a sample of 6×10^{13} muon decays on target.

PACS 11.30.Fs – Global symmetries (*e.g.*, baryon number, lepton number).

PACS 14.60.Ef – Muons.

PACS 13.35.Bv – Decays of muons.

1. – Introduction

In the minimal standard model (SM) the lepton flavour violating (LFV) processes are not allowed at all; leptons are grouped in separated doublets and the lepton flavour conservation is built in by hand assuming vanishing neutrino masses. Nevertheless, the neutrino oscillations are now established facts (for a continuously updated review, see [1]) and the neutrino masses are definitely not vanishing; then, LFV in the neutral sector is an experimental reality, while until now there are no corresponding indications in the charged sector. When massive neutrinos and neutrino oscillations are introduced in the SM, LFV decays of charged leptons are predicted, but at immeasurably small levels (branching fractions $\sim 10^{-50}$ with respect to SM decays). However, Supersymmetric and especially GUT supersymmetric theories (SUSY and SUSY-GUT) naturally accommodate finite neutrino masses and predict relatively large (and probably measurable) branching ratios (BR) for LFV processes (see for example [2-6]). Therefore, sizable flavour violation processes would be strong indications in favour of new physics beyond the SM.

Even if searches for charged LFV effects have, so far, yielded no results, they had a relevant impact on the particle physics development: for example, the non-observation of the $\mu^+ \rightarrow e^+ \gamma$ decay [7] established that the muon and the electron are two distinct leptons [8] and the stronger and stronger constraints on this process were basic arguments for introducing a second neutrino (ν_μ) [9]. At the beginning of the third millennium, the search for charged LFV reactions allows to explore SUSY mass scales up to 1000–10000 TeV (even out of LHC reach) and to give insights about large mass range, parity violation, number of generations, etc.

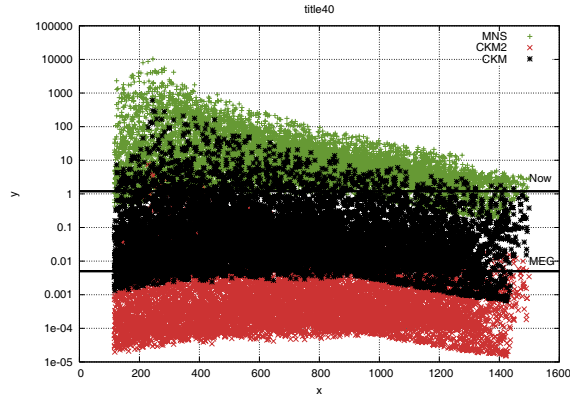


Fig. 1. – Branching ratio of $\mu^+ \rightarrow e^+\gamma$ decay (in units of 10^{-11}) as a function of $M_{1/2}$ (GeV) for three classes of SUSY models [5]. The horizontal line labelled “Now” is the present experimental limit: $BR(\mu^+ \rightarrow e^+\gamma) \leq 1.2 \times 10^{-11}$ [11].

Figure 1 illustrates examples of recent theoretical predictions for charged LFV processes in the SUSY frame: the $\mu^+ \rightarrow e^+\gamma$ BR is shown as a function of $M_{1/2}$ (in GeV) for three different classes of models [5]. A detailed review of the mechanisms which might induce LFV processes and of the relation between LFV and other signs of new physics (like Muon Anomalous Magnetic Moment) can be found in [10].

Many experiments are under way or in preparation which would test the theoretical predictions with unprecedented levels of sensitivity in the μ and in the τ channels.

Note that not only positive results, but also negative results could be very significant, since they would tightly constrain the multi-dimensional SUSY parameter space. We also stress that searching for LFV processes in different channels and with different leptons is one of the most powerful tools to discriminate between different models. Figure 2 shows the improvement with time of the upper limits for some LFV processes. In this paper I present the search for $\mu^+ \rightarrow e^+\gamma$ decay performed by the MEG collaboration.

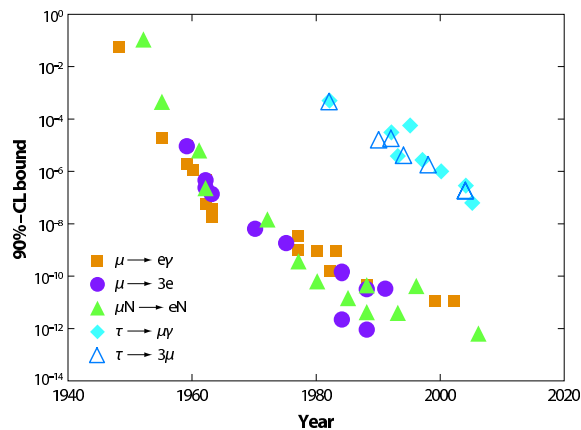


Fig. 2. – Improvement with time of some LFV searches (from [10]).

TABLE I. – The performances of previous $\mu \rightarrow e\gamma$ experiments compared with that expected for MEG. All the quoted resolutions are FWHM. The asterisk shows an average of the numbers given in [11].

Place	Year	$\Delta E_e/E_e$	$\Delta E_\gamma/E_\gamma$	$\Delta t_{e\gamma}$	$\Delta\theta_{e\gamma}$	Upper limit	Refs.
SIN	1977	8.7%	9.3%	1.4 ns	–	$< 1.0 \times 10^{-9}$	[13]
TRIUMF	1977	10%	8.7%	6.7 ns	–	$< 3.6 \times 10^{-9}$	[14]
LANL	1979	8.8%	8%	1.9 ns	37 mrad	$< 1.7 \times 10^{-10}$	[15]
LANL	1986	8%	8%	1.8 ns	87 mrad	$< 4.9 \times 10^{-11}$	[16]
LANL	1999	1.2%*	4.5%*	1.6 ns	17 mrad	$< 1.2 \times 10^{-11}$	[11]
PSI	≈ 2013	0.8%	4.0%	0.15 ns	19 mrad	$< 1 \times 10^{-13}$	MEG

2. – Signal and background

The $\mu \rightarrow e\gamma$ decay is the historical channel where charged LFV is searched for. Positive muons (selected to avoid nuclear captures in the stopping target), coming from decay of π^+ produced in proton interactions on fixed target, are brought to stop and decay at rest, emitting simultaneously a γ and a e^+ in back-to-back directions. Since the e^+ mass is negligible, both particles carry away the same kinetic energy: $E_{e^+} = E_\gamma = m_\mu/2 = 52.83$ MeV. The signature is very simple, but, because of the finite experimental resolution, it can be mimed by two types of background:

- a) The *physical* or *correlated* background, due to the radiative muon decay (RMD): $\mu^+ \rightarrow e^+\bar{\nu}_\mu\nu_e\gamma$. The *BR* of RMD process is $(1.4 \pm 0.2)\%$ of that of usual muon Michel decay $\mu^+ \rightarrow e^+\bar{\nu}_\mu\nu_e$ for $E_\gamma > 10$ MeV.
- b) The *accidental* or *uncorrelated* background, due to the coincidence, within the analysis window, of a e^+ coming from the usual muon decay and a γ coming from RMD, $e^+ - e^-$ annihilation in flight, e^+ bremsstrahlung in a nuclear field, etc.

While signal and RMD rates are proportional to the muon stopping rate R_μ , the accidental background rate is proportional to R_μ^2 , since both particles come from the beam; the accidental background is dominant and sets the limiting sensitivity of a $\mu \rightarrow e\gamma$ experiment. Then, in the search for $\mu^+ \rightarrow e^+\gamma$ decay a continuous muon beam is preferred and R_μ must be carefully chosen to optimize the signal-to-noise ratio. The number of background events depends on the sizes of the signal region, which are determined by the experimental resolutions. Physical effects which degrade the resolution, as multiple scattering and energy loss, are reduced by using “surface” muons, *i.e.* muons produced by pions stopped very close to the surface of π production target, which are efficiently brought to rest in thin targets. Moreover, high resolution detectors are mandatory. table I shows the figures of merit obtained by previous $\mu \rightarrow e\gamma$ experiments compared with the final goals of the MEG [12] experiment; the 90% C.L. upper limits on $\mu \rightarrow e\gamma$ *BR* are also reported.

3. – Detector and calibration systems

The MEG experiment [12] (fig. 3) uses the secondary $\pi E5$ muon beam line extracted from the PSI (Paul Scherrer Institute) proton cyclotron, the most powerful continuous

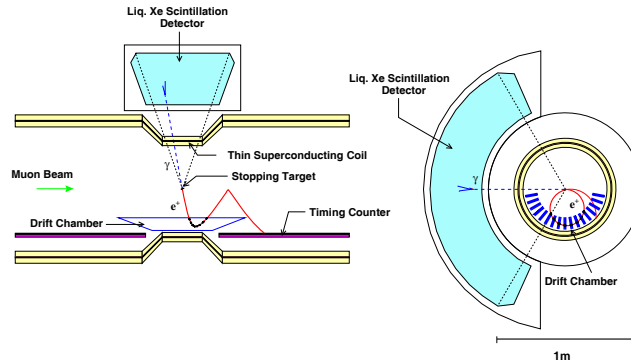


Fig. 3. – Layout of the MEG experiment.

hadronic machine in the world (maximum proton current $I = 2.2 \text{ mA}$). A $3 \times 10^7 \mu^+/\text{s}$ beam is stopped in a $205 \mu\text{m}$ slanted polyethylene target. The e^+ momentum is measured by a magnetic spectrometer, composed by an almost solenoidal magnet (COBRA) with an axial gradient field and by a system of sixteen ultra-thin drift chambers (DC). The e^+ timing is measured by two double-layer arrays of plastic scintillators (Timing Counter, from now on: TC): the external layer is equipped with two sections of 15 scintillating bars each, the internal one with 512 scintillating read by APDs fibers to measure the transverse positron impact coordinate on the scintillating bars. The γ energy, direction and timing are measured in a $\approx 800 \text{ l}$ volume liquid xenon (LXe) scintillation detector. The LXe as scintillating medium was chosen because of its large light yield (comparable with that of NaI) in the VUV region ($\lambda \approx 178 \text{ nm}$), its homogeneity and the fast decay time of its scintillation light ($\approx 45 \text{ ns}$ for γ 's and $\approx 22 \text{ ns}$ for α 's) [17]. The LXe volume is viewed by 846 Hamamatsu $2''$ PMTs, specially produced to be sensitive to UV light and to operate at cryogenic temperatures. Possible water or oxygen impurities in LXe are removed by circulating the liquid through a purification system.

A FPGA-FADC based digital trigger system was specifically developed to perform a fast estimate of the γ energy, timing and direction and of the positron timing and direction; the whole information is then combined to select events which exhibit some similarity with the $\mu \rightarrow e\gamma$ decay. The signals coming from all detectors are digitally processed by a 2 GHz custom made waveform digitizer system to identify and separate pile-up hits.

Several calibration tools (LEDs, point-like α sources deposited on wires [18], Am-Be sources, Michel decays, through going cosmic μ 's, a neutron generator, 55 MeV and 83 MeV γ 's from charge exchange reaction $\pi^-p \rightarrow \pi^0n$, γ -lines from nuclear reactions induced by a CW accelerator, etc.) are frequently used to measure and optimize the detector performances and to monitor their time stability. The experimental resolutions measured in summer of 2010 (the time of this conference) were: $\sigma_p/p = 0.75\%$, $\sigma_\phi = 8 \text{ mrad}$ and $\sigma_\theta = 11 \text{ mrad}$ for e^+ 's, $\sigma_E/E = 2.1\%$ and $\sigma_x = 5.5 \text{ mm}$ for γ 's and $\sigma_{\Delta T} = 142 \text{ ps}$ for $e^+ - \gamma$ relative timing. Significant improvements are expected in the following years, which should make these numbers closer to the table I goals.

A new calibration method for the tracking system is also operative from the 2010, it takes advantage from the elastic Mott scattering of monochromatic positrons into a dedicated polyethylene target. These events can be used to measure the tracker momentum

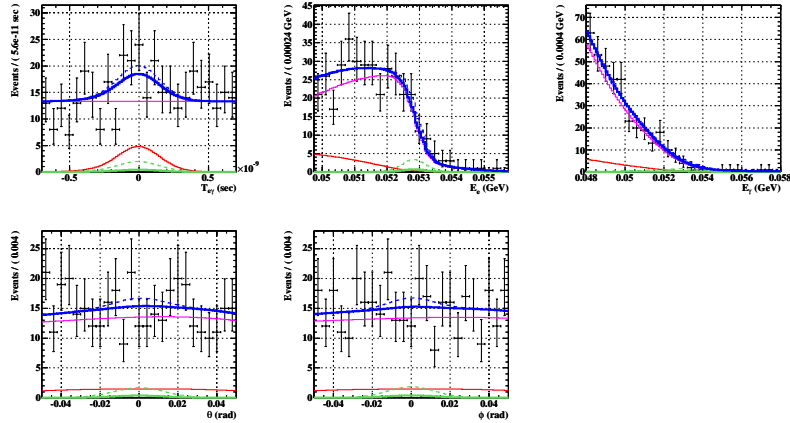


Fig. 4. – (Colour on-line) Results of MEG maximum likelihood analysis. From top to bottom, from left to right: $\Delta T_{e\gamma}$, E_{e^+} , E_γ , $\theta_{e\gamma}$, $\phi_{e\gamma}$. Signal PDFs are in green, RMD PDFs in red, accidental background PDFs in magenta and total PDFs in blue. The black dots represent the experimental data and the dashed lines the 90% C.L. upper limit on the number of signal events.

resolution at the signal energy and investigate systematic uncertainties in the positron track reconstruction.

4. – Data analysis and preliminary result

The data are analysed with a combination of blind and likelihood strategy. Events are pre-selected on the basis of loose cuts, requiring the presence of a track and $|\Delta T_{e\gamma}| < 4$ ns. Preselected data are processed several times with improving calibrations and algorithms and events falling within a tight window (“blinding box”, BB) in the $(E_\gamma, \Delta T_{e\gamma})$ -plane are hidden. The remaining pre-selected events fall in “sideband” regions and are used to optimize the analysis parameters, study the background and evaluate the experimental sensitivity under the zero signal hypothesis. When the optimisation procedure is completed, the BB is opened and a maximum likelihood fit is performed to the distributions of five kinematical variables (E_{e^+} , E_γ , $\Delta T_{e\gamma}$, $\theta_{e\gamma}$ and $\phi_{e\gamma}$), in order to extract the number of Signal (S), RMD (R) and Accidental Background (B) events. Probability Distribution Functions (PDFs) are determined by using calibration measurements and MC simulations for S , theoretical formulae folded with experimental resolution for R ⁽¹⁾ and sideband events for B . Michel positrons are used to calculate the normalization factor needed to convert an upper limit on S into an upper limit on $BR(\mu^+ \rightarrow e^+\gamma)$. The analysis procedure was applied for the first time to the data collected in 2008, with reduced statistics and not optimal apparatus performances, and a first result was published [19]: $BR(\mu \rightarrow e\gamma) \leq 2.8 \times 10^{-11}$ at 90% C.L., about twice worse than the present bound [11]. In 2009 a larger and better quality data sample was collected and the analysis procedure was repeated. 370 events fell in the BB, defined as $48 \text{ MeV} < E_\gamma < 58 \text{ MeV}$ and $|\Delta T_{e+\gamma}| < 0.7$ ns. Figure 4 shows the results of the maximum likelihood fit to the five

⁽¹⁾ In RMD events, the kinematical boundaries introduce a correlation between E_{e^+} , E_γ and positron-gamma relative angle which must be taken into account in the PDF.

kinematical variables for 2009 data. The (preliminary!) best fit result was $S = 3.0$ and $R = 35$. The analysis was repeated by different groups varying the approach (frequentistic and Bayesian), the handling of sideband information and the estimated numbers of R and B in the BB; the best fit value for S ranged between 3 and 4.5 and the corresponding 90% C.L. interval was (0, 15); then, a (preliminary!) 90% C.L. upper limit was set: $BR(\mu \rightarrow e\gamma) \leq 1.5 \times 10^{-11}$, close to the current experimental limit.

5. – Perspectives and conclusions

The MEG collaboration has already performed a new data collection campaign in 2010, collecting a sample twice that of 2009 in comparable running condition and detector performances. The analysis is significantly improved, in particular in the positron reconstruction and the related systematics reduced. A new result with 2009 and 2010 data together is going to be obtained within this summer.

The experiment is expected to run at least until the end of 2012; this will produce a huge increase in statistics and, taking into account further improvements of detector performances, will allow to reach a sensitivity $\sim 5 \times 10^{-13}$, (30–50) times better than the present upper bound.

* * *

I am grateful to the many MEG colleagues who helped me in the preparation of the talk and of these proceedings. A special thank to the Conference Organizers that invited me to present MEG and to enjoy the beautiful slopes of La Thuile.

REFERENCES

- [1] STRUMIA A. and VISSANI F., *Neutrino masses and mixings and ...*, Preprint hep-ph/0606054 (2006).
- [2] BARBIERI R. and HALL L. J., *Phys. Lett. B*, **338** (1994) 212.
- [3] BARBIERI R., HALL L. J. and STRUMIA A., *Nucl. Phys. B*, **445** (1995) 219.
- [4] HISANO J. *et al.*, *Phys. Lett. B*, **391** (1997) 341; *Phys. Lett. B*, **391** (1997) 357(E).
- [5] CABIBBI L. *et al.*, *Phys. Rev. D*, **74** (2006) 116002.
- [6] CABIBBI L. *et al.*, *Proceedings of the Europhysics Conference on High Energy Physics: HEP2009 (Cracow)* (2009) p. 167.
- [7] HINCKS E. P. and PONTECORVO B., *Phys. Rev.*, **73** (1948) 257.
- [8] LOKANATHAN S. and STEINBERGER J., *Phys. Rev. A*, **98** (1955) 240.
- [9] FEINBERG G., *Phys. Rev.*, **110** (1958) 1482.
- [10] MARCIANO W. J., MORI T. and RONEY J. M., *Annu. Rev. Nucl. Part. Sci.*, **58** (2008) 315.
- [11] AHMED M. *et al.* (MEGA COLLABORATION), *Phys. Rev. D*, **65** (2002) 112002.
- [12] BALDINI A. *et al.* (MEG COLLABORATION), Proposal to INFN, see <http://meg.psi.ch> (2002).
- [13] VAN DER SCHAAF A. *et al.*, *Nucl. Phys. A*, **340** (1980) 249.
- [14] DEPOMMIER P. *et al.*, *Phys. Rev. Lett.*, **39** (1977) 113.
- [15] KINNISON W. W. *et al.*, *Phys. Rev. D*, **25** (1982) 2846.
- [16] BOLTON R. D. *et al.*, *Phys. Rev. D*, **38** (1988) 2077.
- [17] BALDINI A. *et al.*, *Nucl. Instrum. Methods A*, **545** (2005) 753.
- [18] BALDINI A. *et al.*, *Nucl. Instrum. Methods A*, **565** (2006) 589.
- [19] MEG COLLABORATION, *Nucl. Phys. B*, **834** (2010) 1.

Search for the rare decays $B_s^0 \rightarrow \mu^+ \mu^-$ and $B^0 \rightarrow \mu^+ \mu^-$ with the LHCb experiment

G. LANFRANCHI on behalf of the LHCb COLLABORATION

INFN, Laboratori Nazionali di Frascati - Frascati (RM), Italy

(ricevuto il 29 Settembre 2011; pubblicato online il 26 Gennaio 2012)

Summary. — A search for the decays $B_s^0 \rightarrow \mu^+ \mu^-$ and $B^0 \rightarrow \mu^+ \mu^-$ is performed with about 37 pb^{-1} of pp collisions at $\sqrt{s} = 7 \text{ TeV}$ collected by the LHCb experiment at the Large Hadron Collider at CERN. The observed numbers of events are consistent with the background expectations. The resulting upper limits on the branching ratios are $\text{BR}(B_s^0 \rightarrow \mu^+ \mu^-) < 5.6 \times 10^{-8}$ and $\text{BR}(B^0 \rightarrow \mu^+ \mu^-) < 1.5 \times 10^{-8}$ at 95% confidence level.

PACS 13.20.He – Decays of bottom mesons.

PACS 12.15.Mm – Neutral currents.

PACS 12.60.Jv – Supersymmetric models.

1. – Introduction

Measurements at low energies may provide interesting indirect constraints on the masses of particles that are too heavy to be produced directly. This is particularly true for Flavour Changing Neutral Currents (FCNC) processes which are highly suppressed in the Standard Model (SM) and can only occur through higher order diagrams.

The SM prediction for the Branching Ratios (BR) of the FCNC decays $B_s^0 \rightarrow \mu^+ \mu^-$ and $B^0 \rightarrow \mu^+ \mu^-$ have been computed [1] to be $\text{BR}(B_s^0 \rightarrow \mu^+ \mu^-) = (3.2 \pm 0.2) \times 10^{-9}$ and $\text{BR}(B^0 \rightarrow \mu^+ \mu^-) = (0.10 \pm 0.01) \times 10^{-9}$.

However New Physics (NP) contributions can significantly enhance this value. For example, within Minimal Supersymmetric extensions of the SM (MSSM), in the large $\tan \beta$ approximation [2], the $\text{BR}(B_s \rightarrow \mu^+ \mu^-)$ is found to be proportional to $\sim \tan^6 \beta$, where $\tan \beta$ is the ratio of vacuum expectation values of the two neutral CP-even Higgs fields. Therefore it could be strongly enhanced for large values of $\tan \beta$.

The most restrictive limits on the search for $B_{(s)}^0 \rightarrow \mu^+ \mu^-$ have so far been achieved at the Tevatron, due to the large $b\bar{b}$ cross-section at hadron colliders. The best limits at 95% CL published so far are obtained using 6.1 fb^{-1} by the D0 Collaboration [3], $\text{BR}(B_s^0 \rightarrow \mu^+ \mu^-) < 5.1 \times 10^{-8}$ and using 2 fb^{-1} by the CDF Collaboration [4], $\text{BR}(B_s^0 \rightarrow \mu^+ \mu^-) < 5.8 \times 10^{-8}$ and $\text{BR}(B^0 \rightarrow \mu^+ \mu^-) < 1.8 \times 10^{-8}$. The CDF Collaboration has also presented preliminary results [5] with 3.7 fb^{-1} that lower the limits to $\text{BR}(B_s^0 \rightarrow \mu^+ \mu^-) < 4.3 \times 10^{-8}$ and $\text{BR}(B^0 \rightarrow \mu^+ \mu^-) < 0.76 \times 10^{-8}$.

The LHCb experiment is well suited for such searches due to its good invariant mass resolution, vertex resolution, muon identification and trigger acceptance.

In addition, LHCb has a hadronic trigger capability which provides large samples of $B_{s,d}^0 \rightarrow h^+h'^-$ decays, where h and h' stand for a hadron (kaon or pion). These are used as control samples in order to reduce the dependence of the results on the simulation.

The measurements presented in this document use about 37 pb^{-1} of integrated luminosity collected by LHCb between July and October 2010 at $\sqrt{s} = 7 \text{ TeV}$. Assuming the SM branching ratio, about 0.7 (0.08) $B_{(s)}^0 \rightarrow \mu^+\mu^-$ ($B^0 \rightarrow \mu^+\mu^-$) are expected to be reconstructed using the $b\bar{b}$ cross-section, measured within the LHCb acceptance, of $75 \pm 14 \mu\text{b}$ [6].

2. – The LHCb detector

The LHCb detector [7] is a single-arm forward spectrometer with an angular coverage from approximately 10 mrad to 300 (250) mrad in the bending (non-bending) plane.

The detector consists of a vertex locator (VELO), a warm dipole magnet with a bending power of $\int Bdl = 4 \text{ Tm}$, a tracking system, two ring-imaging Cherenkov detectors (RICH), a calorimeter system and a muon system.

Track momenta are measured with a precision between $\delta p/p = 0.35\%$ at $5 \text{ GeV}/c$ and $\delta p/p = 0.5\%$ at $100 \text{ GeV}/c$. The RICH system provides charged hadron identification in a momentum range 2–100 GeV/c . Typically kaon identification efficiencies of over 90% can be attained for a $\pi \rightarrow K$ fake rate below 10%. The calorimeter system consists of a preshower, a scintillating pad detector, an electromagnetic calorimeter and a hadronic calorimeter. It identifies high transverse energy (E_T) hadron, electron and photon candidates and provides information for the trigger. Five muon stations provide fast information for the trigger and muon identification capability: a muon identification efficiency of $\sim 95\%$ is obtained for a misidentification rate of about 1–2% for momenta above $10 \text{ GeV}/c$.

LHCb has a two-level flexible and efficient trigger system both for leptonic and purely hadronic B decays. It exploits the finite lifetime and relatively large mass of charm and beauty hadrons to distinguish heavy flavour decays from the dominant light quark processes. The first trigger level (L0) is implemented in hardware and reduces the rate to a maximum of 1 MHz, the read-out rate of the whole detector. The second trigger level (High Level Trigger, HLT) is implemented in software running on an event filter CPU farm. The forward geometry allows the LHCb first level trigger to collect events with one or two muons with p_T values as low as $1.4 \text{ GeV}/c$ for single muon and $p_T(\mu_1) > 0.48 \text{ GeV}/c$ and $p_T(\mu_2) > 0.56 \text{ GeV}/c$ for dimuon triggers. The E_T threshold for the hadron trigger varied in the range 2.6 to 3.6 GeV.

The dimuon trigger line requires muon pairs of opposite charge forming a common vertex and an invariant mass $M_{\mu\mu} > 4.7 \text{ GeV}/c^2$. A second trigger line, primarily to select $J/\psi \rightarrow \mu\mu$ events, requires $2.97 < M_{\mu\mu} < 3.21 \text{ GeV}/c^2$. The remaining region of the dimuon invariant mass is also covered by trigger lines that in addition require the dimuon secondary vertex to be well separated from the primary vertex. Other HLT trigger lines select generic displaced vertices, providing a high efficiency for purely hadronic decays (for instance $B_{s,d}^0 \rightarrow h^+h'^-$).

3. – Analysis strategy

The analysis for the $B_{(s)}^0 \rightarrow \mu^+\mu^-$ search at LHCb is described in detail in [8]. It is done in two steps: first a very efficient selection removes the biggest amount of the background while keeping most of the signal within the LHCb acceptance. Then each event is given a probability to be signal or background in a two-dimensional probability space defined by the dimuon invariant mass and a multivariate analysis discriminant likelihood, the *Geometrical Likelihood* (GL). The compatibility of the observed distribution of events in the GL *vs.* invariant mass plane with a given branching ratio hypothesis is evaluated using the CL_s method [9].

The number of expected signal events is evaluated by normalizing with channels of known branching ratios: $B^+ \rightarrow J/\psi K^+$, $B_s^0 \rightarrow J/\psi \phi$ and $B^0 \rightarrow K^+\pi^-$, where $J/\Psi \rightarrow \mu^+\mu^-$ and $\phi \rightarrow K^+K^-$ ⁽¹⁾. This normalization ensures that knowledge of the absolute luminosity and $b\bar{b}$ production cross-section are not needed, and that many systematic uncertainties cancel in the ratio of the efficiencies.

An important feature of this analysis is to rely as much as possible on data and to restrict to a minimum the use of simulation.

3.1. Event selection. – The selection requires two muon candidates of opposite charge, forming a vertex with a $\chi^2/\text{ndf} < 14$. Tracks are first required to be of good quality and to be displaced with respect to the closest primary vertex. To reject bad combinations before performing the vertex fit, the two tracks are required to have a distance of closest approach of less than 0.3 mm. The secondary vertex is required to be well fitted and must be clearly separated from the primary in the forward direction. When more than one primary vertex is reconstructed, the one that gives the minimum impact parameter significance for the candidate is chosen. The reconstructed candidate has to point to the primary vertex.

Events passing the selection are considered $B_{(s)}^0 \rightarrow \mu^+\mu^-$ candidates if their invariant mass lies within $60 \text{ MeV}/c^2$ of the nominal $B_{(s)}^0$ mass. Assuming the SM branching ratio, 0.3 $B_s^0 \rightarrow \mu^+\mu^-$ and 0.04 $B^0 \rightarrow \mu^+\mu^-$ events are expected after all selection requirements. There are 343 (342) $B_{(s)}^0 \rightarrow \mu^+\mu^-$ candidates selected from data in the $B_s^0(B^0)$ mass window.

The dominant background after the $B_{(s)}^0 \rightarrow \mu^+\mu^-$ selection is expected to be $b\bar{b} \rightarrow \mu\mu X$ [10]. This is confirmed by comparing the kinematical distributions of the sideband data with a $b\bar{b} \rightarrow \mu\mu X$ MC sample.

The muon misidentification probability as a function of momentum obtained from data using $K_S^0 \rightarrow \pi^+\pi^-$, $\Lambda \rightarrow p\pi^-$ and $\phi \rightarrow K^+K^-$ decays is in good agreement with MC expectations. An estimate of the background coming from misidentified hadrons is obtained by reweighting the hadron misidentification probability using the momentum spectrum of the background in the invariant mass sidebands. The single hadron average misidentification probability is measured to be $(7.1 \pm 0.5) \times 10^{-3}$ and the double hadron misidentification probability is $(3.5 \pm 0.9) \times 10^{-5}$, where the correlation between the momenta of the two hadrons is taken into account.

The same selection without the muon identification requirement is applied to the control channel $B_{s,d}^0 \rightarrow h^+h'^-$ and, with a softer pointing requirement, to the $J/\psi \rightarrow \mu\mu$ decay of the control and normalization channels containing J/ψ in the final state.

⁽¹⁾ When the $B_s^0 \rightarrow J/\psi\phi$ and $B^+ \rightarrow J/\psi K^+$ we always assume the decays $J/\psi \rightarrow \mu^+\mu^-$ and $\phi \rightarrow K^+K^-$.

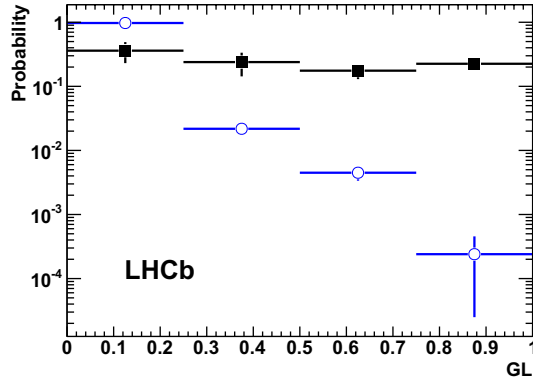


Fig. 1. – Probability of signal events in bins of GL obtained from the inclusive sample of $B_{s,d}^0 \rightarrow h^+h'^-$ events (solid squares). The background probability (open circles) is obtained from the events in the sidebands of the $\mu\mu$ invariant mass distribution in the $B_{(s)}^0$ mass window.

3.2. Signal and background likelihoods. – After the selection the signal purity is still about 10^{-3} for $B_s^0 \rightarrow \mu^+\mu^-$ and 10^{-4} for $B^0 \rightarrow \mu^+\mu^-$ assuming the SM branching ratios. Further discrimination is achieved through the combination of two independent variables: the multivariate analysis discriminant likelihood, GL, and the invariant mass. The GL combines information related with the topology and kinematics of the event as the $B_{(s)}^0$ lifetime, the minimum impact parameter of the two muons, the distance of closest approach of the two tracks, the $B_{(s)}^0$ impact parameter and p_T and the isolation of the muons with respect to the other tracks of the event. These variables are combined in an optimal way by taking their correlations properly into account [11].

The analysis is performed in two-dimensional bins of invariant mass and GL. The invariant mass in the signal regions ($\pm 60 \text{ MeV}/c^2$ around the B_s^0 and the B^0 masses) is divided into six bins of equal width, and the GL into four bins of equal width distributed between zero and one. A probability to be signal or background is assigned to events falling in each bin.

The GL variable is defined using MC events but calibrated with data using $B_{s,d}^0 \rightarrow h^+h'^-$ selected as the signal events and triggered independently on the signal (TIS events) in order to minimize the bias introduced by the hadronic trigger lines [8].

The number of $B_{s,d}^0 \rightarrow h^+h'^-$ events in each GL bin is obtained from a fit to the inclusive mass distribution [12] assigning the muon mass to the two particles. The measured fractions in each GL bin can be seen in fig. 1 and are quoted in table I. The systematic uncertainties are included, estimated by comparing the results from the inclusive $B_{s,d}^0 \rightarrow h^+h'^-$ fit model with those obtained using a double Crystal Ball function [13] and a simple background subtraction.

Two methods have been used to estimate the $B_{(s)}^0 \rightarrow \mu^+\mu^-$ mass resolution from data. The first method uses an interpolation between the measured resolutions for $c\bar{c}$ resonances (J/ψ , $\psi(2S)$) and $b\bar{b}$ resonances ($\Upsilon(1S)$, $\Upsilon(2S)$, $\Upsilon(3S)$) decaying into two muons. Interpolating linearly between the five fitted resolutions to $M_{B_s^0}$ an invariant mass resolution of $\sigma = 26.83 \pm 0.14 \text{ MeV}/c^2$ was estimated.

The systematic uncertainty is estimated to be $1 \text{ MeV}/c^2$ mainly due to the reweighting of the momentum spectrum of the dimuon resonances and the variation of the resolution over the width of the $B_{(s)}^0 \rightarrow \mu^+\mu^-$ signal region. The second method that was used to es-

TABLE I. – Probability of signal events in bins of GL obtained from the inclusive sample of $B_q^0 \rightarrow h^+h'^-$ events. The background probability in the B_s^0 mass window is obtained from the events in the sidebands of the dimuon invariant mass distribution.

GL bin	Signal probability	Background probability
0.0–0.25	0.360 ± 0.130	$0.9735^{+0.0030}_{-0.0032}$
0.25–0.5	0.239 ± 0.096	$0.0218^{+0.0030}_{-0.0028}$
0.5–0.75	0.176 ± 0.046	$0.0045^{+0.0012}_{-0.0010}$
0.75–1.0	0.225 ± 0.036	$0.00024^{+0.00031}_{-0.00015}$

estimate the invariant mass resolution from data is to use the inclusive $B_{s,d}^0 \rightarrow h^+h'^-$ sample. The particle identification requirement would modify the momentum and transverse momentum spectrum of pions and kaons, and thus the mass resolution. Therefore, the fit is performed to the inclusive $B_{s,d}^0 \rightarrow h^+h'^-$ sample without requiring particle identification and assigning the muon mass to the decay products.

The fit has been performed in the GL range [0.25, 1.0] and fitted parameters are the mass resolution, the B^0 and B_s^0 masses, the signal yield, the combinatorial background yields, as well as the fraction of radiative tail and the parameters that describe the combinatorial background. The relative contributions of B^0 and B_s^0 decays are fixed to their known values. The result of the fit for the mass resolution, $\sigma = 25.8 \pm 1.0 \pm 2.3 \text{ MeV}/c^2$, is consistent with the value obtained from the interpolation method.

The weighted average of the two methods, $\sigma = 26.7 \pm 0.9 \text{ MeV}/c^2$, is taken as the invariant mass resolution and considered to be the same for B^0 and $B_{(s)}^0$ decays.

The prediction of the number of background events in the signal regions is obtained by fitting with an exponential function the $\mu\mu$ mass sidebands independently in each GL bin in order to account for potentially different background compositions. The mass sidebands are defined in the range between $M_{B_{(s)}^0} \pm 600(1200) \text{ MeV}/c^2$ for the lower (upper) two GL bins, excluding the two search windows ($M_{B_{(s)}^0} \pm 60 \text{ MeV}/c^2$).

The distribution of the invariant mass for each GL bin is shown in fig. 2.

4. – Normalization factors

As already mentioned, the number of expected signal events is evaluated by normalizing with channels of known branching ratios, $B^+ \rightarrow J/\psi K^+$, $B_s^0 \rightarrow J/\psi\phi$ and $B^0 \rightarrow K^+\pi^-$, as shown in table II, first column.

The first two decays have similar trigger and muon identification efficiency to the signal but a different number of particles in the final state, while the third channel has the same two-body topology but is selected with the hadronic trigger. The branching ratio of the $B_s^0 \rightarrow J/\psi\phi$ decay is not known precisely ($\sim 25\%$) but has the advantage that the normalization of $B_{(s)}^0 \rightarrow \mu\mu$ with a B_s^0 decay does not require the knowledge of the ratio of fragmentation fractions, which has an uncertainty of $\sim 13\%$ [14].

Using each of these normalization channels, the $\text{BR}(B_{(s)}^0 \rightarrow \mu\mu)$ can be calculated as:

$$\begin{aligned}
 (1) \quad \text{BR}(B_{(s)}^0 \rightarrow \mu\mu) &= \text{BR}_{\text{norm}} \times \frac{\epsilon_{\text{norm}}^{\text{REC}} \epsilon_{\text{norm}}^{\text{SEL}} \epsilon_{\text{norm}}^{\text{TRIG}} \epsilon_{\text{norm}}^{\text{SEL}}}{\epsilon_{\text{sig}}^{\text{REC}} \epsilon_{\text{sig}}^{\text{SEL}} \epsilon_{\text{sig}}^{\text{TRIG}} \epsilon_{\text{sig}}^{\text{SEL}}} \times \frac{f_{\text{norm}}}{f_{B_{(s)}^0}} \times \frac{N_{B_{(s)}^0 \rightarrow \mu\mu}}{N_{\text{norm}}} \\
 &= \alpha_{B_{(s)}^0 \rightarrow \mu\mu} \times N_{B_{(s)}^0 \rightarrow \mu\mu},
 \end{aligned}$$

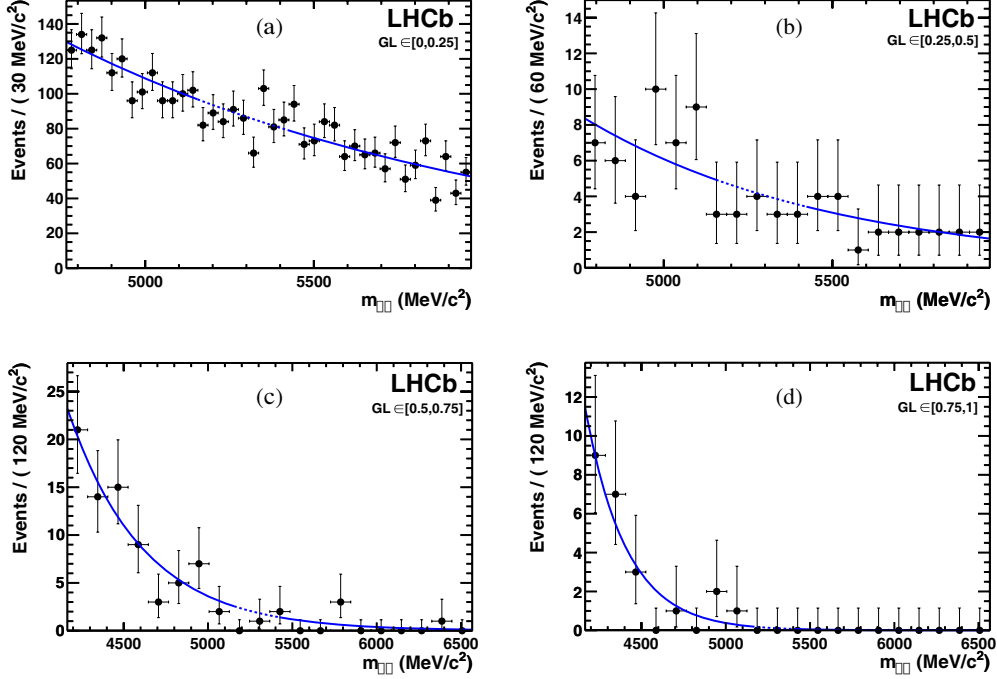


Fig. 2. – (Colour on-line) Distribution of the $\mu\mu$ invariant mass for different GL bins: (a) $[0, 0.25]$, (b) $[0.25, 0.5]$, (c) $[0.5, 0.75]$, (d) $[0.75, 1.0]$. The blue solid lines show the interpolation model used and the dashed line shows the result of the interpolation in the search windows.

where $\alpha_{B_{(s)}^0 \rightarrow \mu\mu}$ denotes the normalization factor, $f_{B_{(s)}^0}$ denotes the probability that a b -quark fragments into a $B_{(s)}^0$ and f_{norm} denotes the probability that a b -quark fragments into the b -hadron relevant for the chosen normalization channel with branching fraction BR_{norm} . The reconstruction efficiency (ϵ^{REC}) includes the acceptance and particle identification, while $\epsilon^{\text{SEL}|\text{REC}}$ denotes the selection efficiency on reconstructed events.

TABLE II. – Summary of the factors and their uncertainties needed to calculate the normalization factors ($\alpha_{B_{(s)}^0 \rightarrow \mu^+\mu^-}$) for the three normalization channels considered. The branching ratios are taken from refs. [15, 16] and includes also the $\text{BR}(J/\psi \rightarrow \mu^+\mu^-)$ and $\text{BR}(\phi \rightarrow K^+K^-)$. The trigger efficiency and number of $B^0 \rightarrow K^+\pi^-$ candidates correspond to only TIS events, as described in the text.

	BR ($\times 10^{-5}$)	$\frac{\epsilon_{\text{norm}}^{\text{REC}} \epsilon_{\text{norm}}^{\text{SEL} \text{REC}}}{\epsilon_{\text{sig}}^{\text{REC}} \epsilon_{\text{sig}}^{\text{SEL} \text{REC}}}$	$\frac{\epsilon_{\text{norm}}^{\text{TRIG} \text{SEL}}}{\epsilon_{\text{sig}}^{\text{TRIG} \text{SEL}}}$	N_{norm}	$\alpha_{B_{(s)}^0 \rightarrow \mu^+\mu^-}$ ($\times 10^{-9}$)	$\alpha_{B^0 \rightarrow \mu^+\mu^-}$ ($\times 10^{-9}$)
$B^+ \rightarrow J/\psi K^+$	5.98 ± 0.22	0.49 ± 0.02	0.96 ± 0.05	$12,366 \pm 403$	8.4 ± 1.3	2.27 ± 0.18
$B_s^0 \rightarrow J/\psi \phi$	3.4 ± 0.9	0.25 ± 0.02	0.96 ± 0.05	760 ± 71	10.5 ± 2.9	2.83 ± 0.86
$B^0 \rightarrow K^+\pi^-$	1.94 ± 0.06	0.82 ± 0.06	0.072 ± 0.010	578 ± 74	7.3 ± 1.8	1.99 ± 0.40

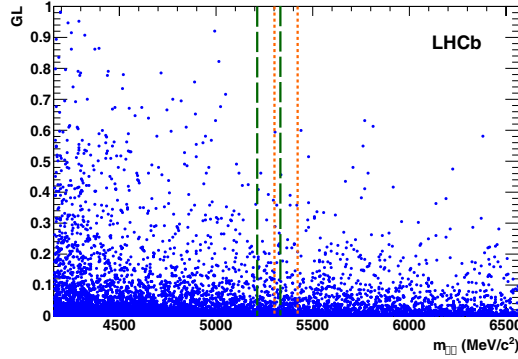


Fig. 3. – (Colour on-line) Observed distribution of selected dimuon events in the GL *vs.* invariant mass plane. The orange short-dashed (green long-dashed) lines indicate the $\pm 60 \text{ MeV}/c^2$ search window around the $B_s^0(B^0)$.

The trigger efficiency on selected events is denoted by $\epsilon^{\text{TRIG|SEL}}$.

The ratios of reconstruction and selection efficiencies are estimated from the simulation and checked on data, while the ratios of trigger efficiencies on selected events are determined from data [8].

The yields needed to evaluate the normalization factor are shown in table II, where the uncertainty is dominated by the differences observed using different models in fitting the invariant mass lineshape.

As can be seen in table II, the normalization factors calculated using the three complementary channels give compatible results. The final normalization factor is a weighted average which takes into account all the sources of correlations, in particular the dominant one coming from the uncertainty on $f_d/f_s = 3.71 \pm 0.47$ [14], with the result

$$\alpha_{B_{(s)}^0 \rightarrow \mu\mu} = (8.6 \pm 1.1) \times 10^{-9},$$

$$\alpha_{B^0 \rightarrow \mu\mu} = (2.24 \pm 0.16) \times 10^{-9}.$$

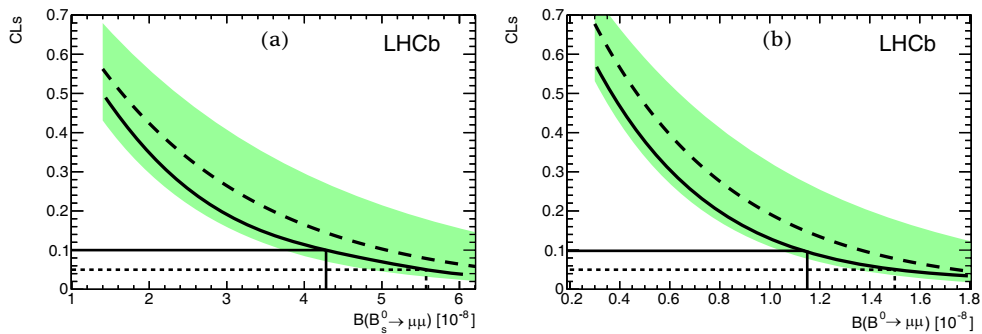


Fig. 4. – (Colour on-line) (a) Observed (solid curve) and expected (dashed curve) CL_s values as a function of $\text{BR}(B_s^0 \rightarrow \mu^+\mu^-)$. The green shaded area contains the $\pm 1\sigma$ interval of possible results compatible with the expected value when only background is observed. The 90% (95%) CL observed value is identified by the solid (dashed) line. (b) The same for $\text{BR}(B^0 \rightarrow \mu^+\mu^-)$.

5. – Results

For each of the 24 bins (4 bins in GL and 6 bins in mass) the expected number of background events is computed from the fits to the invariant mass sidebands described in subsect. 3.2. The expected numbers of signal events are computed using the normalization factors from sect. 4, and the signal likelihoods computed in subsect. 3.2. The distribution of observed events in the GL *vs.* invariant mass plane can be seen in fig. 3.

The compatibility of the observed distribution of events in the GL *vs.* invariant mass plane with a given branching ratio hypothesis is evaluated using the CL_s method [9]. The observed distribution of CL_s as a function of the assumed branching ratio can be seen in fig. 4.

The expected distributions of possible values of CL_s assuming the background-only hypothesis are also shown in the same figure as a green shaded area that covers the region of $\pm 1\sigma$ of background compatible observations. The uncertainties in the signal and background likelihoods and normalization factors are used to compute the uncertainties in the background and signal predictions. These uncertainties are the only source of systematic uncertainty and they are included in the CL_s using the techniques described in ref. [9]. Given the specific pattern of the observed events, the systematic uncertainty on the background prediction has a negligible effect on the quoted limit. The effect of the uncertainty on the signal prediction increases the quoted limits by less than 3%.

The upper limits are computed using the CL_s distributions in fig. 4 with the results:

$$\begin{aligned} BR(B_{(s)}^0 \rightarrow \mu^+ \mu^-) &< 4.3(5.6) \times 10^{-8} \text{ at } 90\% \text{ (95\%) C.L. ,} \\ BR(B^0 \rightarrow \mu^+ \mu^-) &< 1.2(1.5) \times 10^{-8} \text{ at } 90\% \text{ (95\%) C.L. ,} \end{aligned}$$

while the expected values of the limits are $BR(B_s^0 \rightarrow \mu^+ \mu^-) < 5.1(6.5) \times 10^{-8}$ and $BR(B^0 \rightarrow \mu^+ \mu^-) < 1.4(1.8) \times 10^{-8}$ at 90%(95%) CL. The limits observed are similar to the best published limits [3] for the decay $B_s^0 \rightarrow \mu^+ \mu^-$ and more restrictive for $B^0 \rightarrow \mu^+ \mu^-$ the decay [4].

REFERENCES

- [1] BURAS A. J., *Minimal flavour violation and beyond: Towards a flavour code for short distance dynamics*, arXiv:1012.1447; GAMIZ E. *et al.*, *Phys. Rev. D*, **80** (2009) 014503; BURAS A. J., *Phys. Lett. B*, **566** (2003) 115.
- [2] HALL L. J., RATTAZZI R. and SARID U., *Phys. Rev. D*, **50** (1994) 7048; HAMZAOUI C., POSPELOV M. and TOHARIA M., *Phys. Rev. D*, **59** (1999) 095005; BABU K. S. and KOLDA C. F., *Phys. Rev. Lett.*, **84** (2000) 228.
- [3] ABAZOV V. *et al.* (D0 COLLABORATION), *Phys. Lett. B*, **693** (2010) 539.
- [4] AALTONEN T. *et al.* (CDF COLLABORATION), *Phys. Rev. Lett.*, **100** (2008) 101802.
- [5] AALTONEN T. *et al.* (CDF COLLABORATION), *Search for $B_s^0 \rightarrow \mu^+ \mu^-$ and $B^0 \rightarrow \mu^+ \mu^-$ decays in 3.7 fb^{-1} of $p\bar{p}$ collisions with CDF II*, CDF Public Note 9892.
- [6] AAIJ R. *et al.* (LHCb COLLABORATION), *Phys. Lett. B*, **694** (2010) 209.
- [7] ALVES A. A. *et al.* (LHCb COLLABORATION), *JINST*, **3** (2008) S08005, and references therein.
- [8] AAIJ R. *et al.* (LHCb COLLABORATION), *Phys. Lett. B*, **699** (2011) 330.
- [9] READ A. L., *J. Phys. G*, **28** (2002) 2693; JUNK T., *Nucl. Instrum. Methods A*, **434** (1999) 435.
- [10] ADEVA B. *et al.* (LHCb COLLABORATION), *Roadmap for selected key measurements of LHCb*, Chapter 5, v:0912.4179v2.

- [11] KARLEN D., *Computer in Physics*, **12** (1998) 380.
- [12] ADEVA B. *et al.* (LHCb COLLABORATION), *Roadmap for selected key measurements of LHCb*, Chapter 3, v:0912.4179v2.
- [13] GAISER J. E., *Charmonium spectroscopy from radiative decays of the J/ψ and Ψ'* , PhD thesis, SLAC-R-255 (1982), appendix F; SKWARNICKI T., *A study of the radiative cascade transitions between the Υ and Υ' resonances*, PhD thesis, DESY F31-86-02 (1986), appendix E.
- [14] ASNER D. *et al.* (HEAVY FLAVOUR AVERAGING GROUP), *Averages of b -hadron, c -hadron, and τ -lepton properties*, arXiv:1010.1589. Updated values for f_d/f_s available at http://www.slac.stanford.edu/xorg/hfag/osc/end_2009/ have been used for this document, as they include also pre-summer 2010 results which are not contained in [15].
- [15] NAKAMURA K. *et al.* (PARTICLE DATA GROUP), *J. Phys. G*, **37** (2010) 075021.
- [16] LOUVOT R., *$\Upsilon(5S)$ Results at BELLE*, arXiv:0905.4345v2.

Theoretical review on lepton flavour violation

P. PARADISI

Technical University Munich, Physics Department - D-85748 Garching, Germany

(ricevuto il 29 Settembre 2011; pubblicato online il 2 Febbraio 2012)

Summary. — The synergy and interplay of high energy data with flavour precision data are expected to shed some light on the “Flavour Problem”. Lepton flavor violating processes like $\mu \rightarrow e\gamma$ represent “golden channels” where to look for New Physics effects, given their high New Physics sensitivity and the outstanding experimental progress we expect in the upcoming years. If LFV is observed, the next crucial step will be to trace back the New Physics model at work by means of a correlated analysis of various observables.

PACS 14.60.Ef – Muons.

PACS 13.35.Bv – Decays of muons.

1. – Introduction

The most important achievement we expect to reach at the beginning of the LHC era is the understanding of the underlying mechanism accounting for the electroweak symmetry breaking, in particular, whether the Higgs mechanism is realized in nature or not. Moreover, the LHC is also expected to shed light on the hierarchy problem, since a natural solution of it calls for a TeV scale New Physics (NP).

On the other hand, low-energy flavour physics observables provide the most powerful tool to unveil the symmetry properties of the NP theory that will emerge at the LHC, if any. In fact, high-precision measurements at the LHC are made typically challenging by the huge background and by irreducible hadronic uncertainties.

The last decade has established that flavour-changing and CPV processes in $B_{s,d}$ and K systems are well described by the SM. The same is true for electroweak precision tests. This implies automatically tight constraints on flavour-changing phenomena beyond the SM and a potential problem for a natural solution of the hierarchy problem.

On general ground, the main lesson we learned so far from the flavour data is that a TeV scale NP must have a highly non-generic flavour structure in order to satisfy all the existing constraints. Moreover, in order to avoid fine tuning of parameters, natural protection mechanisms suppressing FCNCs generated by NP are required. Famous examples of such mechanisms are MFV, alignment and degeneracy, as arising from Abelian and non-Abelian flavour symmetries.

TABLE I. – *Present [2] and upcoming experimental limits on various leptonic processes at 90% C.L.*

Process	Present bounds	Future bounds	Experiments
$\text{BR}(\mu \rightarrow e\gamma)$	1.2×10^{-11}	$\mathcal{O}(10^{-13})$	MEG, PSI
$\text{BR}(\mu \rightarrow eee)$	1.1×10^{-12}	$\mathcal{O}(10^{-13}\text{--}10^{-14})$	–
$\text{BR}(\mu \rightarrow e \text{ in Ti})$	1.1×10^{-12}	$\mathcal{O}(10^{-18})$	J-PARC
$\text{BR}(\tau \rightarrow e\gamma)$	1.1×10^{-7}	$\mathcal{O}(10^{-8})$	SuperB
$\text{BR}(\tau \rightarrow eee)$	2.7×10^{-7}	$\mathcal{O}(10^{-8})$	SuperB
$\text{BR}(\tau \rightarrow e\mu\mu)$	$2. \times 10^{-7}$	$\mathcal{O}(10^{-8})$	SuperB
$\text{BR}(\tau \rightarrow \mu\gamma)$	6.8×10^{-8}	$\mathcal{O}(10^{-8})$	SuperB
$\text{BR}(\tau \rightarrow \mu\mu\mu)$	2×10^{-7}	$\mathcal{O}(10^{-8})$	LHCb
$\text{BR}(\tau \rightarrow \mu ee)$	2.4×10^{-7}	$\mathcal{O}(10^{-8})$	SuperB

The SM mechanism of flavour mixing has been tested with high accuracy in the quark sector, where all flavour-violating phenomena seem to be well described by the SM Yukawa interaction [1]. Flavour mixing has been observed also in the neutrino sector, indicating the existence of a non-vanishing neutrino mass matrix which cannot be accommodated within the SM.

However, the origin of flavour is still far from being established. The most important open questions can be summarized as follow:

- Which is the organizing principle behind the observed pattern of fermion masses and mixing angles?
- Are there extra sources of flavour symmetry breaking beside the SM Yukawa couplings which are relevant at the TeV scale?

The search for LFV in charged leptons is probably the most interesting goal of flavour physics in the next few years. The observation of neutrino oscillations has clearly demonstrated that lepton flavour is not conserved; however, the smallness of neutrino masses provides a strong indication that neutrinos are generated by an underlying dynamics that violates also the total lepton number. The question is if LFV effects can be visible also in other sectors of the theory, or if we can observe LFV in processes which conserve the total lepton number.

2. – Experimental status for LFV

The status of searches for some selected LFV channels in τ and μ decays is summarized in table I.

In particular, the MEG experiment at PSI [3] should be able to test $Br(\mu \rightarrow e\gamma)$ at the level of $\mathcal{O}(10^{-13})$, and the Super Flavour Factory [4] is planned to reach a sensitivity for $Br(\tau \rightarrow \mu\gamma)$ of $\mathcal{O}(10^{-9})$ and also the planned resolution of SuperKEKB for $\tau \rightarrow \mu\gamma$ is of $\mathcal{O}(10^{-8})$. An impressive improvement is also expected for the upper bound on $\mu - e$ conversion in Ti. The dedicated J-PARC and PRISM/PRIME experiment [5] should

reach the sensitivity of $\mathcal{O}(10^{-18})$, almost six orders of magnitude better than the current upper bound from SINDRUM II at PSI [6].

3. – Flavour violation in charged lepton decays

In the SM with massive neutrinos, the branching ratio for LFV processes like $\mu \rightarrow e\gamma$ is of order $Br(\mu \rightarrow e\gamma)_{\text{SM}} \approx 10^{-54}$, to be compared with the 90% C.L. upper bound from the MEGA Collaboration [7] $Br(\mu \rightarrow e\gamma) < 1.2 \cdot 10^{-11}$. Therefore any observation of LFV would be a clear signal of NP.

On general grounds, if the breaking of the total lepton number occurs at a very high energy scale ($\Lambda_{\text{LN}} > 10^{12}$ GeV), as expected by the smallness of neutrino masses, and the theory has new degrees of freedom carrying lepton-flavour quantum numbers around the TeV scale ($\Lambda_{\text{LFV}} < 10^4$ GeV), then $\mu \rightarrow e\gamma$ should be visible. Indeed, employing an effective theory approach with a minimal breaking of lepton flavour, we find [8]

$$(1) \quad \mathcal{B}(\mu \rightarrow e\gamma) \approx 10^{-13} \left(\frac{\Lambda_{\text{LN}}}{10^{13} \text{ GeV}} \right)^4 \left(\frac{10^4 \text{ GeV}}{\Lambda_{\text{LFV}}} \right)^4.$$

A typical concrete example where this occurs is the MSSM with heavy right-handed neutrinos, where renormalization-group effects generate LFV entries in the left-handed slepton mass matrices at the TeV scale [9]. Once non-vanishing LFV entries in the slepton mass matrices are generated, LFV rare decays are naturally induced by one-loop diagrams with the exchange of gauginos and sleptons. The flavour-conserving component of the same diagrams induces a non-vanishing contribution to the anomalous magnetic moment of the muon, $\Delta a_\mu = (g_\mu - g_\mu^{\text{SM}})/2$. As shown in fig. 1, a strong link between these two observable naturally emerges (see, *e.g.*, [10]). In this context, the value $\Delta a_\mu = \mathcal{O}(10^{-9})$, presently indicated by detailed analyses of g_μ [11], reinforce the expectation of $\mu \rightarrow e\gamma$ within the reach of the MEG experiment.

Beside supersymmetry, there are many other NP models like the Little Higgs model and the Randall-Sundrum models which are able to reach the present bounds and in fact this bounds put already rather stringent constraints on the parameters of these models.

In order to distinguish various NP scenarios, it will be essential to study a large set of decays to three leptons in the final state. Indeed, while in the MSSM [12-14] the dominant role in the decays with three leptons in the final state and in $\mu - e$ conversion in nuclei is played by the dipole operator, in [15,16] it was found that this operator is much less relevant in the LHT model, with Z^0 penguin and box diagrams being the dominant contributions. This implies a striking difference between various ratios of branching ratios of type $Br(l_i \rightarrow 3l_j)/Br(l_i \rightarrow l_j\gamma)$ in the MSSM, where they are typically $\mathcal{O}(10^{-2} - 10^{-3})$ and in the LHT model, where they are $\mathcal{O}(10^{-1})$ [17]. The expected correlations among the branching ratios for the most relevant LFV processes are reported in table II from ref. [18].

4. – Conclusions

The origin of flavour is still, to a large extent, an open question. The synergy and interplay of high energy data with flavour precision data are expected to shed (some) light on this ‘‘Flavour Problem’’. Despite of the remarkable agreement of flavour data with the SM predictions, we still expect New Physics effects to show up in some selected ‘‘golden channels’’ such as LFV processes like $\mu \rightarrow e\gamma$, where an outstanding experimental

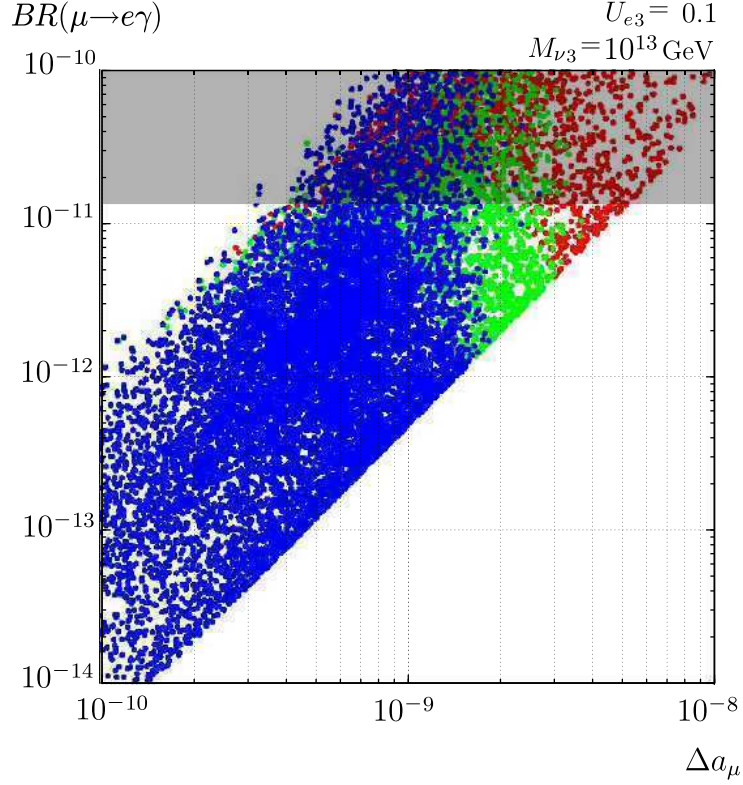


Fig. 1. – Correlation between $\mathcal{B}(\mu \rightarrow e\gamma)$ and Δa_μ in the MSSM with heavy RH neutrinos [10].

TABLE II. – Comparison of various ratios of branching ratios in the LHT model, the MSSM and the SM4. From ref. [18].

Ratio	LHT	MSSM	SM4
$\frac{Br(\mu \rightarrow eee)}{Br(\mu \rightarrow e\gamma)}$	0.02 ... 1	$\sim 2 \cdot 10^{-3}$	0.06 ... 2.2
$\frac{Br(\tau \rightarrow eee)}{Br(\tau \rightarrow e\gamma)}$	0.04 ... 0.4	$\sim 1 \cdot 10^{-2}$	0.07 ... 2.2
$\frac{Br(\tau \rightarrow \mu\mu\mu)}{Br(\tau \rightarrow \mu\gamma)}$	0.04 ... 0.4	$\sim 2 \cdot 10^{-3}$	0.06 ... 2.2
$\frac{Br(\tau \rightarrow e\mu\mu)}{Br(\tau \rightarrow e\gamma)}$	0.04 ... 0.3	$\sim 2 \cdot 10^{-3}$	0.03 ... 1.3
$\frac{Br(\tau \rightarrow \mu ee)}{Br(\tau \rightarrow \mu\gamma)}$	0.04 ... 0.3	$\sim 1 \cdot 10^{-2}$	0.04 ... 1.4
$\frac{Br(\tau \rightarrow eee)}{Br(\tau \rightarrow e\mu\mu)}$	0.8 ... 2	~ 5	1.5 ... 2.3
$\frac{Br(\tau \rightarrow \mu\mu\mu)}{Br(\tau \rightarrow \mu ee)}$	0.7 ... 1.6	~ 0.2	1.4 ... 1.7
$\frac{R(\mu Ti \rightarrow e Ti)}{Br(\mu \rightarrow e\gamma)}$	$10^{-3} \dots 10^2$	$\sim 5 \cdot 10^{-3}$	$10^{-12} \dots 26$

progress is expected in the upcoming years. Once some clear non-standard effects will be established, the next crucial step will be to trace back the New Physics model at work by means of a careful analysis of correlations among various observables.

REFERENCES

- [1] CABIBBO N., *Phys. Rev. Lett.*, **10** (1963) 531; KOBAYASHI M. and MASKAWA T., *Prog. Theor. Phys.*, **49** (1973) 652.
- [2] AMSLER C. *et al.* (PARTICLE DATA GROUP COLLABORATION), *Phys. Lett. B*, **667** (2008) 1.
- [3] YAMADA S., *Nucl. Phys. Proc. Suppl.*, **144** (2005) 185.
- [4] BONA M. *et al.*, *SuperB: A High-Luminosity Asymmetric e^+e^- Super Flavor Factory*, Conceptual Design Report [arXiv:0709.0451].
- [5] MORI Y. *et al.* (PRISM/PRIME WORKING GROUP COLLABORATION), *LOI at J-PARC 50-GeV PS, LOI-25*, <http://psux1.kek.jp/~jhf-np/LOIlist/LOIlist.html>.
- [6] DOHMEN C. *et al.* (SINDRUM II. COLLABORATION), *Phys. Lett. B*, **317** (1993) 631.
- [7] BROOKS M. L. *et al.* (MEGA COLLABORATION), *Phys. Rev. Lett.*, **83** (1999) 1521 [hep-ex/9905013].
- [8] CIRIGLIANO V., GRINSTEIN B., ISIDORI G. and WISE M. B., *Nucl. Phys. B*, **728** (2005) 121 [arXiv:hep-ph/0507001].
- [9] BORZUMATI F. and MASIERO A., *Phys. Rev. Lett.*, **57** (1986) 961.
- [10] HISANO J., NAGAI M., PARADISI P. and SHIMIZU Y., *JHEP*, **0912** (2009) 030 [arXiv:0904.2080 [hep-ph]].
- [11] DAVIER M., HOECKER A., MALAESCU B. and ZHANG Z., arXiv:1010.4180 [hep-ph].
- [12] ELLIS J. R., HISANO J., RAIDAL M. and SHIMIZU Y., *Phys. Rev. D*, **66** (2002) 115013.
- [13] BRIGNOLE A. and ROSSI A., *Nucl. Phys. B*, **701** (2004) 3.
- [14] ARGANDA E. and HERRERO M. J., *Phys. Rev. D*, **73** (2006) 055003.
- [15] BLANKE M., BURAS A. J., DULING B., POSCHENRIEDER A. and TARANTINO C., *JHEP*, **05** (2007) 013.
- [16] DEL AGUILA F., ILLANA J. I. and JENKINS M. D., *JHEP*, **01** (2009) 080.
- [17] BLANKE M., BURAS A. J., DULING B., RECKSIEGEL S. and TARANTINO C., *Acta Phys. Pol. B*, **41** (2010) 657 [arXiv:0906.5454 [hep-ph]].
- [18] BURAS A. J., DULING B., FELDMANN T., HEIDSIECK T. and PROMBERGER C., *JHEP*, **1009** (2010) 104 [arXiv:1006.5356 [hep-ph]].

Search for New Physics at the Fermilab Tevatron $p\bar{p}$ collider

S. ROLLI(*)

Tufts University - 4 Colby St, Medford, MA 02155, USA

(ricevuto il 29 Settembre 2011; pubblicato online il 2 Febbraio 2012)

Summary. — We report on selected recent results from the CDF and D0 experiments on searches for physics beyond the Standard Model using data from the Tevatron collider running $p\bar{p}$ collisions at $\sqrt{s} = 1960$ GeV.

PACS 14.80.Bn – Standard-model Higgs bosons.

1. – Introduction

Over the past decades the Standard Model (SM) of particle physics has been surprisingly successful. Although the precision of experimental tests improved by orders of magnitude no significant deviation from the SM predictions has been observed so far. Still, there are many questions that the Standard Model does not answer and problems it can not solve. Among the most important ones are the origin of the electro-weak symmetry breaking, hierarchy of scales, unification of fundamental forces and the nature of gravity. Recent cosmological observations indicates that the SM particles only account for 4% of the matter of the Universe. Many extensions of the SM (Beyond the Standard Model, BSM) have been proposed to make the theory more complete and solve some of the above puzzles. Some of these extension includes SuperSymmetry (SUSY), Grand Unification Theory (GUT) and Extra Dimensions. At CDF and D0 we search for evidence of such processes in proton-antiproton collisions at $\sqrt{s} = 1960$ GeV. The phenomenology of these models is very rich, although the cross sections for most of these exotic processes is often very small compared to those of SM processes at hadron colliders. It is then necessary to devise analysis strategies that would allow to disentangle the small interesting signals, often buried under heavy instrumental and/or physics background. Two main approaches to search for physics beyond the Standard Model are used in a complementary fashion: model-based analyses and signature based studies. In the more traditional model-driven approach, one picks a favorite theoretical model and/or

(*) Currently at: U.S. Department of Energy, Office of High Energy Physics, Washington, DC 20585, USA.

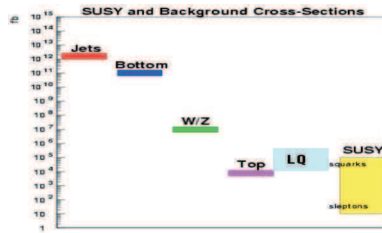


Fig. 1. – Cross sections for typical SM processes at the TeVatron and exotic physics.

a process, and the best signature is chosen. The selection cuts are optimized based on acceptance studies performed using simulated signal events. The expected background is calculated from data and/or Monte Carlo and, based on the number of events observed in the data, a discovery is made or the best limit on the new signal is set. In a signature-based approach a specific signature is picked (*i.e.* dileptons+X) and the data sample is defined in terms of known SM processes. A signal region (blind box) might be defined with cuts which are kept as loose as possible and the background predictions in the signal region are often extrapolated from control regions. Inconsistencies with the SM predictions will provide indication of possible new physics. As the cuts and acceptances are often calculated independently from a model, different models can be tested against the data sample. It should be noticed that the comparison with a specific model implies calculating optimized acceptances for a specific BSM signal. In signature-based searches, there is no such an optimization. Both the experiments have followed a somehow natural approach in pursuing analysis looking at final state signatures characterized by relatively simple physics objects (for example lepton-only final state, where the selection of the leptons is straightforward and can be easily checked with the measurement of electroweak boson production cross sections) and proceeding onto more complex final state, including jets and heavy flavor. Here more sophisticated identification techniques need to be used and issues like jet energy scale calibration play an important role in determining the final result. Given the limited space available for these proceedings, we will focus here on few selected results. Further results are described in http://ncdf70.fnal.gov:8001/presentations/LaThuile2011_Rolli.pdf.

2. – Search for New Physics in dileptons final states

This is a typical example of a signature-based search for new physics. Final states consisting of dileptons are a straightforward signature where to look for new physics, as several resonant states can appear as enhancement of the Drell-Yan cross section. The analysis strategy is very simple: the invariant mass distribution of the dilepton system is compared to the SM expectations, as shown in figs. 2 and 3. Only identification cuts to select a pair of high P_T leptons are placed.

Both CDF [1,2] and D0 [3] have been studying the dilepton invariant mass distribution. The most recent result is a search for new dielectron mass resonances using 5.7 fb^{-1} of data recorded by the CDF II detector. No significant excess over the expected Standard Model prediction is observed, as seen in fig. 2. In this dataset, an event with the highest dielectron mass ever observed ($960 \text{ GeV}/c^2$) has been recorded. The results are interpreted in the framework of the Randall-Sundrum (RS) model [4]. Combined with a similar search performed with 5.4 fb^{-1} of diphoton data [5] the RS-graviton mass limit

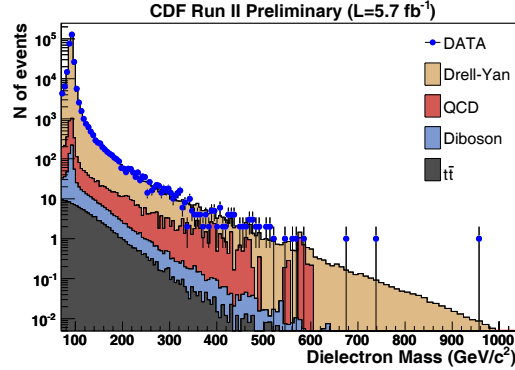


Fig. 2. – Inclusive dielectron mass spectrum at CDF.

for the coupling $k/MP_l = 0.1$ is $1058 \text{ GeV}/c^2$ at 95% CL, making it the strongest limit to date. A similar search is performed in the dimuon channel using 4.3 fb^{-1} of data and no excess is observed (fig. 3). The result is interpreted in terms of Z' production and limits are set on several Z' production scenario: such limits are extending to the kinematical reach of the Tevatron (sequential SM Z' limit is set for example to $1071 \text{ GeV}/c^2$ at 95% CL, making it one of the most stringent in this channel).

3. – Search for extra vector bosons and diboson resonances

A recent result by the D0 Collaboration [6] concerns the search for resonant WW or WZ production. The dataset used corresponds to 5.4 fb^{-1} of integrated luminosity collected by the D0 experiment. The search for these resonances in the diboson decay channel covers the possibility that their coupling to leptons may be lower than the value predicted by the SM. The data are consistent with the standard model background expectation (figs. 4 and 5), and limits are set on a resonance mass using the sequential standard model (SSM) W boson and the Randall-Sundrum model graviton G as benchmarks. D0 excludes a SSM W' boson in the mass range $180\text{--}690 \text{ GeV}$ and a Randall-Sundrum gravi-

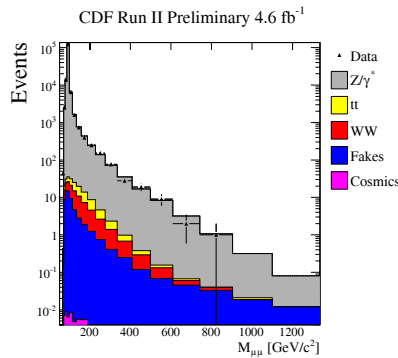


Fig. 3. – Inclusive dimuons mass spectrum at CDF.

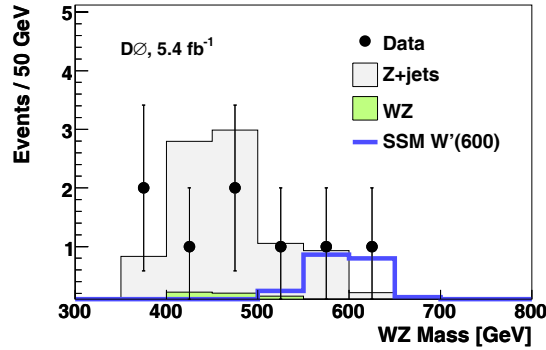


Fig. 4. – Reconstructed WZ mass in the $lvjj, lljj, lll\nu$ channels, D0 Collaboration.

ton in the range 300–754 GeV at 95% CL. There are two recent direct searches for WZ or WW resonances by the CDF and D0 collaborations [7, 8] that exclude WZ resonances with mass below 516 and 520 GeV, respectively, and an RS graviton $G \rightarrow WW$ resonance with mass less than 607 GeV. Indirect searches for new physics in the WW and WZ diboson systems through measurements of the triple gauge couplings also show no deviation from the SM predictions [9–11]. Finally the CDF collaboration has very recently excluded $M(W') < 1.1$ TeV, when assuming the W' boson decays as in the SM [12].

4. – Search for New Physics in complex final states

4.1. *gamma plus jets*. – Many new physics models predict mechanisms that could produce a γ +jets signature. CDF searches in the γ +jets channel, independently of any model, for New Physics using 4.8 fb^{-1} of CDF Run II data [13]. A variety of techniques are applied to estimate the Standard Model expectation and non-collision backgrounds. Several kinematic distributions are examined, including photon ET, invariant masses, and total transverse energy in the event for discrepancies with predictions from the Standard Model (figs. 6 and 7). The data are found to be consistent with Standard

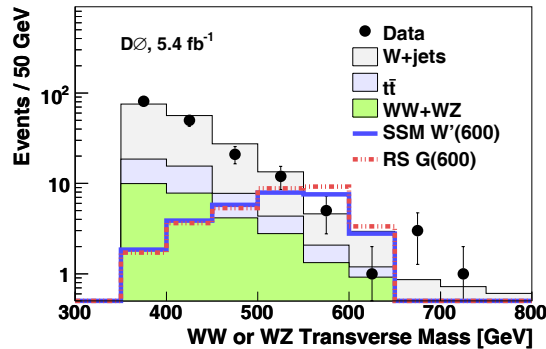


Fig. 5. – Reconstructed WZ or WW transverse mass in the $lvjj$ channel, D0 Collaboration.

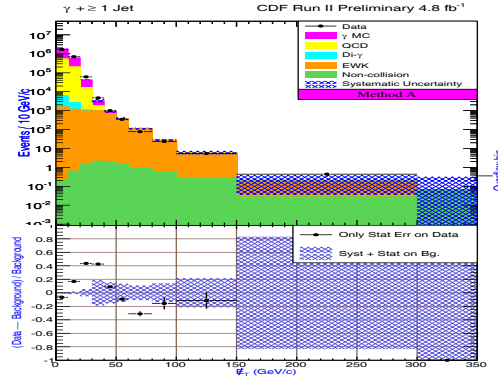


Fig. 6. – Missing energy distribution for $\gamma \pm 1$ jet, CDF Collaboration.

Model expectations. This global search for new physics in γ +jets channel reveals no significant indication of physics beyond Standard Model.

4.2. *gamma plus b-jets plus MET + leptons.* – A search for anomalous production of the signature $l + \gamma + b$ -quark+MET ($l\gamma$ MET b) has been performed by using 6.0 fb^{-1} of data taken with the CDF detector [14]. In addition to the $l\gamma$ MET b signature-based search, CDF also presents for the first time a search for top pair production with an additional radiated photon, $t\bar{t} + \gamma$. 85 events of $l\gamma$ MET b versus an expectation of 99.1 ± 7.61 events. Additionally requiring the events to contain at least 3 jets and to have a total transverse energy of 200 GeV, CDF observes 30 $t\bar{t}\gamma$ candidate events versus an expectation from non-top standard model (SM) sources of 13.0 ± 2.1 . Assuming the difference between the observed number and the predicted non- $t\bar{t}\gamma$ SM total is due to $t\bar{t}\gamma$ production, the collaboration measures the $t\bar{t}\gamma$ cross section to be $0.18 \pm 0.07(\text{stat.}) \pm 0.04(\text{sys.}) \pm 0.01(\text{lum.}) \text{ pb}$. We also measure a ratio of the $t\bar{t}\gamma$ cross section to the $t\bar{t}$ cross section to be 0.024 ± 0.009 .

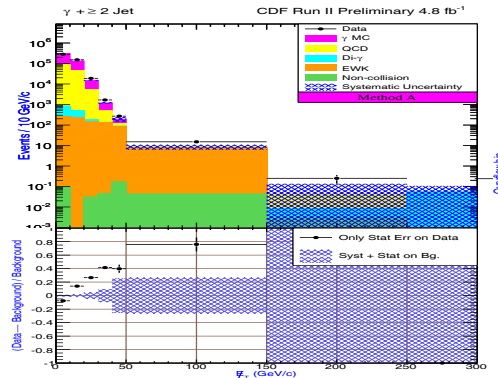


Fig. 7. – Missing energy distribution for $\gamma \pm 2$ jet, CDF Collaboration.

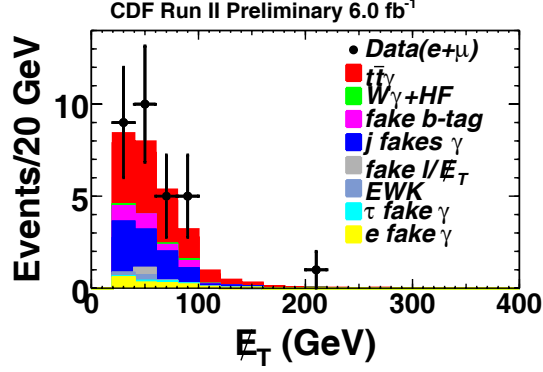
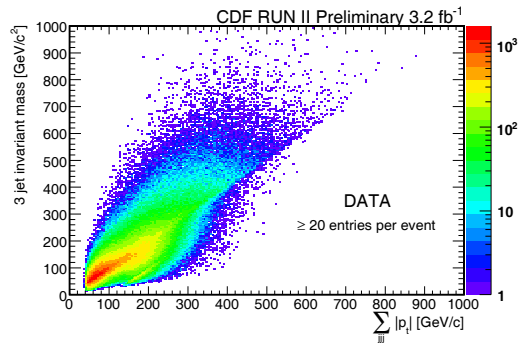
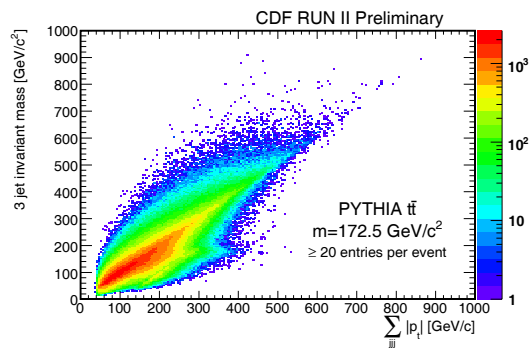
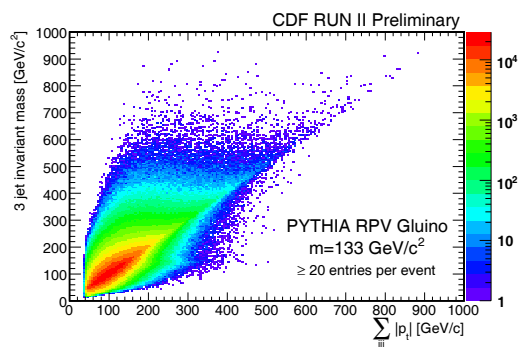


Fig. 8. – Missing energy distribution in $l\gamma$ MET b events, CDF Collaboration.

4.3. Multijets resonances. – A new analysis from CDF has been performed to search for 3-jet hadronic resonances in 3.2fb^{-1} of data [15]. Typical searches for New Physics require either leptons and/or missing transverse energy, however, they might be blind to new physics which have strong couplings and therefore decay into quarks and gluons. The CDF collaboration used 3.2fb^{-1} of data in a model-independent search that reconstructs hadronic resonances in multijet final states. Although the analysis is not optimized for a specific model of new physics, we use as a possible benchmark, R-parity violating supersymmetric (RPV SUSY) gluino pairs production, with each gluino decaying into three objects. Since no significant excess is observed in the data a 95% CL limit is set on $\sigma(pp \rightarrow XX) \times \text{Br}(\tilde{g}\tilde{g} \rightarrow 3\text{jets}+3\text{jets})$, where $X = \tilde{g}, \tilde{q}$, as a function of the gluino invariant mass (fig. 13). To extract signal from the multijet QCD background, kinematic quantities and correlations are used to create an ensemble of jet combinations. Incidentally, the all-hadronic $t\bar{t}$ decay has a signature similar to the signal searched for in this analysis. The biggest challenge of the analysis is the large QCD background that accompanies multijet resonances. A data driven approach is used to parameterize such background. An ensemble consists of 20 (or more) possible jet triplets from the ≥ 6 hardest jets in the event. For every event, we calculate each jet triplet invariant mass, M_{jjj} , and scalar sum p_T , $\Sigma_{jjj}|p_T|$. Using the distribution of M_{jjj} vs. $\Sigma_{jjj}|p_T|$ ensures that the correct combination of jets in pre-defined kinematic regimes is reconstructed, since the incorrect (uncorrelated) triplets tend to have $M_{jjj} = \Sigma_{jjj}|p_T|$. The correct (correlated) triplet produces a horizontal branch in the signal at approximately the invariant mass of the signal that is not present for the background as can be seen in figs. 9, 10, 11, 12.

4.4. Top + MET. – We conclude with a search for a new particle T' decaying to top quark via $T' \rightarrow t + X$, where X is an invisible particle [16]. In a data sample with 4.8fb^{-1} of integrated luminosity collected by the CDF II detector, the search is conducted for pair production of T' in the lepton+jets channel, $p\bar{p} \rightarrow t\bar{t} + X + X \rightarrow l\nu b q\bar{q} + X + X$. Such process would produce extra missing energy and the key observable used in the analysis is the transverse mass distribution of the lepton-missing energy system, which in absence of new physics corresponds to the reconstructed W transverse mass. The results are primarily interpreted in terms of a model where T' are exotic fourth generation quarks and X are dark matter particles [17]. Current direct and indirect bounds on such exotic quarks restrict their masses to be between 300 and $600\text{GeV}/c^2$, the dark matter

Fig. 9. – Distributions of M_{jjj} versus $\Sigma_{jjj}|pT|$.Fig. 10. – Distributions of M_{jjj} versus $\Sigma_{jjj}|pT|$.Fig. 11. – Distributions of M_{jjj} versus $\Sigma_{jjj}|pT|$.

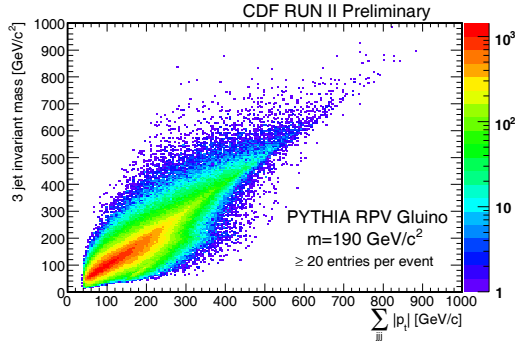


Fig. 12. – Distributions of M_{jjj} versus $\sum_{jjj} |p_T|$ multiple entry (≥ 20).

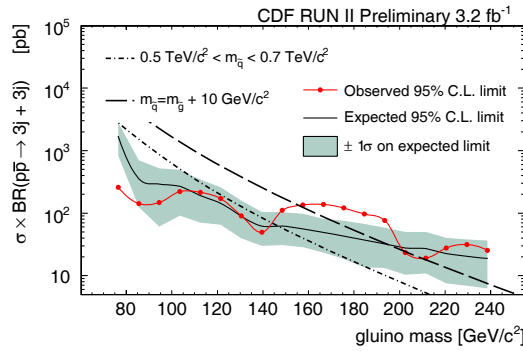


Fig. 13. – The observed and expected limit including systematic uncertainties as well as the theory cross section for $\sigma(p\bar{p} \rightarrow XX) \times \text{Br}(\tilde{g}\tilde{g} \rightarrow 3\text{jets} + 3\text{jets})$ where $X = \tilde{g}, \tilde{q}$, versus gluino invariant mass. The RPV gluino cross-section is from PYTHIA and is corrected by an NLO k -factor.

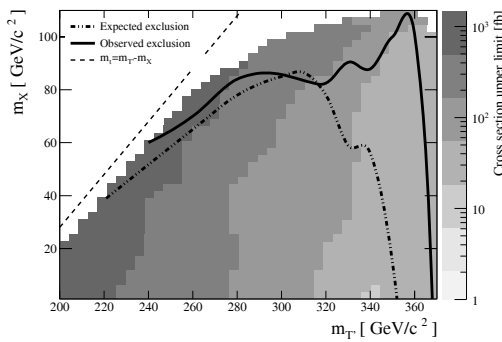


Fig. 14. – Observed versus expected exclusion in (m_T, m_X) along with the cross section upper limits.

particle mass can be anywhere below $m_{T'}$. The data are consistent with standard model expectations, and CDF sets a 95% confidence level limits on the generic production of $TT' \rightarrow t\bar{t} + X + X$, by performing a binned maximum-likelihood fit in the m_W variable, allowing for systematic and statistical fluctuations via template morphing. The observed upper limits on the pair-production cross sections are converted to an exclusion curve in the mass parameter space for the dark matter model involving fourth generation quarks. The current cross section limits on the generic decay, $T' \rightarrow t + X$, may be applied to the many other models that predict the production of a heavy particle T' decaying to top quarks and invisible particles X , such as the supersymmetric process $\tilde{t} \rightarrow t + \chi^0$. Applying these limits to the dark matter model CDF excludes fourth generation exotic quarks T' at 95% confidence level up to $m_{T'} = 360 \text{ GeV}/c^2$ for $m_X < 100 \text{ GeV}/c^2$ (fig. 14).

5. – Conclusions

The CDF and D0 experiments are actively collecting and analyzing data at the Tevatron collider. New physics is searched in a broad manner, using different approaches. In signature based analyses the data are scanned for anomalies pointing to indications of New Physics, while many dedicated searches for specific models are pursued, using the largest possible statistical samples. New results on search for physics beyond the Standard Model are released almost daily. So far there is no evidence for New Physics and numerous limits on new particle masses and cross sections production are set. A broader set of updated results can be found at: <http://www-d0.fnal.gov/Run2Physics/WWW/results/np.htm> and <http://www-cdf.fnal.gov/physics/exotic/exotic.html>.

REFERENCES

- [1] ALTOONEN T. *et al.*, arXiv,1103.4650 (2011).
- [2] ALTOONEN T. *et al.*, *Phys. Rev. Lett.*, **106** (2011) 121801.
- [3] ABAZOV V. M. *et al.*, *Phys. Rev. Lett.*, **104** (2010) 241802.
- [4] RANDALL L. and SUNDRUM R., *Phys. Rev. Lett.*, **83** (1999) 3370.
- [5] ALTOONEN T. *et al.*, *Phys. Rev. D*, **83** (2011) 011102.
- [6] ABAZOV V. M. *et al.*, arXiv.org, 1011.6278 (2010).
- [7] ABAZOV V. M. *et al.*, *Phys. Rev. Lett.*, **104** (2010) 061801.
- [8] AALTONEN T. *et al.*, *Phys. Rev. Lett.*, **104** (2010) 241801.
- [9] ABAZOV V. M. *et al.*, *Phys. Rev. Lett.*, **103** (2009) 191801.
- [10] ABAZOV V. M. *et al.*, *Phys. Rev. D*, **80** (2009) 053012.
- [11] THE LEP COLLABORATIONS, <http://lepewwg.web.cern.ch/> (2005).
- [12] AALTONEN T. *et al.*, *Phys.Rev. D*, **83** (2011) 031102.
- [13] AALTONEN T. *et al.*, CDF Public Note, 10355 (2011).
- [14] AALTONEN T. *et al.*, CDF Public Note, 10437 (2010).
- [15] AALTONEN T. *et al.*, arXiv, 1105.2815 (2011).
- [16] AALTONEN T. *et al.*, *Phys. Rev. Lett.*, **106** (2011) 191801.
- [17] FENG J. *et al.*, arXiv, 1002.3366 (2010).

Searches for New Physics at CMS

H. U. FLÄCHER on behalf of the CMS COLLABORATION

Department of Physics and Astronomy - University of Rochester, Rochester, NY, USA

(ricevuto il 29 Settembre 2011; pubblicato online il 25 Gennaio 2012)

Summary. — The first searches for New Physics with the CMS detector at the LHC are presented. The discussed analyses are based on the data sample recorded in 2010 at a centre-of-mass energy of 7 TeV, which corresponds to an integrated luminosity of about 35 pb^{-1} . Searches for excited vector bosons, leptoquarks, extra dimensions as well as for supersymmetry in different final states are presented. No significant deviations from Standard Model expectations have been observed and thus limits on the parameter space of different New Physics scenarios are derived.

PACS 11.30.Pb – Supersymmetry.

PACS 14.80.Sv – Leptoquarks.

PACS 14.70.Pw – Other gauge bosons.

1. – Introduction

The start of operations at the Large Hadron Collider (LHC) at a centre-of-mass energy of 7 TeV in 2010 has marked the beginning of a new era in the search for physics beyond the Standard Model (SM). In 2010, the CMS experiment [1] recorded a data sample with integrated luminosity of about 35 pb^{-1} of proton-proton collisions. Thanks to the much higher centre-of-mass energy of the collisions, the physics reach is already comparable to or larger than what has been achieved at previous experiments at LEP or the Tevatron. In this article we report the results of the first searches for excited vector bosons, leptoquarks and microscopic black holes. Furthermore, we discuss the results of the first searches for supersymmetry (SUSY) involving missing transverse energy.

2. – W' and Z' searches

Several extensions of the SM predict the existence of further gauge bosons that can be regarded as heavy analogues of the SM gauge bosons W and Z. Examples of such models are left-right symmetric models [2-4], compositeness models [5] and Little Higgs models [6].

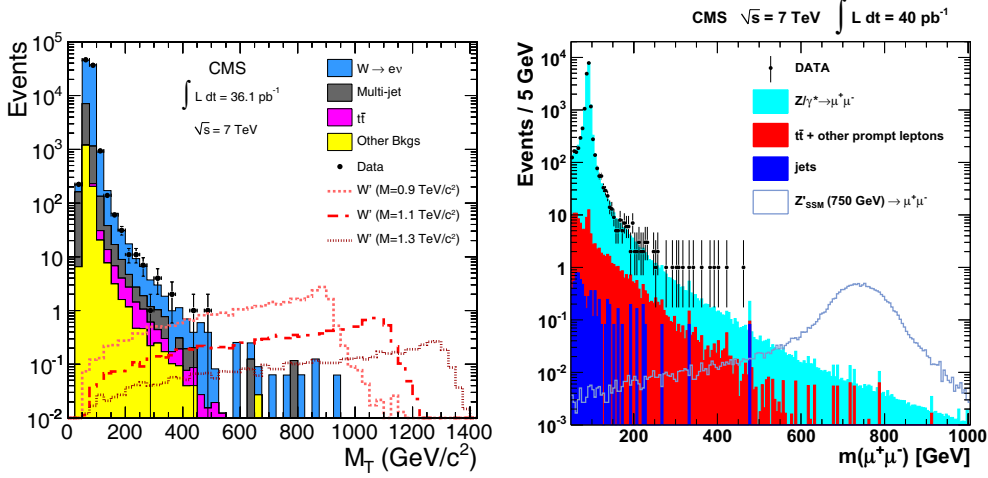


Fig. 1. – Left: transverse mass distributions for selected electron events in the W' search. Right: invariant mass distributions for dimuon events in the Z' search.

The search for an excited W boson, W' , is generally explored using a benchmark model [7] where the W' has the same left-handed fermionic couplings as its SM counterpart and where interactions with the SM gauge bosons are excluded. The most easily identifiable experimental signature thus consists of a high- p_T lepton accompanied by large missing transverse momentum due to the undetected escaping neutrino. The primary discriminating variable is the transverse mass M_T which is the equivalent of the invariant mass of a four-vector computed with only the transverse components of those four-vectors:

$$(1) \quad M_T = \sqrt{2 \cdot E_T^{\text{lep}} \cdot E_T^{\text{miss}} \cdot (1 - \cos \Delta\phi(\text{lep}, E_T^{\text{miss}}))}.$$

As with a W , the M_T distribution of W' events is expected to exhibit a characteristic Jacobian edge at the value of the mass of the decaying particle. Events are selected where an electron with transverse momentum, $p_T > 30$ GeV ($p_T > 25$ GeV for muons) has been identified. As the signal topology is a two-body decay which reconstructs to a high mass, the energy of the neutrino and electron are expected to be mostly balanced in the transverse plane, both in direction and in magnitude. We therefore require $0.4 < E_T^{\text{lep}}/E_T^{\text{miss}} < 1.5$. For the same reason, we require that the angle between the electron and the E_T^{miss} be close to π radians: $\Delta\phi(\text{lep}, E_T^{\text{miss}}) > 2.5$ rad. The main SM background stems from $W \rightarrow \ell\nu$ decays in the tails of the SM W mass distribution. Figure 1 shows the transverse mass distribution for selected events with electrons [8] and the comparison with expected SM backgrounds from Monte Carlo (MC) simulation. In addition, the expected signal from a W' with different masses is overlaid. In the absence of a signal, limits on the mass and production cross-section times branching fraction are set. This is shown in fig. 2. In electron (muon) channel, a W' with SM couplings and branching fractions can be excluded at the 95% confidence level (CL) for masses up to 1.36 (1.40) GeV [8, 9]. Combining the results from the two channels results in an exclusion of W' masses up to 1.58 GeV.

Analogous to the W' searches, a search for a Z' signature has been carried out [10]. Here, the high mass part of the Z resonance tail is studied. Events with two oppositely

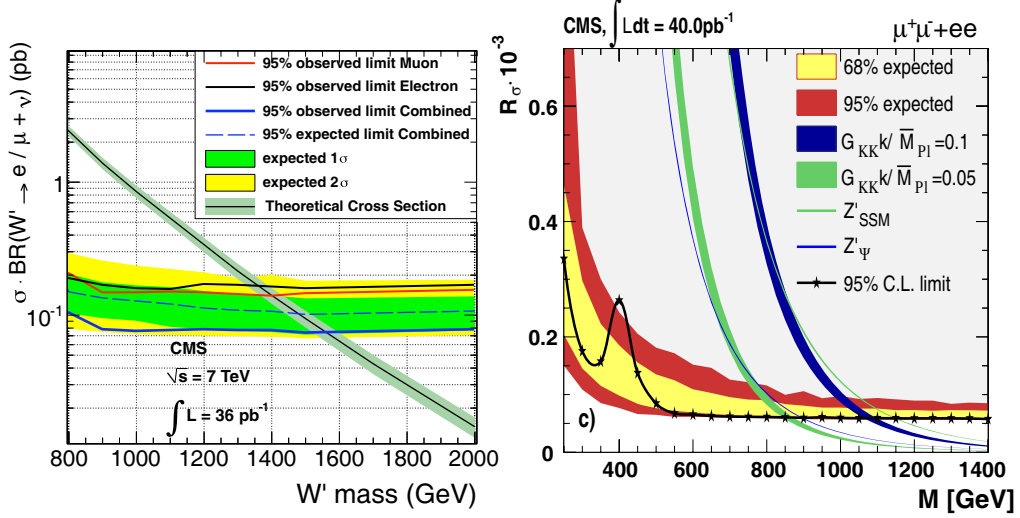


Fig. 2. – Left: upper limits on the production cross section times branching fraction as a function of the W' mass for the electron channel, the muon channel and the combination of both. Right: upper limits on the production ratio R_σ of cross section times branching fraction into lepton pairs for Z'_{SSM} and G_{KK} production and Z'_Ψ boson production as a function of resonance mass M .

charged electrons (muons) with $p_T > 25 \text{ GeV}$ ($p_T > 20 \text{ GeV}$) are selected. The dilepton invariant mass spectrum for di-muon events is shown in fig. 1, together with the expected SM backgrounds and an expected signal from a Z' with mass of 750 GeV. In the absence of an excess of events in the high mass tail over the SM expectation, limits on the production cross section of Z' with respect to SM Z are set as a function of the Z' mass (see fig. 2). By combining the electron and muon channels, the following 95% CL lower limits on the mass of a Z' resonance are obtained [10]: 1140 GeV for the Z'_{SSM} [11], and 887 GeV for Z'_Ψ [11] models. Randall-Sundrum Kaluza-Klein gravitons G_{KK} [12, 13] are excluded below 855 (1079) GeV for values of couplings 0.05 (0.10).

3. – Leptoquark searches

Several extensions of the standard model [14–18] predict the existence of leptoquarks (LQ), hypothetical particles that carry both lepton and baryon numbers and couple to both leptons and quarks. Leptoquarks are fractionally charged and can be either scalar or vector particles. A search for pair-produced first (second) generation leptoquarks is carried out in events with two electrons (muons) and two jets, each with $p_T > 30 \text{ GeV}$. The main backgrounds from Z decays is rejected by requiring $M_{ee} > 125 \text{ GeV}$ ($M_{\mu\mu} > 115 \text{ GeV}$). After this preselection, the main discriminating variable is defined as the scalar sum of the lepton and jet p_T 's: $S_T = E_T(\ell_1) + E_T(\ell_2) + E_T(\text{jet}_1) + E_T(\text{jet}_2)$. The two variables are shown for di-electron events in fig. 3 [19] where good agreement between data and SM expectation is found.

Figure 4 [19, 20] shows the 95% CL upper limit on the LQ pair production cross section times β^2 , where β is the branching fraction for $LQ \rightarrow qe(\mu)^{(1)}$, as a function

⁽¹⁾ $(1-\beta)$ is the branching fraction for $LQ \rightarrow q\nu_e(\nu_\mu)$.

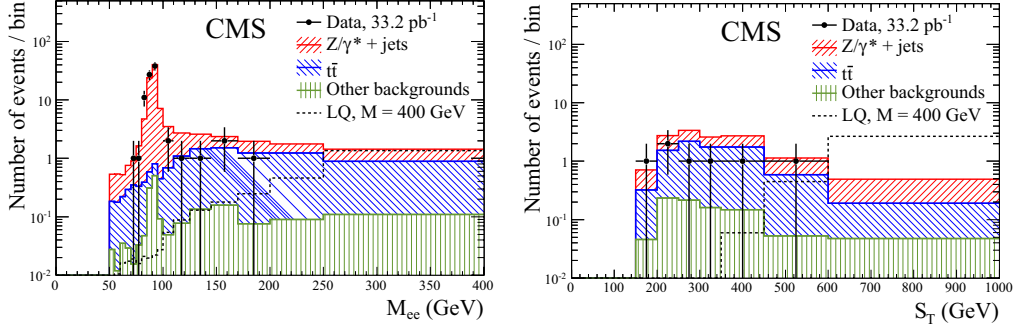


Fig. 3. – Invariant mass distributions for dielectron events after preselection (left) and the S_T distribution after final selection (right).

of the LQ mass. First (second) generation leptoquarks can be excluded at 95% CL for masses up to 384 GeV (394 GeV) for $\beta = 1$ [19, 20].

4. – Searches for microscopic black holes

Extensions to the Standard Model proposing the existence of extra spatial dimensions and low-scale quantum gravity offer the possibility of copious production of microscopic black holes [21, 22]. In this model, the true Planck scale in $4 + n$ dimensions, M_D , is consequently lowered to the electroweak scale, much smaller than the apparent Planck scale of $M_{Pl} \sim 10^{16}$ TeV seen by a 3+1 spacetime observer. The relationship between M_D and M_{Pl} follows from Gauss's law and is given as $M_{Pl}^2 = 8\pi M_D^{n+2} r^n$.

The creation of microscopic black holes is possible when the two partons from colliding beams pass each other at a distance smaller than the Schwarzschild radius corresponding to their invariant mass. The such produced black holes would decay instantly via Hawking

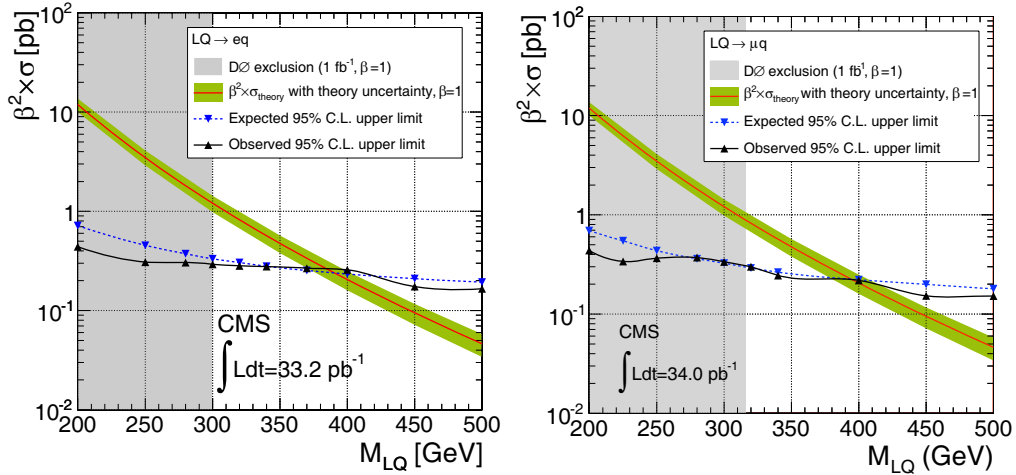


Fig. 4. – Upper limits on the production cross section times branching fraction for first generation leptoquarks (left) and second generation leptoquarks (right).

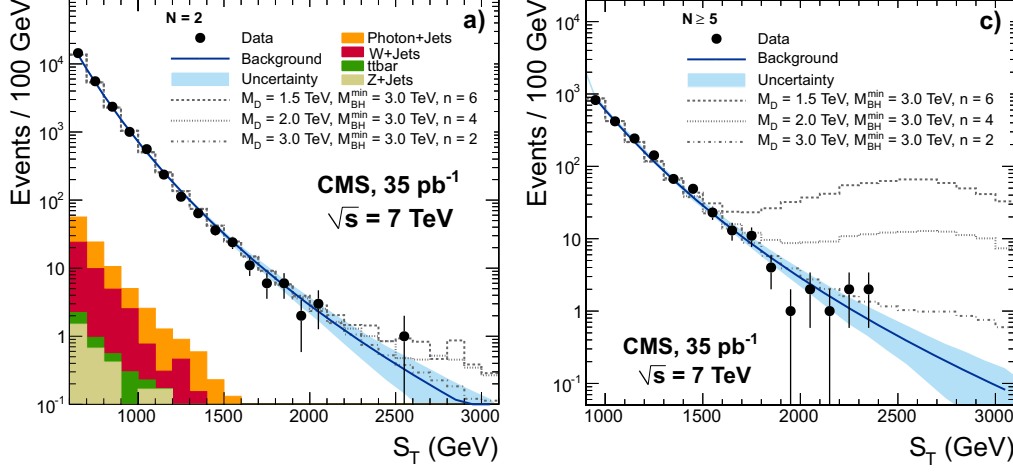


Fig. 5. – The S_T for events with object multiplicity of two (left) and ≥ 5 (right). A possible signal contribution from black hole models with different effective Planck scale M_D and number of extra dimensions n is overlaid.

evaporation with an emission of a large numbers of energetic objects. The search thus uses the scalar sum of all measured physics objects i (jets, muons, electrons, photons, and the missing energy) with transverse energy, $E_T > 50$ GeV as discriminating variable: $S_T = \sum_{i=1}^n E_T^i$.

The main standard model background consists of QCD multi-jet production but it was found that the shape of the S_T distribution does not depend on the object multiplicity. It is thus possible to obtain a purely data driven background estimation for this search, as the S_T shape can be obtained from QCD di-jet events. Due to the small object multiplicity, this sample is basically signal free. The S_T distribution for object multiplicities of two and ≥ 5 is shown in fig. 5 [23]. No excess of events at high S_T over the SM expectation is observed. In fig. 6 the 95% CL upper limits in the black hole production cross section are shown for different values of the effective Planck scale M_D and the number of extra spatial dimensions n . Furthermore, the 95% CL limits on the black hole mass as a function of M_D are shown [23]. The lower limits on the black hole mass at 95% CL range from 3.5 to 4.5 TeV for values of the effective Planck scale up to 3 TeV.

5. – Searches for Supersymmetry

Supersymmetry is one of the most promising extensions to the Standard Model as it provides solutions to several shortcomings of the former. SUSY provides a solution to the hierarchy problem by stabilizing the Higgs mass through the introduction of new particles. In addition, it naturally leads to a unification of the strong and electroweak interactions at a scale around 10^{16} GeV and it predicts electroweak symmetry breaking, which is the basis for understanding all masses via the Higgs mechanism. Finally, it can accommodate a weakly interacting massive stable particle that can serve as a dark matter candidate, thus providing a solution to one of the most intriguing problems in modern particle physics and cosmology. In the following, searches for SUSY based on different event topologies are discussed.

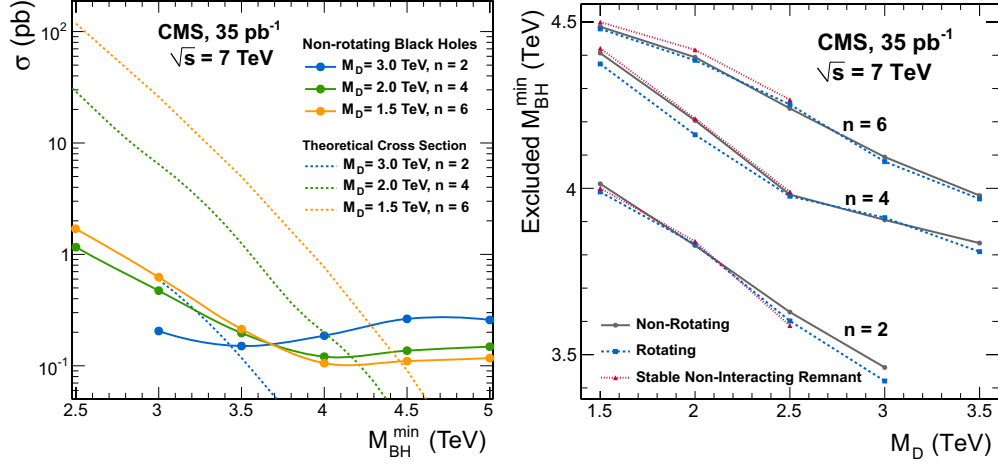


Fig. 6. – Left: the 95% CL upper limits on the black hole production cross section (solid lines) and three theoretical predictions for the cross section (dashed lines), as a function of the black hole mass. Right: the 95% CL limits on the black hole mass as a function of the multidimensional Planck scale M_D for several benchmark scenarios. The area below each curve is excluded by this search.

5.1. The jets + missing energy topology. – The dominant production channels of heavy coloured sparticles at the LHC are squark squark, squark gluino and gluino gluino pair production. In the context of SUSY with R-parity conservation, heavy squarks and gluinos decay into quarks, gluons and other SM particles, as well as a neutralino, *i.e.* the lightest supersymmetric particle (LSP), which escapes undetected, leading to final states with several hadronic jets and large missing transverse energy. While squark squark production usually leads to two jets, gluino production typically results in higher jet multiplicities.

For the jets + missing energy topology the background from multijet production, as predicted by quantum chromodynamics (QCD), is several orders of magnitude larger than the typical signal expected from SUSY. For this type of events, missing transverse energy is introduced through mis-measurements of jets in the detector. For this reason, a kinematic variable, α_T , defined for di-jet events as

$$(2) \quad \alpha_T = \frac{E_T^{\text{jet}_2}}{M_T} = \frac{\sqrt{E_T^{\text{jet}_2}/E_T^{\text{jet}_1}}}{\sqrt{2(1 - \cos \Delta\phi(\text{jet}_1, \text{jet}_2))}},$$

is employed to separate events with real missing energy from those where missing energy is introduced through mis-measurements. For QCD di-jet events, where the jets are expected to be balanced in p_T and back-to-back in azimuthal angle ϕ , this variable has an expectation value of 0.5, and < 0.5 in case the two jets are not p_T balanced, thus exploiting the scalar and angular information of the measured jets. For events with real missing energy, such as SUSY signal but also $t\bar{t}$, $W \rightarrow \ell\nu$, and $Z \rightarrow \nu\nu + \text{jets}$ events with small transverse mass, α_T can take on values > 0.5 . Multi-jet events are reduced to a di-jet topology by constructing pseudo-jets and using these in the calculation of α_T . In the calculation of α_T jets with $E_T > 50$ GeV are considered and $H_T = \sum_{i=1}^n E_T^{\text{jet}_i} > 350$ GeV

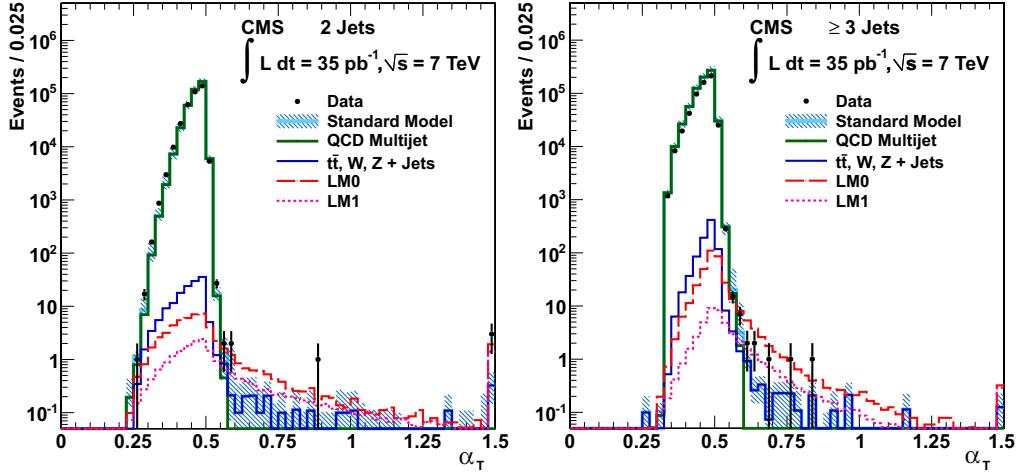


Fig. 7. – α_T distribution for dijet events (left) and events with ≥ 3 jets (right).

is required. Figure 7 shows the α_T distribution for events with two (left) and ≥ 3 jets (right) where the strong rejection power against QCD multi-jets events can be seen. The remaining backgrounds from $t\bar{t}$ and $W \rightarrow \ell\nu$ decays are estimated with an inclusive muon data control sample whereas the background from $Z \rightarrow \nu\nu + \text{jets}$ events is estimated from a photon + jets control sample. The combined background prediction amounts to $10.5^{+3.6}_{-2.5}(\text{stat}) \pm 2.5(\text{syst})$ events compared to 13 events found in data [24]. We use this result to set limits on the parameter space of the constrained minimal supersymmetric extension of the standard model (CMSSM). This is shown in fig. 8 [24] which shows the m_0 vs. $m_{1/2}$ plane, *i.e.* the universal scalar and gaugino mass, respectively. It can be seen that the exclusion exceeds by far the limits set previously by experiments at LEP and the Tevatron.

5.2. The opposite charge dilepton channel. – Pair produced heavy particles such as squarks and gluinos can undergo cascade decays to SM particles, thus producing leptons

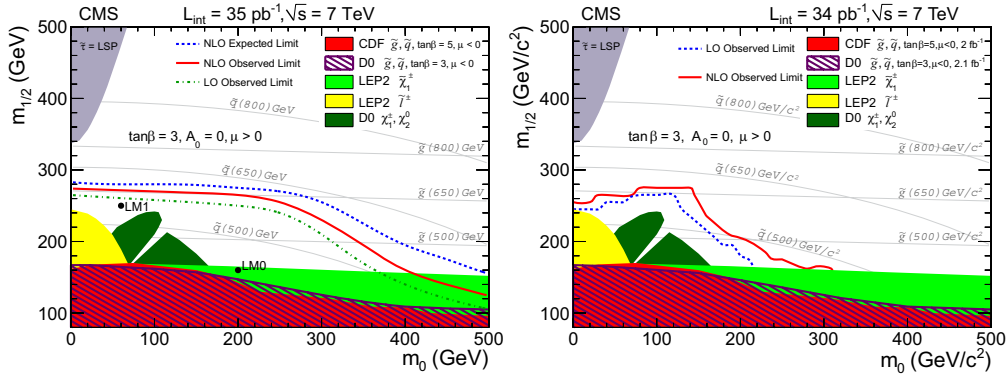


Fig. 8. – 95% CL exclusion in the m_0 vs. $m_{1/2}$ plane of the CMSSM. Left: jets + missing transverse energy analysis based on α_T . Right: opposite charge dilepton analysis. The areas below the solid lines are excluded.

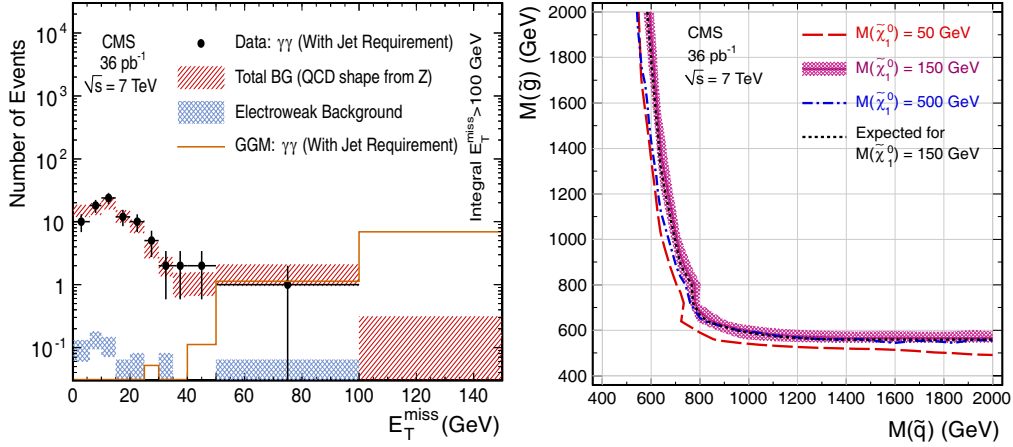


Fig. 9. – Left: missing energy E_T^{miss} distribution for di-photon events and data driven background estimation. Right: lower 95% CL exclusion limits on the squark and gluino masses in the GGM benchmark model for 50, 150, and 500 GeV neutralino masses. The areas below and to the left of the lines are excluded.

in addition to hadronic jets. The requirement of isolated leptons significantly reduces the background from QCD multi-jet events. Requiring two oppositely charged leptons basically only leaves $t\bar{t}$ events as SM background. Events are selected requiring at least one isolated lepton with $p_T > 20$ GeV and the other with $p_T > 10$ GeV. In addition, at least two jets with $p_T > 30$ GeV that are well separated from the leptons are required and the scalar sum of their transverse energies is required to exceed $H_T > 300$ GeV. Furthermore, the missing transverse energy is $E_T^{\text{miss}} > 50$ GeV is required and $y = E_T^{\text{miss}}/\sqrt{H_T} > 8.5\sqrt{\text{GeV}}$, which leaves about 1% of the di-lepton $t\bar{t}$ events. To determine the remaining backgrounds, the fact that H_T and y are nearly uncorrelated is exploited. Defining signal and background regions in both variables, the expected number of background events in the joint signal region can be obtained from the three control regions [25]. A second method exploits the idea that in di-lepton $t\bar{t}$ events the p_T distributions of the charged leptons and neutrinos from W decays are related, because of the common boosts from the top and W decays. This relation is governed by the polarization of the W 's, which is well understood in top decays in the SM and can therefore be reliably accounted for. The observed $p_T(\ell\ell)$ distribution is then used to model the $p_T(\nu\nu)$ distribution, which is identified with E_T^{miss} .

In the signal region with $y = E_T^{\text{miss}}/\sqrt{H_T} > 8.5\sqrt{\text{GeV}}$, one event is observed in data compared with a background expectation of 1.3 ± 0.8 (stat) ± 0.3 (syst) from the first background estimation method and 2.1 ± 2.1 (stat) ± 0.6 (syst) events from the second method. Using the error weighted average of the two background predictions of 1.4 ± 0.8 [25], a 95% CL exclusion limit in the m_0 vs. $m_{1/2}$ plane of the CMSSM is calculated and displayed in fig. 8 [25].

5.3. The diphoton channel. – Supersymmetric models with general gauge mediation (GGM) [26,27] have the gravitino as the lightest supersymmetric particle. In the models considered here, the next-to-lightest supersymmetric particle is the lightest neutralino that is assumed to decay promptly to an escaping gravitino and a photon. The search requires two isolated photons with $E_T > 30$ GeV in the barrel of the electromagnetic

calorimeter and at least one jet with $E_T > 30$ GeV. The main backgrounds arise from SM processes with misidentified photons and/or mismeasured E_T^{miss} . The dominant contribution comes from mismeasurement of E_T^{miss} in QCD processes such as direct diphoton, photon plus jets, and multijet production, with jets mimicking photons in the latter two cases. The E_T^{miss} distribution for $\gamma\gamma$ events is shown in fig. 9 [28]. For $E_T^{\text{miss}} > 50$ GeV, one event is observed in data with a SM background expectation of 1.2 ± 0.4 (stat) ± 0.8 (syst) events. The background expectation is obtained from two different data-driven background estimation methods, selecting two fake photons in a QCD multi-jet sample and two electrons from $Z \rightarrow e^+e^-$ decays, respectively [28]. In the absence of a signal, the observed event yield is used to set limits on the production cross section of GGM models as a function of the squark and gluino mass. The observed 95% confidence level (CL) cross section limits vary between 0.3 and 1.1 pb for squark and gluino masses between 500 and 2000 GeV and a neutralino mass of 150 GeV. These cross section limits can then be turned into lower limits on the squark and gluino masses which are displayed in fig. 9 [28] for different neutralino masses.

6. – Summary

Based on the data collected in 2010, the CMS collaboration has carried out a wide variety of searches for physics beyond the Standard Model. Unfortunately, so far no evidence for a deviation from the SM expectation has been found but the sensitivity of almost all these searches exceeds those of previous experiments at LEP and the Tevatron. In the presented analyses great effort was made to determine the remaining Standard Model backgrounds from data control samples with only small reliance on the Monte Carlo simulation of the involved processes. This bodes well for future searches on the much larger data sample that will be collected in 2011 and 2012.

REFERENCES

- [1] THE CMS COLLABORATION, *JINST*, **3** (2008) S08004.
- [2] MOHAPATRA R. N. and PATI J. C., *Phys. Rev. D*, **11** (1975) 566.
- [3] SENJANOVIC G. and MOHAPATRA R. N., *Phys. Rev. D*, **12** (1975) 1502.
- [4] PATI J. C. and SALAM A., *Phys. Rev. D*, **10** (1974) 275.
- [5] EICHTEEN E., LANE K. D. and PESKIN M. E., *Phys. Rev. Lett.*, **50** (1983) 811.
- [6] HAN T., LOGAN H. E., MCELDRATH B. and WANG L.-T., *Phys. Rev. D*, **67** (2003) 095004 [hep-ph/0301040].
- [7] ALTARELLI G., MELE B. and RUIZ-ALTABA M., *Z. Phys. C*, **45** (1989) 109.
- [8] THE CMS COLLABORATION, *Phys. Lett. B*, **698** (2011) 21 [arXiv:1012.5945 [hep-ex]].
- [9] THE CMS COLLABORATION, *Phys. Lett. B*, **701** (2011) 160 [arXiv:1103.0030 [hep-ex]].
- [10] THE CMS COLLABORATION, *JHEP*, **1105** (2011) 093 [arXiv:1103.0981 [hep-ex]].
- [11] LEIKE A., *Phys. Rep.*, **317** (1999) 143 [arXiv:hep-ph/9805494].
- [12] RANDALL L. and SUNDRUM R., *Phys. Rev. Lett.*, **83** (1999) 4690 [arXiv:hep-th/9906064].
- [13] RANDALL L. and SUNDRUM R., *Phys. Rev. Lett.*, **83** (1999) 3370 [arXiv:hep-ph/9905221].
- [14] BUCHMULLER W., RUCKL R. and WYLER D., *Phys. Lett. B*, **191** (1987) 442; (**448** (1999) 320(E)).
- [15] DIMOPOULOS S. and SUSSKIND L., *Nucl. Phys. B*, **155** (1979) 237.
- [16] DIMOPOULOS S., *Nucl. Phys. B*, **168** (1980) 69.
- [17] EICHTEEN E. and LANE K. D., *Phys. Lett. B*, **90** (1980) 125.
- [18] ANGELOPOULOS V. D., ELLIS J. R., KOWALSKI H., NANOPOULOS D. V., TRACAS N. D. and ZWIRNER F., *Nucl. Phys. B*, **292** (1987) 59.

- [19] THE CMS COLLABORATION, *Phys. Rev. Lett.*, **106** (2011) 201802 [arXiv:1012.4031 [hep-ex]].
- [20] THE CMS COLLABORATION, *Phys. Rev. Lett.*, **106** (2011) 201803 [arXiv:1012.4033 [hep-ex]].
- [21] ARKANI-HAMED N., DIMOPOULOS S. and DVALI G. R., *Phys. Lett. B*, **429** (1998) 263 [hep-ph/9803315].
- [22] ARKANI-HAMED N., DIMOPOULOS S. and DVALI G. R., *Phys. Rev. D*, **59** (1999) 086004 [hep-ph/9807344].
- [23] THE CMS COLLABORATION, *Phys. Lett. B*, **697** (2011) 434 [arXiv:1012.3375 [hep-ex]].
- [24] THE CMS COLLABORATION, *Phys. Lett. B*, **698** (2011) 196 [arXiv:1101.1628 [hep-ex]].
- [25] THE CMS COLLABORATION, *JHEP*, **1106** (2011) 026 [arXiv:1103.1348 [hep-ex]].
- [26] MEADE P., SEIBERG N. and SHIH D., *Prog. Theor. Phys. Suppl.*, **177** (2009) 143 [arXiv:0801.3278 [hep-ph]].
- [27] BUICAN M., MEADE P., SEIBERG N. and SHIH D., *JHEP*, **0903** (2009) 016 [arXiv:0812.3668 [hep-ph]].
- [28] THE CMS COLLABORATION, *Search for Supersymmetry in pp Collisions at $\sqrt{s} = 7$ TeV in Events with Two Photons and Missing Transverse Energy*, arXiv:1103.0953 [hep-ex].

Working Technicolor at the LHC

M. NARDECCHIA

*Centre for Particle Physics Phenomenology, University of Southern Denmark
Odense, Denmark*

(ricevuto il 29 Settembre 2011; pubblicato online il 26 Gennaio 2012)

Summary. — In this talk, we will review the possibility to brake the electroweak symmetry in a dynamical way. We present a class of phenomenologically viable Walking Technicolor models, finally we analyze the potential of the Large Hadron Collider to observe signatures from this kind of models.

PACS 12.60.Nz – Technicolor models.

1. – Introduction

The energy scale at which the Large Hadron Collider (LHC) experiment operates is determined by the need to complete the Standard Model (SM) of particle interactions and, in particular, to understand the origin of the ElectroWeak Symmetry Breaking (EWSB). Together with classical general relativity the SM constitutes one of the most successful models of nature. We shall, however, argue that experimental results and theoretical arguments call for a more fundamental description of nature.

The SM can be viewed as a low-energy effective theory valid up to an energy scale Λ . Above this scale new interactions, symmetries, extra dimensional worlds or any other extension could emerge. At sufficiently low energies with respect to this scale one expresses the existence of new physics via effective operators. The success of the SM is due to the fact that most of the corrections to its physical observables depend only logarithmically on this scale Λ . In fact, in the SM there exists only one operator which acquires corrections quadratic in Λ . This is the squared mass operator of the Higgs boson. Since Λ is expected to be the highest possible scale, in four dimensions the Planck scale (assuming that we have only the SM and gravity), it is hard to explain *naturally* why the mass of the Higgs is of the order of the Electroweak (EW) scale. This is the hierarchy problem. Due to the occurrence of quadratic corrections in the cutoff this SM sector is most sensitive to the existence of new physics.

In the models we will consider here the electroweak symmetry breaks via a fermion bilinear condensate, and the Higgs being a composite object is now free from the naturalness problem. The Higgs sector of the SM becomes an effective description of a more fundamental fermionic theory. This is similar to the Ginzburg-Landau theory

of superconductivity. If the force underlying the fermion condensate driving electroweak symmetry breaking is due to a strongly interacting gauge theory these models are termed Technicolor (TC).

2. – From color to technicolor

One of the main difficulties in constructing such extensions of the SM is the very limited knowledge about generic strongly interacting theories. This has led theorists to consider specific models of TC which resemble ordinary QCD and for which the large body of experimental data at low energies can be directly exported to make predictions at high energies. To reduce the tension with experimental constraints new strongly coupled theories with dynamics different from the one featured by a scaled-up version of QCD are needed.

Let us first review the mechanism of EWSB in QCD. In fact even in complete absence of the Higgs sector in the SM the electroweak symmetry breaks [1] due to the condensation of the following quark bilinear in QCD:

$$(1) \quad \langle \bar{u}_L u_R + \bar{d}_L d_R \rangle \neq 0.$$

This mechanism, however, cannot account for the whole contribution to the weak gauge bosons masses. If QCD was the only source contributing to the spontaneous breaking of the electroweak symmetry one would have

$$(2) \quad M_W = \frac{gF_\pi}{2} \sim 29 \text{ MeV},$$

with $F_\pi \simeq 93 \text{ MeV}$ the pion decay constant. This contribution is very small with respect to the actual value of the W mass that one typically neglects it.

According to the original idea of TC [2,3] one augments the SM with another gauge interaction similar to QCD but with a new dynamical scale of the order of the electroweak one. It is sufficient that the new gauge theory is asymptotically free and has global symmetry able to contain the SM $SU(2)_L \times U(1)_Y$ symmetries. It is also required that the new global symmetries break dynamically in such a way that the embedded $SU(2)_L \times U(1)_Y$ breaks to the electromagnetic Abelian charge $U(1)_Q$. The dynamically generated scale will then be fit to the electroweak one.

The simplest example of TC theory is the scaled-up version of QCD, *i.e.* an $SU(N_{\text{TC}})$ non-Abelian gauge theory with two Dirac Fermions transforming according to the fundamental representation or the gauge group. We need at least two Dirac flavors to realize the $SU(2)_L \times SU(2)_R$ symmetry of the SM discussed in the SM Higgs section. One simply chooses the scale of the theory to be such that the new pion decaying constant is

$$(3) \quad F_\pi^{\text{TC}} = v \simeq 246 \text{ GeV}.$$

The flavor symmetries, for any N_{TC} larger than 2 are $SU(2)_L \times SU(2)_R \times U(1)_V$ which spontaneously break to $SU(2)_V \times U(1)_V$ reproducing the correct mass for the W^\pm and Z^0 bosons.

3. – Extended technicolor

Since in a purely TC model the Higgs is a composite particle the Yukawa terms, when written in terms of the underlying TC fields, amount to four-fermion operators. The latter can be naturally interpreted as a low-energy operator induced by a new strongly coupled gauge interaction emerging at energies higher than the electroweak theory. These type of theories have been termed Extended Technicolor (ETC) interactions [4, 5].

Without specifying an ETC one can write down the most general type of four-fermion operators involving TC particles Q and ordinary fermionic fields ψ . Following the notation of Hill and Simmons [6] we write

$$(4) \quad \alpha_{ab} \frac{\bar{Q}\gamma_\mu T^a Q \bar{\psi}\gamma^\mu T^b \psi}{\Lambda_{\text{ETC}}^2} + \beta_{ab} \frac{\bar{Q}\gamma_\mu T^a Q \bar{Q}\gamma^\mu T^b Q}{\Lambda_{\text{ETC}}^2} + \gamma_{ab} \frac{\bar{\psi}\gamma_\mu T^a \psi \bar{\psi}\gamma^\mu T^b \psi}{\Lambda_{\text{ETC}}^2},$$

where the T s are unspecified ETC generators.

The coefficients parametrize the ignorance on the specific ETC physics. To be more specific, the α -terms, after the TC particles have condensed, lead to mass terms for the SM fermions

$$(5) \quad m_q \approx \frac{g_{\text{ETC}}^2}{M_{\text{ETC}}^2} \langle \bar{Q}Q \rangle_{\text{ETC}},$$

where m_q is the mass of, *e.g.*, a SM quark, g_{ETC} is the ETC gauge coupling constant evaluated at the ETC scale, M_{ETC} is the mass of an ETC gauge boson and $\langle \bar{Q}Q \rangle_{\text{ETC}}$ is the TC condensate where the operator is evaluated at the ETC scale. Note that we have not explicitly considered the different scales for the different generations of ordinary fermions but this should be taken into account for any realistic model.

The β -terms provide masses for pseudo Goldstone bosons and also provide masses for techniaxions [6]. The last class of terms, namely the γ -terms induce FCNCs. For example it may generate the following terms:

$$(6) \quad \frac{1}{\Lambda_{\text{ETC}}^2} (\bar{s}\gamma^5 d)(\bar{s}\gamma^5 d) + \frac{1}{\Lambda_{\text{ETC}}^2} (\bar{\mu}\gamma^5 e)(\bar{e}\gamma^5 e) + \dots,$$

The experimental bounds on these type of operators together with the very *naive* assumption that ETC will generate these operators with γ of order one leads to a constraint on the ETC scale to be of the order of or larger than 10^3 TeV [4]. This should be the lightest ETC scale which in turn puts an upper limit on how large the ordinary fermionic masses can be. The naive estimate is that one can account up to around 100 MeV mass for a QCD-like TC theory, implying that the top quark mass value cannot be achieved.

To better understand in which direction one should go to modify the QCD dynamics, we analyze the TC condensate. The value of the TC condensate used when giving mass to the ordinary fermions should be evaluated not at the TC scale but at the ETC one. Via the renormalization group one can relate the condensate at the two scales via

$$(7) \quad \langle \bar{Q}Q \rangle_{\text{ETC}} = \exp \left(\int_{\Lambda_{\text{TC}}}^{\Lambda_{\text{ETC}}} d(\ln \mu) \gamma_m(\alpha(\mu)) \right) \langle \bar{Q}Q \rangle_{\text{TC}},$$

where γ_m is the anomalous dimension of the techniquark mass operator. The boundaries of the integral are at the ETC scale and the TC one.

The tension between having to reduce the FCNCs and at the same time provide a sufficiently large mass for the heavy fermions in the SM as well as the pseudo-Goldstones can be reduced if the theory has a near conformal fixed point. This kind of dynamics has been denoted as of *walking* type.

In the walking regime

$$(8) \quad \langle \bar{Q}Q \rangle_{\text{ETC}} \sim \left(\frac{\Lambda_{\text{ETC}}}{\Lambda_{\text{TC}}} \right)^{\gamma_m(\alpha^*)} \langle \bar{Q}Q \rangle_{\text{TC}},$$

which is a much larger contribution than in QCD dynamics [7-10]. Here γ_m is evaluated at the would be fixed point value α^* . Walking can help resolving the problem of FCNCs in TC models since with a large enhancement of the $\langle \bar{Q}Q \rangle$ condensate the four-Fermi operators involving SM fermions and technifermions and the ones involving technifermions are enhanced by a factor of $\Lambda_{\text{ETC}}/\Lambda_{\text{TC}}$ to the γ_m power while the one involving only SM fermions is not enhanced.

Another relevant point is that a near conformal theory would still be useful to reduce the contributions to the precision data and, possibly, provide a light composite Higgs of much interest to LHC physics [11].

4. – Minimal models with walking dynamics

The existence of a new weak doublet of technifermions amounting to, at least, a global $SU(2)_L \times SU(2)_R$ symmetry later opportunely gauged under the electroweak interactions is the bedrock on which models of TC are built on.

It is therefore natural to construct first minimal models of TC passing precision tests while also reducing the FCNC problem by featuring near conformal dynamics. By minimal we mean with the smallest fermionic matter content. These models were put forward recently in [12, 11]. To be concrete we describe here the Minimal Walking Technicolor extension of the SM.

The extended SM gauge group is now $SU(2)_{\text{TC}} \times SU(3)_C \times SU(2)_L \times U(1)_Y$ and the field content of the TC sector is constituted by four techni-fermions and one techni-gluon all in the adjoint representation of $SU(2)_{\text{TC}}$. The model features also a pair of Dirac leptons, whose left-handed components are assembled in a weak doublet, necessary to cancel the Witten anomaly [13] arising when gauging the new technifermions with respect to the weak interactions. Summarizing, the fermionic particle content of the MWT is given explicitly by

$$(9) \quad Q_L^a = \begin{pmatrix} U^a \\ D^a \end{pmatrix}_L, \quad U_R^a, \quad D_R^a, \quad a = 1, 2, 3,$$

with a being the adjoint color index of $SU(2)$. The left handed fields are arranged in three doublets of the $SU(2)_L$ weak interactions in the standard fashion. The condensate is $\langle \bar{U}U + \bar{D}D \rangle$ which correctly breaks the electroweak symmetry as already argued for ordinary QCD in eq. (1).

To discuss the symmetry properties of the theory it is convenient to use the Weyl basis for the fermions and arrange them in the following vector transforming according to the fundamental representation of $SU(4)$

$$(10) \quad Q = \begin{pmatrix} U_L \\ D_L \\ -i\sigma^2 U_R^* \\ -i\sigma^2 D_R^* \end{pmatrix},$$

where U_L and D_L are the left-handed techniup and technidown, respectively and U_R and D_R are the corresponding right-handed particles. Assuming the standard breaking to the maximal diagonal subgroup, the $SU(4)$ symmetry spontaneously breaks to $SO(4)$. Such a breaking is driven by the following condensate:

$$(11) \quad \langle Q_i^\alpha Q_j^\beta \epsilon_{\alpha\beta} E^{ij} \rangle = -2 \langle \bar{U}_R U_L + \bar{D}_R D_L \rangle,$$

where the indices $i, j = 1, \dots, 4$ denote the components of the tetraplet of Q , and the Greek indices indicate the ordinary spin. The matrix E is a 4×4 matrix defined in terms of the 2-dimensional unit matrix as

$$(12) \quad E = \begin{pmatrix} 0 & \mathbb{1} \\ \mathbb{1} & 0 \end{pmatrix}.$$

Here $\epsilon_{\alpha\beta} = -i\sigma_{\alpha\beta}^2$ and $\langle U_L^\alpha U_R^{*\beta} \epsilon_{\alpha\beta} \rangle = -\langle \bar{U}_R U_L \rangle$. A similar expression holds for the D techniquark. The above condensate is invariant under an $SO(4)$ symmetry. This leaves us with nine broken generators with associated Goldstone bosons, of which three become the longitudinal degrees of freedom of the weak gauge bosons.

Another example is the Next to Minimal Walking Technicolor (NMWT). The theory with three technicolors contains an even number of electroweak doublets, and hence it is not subject to a Witten anomaly. The doublet of technifermions, is then represented again as

$$(13) \quad Q_L^{\{C_1, C_2\}} = \begin{pmatrix} U^{\{C_1, C_2\}} \\ D^{\{C_1, C_2\}} \end{pmatrix}_L, \quad Q_R^{\{C_1, C_2\}} = \left(U_R^{\{C_1, C_2\}}, D_R^{\{C_1, C_2\}} \right).$$

Here $C_i = 1, 2, 3$ is the technicolor index and $Q_{L(R)}$ is a doublet (singlet) with respect to the weak interactions. Since the two-index symmetric representation of $SU(3)$ is complex the flavor symmetry is $SU(2)_L \times SU(2)_R \times U(1)$. Only three Goldstones emerge and are absorbed in the longitudinal components of the weak vector bosons.

Despite the different envisioned underlying gauge dynamics it is a fact that the SM structure alone requires the extensions to contain, at least, the following chiral symmetry breaking pattern (insisting on keeping the custodial symmetry of the SM):

$$(14) \quad SU(2)_L \times SU(2)_R \rightarrow SU(2)_V.$$

Based on the previous symmetry breaking pattern we describe the low-energy spectrum in terms of the lightest spin one vector and axial-vector iso-triplets $V^{\pm,0}, A^{\pm,0}$ as well as the lightest iso-singlet scalar resonance H . In QCD the equivalent states are the $\rho^{\pm,0}, a_1^{\pm,0}$ and the $f_0(600)$. It has been argued in [14], using large-N arguments, and in [11], using the saturation of the trace of the energy momentum tensor, that models of dynamical electroweak symmetry breaking featuring (near) conformal dynamics contain a composite Higgs state which is light with respect to the new strongly coupled scale ($4\pi v$ with $v \simeq 246$ GeV). These indications have led to the construction of models of TC with a naturally *light composite* Higgs. Recent investigations using Schwinger-Dyson [15] and gauge-gravity dualities [16] also arrived to the conclusion that the composite Higgs can be light. The 3 technipions $\Pi^{\pm,0}$ produced in the symmetry breaking become the longitudinal components of the W and Z bosons.

The composite spin one and spin zero states and their interaction with the SM fields are described via the following effective Lagrangian:

$$(15) \quad \mathcal{L}_{\text{boson}} = -\frac{1}{2}\text{Tr}[\widetilde{W}_{\mu\nu}\widetilde{W}^{\mu\nu}] - \frac{1}{4}\widetilde{B}_{\mu\nu}\widetilde{B}^{\mu\nu} - \frac{1}{2}\text{Tr}[F_{L\mu\nu}F_L^{\mu\nu} + F_{R\mu\nu}F_R^{\mu\nu}] \\ + m^2\text{Tr}[C_{L\mu}^2 + C_{R\mu}^2] + \frac{1}{2}\text{Tr}[D_\mu M D^\mu M^\dagger] - \tilde{g}^2 r_2 \text{Tr}[C_{L\mu} M C_{R\mu}^\dagger M^\dagger] \\ - \frac{i\tilde{g}r_3}{4}\text{Tr}[C_{L\mu}(M D^\mu M^\dagger - D^\mu M M^\dagger) + C_{R\mu}(M^\dagger D^\mu M - D^\mu M^\dagger M)] \\ + \frac{\tilde{g}^2 s}{4}\text{Tr}[C_{L\mu}^2 + C_{R\mu}^2] \text{Tr}[M M^\dagger] + \frac{\mu^2}{2}\text{Tr}[M M^\dagger] - \frac{\lambda}{4}\text{Tr}[M M^\dagger]^2,$$

where $\widetilde{W}_{\mu\nu}$ and $\widetilde{B}_{\mu\nu}$ are the ordinary electroweak field strength tensors, $F_{L/R\mu\nu}$ are the field strength tensors associated to the vector meson fields $A_{L/R\mu}$ and the $C_{L\mu}$ and $C_{R\mu}$ fields are

$$(16) \quad C_{L\mu} \equiv A_{L\mu} - \frac{g}{\tilde{g}}\widetilde{W}_\mu, \quad C_{R\mu} \equiv A_{R\mu} - \frac{g'}{\tilde{g}}\widetilde{B}_\mu.$$

The 2×2 matrix M is

$$(17) \quad M = \frac{1}{\sqrt{2}}[v + H + 2i\pi^a T^a], \quad a = 1, 2, 3,$$

where π^a are the Goldstone bosons produced in the chiral symmetry breaking, $v = \mu/\sqrt{\lambda}$ is the corresponding VEV, H is the composite Higgs, and $T^a = \sigma^a/2$, where σ^a are the Pauli matrices. The covariant derivative is

$$(18) \quad D_\mu M = \partial_\mu M - ig\widetilde{W}_\mu^a T^a M + ig' M \widetilde{B}_\mu T^3.$$

When M acquires a VEV, the Lagrangian of eq. (15) contains mixing matrices for the spin one fields. The mass eigenstates are the ordinary SM bosons, and two triplets of heavy mesons, of which the lighter (heavier) ones are denoted by R_1^\pm (R_2^\pm) and R_1^0 (R_2^0). These heavy mesons are the only new particles, at low energy, relative to the SM.

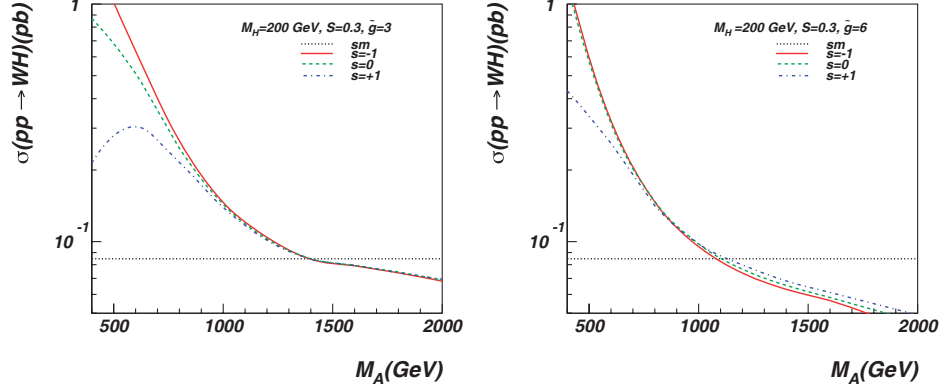


Fig. 1. – The cross section for $pp \rightarrow WH$ production at 7 TeV in the center of mass (W^+H and W^-H modes are summed up) versus M_A for $S = 0.3$, $s = (+1, 0, 1)$ and $\tilde{g} = 3$ (left) and $\tilde{g} = 6$ (right). The dotted line at the bottom indicates the SM cross section level.

5. – Phenomenological implications

New physics signals are expected from the vector meson and the composite Higgs sectors.

The heavy spin-one resonances, $R_{1,2}^0$ and $R_{1,2}^\pm$, can be produced through DY processes. In particular very important signatures are given by the following processes with lepton signatures:

- 1) $\ell^+\ell^-$ signature from the process $pp \rightarrow R_{1,2}^0 \rightarrow \ell^+\ell^-$,
- 2) $\ell + \cancel{E}_T$ signature from the process $pp \rightarrow R_{1,2}^\pm \rightarrow \ell^\pm\nu$,
- 3) $3\ell + \cancel{E}_T$ signature from the process $pp \rightarrow R_{1,2}^\pm \rightarrow ZW^\pm \rightarrow 3\ell\nu$,

where ℓ denotes a charged lepton (electron or muon) and \cancel{E}_T is the missing transverse energy. A detailed analysis of this and other channels is presented in [17, 18].

The presence of the heavy vectors is prominent in the associated production of the composite Higgs with SM vector bosons, as first pointed out in [19].

The resonant production of heavy vectors can enhance HW and ZH production by a factor 10 as one can see in fig. 1 (right). This enhancement occurs for low values of the vector meson mass and large values of \tilde{g} .

6. – Conclusions

We introduced extensions of the SM in which the Higgs emerges as a composite state. In particular we motivated TC, constructed underlying gauge theories leading to minimal models of TC and constructed the low-energy effective theory.

LHC can be sensitive to spin one states as heavy as 2 TeV. One TeV spin one states can be observed already with 100 pb^{-1} integrated luminosity in the dilepton channel. The enhancement of the composite Higgs production is another promising signature.

REFERENCES

- [1] FARHI E. and SUSSKIND L., *Phys. Rep.*, **74** (1981) 277.
- [2] WEINBERG S., *Phys. Rev. D*, **19** (1979) 1277.
- [3] SUSSKIND L., *Phys. Rev. D*, **20** (1979) 2619.
- [4] EICHTEIN E. and LANE K. D., *Phys. Lett. B*, **90** (1980) 125.
- [5] DIMOPOULOS S. and SUSSKIND L., *Nucl. Phys. B*, **155** (1979) 237.
- [6] HILL C. T. and SIMMONS E. H., *Phys. Rep.*, **381** (2003) 235; **390** (2004) 553(E) (arXiv:hep-ph/0203079).
- [7] YAMAWAKI K., BANDO M. and MATUMOTO K. I., *Phys. Rev. Lett.*, **56** (1986) 1335.
- [8] HOLDOM B., *Phys. Lett. B*, **150** (1985) 301.
- [9] HOLDOM B., *Phys. Rev. D*, **24** (1981) 1441.
- [10] APPELQUIST T. W., KARABALI D. and WIJEWARDHANA L. C. R., *Phys. Rev. Lett.*, **57** (1986) 957.
- [11] DIETRICH D. D., SANNINO F. and TUOMINEN K., *Phys. Rev. D*, **72** (2005) 055001 (arXiv:hep-ph/0505059).
- [12] SANNINO F. and TUOMINEN K., *Phys. Rev. D*, **71** (2005) 051901 (arXiv:hep-ph/0405209).
- [13] WITTEN E., *Phys. Lett. B*, **117** (1982) 324.
- [14] HONG D. K., HSU S. D. H. and SANNINO F., *Phys. Lett. B*, **597** (2004) 89 (arXiv:hep-ph/0406200).
- [15] DOFF A., NATALE A. A. and RODRIGUES DA SILVA P. S., *Phys. Rev. D*, **77** (2008) 075012 (arXiv:0802.1898 [hep-ph]).
- [16] FABBRICHESI M., PIAI M. and VECCHI L., *Phys. Rev. D*, **78** (2008) 045009 (arXiv:0804.0124 [hep-ph]).
- [17] BELYAEV A., FOADI R., FRANSEN M. T., JARVINEN M., SANNINO F. and PUKHOV A., *Phys. Rev. D*, **79** (2009) 035006 (arXiv:0809.0793 [hep-ph]).
- [18] ANDERSEN J. R. *et al.*, arXiv:1104.1255 [hep-ph].
- [19] ZERWEKH A. R., *Eur. Phys. J. C*, **46** (2006) 791 (arXiv:hep-ph/0512261).

SESSION VIII - PHYSICS AND SOCIETY

Rolf-Dieter Heuer

CERN and the future of particle physics

CERN and the future of particle physics

R.-D. HEUER

CERN - CH-1211 Geneva 23, Switzerland

(ricevuto il 29 Settembre 2011; pubblicato online il 25 Gennaio 2012)

Summary. — This paper presents CERN and its current scientific programme and outlines options for high-energy colliders at the energy frontier for the years to come. The immediate plans include the exploitation of the LHC at its design luminosity and energy as well as upgrades to the LHC and its injectors. This may be followed by a linear electron-positron collider, based on the technology being developed by the Compact Linear Collider and by the International Linear Collider, or by a high-energy electron-proton machine, the LHeC. This contribution describes the past, present and future directions, all of which have a unique value to add to experimental particle physics, and concludes by outlining key messages for the way forward.

PACS 14.80.Da – Supersymmetric Higgs bosons.

PACS 12.60.Jv – Supersymmetric models.

PACS 12.38.Mh – Quark-gluon plasma.

PACS 12.15.Ff – Quark and lepton masses and mixing.

1. – CERN - A global laboratory for particle physics

The mission of CERN is fourfold:

- Push back the frontiers of knowledge. This includes gaining further understanding of the secrets of the early Universe shortly after the Big Bang and the nature of matter within the first moments of the Universe's existence.
- Develop new technologies for accelerators, detectors and computing. These technologies can subsequently be transferred to other applications, something which has happened with the World Wide Web and the Grid in information technology and with diagnosis and therapy techniques in medicine.
- Train the scientists and engineers of tomorrow.
- Unite people from different countries and cultures.

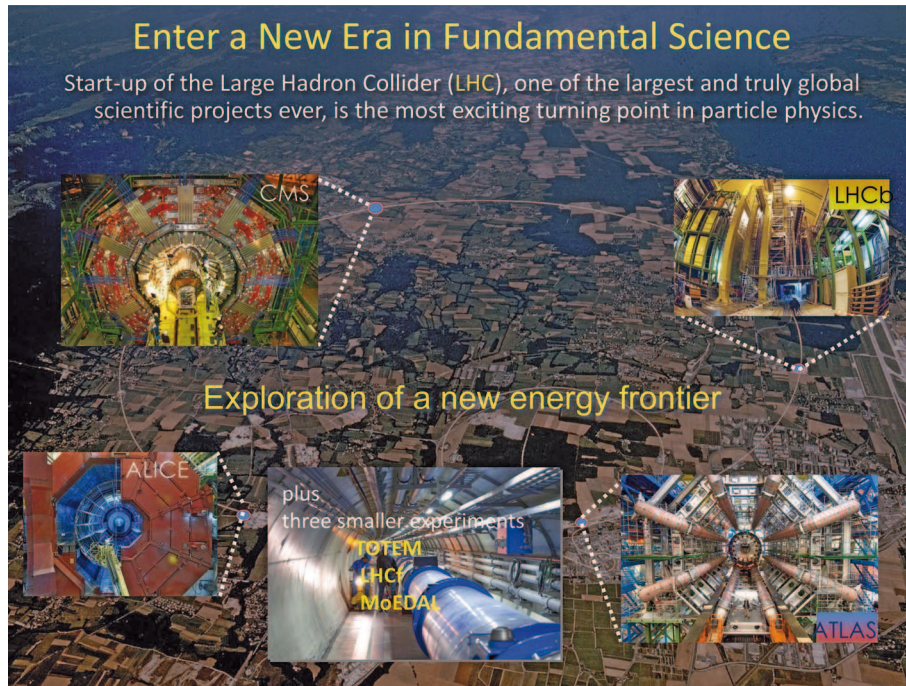


Fig. 1. – The LHC accelerator and the ALICE, ATLAS, CMS and LHCb experiments. There are also three smaller experiments - LHCf, MoEDAL and TOTEM.

The above mission is supported by the more than 10 000 scientific users from the Member States, Observer States and states with which CERN has concluded co-operation agreements. A survey conducted in March 2009 shows that the age of scientists at CERN peaks in the 20s and that there are more than 2 500 PhD students in the LHC experiments alone. Earlier surveys of the destination of students during the LEP period showed that after completing their PhDs most students went on to careers in the private sector.

Amongst the numerous education and training programmes, the CERN Summer Student Programme is of particular note. About 250 advanced undergraduate students joined the programme in 2010, originating from both Member States and non-Member States. Moreover, the High School Teacher Programme has been highly successful in bringing to CERN about 3 000 teachers during the period 1998-2010, with close to 1 000 teachers in 2010 alone. The knowledge and skills they obtain during their stays at CERN is then transferred to the classroom, with highly visible effects in capturing the interest and imagination of the next generation of would-be scientists.

2. – The Large Hadron Collider

2.1. The Physics. – The Large Hadron Collider (LHC) [1] is primarily a proton-proton collider (see fig. 1) with a design centre-of-mass energy of 14 TeV and nominal luminosity of $10^{34} \text{ cm}^{-2} \text{ s}^{-1}$, and will also be operated in heavy-ion mode. The high 40 MHz proton-proton collision rate and the tens of interactions per crossing result in an enormous challenge for the experiments and for the collection, storage and analysis of the data.

By colliding unparalleled high-energy and high-intensity beams, the LHC is opening up previously unexplored territory at the TeV scale in great detail, allowing the experiments to probe deeper inside matter and providing further understanding of processes that occurred very early in the history of the Universe.

Of central importance to the LHC is the elucidation of the nature of electroweak symmetry breaking, for which the Higgs mechanism and the accompanying Higgs boson(s) are presumed to be responsible. In order to make significant inroads into the Standard Model Higgs Boson search, sizeable integrated luminosities of several fb^{-1} are needed. However, even with 1fb^{-1} per experiment, discovery of the Standard Model Higgs Boson is still possible in mass regions beyond the lower limit of 114.4 GeV from direct searches at LEP2. At the initial LHC centre-of-mass energy of 7 TeV and with 1fb^{-1} per experiment, combining the results from ATLAS and CMS would provide a 3σ sensitivity to a Standard Model Higgs Boson mass in the range 135 GeV to 475 GeV, and will exclude the Standard Model Higgs Boson between 120 GeV and 530 GeV at 95% CL. Combining the results from ATLAS and CMS at 7 TeV centre-of-mass energy and assuming about 10fb^{-1} per experiment would exclude at 95% CL the mass range from 600 GeV down to the LEP2 lower limit and would also provide a 3σ sensitivity to a Standard Model Higgs Boson in the same mass range.

The reach for new physics at the LHC is considerable already at LHC start-up. In Supersymmetry (SUSY) theory, due to their high production cross-sections, squarks and gluinos can be produced in significant numbers even at modest luminosities. This would enable the LHC to start probing the nature of dark matter. The LHC discovery reach for SUSY particles is up to a mass of about 700 GeV for 1fb^{-1} per experiment at 7 TeV centre-of-mass energy.

The discovery reach for new heavy bosons Z' and W' is about 1.6 TeV and 2.1 TeV, respectively, for 1fb^{-1} per experiment at 7 TeV centre-of-mass energy.

The LHC will also provide information on the unification of forces, the number of space-time dimensions and on matter-antimatter asymmetry. With the heavy-ion collision mode, the LHC will probe the formation of the quark-gluon plasma at the origin of the Universe.

2.2. LHC Operations

2.2.1. The Past. The start-up of the LHC on 10 September 2008 was a great success for both the accelerator and the experiments. Circulating beams were established rapidly and the beams were captured by the radiofrequency system with optimum injection phasing and with the correct reference. The incident of 19 September 2008, caused by a faulty inter-magnet bus-bar splice, resulted in significant damage in Sector 3-4 of the accelerator. Actions were taken immediately to repair the damage and to introduce measures to avoid any re-occurrence. The damaged thirty-nine main dipole magnets and fourteen quadrupole magnets were removed and replaced. Fast pressure release valves (DN200) were added on the main magnets, an improved anchoring on the vacuum barriers was introduced around the ring, and most importantly an enhanced quench protection system was implemented. Any remaining risks to the LHC, due to the shortcomings of copper-stabilizer joints of the main LHC magnets, are minimized by limiting the top beam energy in the first years of LHC operation.

Excellent progress was made in the above-mentioned repair, consolidation and improvement work, and first collisions at the LHC were recorded by the experiments on 23 November 2009 at a centre-of-mass energy of 900 GeV. During this first physics run at

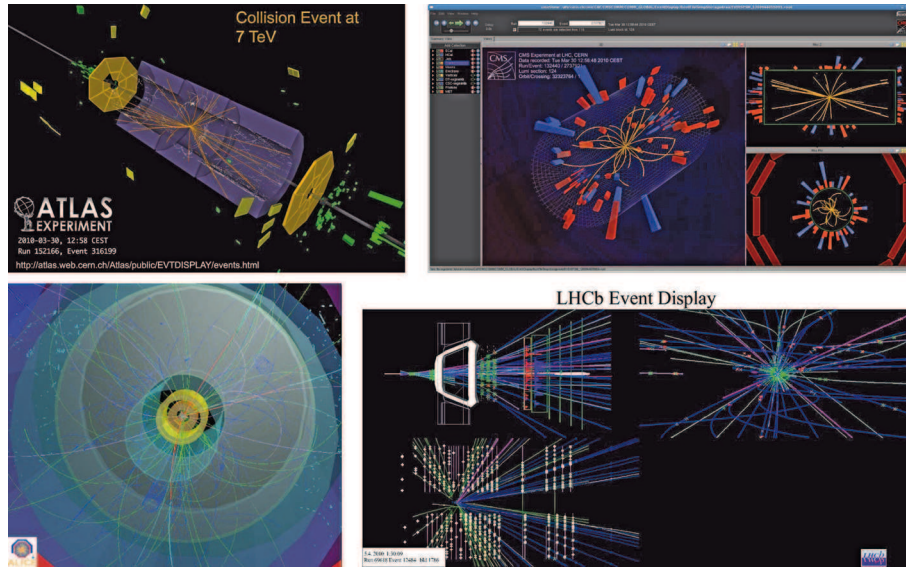


Fig. 2. – First collisions at 7 TeV centre-of-mass energy.

the end of 2009, the LHC accelerator performed exceptionally and the readiness of the experiments and the computing Grid was excellent, resulting in impressive preliminary results provided already at an open seminar held at CERN on 18 December 2009 and the prompt publication of the first physics results by year's end.

First LHC beams for 2010 were available on 27 February for commissioning the accelerator with beam. This was followed by first physics collisions at 7 TeV centre-of-mass energy on 30 March (see fig. 2) and by the first physics runs with a stronger focusing at the interaction points. During the 2009 and 2010 LHC physics runs, data has been collected at 900 GeV, 2.36 TeV and 7 TeV centre-of-mass energies with increasing instantaneous luminosities.

The main LHC achievements for 2010 can be summarized as follows:

- Excellent performance of the LHC machine for both proton and Pb-ion beams. Beam operation availability was 65% on average. Peak instantaneous luminosities of $2 \times 10^{32} \text{ cm}^{-2} \text{ s}^{-1}$ were attained for proton-proton collisions, which were a factor of two above the 2010 goal and which resulted in almost 50 pb^{-1} of integrated luminosity delivered to the experiments. Following a short 4-day switch-over to Pb-ion beams, peak luminosities of $3 \times 10^{25} \text{ cm}^{-2} \text{ s}^{-1}$ were attained for Pb-Pb collisions with almost $10 \mu\text{b}^{-1}$ of integrated luminosity delivered to the experiments.
- The experiments took data of excellent quality and with high efficiency. The physics analyses re-measured the science of the Standard Model of Particle Physics, in many instances superseding limits set at the Tevatron while taking the LHCs first steps into new territory. As a result, 54 physics papers based on the 2010 data were published and more than 1140 conference presentations were made by the LHC experiments.
- The performance of the LHC Computing Grid was also outstanding, exceeding the design bandwidth and allowing a very fast reconstruction and analysis of the data.

2.2.2. The Present. At the LHC Performance Workshop in Chamonix, held at the end of January 2011, the current state of the LHC was evaluated and presented, leading subsequently to the following decisions:

- The LHC will be operated during 2011 and 2012 with target integrated luminosities of 1 fb^{-1} by the end of 2011 at 3.5 TeV/beam and of several fb^{-1} by the end of 2012. Heavy-ion runs are scheduled at the end of both years, each of about 4 weeks duration. A technical stop of about 3 months around Christmas 2011 is needed.
- This extended operations period will be followed by a long shutdown (of about 20 months beam-to-beam) starting at the end of 2012 to repair and consolidate the inter-magnet copper-stabilizers (splices) to allow for safe operation up to 7 TeV/beam for the lifetime of the LHC.
- In the shadow of the inter-magnet copper-stabilizer work, the installation of the pressure rupture disks (DN200) will be completed and around 20 magnets which are known to have problems for high energy will be repaired or replaced. In addition, PS and SPS consolidation and upgrade work will be carried out.
- During this shutdown, the collimation system will also be upgraded at region Point 3 of the LHC.
- The experiments will use the shutdown to implement a programme of consolidation, improvements and upgrades.

2.2.3. The Future. The coming years will lay the foundation for the next decades of high-energy physics at the LHC. The LHC research programme until around 2030 is determined by the full exploitation of its physics potential, consisting of the design luminosity and the high-luminosity upgrade (HL-LHC), together with superconducting higher-field magnets for a higher-energy proton collider (HE-LHC), if necessitated by the physics. These initiatives will position CERN as the laboratory at the energy frontier.

The strategy for the LHC for the coming years is the following:

- Exploitation of the physics potential of the LHC up to design conditions in the light of running experience and by optimizing the schedule for physics.
- Preparation of the LHC for a long operational lifetime through appropriate modifications and consolidation to the machine and detectors and through the build-up of an adequate spares inventory.
- In the years 2015, 2016 and 2017, the LHC will be operated towards 7 TeV/beam with increased intensities and luminosities.
- In 2017/2018, a long shutdown is scheduled to connect LINAC4 [2], to complete the PS Booster energy upgrade, to finalize the collimation system enhancement and to install LHC detector improvements. After this shutdown, a further period of three years of LHC operation at 7 TeV/beam and at least the design luminosity is planned (with short technical stops around the end of each year).
- The ambitious longer-term plans include a total integrated luminosity of the order of 3000 fb^{-1} (on tape) by the end of the life of the LHC. This High-Luminosity LHC (HL-LHC) implies an annual luminosity of about $250\text{-}300 \text{ fb}^{-1}$ in the second decade

of running the LHC. The HL-LHC upgrade is also required to implement modifications to elements in the insertion regions of the machine whose performance has deteriorated due to radiation effects, such as the inner triplet quadrupole magnets. The HL-LHC upgrade is scheduled for the 2021/2022 long shutdown.

- LHC detector R&D and upgrades to make optimal use of the LHC luminosity.

This strategy is also driven by the necessity to bring the LHC injector chain and the technical and general infrastructure up to the high standards required for a world laboratory in order to ensure reliable operation of the CERN complex.

3. – Fixed-target physics

CERN has a rich fixed-target physics programme, consisting of experiments at the facilities of the Antiproton Decelerator (AD) [3], the neutron Time-of-Flight (nTOF) [4], the On-Line Isotope Mass Separator (ISOLDE) [5], the axion search experiments [6] and at the external lines of the Proton Synchrotron (PS) and Super Proton Synchrotron (SPS). Information on all fixed-target experiments can be found in the CERN Database of Experiments [7] and only a few examples are given here.

The Antiproton Decelerator is a unique machine providing low-energy antiprotons for studies of antimatter and in particular for creating anti-atoms. In 2002 the ATHENA and ATRAP experiments at the AD successfully made large numbers of anti-atoms for the first time. Currently, the AD serves three experiments that are studying antimatter: ALPHA, ASACUSA and ATRAP. A fourth experiment, ACE, also uses antiprotons, in this case to assess the suitability of antiprotons for cancer therapy. The highlight for 2010 was the first trapping of anti-hydrogen atoms by the ALPHA and ASACUSA experiments, which attracted much interest in the international media and which was cited as Breakthrough of the Year by the Physics World Magazine.

The CERN Neutrinos to Gran Sasso (CNGS) [8] programme has the aim of studying neutrino oscillations. The CNGS beam consists primarily of muon neutrinos sent from CERN to the Gran Sasso National Laboratory (LNGS), 732 km away in Italy. There, two experiments, OPERA [9] and ICARUS [10], measure the oscillation of muon neutrinos to tau neutrinos in the intervening long baseline. Recently, OPERA has observed the first tau neutrino candidate event in their detector and ICARUS has detected the first neutrino interaction in their T600 module.

The CLOUD experiment [11] is using a cloud chamber to study the possible link between cosmic-rays and cloud formation. The CLOUD experiment recorded very clean data in 2010, which allowed the first measurement of the critical cluster at the molecular level for various temperatures.

4. – The way forward and the European strategy for particle physics

The LHC will provide a first indication of any new physics at energies of the TeV scale. Many of the questions left open by the LHC and its upgrades may be addressed best by an electron-positron collider, based on technology developed by the Compact Linear Collider (CLIC) [12] and International Linear Collider (ILC) [13] Collaborations. Moreover, the option of a high-energy electron-proton collider (LHeC) [14] is being considered for the high-precision study of QCD and of high-density matter.

Great opportunities are in store at the TeV scale and a fuller understanding of Nature will come about through a clearer insight at this energy level. The discovery of the

Standard Model over the past few decades has advanced through the synergy of hadron-hadron (*e.g.*, SPS and the Tevatron), lepton-hadron (HERA) and lepton-lepton colliders (*e.g.*, LEP and SLC). Such synergies should be continued in the future and thus a strategy has been developed along these lines. An upgrade to the LHC will not only provide an increase in luminosity delivered to the experiments, but will also provide the occasion to renew the CERN accelerator complex. The ILC could be constructed now whereas further R&D is needed for CLIC. There is a drive to converge towards a single electron-positron linear collider project. The above effort on accelerators should advance in parallel with the necessary detector R&D. First results from the LHC will be decisive in indicating the direction that particle physics will take in the future.

European particle physics is founded on strong national institutes, universities and laboratories, working in conjunction with CERN. The increased globalization, concentration and scale of particle physics require a well-coordinated European strategy. This process started with the establishment of the CERN Council Strategy Group, which organized an open symposium in Orsay in 2006, a final workshop in Zeuthen in May 2006 and with the strategy document being signed unanimously by Council in July 2006 in Lisbon [15]. CERN considers experiments at the high-energy frontier to be the premier physics priority for the coming years. This direction for future colliders at CERN follows the priorities set in the strategy document. The European Strategy for Particle Physics includes several other key areas of research, all in line with the plans of CERN for the future directions. The start of the LHC physics exploitation is leading to important input for the update of the European strategy for particle physics planned for 2012.

CERN Council opened the door to greater integration in particle physics when it recently unanimously adopted the recommendations to examine the role of CERN in the light of increasing globalization in particle physics. The key points agreed by Council include a) all states shall be eligible for CERN Membership, irrespective of their geographical location; b) a new Associate Membership status is to be introduced to allow non-Member States to establish or intensify their institutional links with CERN; and c) the participation of CERN in global projects is to be enabled wherever they are sited.

5. – Future high-energy linear colliders

5.1. *The Compact Linear Collider (CLIC)*. – The conceptual lay-out of CLIC is based on using lower-energy electron beams to drive high-energy beams. The fundamental principle is that of a conventional AC transformer. The lower-energy drive beam serves as an RF source that accelerates the high-energy main beam with a high-accelerating gradient. The nominal centre-of-mass energy is up to 3 TeV, the luminosity exceeds $10^{34} \text{ cm}^{-2} \text{ s}^{-1}$, the main linear accelerator frequency is 12 GHz, the accelerating gradient is 100 MeV/m and the total length of the main linear accelerators is 48.3 km.

CLIC requires more R&D. In particular, the target accelerating gradient is considerably high and requires very aggressive performance from the accelerating structures. The nominal CLIC accelerating gradient has been exceeded in an unloaded structure with a very low breakdown probability of less than 3×10^{-7} per metre after RF conditioning for 1200 hours.

The mandate of the CLIC team is to demonstrate the feasibility of the CLIC concept by the year 2012 in a Conceptual Design Report. If this effort is successful, and if the new physics revealed by the LHC warrants, the next phase of R&D on engineering and cost issues will be launched. This would serve as the basis for a Technical Design Report and a request for project approval.

5.2. *The International Linear Collider (ILC).* – The ILC, which is an option for a linear electron-positron collider at lower energies than CLIC, is based on a more conventional design for acceleration using superconducting standing wave cavities with a nominal accelerating field of 31.5 MeV/m and a total length of 31 km at 500 GeV centre-of-mass energy and upgradable to around 1 TeV. A two-stage technical design phase during 2010-2012 is presently underway. A major contribution from Europe and from DESY to the ILC Global Design Effort is the European X-ray Laser Project XFEL at DESY. The purpose of the facility is to generate extremely brilliant and ultra-short pulses of spatially-coherent X-rays. The electron energy is brought up to 20 GeV through a superconducting linear accelerator, of length one-tenth that of the ILC superconducting linear accelerator, and conveyed to long undulators where the X-rays are generated and delivered to the experimental stations. The XFEL technical design is ready and the aim is to start operation of the XFEL in 2015.

The strategy to address key issues common to both linear colliders involves close collaboration between ILC and CLIC. Recent progress has been encouraging in this respect and common meetings between ILC and CLIC are being held regularly.

5.3. *Detector challenges.* – R&D on key components of the detector for a linear collider is mandatory and also well underway. High-precision measurements demand a new approach to the reconstruction. Particle flow, namely reconstruction of all particles, is thus proposed requiring unprecedented granularity in three dimensions of the detection channels.

6. – Key messages

Particle physics will need to adapt to the evolving situation. Facilities for high-energy physics (as for other branches of science) are becoming larger and more expensive. Funding is not increasing and the timescale for projects is becoming longer, both factors resulting in fewer facilities being realized. Moreover, many laboratories are changing their missions. All this leads to the need for more co-ordination and more collaboration on a global scale. Expertise in particle physics needs to be maintained in all regions, ensuring the long-term stability and support through-out. It will be necessary to engage all countries with particle physics communities and to integrate the communities in the developing countries. The funding agencies should in their turn provide a global view and synergies between various domains of research, such as particle physics and astroparticle physics should be exploited.

Particle physics is now entering a new era. The start-up of the LHC allows particle physics experiments at the highest collision energies. The expectations from the LHC are great, as it could provide revolutionary advances in the understanding in particle physics and a fundamental change to our view of the early Universe. Due to the location of the LHC, CERN is in a unique position to contribute to further understanding in particle physics in the long term.

Results from the LHC will guide the way in particle physics for many years. It is expected that the period of decision-making concerning the energy frontier will be in the next few years. Particle physics is now in an exciting period of accelerator planning, design, construction and running and will need intensified efforts in R&D and technical design work to enable the decisions for the future course. Global collaboration coupled with stability of support over long time scales is mandatory.

The particle physics community needs to define now the most appropriate organizational form and needs to be open and inventive in doing so, and there should be a dialogue between scientists, funding agencies and governments. It is mandatory to have accelerator laboratories in all regions as partners in accelerator development, construction, commissioning and exploitation. Furthermore, planning and execution of high-energy physics projects today require world-wide partnerships for global, regional and national projects, *i.e.* for the whole particle physics programme. The exciting times ahead should be used to establish such partnerships.

7. – Conclusions

In this paper we have provided an overview of CERN, focusing on the LHC and some aspects of the fixed-target physics programme as well as on future projects in particle physics at the energy frontier, such as high-energy linear electron-positron colliders and an electron-positron collider. In the coming years, the priorities are the full exploitation of the LHC, together with preparation for a possible luminosity upgrade and the consolidation and optimization of the CERN infrastructure and the LHC injectors. It will be necessary to keep under review the physics drivers for future proton accelerator options and it will be necessary to compare the physics opportunities offered by proton colliders with those available at a linear electron-positron collider and an electron-proton collider. The R&D associated with future colliders needs to continue in parallel.

* * *

I would like to thank the organizers for the invitation to make this contribution and for the excellent organization of the very interesting conference, which included new results from the LHC. Many thanks go to EMMANUEL TSESMELIS for his assistance in preparing this contribution.

REFERENCES

- [1] LHC Design Report, Volumes I, II and III, <http://lhc.web.cern.ch/lhc/LHC-DesignReport.html>.
- [2] <http://linac4.web.cern.ch/linac4/>.
- [3] <http://psdoc.web.cern.ch/PSDoc/acc/ad/>.
- [4] <http://pceet075.cern.ch/>.
- [5] <http://isolde.web.cern.ch/isolde/>.
- [6] <http://cast.web.cern.ch/CAST/>
<http://cdsweb.cern.ch/record/1045979>.
- [7] <http://greybook.cern.ch/>.
- [8] <http://proj-cnsgs.web.cern.ch/proj-cnsgs/>.
- [9] <http://operaweb.lngs.infn.it/>.
- [10] <http://www.nu.to.infn.it/exp/all/icarus/>.
- [11] <http://cloud.web.cern.ch/cloud/>.
- [12] <http://clic-study.org>.
- [13] <http://www.linearcollider.org/>.
- [14] <http://lhcc.web.cern.ch/lhcc>.
- [15] THE EUROPEAN STRATEGY FOR PARTICLE PHYSICS, <http://council-strategygroup.web.cern.ch/council-strategygroup/Strategy.Statement.pdf>.

SESSION IX - PERSPECTIVES

<i>Angela Fava</i>	Icarus and status of Liquid-Argon technology
<i>Christopher Naumann</i>	The (future) Cherenkov Telescope Array CTA
<i>Guy Wormser</i>	Status of the SuperB project
<i>Yasuyuki Horii</i>	Status and physics prospects of the SuperKEKB/Belle II project

Icarus and status of Liquid-Argon technology

A. FAVA for the ICARUS COLLABORATION

INFN, Sezione di Padova - Via Marzolo 8, I-35131, Padova, Italy

(ricevuto il 29 Settembre 2011; pubblicato online il 25 Gennaio 2012)

Summary. — ICARUS-T600 at the INFN-LNGS Gran Sasso Laboratory is the first underground large-mass Liquid-Argon TPC: exposed to the CNGS neutrino beam from CERN, it has been taking data since May 2010. Thanks to its excellent resolution and 3D imaging, it allows an unprecedented event visualization quality combined with a good calorimetric reconstruction and the electronic event processing. After a first commissioning phase, it has started an interesting physics program, ranging from $\nu_\mu \rightarrow \nu_\tau$ oscillation search in appearance to matter stability study, thus demonstrating the feasibility and effectiveness of the Liquid-Argon TPC technique. Furthermore, ICARUS-T600 represents a major milestone towards the realization of much larger Liquid-Argon detectors for future rare events physics. The idea to use a LAr-TPC experiment at a refurbished CERN-PS neutrino beam is presented as a possible solution to the sterile neutrino puzzle.

PACS 95.55.Vj – Neutrino, muon, pion, and other elementary particle detectors; cosmic ray detectors.

PACS 13.15.+g – Neutrino interactions.

PACS 07.05.Fb – Design of experiments.

1. – LAr TPC technique: working principle and performance

The idea of a Liquid-Argon Time Projection Chamber (LAr-TPC) was first proposed by C. Rubbia in 1977 [1] as a powerful detection technique to provide a 3D imaging of any ionizing event. Nowadays LAr-TPC can be considered the heir of the bubble chamber detector, because of the high granularity and excellent spatial resolution and calorimetric properties; but it has some interesting additional features, being continuously sensitive and self-triggering detector, and the advantage of being scalable to bigger masses.

The working principle of the LAr-TPC (fig. 1) is based on the two processes by which charged particles lose energy in liquid argon, *i.e.* scintillation and ionization. Scintillation light, emitted in the infrared at 128 nm wavelength with 5000 γ /mm yield, provides a prompt signal made by a fast (~ 6 ns) and a slow (~ 1.6 μ s) component. By means of ionization, instead, each charged particle produces ~ 6000 electrons per mm, which are drifted by a uniform and intense electric field towards several (transparent)

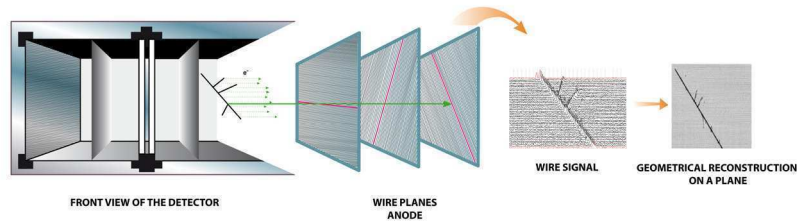


Fig. 1. – Simple scheme of the LAr-TPC working principle: from the interaction of the incoming particle with LAr to the readout system.

wire arrays where the signal is recorded in a nondestructive way, ensuring a redundant tridimensional track reconstruction. A key feature for LAr-TPC experiments is the level of purity of liquid argon, since electro-negative molecules (mainly O_2 , H_2O and CO_2) could eventually capture the drifting electrons before they reach the anode plane.

The high resolution and granularity of this detection technique (less than 1 mm^3) allows a precise reconstruction of events topology and the recognition of the particles produced in interactions in LAr. Calorimetric measurement is also possible over a very wide energy range, from MeV to several tens of GeV, allowing particle identification via dE/dx ionization signal.

For long muon tracks escaping the detector, momentum is determined exploiting their multiple scattering by a Kalman filter algorithm, *i.e.* studying the track displacements with respect to a straight line; this procedure, validated on cosmic rays stopping muons, allows a resolution $\Delta p/p$ down to 10%, depending mainly on the track length [2]. Electrons, instead, are identified with full efficiency by the characteristic electromagnetic showering, well separated from π^0 combining γ reconstruction, dE/dx signal comparison and π^0 invariant-mass measurement at the level of 10^{-3} [3]. This feature guarantees a 90% efficiency identification of the leading electron in ν_e CC interactions, while rejecting NC interactions to a negligible level.

The electromagnetic energy resolution $\sigma(E)/E = 0.03/\sqrt{E(\text{GeV})} \oplus 0.01$ is estimated in agreement with the $\pi^0 \rightarrow \gamma\gamma$ invariant mass measurements in the sub-GeV energy range. The measurement of the Michel electron spectrum from muon decays, where bremsstrahlung photons emission is taken into account [4], provided the energy resolution below critical energy ($\sim 30\text{ MeV}$), $\sigma(E)/E = 0.11/\sqrt{E(\text{MeV})} \oplus 0.02$. At higher energies the estimated resolution for hadronic showers is $\sigma(E)/E = 0.30/\sqrt{E(\text{GeV})}$. However the LAr-TPC detector allows to identify and measure, track by track, each hadron produced in interactions, through ionization and range, leading to a much better energy resolution.

2. – ICARUS-T600 experiment

The ICARUS T600 LAr-TPC detector, presently taking data in the Hall B of the INFN Gran Sasso underground National Laboratory (LNGS), is the largest Liquid-Argon TPC ever built, with the cryostats containing more than 600 tons of LAr. Its detection technique offers the possibility to collect “bubble chamber like” events to address a wide physics program: the main goal is the observation of the $\nu_\mu \rightarrow \nu_\tau$ oscillation in the CNGS neutrino beam from CERN to Gran Sasso, but this detector can also be used to study solar and atmospheric neutrino events and to improve the limit on proton decay in some background free channels.

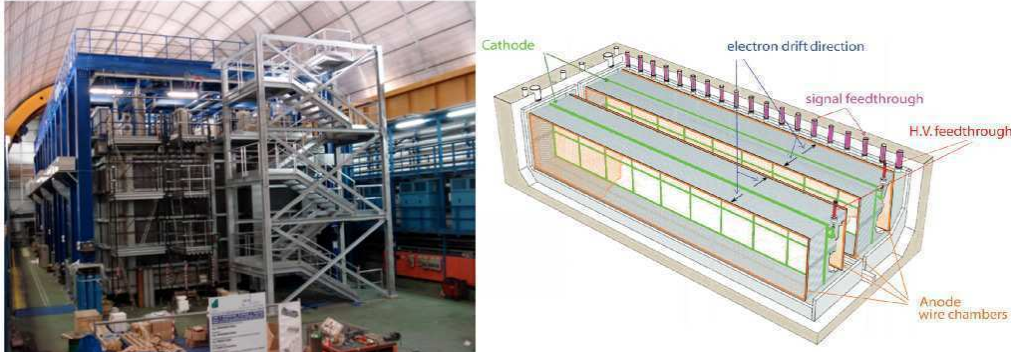


Fig. 2. – The ICARUS T600 detector in Hall B at the LNGS underground laboratory (left) and a simple sketch of the inner TPCs structure (right).

2.1. Detector overview. – The ICARUS-T600 detector [5] (see fig. 2) consists of a large cryostat split into two identical, adjacent and independent half-modules, with an overall volume of about 760 tons of ultra-pure liquid Argon at 89 K temperature. Each half-module, with internal dimensions $3.6 \times 3.9 \times 19.6 \text{ m}^3$, houses two Time Projection Chambers (TPC) separated by a common cathode. The anode of each TPC is made of three parallel wire planes, 3 mm apart, oriented at 0° and $\pm 60^\circ$ w.r.t. the horizontal direction: in all 53248 wires, with length up to 9 m, are installed. By appropriate voltage biasing, the first two planes (Induction-1 and Induction-2 planes) are transparent to drift electrons and measure them in a non-destructive way, whereas the ionization charge is finally collected by the last one (Collection plane). The application of an electric field $E_D = 500 \text{ V/cm}$, kept uniform by appropriate field shaping electrodes, ensures that the 1.5 m maximum drift distance is covered in 1 ms. The signals coming from each wire are continuously read and digitized at 25 MHz (thus 1 t-sample $\sim 400 \text{ ns}$) and recorded in multi-event circular buffers.

A prompt detection of the scintillation light is also necessary to determine the absolute time of the ionizing events. For this purpose arrays of Photo Multiplier Tubes (PMTs), operating at the LAr cryogenic temperature [6] and made sensible to VUV scintillation light ($= 128 \text{ nm}$) by applying a wavelength shifter layer (TPB), are installed behind the wire planes.

2.2. The Liquid-Argon purity. – The main technological challenge in the development of a large mass LAr-TPC is the capability to ensure and maintain a high LAr purity level. In ICARUS-T600 detector an elaborate cryogenic plant, comprehensive of Oxysorb/Hydrosorb filters, performs both gas and liquid recirculation to reduce and keep at an exceptionally low level the electro-negative impurities, especially water and oxygen, in order to obtain free electron lifetime of several milliseconds.

The electron lifetime is continuously monitored studying the attenuation of the charge signal as a function of the drift time along “clean” through-going muon tracks in Collection view, *i.e.* straight tracks without clear δ -rays and associated γ 's; the negative signal induced by the PMTs on the wires (fig. 3) marks the time at which the track entered the detector. About 50 muon tracks are sufficient to measure day-by-day the electron charge attenuation within a 3% precision, dominated by residual Landau charge fluctuations.

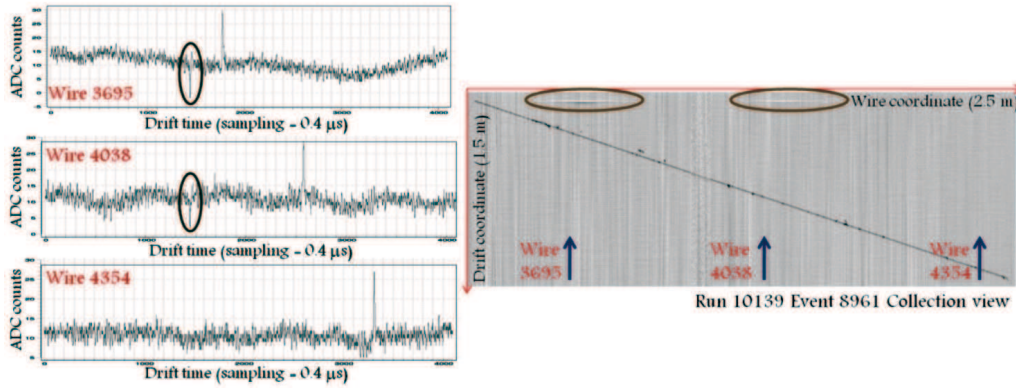


Fig. 3. – A muon track candidate for the purity measurement (right) and three different wire signals (left) in Collection view. The $t = 0$ signal, induced by PMTs on the wires, are circled.

With the liquid recirculation turned on, the LAr purity steadily increased, reaching values of free electron lifetime (τ_e) exceeding 6 ms in both half-modules after few months of operation (fig. 4). This corresponds to 0.05 ppb O_2 equivalent impurity concentration, producing a maximum 16% charge attenuation, at the maximum 1.5 m drift distance.

2.3. Physics programme. – ICARUS-T600 is the major milestone towards the realization of a multikiloton LAr-TPC detector [7], but it can also address some interesting physics in itself, thanks to its high resolution, $\sim mm^3$ granularity, information redundancy and particle identification capability [8].

The main goal is the search for $\nu_\mu \rightarrow \nu_\tau$ oscillation in the CNGS beam, *i.e.* a beam almost pure in ν_μ with average energy $E_\nu \sim 17.4$ GeV, traveling over 732 km from CERN to Gran Sasso. ICARUS-T600 looks for ν_τ appearance in the electron decay channel $\tau \rightarrow e\nu\nu$ of the τ produced by ν_τ CC interaction in LAr: in 2011–2012 run almost 3000 ν_μ CC interactions are expected ($1.1 \cdot 10^{20}$ pot), leading to 3 $\tau \rightarrow e$ events over 7 ν_e CC

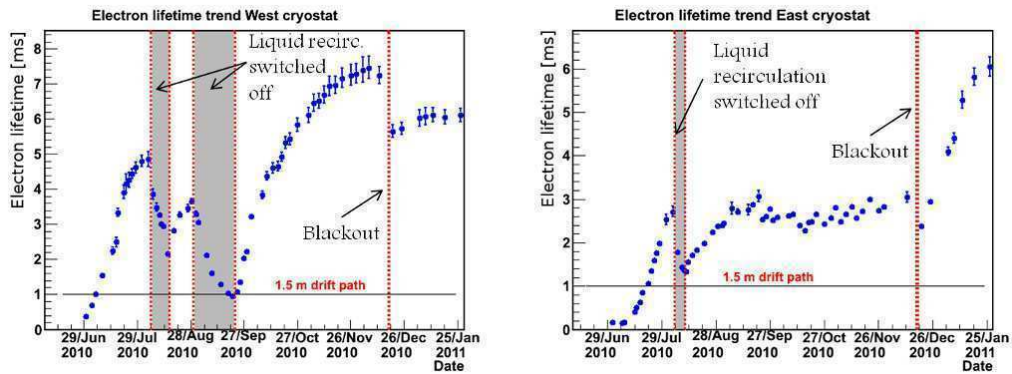


Fig. 4. – Free electron lifetime monitoring in 2010 run, for both cryostats.

background events due to the intrinsic beam contamination. The background can be rejected with kinematical selection criteria based on missing transverse momentum, thus eventually allowing to detect 1-2 ν_τ CNGS events in next 2 years. On the same beam the search for sterile neutrinos in LNSD parameter space can be also performed, looking at an excess of ν_e CC events.

ICARUS-T600 is studying also neutrinos from natural sources: ~ 80 unbiased CC atmospheric neutrino interactions are expected per year, and solar electron neutrino interactions with energy greater than 8 MeV can be detected.

Finally, thanks to the powerful background rejection and its 3×10^{32} nucleons, ICARUS-T600 can play a role in the long sought for proton decay search, in particular in interesting exotic channels not accessible to Čerenkov detectors. With an exposure of a few years its sensitivity on some “super-symmetric favored” nucleon decay channels will exceed the present known limits.

2.4. 2010 physics run. – ICARUS-T600 started its operation in May 2010, after a long R&D and installation phase, collecting right from the beginning both cosmic rays and CNGS neutrino events. The trigger system relies on the scintillation light signals, with a starting layout based, for each of the four TPC chambers, on the analog sum of signal from PMTs with a 100 photo-electron discrimination threshold. The trigger for cosmic rays exploits the coincidence of the PMTs sum signals of the two adjacent chambers in the same half-module, relying on the 50% transparency of the cathode mechanical structure: this allows an efficient reduction of the spurious signals maximizing the detection of low energy events. An overall acquisition rate of 25 mHz has been achieved well below the maximum allowed DAQ rate, resulting in about 83 cosmic events per hour. For CNGS neutrino events the proton extraction time information is also available, since an “early warning” signal is sent from CERN to LNGS 80 ms before the first proton spill extraction. Thus, accounting for the CNGS SPS cycle structure, *i.e.* two spills 50 ms apart and lasting 10.5 μ s each, a dedicated trigger strategy has been chosen for the CNGS neutrino interactions, based on the presence of the PMT signal within a $\sim 50 \mu$ s gate opened in correspondence to the predicted extraction times delayed by the neutrino time of flight (2.44 ms) from CERN to LNGS. A trigger rate of about 1 mHz is obtained, including neutrino interactions inside the detector and muons from neutrino interactions in the upstream rocks.

The CNGS run started in stable conditions on October 1st and continued till the beam shutdown, on November 22nd; in this period $5.8 \cdot 10^{18}$ pot were collected out of the $8 \cdot 10^{18}$ delivered by CERN, with a detector lifetime up to 90% since November 1st (fig. 5, top). The 78% of the whole collected sample of events, corresponding to $4.52 \cdot 10^{18}$, has been preliminarily analyzed: 94 ν_μ CC and 32 NC events have been identified by means of visual scanning into a 434 tons fiducial volume, while 6 events need for further analysis to be classified (being at edges, with μ track too short do be visually recognized); this result is in full agreement with the number of interactions predicted in the whole energy range up to 100 GeV ($(2.6 \nu_\mu \text{ CC} + 0.86 \nu \text{ NC}) \cdot 10^{-17}/\text{pot}$), to be corrected for fiducial volume and DAQ dead-time.

The analysis of the time distributions of this event sample, compared with the CNGS proton extraction time, allows to reconstruct the 10.5 μ s spill duration (fig. 5, bottom), suggesting an excellent precision in the events timestamp.

The neutrino interaction events are then fully 3D reconstructed: muons, pions, protons and kaons are identified by studying the event topology and the energy deposition per track length unit as a function of the particle range (dE/dx versus range) with

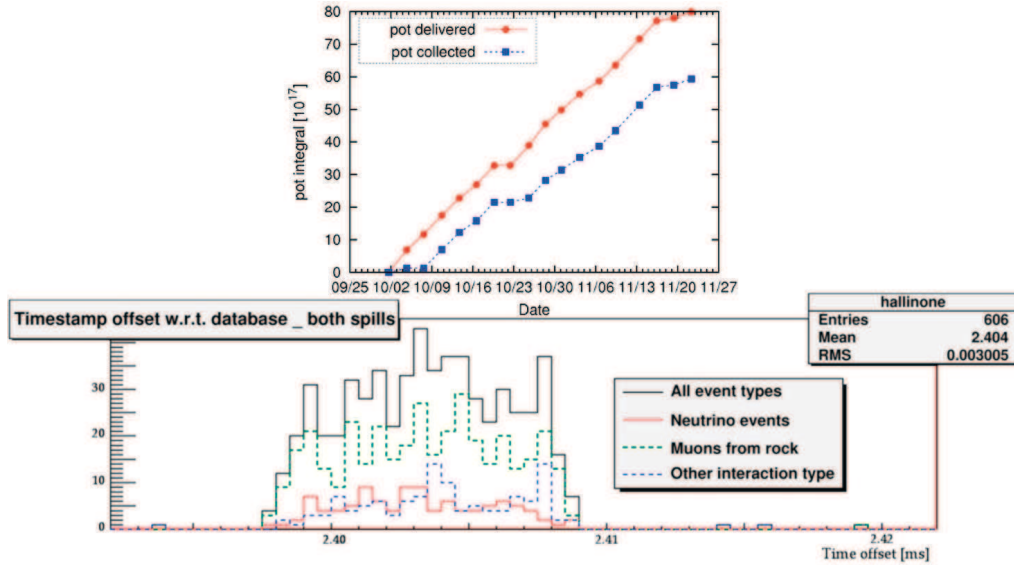


Fig. 5. – Top: number of pot collected by ICARUS-T600 in the Oct.1st–Nov.22nd run compared with the beam intensity delivered by CERN. Bottom: distribution of the difference between the neutrino interaction timestamp and the corresponding CNGS proton extraction time.

a dedicated reconstruction program based on the polygonal line algorithm [9] and on neural network. Electrons are recognized by the characteristic electromagnetic showering. Momentum of long muon tracks escaping the detector momentum is determined by multiple scattering. An example of event reconstruction is reported in fig. 6.

3. – A two LAr-TPC experiment at a CERN-PS neutrino beam to solve the sterile neutrino puzzle

Recently a sterile neutrino puzzle is growing, catching the interest of the particle physics community, due to the increasing number of experimental anomalies. On one side the $3.8 \sigma \bar{\nu}_e$ excess signal in a $\bar{\nu}_\mu$ beam first observed by LSND has been confirmed by the MiniBooNE experiment, suggesting a possible $\bar{\nu}_\mu \rightarrow \bar{\nu}_e$ oscillation with large Δm^2 ($0.2 < \Delta m^2 < 2.0 \text{ eV}^2$, $\sin^2 2\theta < 10^{-3}$) beyond the 3ν flavour oscillation scheme

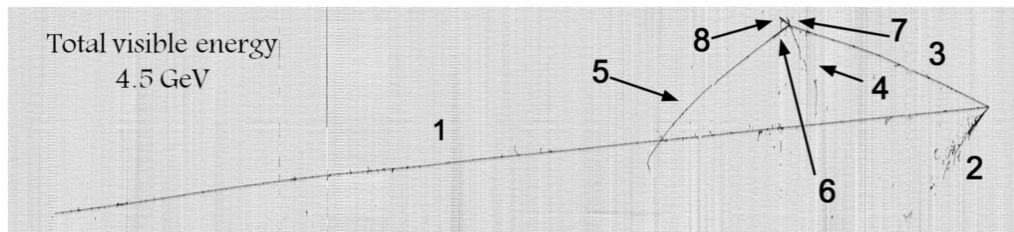


Fig. 6. – Example of a fully reconstructed CNGS ν_μ CC event, collected in 2010 run.

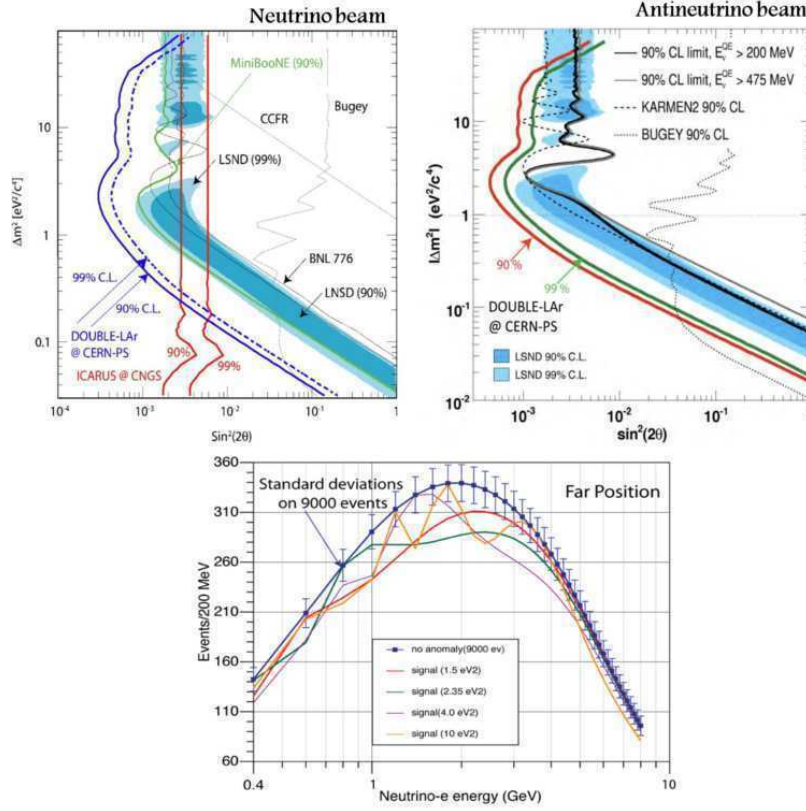


Fig. 7. – Top: sensitivity of the CERN-PS experiment to the ν_e appearance signal in 2 years (left) and 4 years (right) data taking with in neutrino and antineutrino beam mode, respectively. Bottom: sensitivity to the disappearance reactor anomaly at the far detector.

as observed in solar/atmospheric neutrino experiments. On the other side, a recent re-evaluation of the $\bar{\nu}_e$ reactor spectra ($\sim 3\%$ flux increase) brought out a $\bar{\nu}_e$ deficit at many short-baseline reactor experiments and revived the SAGE/GALLEX ν_e deficit from the MegaCurie radioactive source, hinting at a fast disappearance rate ($\Delta m^2 > 1.5 \text{ eV}^2$, $0.02 < \sin^2 2\theta < 0.23$ at 99.7% C.L.). Finally, the latest WMAP data seem not to exclude, or even to prefer, a scenario with more than 3 neutrinos.

To clarify the situation a definitive experiment is envisaged: the proposal to use 2 strictly identical LAr-TPC detectors on a refurbished neutrino beam at the CERN-PS represents a possible solution [10]. The neutrino beam would be a low energy ν_μ beam produced by 19.2 GeV protons of at least $1.25 \cdot 10^{20}$ pot/y intensity. The far detector, located at ~ 850 m from the target, could be ICARUS-T600 itself, while the near detector, at ~ 127 m, would be a ~ 150 tons active mass LAr-TPC (possibly a clone of a ICARUS-T600 semi-module with length reduced by a factor 2). The LAr-TPC technique appears the ideal detector for the study of low-energy neutrino events thanks to its very high ν_e detection efficiency combined with an extremely high rejection of associated NC background events. Moreover the usage of two identical detectors together with the very similar intrinsic ν_e spectra in the two positions, ensure the canceling out

of experimental and cross-section biases. It would thus be possible to perform the search for both $\nu_\mu \rightarrow \nu_e$ LSND appearance signal and $\nu_e \rightarrow \nu_x$ reactor disappearance anomaly, with promising sensitivity in only 2(4) years data taking in $\nu(\bar{\nu})$ mode (fig. 7).

4. – Conclusions

The ICARUS-T600 detector, installed underground at the LNGS laboratory, has started data taking during 2010 after a long R&D and installation phase. The successful assembly and operation of this LAr-TPC is the experimental proof that this technique is mature. It has demonstrated to have unique imaging capability, spatial and calorimetric resolutions and the possibility to efficiently distinguish electron from π^0 signals, thus allowing to reconstruct and identify events in a new way with respect to the other neutrino experiments.

After a short commissioning phase this experiment is ready for the 2011–2012 run, addressing a wide physics programme. The main goal is to collect events from the CNGS neutrinos beam from CERN-SPS to search for the $\nu_\mu \rightarrow \nu_\tau$ oscillation and LSND-like ν_e excess, but also to study solar and atmospheric neutrino and explore in a new way the nucleon stability in particular channels beyond the present limits.

Furthermore ICARUS-T600 is so far the major milestone towards the realization of a much more massive LAr detector. Actually the employment of this technique at a refurbished CERN-PS ν beam has been proposed after the ICARUS-T600 exploitation at LNGS to definitely solve the sterile neutrino puzzle.

REFERENCES

- [1] RUBBIA C., *The Liquid-Argon Time Projection Chamber: A new Concept for Neutrino Detector*, CERN-EP/77-08 (1977).
- [2] ANKOWSKI A. *et al.* (ICARUS COLLABORATION), *E. Phys. J. C*, **48** (2006) 667.
- [3] ANKOWSKI A. *et al.* (ICARUS COLLABORATION), *Acta Phys. Polon. B*, **41** (2010) 103.
- [4] AMORUSO S. *et al.* (ICARUS COLLABORATION), *E. Phys. J. C*, **33** (2004) 233.
- [5] AMERIO S. *et al.* (ICARUS COLLABORATION), *Nucl. Instrum. Methods A*, **527** (2004) 329.
- [6] ANKOWSKI A. *et al.* (ICARUS COLLABORATION), *Nucl. Instrum. Methods A*, **556** (2005) 146.
- [7] BAIBUSSINOV B. *et al.*, *Astropart. Phys.*, **29** (2008) 174.
- [8] ARNEODO F. *et al.* (ICARUS COLLABORATION), *ICARUS initial physics program*, LNGS P28/01, LNGS-EXP 13/89 add. 1/01.
- [9] KEGL B., KRZYZAK A., LINDER T. and ZEGER K., *IEEE Trans. Pattern Anal. Machine Intell.*, **22** (2000) 281.
- [10] BAIBUSSINOV B. *et al.*, *A new search for anomalous neutrino oscillations at the CERN-PS*, arXiv:0909.0355; RUBBIA C. (ICARUS/CNGS2-P323 COLLABORATION), *Physics Programme for ICARUS after 2012*, CERN-SPSC-2011-012, SPSC-M-773 (2011).

The (future) Cherenkov Telescope Array CTA

C. L. NAUMANN(*) on behalf of the CTA CONSORTIUM

LPNHE Paris - 4 place Jussieu, F-75252 Paris Cedex 05, France

(ricevuto il 29 Settembre 2011; pubblicato online il 25 Gennaio 2012)

Summary. — The international CTA consortium has recently entered the preparatory phase towards the construction of the next-generation Cherenkov Telescope Array CTA. This experiment will be a successor to and will benefit from the return of experience from the three major current-generation arrays H.E.S.S., MAGIC and VERITAS. It aims to significantly improve upon the sensitivity as well as the energy range of its highly successful predecessors. Construction is planned to begin by 2014, and when finished, CTA will be able to explore the highest-energy gamma-ray sky in unprecedented detail. The current status of the CTA project is presented, together with its expected performance based on Monte Carlo studies.

PACS 95.55.Ka – X- and gamma-ray telescopes and instrumentation.

PACS 95.85.Pw – γ -ray.

1. – Introduction: Cherenkov telescopes

1.1. *Physical motivation.* – The observation of photons of different wavelengths has for a long time been the most important tool in astronomy. Initially using only visible light, this effort now spans the whole wavelength band from radio waves to gamma rays. At the highest energies (above ~ 100 GeV), the Imaging Atmospheric Cherenkov telescope is currently the most successful technology for the detection and observation of both galactic and extragalactic TeV gamma-ray sources. Among others, possible extragalactic targets of interest are the nuclei of active galaxies (AGNs), including blazars and radio galaxies, and gamma-ray bursts (GRBs). Galactic source candidates in this energy range are pulsars and their wind nebulae (PWNs), supernova remnants, binary systems and microquasars. As these possible targets are not uniformly distributed over the sky, the scientific impact of a Cherenkov observatory will depend on its location: As the galactic plane is mainly confined to the Southern sky, observation of galactic sources are best carried out from Southern locations, while Northern sites are more suited to extragalactic observations.

(*) E-mail: naumann@lpnhe.in2p3.fr

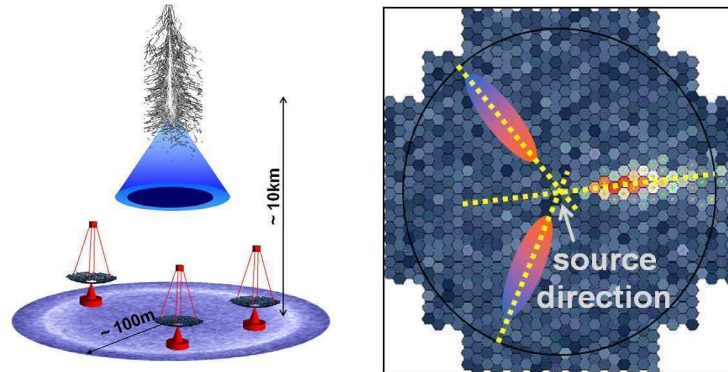


Fig. 1. – Left: Sketch of the detection technique. Not to scale. Right: Shower image in one camera, overlaid with reconstructed shower images from other cameras.

Cherenkov telescopes are also important contributors to multi-wavelength and multi-messenger campaigns, where they observe jointly with instruments operating in other wavelength domains (such as optical or X-ray) or observation channels (such as neutrinos or gravitational waves).

In addition to those astrophysical sources, Cherenkov telescopes also contribute to the search for new physics, such as dark matter or quantum gravity.

1.2. Detection technique. – To detect the decreasing fluxes of gamma rays at multi-TeV energies, very large detection volumes are necessary. In gamma Cherenkov telescopes, this is achieved by using the Earth’s atmosphere as detector (as sketched in fig. 1): The primary gamma rays interacting in the upper atmosphere are converted to electromagnetic showers, whose charged components emit Cherenkov light in a narrow cone along the shower’s direction (opening angle about 1 degree). This light can be detected several kilometres below by an array of optical telescopes equipped with very sensitive high-speed cameras. From the light distribution in these cameras, the original shower geometry can be reconstructed, giving the direction, energy and type of the primary particle. In systems with several telescopes, the individual camera images can be combined to provide a stereoscopic view of the shower, significantly improving the system’s resolution and background suppression capabilities (fig. 1, right). In order to detect the faint Cherenkov light of the atmospheric showers, the atmospherical quality at the telescope site is subject to stringent requirements, in particular high altitude, clean and dry air, and the absence of light pollution. Consequently, all current systems are generally located in remote locations such as deserts or mountain tops.

1.3. Current generation of Cherenkov telescopes. – The gamma Cherenkov technology has steadily evolved over the last few decades, with several subsequent generations of instruments, each improving in sensitivity upon its predecessors. The current generation is represented by three systems in different locations on the Earth, the H.E.S.S. array in Namibia, the MAGIC telescopes on the Canary Islands and the VERITAS system in Arizona.

- The High Energy Stereoscopic System H.E.S.S.: Phase 1 of the H.E.S.S. system comprises four telescopes, of 107 m^2 surface area each, that are operated at an altitude of 1800 m in the Khomas highland in Namibia [1].

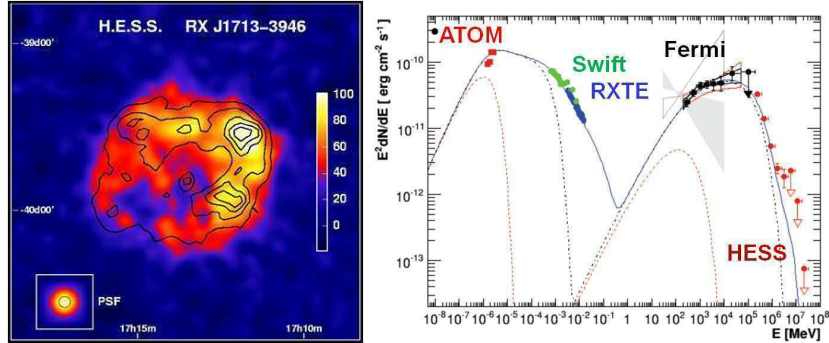


Fig. 2. – Example results for current-generation systems. Left: Extended source RX-J1713 as measured by H.E.S.S., showing clear shell-like sub-structures. Right: Multiwavelength spectrum obtained by H.E.S.S. together with several ground- and space-based telescopes, from [4].

- MAGIC I+II: Located on the top of the Canary Island of La Palma, at an altitude of 2225 metres. In contrast to the four medium-sized telescopes used in the H.E.S.S. array, the MAGIC project used in its first phase of operation a single, large telescope (234 m^2) to decrease the energy threshold at the expense of sensitivity at higher energies. This telescope has recently been joined by a second large telescope, in the MAGIC-II phase [2].
- VERITAS: The second system on the Northern hemisphere is located in Arizona, USA, at the Fred Lawrence Whipple Observatory. It consists of four 106 m^2 telescopes in an array, similar to the H.E.S.S. system [3].
- System upgrades: To increase their performance, and to cover the time until the arrival of a next-generation system, both the H.E.S.S. and the MAGIC telescope systems are currently undergoing technical upgrades: a second telescope was added to the MAGIC site in 2009 to allow stereoscopic observations, and at the H.E.S.S. site a single large telescope (23 m diameter) is currently under construction, to significantly improve the system’s sensitivity at lower energies.

1.4. *Example results.* – Due to their relatively good angular resolution and sensitivity, the current telescope systems have, for the first time, been able to provide spatially resolved images of a variety of extended objects, such as shell-type supernova remnants, and have made it possible to study their emission morphology (fig. 2, left). On the other hand, the unprecedented flux sensitivity offers the possibility to follow the temporal development of variable emitters, such as either periodic (like pulsars) or flaring sources (such as AGNs). In addition to dedicated observations of individual sources, sky surveys have also been performed. These have led to the detection of many sources with or without prior-known counterparts at other wavelength bands. Cherenkov telescopes have played an important role in recent multi-wavelength campaigns, together with satellites and ground-based telescopes operating in other wavelength bands (see, for example, fig. 2, right, for a spectrum measured in a multi-wavelength campaign where H.E.S.S. contributed in the high-energy cut-off region important for model discrimination).

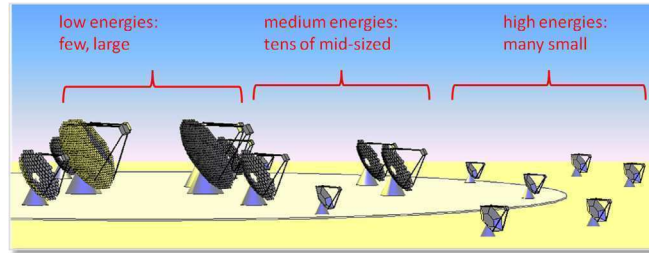


Fig. 3. – Artist’s sketch of the different telescope types.

2. – The next-generation array CTA

2.1. Motivation. – While the current-generation Cherenkov telescopes have provided many discoveries and important scientific results, it has become clear that there is a range of phenomena and source types which are just out of reach of their sensitivity, or whose detailed analysis would require significantly better statistics than currently available. This required improvement in statistical power could be achieved by improving the differential flux sensitivity by about an order of magnitude. Possible new sources within reach of such an improved system could include among others: colliding supernova winds (galactic), starburst galaxies, galaxy clusters and gamma-ray bursts (all extra-galactic). In addition, improved limits on dark matter models and quantum gravity effects—or their discovery—are also be expected.

2.2. The array. – For this purpose, the CTA consortium is working on the design of a next-generation telescope system, the Cherenkov Telescope Array (CTA). It will consist of a large number (up to 100) of telescopes of three different sizes, at two sites (one Northern, one Southern). To improve the sensitivity at the lowest energies (below ~ 100 GeV, moving the threshold down to about 20 GeV), several large-size telescopes (LST) with diameters around 24 metres will be used to collect the faint light emitted by those showers. At the highest energies (several tens to hundreds of TeV), the limiting factor is the dwindling flux of particles; to compensate for that, CTA will use a large number of sparsely distributed small-size telescopes (SST), offering a total detection area greater than a few km^2 at a reasonable cost. The workhorse of the system will be an array of medium-sized telescopes (MST), whose main goal is to improve the flux sensitivity in the mid-energy range (between 100 GeV and > 30 TeV) down to the milli-Crab level.

In accordance with the different physics goals for the Northern and Southern site, the two arrays will likely have a different combination of the three telescope sizes.

2.3. The CTA consortium. – The construction and operation of such a system of up to 100 telescope units will require substantial funding and manpower; in particular, it will not be possible without a major international collaboration. For that reason, the CTA consortium has been founded, which now comprises most of the members of the three current-generation collaborations (H.E.S.S., MAGIC and VERITAS), as well as several other groups from all around the world. The CTA project is supported by the European ESFRI⁽¹⁾ roadmap [5] and has received funding both from national agencies and from

⁽¹⁾ The *European Strategy Forum on Research Infrastructures*.

the European Union for the design study and preparatory phase. The CTA consortium received funding from ESFRI for the preparation of the construction within 3 years. In addition, it was cited as one of the top-priority near-term projects on the ASPERA⁽²⁾ 2008 roadmap [6], as well as being one of the two projects targeted by the 2009 ASPERA common call for cross-national funding.

The CTA design study was finished in 2010 [7]. Prototyping is planned for 2011 to 2013, Construction is expected to begin by 2014. Observation with the partial array will start soon after, while the full array is still under construction.

2.4. CTA as a gamma observatory. – One particularity that will set CTA apart from its predecessors is the plan to operate it - at least partially - as an open observatory, where access to the data is not limited to members of the collaboration. Instead, it is envisaged that external groups can apply for observation time on the array. The different observation proposals will be evaluated by a peer-review process, and selected proposals granted observation time. The observation itself will be performed by experts from the CTA consortium, so that no technical knowledge of the system will be required for the submitters of the proposals. Likewise, it is foreseen that a suite of analysis tools will be made available, to perform standard analyses on the data without deeper knowledge of the CTA software.

In addition to these on-demand observations, it is foreseen to produce a set of *legacy data* in the form of sky scans (either in-depth scans of the galactic plane or a full-sky survey at lower exposure).

3. – Towards the array

The design goals for the CTA array are: an improvement of the sensitivity at TeV energies by about a factor 10 with respect to current experiments with, at the same time, a lowered energy threshold (a few tens of GeV) and a larger energy reach up to and beyond a few hundred TeV. Also, to allow for higher precision studies of extended sources, a better angular resolution (below 0.1 degrees above 100 GeV and 0.05 degrees above 1 TeV⁽³⁾) and a wide field of view are required. This will for the first time make it possible to resolve the inner structures of extended objects at a level of detail up to now visible only in other wavelength bands. With the large detection area, and thus high sensitivity, more precise studies of time-dependent sources, down to sub-minute time scales, will also be feasible.

3.1. Site search. – Currently, several sites are under study for the Northern and Southern array, each of which fulfill the base requirements for the CTA observatory (altitude, clean and dry air, little light pollution). Apart from these physics requirements, there are other factors that are equally important for site selection. While for example remote sites typically offer the best observation conditions, they often have very limited available infrastructure (roads, power and data connections), making construction and operation of a large array difficult. The site should also be not prone to natural disasters (such as earthquakes or tornadoes). Current candidates include locations near the sites of the MAGIC and H.E.S.S. telescopes (the Canary Islands and the Khomas Highland

⁽²⁾ The *ASTroParticle ERANet*, a network of national government agencies responsible for coordinating and funding national research efforts in Astroparticle Physics.

⁽³⁾ 80% containment radius.

in Namibia, respectively), a site in the Baja California (Mexico) and in Arizona, as well as two sites in Argentina (El Leoncito and Salta). The task of choosing the final sites will be performed by the SITE work package in CTA.

3.2. Technology development. – Being a successor to the currently operating telescope arrays, the development for CTA will profit strongly from existing designs and experience. In particular, working designs for the medium and large size telescopes exist already in the form of the H.E.S.S., VERITAS and MAGIC telescopes, as well as proven technology for the cameras and readout hardware. The construction of a large array of those telescopes, however, will not be possible without substantial modification and optimisation of those designs, as they were not conceived for mass-production or a high level of reliability (both of which are key requirements for CTA).

The task of technology development is currently shared by several workpackages in CTA, including one responsible for electronics, for the focal-plane instrumentation, for telescope mechanics, for data transfer, for mirrors, and others. Each of these groups is lead by experts from the current telescopes, and pursues several different technological options. For example, for the cameras there exist designs based on fully analogue schemes for triggering and readout, as well as designs using fully digital cameras.

For each of the most promising technological possibilities, prototypes will be developed. The final choice of the technology to use for CTA will be made on the basis of the performance of those prototypes, as well as on the cost and reliability of the different options. As several different telescope sizes will be used on two sites, it is possible that different technological options will be chosen for the various telescope types.

3.3. Data storage and transfer. – To be able to handle the large amount of data that will be recorded by the system, substantial efforts are made for a GRID integration of CTA. This includes the development of software for easy access to the data from all participating institutions, as well as for data processing and analysis optimised for grid computing. For this purpose, the consortium has set up a CTA Virtual Observatory within the EU-funded EGEE project (Enabling Grids for E-Science). This is facilitated by the fact that several CTA member institutes are Tier 1 or 2 centres of the LHC computing grid and participate in the Cosmograd.

While the main purpose of the GRID integration will be for storage, transfer and analysis of real data from the telescope system, the GRID is already being used for the extensive Monte Carlo simulations performed for the optimisation of the array's design.

3.4. Telescope structure. – Each of the three telescope sizes envisaged for CTA will pose different kinds of challenges for its construction and operation:

For the large size telescope, the main challenge is the large size and weight of the structure. To guarantee good and stable optical properties of the telescope, it is important that the mirror does not deform under its own weight, or compensations must be done for any such deformation. This is also true for the mounting of the several-ton camera. For this reason, the use of strong, yet light, carbon-fibre based materials is evaluated. This will also help to keep the total weight low enough to allow sufficiently fast slewing of the telescopes. To compensate for any remaining deformation of the optical system, an active mirror control system could be employed, as is already the case for the MAGIC telescopes. The only design option being pursued for the LST is a single, faceted mirror, mounted on a rail support structure, such as used in H.E.S.S. and in MAGIC.

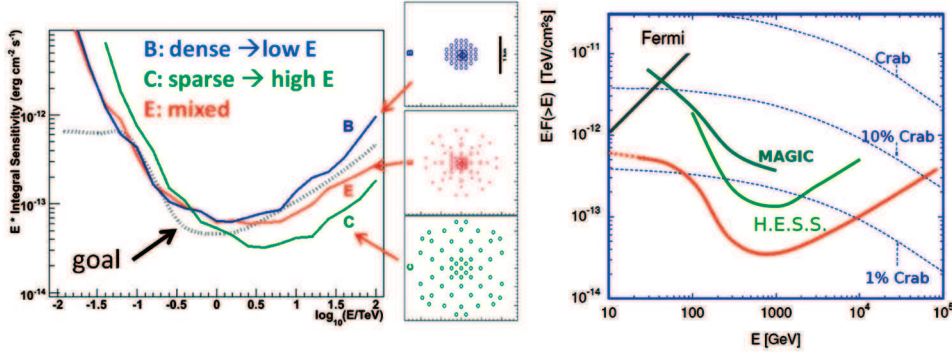


Fig. 4. – Left: Sensitivity of different sub-arrays from the simulation (B: dense, C: sparse, E: compromise), compared to the CTA design goal (dashed). Right: Expected sensitivity compared to current-generation Cherenkov telescopes and the Fermi satellite. Adapted from [7].

For the small-size telescopes, however, of which the largest number will be installed, ease of construction, a low unit cost and simplicity of operation are paramount. Currently, several possible designs for the SST are under evaluation. As a wide field of view is essential for the SSTs' operation (up to 10 degrees), a standard Davies-Cotton design [8] with a single mirror would require a relatively large, and rather expensive, camera. A possible alternative would be the use of a dual-mirror Schwarzschild-Couder design [9], which would allow for a much smaller camera, at the expense of a more complicated and costly mirror system. In this case, the camera would require smaller pixel sizes. Which of those options will be chosen for the final design will have to be determined based on feasibility and cost, and from experience with prototypes developed during the preparatory phase.

For the medium size telescopes, the technical challenges are less severe than for the LST. However, as this telescope type will serve as the workhorse of the CTA observatory, a significant number of those will have to be built, so that simplicity of design, robustness and reliability are crucial. Currently, as for the SST, several possible options are being studied, and prototypes planned. The preferred design uses of a single-mirror system, either rail- or tower-mounted.

In addition to these three telescope types, a 50 m^2 dual-mirror Schwarzschild-Couder design is being investigated.

3.5. Monte-Carlo simulations. – To evaluate the expected performance of the array, depending on the technological choices made and the different possible sites, extensive Monte Carlo studies are being undertaken. As the aim is to find the best possible combination of array geometry, telescope types and triggering and readout options for a given total cost, a large number of different options has to be simulated. For this purpose, a single “super-array” of several hundred telescopes in all sizes is simulated, and then split into appropriate sub-arrays of a comparable cost (around 80 million Euros for the Southern and 40 million for the Northern array). For these sub-arrays the system's effective area, as well as its sensitivity to different kinds of sources, can be calculated and compared (fig. 4, left). Most of this work is done with a standardised detector simulation [10] based on the CORSIKA shower propagation code [11]; for this purpose, a vast library containing on the order of 10^{11} showers has been produced. In addition to

that, several dedicated simulations have been written for in-detail study of aspects such as alternative triggering and readout schemes.

As different arrays will not perform equally well at high and low energies, the final design choice will strongly depend on the physics goals pursued with CTA and will differ for the North and South array.

4. – Expected performance

Monte Carlo simulations have shown that with current designs the CTA science goals can be reached. Depending on the array configuration used, a milli-Crab sensitivity in the focus energy region seems realistic. A comparison (fig. 4, right) shows that CTA will indeed be much more sensitive (by a factor of about ten) than current experiments, over a wider energy range. The envisaged improvement of the angular resolution will also be achievable with the preferred candidate arrays. In addition, its sensitivity at low energies should provide a good overlap with satellite experiments (such as Fermi). As the reconstruction and analysis methods are still under development, those results are likely to improve in the future.

5. – Conclusions

Having finished the Design Study phase, the CTA consortium is now in the process of converging towards a final design for the telescope array. Technology development is well under way, so that array construction should proceed as planned. Monte Carlo studies confirm that the design sensitivity is reachable. With this expected sensitivity, TeV gamma astronomy will enter a new era, passing from the stage of first detections to precision measurements. While its predecessors have been able to detect and measure of the order of a hundred objects, CTA is expected to study ten times as many at much higher precision, to literally “mass-produce physics discoveries”. In this respect, it will be on par with the most successful last-generation experiments in other wavelength bands, such as Fermi for the soft gamma rays.

* * *

We gratefully acknowledge support from the agencies and organisations listed in this page: <http://www.cta-observatory.org/?q=node/22>.

REFERENCES

- [1] *The H.E.S.S. project homepage* <http://www.mpi-hd.mpg.de/hfm/HESS/HESS.html>.
- [2] *The MAGIC project homepage* <http://www.magic.mppmu.mpg.de/>.
- [3] *The VERITAS project homepage* <http://veritas.sao.arizona.edu/>.
- [4] THE H.E.S.S. and FERMI-LAT COLLABORATIONS, *Astrophys. J. Lett.*, **696** (2009) 150.
- [5] ESFRI, ftp://ftp.cordis.europa.eu/pub/esfri/docs/esfri_roadmap_update_2008.pdf.
- [6] ASPERA, <http://www.aspera-eu.org/images/stories/files/Roadmap.pdf>.
- [7] THE CTA CONSORTIUM, arXiv:1008.3/03v2 [astro-ph.IM].
- [8] DAVIES J. M. and COTTON E. S., *J. Solar Energy Sci. Eng.*, **1** (1957) 16.
- [9] SCHWARZSCHILD K., *Untersuchungen zur geometrischen Optik II Abhandlungen der Gesellschaft der Wissenschaften in Göttingen, Bd 4*, **2** (1905) 1.
- [10] BERNLÖHR K., *Astropart. Phys.*, **30** (2008) 149.
- [11] HECK D. *et al.*, <http://www-ik.fzk.de/corsika/>.

Status of the SuperB project

G. WORMSER

LAL, Univ Paris-Sud, CNRS/IN2P3 - Orsay, France

(ricevuto il 29 Settembre 2011; pubblicato online il 25 Gennaio 2012)

Summary. — The SuperB project is a very ambitious program whose goal is to build, in the immediate vicinity of the Frascati National Laboratory, an e^+e^- collider operating in the $\Upsilon(4S)$ region with a luminosity in excess of 10^{36} Hz/cm⁻², surpassing by two orders of magnitude the present generation. Such a progress has been made possible by the new Crab Waist colliding scheme together with the design of very low emittance rings. The physics goal of this machine is to determine the structure of the new physics (NP) at the Terascale that is likely to show up at the LHC. This will be possible through a very detailed scrutiny of all NP induced indirect effects in rare (or even forbidden in the Standard Model) decays and precision measurements in the quark and lepton sectors. The project, an official element of the European HEP Strategy, has been recently approved and fully funded by the Italian government. The Nicola Cabibbo Laboratory will be created as a consortium to host and manage the project. The site has been selected and the detector collaboration is currently being formed. The first beams are expected in 2016, with a yearly integrated luminosity of 15 ab^{-1} .

PACS 11.30.Er – Charge conjugation, parity, time reversal, and other discrete symmetries.

PACS 11.30.Hv – Flavor symmetries.

PACS 13.35.-r – Decays of leptons.

PACS 29.20.-c – Accelerators.

1. – Introduction

All major discoveries concerning the flavour sector have, as strange as it may seem, been first made by indirect observations. The existence and properties of the 4th, 5th and 6th quarks have been demonstrated a few years before their direct observations through the non-observation of neutral currents reactions (GIM mechanism), CP violation in the K sector (KM hypothesis), rate of the B mixing. These indirect measurements not only provided information on the existence and mass of these quarks but also on the organisation of the quark sector in the Standard Model. The SuperB project goal is to repeat this brilliant history but now for the New Physics Beyond the Standard Model (BSM or NP). There is good hope that this approach will be very successful since we

Observable/mode	H^+	MFV	non-MFV	NP	Right-handed	LTH	SUSY				
	high $\tan\beta$			Z penguins	currents		AC	RVV2	AKM	δLL	FBMSSM
✓ $\tau \rightarrow \mu\gamma$							***	***	*	***	***
✓ $\tau \rightarrow \ell\ell\ell$						***					
✓ $B \rightarrow \tau\nu, \mu\nu$	*** (CKM)										
✓ $B \rightarrow K^{(*)}\nu\bar{\nu}$			*	***			*	*	*	*	*
✓ S in $B \rightarrow K_S^0\pi^0\gamma$					***						
✓ S in other penguin modes			*** (CKM)		***		***	***	*	***	***
✓ $A_{CP}(B \rightarrow X_s\gamma)$			***		***		*	*	*	***	***
✓ $BR(B \rightarrow X_s\gamma)$		***	*		*						
✓ $BR(B \rightarrow X_s\ell\ell)$			*	*	*						
✓ $B \rightarrow K^{(*)}\ell\ell$ (FB Asym)							*	*	*	***	***
$B_s \rightarrow \mu\mu$							***	***	***	***	***
β_s from $B_s \rightarrow J/\psi\phi$							***	***	***	*	*
✓ a_{sl}						***					
✓ Charm mixing							***	*	*	*	*
✓ CPV in Charm	**									***	

Fig. 1. – (Colour on-line) List of golden mode channels for SuperB and their relevance for various New Physics Models. The modes with a red tick are accessible to SuperB, the ones without are only available with hadron machines.

already know that strong constraints already exist when building any BSM model to avoid producing effects in the flavour sector in contradiction with current observations. The detailed understanding of the unknown physical source of these constraints and the identification of the BSM model that Nature has chosen to implement is the ultimate goal of SuperB. This task will be made easier when LHC will have discovered some new particles in the mass range between 200 GeV and 1 TeV, because this will precisely set the mass scale for the indirect effects induced by this new particle at SuperB. The requirement which was used to specify the integrated luminosity needed for the SuperB physics case is that a 3σ effect should be detected at SuperB in one of the accessible channels for a 1 TeV particle given the fact that its couplings phase should be at minimum the SM phase (its couplings cannot be lower as is explained in the so-called Minimum Flavour Violation scheme). The minimum integrated luminosity to reach this goal is 75 ab^{-1} , which can be recorded in 5 years of data taking at SuperB.

2. – SuperB physics goals

The general goal of the SuperB physics program is to understand in depth the underlying structure of the new physics (NP) beyond the Standard Model (BSM). It has been demonstrated in great detail [1] that by measuring deviations from SM expectations in a variety of different channels, one could gather very precious information about the structure of the NP. This is because all new particles with masses below 1 TeV will generate deviations from SM even if their couplings to normal quarks and leptons is minimum. Figure 1 shows the relative sensitivity of the key superB observables with respect to various theoretical frameworks. Several lessons can be learned from this figure: firstly, the golden channels lists must be quite comprehensive to be able to disentangle all the various scenarios; secondly that this golden channel list contains many modes that are only accessible to a SuperB factory. Some modes will be well measured by the LHCb experiment which will have completed its first data taking phase when SuperB will start and integrated around 5 fb^{-1} , as can be seen from fig. 2 but many others just cannot be measured at all (or not measured with the needed precision) without SuperB because they

Observable/mode	Current (now)	LHCb (2017)	SuperB (2021)	LHCb upgrade (2030?)	theory
τ Decays					
$\tau \rightarrow \mu\gamma$	Yellow	Yellow	Green	Yellow	Green
$\tau \rightarrow e\gamma$	Yellow	Yellow	Green	Yellow	Green
$B_{u,d}$ Decays					
$B \rightarrow \tau\nu, \mu\nu$	Yellow	Red	Blue	Red	Blue
$B \rightarrow K^{(*)+} \nu\bar{\nu}$	Red	Red	Green	Red	Green
S in $B \rightarrow K_S^0 \pi^0 \gamma$	Yellow	Red	Green	Red	Yellow
S in other penguin modes	Yellow	Red	Blue	Red	Yellow
$A_{CP}(B \rightarrow X_s \gamma)$	Blue	Yellow	Green	Yellow	Green
$BR(B \rightarrow X_s \gamma)$	Blue	Yellow	Green	Yellow	Green
$BR(B \rightarrow X_s \ell\ell)$	Yellow	Red	Green	Red	Green
$BR(B \rightarrow K^{(*)} \ell\ell)$	Yellow	Blue	Green	Green	Yellow
B_s Decays					
$B_s \rightarrow \mu\mu$	Red	Blue	Red	Green	Green
β_s from $B_s \rightarrow J/\psi\phi$	Red	Blue	Red	Green	Green
$B_s \rightarrow \gamma\gamma$	Red	Blue	Red	Red	Green
a_{sl}	Red	Blue	Green	Green	Green
D Decays					
mixing parameters	Yellow	Blue	Green	Green	Green
CPV	Red	Blue	Green	Green	Green
Precision EW					
$\sin^2 \theta_W$ at $\Upsilon(4S)$	Red	Blue	Green	Red	Green
$\sin^2 \theta_W$ at Z-pole	Red	Blue	Red	Green	Yellow

Fig. 2. – (Colour on-line) Sensivity of SuperB and LHCb to various physics modes. The colour code is as follows. Red: no measurement, yellow: not precise, blue: precise, green: very precise. For the theory column, the color code is: yellow: moderately clean mode, blue: clean mode but requires lattice computations, green: very clean mode

involve one or more neutrinos and are based on inclusive measurements. The rightmost column of this table indicates in green the modes which can be best predicted in the SM framework, and which therefore can be the best candidates for unambiguous deviations from SM predictions. There is a strong correlation between these clean modes and the moes who can be accessed only by SuperB. It has to be noted that the physics program of SuperB is not restricted to the study of B decays at the $\Upsilon(4S)$ resonance. The search for lepton flavour violation is one of the major physics goals and the present limits on the decay $\tau \rightarrow \mu\gamma$ and τ to three charged leptons can be improved by a factor 10, reaching BR level from 10^{-9} to a few 10^{-10} becoming quite competitive and complementary with the related search $\mu \rightarrow e\gamma$. A key asset in this search is the fact that SuperB will benefit of an 80% polarized electron beam. This will allow the search for $\tau \rightarrow \mu\gamma$ to benefit from a very significant background rejection. This extra factor will be quite important since many NP models predict BR for such very rare decays in the 10^{-9} range. The beam polarization also offers the possibility to perform search for CP violation in τ decays, and to try to perform the first measurement of τ magnetic moment. In addition to this key role in the lepton sector, the beam polarization will allow to measure the $\mu^+\mu^-$ forward-backward asymmetry at 10 GeV, adding a measurement of comparable precision to the one performed at LEP. This will again allow a good sensitivity to NP. Another feature of the SuperB physics program is to run at charm threshold with asymmetric beam energies, giving access for the first time to time-dependant CP asymmetries in the charm sector. The very high luminosity (10^{35}) foreseen at 4 GeV will allow unprecedented precision in the charm sector.

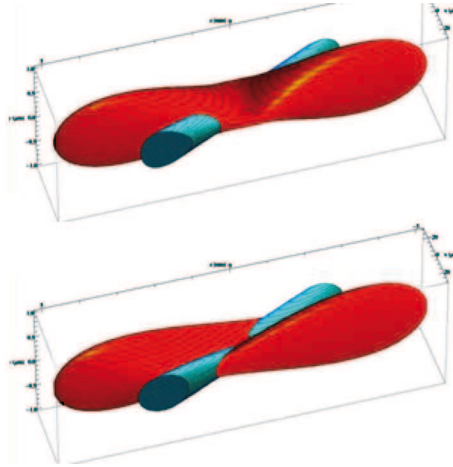


Fig. 3. – Profiles of the two colliding beams without (top) and with (bottom) Crab Waist scheme. The predistortion of the beams allow the minimum waist of one beam to be aligned with the other.

3. – The SuperB accelerator

The SuperB accelerator concept stems from a series of very innovative ideas developed in the accelerator community in the last ten years. Previous experience with PEP-II and KEKB rings showed it would be extremely difficult to increase in a significant manner the beam currents. Therefore the only solution left to reach 10^{36} luminosity is to collide nanometer size beam. This requires the production of extremely low emittance beams in the electron and positron sources and in the linac, the low emittance conservation in the rings and the design a final focus system capable to generating and putting in stable collisions 50 nm vertical size beams. This has been made possible in particular thanks to the development of all the accelerator R&D performed in the framework of the International Linear Collider project where the issues are exactly the same. One must also point out that SuperB rings have also benefitted from the development of very high-brilliance 3rd-generation light sources. But the collision of such dense beams creates, if no counter measures are taken, very large beam-beam resonances which will immediately blow up the beams. The Crab Waist scheme, which consists in the addition of two sextupoles very near the Interaction point, has been precisely invented by Pantaleo Raimondi [2] in order to suppress these beam-beam effects by predistorting the beams before the collision in order to minimize the beam-beam effects. The effect of the Crab Waist sextupoles of the beam profiles are displayed in fig. 3. The tune space, which was previously heavily populated by beam killing resonances, offers now very large resonance-free zones (see [3], p. 54). The crab waist scheme was very successfully demonstrated on the DAFNE storage ring in 2008-2009 [4]. DAFNE luminosity has been increased by a factor 3 compared to the absence of sextupoles, as predicted by the simulations. It is often asked how to compare this sizable but modest gain with the factor 100 expected between SuperB and present colliders. As mentioned above, the very large luminosity increase will be due to the very small size of the beams, going from micrometer to nanometer vertical size. The Crab waist technique is the key enabling factor, making possible the collision of such dense beams without detrimental beam-beam effects.



Fig. 4. – Layout of the SuperB accelerator on the Tor Vergata site (preliminary).

The detailed description of the accelerator design has been recently updated and is described in [3]. The preliminary layout of the accelerator on the SuperB site (see below) is indicated on fig. 4. It consists of a polarized electron source, a high-yield positron source coupled to a positron damping ring, a 7 GeV Linac and of two 1250 m rings. As a result of the partnership with the Italian Institute of Technology, SuperB rings will also be used to produce top class synchrotron beam lines. Six such beam lines are tentatively indicated on fig. 4, located on the High-Energy Ring, since 7 GeV light sources are much more difficult to find than 4 GeV ones. The brilliance of such beamlines will be higher than any other presently running machine, given the very low emittance and relatively high current (2 A) of the Super B ring (see [3], p. 144).

4. – The SuperB site

Given the revolutionary character of the SuperB machine, no present ring or tunnel in Europe is capable of hosting the SuperB project. It has been therefore necessary to explore green field scenarios. The SuperB project has issued a Site Specifications document, which has been reviewed by an international Site Committee. The specifications address the following issues: site size given the machine circumference (1250 meters), the space needed for synchrotron beam lines, and office and utility spaces, geology, vibration level, constructibility, ease of access for people and components, availability of energy and cooling, proximity of a nearby INFN structure, industrial expertise level in the vicinity. A clear desire has also been expressed towards a site allowing a shallow tunnel since the presence of several synchrotron light beamlines make this possibility extremely cost effective. Although several site candidates have been identified throughout Italy, the INFN management indicated its marked preference for a site in the immediate vicinity of the Frascati National Laboratory where the accelerator design team is located. Two sites have been finally considered, the LNF site itself where the machine has to be deeply underground given the strong slopes on this site and the nearby Tor-Vergata University site (fig. 4). The geological structure of Tor Vergata is very favorable because of its flat-

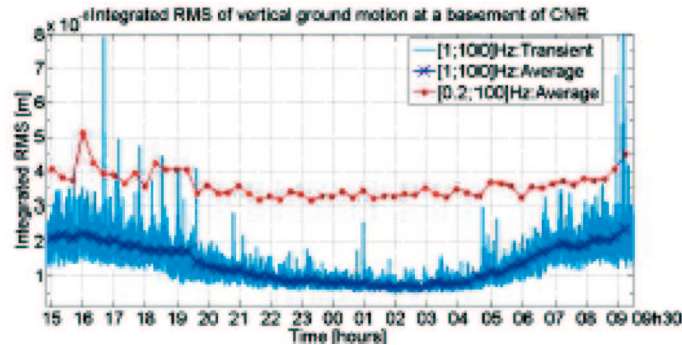


Fig. 5. – Long-term measurement of the RMS vertical displacement at a point on Tor Vergata site, close to the future SuperB Interaction Region. The RMS varies between 10 and 20 nm, when the noise is integrated between 1 and 100 Hz.

ness, uniformity and the good vibration damping properties of the pyroclastic material. A intensive vibration measurement campaign has been performed by the LAPP Annecy team and the results show that the RMS vertical motion along the ring or at the IP is between 20 and 40 nm, much below the 300 nm required, in spite of the presence of the Rome-Naples highway 100 m away (fig. 5). Given all these nice properties (the site has also been checked against archeological remains), the Tor Vergata site has been formally selected and officially proposed by the Tor Vergata University to INFN for SuperB use. INFN has endorsed this proposal and therefore, the Tor vergata site has been definitively selected as SuperB site.

5. – The SuperB detector

Since the BABAR and SuperB physics requirements are very similar, the SuperB detector can and will reuse very significant parts of the BABAR detector in order to save costs and time, and because its very good properties: magnet, iron yoke, CsI(Tl)-based crystal calorimeter, and the quartz bars of the Particle IDentification system (PID). The overall structure of the SuperB detector shown in fig. 3 is therefore very similar to BABAR. However, several main differences exist. The much higher luminosity in SuperB will force the SuperB vertex detector to be much more radiation resistant both in terms of integrated dose and instantaneous occupancy than the BABAR one. In addition, the smaller boost (0.238 instead of 0.56) in SuperB forces the first SVT layer to be closer to the beam pipe, in order to retain a comparable or better proper time resolution. The SuperB physics program calls for a better Hermeticity of the detector because of the renewed importance of the mode involving one or two neutrinos in the final state. SuperB will therefore be equipped, budget permitting, of a forward PID device and of a backward calorimeter. These two additions will increase in total by 10% superB efficiency to the very rare modes described above. The detailed description of the SuperB detector can be found in [5, 6]. It is displayed in fig. 6.

Some modifications will be implemented on the parts coming from BABAR: the flux-return will be augmented with additional absorber to increase the number of interaction lengths for muons to roughly 7λ ; the DIRC camera will be replaced by a twelvefold modular camera using multi-channel plate (MCP) photon detectors in a focusing con-

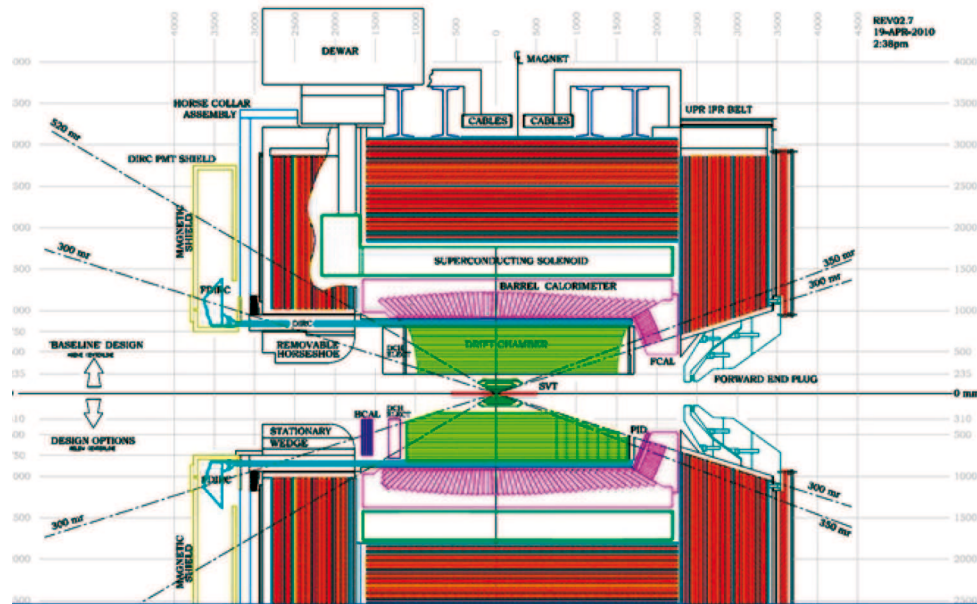


Fig. 6. – Cross section of the SuperB detector. the bottom part includes the two options considered to improve SuperB Hermiticity: a backward calorimeter and a forward PID device.

figuration using fused silica optics to reduce the impact of beam related backgrounds and improve performance; the forward EMC will feature cerium-doped LYSO (lutetium yttrium orthosilicate) crystals, which have a much shorter scintillation time constant, a lower Molière radius and better radiation hardness than the current CsI(Tl) crystals, again for reduced sensitivity to beam backgrounds and better position resolution.

The tracking detectors for SuperB will be new. To maintain sufficient proper-time difference (Δt) resolution for time-dependent CP violation measurements with the SuperB boost of $\beta\gamma = 0.24$, the vertex resolution will be improved by reducing the radius of the beam pipe, placing the innermost layer of the SVT at a radius of roughly 1.2 cm. This innermost layer of the SVT will be constructed of either silicon striplets or Monolithic Active Pixel Sensors (MAPS) or other pixelated sensors, depending on the estimated occupancy from beam-related backgrounds. Likewise, the design of the cell size and geometry of the DCH will be driven by occupancy considerations. The hermeticity of the SuperB detector, and, thus, its performance for certain physics channels will be improved by including a backwards veto-quality EMC detector comprising a lead-scintillator stack.

6. – The SuperB project status

Between December 2010 and May 2011, the SuperB project has successfully cleared all the governmental milestones to become a fully funded project. SuperB has been ranked first among a list of 14 Flagship Projects forming the core of the 2011-2013 National Research Plan in Italy. This Plan has been approved by the government and voted at both Houses of the Italian Parliament in December 2010, together with a generic funding mechanism. This resulted in an immediate release of 19 M towards the construction of SuperB. The details of the SuperB funding, and especially its pluriannual investment profile have been recently endorsed by the interministerial CIPE committee. A budget

of 50 M in 2011 has been allocated to the project. according to the INFN triennial plan indicated below. The scope of the SuperB project consisting of a HEP accelerator and a synchrotron light source, a consortium will be made within the following months between INFN, IIT (The Italian Institute of Technology, in charge of the light source sector), Tor Vergata University (mainly in charge of the civil construction on the site) and the Italian Ministry for Research. The decision has been taken to name this consortium Nicola Cabibbo laboratory. The intention of the Italian Government is to make this structure evolve into an ERIC (European Research Infrastructure Consortium) in a few years. The Nicola Cabibbo Laboratory will be very active to seek international partnerships for the construction of the SuperB accelerator.

7. – Conclusion

The launch of the SuperB project is a very rare and important event in European particle physics. Only once every 25 years or so, a large scale project is created in Europe besides the CERN projects, the last example of such an initiative being HERA in Hamburg. It is of course very clear that the concentration of European investments at CERN is essential, but the added diversity by such national or regional programs is also important and was recognized as such in the European Strategy document adopted in Lisbon in July 2006. The exceptional scientific and technological merits of the SuperB project make this new adventure particularly exciting. Recent decisive progress have been accomplished with the final approval and funding of the machine by the Italian Government, the final site selection on the campus of the Tor Vergata University, the decision to create the Nicola Cabibbo Laboratory consortium, the formal launch of the detector collaboration formation. In parallel to these major milestones, the detailed technical design of the accelerator, synchrotron light beam lines and detector is taking place, with the publication of Technical Design Reports documents in 2012. Given all this activity, machine commissioning can be expected in 2016, in a time frame a little later but comparable to the similar program, SUPERKEKB and BELLE-II, being pursued in Japan. The competition with this project will be accompanied with a very substantive collaboration, as was already the case in the PEP-II/BABAR-KEKB/BELLE lifetime and will certainly turn out to be very fruitful. Major scientific breakthroughs, in terms of a deep understanding of the organisation of the physics beyond the Standard Model, in partnership with the LHC results, can therefore be confidently expected around 2020, when SuperB will have collected its nominal integrated luminosity of 75 ab^{-1} .

REFERENCES

- [1] Physics, SuperB Collaboration, SuperB Progress Reports, INFN/AE-10/2,LAL 10-110, arXiv:1008.1541[hep-ex].
- [2] RAIMONDI P. *et al.*, Suppression of beam-beam resonances in crab waist collisions, *EPAC08-WEPP045*, July 2008, in *Conf. Proc. C08006223* (2008) WEPP045.
- [3] Accelerator, SuperB Collaboration, SuperB Progress Reports, arXiv:1009.6178(physics.acc-ph).
- [4] ZOBOV M. *et al.*, Tests of crab-waist collisions at DAFNE Phi Factory, *Phys. ReV. Lett.*, **104** (2010) 174801.
- [5] BONA M. *et al.*, SUPERB: A High-Luminosity Heavy Flavour Factory. Conceptual Design Report, arXiv:0709.0451v2 [hep-ex], INFN/AE-07/2, SLAC-R-856, LAL 07-15, also available at <http://www.pi.infn.it/SuperB/CDR>.
- [6] GRAUGES E. *et al.*, SuperB Progress Reports: Detector, SuperB Collaboration, INFN/AE-10/4,LAL 2010-115, arXiv:1007.4241[physics.ins-det].

Status and physics prospects of the SuperKEKB/Belle II project

Y. HORII(*)

*Kobayashi-Maskawa Institute, Nagoya University - Furo-cho, Chikusa-ku, Nagoya
464-8602, Japan*

(ricevuto il 29 Settembre 2011; pubblicato online il 26 Gennaio 2012)

Summary. — Measurements at the KEKB collider and the Belle detector have provided important insights into the flavor structure of elementary particles. By upgrading to the SuperKEKB collider and the Belle II detector, we expect ~ 40 times higher luminosity with improved detections in several aspects. Measurements at the upgraded apparatus will over-constrain the parameter space of the Standard Model and its extensions and will shed light on the nature of new physics. This paper describes the status and physics prospects of the SuperKEKB/Belle II project.

PACS 12.60.-i – Models beyond the standard model.

1. – Introduction

Measurements at the KEKB collider and the Belle detector have provided important insights into the flavor structure of elementary particles. Especially, the observation of the CP violation in the B meson system is a tremendous success in confirming the picture of quark flavor sector proposed by N. Cabibbo, M. Kobayashi, and T. Maskawa [1, 2]. Much larger data sample will be available at the upgraded experiment based on the SuperKEKB collider and the Belle II detector. In this experiment, we will quest for the physics beyond the Standard Model by searching for the deviations from the predictions of the Standard Model. Our high-precision studies will play a complementary role to the direct searches of new physics at the energy frontier. This paper describes the status and physics prospects of the SuperKEKB/Belle II project.

2. – SuperKEKB collider

The KEKB collider [3], which is an asymmetric-energy e^+e^- collider located at the High Energy Accelerator Research Organization (KEK) in Japan, will be upgraded to

(*) Representing the Belle II Collaboration.

TABLE I. – *Parameters of the SuperKEKB and KEKB colliders. We show the design values for the SuperKEKB and the achieved values for the KEKB. The two values separated by a slash indicate the values for e^+ and e^- beams, respectively. The vertical beta function at IP, the beam current, and the beam-beam parameter are the crucial parameters related to the peak luminosity.*

Parameters	SuperKEKB	KEKB
Peak luminosity ($10^{35} \text{ cm}^{-2} \text{ s}^{-1}$)	8.0	0.21
Vertical beta function at IP (mm)	0.27/0.30	5.9/5.9
Beam current (A)	3.6/2.6	1.64/1.19
Beam-beam parameter	0.09/0.08	0.129/0.090
Energy (GeV)	4.0/7.0	3.5/8.0

the SuperKEKB collider [4]. The design value of the center-of-mass energy for the SuperKEKB is on the $\Upsilon(4S)$ resonance, which is the same as the KEKB. On the other hand, the design luminosity for the SuperKEKB is $8.0 \times 10^{35} \text{ cm}^{-2} \text{ s}^{-1}$, which is about 40 times larger than the current world record of $2.1 \times 10^{34} \text{ cm}^{-2} \text{ s}^{-1}$ achieved by the KEKB.

Table I shows the parameters for the SuperKEKB and the KEKB. The upgrade is based on the “nano-beam” scheme, which was first proposed for the INFN SuperB project [5]. We reduce the vertical beta function at the interaction point (IP) by a factor of about 1/20, providing a luminosity improvement by a factor of about 20. To introduce this improvement, we set the final focus magnets closer to the IP by changing the beam-crossing angle from 22 mrad to 83 mrad. The other improvement of the luminosity is available from the increase of the beam current by a factor of about 2. The design value of the beam-beam parameter, which is additional crucial parameter related to the luminosity, is at a similar level as at the KEKB.

To mitigate the emittance growth due to intra-beam scattering and the short beam lifetime due to the Touschek effect, the beam energy for the e^+ beam is changed from 3.5 GeV to 4.0 GeV. The beam energy for the e^- beam is changed from 8.0 GeV to 7.0 GeV accordingly. The effects of the reduction of the beam-energy asymmetry on the vertex measurements are found to be safely small.

Figure 1 shows the milestone for the integrated and peak luminosities for the SuperKEKB project. After the shutdown for about four years, the commissioning will start in the second half of Japanese fiscal year 2014. The integrated luminosity will reach 50 ab^{-1} in 2020–2021, which is 50 times larger than the data size for the KEKB.

3. – Belle II detector

The Belle detector [6] will be upgraded to the Belle II detector [4]. The main concern for the Belle II detector is the higher-background environment. For evaluating the effects of the backgrounds on the detector performance, we extrapolate the results of the operations of KEKB and Belle by accounting for scaling for each component of backgrounds. The Belle II detector is designed to cope with this estimation conservatively, and has better performance than the Belle detector in some aspects.

Figure 2 shows the dimensions of the Belle II and Belle detectors. Just outside the beam pipe, the four-layer silicon strip detector is replaced by a two-layer silicon pixel detector based on the DEPFET (DEpleted P-channel Field Effect Transistor) and a four-layer silicon strip detector. The impact parameter resolution in the beam direction is



Fig. 1. – Milestone for the SupreKEKB project.

improved mainly due to the pixel detector by a factor of around two for momenta below 1 GeV. The efficiency for reconstructing K_S decays to two charged pions is improved due to the larger outer radius of the strip detector. The central tracking chamber has smaller drift cells, larger outer radius, and fast readout electronics, providing higher performance

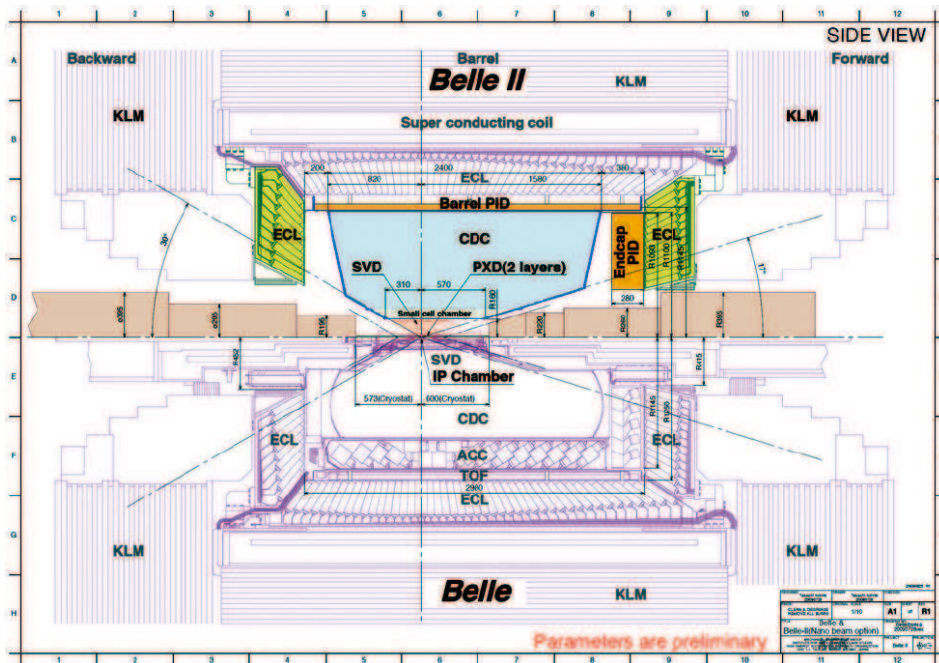


Fig. 2. – Dimensions for the Belle II (top half) and Belle (bottom half) detectors.

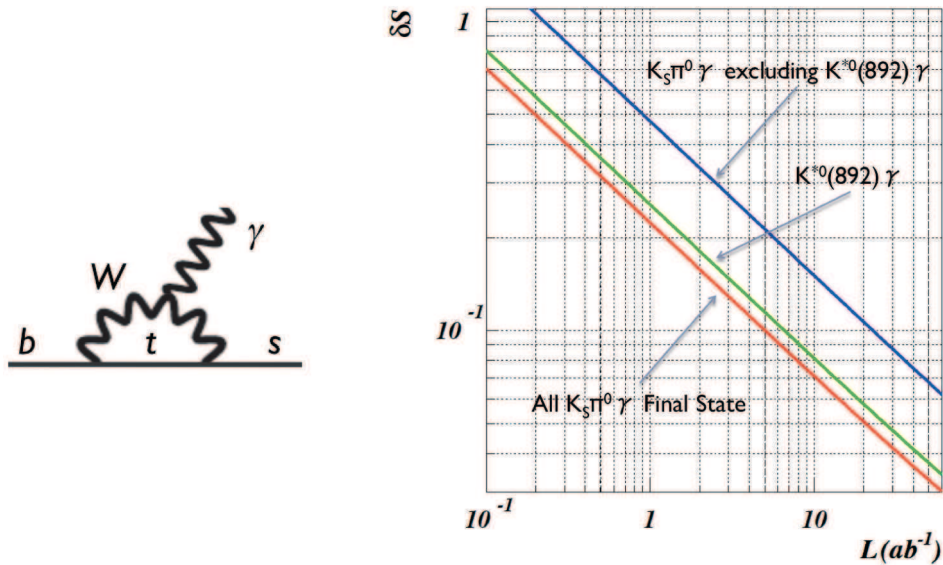


Fig. 3. – Feynman diagram for the process $b \rightarrow s\gamma$ (left). Expected precision for the mixing-induced asymmetries for $B \rightarrow K^{*0}(892)\gamma$ (green), other $K_S\pi^0\gamma$ (blue), and all $K_S\pi^0\gamma$ final state (red) as a function of integrated luminosity.

against the background. The particle identification system based on Cherenkov-threshold detectors is replaced by a lower-material system based on Cherenkov-imaging detectors. The probability of misidentifying a charged pion (kaon) as a charged kaon (pion) is improved from $\sim 10\%$ to $\sim 1\%$ for the kaon (pion) selection efficiency of $\sim 95\%$ at the kinematic limit of the momentum $\sim 4\text{ GeV}/c$. The electronics of the electromagnetic calorimeter employs a wave-form-sampling type to cope with the longer time constant $\sim 1\mu\text{s}$ of the CsI(Tl) crystals, reducing accidental overlaps by a factor of around seven. For the crystals in the endcaps, we have options for shorter time constant, *e.g.*, pure CsI, for further upgrade. For the K_L and muon detector in the endcaps, we use scintillators instrumented with silicon photomultiplier tubes as the alternative to the resistive plate chambers to reduce the dead time. The new data acquisition system meets the requirements of a considerably higher event rates.

4. – Physics at SuperKEKB/Belle II

At the SuperKEKB collider and the Belle II detector, we have broad physics program in the fields of heavy-flavor physics [7]. Our measurements will over-constrain the parameter space of the Standard Model and its extensions and will shed light on the nature of new physics by exploiting the correlations among various observables. Compared to the LHCb experiment, we have advantages in the studies of the decay modes with neutral particles in the final state. From the large number of planned measurements, several important examples on $B \rightarrow X_s\gamma$, $B \rightarrow \tau\bar{\nu}$, $B \rightarrow K\pi$, and lepton-flavor-violating τ decays are explained in the following sections.

4.1. $B \rightarrow X_s\gamma$. – The decay $B \rightarrow X_s\gamma$ occurs at one-loop order as shown in fig. 3 (left), but still has a relatively large branching fraction of order 10^{-4} due to the top

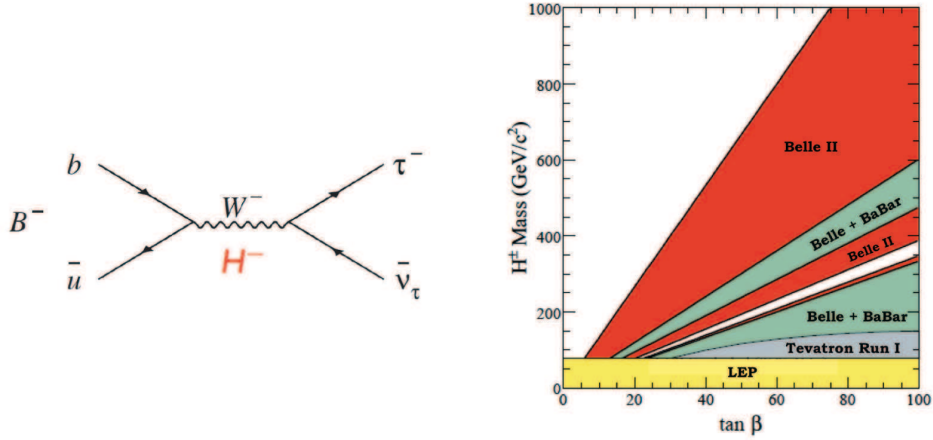


Fig. 4. – Feynman diagram for the decay $B^- \rightarrow \tau^- \bar{\nu}_\tau$ (left). 5σ -discovery region for Belle II at an integrated luminosity of 50 ab^{-1} (red) and current exclusion regions at 95% CL by B factories (green), Tevatron (gray), and LEP (yellow) on the plane of m_H and $\tan \beta$ (right).

quark contribution. Since heavy virtual particles can be exchanged in the loop, the decay $B \rightarrow X_s \gamma$ is sensitive to new physics effects. The branching fraction, the direct CP asymmetry, and the mixing-induced CP asymmetries for the exclusive final states such as $K_S \pi^0 \gamma$ could provide important information for investigating the new physics.

Various related measurements have been obtained at the Belle experiment [8-11]. The measurement of the branching fraction is challenging even at the Belle II experiment, since accurate background subtraction is needed. We expect the precision of 6% at an integrated luminosity of 50 ab^{-1} , which is at the same level as the precision of the theoretical predictions. The magnitude of the direct CP -violating asymmetry predicted by the Standard Model is below 1%, while it could be above 10% in many extensions of the Standard Model [12,13]. Expected sensitivity for the CP asymmetry at 50 ab^{-1} is 0.5% including systematic uncertainties. The magnitude of the mixing-induced CP -violating parameter, usually denoted by S , of the final state $K_S \pi^0 \gamma$ is estimated to be 0.04 in the Standard Model, while it could be as high as 0.5 in left-right symmetric models [14]. As shown in fig. 3 (right), expected sensitivity at 50 ab^{-1} is 0.03.

4.2. $B \rightarrow \tau \bar{\nu}$. – Many models beyond the Standard Model include more than one Higgs doublet. In the so-called type II of two Higgs doublet models, one doublet yields masses of u -type quarks and the other doublet yields masses of d -type quarks. In these models, the decay rate of $B \rightarrow \tau \bar{\nu}$ is affected by the charged Higgs contribution as shown in fig. 4 (left). The branching fraction could be modified from the value of the Standard Model by a factor $(1 - m_B^2 \tan^2 \beta / m_H^2)^2$, where m_B and m_H are the masses of charged B meson and charged Higgs boson, respectively, and $\tan \beta$ is the ratio of the vacuum expectation values of the two Higgs doublets [15].

The first evidence for the decay $B \rightarrow \tau \bar{\nu}$ has been obtained by the Belle experiment by using the residual energy detected in the electromagnetic calorimeter after removing the accompanying B meson and charged decay products of the tau lepton [16]. The accompanying B meson is reconstructed in hadronic modes. The Belle has also obtained the evidence by a reconstruction of the accompanying B meson in semileptonic modes [17].

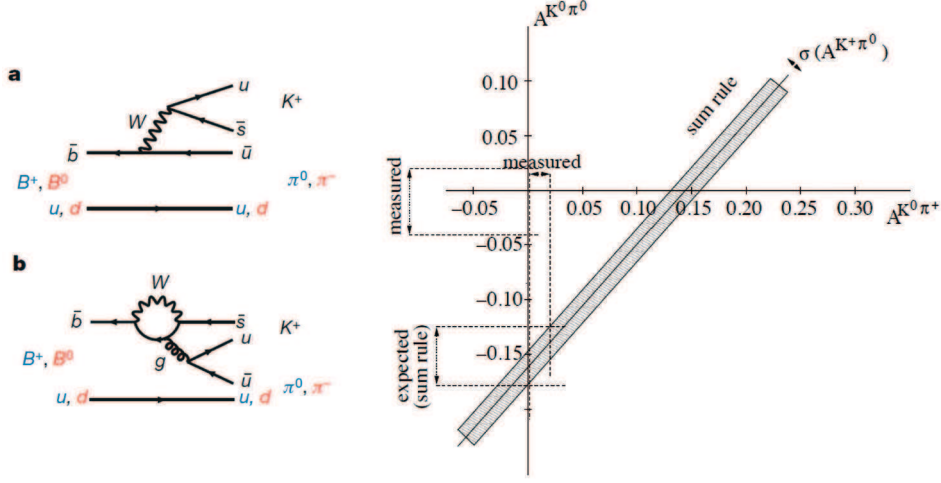


Fig. 5. – Feynman diagrams for the decays $B^+ \rightarrow K^+\pi^0$ and $B^0 \rightarrow K^+\pi^-$ (left). The sum rule for $B \rightarrow K\pi$ with the current central values of the observables and the accuracies expected for an integrated luminosity of 50 ab^{-1} (right).

The world average of the branching fraction is obtained to be $(1.64 \pm 0.34) \times 10^{-4}$ [18], while the global fit assuming the Standard Model without including direct measurements shows $(0.763_{-0.061}^{+0.114}) \times 10^{-4}$ [19]. The measurements at Belle II will provide important information for the tension between the direct measurement and the Standard-Model expectation. In fig. 4 (right), we show expected $(m_H, \tan\beta)$ region of 5σ discovery for the charged Higgs boson at Belle II with an integrated luminosity of 50 ab^{-1} , as well as the current exclusion regions at 95% CL. The Belle II will cover large regions in the space of m_H and $\tan\beta$.

4.3. $B \rightarrow K\pi$. – The decays $B \rightarrow K\pi$ proceed through a tree diagram and a loop penguin diagram as depicted in fig. 5 (left). Since the tree process is suppressed by the small CKM matrix element $|V_{ub}|$, the contribution of the loop penguin process is of similar magnitude. The interference of the two decays could lead to direct CP violation, which is equivalent to non-zero value of $A^f = [\Gamma(\bar{B} \rightarrow f) - \Gamma(B \rightarrow f)]/[\Gamma(\bar{B} \rightarrow f) + \Gamma(B \rightarrow f)]$ with f indicating a certain final state. As suggested in the diagrams in fig. 5 (left), the processes for the neutral and the charged B meson decays are similar, and thus the difference $\Delta A = A^{K^+\pi^0} - A^{K^+\pi^-}$ should be close to zero.

The measurement by the Belle experiment has shown a significant difference $\Delta A = 0.164 \pm 0.035 \pm 0.013$ [20]. The difference could be due to the neglected diagrams contributing to the charged B meson decays only, for which the theoretical uncertainties are still large, or due to some unknown effect by the new physics. To make a test free of theoretical uncertainties, one can use a sum rule for various measurements in $B \rightarrow K\pi$ including $B \rightarrow K^0\pi^+$ and $B \rightarrow K^0\pi^0$ [21]. Figure 5 (right) shows the accuracies expected for Belle II at an integrated luminosity of 50 ab^{-1} . The Belle II will provide a good environment even for the all neutral final state $K^0\pi^0$, which is the most critical mode for the test using the sum rule.

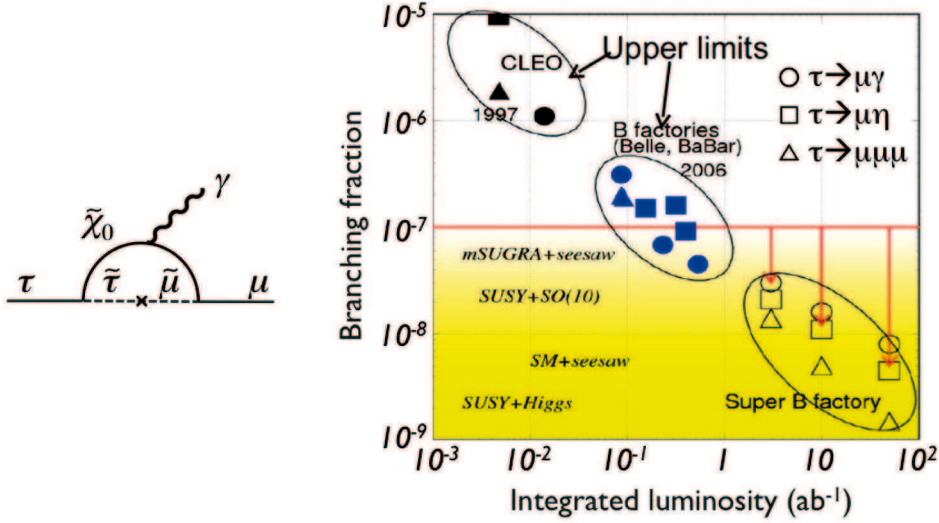


Fig. 6. – Example of the Feynman diagrams for $\tau \rightarrow \mu \gamma$ (left). History and anticipated upper limits on the branching fractions for $\tau \rightarrow \mu \gamma$, $\tau \rightarrow \mu \eta$, and $\tau \rightarrow \mu \mu \mu$ decays as a function of the integrated luminosity (right).

4.4. *Lepton-flavor-violating τ decays.* – The lepton-flavor-violating decays could be induced by the oscillations of massive neutrinos. However, such processes are highly suppressed and far beyond the experimental reach. The situation is quite different if there is new physics including a particle that has mass of the order of the weak scale and couples to leptons. Example of the diagrams is shown for the decay $\tau \rightarrow \mu \gamma$ in fig. 6 (left).

Upper limits on various lepton-flavor-violating τ decays have been obtained by the Belle experiment [22-24]. As shown for the decays $\tau \rightarrow \mu \gamma$, $\tau \rightarrow \mu \eta$, and $\tau \rightarrow \mu \mu \mu$ in fig. 6 (right), the current limits are typically on the order of 10^{-8} . At the Belle II experiment, the anticipations for the upper limits will reach the order of 10^{-9} , by which large parameter spaces of many new physics models will be covered [25-27]. Since there are strong correlations between the expected rates of various channels, the measurements for different modes could provide important information to identify the underlying mechanism.

5. – Conclusion

At the SuperKEKB collider and the Belle II detector, we expect ~ 40 times higher luminosity and improved detection in several aspects. Of the broad physics program in the fields of heavy flavor physics, examples for $B \rightarrow X_s \gamma$, $B \rightarrow \tau \bar{\nu}$, $B \rightarrow K \pi$, and lepton-flavor-violating τ decays are shown. We will provide important information for investigating the physics beyond the Standard Model.

REFERENCES

- [1] CABIBBO N., *Phys. Rev. Lett.*, **10** (1963) 531.
- [2] KOBAYASHI M. and MASKAWA T., *Prog. Theor. Phys.*, **49** (1973) 652.
- [3] KUROKAWA S. and KIKUTANI E., *Nucl. Instrum. Methods Phys. Res. A*, **499** (2003) 1, and other papers included in this volume.

- [4] ABE T. *et al.*, KEK Report 2010–1, arXiv:1011.0352 (2010).
- [5] RAIMONDI P., *Talk given at the 2nd SuperB workshop, Frascati, 2006*, <http://www.lnf.infn.it/conference/superb06/talks/raimondi1.ppt>.
- [6] ABASHIAN A. *et al.* (BELLE COLLABORATION), *Nucl. Instrum. Methods Phys. Res. A*, **479** (2002) 117.
- [7] AKEROYD A. G. *et al.*, KEK Report 2009–12, arXiv:1002.5012 (2010).
- [8] ABE K. *et al.* (BELLE COLLABORATION), *Phys. Lett. B*, **511** (2001) 151.
- [9] NISHIDA S. *et al.* (BELLE COLLABORATION), *Phys. Rev. Lett.*, **93** (2004) 031803.
- [10] NAKAO M. *et al.* (BELLE COLLABORATION), *Phys. Rev. D*, **69** (2004) 112001.
- [11] USHIRODA Y. *et al.* (BELLE COLLABORATION), *Phys. Rev. D*, **74** (2006) 111104(R).
- [12] KAGAN A. L. and NEUBERT M., *Phys. Rev. D*, **58** (1998) 094012.
- [13] BAEK S. and KO P., *Phys. Rev. Lett.*, **83** (1999) 488.
- [14] ATWOOD D., GRONAU M. and SONI A., *Phys. Rev. Lett.*, **79** (1997) 185.
- [15] HOU W.-S., *Phys. Rev. D*, **48** (1993) 2342.
- [16] IKADO K. *et al.* (BELLE COLLABORATION), *Phys. Rev. Lett.*, **97** (2006) 251802.
- [17] HARA K. *et al.* (BELLE COLLABORATION), *Phys. Rev. D*, **82** (2010) 071101(R).
- [18] ASNER D. *et al.* (HEAVY FLAVOR AVERAGING GROUP), arXiv:1010.1589, and online update for rare decays at <http://www.slac.stanford.edu/xorg/hfag>.
- [19] CHARLES J. *et al.* (CKMFITTER GROUP), *Eur. Phys. J. C*, **41** (2005) 1, and online update at: <http://ckmfitter.in2p3.fr>.
- [20] LIN S.-W. *et al.* (BELLE COLLABORATION), *Nature*, **452** (2008) 332.
- [21] GRONAU M., *Phys. Lett. B*, **627** (2005) 82.
- [22] MIYAZAKI Y. *et al.* (BELLE COLLABORATION), *Phys. Lett. B*, **648** (2007) 341.
- [23] HAYASAKA K. *et al.* (BELLE COLLABORATION), *Phys. Lett. B*, **666** (2008) 16.
- [24] HAYASAKA K. *et al.* (BELLE COLLABORATION), *Phys. Lett. B*, **687** (2010) 139.
- [25] ELLIS J. R., HISANO J., RAIDAL M. and SHIMIZU Y., *Phys. Rev. D*, **66** (2002) 115013.
- [26] BRIGNOLE A. and ROSSI A., *Nucl. Phys. B*, **701** (2004) 3.
- [27] CALIBBI L., FACCIA A., MASIERO A. and VEMPATI S. K., *Phys. Rev. D*, **74** (2006) 116002.

PARTICIPANTS

ALTARELLI Guido	Università di Roma Tre	Rome	Italy
AMALDI Ugo	CERN	Geneva	Switzerland
AMIDEI Dante	Michigan University	Ann Arbor	USA
ARNOWITT Richard	Texas A&M University	College Station	USA
ARTUSO Marina	Syracuse University	Syracuse	USA
ASHERY Daniel	Tel Aviv University	Tel Aviv	Israel
BALDINI Luca	INFN-Pisa	Pisa	Italy
BALEV Spasimir	CERN	Geneva	Switzerland
BARBIERI Riccardo	SNS-Pisa	Pisa	Italy
BARONCELLI Antonio	Università di Roma Tre	Rome	Italy
BELLETTINI Giorgio	Università di Pisa/INFN	Pisa	Italy
BERNARDINI Paolo	Università del Salento	Lecce	Italy
BERTOLINI Enzo	Aosta		Italy
BILOKON Halina	INFN-LNF	Frascati	Italy
BLANKENBURG Gianluca	Università Roma Tre	Rome	Italy
BOHACOVA Martina	Institute of Physics	Prague	Czech Republic
BRAMON Albert	Universitat Autònoma de Barcelona	Barcelona	Spain
BUEHLER Marc	University of Virginia	Charlottesville	USA
CACCIANIGA Barbara	Università di Milano	Milano	Italy
CACCIARI Matteo	LPTHE Paris	Paris	France
CAPONE Antonio	Università di Roma I	Rome	Italy
CASELLE Michele	Università di Torino	Torino	Italy
CHANG Ming-Chuan	Fu Jen Catholic University	New Taipei	Taiwan
CHENG Chih-hsiang	Caltech	Pasadena	USA
CHIARELLI Giorgio	INFN-Pisa	Pisa	Italy
CIUCHINI Marco	Università di Roma Tre	Roma	Italy
COLANGELO Gilberto	ITP Bern	Bern	Switzerland
CORCORAN Marjorie	Rice University	Houston	USA
CRIVELLIN Andreas	ITP Bern	Bern	Switzerland
DAINESE Andrea	INFN-Padova	Padova	Italy
DAR Arnon	Technion	Haifa	Israel
DAWSON Jaime	Lab. Astroparticule Cosmologie	Paris	France
DE GRUTTOLA Michele	University of Florida	Gainesville	USA
DE RÚJULA Alvaro	CERN	Geneva	Switzerland
DEDOVICH Dmitry	JINR	Dubna	Russia
DEGRASSI Giuseppe	Università di Roma Tre	Roma	Italy
DELL'AGNELLO Simone	INFN-LNF	Frascati	Italy
DI VITA Stefano	Università di Roma Tre and INFN	Roma	Italy
DJOUADI Abdelhak	Université Paris-Sud	Orsay	France
DOBBS Sean	Northwestern University	Evanston	USA
DOKUCHAEV Vyacheslav	Russian Academy of Sciences	Moscow	Russia
DOLGOV Alexander	INFN-Ferrara	Ferrara	Italy
ERMOLAEV Boris	Ioffe Physico-Technical Institute	St. Petersburg	Russia

FAVA Angela	INFN-Padova	Padova	Italy
FERRARI Ruggero	Università di Milano	Milano	Italy
IORE Salvatore	Università di Roma I/INFN-Roma I	Roma	Italy
FLÄCHER Henning	University of Rochester	Rochester	USA
FREDERIX Rikkert	University of Zurich	Zurich	Switzerland
GALBIATI Cristiano	Princeton University	Princeton	USA
GALLI Luca	INFN-Pisa	Pisa	Italy
GASTALDI Ugo	INFN-LNL	Legnaro	Italy
GERVINO Gianpiero	INFN-Torino	Torino	Italy
GIUNTI Carlo	INFN-Torino	Torino	Italy
GOLUTVIN Andrey	Imperial College/ITEP/CERN	Crozet	France
GRECO Mario	Università di Roma Tre	Roma	Italy
GROSS Eilam	Weizmann Institute of Science	Rehovot	Israel
HESKETH Gavin	University College	London	UK
HEUER Rolf	CERN	Geneva	Switzerland
HORII Yasuyuki	Tohoku University	Sendai	Japan
ISIDORI Gino	LNF-INFN	Frascati	Italy
KAZAKOV Dmitry	JINR(Dubna)/ITEP(Moscow)	Dubna	Russia
KOHN Fabian	Universitaet Goettingen	Goettingen	Germany
KOSE Umut	INFN-Padova	Padova	Italy
KOTZINIAN Aram	Università di Torino/INFN-Torino	Torino	Italy
LANFRANCHI Gaia	INFN-LNF	Frascati	Italy
LAVAGNO Andrea	Politecnico di Torino	Torino	Italy
LEE Hyun Su	University of Chicago	Chicago	USA
LEONE Sandra	INFN-Pisa	Pisa	Italy
LEROY Olivier	CPPM CNRS/IN2P3/Aix-Marseille Univ.	Marseille	France
LEWIS Jonathan	Fermilab	Batavia	USA
LISS Tony	University of Illinois	Urbana	USA
LOPEZ HONOREZ Laura	Université Libre de Bruxelles	Bruxelles	Belgium
LUBICZ Vittorio	Università di Roma Tre	Roma	Italy
MANGANO Michelangelo	CERN	Geneva	Switzerland
MASIERO Antonio	Università di Padova/INFN-Padova	Padova	Italy
MASO Eduard	Universidad Autónoma de Barcelona	Barcelona	Spain
MEONI Evelin	Universidad Autónoma de Barcelona	Barcelona	Spain
MINAMINO Akihiro	Kyoto University	Kyoto	Japan
MIZUK Roman	ITEP	Moscow	Russia
MONACELLI Piero	LNGS- Università di L'Aquila	L'Aquila	Italy
NARDECCHIA Marco	CP3-Origins	Odense	Denmark
NATOLI Paolo	Università di Ferrara	Ferrara	Italy
NAUMANN Christopher	LPNHE	Paris	France
NOVIKOV Victor	ITEP	Moscow	Russia
PARADISI Paride	TUM	Munich	Germany
PERUZZI Ida	INFN-LNF	Frascati	Italy
PICCOLO Marcello	INFN-LNF	Frascati	Italy
PUNZI Giovanni	INFN-Pisa	Pisa	Italy
REDI Michele	CERN/INFN	Geneva	Switzerland
ROJO Juan	Università di Milano	Milano	Italy
ROLLI Simona	Tufts University	Batavia	USA
ROTH Itamar	Weizmann Institue of Science	Rehovot	Israel
SAHBAEI Sajjad	Lund University	Lund	Sweden
SAMTLEBEN Dorothea	NIKHEF	Amsterdam	Netherlands
SANDSTRÖM Rikard	Max-Planck-Institut	Munich	Germany

SCOMPARIN Enrico	INFN-Torino	Torino	Italy
SEKARIC Jadranka	University of Kansas	Naperville	USA
SINITSYNA Vera Georgievna	P. N. Lebedev Physical Institute	Moscow	Russia
SINITSYNA Vera Yurievna	P. N. Lebedev Physical Institute	Moscow	Russia
SOKOLOWSKA Dorota	University of Warsaw	Warsaw	Poland
SPAGNOLO Paolo	INFN-Pisa	Pisa	Italy
SRIVASTAVA Yogendra	INFN-Perugia	Perugia	Italy
STEINBERG Peter	Brookhaven National Laboratory	Upton	USA
STONE Sheldon	Syracuse University	Syracuse	USA
STRAUB David	SNS-Pisa	Pisa	Italy
STUDENIKIN Alexander	Moscow State University	Moscow	Russia
TARANTINO Cecilia	Università di Roma Tre	Rome	Italy
TIBALDO Luigi	INFN-Padova	Padova	Italy
TISSERAND Vincent	LAPP	Annecy	France
TONELLI Guido	Università di Pisa	Pisa	Italy
TONER Ruth	University of Cambridge	Cambridge	UK
TOUKAN Khaled	SESAME	Allan	Jordan
TRUC Fabio	Aosta		Italy
TURINI Nicola	Università di Siena/INFN-Pisa	Siena	Italy
TURNER Michael	Kavli Institute for Cosmological Physics	Chicago	USA
VIVES Francesc	IFAE	Barcelona	Spain
VORWERK Volker	IFAE Barcelona	Barcelona	Spain
VYSOTSKY Mikhail	ITEP	Moscow	Russia
WORMSER Guy	LAL	Orsay	France
YAO WeiMing	LBNL	Berkeley	USA

FRASCATI PHYSICS SERIES VOLUMES

Volume I

Heavy Quarks at Fixed Target
Eds.: S. Bianco and F.L. Fabbri
Frascati, May 31–June 2, 1993
ISBN 88-86409-00-1

Volume II – Special Issue

*Les Rencontres de Physique de la Vallée d'Aoste –
Results and Perspectives in Particle Physics*
Ed.: M. Greco
La Thuile, Aosta Valley, March 5–11, 1995
ISBN 88-86409-03-6

Volume III

Heavy Quarks at Fixed Target
Ed.: B. Cox
University of Virginia, Charlottesville
October 7–10, 1994, 11
ISBN 88-86409-04-4

Volume IV

Workshop on Physics and Detectors for DAΦNE
Eds.: R. Baldini, F. Bossi, G. Capon, G. Pancheri
Frascati, April 4–7, 1995
ISBN 88-86409-05-2

Volume V – Special Issue

*Les Rencontres de Physique de la Vallée d'Aoste –
Results and Perspectives in Particle Physics*
Ed.: M. Greco
La Thuile, Aosta Valley, March 3–9, 1996
ISBN 88-86409-07-9

Volume VI

Calorimetry in High Energy Physics
Eds.: A. Antonelli, S. Bianco, A. Calcaterra, F.L. Fabbri
Frascati, June 8–14, 1996
ISBN 88-86409-10-9

Volume VII

Heavy Quarks at Fixed Target
Ed.: L. Köpke
Rhinefels Castle, St. Goar, October 3–6, 1996
ISBN 88-86409-11-7

Volume VIII

ADONE a milestone on the particle way

Ed.: V. Valente 1997

ISBN 88-86409-12-5

Volume IX – Special Issue

*Les Rencontres de Physique de la Vallée d'Aoste –
Results and Perspectives in Particle Physics*

Ed.: M. Greco

La Thuile, Aosta Valley, March 2–8, 1997

ISBN 88-86409-13-3

Volume X

Advanced ICFA Beam Dynamics

Workshop on Beam Dynamics Issue for e^+e^- Factories

Eds.: L. Palumbo, G. Vignola

Frascati, October 20–25, 1997

ISBN 88-86409-14-1

Volume XI

*Proceedings of the XVIII International Conference on
Physics in Collision*

Eds.: S. Bianco, A. Calcaterra, P. De Simone, F. L. Fabbri

Frascati, June 17–19, 1998

ISBN 88-86409-15-X

Volume XII – Special Issue

*Les Rencontres de Physique de la Vallée d'Aoste –
Results and Perspectives in Particle Physics*

Ed.: M. Greco

La Thuile, Aosta Valley, March 1–7, 1998

ISBN 88-86409-16-8

Volume XIII

Bruno Touschek and the Birth of e^+e^-

Ed.: G. Isidori

Frascati, 16 November, 1998

ISBN 88-86409-17-6

Volume XIV – Special Issue

*Les Rencontres de Physique de la Vallée d'Aoste –
Results and Perspectives in Particle Physics*

Ed.: M. Greco

La Thuile, Aosta Valley, February 28–March 6, 1999

ISBN 88-86409-18-4

Volume XV

Workshop on Hadron Spectroscopy

Eds.: T. Bressani, A. Feliciello, A. Filippi

Frascati, March 8-2 1999

ISBN 88-86409-19-2

Volume XVI

Physics and Detectors for DAΦNE

Eds.: S. Bianco, F. Bossi, G. Capon, F.L. Fabbri,

P. Gianotti, G. Isidori, F. Murtas

Frascati, November 16-19, 1999

ISBN 88-86409-21-4

Volume XVII – Special Issue

*Les Rencontres de Physique de la Vallée d'Aoste –
Results and Perspectives in Particle Physics*

Ed.: M. Greco

La Thuile, Aosta Valley, February 27-March 4, 2000

ISBN 88-86409-23-0

Volume XVIII

LNf Spring School

Ed.: G. Panzeri

Frascati, 15-20 May, 2000

ISBN 88-86409-24-9

Volume XIX

XX Physics in Collision

Ed.: G. Barreira

Lisbon June 29-July 1st. 2000

ISBN 88-86409-25-7

Volume XX

Heavy Quarks at Fixed Target

Eds.: I. Bediaga, J. Miranda, A. Reis

Rio de Janeiro, Brasil, October 9-12, 2000

ISBN 88-86409-26-5

Volume XXI

*IX International Conference on Calorimetry in
High Energy Physics*

Eds.: B. Aubert, J. Colas, P. Nédélec, L. Poggioli

Ancey Le Vieux Cedex, France, October 9-14, 2000

ISBN 88-86409-27-3

Volume XXII – Special Issue

*Les Rencontres de Physique de la Vallée d'Aoste –
Results and Perspectives in Particle Physics*

Ed.: M. Greco

La Thuile, Aosta Valley, March 4–10, 2001

ISBN 88–86409–28–1

Volume XXIII

XXI Physics in Collision

Ed.: Soo-Bong Kim

Seoul, Korea, June 28–30, 2001

ISBN 88–86409–30–3

Volume XXIV

*International School of Space Science – 2001 Course on:
Astroparticle and Gamma-ray Physics in Space*

Eds.: A. Morselli, P. Picozza

L'Aquila, Italy, August 30–September 7, 2000

ISBN 88–86409–31–1

Volume XXV

*TRDs for the 3rd Millennium Workshop on
Advanced Transition Radiation Detectors for
Accelerator and Space Applications*

Eds. N. Giglietto, P. Spinelli

Bari, Italy, September 20–23, 2001

ISBN 88–86409–32–X

Volume XXVI

KAON 2001 International Conference on CP Violation

Eds.: F. Costantini, G. Isidori, M. Sozzi

Pisa Italy, June 12th–17th, 2001

ISBN 88–86409–33–8

Volume XXVII – Special Issue

*Les Rencontres de Physique de la Vallée d'Aoste –
Results and Perspectives in Particle Physics*

Ed.: M. Greco

La Thuile, Aosta Valley, March 3–9, 2002

ISBN 88–86409–34–6

Volume XXVIII

Heavy Quarks at Leptons 2002

Eds.: G. Cataldi, F. Grancagnolo, R. Perrino, S. Spagnolo

Vietri sul mare (Italy), May 27th–June 1st, 2002

ISBN 88–86409–35–4

Volume XXIX

*Workshop on Radiation Dosimetry: Basic Technologies,
Medical Applications, Environmental Applications*

Ed.: A. Zanini

Rome, Italy, February 56, 2002

ISBN 88-86409-36-2

Volume XXIX – Suppl.

*Workshop on Radiation Dosimetry: Basic Technologies,
Medical Applications, Environmental Applications*

Ed.: A. Zanini

Rome, Italy, February 56, 2002

ISBN 88-86409-36-2

Volume XXX – Special Issue

*Les Rencontres de Physique de la Vallée d'Aoste –
Results and Perspectives in Particle Physics*

Ed.: M. Greco

La Thuile, Aosta Valley, March 9–15, 2003

ISBN 88-86409-39-9

Volume XXXI

*Frontier Science 2002 – Charm, Beauty and CP,
First International Workshop on Frontier Science*

Eds.: L. Benussi, R. de Sangro, F.L. Fabbri, P. Valente

Frascati, October 6–11, 2002

ISBN 88-86409-37-0

Volume XXXII

19th International Conference on x-ray and Inner-Shell Processes

Eds.: A. Bianconi, A. Marcelli, N.L. Saini

Università di Roma La Sapienza June 24–28, 2002

ISBN 88-86409-39-07

Volume XXXIII

Bruno Touschek Memorial Lectures

Ed.: M. Greco, G. Pancheri

Frascati, May 11, 1987

ISBN 88-86409-40-0

Volume XXXIV – Special Issue

*Les Rencontres de Physique de la Vallée d'Aoste –
Results and Perspectives in Particle Physics*

Ed.: M. Greco

La Thuile, Aosta Valley, February 29 – March 6, 2004

ISBN 88-86409-42-7

Volume XXXV

Heavy Quarks And Leptons 2004

Ed.: A. López

San Juan, Puerto Rico, 1–5 June 2004

ISBN 88–86409–43–5

Volume XXXVI

DAΦNE 2004: Physics At Meson Factories

Eds.: F. Anulli, M. Bertani, G. Capon, C. Curceanu–Petrascu,

F.L. Fabbri, S. Miscetti

Frascati, June 7–11, 2004

ISBN 88–86409–53–2

Volume XXXVII

Frontier Science 2004, Physics and Astrophysics in Space

Eds.: A. Morselli, P. Picozza, M. Ricci

Frascati, 14–19 June, 2004

ISBN 88–86409–52–4

Volume XXXVIII

II Workshop Italiano sulla Fisica di ATLAS e CMS

Eds.: Gianpaolo Carlino and Pierluigi Paolucci

Napoli, October 13 – 15, 2004

ISBN 88–86409–44–3

Volume XXXIX – Special Issue

Les Rencontres de Physique de la Vallée d’Aoste –

Results and Perspectives in Particle Physics

Ed.: M. Greco

La Thuile, Aosta Valley, February 27 – March 5, 2005

ISBN 88–86409–45–1

Volume XL

Frontier Science 2005 – New Frontiers in Subnuclear Physics

Eds.: A. Pullia, M. Paganoni

Milano, September 12 - 17, 2005

ISBN 88–86409–46–X

Volume XLI

Discoveries in Flavour Physics at e^+e^- Colliders

Eds.: L. Benussi, S. Bianco, C. Bloise, R. de Sangro, C. Gatti,

G. Isidori, M. Martini, F. Mescia, S. Miscetti

Frascati, February 28th - March 3rd, 2006

ISBN 88–86409–51–6

Volume XLII – Special Issue

*Les Rencontres de Physique de la Vallée d'Aoste –
Results and Perspectives in Particle Physics*

Ed.: M. Greco

La Thuile, Aosta Valley, March 5 - March 11, 2006

ISBN 88-86409-47-8

Volume XLIII – Special Issue

*Neutral Kaon Interferometry at A Phi-Factory: from Quantum Mechanics
to Quantum Gravity*

Ed.: A. Di Domenico

Frascati, March 24th 2006

ISBN 978 88-86409-50-8

Volume XLIV – Special Issue

*Les Rencontres de Physique de la Vallée d'Aoste –
Results and Perspectives in Particle Physics*

Ed.: M. Greco

La Thuile, Aosta Valley, February 28th - March 5th, 2007

ISBN 978 88-86409-49-4

Volume XLV Frontier Science – Science with the New Generation

High Energy Gamma-ray Experiments

Eds.: A. Lionetto, A. Morselli

Villa Mondragone, Monteporzio, Italy, June 18 -20, 2007

ISBN 978 88-86409-54-0

Volume XLVI

XII International Conference on Hadron Spectroscopy

Eds.: L. Benussi, M. Bertani, S. Bianco, C. Bloise, R. de Sangro, P. de Simone,
P. di Nezza, P. Giannotti, S. Giovanella, M.P. Lombardo, S. Pacetti

Laboratori Nazionali di Frascati, October 7-13, 2007

ISBN 978-88-86409-55-1

Volume XLVII – Special Issue

*Les Rencontres de Physique de la Vallée d'Aoste –
Results and Perspectives in Particle Physics*

Ed.: M. Greco

La Thuile, Aosta Valley, February 24th - March 1st, 2008

ISBN 978-88-86409-56-8

Volume XLVIII

*The XIV LNF Spring School “Bruno Touschek” in Nuclear,
Subnuclear and Astroparticle Physics
Young Researchers Workshop “Physics Challenges in the LHC Era”*
Ed.: E. Nardi

Laboratori Nazionali di Frascati, Frascati, May 11th - May 14th, 2009
ISBN 978-88-86409-57-5

Volume XLIX

Workshop on Monte Carlo’s, Physics and Simulations at the LHC
Ed. P. Nason

Laboratori Nazionali di Frascati, Frascati, February 27-28, 2006
ISBN 978-88-86409-58-2

Volume L – Special Issue

*Les Rencontres de Physique de la Vallée d’Aoste –
Results and Perspectives in Particle Physics*
Ed.: M. Greco

La Thuile, Aosta Valley, March 1st - 7th, 2009
ISBN 978-88-7438-053-4

Volume LI

*Second Young Researchers Workshop
“Physics Challenges in the LHC Era” 2010*

Ed. E. Nardi
Laboratori Nazionali di Frascati, Frascati, May 10-13, 2010
ISBN 978-88-86409-60-5

Volume LII – Special Issue

*Les Rencontres de Physique de la Vallée d’Aoste –
Results and Perspectives in Particle Physics*
Ed.: M. Greco

La Thuile, Aosta Valley, February 28th - March 6th, 2010
ISBN 978-88-7438-060-2

FRASCATI PHYSICS SERIES VOLUMES – Italian Collection

Collana: Scienza Aperta Vol. I (2006) - Comunicare Fisica 2005

Atti 1° Convegno “Comunicare Fisica e altre Scienze”,

Frascati, 24-27 Ottobre, 2005

Eds: Franco L. Fabbri, Piero Patteri

ISBN 88-86-409-48-6

Finito di stampare
nel mese di Febbraio 2012
Compositori Industrie Grafiche - Bologna